343038

PB 260 843

REPORT NO.
EERC 76-2
MAY 1976

EARTHQUAKE ENGINEERING RESEARCH CENTER

EXPERIMENTAL AND ANALYTICAL STUDIES ON THE HYSTERETIC BEHAVIOR OF REINFORCED CONCRETE RECTANGULAR AND T-BEAMS

by
SHAO-YEH M. MA
VITELMO V. BERTERO
EGOR P. POPOV

Report to Sponsor:
National Science Foundation

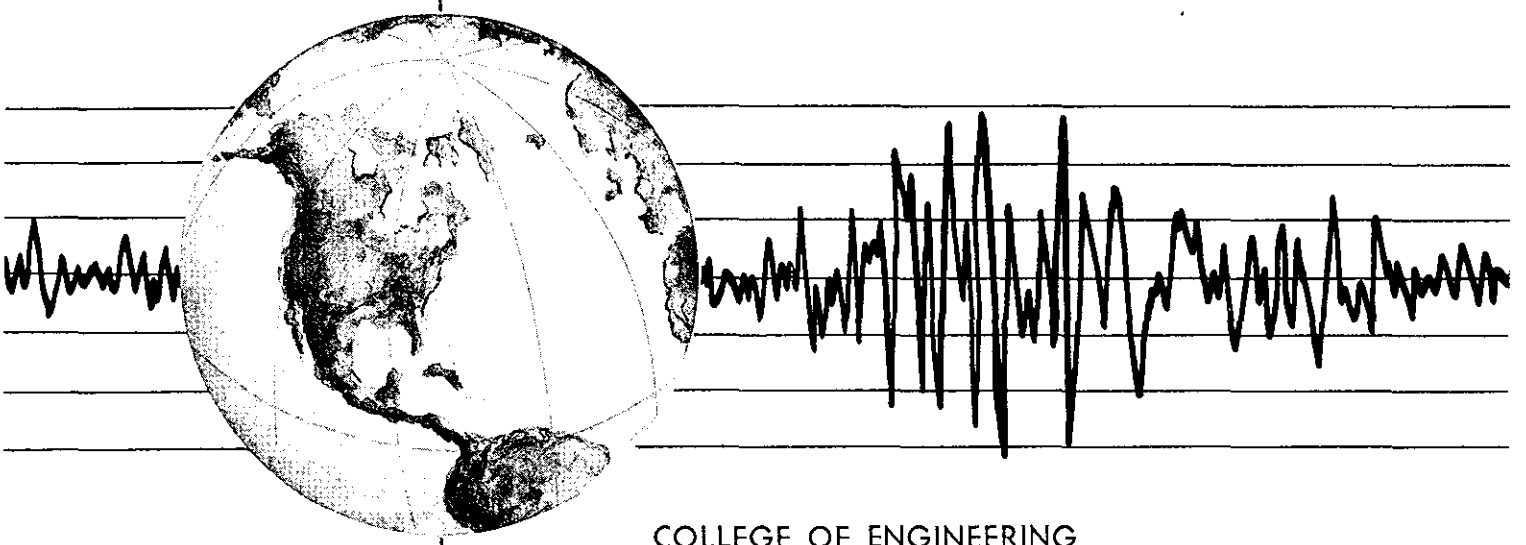

COLLEGE OF ENGINEERING
UNIVERSITY OF CALIFORNIA · Berkeley, California

REPRODUCED BY

EXPERIMENTAL AND ANALYTICAL STUDIES ON HYSTERETIC BEHAVIOR OF REINFORCED CONCRETE RECTANGULAR AND T-BEAMS

by

SHAO-YEH M. MA
Senior Engineer
Bechtel Power Corp., San Francisco

and

VITELMO V. BERTERO and EGOR P. POPOV
Professors of Civil Engineering
University of California, Berkeley

A report on research sponsored by
the National Science Foundation

Report No. EERC 76-2
Earthquake Engineering Research Center
College of Engineering
University of California
Berkeley, California

May 1976

ABSTRACT

This report describes an experimental and analytical study program carried out for investigating the inelastic behavior of critical regions that may develop in a beam near its connection with the column of a reinforced concrete ductile moment-resisting space frame when subjected to severe earthquake excitations.

In the experimental program, a series of nine cantilever beams, representing half-scale models of the lower story girder of a 20-story ductile moment-resisting reinforced concrete office building, was designed according to present seismic codes. These beams were designed in order to study the effects of (1) the slab by testing T-beams with a top slab width equal to the effective width specified by the ACI (318-71) Code; (2) relative amounts of top and bottom reinforcement by varying the amounts of bottom reinforcement; (3) supplementary ties by providing hairpin ties around main bars not restrained by the corners of stirrup ties; (4) the high shear force by varying the shear-span ratio; and (5) loading histories by testing some beams under loading reversals inducing a gradually increased deformation, and others, under monotonic loadings to large deformations in one direction. Detailed descriptions of the specimens, testing procedures, experimental data, and results obtained are presented. The significance of the experimental results in relation to the seismic design of the reinforced concrete critical region is also discussed.

The results showed that the main effect of the slab in T-beams was an increase in the moment capacity of the beam in one direction due to the slab reinforcement at the top. By increasing the bottom steel area up to the same amount as that of the top steel area, the energy dissipation capacity of the beam increased between 27 and 54 percent; by providing supplementary ties for supporting main compression bars not restrained by the corner of ties, the energy dissipation capacity increased about 74 percent. The development of a maximum nominal shear stress, v_{max}, of $5.3\sqrt{f'_c}$ in the shortest beam reduces the energy dissipation by one half when compared with a similar, but longer, beam with a v_{max} of $3.5\sqrt{f'_c}$. Greater amounts of energy can be dissipated by subjecting the beam to loading reversals of gradually increasing amplitude than by subjecting it directly to loading reversals of large amplitude. The inelastic rotations obtained from the test beams reached peak values in each sense ranging from 0.026 rad. to 0.058 rad. These values are considered to be adequate for the efficient design of a ductile moment-resisting frame member.

Photogrammetric measurements proved to be useful for studying the deformation patterns of the beam critical region subjected to reversed loadings. These measurements were especially useful for detecting shear deformation occurring along large cracks that were forming across the entire beam section.

Analytical studies were carried out to gain a better understanding of the flexure, shear, and bond resisting mechanisms in the reinforced concrete critical regions subjected to inelastic load reversals. The analytical studies include: (1) a moment-curvature analysis, based on a hysteretic stress-strain model of reinforcing steel developed from tests on machined main reinforcing bars; (2) a finite element analysis of stress transfer (bond) between concrete and anchored main bars; and (3) an analysis of the shear force-shear deformation hysteretic relationship of reinforced concrete beams considering aggregate interlocking, stirrup-tie resistance, dowel action of main bars, and shear resistance offered by uncracked concrete. The significance of these studies is discussed and summarized.

ACKNOWLEDGMENTS

This report is based on the dissertation written for the degree of Doctor of Philosophy in Engineering by Dr. Ma under the guidance of Professors Popov and Bertero.

The research reported herein, part of a continuing investigation on the hysteretic behavior of structural members and systems, was sponsored by the National Science Foundation under grant numbers GI-36387, sub-project 0-21887, and AEN-07732 A02, sub-project 0-21987. The use of computer facilities was provided by the computer center of the University of California, Berkeley. The tests were conducted in the Structural Engineering Laboratory of the Department of Civil Engineering, University of California, Berkeley. The assistance of the machine shop and the electronics shop personnel is acknowledged with gratitude.

The authors would like to express their deepest appreciation to Dr. H. Krawinkler for his assistance in the initial phase of the experimental program, and students S. Viwathanatepa, D. Soleimani, T. Y. Wang, P. Wong, T. Whitford, and D. Clyde for their willingness to assist with tests and some of the data reduction.

Lastly, the authors are grateful to Mr. R. Altenhofen, Head of the Photogrammetric Division of the U.S. Geological Survey in Menlo Park, California, and to Professor F. Moffit who arranged for the use of the photogrammetric facilities.

TABLE OF CONTENTS

	Page
ABSTRACT	i
ACKNOWLEDGEMENTS	ii
TABLE OF CONTENTS	iii
LIST OF NOTATIONS	ix
1. INTRODUCTION	1
1.1 General	1
1.2 Review of Past Studies	1
1.2.1 Experimental Studies	1
1.2.2 Analytical Studies	3
1.3 Objectives and Scope	4
1.3.1 Experimental Studies	4
1.3.2 Analytical Studies	4
2. EXPERIMENTAL PROGRAM	7
2.1 Selection and Design of Test Specimens	7
2.1.1 Longitudinal Reinforcements	7
2.1.2 Web Reinforcements	8
2.1.3 Contribution of Floor Slab in T-beams	9
2.1.4 Beam Span Length	9
2.2 Properties of Reinforcing Steel	9
2.3 Properties of Concrete	10
2.4 Fabrication of Test Specimens	10
3. EXPERIMENTAL SETUP AND TESTING PROCEDURE	11
3.1 Loading and Support Arrangements	11
3.2 Specimen Instrumentation	11
3.3 Photogrammetric Measurements	12
3.4 Loading Program and Testing Procedure	12
4. EXPERIMENTAL RESULTS	15
4.1 General Remarks	15
4.2 General Observations on Crack Development and Failure Modes	15
4.2.1 Crack Development	15
4.2.2 Failure Modes	16
4.3 Continuously Recorded Force-Deformation Relationships	17
4.3.1 P-δ Diagrams	17
4.3.2 M-ϕ_{av} Diagrams	17
4.3.3 M-θ_{FE} Diagrams	18
4.3.4 V-γ_{av} Diagrams	18
4.3.5 V-ε_{st} Diagrams	18

Page

4.4 Steel Strains in the Main Beam and Slab Reinforcement 19

4.4.1 Strain Variation along Reinforcement of T-beam Slab 19

4.5 Strength, Deformation and Energy Dissipation Capacities 19

4.6 Test Results regarding Effects of Main Parameters 21

4.6.1 Effect of Loading History 21

4.6.2 Effect of Floor Slab in T-beams 22

4.6.3 Effect of Relative Amounts of Top and Bottom Reinforcement 23

4.6.4 Effect of Supplementary Ties 24

4.6.5 Effect of High Shear Force 25

A4. APPENDIX TO CHAPTER 4 -- ESTIMATION OF TIP DEFLECTION COMPONENTS 27

5. EVALUATION OF FLEXURAL BEHAVIOR 29

5.1 General Remarks 29

5.2 Computer Program 29

5.3 Analysis Method and Idealizations 29

5.4 Step-by-step Determination of Internal Moment for a Prescribed Section Deformation History 31

5.5 Required Computing Time 32

5.6 Examples of Moment-curvature Analysis 32

5.7 Effects of Loading Reversals on Different Beam Sections 32

5.7.1 Steel Force-couple Response 33

5.7.2 Effect of Loading Reversals on Stiffness 33

5.7.3 Effect of Loading Reversals on Strength 33

5.8 Effect of Steel Ratio 34

5.9 Effect of Slab in T-beams 34

5.10 Comparison between Theoretical and Measured Responses 37

5.10.1 Beam T-2 (ρ'/ρ_t = 0.34) 37

5.10.2 Beam R-3 (ρ'/ρ_t = 0.53) 37

5.10.3 Beam R-6 (ρ'/ρ_t = 1.0) 38

5.11 Concluding Remarks 39

A5. APPENDIX TO CHAPTER 5 -- DEVELOPMENT OF HYSTERETIC MODEL FOR MATERIALS 41

A5.1 Model for Reinforcing Steel 41

A5.1.1 Cyclic Tests on Reinforcing Steel 41

A5.1.2 Test Results 42

A5.1.3 Hysteretic Model for Stress-Strain Relationship of Reinforcing Steel 42

A5.1.4 Hysteretic Rules 44

A5.1.5 Comments on Hysteretic Rules 45

A5.1.6 Accuracy of Model 46

A5.2 Model for Concrete Stress-Strain Relationships 46

A5.2.1 Model for Monotonic Stress-Strain Curve 47

A5.2.2 Model for Concrete Behavior under Cyclic Loading 47

A5.2.3 Crushing of Unconfined Concrete 48

BIBLIOGRAPHIC DATA SHEET	1. Report No. EERC 76-2	2.	3. Recipient's Accession No.
4. Title and Subtitle Experimental and Analytical Studies on the Hysteretic Behavior of Reinforced Concrete Rectangular and T-Beams			5. Report Date May 1976 6.
7. Author(s) Shao-Yeh M. Ma, Vitelmo V. Bertero and Egor P. Popov			8. Performing Organization Rept. No. 76-2
9. Performing Organization Name and Address Earthquake Engineering Research Center University of California, Berkeley 1301 S. 46th Street Richmond, California 94804			10. Project/Task/Work Unit No. (a) 0-21887 (b) 0-21987 11. Contract/Grant No. (a) GI36387 (b) AEN-07732
12. Sponsoring Organization Name and Address National Science Foundation 1800 G. Street, N.W. Washington, D. C. 20550			13. Type of Report & Period Covered 14.
15. Supplementary Notes			

16. Abstracts

This report describes an experimental and analytical study program carried out for investigating the inelastic behavior of critical regions that may develop in a beam near its connection with the column of a reinforced concrete ductile moment-resisting space frame when subjected to severe earthquake excitations.

In the experimental program, a series of nine cantilever beams, representing half-scale models of the lower story girder of a 20-story ductile moment-resisting reinforced concrete office building, was designed according to present seismic codes. These beams were designed in order to study the effects of (1) the slab by testing T-beams with a top slab width equal to the effective width specified by the ACI (318-71) Code; (2) relative amounts of top and bottom reinforcement by varying the amounts of bottom reinforcement; (3) supplementary ties by providing hairpin ties around the main bars not restrained by the corners of stirrup ties; (4) the high shear force by varying the shear-span ratio; and (5) loading histories by testing some beams under loading reversals inducing a gradually increased deformation, and others, under monotonic loadings to large deformations in one direction. Detailed descriptions of the specimens, testing procedures, experimental data, and results obtained are presented. The significance of the experimental results in relation to the seismic design of the reinforced concrete critical region is also discussed.

The results showed that the main effect of the slab in T-beams was an increase in the moment capacity of the beam in one direction due to the slab reinforcement at the top. By increasing the bottom steel area up to the same amount as that of the top steel area, the energy dissipation capacity of the beam increased between 27 and 54 per cent; by providing supplementary ties for supporting main compression bars not restrained by the corner of ties, the energy dissipation capacity increased about 74 percent. The development of a maximum nominal shear stress, v_{max}, of $5.3\sqrt{f'_c}$ in the shortest beam reduces the energy dissipation by one half when compared with a similar, but longer, beam with a v_{max} of $3.5\sqrt{f'_c}$. Greater amounts of energy can be dissipated by subjecting the beam to loading reversals of gradually increasing amplitude than by subjecting it directly to loading reversals of large amplitude. The inelastic rotations obtained from the test beams reached peak values in each sense ranging from 0.026 rad. to 0.058 rad. These values are considered to be adequate for the efficient design of a ductile moment-resisting frame member.

Photogrammetric measurements proved useful for studying the deformation patterns of

18. Availability Statement	19. Security Class (This Report)	21. No. of Pages
Release Unlimited	UNCLASSIFIED	264
	20. Security Class (This Page) UNCLASSIFIED	22. Price 9.00

FORM NTIS-35 (REV. 3-72) USCOMM-DC 14952-P72

INSTRUCTIONS FOR COMPLETING FORM NTIS-35 (10-70) (Bibliographic Data Sheet based on COSATI Guidelines to Format Standards for Scientific and Technical Reports Prepared by or for the Federal Government, PB-180 600).

1. **Report Number.** Each individually bound report shall carry a unique alphanumeric designation selected by the performing organization or provided by the sponsoring organization. Use uppercase letters and Arabic numerals only. Examples FASEB-NS-87 and FAA-RD-68-09.

2. Leave blank.

3. **Recipient's Accession Number.** Reserved for use by each report recipient.

4. **Title and Subtitle.** Title should indicate clearly and briefly the subject coverage of the report, and be displayed prominently. Set subtitle, if used, in smaller type or otherwise subordinate it to main title. When a report is prepared in more than one volume, repeat the primary title, add volume number and include subtitle for the specific volume.

5. **Report Date.** Each report shall carry a date indicating at least month and year. Indicate the basis on which it was selected (e.g., date of issue, date of approval, date of preparation.

6. **Performing Organization Code.** Leave blank.

7. **Author(s).** Give name(s) in conventional order (e.g., John R. Doe, or J.Robert Doe). List author's affiliation if it differs from the performing organization.

8. **Performing Organization Report Number.** Insert if performing organization wishes to assign this number.

9. **Performing Organization Name and Address.** Give name, street, city, state, and zip code. List no more than two levels of an organizational hierarchy. Display the name of the organization exactly as it should appear in Government indexes such as **USGRDR-I.**

10. **Project/Task/Work Unit Number.** Use the project, task and work unit numbers under which the report was prepared.

11. **Contract/Grant Number.** Insert contract or grant number under which report was prepared.

12. **Sponsoring Agency Name and Address.** Include zip code.

13. **Type of Report and Period Covered.** Indicate interim, final, etc., and, if applicable, dates covered.

14. **Sponsoring Agency Code.** Leave blank.

15. **Supplementary Notes.** Enter information not included elsewhere but useful, such as: Prepared in cooperation with . . . Translation of . . . Presented at conference of . . . To be published in . . . Supersedes . . . Supplements . . .

16. **Abstract.** Include a brief (200 words or less) factual summary of the most significant information contained in the report. If the report contains a significant bibliography or literature survey, mention it here.

17. **Key Words and Document Analysis. (a). Descriptors.** Select from the Thesaurus of Engineering and Scientific Terms the proper authorized terms that identify the major concept of the research and are sufficiently specific and precise to be used as index entries for cataloging.
(b). Identifiers and Open-Ended Terms. Use identifiers for project names, code names, equipment designators, etc. Use open-ended terms written in descriptor form for those subjects for which no descriptor exists.
(c). COSATI Field/Group. Field and Group assignments are to be taken from the 1965 COSATI Subject Category List. Since the majority of documents are multidisciplinary in nature, the primary Field/Group assignment(s) will be the specific discipline, area of human endeavor, or type of physical object. The application(s) will be cross-referenced with secondary Field/Group assignments that will follow the primary posting(s).

18. **Distribution Statement.** Denote releasability to the public or limitation for reasons other than security for example "Release unlimited". Cite any availability to the public, with address and price.

19 & 20. **Security Classification.** Do not submit classified reports to the National Technical

21. **Number of Pages.** Insert the total number of pages, including this one and unnumbered pages, but excluding distribution list, if any.

22. **Price.** Insert the price set by the National Technical Information Service or the Government Printing Office, if known.

BIBLIOGRAPHIC DATA SHEET	1. Report No. EERC 76-2	2.	3. Recipient's Accession No.
4. Title and Subtitle (Continued from page 1)			5. Report Date
			6.
7. Author(s)			8. Performing Organization Rept. No.
9. Performing Organization Name and Address			10. Project/Task/Work Unit No.
			11. Contract/Grant No.
12. Sponsoring Organization Name and Address			13. Type of Report & Period Covered
			14.
15. Supplementary Notes			

16. Abstracts (Continued from page 1)

the beam critical region subjected to reversed loadings. These measurements were especially useful for detecting shear deformation occurring along large cracks that were forming across the entire beam section.

Analytical studies were carried out to gain a better understanding of the flexure, shear, and bond resisting mechanisms in the reinforced concrete critical regions subjected to inelastic load reversals. The analytical studies include: (1) a moment-curvature analysis, based on a hysteretic stress-strain model of reinforcing steel developed from tests on machined main reinforcing bars; (2) a finite element analysis of stress transfer (bond) between concrete and anchored main bars; and (3) an analysis of the shear force-shear deformation hysteretic relationship of reinforced concrete beams considering aggregate interlocking, stirrup-tie resistance, dowel action of main bars, and shear resistance offered by uncracked concrete. The significance of these studies is discussed and summarized.

17c. COSATI Field/Group

18. Availability Statement	19. Security Class (This Report)	21. No. of Pages
Release Unlimited	UNCLASSIFIED	260
	20. Security Class (This Page) UNCLASSIFIED	22. Price

FORM NTIS-35 (REV. 3-72) USCOMM-DC 14952-P72

INSTRUCTIONS FOR COMPLETING FORM NTIS-35 (10-70) (Bibliographic Data Sheet based on COSATI Guidelines to Format Standards for Scientific and Technical Reports Prepared by or for the Federal Government, PB-180 600).

1. **Report Number.** Each individually bound report shall carry a unique alphanumeric designation selected by the performing organization or provided by the sponsoring organization. Use uppercase letters and Arabic numerals only. Examples FASEB-NS-87 and FAA-RD-68-09.

2. Leave blank.

3. **Recipient's Accession Number.** Reserved for use by each report recipient.

4. **Title and Subtitle.** Title should indicate clearly and briefly the subject coverage of the report, and be displayed prominently. Set subtitle, if used, in smaller type or otherwise subordinate it to main title. When a report is prepared in more than one volume, repeat the primary title, add volume number and include subtitle for the specific volume.

5. **Report Date.** Each report shall carry a date indicating at least month and year. Indicate the basis on which it was selected (e.g., date of issue, date of approval, date of preparation.

6. **Performing Organization Code.** Leave blank.

7. **Author(s).** Give name(s) in conventional order (e.g., John R. Doe, or J.Robert Doe). List author's affiliation if it differs from the performing organization.

8. **Performing Organization Report Number.** Insert if performing organization wishes to assign this number.

9. **Performing Organization Name and Address.** Give name, street, city, state, and zip code. List no more than two levels of an organizational hierarchy. Display the name of the organization exactly as it should appear in Government indexes such as **USGRDR-I.**

10. **Project/Task/Work Unit Number.** Use the project, task and work unit numbers under which the report was prepared.

11. **Contract/Grant Number.** Insert contract or grant number under which report was prepared.

12. **Sponsoring Agency Name and Address.** Include zip code.

13. **Type of Report and Period Covered.** Indicate interim, final, etc., and, if applicable, dates covered.

14. **Sponsoring Agency Code.** Leave blank.

15. **Supplementary Notes.** Enter information not included elsewhere but useful, such as: Prepared in cooperation with . . . Translation of . . . Presented at conference of . . . To be published in . . . Supersedes . . . Supplements . . .

16. **Abstract.** Include a brief (200 words or less) factual summary of the most significant information contained in the report. If the report contains a significant bibliography or literature survey, mention it here.

17. **Key Words and Document Analysis. (a). Descriptors.** Select from the Thesaurus of Engineering and Scientific Terms the proper authorized terms that identify the major concept of the research and are sufficiently specific and precise to be used as index entries for cataloging.
(b). Identifiers and Open-Ended Terms. Use identifiers for project names, code names, equipment designators, etc. Use open-ended terms written in descriptor form for those subjects for which no descriptor exists.
(c). COSATI Field/Group. Field and Group assignments are to be taken from the 1965 **COSATI Subject Category List.** Since the majority of documents are multidisciplinary in nature, the primary Field/Group assignment(s) will be the specific discipline, area of human endeavor, or type of physical object. The application(s) will be cross-referenced with secondary Field/Group assignments that will follow the primary posting(s).

18. **Distribution Statement.** Denote releasability to the public or limitation for reasons other than security for example "Release unlimited". Cite any availability to the public, with address and price.

19 & 20. **Security Classification.** Do not submit classified reports to the National Technical

21. **Number of Pages.** Insert the total number of pages, including this one and unnumbered pages, but excluding distribution list, if any.

22. **Price.** Insert the price set by the National Technical Information Service or the Government Printing Office, if known.

Page

A5.3 Data Input to Program CYCMC (Cyclic Moment-curvature Analysis Program) . . . 48

A5.3.1 Heading Card (12A6) . . . 48

A5.3.2 Data Cards . . . 48

A5.4 Data Input to Program BAUSH (Program for Calculation of Cyclic Stress-Strain Response of Reinforcing Steel . . . 50

A5.4.1 Heading Cards (12A6) two cards . . . 50

A5.4.2 Data for Monotonic Stress-Strain Curve [Fig. A5.15(b)] . . . 50

A5.4.3 Steel Strain Values Defining Cyclic History . . . 50

6. EVALUATION OF BEHAVIOR OF ANCHORED MAIN BARS . . . 53

6.1 General Remarks . . . 53

6.2 Nature of Bond between Steel and Concrete . . . 53

6.2.1 Effect of Loading History of Bond Deterioration . . . 53

6.2.2 Bond Deterioration Mechanism . . . 54

6.3 Theory on Bond Deterioration Mechanism . . . 54

6.3.1 Monotonic Response (Specimen A25-4-MN) . . . 55

6.3.2 Repeated Loading in One Sense (Specimen A25-12-RP) . . . 55

6.3.3 Behavior under Reversed Loading (Specimen A25-11-RV) . . . 56

6.4 Anchorage Behavior of Test Beams . . . 56

6.4.1 Reduction of Steel Strain Distribution Data . . . 57

6.4.2 Computation of Steel Strain and Average Bond Stress . . . 57

6.4.3 Behavior under Monotonic Loading . . . 57

6.4.4 Behavior under Cyclic Loading . . . 58

6.5 Concluding Remarks . . . 61

A6. APPENDIX TO CHAPTER 6 -- ANALYTICAL STUDY OF BOND BEHAVIOR . . . 63

A6.1 General Remarks . . . 63

A6.2 Bresler and Bertero Study . . . 63

A6.3 Finite-element Model . . . 63

A6.4 Finite Elements . . . 64

A6.5 Material Model for Concrete . . . 65

A6.6 Material Model for Steel . . . 66

A6.7 Material Properties and Rebar Characteristics used in the Model . . . 66

A6.8 Nonlinear Analysis Solution Procedure . . . 66

A6.9 Analytical Results . . . 67

A6.9.1 Stress Distribution in Uncracked Prism - Linear-elastic Solution . . . 67

A6.9.2 Predicted Crack Development in Concrete Layer around Anchored Main Bar and Its Effect on Bond Behavior . . . 67

A6.9.3 Significance of Results Related to Pull-out of Anchored Main Bars . . . 69

A6.10 Suggestions for Future Studies . . . 69

7. EVALUATION OF SHEAR BEHAVIOR . . . 71

7.1 General Remarks . . . 71

7.2 Basic Mechanisms of Shear Transfer and Shear Resistance in Cracked Regions . . . 71

Page

7.2.1 Mechanisms under Monotonic Loading (Beam T-2) 71

7.2.2 Mechanisms under Loading Reversals (Beam T-3) 72

7.3 Mechanism of Shear Distortion in R/C Beams 72

7.3.1 Uncracked Beam 72

7.3.2 Cracked Beam 72

7.4 Measurement of Shear Distortion by Diagonal Clip Gages 73

7.5 Photogrammetric Study of Deformation Patterns in Critical Region 73

7.5.1 LP 49 to LP 49A (From 0 kips to 6 kips) 73

7.5.2 LP 49A to LP 50 (From 6 kips to 35 kips) 74

7.5.3 LP 59 to LP 51 (From P = 35 kips to 0 kips) 74

7.6 Shear Degradation Mechanism under Repeated Reversed Loadings 74

7.6.1 Shear Degradation Mechanism 74

7.6.2 Shear Degradation due to Increase in Applied Beam Displacement 75

7.7 Shear Distortion Response of Test Beams 75

7.7.1 Effect of Loading History 76

7.7.2 Effect of Relative Amounts of Top and Bottom Steel Reinforcement 76

7.7.3 Effect of Slab in T-beam 76

7.7.4 Effect of High Shear Force 76

7.8 Concluding Remarks 77

A7. APPENDIX TO CHAPTER 7 -- ANALYSIS OF THE HYSTERETIC SHEAR FORCE-SHEAR DEFORMATION RELATIONSHIP IN R/C BEAMS SUBJECTED TO INELASTIC LOAD REVERSALS 79

A7.1 General Remarks 79

A7.2 Analytical Method 79

A7.3 Mathematical Model for Computing Shear Deformation Cracks 80

A7.3.1 End of Initial Loading Stage 81

A7.3.2 Shear Deformation after Initial Loading Stage of Inelastic Load Reversal 82

A7.3.3 Aggregate Interlocking Resistance (Stiffness) 82

A7.3.4 Stirrup Resistance (Stiffness) 83

A7.3.5 Dowel Stiffness of Longitudinal Steel 84

A7.4 Comparison between Predicted Shear Force-Shear Deformation and Measured Shear Force-Shear Distortion Response 85

A7.5 Loading Reversals at a Ductility of One 86

A7.5.1 Determination of Overall Shearing Stiffness at Beginning of Loading 86

A7.5.2 Estimation of End of Initial Loading Stage 88

A7.5.3 Check for Gap Closures 89

A7.5.4 Repeated Cycles at a Ductility of One 89

A7.5.5 Comparison of Analytical Results with Measured Values 89

A7.6 Inelastic Loadings at a Ductility of Two 90

A7.7 Inelastic Loadings at a Ductility Greater than Two 92

A7.8 Concluding Remarks 93

Page

8. CONCLUSIONS, RECOMMENDATIONS FOR IMPROVING DESIGN CODE PROVISIONS, AND SUGGESTIONS FOR FUTURE RESEARCH 95

8.1 Conclusions from Experimental Studies 95

8.1.1 Performance of Testing Facility and Instrumentation 95

8.1.2 Performance of R/C Beams 95

8.2 Conclusions from Analytical Studies 97

8.3 Recommendations for Improving Present Seismic Design Provisions . . . 98

8.4 Suggestions for Future Research 99

REFERENCES 101

TABLES 105

FIGURES 133

LIST OF EERC REPORTS 243

LIST OF NOTATIONS

a	=	shear span (for cantilever beams, $a=\ell$)
A	=	cross-section area of beam
A_b	=	area of reinforcing bar
A_s	=	area of top reinforcing steel
A'_s	=	area of bottom reinforcing steel
A''_s	=	area of slab reinforcement
b	=	width of beam section
b''	=	width of confined concrete core
C	=	compression force
C_c	=	compression force carried by concrete
C_s	=	compression force carried by steel
d	=	effective depth (distance from bottom side to centroid of top steel)
d'	=	distance from bottom side to centroid of bottom steel
d''	=	distance from bottom side to centroid of the slab reinforcement
d_b	=	diameter of reinforcing bar
e_p	=	distance from bottom side to plastic centroid of a R/C section
E	=	modulus of elasticity
E_c	=	modulus of elasticity of concrete
$E_{c_{0.45}}$	=	E_c within the range $0 < \lvert\sigma_c\rvert < 0.45\ f'_c$
E_{diss}	=	amount of energy dissipation
E_s	=	modulus of elasticity (steel)
F	=	applied force
f'_c	=	concrete compressive strength
f_h	=	tensile stress developed at a standard hook [1.11]
f_r	=	modulus of rupture
f_y	=	yield strength of steel
G	=	shear modulus
G^*	=	shear modulus of cracked concrete
Gap^c	=	gap between main reinforcement (dowel) and confined concrete core
Gap^s	=	vertical gap between two inclined crack faces
Gap^t	=	gap between main reinforcement (dowel) and stirrup-ties
h	=	height of beam cross-section
I_s	=	moment of inertia of steel bars
K_{ag}	=	aggregate interlocking stiffness
$K^i_{ag,(i=A,B,C)}$	=	K_{ag} at cracks A,B,C
K^c	=	shear stiffness of solid R/C pieces separated by cracks
K_{crack}	=	shear stiffness due to elements resisting shear at cracks
K_{dw}	=	dowel stiffness of longitudinal main reinforcement

K_{dw}^t, K_{dw}^b	=	K_{dw} of the top and bottom bars
K_{st}	=	axial stiffness of ties across an inclined crack
ℓ	=	span of beam
ℓ_a	=	effective embedment of an anchored rebar
ℓ_{crit}	=	length of critical region
ℓ_d	=	development length of anchored steel
ℓ_d^ℓ	=	ℓ_d of tie in concrete block on left side of an inclined crack
ℓ_d^r	=	ℓ_d of tie in concrete block on right side of an inclined crack
ℓ_e	=	equivalent embedment length of an end hook
ℓ_p	=	yielded length of main reinforcement of beam
ℓ_x^ℓ	=	required development length of tie in concrete block on left side of an inclined crack
ℓ_x^r	=	required development length of tie in concrete block on right side of an inclined crack
L	=	center to center span between two adjacent columns
L_c	=	clean span between two adjacent columns
L_s	=	transverse center to center span between two adjacent columns
LP	=	Load Point
M_c	=	$V_c \cdot \ell$
M_{cr}	=	$V_{cr} \cdot \ell$
M_{max}	=	$V_{max} \cdot \ell$
M_u	=	ultimate moment of a R/C section [1.11]
M_{ult}	=	$V_{ult} \cdot \ell$
$M_{w\ell}$	=	$V_{w\ell} \cdot \ell$
M_y	=	$V_y \cdot \ell$
N	=	normal force applied on a beam section
R/C	=	Reinforced Concrete
S	=	stirrup spacing
P	=	force applied on beam at first flexural yielding
P_y	=	force applied on beam at first flexural yielding
q	=	reinforcing index
u	=	bond stress
u_{max}	=	maximum nominal bond stress = $\frac{\Delta\sigma_s A_b}{\Sigma o \Delta x}$
v_{max}	=	V_{max}/bd, maximum nominal shear stress
V	=	shear force
V_{ag}	=	shear force carried by aggregate interlocking
V_c	=	shear capacity contributed by concrete
V_{cr}	=	shear force at first (flexural) cracking
V_{dw}	=	shear carried by dowel (longitudinal steel)
V_{max}	=	maximum shear force
V_s	=	shear capacity contributed by web reinforcement

V_{st}	=	shear carried by stirrup
V_u	=	$\frac{M_u}{\ell}$
V_{ult}	=	V_s+V_c
$V_{w\ell}$	=	shear force at work stress level
V_y	=	shear force at first flexural yielding
x	=	longitudinal distance along a bar
α	=	Ramberg-Osgood equation parameter (Eq. A5.1)
β	=	Ramberg-Osgood equation parameter (Eq. A5.1)
γ_{av}	=	measured average shear distortion (angle)
Δ	=	variable proceeded by Δ means it is an incremental quantity
Δ_c	=	crack width
Δ_c^i, (i=A,B,C)	=	Δ_c at cracks A,B,C
Δ_{cy}	=	elongation of embedded rebar due to effect of cyclic loading (Eq. 6.3)
Δ_m	=	elongation of embedded rebar under monotonic loading (Eq. 6.3)
Δ_p	=	elongation of tie at inclined crack interface
δ	=	tip deflection of beam
δ_b	=	elongation of the steel bar
δ_{bc}	=	increase in δ_b due to cracking
δ_{crack}	=	shear deformation due to cracks
δ_{crack}^i,(i=A,B,C)	=	δ_{crack} at cracks A, B, C
δ_{crk}	=	deformation due to cracks = δ_{crack} + $\delta_{flex,\ crk}$
δ_{dw}	=	dowel displacement
δ_{flex}^e	=	flexural deformation of an elastic beam
$\delta_{flex,crk}$	=	beam displacement due to flexure deformation at cracks
δ_{FE}	=	tip deflection caused by beam fixed-end rotation
δ_{max}	=	maximum tip deflection of beam
δ_{res}	=	residual shear deformation
δ_{shear}	=	measured shear deformation of critical region
δ_{sh}	=	abbreviated form of δ_{shear} or simply shear deformation
δ_{sh}^c	=	shear deformation of uncracked solid concrete
δ_{sh}^e	=	shear deformation of an elastic beam
δ_t	=	total tip deflection occurred during loading phase
δ_{tip}	=	estimated tip deflection of beam
δ_y	=	beam tip deflection at first flexural yielding

ε	=	strain
ε_c	=	concrete strain
$\varepsilon_{c\ max}$	=	maximum concrete strain
ε_o	=	concrete strain at concrete stress of f'_c
$\varepsilon_{p\ max}$	=	maximum plastic steel strain
ε_s	=	steel strain
ε_{sh}	=	steel strain at point of strain-hardening under monotonic loading
ε_{st}	=	stirrup strain
ε_u	=	ultimate strain
ζ_ϕ	=	strain distribution at a curvature, ϕ
θ	=	angle of rotation
θ_{FE}	=	fixed-end rotation of the beam
θ_{PL}	=	inelastic rotation (Fig. 4.15)
θ^t_{PL}	=	total inelastic rotation (Fig. 4.15)
θ_{tip}	=	rotation at the tip of the beam
λ	=	bond deterioration index
μ_δ	=	tip deflection ductility factor (Fig. 4.15)
μ^t_δ	=	cyclic deflection ductility factor (Fig. 4.15)
ν	=	Poisson's ratio
ρ	=	top steel reinforcement ratio, A_s/bd
ρ'	=	bottom steel reinforcement ratio, A'_s/bd
ρ''	=	volume of stirrup-tie/volume of bound concrete core
ρ_b	=	balanced reinforcement ratio
ρ_t	=	top steel reinforcement ratio, $(A_s+A''_s)/bd$
σ	=	stress
σ_c	=	concrete stress
σ_s	=	steel stress
Σ_o	=	perimeter of reinforcing bars
ϕ	=	curvature
ϕ_{av}	=	average curvature
$\bar{\phi}$	=	average curvature between face of beam support and a beam section
ϕ	=	average curvature between two beam sections
ϕ_{max}	=	maximum curvature
ϕ_y	=	curvature at first flexural yielding

1. INTRODUCTION

1.1 GENERAL

The Structural Engineers' Association of California has recommended that buildings be designed to resist major earthquakes of the intensity of the strongest experienced in California such that structural and the nonstructural damages incurred from the earthquake do not lead to the collapse of the structure or to the endangerment of human life [1.1] This criterion imposes demands on the ability of the structure to absorb and dissipate the energy fed into it from ground motions. The manner in which these energy requirements are met varies with the structural system used for the building. For medium-rise reinforced concrete (R/C) buildings up to 20 stories high, the necessary lateral stiffness and energy capacity requirements can be met by using a ductile moment-resisting space frame alone. For higher R/C buildings, however, a combined lateral resisting frame-wall system is generally desirable for controlling deformations and, therefore, damages. In this combined system, the moment-resisting space frame is used as a secondary structural resistant system to provide ductility.

Reinforced concrete structures designed as ductile moment-resisting space frames for earthquake loading provisions specified in the Uniform Building Code [1.2] are expected to rely on the inelastic deformability of its structural components for absorbing and dissipating energy fed into the structures from severe earthquake motions. The inelastic deformations are usually developed at certain critical regions in the structural frame. These critical regions are often located at points of maximum internal forces (moments).

The locations of critical regions in one floor of a R/C moment-resisting frame are illustrated in Fig. 1.1. These regions can be conveniently classified [1.3] according to their controlling states of stress: (1) at midspan of the girder (region 1) where inelastic behavior is usually controlled by bending; (2) at the ends of the girder (regions 2 and 3) where inelastic behavior can be controlled by either bending alone or bending and shear; and (3) at the ends of the column (regions 4-7) and at the beam-column joints (regions 8 and 9) where behavior can be controlled by the combination of high shear and axial forces, and bond stresses (transfer of stresses from steel to concrete) rather than bending.

The study reported herein is an attempt to investigate the inelastic behavior of critical regions at the ends of the girder near the column joint. Considerable efforts have been devoted to studying the behavior of this critical region and a review of these studies follows.

1.2 REVIEW OF PAST STUDIES

1.2.1 Experimental Studies

Previous experimental studies have attempted to study the inelastic behavior of R/C critical regions subjected to reversed bending and shear [1.4-1.9]. In these investigations the behavior of the critical region was determined by performing tests on isolated, statically determinate R/C beams. The variables which were found to affect the inelastic behavior of the region are discussed below.

(a) Amount of tensile and compressive reinforcement, ρ and ρ'. - It is well known that the flexural strength and ductility of R/C critical regions are influenced by the amount of flexural reinforcement as well as by the characteristics of the steel and concrete reinforcements. The effect of these parameters can be conveniently described in terms of a generalized reinforcing index, $q = (\rho - \rho') f_y/f'_c$ [1.10].

According to present codes [1.2, 1.11] for developing the flexural strength, M_u, assumed in the ultimate strength design method, a minimum amount of shear reinforcement is required in the flexural member to prevent shear failure before M_u is attained. Furthermore, to attain sufficient ductility to permit some redistribution, an upper bound on ρ not more than 0.75 of that producing the balanced condition, and a minimum amount of tensile reinforcement of $200/f_y$ are required.

Because of uncertainties regarding the characteristics of future earthquake ground motions, seismic designs should provide high ductility in possible critical regions. The need for more stringent requirements of tensile reinforcement has been reflected in present codes. The UBC [1.2] specifies that the value of ρ should not exceed 0.025 while the ACI Code [1.11] requires this value to be not more than 0.5 of that producing the balanced condition.

Since a partial or full reversal of moment deformation may occur in a critical region subjected to seismic overloads, a minimum amount of bottom steel, not less than 50 percent of that of the top steel, is also required.

Brown and Jirsa [1.4] tested a series of R/C cantilever beams with different amounts of top and bottom steel reinforcements under constant amplitude inelastic load reversals. They found that increasing the amount of top and bottom steel or increasing the amount of bottom steel will reduce the number of cycles to reach failure. Failure was of a generally shear-compression type in which the main bars buckled. This type of failure was reportedly due to the increased shear and compressive forces acting in the beam. However, this conclusion was based on test beams with a tie spacing of about d/2 which does not satisfy the minimum spacing of d/4 required in the design of girder critical regions of ductile moment-resisting R/C frames [1.2,1.11].

(b) Amount and arrangement of lateral ties. - Lateral ties are used to provide shear to the critical region, confinement to the concrete core, and lateral restraints to the compressive steel in order to delay the inelastic buckling of the steel.

Current seismic codes emphasize the use of closely spaced vertical stirrup-ties (tie spacing not more than d/4) to provide effective confinement of concrete and support for the main reinforcement. This requirement will usually provide an amount of shear reinforcement exceeding that required by the codes.

In the past, tests on R/C beams subjected to inelastic load reversals [1.4-1.8] have shown that the energy dissipation of the beam can be improved by increasing the amount of web reinforcement, or, more effectively, by providing closed stirrups or ties at reduced spacings.

(c) Moment-to-shear or shear-span ratios. - Tests on R/C cantilever beams with different spans [1.4, 1.8] have indicated that for beams with a shorter span or with a higher nominal shearing stress, it takes fewer cycles to reach failure and the recorded load-deflection hysteretic loops will exhibit a progressive pinching of loops due to shear deformations. This in turn will lead to a reduction in the energy dissipation capacity of the beam.

(d) Loading history. - A number of tests have been conducted [1.4, 1.9] to study the effect of different loading histories on the behavior of R/C beams subjected to bending and shear. It was found that the strength and, particularly, the stiffness were very sensitive to the loading history. In general, the results indicate that the continuous application of cyclic loading with full reversals of deformations will induce the most damage, and the greater the peak deformations imposed by each cycle of reversal, the fewer the cycles required to reach failure.

(e) Rate of loading. - Celebi and Penzien [1.8] and Mahin and Bertero [1.13], have recently studied the effect of the rate of loading on the behavior of R/C flexural members. It was found that the rate of loading mainly affects the moment capacity in the first excursion beyond yield.

One important parameter that is consistently neglected in experimental studies is the effect of the floor slab on the inelastic behavior of the R/C critical region. In most cyclic loading tests, rectangular cross-section beams were used. Since girders are usually cast integrally with the floor slab, they must deform together with the slab; consequently, this floor slab must affect the strength, stiffness, ductility, and energy dissipation characteristics of the critical region. Underestimating or neglecting the effect of floor slabs on the strength of the girders may lead to a design with weak columns that are incapable of resisting forces, particularly, the moment that could be developed according to the actual strength of the girders interacting with the slab under lateral loads. As a result, the critical region may develop in the columns. This is undesirable because if a partial mechanism is developed in the frame under strong seismic loadings, it will require large concentrated inelastic rotations at the ends of the columns which generally have less available ductility than the girders.

1.2.2 Analytical Studies

To predict analytically the history of inelastic response of large R/C structures under dynamic earthquake loading, simple practical hysteretic models for reinforced concrete must be used. Among these models are the bilinear model, the degrading model proposed by Clough and Johnston [1.14] (known as the Clough model), and a similar model proposed by Takeda et al. [1.15]. More refined analytical methods based on postulated material behavior have been employed [1.5, 1.16-1.19] to predict the inelastic response of isolated R/C members.

In the works of Sargin [1.16] and Park, Kent, and Sampson [1.5], only the flexural behavior of R/C beams was analyzed, assuming that no interaction between shear and flexural behavior can occur. Whereas other studies [1.17-1.19] modeled R/C members as an assemblage of two- or three-dimensional finite elements, these studies considered the combined states of stress in concrete and the effect of shear. Because of the complexity involved in modeling the actual behavior of reinforced concrete, particularly with regard to concrete cracking, shear resistance at the crack interface and bond slippage, most of the analytical studies have been based on highly questionable simplified models [1.20].

To account for the effect of cracking, it is common to reduce the stiffness in the principal stress or strain direction where cracking strength has been exceeded by modifying the concrete constitutive relationships. However, this cracking model does not consider the physical discontinuity introduced by the cracks, the crack spacing, or the individual crack width. This makes it difficult to incorporate the effect of interface shear resistances such as the aggregate interlocking and the dowel action of steel reinforcement, into the cracking model.

Besides the complexities involved in modeling, the main difficulty encountered in the development of effective mathematical models for shear and bond behavior of R/C members is the lack of knowledge regarding the actual physical mechanism of shear and bond resistance under general excitations. For this reason, it was decided to investigate further the behavior of critical regions which may develop near column connections.

1.3 OBJECTIVES AND SCOPE

The objectives of the work reported herein were to investigate and predict analytically the behavior of R/C critical regions at the ends of girders in high-rise framed buildings when subjected to bending and shear actions similar to those expected during severe earthquakes. To achieve these objectives, experimental studies were carried out to investigate the strength, stiffness, deformational capacity, and energy absorption and dissipation characteristics of such critical regions and to formulate reliable mechanical and mathematical models for implementation in the analytical prediction of their behavior.

1.3.1 Experimental Studies

For a realistic representation of the R/C critical region at the ends of the girder, half-scale models of girders in a 20-story moment-resisting R/C frame were adapted for the experimental study.

A series of nine under-reinforced ductile R/C cantilever beams was tested. The cross-sections of the beams were 9 in. x 16 in. with a span length of either 38.5 in. or 62.5 in. The beams were reinforced with four #6 bars at the top and either four #6 or three #5 bars at the bottom. Three of the nine beams were cast integrally with a portion of the floor slab and crossbeam stubs.

The tests were conducted to investigate the effects of the following parameters on the response of test beams under a prescribed loading history.

(1) Slab: examined using three pairs of identical beams, three with slab and three without.

(2) Relative amounts of top and bottom reinforcement: examined by varying the amount of bottom steel reinforcement.

(3) High shear forces: evaluated by comparing results obtained from similar beams of different shear-span ratios.

(4) Loading history: studied using two basic types of loading programs. In the first, beams were subjected to a series of symmetrical or unsymmetrical stepwise increasing load/deformation cycles until failure. In the second type, beams were subjected directly to a very large reversed cycle which was repeated until deflection failure.

The loading was applied in a pseudo-static manner to permit a detailed study of the beams under failure as well as of the progressive strength and stiffness deteriorations. Extensive instrumentation was used to obtain the data necessary for studying the inelastic behavior of the beam critical region. These include measurements of flexural strength and deformation, shear strength and shear distortion, and fixed-end rotation caused by pull-out of the main bars in the beam anchorage zone. In addition, photogrammetric measurements were taken to study the deformation patterns of the beam critical region.

Additional tests were carried out to study the hysteretic stress-strain behavior of the materials used in the fabrication of the test beams. A number of machined specimens of the reinforcing bars were tested under a loading history necessary for inducing a strain history similar to the recorded strain history of steel reinforcing bars in the critically-strained beam regions.

1.3.2 Analytical Studies

Analytical studies were carried out to gain a better understanding of the flexure, shear, and bond resisting mechanisms of R/C critical regions subjected to inelastic load

reversals. These studies included: (1) moment-curvature analysis of a hysteretic stress-strain model of reinforcing steel developed from tests on machined main reinforcing bars; (2) finite element analysis of stress transfer or bond between concrete and anchored main bars; and (3) analysis of shear force-shear deformation hysteretic relationship of R/C beams, considering aggregate interlocking, stirrup-tie resistance, dowel action of main bars, and shear resistance offered by uncracked concrete.

2. EXPERIMENTAL PROGRAM

2.1 SELECTION AND DESIGN OF TEST SPECIMENS

The main purpose of the experimental program was to study the behavior of R/C critical regions such as those occurring in beams near the column face. In order to model realistically these critical regions, a basic test specimen was adapted to simulate the lower-story girders of a 20-story ductile moment-resisting concrete frame. The design of the test specimen is reported in Ref. 2.1. This frame will be referred to herein as the prototype.

The relationship between the selected test specimen and the actual girder in the prototype is illustrated in Fig. 2.1. The test specimen represents an isolated part of the integral girder-slab structure near the column connections. Except for one specimen, the overall dimensions of the test specimens were just one-half the dimensions of the prototype. This model scale was dictated by the capacity of the available testing facility (Sect. 3.1).

The specimens were supported by an enlarged end block simulating a rigid column stub and loaded at the tip as cantilever beams so that the critical region would develop near the column face such as that expected to occur in the corresponding girder of the prototype subjected to lateral loading (Fig. 2.2). With the system of loading adopted, the force and deformation applied to the critical region could be directly controlled by the applied load or deformation at the tip of the cantilever beam.

Nine beams were tested in this experimental program, six R/C beams having rectangular cross-sections and three T-beams having tee-sections. Three pairs of beams (R-1 and R-2, R-3 and R-4, and T-1 and T-2) were made identical for studying the effect of the loading history. The selected loading programs for these pairs of beams will be discussed in Sect. 3.4.

In order to study the remaining parameters (effects of slab, relative amount of top and bottom reinforcement, lateral web reinforcement and high shear force), the design of test beams was varied according to which parameter was being investigated. The four basic section types used in the test beams are shown in Fig. 2.3. The basic properties of the beams and their computed strengths are listed in Tables 2.1 and 2.2, and the dimensions and reinforcement details for each beam are presented in Figs. 2.4 to 2.8. The principal parameters (variables) in each specimen are listed in Table 2.3 and discussed in the following sections.

2.1.1 Longitudinal Reinforcements

All the test beams were reinforced with four #6 bars at the top and four #6 or three #5 bars at the bottom. This gives a maximum tensile reinforcement ratio of 0.014 which is below the 0.5 balanced steel, ρ_b, ratio* required by present seismic code provisions [1.2, 1.11]. The three bottom #5 bars used in Beams R-1 to R-4, T-1 and T-2 provided an upward moment capacity of slightly more than 50 percent of the downward moment capacity corresponding to the four main top #6 bars (Fig. 2.2). This satisfied the moment capacity required by seismic codes for the positive moment direction in R/C critical regions near column connections.

The effect of relative amounts of top and bottom steel was studied by comparing the performance of beams which were similar, but having different amounts of bottom reinforcement, i.e., Beams R-3 and R-6, and Beams T-1 and T-3.

---

* In the design computations, a concrete strength, f'_c, of 4 ksi and a steel strength, f_y, of 60 ksi were used, giving a ρ_b of 0.029. The calculated ρ_b based on the actual f'_c and f_y varies from 0.026 to 0.030 (Table 2.1).

Preceding page blank

The anchorage for the main steel reinforcement of the test beams was designed to avoid failure in the beam anchorage zone so that the ultimate load and deformation capacities of the critical region developed in the girder portion could be attained. The anchorage for the main reinforcement, top #6 bars, and bottom #5 and #6 bars, was provided by a straight embedment length of 26.25 in. plus a standard 180 degree end hook in the R/C column block (Figs. 2.7 and 2.8). The equivalent embedment length, ℓ_e, of the hooks can be computed by applying Sect. 12.8 of the ACI Code [1.11], and the combined development length, ℓ_a, by applying Sect. 12.9:

$$\ell_a = \text{straight bar length } (\ell_s) + \text{equivalent length for end hook } (\ell_e)$$
$$= 26.25 \text{ in.} + 0.04\, A_b\, f_h/\sqrt{f'_c}$$

where

A_b = area of bar

$f_h = \xi \sqrt{f'_c}$, where ξ = 540 for #5 bar, 450 for top #6 bar, 540 for bottom #6 bar (see Table 12.8.1 of Ref. 1.11)

f'_c = concrete compressive strength (the specified strength of 4000 psi was used)

$$\left.\begin{array}{ll} \text{top \#6 bar} & \ell_a = 26.25 + 7.92 = 34.2 \text{ in.} \\ \text{bottom \#5 bar} & \ell = 26.25 + 6.70 = 33.0 \text{ in.} \\ \text{bottom \#6 bar} & \ell = 26.25 + 9.50 = 35.8 \text{ in.} \end{array}\right\} \quad (2.1a)$$

The required development length, ℓ_d, for the bars computed from Sect. 12.5(a), and 12.5(b) of the ACI Code is:

$$\ell_d = \ell'_d \times (1.4) \times \left[2 - \frac{60{,}000}{f_y(\text{psi})}\right]$$

where

$\ell'_d = 0.04\, A_b\, f_y/\sqrt{f'_c}$ or

$0.0004\, d_b\, f_y(\text{psi})$, whichever is greater

f_y = yielding strength of steel

1.4= correction factor for concrete sedimentation [this factor applies to the top bars since there is 12 in. of concrete cast vertically below the bars (Sect. 2.4)]

$(2 - \frac{60{,}000}{f_y})$ = correction factor for bars with f_y higher than 60,000 psi.

d_b = diameter of bar (in.)

A_b = area of bar (in.^{2})

For a #5 bar with an f_y = 66.5 ksi, and a #6 bar with an f_y = 65.5 ksi, the computed required development lengths for the bars are:

$$\left.\begin{array}{ll} \text{top \#6 bar} & \ell_d = 29.7 \text{ in.} \\ \text{bottom \#5 bar} & \ell_d = 18.3 \text{ in.} \\ \text{bottom \#6 bar} & \ell_d = 21.2 \text{ in.} \end{array}\right\} \quad (2.1b)$$

Comparing (2.1a) and (2.1b) it is clear that the supplied embedment length satisfies the code requirements.

2.1.2 Web Reinforcements

In all specimens, vertical stirrup-ties were used as the web reinforcement and were designed to meet the seismic code requirements for the detailing of R/C critical regions close to column connections [1.2, 1.11]. These ties were made of deformed #2 bars and the

details of their design are shown in Figs. 2.7 and 2.8.

The design of web reinforcement used in the test specimen was dictated by the minimum spacing requirement of d/4, Sect. A5.9 of Ref. 1.11. The calculated shear strength, V_{ult}, is considerably greater than that needed to develop the flexural strength of the beam, M_u (compare V_{ult} and V_u in Table 2.2).

Single hoop stirrup-ties which gave a binding ratio (volume of lateral ties/volume of bound concrete core) of 0.0053 were used in Beams R-1 and R-2. Supplementary hairpin or double-hoop ties were used to minimize the buckling of the center longitudinal bars in the remaining test beams. This increased the binding ratio of these beams to 0.01. The present code offers no specific requirement for the arrangement of ties for supporting the compression bars in beams or girders. The use of single ties is permitted, provided the size and spacing limitations are satisfied: ties must be at least #3 bar in size, spaced at not more than 16 times the bar diameter, or 48 times the tie diameter (Sects. 7.12.5, and A5.10 of Ref. 1.11). In the half-scale experimental beams, #2 bars were used for the ties corresponding to #4 bars in the prototype. The spacing of the #2 ties was kept at d/4 = 3.5 in. which is less than 16 times the diameter of the compressive #5 or #6 bars, and less than 48 times the diameter of the #2 ties. Beams R-1 and R-3 were tested to study the effect of web reinforcement.

2.1.3 Contribution of Floor Slab in T-beams

The detailing of the floor slab in T-beams is shown in Fig. 2.8. The width and thickness of the slab are 36 in. and 2.25 in., respectively. The selected width of the slab is the same as the allowable effective slab width specified in Sect. 8.7.2 of the ACI Code [1.11].

The top and bottom layers of the longitudinal deformed #2 reinforcing bars used in the T-beam slab represent the principal #4 bar reinforcement of the one-way slab system of the prototype [Fig. 2.1(b)]. The spacing and concrete cover for these #2 bars were designed in accordance with Sects. 7.4.3 and 7.14.1 of the ACI Code. The top and bottom slab reinforcement ratio is 0.0044 as compared with the minimum acceptable value of $200/f_y = 0.0033$ for tensile steel. The amount and spacing of the transverse slab reinforcement in the T-beams were designed in accordance with Sect. 7.13 of the ACI Code.

2.1.4 Beam Span Length

For shorter beams, a greater shear force is required to develop the same amount of moment at a fixed beam end. Therefore, the influence of large shear force could be studied by comparing the relative performances of similar beams made with different span lengths. In the present experimental program, all beams except R-5 had a span length, ℓ, of 62.5 in. and a shear span ratio, ℓ/d, of 4.46. The span length corresponds to one-half the clear span length, L_c, of the lower floor girders of the prototype (Fig. 2.2). Figure 2.2 shows that as the frame is deflected laterally, the points of inflection are located around the midspan of the girders, and maximum moment occurs near the column connections. Therefore, by applying the load at the tip of cantilever beams having a ℓ of $L_c/2$, a moment gradient similar to that in the prototype can be generated. The span length of Beam R-5 was reduced to 38.5 in. ($\ell/d = 2.75$) in order to study the effect of high shear force.

2.2 PROPERTIES OF REINFORCING STEEL

The main reinforcements used in fabricating the test beams were deformed #5 and #6 bars of 60 grade steel conforming to an ASTM designation of A615. Beam web reinforcement and slab reinforcement used a deformed #2 bar. The stress-strain curves obtained from con-

ventional tension tests on #5, #6, and #2 rebar specimens are shown in Fig. 2.9 which also lists their most important mechanical characteristics. The curves represent averaged results of several tests. The yield strength of #6 and #5 bars were 65.6 ksi and 66.5 ksi, respectively. The onset of strain-hardening occurred at about 0.0134 in./in. for the #6 bar and 0.0116 in./in. for the #5 bar. The stress-strain curve of the deformed #2 bar indicates a yielding strength of 60 ksi, and a pronounced yield plateau which was about twice as long as that of a #5 or #6 bar. The steel moduli at the initiation of steel strain-hardening, E_{sh}, were 1050 ksi for the #6 bar, 1010 ksi for the #5 bar, and 750 ksi for the #2 bar (Fig. 2.9).

Additional tests were carried out to investigate the hysteretic behavior of the main reinforcing bars. These tests and their results are discussed in Appendix A5.

2.3 PROPERTIES OF CONCRETE

Type II Portland Cement and normal-weight aggregate were used for the concrete. It was designed to have a compressive strength of about 4000 psi at 14 days. The typical mix proportion specified by weight (SSD) was one part Type II Portland Cement to 2.3 parts of #0 sand (fineness modulus = 2.74), to 2.6 parts of Santa Cruz coarse aggregate ranging in size from #4 to 1/2 in. The water-cement ratio for the fresh concrete was 0.55. The slump was about 5 in.

To determine the actual concrete characteristics of each specimen, numerous 6-in. diameter by 12-in. control cylinders and 5-in. x 6-in. x 20-in. flexural beams were cast from each concrete batch. Compressive strength was evaluated at seven and fourteen days for each batch. The compressive strength, stress-strain relationships, and modulus of rupture were determined for each beam during testing.

The stress-strain curves of concrete used in each test beam obtained from the standard compression test at about 14 days are shown in Fig. 2.10. The estimated modulus of concrete elasticity, $E_{c_{0.45}}$, from these curves and the computed E_c from Sect. 8.3.1 of the ACI Code [1.11] are also listed in Fig. 2.10. The difference between experimental and ACI values did not exceed 10 percent.

2.4 FABRICATION OF TEST SPECIMENS

After the steel reinforcement cage was assembled, as shown in Figs. 2.7 and 2.8, it was placed in the formwork. Test specimens were then cast in a vertical position as they would be in actual construction. The concrete was poured in three steps and compacted with a high frequency vibrator. In the first step, concrete was poured into the anchorage block (column) to the level of the bottom of the cantilever beam; in the second step, to the top level of the beam; and in the third step, to the top level of the anchorage block. At the end of the first and second steps, the concrete was allowed to set for several hours until it stopped bleeding. The specimens were cured in the forms with wet burlap covered by a plastic cover for seven days. After seven days, the forms were removed and the specimens were moved to the test area and fastened to the reaction fixture by means of prestressing rods. The specimens were then left to cure in the 70 percent relative humidity and the 70°F ambient temperature of the laboratory surroundings for seven days or until the desired concrete strength of 4000 psi was attained.

3. EXPERIMENTAL SETUP AND TESTING PROCEDURE

3.1 LOADING AND SUPPORT ARRANGEMENTS

The half-size beam specimens were tested in a facility developed for the testing of full-size structural steel components [3.1]. The loading and support arrangements for the specimens are shown schematically in Fig. 3.1. Both the loading and reaction fixtures shown in this figure were anchored to the structural test floor slab by means of prestressing rods. The enlarged end block of each specimen was secured in the test position to the front face of the reaction fixture by eight 1-in. diameter prestressing rods. The applied load to the tip of the specimen was provided by a Miller Model H double-acting hydraulic actuator with a maximum capacity of approximately 460 kips. The loading ram of the actuator was pin-connected to the tip of the test specimen. The load applied to the specimen was measured by a load cell specially designed for the loading range used in these tests. The load cell was calibrated on a testing machine to a maximum value of 50 kips in compression and then installed at the mid-portion of the actuator ram (Fig. 3.1).

3.2 SPECIMEN INSTRUMENTATION

Various transducers of clip gages, linear potentiometers, and strain gages were used to monitor the applied load, displacement rotations, and steel strains in the specimen. Figure 3.2 illustrates the typical arrangement of the instrumentation. Except for Beam R-1, the following variables were continuously plotted for each test on X-Y and X-Y-Y' recorders against the applied load at the tip of the cantilever beam, P: beam tip deflection, rotation of the critical region, and shear distortion in the critical region. Steel strains and most of the other displacement variables were monitored at selected points in the loading of the specimen on a low-speed scanner controlled by a small NOVA computer. The readings were stored and then printed out on a teletype. The general test setup and low-speed scanner equipment are shown in Fig. 3.3. The description of the measurement procedure is presented below.

(a) Displacements at beam tip. - The tip deflection, δ, of the test beam was measured with a linear potentiometer, P1, attached to a fixed stand on the floor (Fig. 3.2). The beam tip rotation, θ_{tip}, was estimated from the displacements at the two ends of a long aluminum rod rigidly attached to the end of the beam, and the end displacements of the rod were measured with two linear potentiometers, P2 and P3 (Fig. 3.2).

(b) Rotations in the critical region. - Clip gages were used to measure the relative rotation between cross-sections located at a distance of 0 in., 7 in., 14 in., and 21 in. from the fixed-end of the beam. The length of measurement was therefore 7 in., one-half the effective depth, d. The clip gages used for measuring rotation were either supported by rectangular aluminum frames mounted perpendicularly to the longitudinal axis of the beam as shown in Fig. 3.4, or were supported on steel pins which were silver-soldered to the longitudinal reinforcement (Fig. 3.5).

The average curvature, ϕ_{av}, used later in the test was obtained by dividing the measured rotation between two sections, $\Delta\theta$, by the gage length, ℓ_g. The equation used for computing $\Delta\theta$ and ϕ_{av} from the clip gage measurements (Δ, $\bar{\Delta}$) is shown in Fig. 3.5.

(c) Average shear distortion. - A special instrument was used to measure the deformations resulting from the shear force of the beam critical region, γ_{av}. These deformations are referred to as "shear distortions." The instrument consisted of a pair of clip gages mounted on diagonally-opposite corner points of the critical region (Figs. 3.2 and 3.4).

A similar instrument has been used for measuring the shear distortion of shear panel in steel beam-to-column subassemblages [3.2].

Each of the two clip gages provided a measurement of the relative movement of two diagonally oriented points. From these measurements, the average shear distortion can be obtained geometrically as:

$$\gamma_{av} = \frac{\Delta - \bar{\Delta}}{2} \frac{d}{bh} \tag{3.1a}$$

Because of this shear distortion, the change in the beam deflection is given by:

$$\delta_{sh} = \gamma_{av}\, b = 1/2\, \frac{(\Delta - \bar{\Delta})\, d}{h} \tag{3.1b}$$

where the notations are indicated in Fig. 3.6(a). The limitations of this equation and the nature of the measured shear distortion are discussed in Chapter 7.

(d) Beam fixed-end rotation. - The amount of fixed-end beam rotation, θ_{FE}, caused by pull-out of the main reinforcing bars from their anchorage zone was estimated on the basis of the difference in the longitudinal displacements of the top, Δ_t, and bottom, Δ_b, anchored bars. The relationship between θ_{FE} and these displacements is indicated in Fig. 3.6(b). Displacements Δ_t and Δ_b were measured by a pair of linear potentiometers supported on the surface of the anchorage block (column stub). These gages are shown in Fig. 3.7.

(e) Strains in steel reinforcement. - Several microdot strain gages (with a strain range of about ± 0.030 in./in.) were mounted on the main top and bottom reinforcement in the anchorage zone and on the stirrups, as well as on the longitudinal slab reinforcement. The average steel strain in the top and bottom steel reinforcements was measured with clip gages mounted on steel pins silver-soldered to the bar. This measuring system was also used for the #2 slab reinforcement of Beam T-3 (Fig. 3.8).

3.3 PHOTOGRAMMETRIC MEASUREMENTS

Photographic equipment for the study consisted of a fixed-lens camera with a supporting stand, as shown in Fig. 3.3(a). The camera was positioned such that the axis of the lens was perpendicular to the surface to be measured. Fine grid lines were drawn on the top surface of the test beam and on the adjoining column block to provide reference lines for such a study (Fig. 3.4). To determine the deformation pattern, points at the intersection of the grid lines were read. Breaks in the continuous grid lines were due to cracking; these were also measured at various positions in the critical region. All photographs were taken on glass plates to stabilize the records. These records were then analyzed using a Mann comparator at the U.S. Geological Survey facility in Menlo Park, California. Although the comparator has a very high resolution (0.001 mm), most errors are introduced from reading the record on the glass plates, where images of the intersecting points of grid lines are difficult to locate accurately. Selected photogrammetric results can be found in Chapter 7.

3.4 LOADING PROGRAM AND TESTING PROCEDURE

The selected loading sequences for the nine test specimens are expressed in terms of peak tip deflections and peak loads of each cycle as shown in Figs. 3.9-3.12.

Most of the beams were subjected to a series of gradually increasing load reversals until failure. This gradually increasing cyclic load sequence somewhat resembles the development of force applied on the structure during the initial buildup phase of a strong seismic motion. The details of this loading sequence are described below:

(a) Load-controlled cycles (pre-yielding cycles). - In the cycles preceding yielding of the steel reinforcement, loading was controlled by the magnitude of the applied load. Several cycles at working stress level were made before applying a load high enough to cause the yielding of steel.

(b) Displacement-controlled cycles (post-yielding cycles). - After yielding of the steel reinforcement, loading was controlled by the magnitude of the measured tip deflection, δ. The tip deflection was increased in steps corresponding to deflection ductility ratio (δ/δ_y) increments of one unit. The deformation cycle at each step, i.e., at a constant tip deflection, was repeated several times to study the degradation of stiffness and strength at each ductility level. The procedure was repeated until a sudden drop in strength occurred which constituted failure of the specimen.

Except for Beam R-2, the specimens were cycled between symmetrical peak tip deflections. In the loading program for Beam R-2, the cyclic peak deformations in one direction were larger than those in the other direction [Fig. 3.10(a)].

The study of the effects of the variables was made under the symmetrical stepwise increasing loading program.

Test beams T-2 and R-4 were loaded directly to the largest deformation permitted by the stroke of the actuator (about 4 in.). A loading reversal was then applied, causing the beam to deform an equal amount in the opposite direction, and then repeated until failure of the beam. This direct monotonic loading sequence simulates the loading of the structure as it is subjected to a strong lurch in one direction under a severe earthquake motion.

During testing, load deformation data were continuously recorded until the beam failed or until the measured deformation reached such a magnitude that continued recording might have impaired the function of the clip gages. At preselected load points, the load was slightly reduced and kept constant for a short period of time to permit marking of the crack propagation, taking of photos, and recording of scanner data. Tests were usually conducted with a personnel of four whose tasks included operating the actuator pump, attending the instrumentation, marking and recording the crack pattern, and operating the low-speed scanner.

4. EXPERIMENTAL RESULTS

4.1 GENERAL REMARKS

In this chapter most of the important test results obtained from the experimental program are presented in tables and in graphs as hysteretic diagrams.

The hysteretic diagrams consist of continuous plots of load-tip deflection, P-δ, moment-average curvature, M-ϕ_{av}, shear force-average shear distortion, V-γ_{av}, moment fixed-end rotation, M-θ_{FE}, and shear force stirrup strain, V-ε_{st}.

The different modes of beam failure observed in the tests are presented, followed by a brief discussion of the hysteretic diagrams and the strain gage data of the steel reinforcement. The principal test results are given, together with observations on the effects of the parameters under investigation (Table 2.3). A method of estimating tip deflection from the measured flexural, shearing, and fixed-end deformations is presented in the appendix to this chapter.

4.2 GENERAL OBSERVATIONS ON CRACK DEVELOPMENT AND FAILURE MODES

4.2.1 Crack Development

Important observations on the crack development in test beams are summarized below:

(a) Influence of shear. - Before cracking, the stress field developed in the beam is similar to that shown in Fig. 4.1(a). On the upper and lower sides of the beam, the flexural stresses are dominant but toward the mid-depth and tip of the beam, the shear stresses are relatively greater than the flexural ones. Since cracks tend to form in the direction of principal tensile stress or strain, the initial cracks that developed in the upper or lower sides of the beam were observed to be nearly vertical. As cracks extended toward the center and tip of the beam, they became increasingly inclined due to the effect of shear stresses [Fig. 4.1(b)]. A comparison of the crack pattern of the short beam, R-5, with that of the longer beam, R-6 [Fig. 4.1(b)], showed that a more inclined crack pattern developed in Beam R-5 due to the relatively higher shear-to-moment ratio.

(b) Influence of loading reversals. - Figure 4.2 compares the crack patterns of Beams T-2 and R-4 subjected to monotonically increasing loads with those of comparable beams, T-1 and R-3, which were subjected to stepwise increasing full displacement reversals. These crack patterns were recorded at peaks of downward loading, corresponding to a tip displacement ductility ratio of 4, 5, 5.5, and 7.

The crack pattern of Beams R-3 and T-1 shows that after the critical region underwent a number of loading reversals, some of the cracks developed on the upper side of the beam and traversed those that developed on the lower side. The concrete in the critical region became fractured into a series of concrete blocks. These blocks were held or stitched together by the longitudinal and web reinforcement in the region.

(c) Crack development in T-beam slab. - Typical crack development in a T-beam slab can be seen in the photographs presented in Fig. 4.3. At about half of the yield load (15.7 kips), most of the cracks were observed to have extended across the entire width (36 in.) of the slab, except in regions near the tip of the beam where the flexural stresses were relatively low.

As load increased to 32 kips (yield load), tensile steel stress in the top reinforcement increased further due to flexure; cracks were observed to form between the previously developed cracks. Most of these new cracks formed in the region of the slab connected to the beam stem. This indicates that due to the shear lag effect, the slab reinforcements

Preceding page blank

placed at or near the beam stem were subjected to higher flexural stress.

4.2.2 Failure Modes

The observed failure modes of test beams are discussed below. The load-tip deflection of each test beam at the last series of cycles before failure is given in Figs. 4.4 to 4.6 to provide a quantitative indication of the behavior of a beam near its failure stage.

(a) Beams R-1 to R-4 and Beam T-1. - In these beams, failure was initiated by the inelastic buckling of the bottom #5 bars at the region close to the face of the column stub. Since the moment capacity of these beams in the downward direction was greater than that in the upward direction, the bottom concrete and steel bars were subjected to a larger compressive force than the corresponding ones at the top during reversal of the load. Thus, after a number of large loading reversals, the concrete cover in the bottom part of the beam was severely crushed, leaving the compressive #5 bar steel free to buckle between the ties. The inelastic buckling of the main bars could also be triggered or accelerated by the dowel action in the compressive steel due to the existence of open cracks extending across the entire beam section after numerous repeated inelastic load reversals.

The rate of decrease in resistance or strength in successive cycles during failure of these beams can be seen in Figs. 4.4 and 4.5(a). As inelastic buckling occurred, a substantial drop in strength in the downward loading direction was observed. An example of this type of failure is indicated by Beam T-1 shown in Fig. 4.7. This figure shows the beam after additional loading reversals were applied beyond the first observed severe drop in resistance.

(b) Beam T-2. - Failure of this beam occurred at the face of the column stub when loading approached the downward peak of the first cycle [Fig. 4.5(b)]. Failure was caused by the premature fracture of the bottom longitudinal reinforcing bar to which the clip gage support pin was soldered. It is believed that this beam could have withstood more loading cycles if the steel had not failed.

(c) Beams R-5 and R-6. - For these symmetrically reinforced beams ($\rho=\rho'$) failure was indicated by gradually decreasing strength [Figs. 4.6(a) and 4.6(b)]. The failure of these beams is believed to have been caused by the gradual loss of shear resisting capacity in the beam critical region. At the first observation of unloading (LP 62) for Beam R-5, large shear displacement could be seen at the cracks that developed across the entire section of the beam [Fig. 4.8(a)]. After three additional repeated reversals, local buckling of the bottom longitudinal main #6 bar near the column face (beam support) was observed.

(d) Beam T-3. - An unusual mode of failure was observed in this beam. As the beam was being deflected downward toward the peak point (LP 58) of the third cycle at a displacement ductility ratio of four [Fig. 4.6(c)], the splitting cracks previously developed at the beam slab interface near the beam support suddenly widened and extended along the entire length of the slab [Fig. 4.8(b)]. This separation of the slab from the beam portion caused a significant drop in the strength of the beam as indicated in the P-δ response at LP 58, [see Fig. 4.6(c) or 4.9(i)]. Since the shear transfer between slab and beam was ineffective at this stage, the load was mostly resisted by the beam stem, and the contribution of slab reinforcement to the downward moment capacity was reduced, causing a corresponding reduction in load-carrying capacity.

The separation failure is believed to have been caused by the presence of the top four #6 bars near the beam slab interface [(see Fig. 4.8(b)]. As the top bars were subjected

to repeated tension and compression of increasing magnitude, they triggered a splitting crack across the beam at the interconnecting face with the slab where these highly strained steel bars were located [Fig. 4.8(b)]. A large portion of the shear that developed in the slab had to be transferred by aggregate interlocking and friction along the horizontally split crack at the interface. Consequently, after some reversals with large loading amplitude, the interface resistance became increasingly less effective, leading finally to complete separation.

A better design would have been to move the top #6 bars toward the middle surface of the slab and to spread them along the width of the slab. This change in design would have reduced the tendency to initiate cracks (failure planes) resulting from the stress concentration of top bars present near the beam-slab interface. More importantly, if the ties had been extended vertically to the top bars, they could have served as an effective web reinforcement for the horizontal section at the beam-slab interface.

4.3 CONTINUOUSLY RECORDED FORCE-DEFORMATION RELATIONSHIPS

A description of the general characteristics of the continuously recorded beam force-deformation diagrams is given below. In all the hysteretic diagrams shown in Figs. 4.9 to 4.13, the first cycle of each loading step is indicated by solid lines and the repeated cycles, by dashed lines. To identify the test beam, the following basic variables are given in each diagram: the steel ratio, ρ'/ρ_t, where ρ_t is the percentage of top steel and slab reinforcements and ρ' is the percentage of bottom steel reinforcements; the binding ratio, ρ'' (volume of stirrup ties/volume of concrete core); and the span ratio, ℓ/d.

4.3.1 P-δ Diagrams

These diagrams are shown in Figs. 4.9(a) to 4.9(i). The applied load, P, at the tip of the cantilever is plotted against the tip deflection, δ. These diagrams provide the most significant data for evaluating the overall performance of the test beams. The amount of energy dissipated by the beams can be estimated from the area enclosed in the hysteretic P-δ loops. The stiffness deterioration and strength characteristics of the beam can also be readily obtained from these diagrams. To trace the cause of stiffness and strength deteriorations observed in the P-δ response at different stages of loading, as well as to interpret the overall behavior of an R/C beam, it is desirable to know the complete response history of the following deformation components: flexure, shear, and fixed-end rotation. In general, the results indicate that for test beams subjected to reversed bending with small shear (this excludes Beam R-5), the hysteretic P-δ loops are of shapes similar to the corresponding M-ϕ loops [Figs. 4.10(a) to 4.10(h)], indicating that the tip deflection in these beams is governed by flexural deformations. For Beam R-5 with a ℓ/d of 2.75, the P-δ diagram [Fig. 4.9(e)] shows a distinct pinching of loops resulting from a relatively large contribution of shear distortion [Fig. 4.12(d)].

4.3.2 M-ϕ_{av} Diagrams

These diagrams are indicated in Figs. 4.10(a) to 4.10(h). The average curvature in the first 7-in. (d/2) interval vs. moment is plotted for each test beam. Continuous plots of the M-ϕ_{av} for the second 7-in. interval are also given for Beams R-1, R-3, R-5, and T-1. In most beams, the average curvature in the first interval was measured with respect to the column face. Consequently, this measurement included the θ_{FE} due to the slippage of the longitudinal bars in the anchorage zone. Since it is desirable to know the amount of beam deflection caused by the slippage of bars in the anchorage zone, continuous recording of

the θ_{FE} and applied loads was made for Beams T-2 and T-3.

The hysteretic M-ϕ_{av} loops of all test beams were mainly spindle-shaped and reminiscent of the mechanical characteristics of steel under cyclic loading. This can be explained by the fact that after several inelastic cycles, the concrete in the critical region was thoroughly cracked, and remained so for much of the loading history; consequently, the flexural behavior of this region was controlled mainly by the mechanical characteristics of the reinforcing steel. Therefore, the prediction of the M-ϕ_{av} response of test beams while cracks remain open can essentially be based on the hysteretic stress-strain relationship of steel. Such a prediction is presented in Chapter 5.

4.3.3 M-θ_{FE} Diagrams

In these diagrams, shown in Figs. 4.11(a) and 4.11(b), the fixed-end moment, M, vs. the fixed-end rotation, θ_{FE}, caused by the slippage of the main reinforcement from the beam anchorage zone is represented by a continuous curve. For Beam T-2, the beam deflection was increased directly to large ductility without cycling [Fig. 4.9(h)]. The amount of fixed-end rotation that occurred [Fig. 4.11(a)] was considerably smaller than that of Beam T-3 [Fig. 4.11(b)] which was subjected to stepwise increasing load reversals [Fig. 4.9(i)]. The reason for this observed difference in behavior could be due to the increased rate of bond deterioration along the anchored main bars of Beam T-3 caused by the effect of loading reversals.

4.3.4 V-γ_{av} Diagrams

These diagrams are shown in Figs. 4.12(a) to 4.12(g). The applied shear force, V, is plotted aginst the average angle of distortion, γ_{av}, measured in the region within 1-1/2 in. to 14 in. (one d) from the fixed end of the cantilever.

When similar deflection cycles were carried out at a loading step, the shear distortion increased from cycle to cycle, and no stabilization of loops was observed. This lack of stabilization increased as the tip displacement was increased, indicating that the shear stiffness in the critical region is highly susceptible to deterioration under cyclic loading. The magnitude of shear distortion and the rate of deterioration seem to be proportional to the magnitude of the applied tip deflection.

After a number of cycles in the inelastic range and the start of each reloading near zero load, the loops exhibited very low stiffness. The explanation for this low reloading stiffness is as follows. Due to the previous load reversals, flexural and diagonal tension cracks occurred on both sides of the beam. Since the reinforcement was strained inelastically, these cracks remained open after unloading. At reloading, the shear was mostly resisted by the dowel action of the main reinforcement, the degrading aggregate interlocking, and the friction along the cracks. The stiffness increased again only when the cracks closed, the effectiveness of interlocking and friction increased, and the composite action of the concrete and the web reinforcement started to resist shear. The wider the crack width and the greater the number of reversals, the less effective will be the aggregate interlocking resistance and the greater will be the range of low stiffness.

4.3.5 V-ε_{st} Diagrams

The typical variation of steel strain at mid-height of a stirrup in the critical region as a function of the applied shear force is shown in Fig. 4.13(a). The stirrup strain was recorded for the second stirrup-tie of Beam T-3 at about 4.5 in. from the beam fixed-end [Fig. 4.13(b)].

The inclined cracks were first observed when the load was increased to load point A [Fig. 4.13(a)]. Prior to this, nearly all the applied shear had been carried by the concrete, and the stirrup underwent little straining. For example, the measured strain of the second stirrup was relatively small before reaching point A. At load point B, the beam was deflected to a ductility ratio of 1.3, and the stirrup strain increased to 0.0006 in./in.

After the applied shear was released, most of the tensile stirrup strain was recovered at point C. As the loading was reversed, i.e., as the beam was pushed upwards, crack B started to close, while crack C started to widen [loading stage C to C', Fig. 4.13(c)]. During the closure of crack B, the mid-height of the second tie was forced into compression. This reduced the tensile stirrup strain to zero and even resulted in some compression [Fig. 4.13(a)]. However, as crack B closed and crack C developed across the mid-height of the second tie [loading stage C' to D, Fig. 4.13(d)], the transfer of shear across crack C forced the tie into tension. Accordingly, the strain gage reading again registered tension.

4.4 STEEL STRAINS IN THE MAIN BEAM AND SLAB REINFORCEMENT

Steel strain measurements were taken along the main reinforcement in the critically strained regions of the beam and slab. The results of measurements on strains along the reinforcement of the T-beam slab near the beam support end are presented in this chapter. Results of measurements for strains along the portion of the main reinforcement embedded in the anchorage zone close to the beam-column interface and those along the main reinforcement in the critical region of the beam will be presented in Chapters 5 and 6.

4.4.1 Strain Variation along Reinforcement of T-Beam Slab

The measured strains in the #2 slab reinforcements at a section close to the fixed end of the beam are plotted in Figs. 4.14(a) and 4.14(b) for Beams T-2 and T-3, respectively. The corresponding stress values determined by the hysteretic steel σ-ε relationship model (Sect. A5.1) are also shown in these figures.

For Beam T-2, microdot strain gages were used to measure the strain of #2 slab reinforcement located at a section 4 in. away from the column face. Unfortunately, most gages failed immediately after LP 6 ($\delta/\delta_y = 2$) during the initial monotonic loading; hence, little data were obtained. For the cyclically loaded beam, T-3, clip gages were used to measure the average strains in the slab reinforcements, thereby permitting large strain readings.

The results generally indicated that during the post-yield loadings, the inner slab reinforcing bars close to the beam stem experienced greater straining than the outer reinforcing bars. This lag in steel strains increased with the magnitude of deflection applied at the tip of the beam. On the other hand, stress variation across the width of the slab was not appreciable at the recorded peak loading points. This is because the steel had yielded at the peak of inelastic cycles, making the maximum steel stress insensitive to the increase in inelastic strains.

4.5 STRENGTH, DEFORMATION AND ENERGY DISSIPATION CAPACITIES

The measured strengths at some of the most significant limits of usefulness are compared with the computed strengths to identify the potential variations between actual and predicted load resisting capacities of flexural critical regions. The limits of usefulness considered are at cracking, yield, and maximum loads reached before failure of the beam. The experimental values of these strengths are listed in Table 4.1. The computed cracking and yielding loads are found in Table 2.2. The strengths were either expressed as the applied tip force, P or V,

or as the fixed-end moment, M, of the beam.

For each beam tested, Table 4.1 also lists the value of the tip deflection at the first yielding of the reinforcement, as well as the maximum value attained for this deflection. The ratio of deflection, usually defined as the displacement or deflection ductility factor, is shown in Fig. 4.2 together with the average curvature ductility factor, defined as the ratio of maximum average curvature at a region to the average curvature at the first yielding of the main reinforcement; and the steel strain ductility factor, defined as the ratio of maximum average strain induced at certain steel regions to the average strain at the first yielding.

Also included in the table is the cyclic deflection ductility factor, μ_δ^t [1.6]. This value is obtained by dividing the maximum total deformation which occurred in one full reversal before failure, δ_t, by the yield deflection, δ_y (Fig. 4.15). This parameter is useful for indicating the overall ductility that can be achieved during the most severe cycle of reversed deformation.

The expression for the maximum plastic rotation, θ_{PL}, and the cyclic maximum plastic rotation, θ_{PL}^t, is shown in Fig. 4.15. The quantity θ_{PL} is equal to $|\delta_{max} - \delta_y|/\ell$ where δ_{max} is the maximum tip deflection in any loading direction (upward or downward). Physically, θ_{PL} corresponds to the plastic rotation of the girder end when the girder is deformed in a double curvature deflection curve under lateral seismic loading (Fig. 2.2). The quantity θ_{PL}^t is equal to $|\delta_t - \delta_y|/\ell$, which is the maximum amount of plastic rotation achieved in one full reversal before failure.

It should be noted that the values of the ductility factor and the maximum plastic rotation listed in Table 4.2 are dependent on the loading or deformation history selected for the beam (Sect. 3.4). Therefore, in comparing the ductility factors and maximum plastic rotations between test beams, differences in the loading history should be considered.

The energy dissipation capacity is estimated from the sum of areas enclosed in the P-δ loops before failure occurs. Because its magnitude is affected by the history of force-deformation response before failure, it is a better index than ductility factors and plastic rotations for evaluating the relative performance of test beams.

The following observations can be made from the values listed in Tables 2.2, 4.1, and 4.2:

(1) As shown in Table 4.1, the observed downward flexural cracking moment was about 250 k/in. to 300 k/in. for rectangular beams (R-1 to R-6) and about 625 k/in. for T-beams (T-1 to T-3). These values are 10 to 20 percent higher than the computed downward flexural cracking loads, M_{cr}, listed in Table 2.2, assuming that the concrete cracks when stress reaches the value of the modulus of concrete rupture, f_r (Table 2.1).

(2) The observed yielding moment of rectangular beams was about 1500 k/in. in the downward direction and about 850 k/in. in the upward direction. For T-beams, the yielding moment in the downward direction with top steel in tension was about 2000 k/in. or about 33 percent greater than that of rectangular beams (Table 4.1). These observed values of yielding moment, although slightly higher, generally agree well with the values computed for ultimate flexural strength, M_u, using the ACI Code (Table 2.2). It should be noted, however, that the computed value of M_u is based on internal section forces corresponding to a peak compressive concrete strain of -0.003 in./in. rather than on first yielding of steel. The reason for this close agreement can be explained by the small change of internal moment

after yielding of the tensile steel, to the time when concrete strain reached -0.003 in./in. As the tensile steel yielded, the internal moment was controlled by the yielding force and the moment arm between tensile force and resultant compressive force. Due to the relatively small depth of the compression zone after yielding, the moment arm barely changed. Correspondingly, changes in the internal moment were small.

(3) Deflection ductility factors were consistently lower than other ductility factors while steel strain ductility factors were the highest observed (Table 4.2).

(4) Beams T-2 and R-4, loaded monotonically in one direction, attained greater deflection and curvature ductilities than beams subjected to stepwise increasing cyclic loading (Table 4.2).

(5) Cyclic deflection ductility factors were greater than the corresponding deflection ductility factors. This is due to the fact that the total deflection amplitude reached in each beam was greater than that reached in only one direction (Table 4.2). A similar observation was made between the relationship of maximum and maximum cyclic plastic rotation.

(6) The maximum plastic rotations achieved in test beams ranged from 0.026 rad. to 0.058 rad. (Table 4.2). Beam R-5, which was subjected to a series of stepwise increasing load reversals, had the smallest value of θ_{PL} among the beams. The largest value of θ_{PL} was attained by Beam R-4 subjected to a monotonically increasing load. Since an efficient design of a ductile moment-resisting space frame against severe earthquake excitations requires an expected maximum plastic rotation on the order of 0.03 rads. [1.7], the design of critical regions of the test beams can be considered to be satisfactory.

(7) The energy dissipation values, E_{diss}, listed in Table 4.2 indicate superior energy dissipation capacity for beams with a greater amount of bottom reinforcement, R-6 and T-3. The increase in E_{diss} ranges from 27 to 54 percent. From 74 to 120 percent more energy is dissipated in beams subjected to stepwise increased loading and/or deformation than that in the corresponding beams subjected to cycling between large deflection limits. This can be seen by comparing the E_{diss} for Beams T-1 and R-3 with that of Beams T-2 and R-4. The results also showed a 75 percent improvement in energy dissipation for beams wherein a supplementary hairpin tie was provided for restraining the bottom center bar which was not supported by the corners of the stirrup tie. This is clearly seen by comparing the E_{diss} of Beam R-1 with that of Beam R-3.

4.6 TEST RESULTS REGARDING EFFECTS OF MAIN PARAMETERS

Table 2.3 shows the variation of parameters in each test beam.

4.6.1 Effect of Loading History

(a) Effect of repeated load reversals.- The effect of applying load reversals at working stress levels can be seen by comparing the initial responses of rectangular beams R-3 and R-4, and T-beams T-1 and T-2 as shown in Fig. 4.16. Three cycles at a working stress level were carried out only for Beams R-3 and T-1 before being loaded to yielding in the downward direction. This limited cycling did not seem to affect the initial response or the developed yielding strength of the beam. The behavior of test beams was mainly affected by loading reversals in the inelastic range when yielding capacities of the test beams were exceeded in the two loading direction.

It was found that for unsymmetrically reinforced beams, T-1 and R-3, repeated full bending and shear reversals with increasing deformation tended to induce early spalling

of concrete on the less reinforced side of the beam. The spalling of the concrete and the development of dowel action in the compressive steel led the beam to fail by the inelastic buckling of the bottom bars. The flexural failure mechanism of these beams can be summarized as follows:

(1) Since the bottom steel area of most beams was smaller than that at the top, as the beam was deflected to the peak of downward loading, the previously opened bottom cracks had to be closed in order to develop the compressive force required to counterbalance the tensile force at the top. Therefore, the bottom concrete cover was compressed at each downward loading.

(2) At the peak of upward loading, as the bottom side of the beam was strained in tension, the wedging action of the reinforcing bar lug caused splitting cracks to develop along these highly strained steel bars. These cracks joined the vertical flexural cracks and caused the concrete cover to fracture into pieces. Therefore, as the beam was cycled between increasing limits of deformation, the extent of damage sustained by the bottom concrete cover increased. The cover soon crushed and eventually spalled off under compression. Compressive steel restraint against inelastic buckling was reduced to tie restraint. The buckling failure of these bars could be triggered and/or accelerated by the development of large dowel action as a result of cracks traversing the entire section after numerous large inelastic load reversals. Under monotonically increasing loads, the concrete in the bottom compression zone was under constant compression and was not subjected to damage from the action of alternating tension and compression as described above. Furthermore, since the concrete remained uncracked, the shear resistance provided by the compression zone was relatively large. Consequently, monotonically loaded beams R-4 and T-2 were able to attain a higher ductility level in the downward loading direction than the corresponding cyclically loaded beams, R-3 and T-1, without inducing flexural failure [Figs. 4.9(d) and 4.9(h)].

(b) Effect of applying unsymmetrical inelastic loading reversals. - This effect is studied by evaluating the relative performances of similar beams, R-1 and R-2. In the loading of Beam R-2 [Fig. 3.10(a)], the beam was deflected to yield first in the upward direction. Several cycles of loading and unloading in this direction up to a ductility ratio of three followed, after which the beam was loaded in the downward direction.

The results showed that the difference in loading pattern in Beams R-1 and R-2 [see Figs. 3.9(a) and 3.10(a)] did not cause a change in the mode of failure: both beams failed due to local inelastic buckling of the bottom #5 bars. The energy dissipated in Beam R-2 before failure was 267 k/in. which is 20 percent less than the 335 k/in. dissipated in Beam R-1 subjected to a symmetrical deformation pattern [Fig. 3.9(a)].

The relatively early failure of Beam R-2 can be explained by the fact that this beam was repeatedly deflected to a greater deflection limit in the upward direction prior to failure; thus, more cracking and splitting of the bottom concrete cover occurred in Beam R-2. Therefore, as the beam was deflected downwards, with the bottom side under compression, the fractured bottom concrete cover in the critical region did not offer significant lateral restraint to the bottom compressive #5 steel bars. As a result, inelastic buckling was initiated in the downward direction at a ductility ratio of 2.8, a value less than the ductility ratio of 4.28 reached by Beam R-1.

4.6.2 Effect of Floor Slab in T-beams

The effect of the composite action between floor slab and girder on the inelastic behavior of the R/C critical region close to column connections was studied by comparing

the relative performances of Beams R-3 and T-1. The P-δ responses of Beams T-1 and R-3 are superimposed in Fig. 4.17(a) with the response of Beam R-3 drawn in solid lines and that of Beam T-1 in dashed lines.

Comparison of the hysteretic loops of the two beams indicates that they offer similar resistance in the upward direction. This was as expected since strength in the upward direction for both beams is controlled by the bottom steel with three #5 bars.

The general stiffness characteristics of the two beams can be seen in the slope variation of the P-δ response [Fig. 4.17(a)]. Attention is drawn to the similarity between the stiffness characteristics of the two beams during the upward and initial downward loading before stiffness increased due to the closure of the bottom cracks at about 14 kips. After a couple of cycles of inelastic reversals during the early stages of loading, cracks crossed the entire beam section and remained open. At these stages, the moment was carried only by the top and the bottom steel. Since the main reinforcement used for both beams is the same, the stiffness characteristics during these stages of response are therefore similar.

As the beam was deflected toward the peak of downward loading, the bottom cracks finally closed and the stiffness increased, resulting in a distinct pinching of the hysteretic loops of both beams. A small amount of shear pinching at small load can also be observed in these loops. This shear pinching becomes progressively more pronounced as the number of cycles increases. Such behavior is apparently caused by the progressively increased contribution of shear distortion in the tip deflection of the beam [Figs. 4.12(b) and 4.12(f)].

The energy dissipated per cycle in the two beams can be compared in Fig. 4.17(b) with the number of cycles. The results indicate that the amount of energy dissipated per cycle in Beam T-1 was consistently greater than that in Beam R-3. However, due to an earlier failure in Beam T-1 the total amount of energy dissipated in Beam T-1 was less than that of Beam R-3 (519 k/in. vs. 583 k/in.).

4.6.3 Effect of Relative Amounts of Top and Bottom Reinforcement

Since the moment capacities of test beams in the two loading directions are controlled by the amount of corresponding tensile steel reinforcements, the effect of relative moment capacities in the two loading directions is used to study the effect of relative amounts of top and bottom reinforcement.

Test results of rectangular beams R-3 and R-6 and T-beams T-1 and T-3 were selected for analysis. The amount of bottom steel was varied, using either three #5 bars (Beams R-3 and T-1) or four #6 bars (Beams R-6 and T-3).

The general effect of relative amounts of top and bottom steel reinforcement on the stiffness, strength, and energy dissipation capacities of the R/C beam is discussed based on the behavior of Beams T-1 and T-3. Similar results were obtained from the behavior of Beams R-3 and R-6. A comparison between the P-δ response of Beam T-3, indicated by dashed lines, and that of Beam T-1, by solid lines, is shown in Fig. 4.18.

Because of the larger amount of bottom steel used in Beam T-3, the moment developed during the peak upward loadings was greater than that of Beam T-1 (Fig. 4.18). As a result, there was more energy dissipated in Beam T-3 during the half-cycle loading in the upward direction. The shear applied to Beam T-3 in this direction was also increased; for example, at LP 40 the shear force was 28.5 kips in Beam T-3 (nominal shear stress = 2.95 $\sqrt{f'_c}$),

and 16.1 kips in Beam T-1, (nominal shear stress = 1.62 $\sqrt{f'_c}$). The increased shear caused more shear distortion to occur in Beam T-3 than in T-1 (Tables 4.3g and 4.3i), although the magnitude of the shear distortion was still small: below 12 percent of the tip deflection, up to a ductility ratio of four at LP 52 (Table 4.3i).

The reason for the small contribution of shear distortion in Beam T-3 is that the increased shear applied in the upward direction was still small, i.e., below $3\sqrt{f'_c}$, while the shear capacity was large. This large shear capacity is attributed to the double stirrup-tie reinforcements spaced at d/4 intervals in the web.*

The total energy dissipated in Beam T-3 before failure was 803 k/in., which is 54 percent higher than that (519 k/in.) dissipated in Beam T-1 (Table 4.2). This increase in the energy dissipation of Beam T-3 is a consequence of the higher moment developed in the upward direction and of the early failure of Beam T-1 due to local buckling of the bottom #5 bars near the beam support. Since Beam T-1 has less steel in the bottom than the top, the bottom concrete must take a higher percentage of compression, making it more compressed during downward loadings. Thus, the concrete cover tends to spall off sooner, leaving the bottom bar unrestrained against buckling between the ties. This made it more difficult to maintain moment capacity in the downward direction. An additional factor for the early failure was due to the fact that the bottom bar #5 used in Beam T-1 has smaller than that (#6) used in Beam T-3. For the same restrained length, the smaller bar proves more vunerable to buckling failure since it has a lower buckling strength. An indication of the relative buckling strength of #5 and #6 bars can be seen by the ratio of moment of inertias of the two bars (0.48).

4.6.4 Effect of Supplementary Ties

The failure of the first two beams, R-1 and R-2, was caused by the buckling of the center bottom #5 bar which was not directly restrained by the corner of ties (Fig. 2.7). It was thought that an improved performance could be obtained by providing supplementary ties in the form of hairpins (Fig. 2.7) to restrain directly the center #5 bar from early buckling. To investigate this effect, Beam R-3, with hairpin ties, was tested under a loading history similar to that used for the test of Beam R-1 [Fig. 3.9(a)]. As a result of added hairpin ties in Beam R-3, not only were all the main bars restrained, but the amount of concrete confinement and the shear-resisting capacity of the beam were correspondingly increased. The binding ratio was increased from 0.0053 to 0.010, and the calculated shear capacity, from 42.8 kips to 66.9 kips (Tables 2.1 and 2.2).

The test results indicate that the major effect of added hairpin ties in Beam R-3 was to delay the buckling of the bottom center #5 bar. Consequently, the moment resistance of Beam R-3 was maintained up to a ductility level of about five and failed in the second cycle at this ductility due to the inelastic buckling of bottom #5 bars. On the other hand, for Beam R-1, buckling failure occurred earlier in the second cycle at a ductility level of about four.

The improved performance of Beam R-3 is best indicated by the relative amounts of energy dissipated in the two beams. The results show a value of 583 k/in. dissipated in Beam R-3, as compared with the 335 k/in. dissipated in Beam R-1, an increase of 74 percent (Table 4.2).

---

* The shear capacity of web reinforcement, V_s, was about 40 percent higher than the maximum applied shear, V_{max} (Tables 2.2 and 4.1).

4.6.5 Effect of High Shear Force

The study of the effect of high shear force on the inelastic behavior of the R/C critical region is based on test results of the two symmetrically reinforced beams, R-5 and R-6, subjected to a stepwise increasing loading program (Table 2.3). The maximum nominal shear stresses, V_{max}/bd, induced during inelastic reversals are $5.3\sqrt{f'_c}$ for Beam R-5 and $3.5\sqrt{f'_c}$ for Beam R-6 (Table 4.1).

The effect of shear became significant after the flexural steel was strained to yielding. For the short beam, R-5, the contribution of shear distortion to the tip deflection increased from 8.6 percent at initial yielding (LP 26) to 36.5 percent at a δ/δ_y of about four (LP 62) at the first distinct decrease in strength. In the corresponding beam, R-6, the increase was from 2.4 percent at initial yielding (LP 14) to 12.2 percent at a δ/δ_y of about four. In Beam R-5, the shear force acting in the two loading directions was larger than that of Beam R-6. This led to more grinding and crushing of the concrete along shear cracks in the critical region of Beam R-5. Shear degradation was consequently larger, and caused more shear distortion as well as a stronger pinching of hysteretic P-δ loops at large ductility cycles, Fig. 4.19. To facilitate comparison, the P-δ loops in this figure are plotted in nondimensional scales, P/P_y and δ/δ_y.

The energy dissipated in Beam R-6 computed from the area enclosed in P-δ loops before failure was 738 k/in. versus a value of 349 k/in. dissipated in Beam R-5, i.e., a ratio of two-to-one. The lower amount of energy dissipated in Beam R-5 is mainly due to a higher degree of degradation of shear resistance which occurred in the critical region of Beam R-5 with an increasing number of inelastic load reversals.

A more deatiled discussion of the effect of shear on the behavior of beam critical regions is presented in Chapter 7.

A4. APPENDIX TO CHAPTER 4

ESTIMATION OF TIP DEFLECTION COMPONENTS

Tables 4.3a to 4.3i summarize the contribution of each displacement component to total tip deflection at different load points for each test beam. Similar information is given graphically in Figs. A4.1 to A4.8, which illustrate the importance of each component. The amount of error involved in the interpretation of data is also indicated in these figures.

The tip deflection is assumed to be a summation of three basic displacement components:

$$\delta_{Tip} = \delta_{Flex} + \delta_{Shear} + \delta_{FE} \tag{A4.1}$$

The quantity δ_{Flex} is the estimated contribution from flexural deformation occurring in the beam. This quantity is further subdivided into $\delta_{Flex\ 1}$ and $\delta_{Flex\ 2}$, where $\delta_{Flex\ 1}$ is caused by the flexural deformation within one d (14 in.) from the beam fixed-end. The quantity $\delta_{Flex\ 2}$ accounts for the flexural deformation contributed by the remainder of the beam. The quantity $\delta_{Flex\ 1}$ is estimated from readings of clip gages placed on the main bars over the distances of 0 to 7 in. and 7 in. to 14 in. from the beam fixed-end. The value of $\delta_{Flex\ 2}$ is calculated from the clip gage readings in the beam span 14 in. to 21 in. from the beam fixed-end and from the deflection in the remainder of the beam by assuming a triangular curvature distribution:

$$\delta_{Flex\ 2} = \theta_3 L_3 + \frac{1}{3}\frac{PL_2^3}{(EI)_2} \tag{A4.2}$$

where θ_3 is the measured rotation over the third 7-in. interval (14 in. to 21 in.); L_3 is the effective arm; and L_2, the length of the remainder of the beam. The sectional stiffness, $(EI)_2$, is estimated from the initial unloading stiffness in the recorded M-ϕ_2 diagrams, i.e., from LP A to LP B (Fig. A4.9).

The measured values of $(EI)_2$ are observed to be up to 15 percent greater than the values calculated for cracked concrete sections using moment-curvature analysis as described in Chapter 5.

The quantity δ_{Shear} represents the amount of shear distortion taking place in the critical region. This value is equal to the average shear distortion, γ_{av} [Figs. 4.12(a) to 4.12(g)], times the length of the region (12.5 in.) over which shear distortion measurements were taken.

The quantity δ_{FE} is estimated from the rotation of the beam fixed-end, θ_{FE}, by multiplying θ_{FE} by the length of the beam. This quantity includes the support rotation and the relative rotation occurring at the interface of the cantilever beam and the anchorage block due to slippage of the main bars from the anchorage zone. The support rotation has been measured with dial gages and was found to contribute only a negligible amount to the tip deflection. For most of the test beams, θ_{FE} was calculated by substituting the rotations which took place in the beam from the measured tip rotation, θ_{Tip}:

$$\theta_{FE} = \theta_{Tip} - (\theta_{Flex\ 1} + \theta_{Flex\ 2}) \tag{A4.3}$$

This method of determining θ_{FE} is considered to be fairly accurate, since θ_{Tip} is directly measured from the tip of the cantilever beam [Sect. 3.2(a)], and $\theta_{Flex\ 1}$ is measured from clip gages mounted on the longitudinal reinforcement over the first 14 in. (one d) from the beam support face. Quantity $\theta_{FLEX\ 2}$ is computed from θ_3 (Eq. A4.2) and from assuming a triangular curvature distribution in the remainder of the beam. The possible error in $\theta_{FLEX\ 2}$ is not expected

Preceding page blank

to be important since most of the inelastic deformation at the peak of inelastic cycles occurred within one d from the beam support face. For Beams T-2 and T-3, directly measured θ_{FE} quantities were used. Data on θ_{Tip} for Beams R-2 and R-5 were lost due to a malfunctioning in the scanner equipment. For these cases, the fixed-end rotation was estimated from photogrammetric measurements (Sect. 3.3).

The agreement in percentage between estimated tip deflection, δ_{Tip}, and the measured deflection, δ_{Meas}, is indicated in column 8 of Tables 4.3a to 4.3i. The general agreement between the measured and estimated δ is fairly good. The contribution of each component to the total δ_{Meas} is listed in the bottom half of the table.

The possible sources of error are discussed below:

(1) In the case of Beam R-1, data on δ_{Shear} were not available and therefore not included in the estimated δ. The results in Table 4.3a show that the estimated values of δ are consistently lower (about 15 percent less) than those measured. If δ_{Shear} had been included, the agreement might have been better.

(2) In all beams, only the shear distortion in the region 1.5 in. to 14.0 in. from the beam fixed-end was accounted for. Therefore, one source of error is from neglecting the contribution of shear distortion from the remainder of the beam, especially at the 1.5 in. region adjacent to the face of the column, where, in most of the beams, large cracks opened up, enabling relatively large shear distortion to take place.

(3) Other sources of errors are introduced from making calculations, reading data, and from inherent inaccuracies in the measuring devices.

The results in Tables 4.3a to 4.3i indicate that the contribution of shear distortion to tip deflection was relatively small (less than 13 percent) in the test beams with a ℓ/d of 4.46. On the other hand, the shear distortion of Beam R-5 with a ℓ/d of 2.75 contributed to 36.5 percent of the total δ_{Meas}. Both the fixed-end rotation and the flexural component account for a large portion of the tip deflection in all beams. For beams subjected to monotonic loading, Beams R-4 and T-2, the percentage of δ_{FE} tends to decrease with increasing tip deflection, and an increased contribution from flexural deformation may be observed (Tables 4.3d and 4.3h). The opposite behavior is true for beams subjected to repeated reversed loading. This indicates that bond along the embedment length of bars tends to deteriorate more under cyclic, rather than monotonically increased, loading. This bond deterioration, in turn, causes a corresponding increase in degradation of initial stiffness which gives rise to an increase in the overall flexibility of the beam.

5. EVALUATION OF FLEXURAL BEHAVIOR

5.1 GENERAL REMARKS

The results reported in the preceding chapter show that the inelastic flexural behavior of the critical region has a significant effect on the general inelastic behavior of the beams tested. This can be noted by comparing the general characteristics of load vs. tip deflection (P-δ) hysteretic loops [Figs. 4.9(a)-4.9(i)] with those of moment-average curvature (M-ϕ_{av}) loops taken within a distance of one d from the fixed-end of the beam [Figs. 4.10(a)-4.10(h)]. The estimated components of tip deflection listed in Tables 4.3a to 4.3i indicate that a large component of δ can be attributed to the inelastic flexural deformation taking place in the region near the fixed-end of the beam. The shape of both the P-δ and M-ϕ_{av} loops suggests the strong influence of the Bauschinger effect of steel.

According to the results, it is therefore desirable to investigate the possibility of predicting the measured inelastic moment-average curvature response within the critical region on the basis of the mechanical behavior of the constituent materials, i.e., the reinforcing steel and the concrete. This would provide a better understanding of the basic flexural resistance mechanism operating during inelastic load reversals.

The M-ϕ_{av} analysis reported in this chapter is based on equilibrium and compatibility conditions for a beam section with the appropriate stress-strain relationships of steel and concrete. A computer program was written for implementing this analysis. The description of the program is given in Sect. 5.2, where the method of analysis and the assumptions on which the method is based are also discussed. The material hysteretic stress-strain models of reinforcing steel and concrete to be used in the M-ϕ_{av} analysis are presented in the appendix to this chapter.

The effects of loading history, steel ratio, ρ'/ρ, and slab on T-beams were studied by computing the moment-average curvature of the R/C beam sections shown in Fig. 2.3. The moment-average curvature response of some long-span test beams ($\ell/d = 4.46$) was predicted and compared with the experimental results.

5.2 COMPUTER PROGRAM

A computer program, CYCMC, has been written for the purpose of computing the moment-curvature response of general R/C regions under cyclic loading with or without axial load.

Since the cyclic moment-curvature response is history dependent, the analysis is carried out incrementally. The loading history to be studied is defined by a series of curvature points. Other required input data include (1) stress-strain relationships for both top and bottom reinforcement obtained from experiments with monotonically increasing loads; (2) parameters defining the confinement of concrete; and (3) the applied axial load. The flow chart for the computer program is given in Fig. 5.1 and the specifications for preparing the input data are given in Appendix A5.3.

5.3 ANALYSIS METHOD AND IDEALIZATIONS

To predict the cyclic moment-curvature response of R/C regions subjected to bending reversals, the R/C region is discretized into imaginary layers or fibers of steel and concrete [Fig. 5.2(a)] as done in Ref. 1.5. These layers are allowed to stretch and contract axially under flexure.

The longitudinal strain in the steel and concrete at various levels is assumed to be directly proportional to the distance from the neutral axis [Fig. 5.2(b)], i.e., a linear strain-distribution across the beam section is assumed. The loss of concrete strength due to cracking under tension is accounted for by assigning zero stiffness to the cracked concrete fibers. With this idealization [Fig. 5.2(b)], the strain at each material layer is given by:

$$\varepsilon_s^t \text{ (top steel)} = \varepsilon_{c_{max}} + \phi d \tag{5.1}$$

$$\varepsilon_s^b \text{ (bottom steel)} = \varepsilon_{c_{max}} + \phi d' \tag{5.2}$$

and

$$\varepsilon_{c_i} = \varepsilon_{c_{max}} + \phi d' \tag{5.3}$$

where

ϕ = curvature

$\varepsilon_{c_{max}}$ = concrete strain in extreme compression layer

d = distance from extreme compression side to centroid of top steel

d' = distance from extreme compression side to centroid of bottom steel

y_i = distance from bottom side to i^{th} material layer.

The corresponding stress in each material layer is computed from the corresponding σ-ε relation specified by the hysteretic models for concrete or steel (Sects. A5.1 and A5.2). The internal resisting forces (axial force and moment) are obtained by summing the forces in each layer as follows [Fig. 5.2(b)]:

$$\text{Net section axial force } N = C_c + C_s + T_s \tag{5.4}$$

where C_c is the force resisted by the concrete and is given by:

$$C_c = \sum_{i=1}^{m} \sigma_{c_i}\, b_f \frac{h_f}{m} + \sum_{i=m}^{n+m} \sigma_{c_i}\, b_w \frac{h_w}{n} \tag{5.5}$$

in which

m = number of concrete layers in flange

n = number of concrete layers in beam web

σ_{c_i} = stress in i^{th} concrete layer

b_f, h_f = width and depth of flange, respectively

b_w, h_w = width and depth of beam web (stem), respectively

The forces resisted by tensile and compressive steel are:

$$T_s = A_s\, \sigma_s \text{ and } C_s = A_s'\, \sigma_s' \tag{5.6}$$

The internal resisting moment is obtained by summing the forces in the material layers and multiplying by the respective moment arms; thus:

$$M = \sum_{i=1}^{m} \left(\sigma_{c_i}\, b_f \frac{h_f}{m}\right) y_i + \sum_{i=m}^{n+m} \left(\sigma_{c_i}\, b_w \frac{h_w}{n}\right) y_i + A_s'\, \sigma_s'\, d' + A_s \sigma_s d + N \cdot e_p \tag{5.7}$$

where e_p is the distance from the bottom side to the plastic centroid of the section.

5.4 STEP-BY-STEP DETERMINATION OF INTERNAL MOMENT FOR A PRESCRIBED SECTION DEFORMATION HISTORY

Before calculating the internal resisting moment, M, from Eq. 5.7 for each curvature point in the prescribed loading history (Fig. 5.3), it is necessary to establish the correct strain distribution in the section in order to satisfy equilibrium and compatibility conditions.

Since linear distribution is assumed across the depth of the section and the slope of the strain distribution is given by the curvature, $d\varepsilon(y)/dy = \phi$ (Fig. 5.3), a strain distribution which will satisfy the force equilibrium condition must be sought. The method usually adopted by other investigators [1.16, 5.1] is to adjust the neutral axis position until the equilibrium condition is satisfied.

Under cyclic loading, the neutral axis can vary from $\pm\infty$ to $\mp\infty$ many times as the curvature changes sign at zero curvature value. Adjusting the neutral axis position within this wide range of values usually requires many iterations to converge [5.1] and is therefore undesirable. To overcome this difficulty, a more efficient method has been devised in the present computer program. The basic numerical procedure is illustrated by an example shown in Fig. 5.4.

For a given curvature, ϕ_i, the problem is to determine a strain distribution, ζ_{ϕ_i}, with forces C and T which will satisfy the equilibrium condition whereby C + T = 0 (equilibrium is checked in the program against a user-specified force tolerance). The basic computation steps are explained below:

(1) Establish two strain distributions, $\zeta_{\phi_i}^1$ and $\zeta_{\phi_i}^2$ [indicated by dashed lines in Fig. 5.4(a)] with reference to the previous strain distribution at ϕ_{i-1} or $\zeta_{\phi_{i-1}}$ [indicated by the solid line in Fig. 5.4(a)] for which the equilibrium condition has been satisfied (300 - 300 = 0). Strain distribution $\zeta_{\phi_i}^1$ has the same tensile steel strain, ε_s, as that of $\zeta_{\phi_{i-1}}$, while $\zeta_{\phi_i}^2$ has the same value as $\varepsilon_{c_{max}}$. Since $\phi_i > \phi_{i-1}$, strain distribution $\zeta_{\phi_i}^1$ causes more concrete to be in compression, and the sum of $T^1 + C^1$ is negative, i.e., -700 compression [Fig. 5.4(b)]. Since strain distribution $\zeta_{\phi_i}^2$ creates more tensile force in the top steel, the sum of $T^2 + C^2$ is positive, i.e., +750 in tension [Fig. 5.4(c)].

(2) Since neither $\zeta_{\phi_i}^1$ nor $\zeta_{\phi_i}^2$ satisfies the force equilibrium criterion of C + T = 0, a new strain distributor, $\zeta_{\phi_i}^3$ is established by taking the average of $\zeta_{\phi_i}^1$ and $\zeta_{\phi_i}^2$ [Fig. 5.4(d)] For example, the strain for $\zeta_{\phi_i}^3$ at level y_i is $\varepsilon^3(y_i) = 1/2\ [\varepsilon^1(y_i) + \varepsilon^2(y_i)]$. The averaged strain distribution, $\zeta_{\phi_i}^3$, gives a better approximation of the solution because if it has an unbalanced force in compression, as in the case shown in Fig. 5.4(e), its magnitude will be less than that of $\zeta_{\phi_i}^1$ [Fig. 5.4(b)], since $C^3 > C^1$ and $T^3 > T^1$. Similarly, if the sum of C + T in $\zeta_{\phi_i}^3$ is in tension, the result will be less unbalanced tensile force than that in $\zeta_{\phi_i}^2$ [Fig. 5.4(c)], since $C^3 < C^2$ and $T^3 < T^2$. Therefore, one can always obtain a strain distribution that gives a better equilibrium balance by repeating the averaging procedure [Figs. 5.4(f) and 5.4(g)].

It was found that generally not more than five trials are needed to converge to the strain distribution of less than 1 percent unbalanced force. After the correct strain distribution is established, the corresponding internal resisting moment is computed from Eq. 5.7.

The above described procedure is carried out in a stepwise manner for each curvature point in the loading history. Therefore, a complete moment-curvature response of the R/C beam section can be obtained.

5.5 REQUIRED COMPUTING TIME

The M-ϕ analysis procedure was coded in FORTRAN for execution on a CDC 6400 computer. For solving a complete M-ϕ response of Beam R-3 (Fig. 5.11) consisting of about 170 curvature points, the central computer processing (CP) time was about 7.5 seconds and peripheral processing (PP) time was about 3.7 seconds.

5.6 EXAMPLES OF MOMENT-CURVATURE ANALYSIS

The method of analysis described in Sects. 5.3 and 5.4 is used for predicting the M-ϕ response of critical R/C regions subjected to reversed bending and shear. There are, however, a number of limitations inherent in this approach and these should be kept in mind when the proposed analytical method is applied:

(1) It has been tacitly assumed that cracking takes place mainly in a vertical plane perpendicular to the axis of bending. This assumption is acceptable for analyzing the M-ϕ response of the beams in which the critical regions are subject to bending with small shear. In this case, the concrete cracking is mainly controlled by flexure, and, consequently, takes place in nearly vertical planes. For Beam R-5 which is subjected to bending with high shear, the cracks in the critical region are strongly inclined; therefore, equilibrium should be taken at an inclined cracked section rather than on a vertical plane. Thus, the application of the described M-ϕ analysis procedure for this case is questionable.

(2) A continuous displacement field---linear strain distribution---is assumed in the layered system. The possible relative movement between the adjacent concrete and steel layers caused by failure of the composite action (bond) is not simulated nor is the variation in concrete and steel stress strain between cracks accounted for.

(3) The obtained M vs. ϕ curve represents an effective moment vs. average curvature of a region between two main cracks, or more precisely, of a region bridging a main crack having a length equal to the spacing of the main flexural crack.

(4) The influence of shear deformation in the critical region on the flexural force-deformation, M-ϕ response, was not considered (Sect. 5.10.2).

5.7 EFFECTS OF LOADING REVERSALS ON DIFFERENT BEAM SECTIONS

The M-ϕ response of the four basic sections (Fig. 2.3) used in the experimental program (Chapter 2) under a prescribed history of loading is computed. The prescribed loading program for each section is the same, so that the effect of different section designs can be studied. Two cycles are carried out between maximum curvature values of $\pm$ 0.005 rad./in. (= $\pm$ 20 ϕ_y). This loading history is somewhat similar to the measured M-ϕ_1 history from Beams T-2 and R-4 [Fig. 4.10(d)].

The analytical results of M-ϕ responses of the four sections are given in Figs. 5.5, 5.7(a), and 5.8(a). The corresponding stress-strain responses of top and bottom steel bars are shown in Figs. 5.6, 5.7(b), and 5.8(b). Significant analytical results are listed in Table 5.1. The concrete characteristics used in the analysis are compressive strength, f'_c = 4.6 ksi; concrete strain at f'_c, ε_0 = -0.0225 in./in.; and binding ratio, ρ'' = 0.01. These values are typical of the concrete used in the test beams (Table 2.1 and Fig. 2.10).

In the analyzed beam sections, the web of the beam was discretized into 40 concrete layers; the flange of T-sections, into 5 concrete layers. One top steel layer and one bottom steel layer were used in all sections.

5.7.1 Steel Force-couple Response

It was found that over a large portion of the M-ϕ response, the bending moment was carried by tensile and compressive forces in steel alone, viz., $M = T_s(d-d')$ with $T = C_s$, where T_s and C_s were the forces carried by tensile and compressive steel, respectively. During this stage of the response, the cracks in the compression zone remained open due to the residual inelastic tensile strains in the compressive steel. These residual strains resulted from the previous loading which strained the steel well into the plastic range. Thus, the concrete was not effective in carrying the compressive load. Consequently, the stiffness and strength of the section were determined entirely by the behavior of both the top and bottom steel at this stage of the response. The extent of this stage in the M-ϕ response is shown in Figs. 5.5, 5.7(a), and 5.8(a) by dashed lines. This includes almost all of the reloading curves, except the part toward the ends of the curves where the concrete goes into contact.

The effect of this type of moment-resisting mechanism on the stiffness and strength characteristics of the section is further discussed in the following sections.

5.7.2 Effect of Loading Reversals on Stiffness

The stiffness degradation occurring at different stages of the response is illustrated the M-ϕ diagram for beam section R-6 in Fig. 5.5.

(a) First and second cycles of loading. - As the section was deformed to the peak of downward loading at LP 1, a large inelastic strain was produced in the top steel of Beam R-6 [Fig. 5.6(a)]. As the load reversed to the upward moment region, the stiffness of the section was controlled by the steel force-couple until reaching LP 2A (Fig. 5.5). The stiffness degradation observed at this stage of loading was mainly caused by the cyclic strain-softening (Sect. A5.1.1) which occurred in the top steel as stress reversed from tension to compression, from LP 2 to LP 3 [Fig. 5.6(a)]. The stiffness degradation observed in the second cycle, from LP 3A to LP 4 and from LP 6 to LP 7 (Fig. 5.5), was caused by the cyclic strain-softening of both the top and bottom steel [Fig. 5.6(a) and 5.6(b)]. This strain-softening occurred in the bottom steel after the steel underwent yielding during the previous loading to LP 3.

When the crack closed during loading, the tangential stiffness of the section increased as the concrete resisted part of the compression due to flexure. This trend is observable in the M-ϕ response from LP 4 to LP 5 of beam section R-4 [Fig. 5.5].

(b) Third and subsequent cycles of loading. - From the third cycle on, the section was cycled between the previous deformation (curvature) limits; no further inelastic strain was produced in the top and bottom steel. Because the degradation in stiffness caused by the strain-softening of the steel became stabilized, the response between the second and third cycles was "shaken down" to a stabilized hysteretic loop, thereby producing little stiffness deterioration. In actual cases, some extra degradation could occur due to bond deterioration between the cracks.

5.7.3 Effect of Loading Reversals on Strength

During the stages in which cracks remained open throughout the cross-section, the moment capacity of the beam section was given by:

$$M = F(d-d') \tag{5.8}$$

where F is either the capacity in tension or compression of the top or bottom steel, whichever is smaller, and d-d' is the distance between the top and bottom steel.

5.8 EFFECT OF STEEL RATIO

Beam section R-6 is reinforced with four #6 bars at both the top and bottom, having a steel ratio, ρ'/ρ, of 1.0. Beam R-4 is also reinforced with four #6 bars at the top, but with three #5 bars at the bottom, having a ρ'/ρ equal to 0.53. In every other respect, the two sections are identical. The observed differences in the behavior of these two beam sections is discussed below.

(1) During the monotonic loading from LP 0 to LP 1 (Fig. 5.5) of Beam R-4, the concrete in the compression zone must have a higher percentage of compression. As a result, the neutral axis position is higher [Fig. 5.6(a)], and the tensile strain in the top steel of Beam R-6 at a given curvature is greater. As the loading reached LP 1, yielding occurred in the compressive steel of Beam R-4 but not in that of R-6.

(2) During the upward loading (Fig. 5.5), the moment capacity was controlled by the bottom steel in tension. Beam R-6, with nearly twice as much bottom steel as Beam R-4, was able to carry about twice the amount of moment. This means that about twice the amount of compressive force was being applied on the top steel of R-6. The residual inelastic strain in the top steel of this beam was considerably reduced compared to that of R-4. As loading approached LP 3 (Fig. 5.5), cracks at the top of Beam R-6 could have closed, whereas those in R-4 remained open throughout the loading process from LP 2 to LP 3. During this loading process, considerably more inelastic straining occurred in the bottom steel of R-4 [Fig. 5.6(b)].

(3) The stiffness of Beam R-6 was greater than that of R-4 during unloading from LP 3 to LP 3A (Fig. 5.5). This is due to that fact that the concrete was initially in contact during the unloading of Beam R-6.* From LP 3A to LP 4, the top steel reinforcements of the beam were in tension; the moment was resisted by the top and bottom bars alone. In Beam R-4, the amount of bottom compressive steel was about half the top tensile steel; therefore, the moment was controlled by the compressive force that could be resisted by the bottom steel wherein $M = C_s(d-d')$. For Beam R-6, the full moment capacity corresponding to tensile steel strength could be developed due to the equal amount of tensile and compressive steel.

(4) From LP 4 to LP 5, the bottom crack of Beam R-4 began to close and compressive load was again effectively carried by concrete. This enabled the downward moment capacity to develop and resulted in a sharp increase in sectional stiffness during this loading process. On the other hand, the closure of the bottom crack of Beam R-6 resulted in no significant increase in stiffness. This was because the steel resistance alone permitted nearly the full moment-resisting capacity of the section to develop. For the purpose of increasing the energy dissipated through flexural deformations, it is therefore desirable to keep the steel ratio close to one.

5.9 EFFECT OF SLAB IN T-BEAMS

The longitudinal slab reinforcement for T-beams was also effective in increasing the beam's moment capacity. For this reason, the longitudinal slab reinforcement must be regarded as a part of the top longitudinal reinforcement. In the analysis, the areas of #2 slab reinforcement and the top #6 bars are lumped together as:

$$\text{Total area of top reinforcement} = A_s + A_s'' \qquad (5.9)$$

* Stiffness in Beam R-6 is also provided by four top and bottom #6 bars, compared to four top #6 bars and three bottom #6 bars in Beam R-4.

Effective distance, $d = (f_y A_s d + f''_y A''_s d'')/f_y(A_s + A''_s)$ (5.10)

where

A_s = area of four top #6 bars = 1.76 sq. in.

A''_s = area of twelve #2 slab reinforcement = 0.60 sq. in.

f_y, f''_y = yield strengths of #6 and #2 bars (Table 2.1), respectively

d, d" = distance from the bottom side to the top #6 bars and to the centroid of the slab reinforcement, respectively.

The calculated effective distance for T-beam sections was 14.22 in. as compared with a value of 14 in. for the rectangular beam sections, in this case, Beam R-4.

The concrete in the top flange of the T-beam section did not affect appreciably the inelastic M-ϕ response of these sections. After cracks developed through the T-beam flange and remained open for the remainder of the response history due to the development of residual inelastic tensile strains in the reinforcement, the behavior of the T-beam section became identical to that of the rectangular section with the same amount of top reinforcement. Even if the top cracks were to close under compression during upward loadings, the effect would be to shift the neutral axis toward the top side of the beam section. This shift would then result in a slight increase in the upward moment capacity of the section due to the larger moment arm developed between tensile and compressive forces. This fact can be seen by comparing the upward moment resistance developed in Beam R-4 (Fig. 5.5) with that developed in Beam T-2 [Fig. 5.7(a)].

According to the above discussion, most of the M-ϕ response changes caused by a portion of the slab at the top of the beam section are the result of increasing the area of reinforcement (or the moment capacity) by an amount equal to the area of slab reinforcement. With an increase in the amount of top reinforcement, there would be more tensile steel at the top, and, consequently, an increased downward moment capacity. Considering the slab reinforcement, the distribution of steel at the top and bottom of the four sections is as follows:

$$\begin{aligned} &\text{Section T-2} \quad \rho'/\rho_t = 0.39^* \\ &\text{Section R-4} \quad \rho'/\rho_t = 0.53 \\ &\text{Section T-3} \quad \rho'/\rho_t = 0.75 \\ &\text{Section R-6} \quad \rho'/\rho_t = 1.00 \end{aligned} \tag{5.11}$$

where ρ_t is the percentage of steel area at the top including the area of slab reinforcement, and ρ' is the percentage of steel area at the bottom.

A comparison between the M-ϕ response of T-beams [Figs. 5.7(a), 5.8(a)] and rectangular beams (Fig. 5.5) indicates that the downward yielding moment increases about 33 percent, i.e., from about 1500 k/in. to 2000 k/in. These analytical results correlate well with the experimentally observed flexural yielding moments (Table 4.2). For the T-beam and rectangular beam sections with the same amount of bottom reinforcement, i.e., Beams T-2 and R-4, and Beams T-3 and R-6, the theoretical M-ϕ responses are similar in the region in which behavior is controlled by the steel force-couple (from LP 2 to LP 4). This is because in the response range for the steel force-couple, stiffness and strength characteristics are controlled by the capacity of the bottom steel which has less area than that at the top (Sect. 5.7).

---

* This ratio does not satisfy the minimum negative steel-to-positive steel ratio of 0.5 required for the critical regions of girders of ductile moment-resisting frames [1.2,1.11].

The important results from the theoretical M-ϕ analysis of the four beam sections, R-4, R-6, T-2, and T-3, are summarized in Table 5.1. The results indicate that when loaded in a downward direction, concrete crushed earlier in sections with relatively smaller amounts of bottom steel. This is because the bottom concrete of these sections must carry a higher percentage of compressive load as a result of a smaller amount of bottom compressive steel. For the same reason, the beams with relatively smaller amounts of bottom steel had greater degrees of straining in the bottom than in the top.

The behavior of the four beam sections in the two cycles of loading can be compared using the energy dissipation parameter. The energy dissipated, E_{diss}, through M-ϕ loops and through the materials are listed in Table 5.2. These values are expressed in kip-in. of energy per inch of beam length.

The energy dissipated in the top or bottom steel for a given cycle is equal to the area enclosed in the hysteretic σ-ε loop times the steel area. The energy dissipated in the concrete for a given cycle was estimated from the following energy balance:

$$E_{diss_{\text{in concrete}}} = D_{diss_{\text{in the M-}\phi\text{ loop}}} - E_{diss_{\text{in top and bottom bars}}}$$

Table 5.2 also lists the values of energy dissipated through the material of each section, expressed as a percentage of the energy dissipated in the M-ϕ loop. Because all the beams are loaded under the same prescribed deformation (curvature) history, results are comparable.

The following observations can be made from the results given in Table 5.2:

(1) For beams with amounts of bottom steel relatively smaller than top steel, the percentage of energy dissipated through the bottom steel will be greater, i.e., Beams R-4 and T-2.

(2) Since the concrete in beams with relatively small amounts of bottom steel must take a greater percentage of compression, the concrete energy dissipation in these sections is greater. This can be seen by comparing the $E_{diss_{\text{in concrete}}}$ in Beams R-4 and T-2 with those in Beams R-6 and T-3.

(3) Adding more steel to either the top or bottom section will result in an increase in the amount of the total $E_{diss(M-\phi)}$ (Table 5.3). As shown in the results presented in Table 5.3, however, the value of E_{diss} does not increase directly in proportion to the amount of steel added. The increase in E_{diss} depends on the ρ'/ρ_t of the beam after the steel is added. If the added steel brings the ρ'/ρ_t closer to one, the increase of E_{diss} will be greater than if the ratio is decreased. For example, although Beam T-2 has 22 percent more steel at the top than Beam R-4, the increase in E_{diss} is under 11 percent for the first and second cycles. This is because the increased steel causes a reduction in the ρ'/ρ_t from 0.53 to 0.39. On the other hand, by adding 25 percent more steel at the bottom of Beam T-2, converting Beam T-2 to Beam T-3, the increase in E_{diss} for the first and second cycles is above 43 percent. This is due to the fact that the added steel helps to bring the ρ'/ρ_t closer to one, from 0.39 to 0.75.

The above analytical results indicate that in order to increase energy dissipation through flexural deformations under fully reversed loadings, the steel ratio should be kept as close as possible to one.

5.10 COMPARISON BETWEEN THEORETICAL AND MEASURED RESPONSES

To assess the accuracy of the theoretical M-ϕ analysis, the measured and predicted M-ϕ responses are compared for three selected examples shown in Figs. 5.10, 5.11, 5.12, and 5.15. The first example considers the M-ϕ response of Beam T-2 with a ρ'/ρ_t of 0.34, measured within a 7-in. distance from the beam fixed-end. The M-ϕ response of Beam R-3 with a ρ'/ρ_t of 0.53, measured within a 7 to 14 in. distance from the beam fixed-end, is considered in the second example. The third example accounts for the M-ϕ response of Beam R-6, with a ρ'/ρ_t of 1.0 measured within a 7-in. distance from the beam fixed-end.

5.10.1 Beam T-2 (ρ'/ρ_t = 0.34)

In the initial monotonic M-ϕ response of Beam T-2, the predicted curve showed a slightly higher value (6 percent) of yield moment. An earlier and stronger increase in moment strength was observed in the inelastic response (Fig. 5.10).

The slightly higher moment at yield could be due to the fact that in the theoretical model the slab reinforcement is assumed to be effective over the whole width of the flange. In actuality, as observed in the plotted strain data of slab reinforced Beam T-2 [Fig. 4.14(a)], the steel is not strained uniformly across the width of the slab; the slab reinforcement adjacent to the beam stem reached yielding earlier than the remaining slab reinforcement. Therefore, the moment capacity corresponding to the yield strength of the entire reinforcing slab was not developed until a later stage.

The difference in the later monotonic M-ϕ response could be traced to the inadequate representation of the strain-hardening effect of the #2 slab reinforcement in the M-ϕ analysis. In the analysis, the top #6 reinforcement and #2 slab reinforcement are lumped together and the σ_s vs. ε_s relationship for #6 bars is adopted for the lumped steel. Since the #2 bars have a yield plateau about twice as long as that of the #6 bars (Fig. 2.9), lumping the steel together would overestimate the strain-hardening effect.

Another noticeable difference can be seen by comparing the predicted and measured loading curves in the upward moment region (Fig. 5.10). Greater degradation of stiffness was observed in the measured M-ϕ_{av} response. The reason for this could be as follows. Because of the severity of the initially applied half-cycle (δ/δ_y reached about 5.5), some crushing of concrete at the bottom of the beam and some buckling of the bottom compressive #5 bars probably took place. On applying loading in the opposite upward direction, the slightly bent bottom bars would be less stiff than the straight bars assumed in the analysis.

5.10.2 Beam R-3 (ρ'/ρ_t = 0.53)

The predicted and measured M-ϕ_{av} responses for Beam R-3 are shown in Fig. 5.11 and the cycle-to-cycle comparisons are given in Fig. 5.12.

The major difference is observed in the upper part of the downward loading curves. Initially, the stiffness (slope) of these curves was relatively small due to the opening of cracks at the bottom compression zone. After the bottom cracks started to close, stiffness increased. An earlier and more gradual rise in stiffness is observed in the measured downward loading curves. This indicates that in reality, some compression can be developed in the concrete across the bottom cracks before these cracks are fully closed. This could be due to the presence of loosened concrete granules entrapped in the cracks. As they bridged the cracks, the granules provided a path for the transmission of compressive force. The early transfer of compression could also be caused by some relatively vertical shear displacement

between the faces of the crack (Fig. 5.13), causing concrete to contact earlier.

Another reason for the much delayed crack closing in the theoretical response could be due to the fact that the concrete is assumed to unload and reload elastically in compression [Fig. 5.14(a)]. If concrete is compressed inelastically, inelastic strains will develop in the concrete layer. On the next loading, the cracks will not close until the concrete compressive strain reaches a value equal to the compressive inelastic strain. [The cracks close at LP 4 as shown in Fig. 5.14(a)]. This would delay the participation of the concrete in resisting compression. To investigate the effect of crack closure in the bottom, a different unloading and reloading behavior is assumed [Model 2, Fig. 5.14(b)]. This behavior assumes that cracks start to close immediately as strain becomes compressive, and loading starts from the origin. Unloading in compression is also assumed to end at the origin. The theoretical M-ϕ analysis results using Models 1 and 2 are shown in Fig. 5.14(c). As can be seen from this figure, very little change has occurred. Concrete resistance to load begins a little earlier in the response obtained from Model 2, but is still much later than that observed in the measured response (Fig. 5.11).

It can be concluded that in order to predict effectively the behavior of crack closure at downward (strong direction) loading, it may be necessary to consider the effect of concrete granules trapped in the cracks and the effect of shear displacement across the crack (Fig. 5.13).

From both the experimental and analytically predicted downward loading curves, it can be observed that the presence of open cracks in the bottom compression zone, which eventually close, caused a sharp increase in the stiffness of the downward curves. As a result, the hysteretic M-ϕ_{av} loops became pinched at the top. This pinching effect was accentuated when the section had a steel ratio of less than one and can be referred to as "flexural pinching of loops" to differentiate it from the type of pinching of loops which often takes place at small loads and is due to shear effects. A strong degree of flexural pinching is evident in the recorded M-ϕ_{av} and P-δ response of beams with unequal steel ratios, Beams R-1 and R-4, and Beams T-1 to T-3 (Figs. 4.9 and 4.10).

Comparison of the energy dissipated in theoretical loops with that obtained from the measured loops shows that the analysis underestimates the energy dissipated by less than 20 percent, mostly due to the disagreement in the downward loading curves.

5.10.3 Beam R-6 (ρ'/ρ_t = 1.0)

This section had equal amounts of steel in both the top and bottom. Even if cracks remain open in the compression zone under reversed loading, the section can usually develop its moment capacity corresponding to the capacity of the tensile steel. The equal amount of compressive steel acts to counterbalance the tensile force.

In the case of Beam R-6, the measured moment-curvature response at large ductility ratios was strongly influenced by the shear distortion that took place in the two regions where ϕ_1 and ϕ_2 were measured [Fig. 4.10(f)]. This led to distortions in the moment-curvature responses, M-ϕ_1 and M-ϕ_2, at the initial stages of loading reversals. Since the present M-ϕ analysis does not account for this distortion, only the M-ϕ_1 response up to a ductility ratio of two was predicted (Fig. 5.15). The predicted M-ϕ loops shown are in good agreement with the measured loops except that at a δ/δ_y of one [Fig. 5.15(a)], a distinct increase in stiffness and moment resistance in the upward direction can be observed in the theoretical M-ϕ curve. This

increase is due to a large concrete cover at the top (Fig. 2.3) which is the result of an upward shift in the centroid of resultant compressive forces C_c and C_s [Fig. 5.2(b)] once cracks started to close at the top. This creates a larger moment arm; hence, a larger moment capacity in the upward direction. The comparison between the amount of energy dissipated in the theoretical M-ϕ loops and that in the experimental loops showed a 5 percent difference.

5.11 CONCLUDING REMARKS

Comparison between the predicted M-ϕ loops with the experimental results (Sect. 5.10) demonstrates that the presently developed moment-curvature model was able to predict reasonably well the energy dissipation and characteristics of the hysteretic M-ϕ_{av} loops obtained from experimental beams subjected to reversed bending with small shear. The analysis showed that for beams with less steel in the bottom than in the top, the bottom cracks must close during downward loadings in order to develop the moment capacity corresponding to the top steel. Closure of the cracks usually caused an increase in stiffness, as clearly observed in the experimental hysteretic M-ϕ diagrams. The analytical model also predicted such an increase in stiffness, but in a manner more pronounced and at a larger curvature and a lower moment than those depicted by the measured curve. This may be attributed to the influence of entrapped concrete granules in the cracks and the effect of shear displacement along the cracks.

A5. APPENDIX TO CHAPTER 5
DEVELOPMENT OF HYSTERETIC MODEL FOR MATERIALS

A5.1 MODEL FOR REINFORCING STEEL

A5.1.1 Cyclic Tests on Reinforcing Steel

For the purpose of establishing an analytical model for the cyclic stress-strain relationship of reinforcing steel, a number of uniaxial tests on reinforcing steel specimens were carried out. The test specimens consisted of six machined #5 and #6 bars with dimensions as shown in Fig. A5.1. The results obtained in five of the six specimens are described in detail herein. The sixth specimen was made from a #5 bar tested under a cyclic loading program similar to that applied to Specimen 2 with a #6 bar (Fig. A5.6). No details of the sixth specimen are presented as the results of these two specimens showed no appreciable difference.

A 50-kip MTS servo-controlled system was used for testing [Fig. A5.2(a)]. A displacement transducer for measuring the average axial strain consisted of a pair of Daytronic LVDT's [having a total travel of about 0.05 in. and a gage length of 1 in. placed on opposite sides of the test specimen, as shown in Fig. A5.2(b)]. The applied force on the specimen was measured by an internal load cell built into the MTS testing system. Average readings of the two LVDT's and the applied load were continuously read on an X-Y recorder [Fig. A5.2(a)].

The specific loading program for each specimen was selected to provide reliable data for the formulation of an analytical hysteretic σ-ε model for the main reinforcing steel bars. The loading program was carried out by controlling the average strain over the 1-in. gage length of the specimen.

Loading for each specimen was carried out at two different strain rates. For loading within strain limits of about ± 0.01 in./in., the applied strain rate was about 50 μ-in./in./sec.; for larger strain values, the strain rate was increased to about 200 μ-in./in./sec.

Before proceeding to the discussion of test results, it is necessary to clarify some terms used in the text for characterizing the cyclic σ-ε response for reinforcing steel. These terms are illustrated in Fig. A5.3.

Bauschinger effect of steel. - If steel is stressed in one sense into the inelastic range and then loading is reversed, softening of the steel resistance (yielding) will often occur before the magnitude of stress during loading in the opposite sense reaches the value of the initial yielding stress of the material. This phenomenon is referred to as the Bauschinger effect of steel and is shown in Fig. A5.3(a).

Cyclic strain-hardening*. - This term denotes the increase of material resistance during loading reversals beyond the value of the initial yielding stress of the material [Fig. A5.3(b)].

Cyclic strain-softening*. - This term is used to denote the stiffness degradation of the steel or, more specifically, the reduction of the instantaneous tangent modulus of steel that occurs during inelastic reversals [Fig. A5.3(c)].

Cyclic mean stress relaxation. - If a steel specimen is subjected to a series of stress reversals by cycling it between two fixed strain limits (the associated peak stresses are noted by σ^+ and σ^-), the decrease in the average mean stress, i.e., $(\sigma^+ + \sigma^-)/2$ with each cycle of stress reversal [5.3], will be denoted as the cyclic mean stress relaxation [Fig. A5.3(d)].

---

* Note the difference in meaning between these terms and similar terms generally used in the literature [5.2] (Fig. A5.3).

Preceding page blank

A5.1.2 Test Results

(a) Specimens 1 (#6 bar) and 5 (#5 bar). - Specimens 1 and 5 were machined. The initial monotonic σ-ε curve of these specimens is compared in Fig. A5.4 with that obtained from unmachined bars. The machined specimens showed a slightly higher upper yielding point and a higher strain-hardening curve than the unmachined bars, although the difference in stress value was less than 5 percent. Two possible explanations for this difference may be postulated. Machining could have modified the residual stress that might have been built into the deformed bar during its fabrication, or the difference could have been due to nonuniform mechanical characteristics along the bar.

Specimens 1 and 5 were initially loaded to a strain value of 0.045 in./in. to simulate the straining of top bars in monotonically loaded beams R-4 and T-2. These specimens were then subjected to stress reversals which varied between 90 ksi and -66 ksi, Fig. A5.5.

The complete stress-strain response of Specimen 1 is shown in Fig. A5.5. The hysteretic loops exhibited a pronounced Bauschinger effect. The specimen was also observed to undergo the cyclic stress relaxation phenomenon. At the first cycle, the value of mean stress was 11 ksi, but after three repeated cycles, this value was reduced to 7 ksi. The results show that the reduction of mean stress was greater from the first to the second cycle than from the second to the third. This behavior seems to indicate the beginning of a shakedown of the response to a stabilized loop.

(b) Specimens 2 (#6 bar) and 5 (#6 bar). - The loading program used for Specimen 2 was controlled by strain. The programmed strain input was similar to the recorded strain history of the top steel in the critical region of Beam T-3. Similarly, the programmed strain input for Specimen 3 approximated that of the bottom steel of Beam T-3 in the same region. The stress-strain response of these two specimens is shown in Figs. A5.6 and A5.7, respectively. The monotonic σ-ε response of Specimen 1 is also indicated in the two figures for comparison. The shaded areas emphasize the difference between the monotonic curves and the upper envelope of the hysteretic σ-ε loops.

In general, the cyclic σ-ε test results show that the Bauschinger effect became more pronounced as the magnitude of plastic strain increased; also, the descending and ascending curves of the hysteretic σ-ε loops were noticeably similar in shape. The upper envelope of hysteretic σ-ε loops may be either slightly lower (Specimen 2, Fig. A5.6) or slightly higher (Specimen 3, Fig. A5.7) than the corresponding monotonic curve, depending on the previous loading history. Although the observed differences are small, this indicates that the cyclic strain-hardening behavior (Sect. A5.1.1) is strain-history dependent and that the monotonic σ-ε curve may not be an accurate envelope for defining the maximum stress that can be attained by cyclically loaded reinforcing steel.

(c) Specimen 4 (#6 bar). - The loading sequence of Specimen 4 was arbitrarily chosen. The specimen was first subjected to a cycle with peak strains at about $\pm$ 0.01 in./in., and then loaded to failure (Fig. A5.8).

In the first cycle, the hysteretic loop exhibited a pronounced Bauschinger effect. As loading continued in tension to the large strain value of about 0.08 in./in., the difference between the monotonic σ-ε curve of Specimen 1 and the cyclic σ-ε curve of Specimen 4 became negligible.

A5.1.3 Hysteretic Model for Stress-Strain Relationship of Reinforcing Steel

The hysteretic model for the σ-ε relationship of the reinforcing bars was developed on the basis of the uniaxial test results reported in the previous section. The model was developed to meet the following needs:

(1) To determine the steel stress corresponding to the measured steel strain. Once the steel has yielded and strain reversal has taken place, the stress-strain relationship becomes history dependent. Since there is no direct way of measuring steel stress in the beam tests, the corresponding stress is computed from the measured strain value.

(2) To establish the hysteretic σ-ε behavior of reinforcing steel for the analytical prediction of the inelastic behavior of R/C members. Previously reported tests [1.4-1.9] have shown that reinforcing steel plays a dominant role in the inelastic behavior of R/C members.

Several investigators [1.5, 5.3, 5.4] have attempted to model the hysteretic stress-strain behavior of reinforcing steel, usually made with intermediate-grade steel having distinct yield plateaus. The most comprehensive study was made by Park, Kent, and Sampson [1.5]. In their model, the Ramberg-Osgood function [5.6] was used to describe analytically the Bauschinger and cyclic strain-hardening effects. The analytical results indicated good prediction of the observed Bauschinger effect, but in many cases, the effect of cyclic strain-hardening was overestimated.

Kato [5.7] has proposed a hysteretic σ-ε model for structural steel. In his study, the monotonic strain-hardening relationship was used to approximate the cyclic strain-hardening in steel, while a nonlinear relationship was used to approximate the effect of strain-softening during reversals. The model was developed by matching results with symmetrical deformation σ-ε loops obtained from the experiments.

(a) Internal straining of reinforcing steel in R/C flexural members subjected to loading reversals. - It should be recognized that during loading reversals, concrete in the compression zone prevents the development of high compressive strain in the compressive steel. Therefore, unless concrete loses its resistance, as in the case of concrete spalling, the development of high compressive strain in reinforcing steel is unlikely. On the other hand, concrete offers practically no resistance to tension; therefore, as the steel is strained in tension, high tensile strain may develop. These observations explain why the hysteretic σ-ε loops of the main reinforcing bars obtained in present and past tests [1.6-1.8] remain primarily in the tensile strain range.

In developing a practical hysteretic σ-ε model of reinforcing steel based on tests of reinforcing bar specimens, emphasis should be placed on selecting a loading history which reflects actual characteristics of steel strains. For this reason, the recorded strain history from beam tests serve as the basis for selecting the loading histories applied in the MTS tests (Sect. A5.1.2).

(b) Hysteretic model of reinforcing steel. - In the proposed hysteretic model for uniaxial σ-ε relationship of the reinforcing steel, the Ramberg-Osgood function is used to describe the effect of strain-softening under reversed loadings. A separate set of hysteretic rules are used to describe the cyclic strain-hardening behavior in the reinforcing steel. A computer program, BAUSCH, contains the analysis routine for the proposed hysteretic model. Specifications for preparing the input data for this computer program are given in Sect. A5.4.

The user provides seven stress-strain points to define the σ-ε curve of the reinforcing steel under monotonic loading [Fig. A5.9(a)]. With these stress-strain points the following parameters can be established: yield stress, σ_y; strain at yield, ε_y; elastic modulus, E_s; strain-hardening strain, ε_{sh}; the shape of the σ-ε curve in the strain-hardening range; maximum stress, σ_{max}; and ultimate strain, ε_u [Fig. A5.9(a)].

A5.1.4 Hysteretic Rules

The following proposed rules are primarily based on the general pattern of stress-strain response observed in the experimental results and on suggestions made by previous investigators. The physical and intuitive basis for these rules will be discussed later.

The hysteretic rules used for constructing σ-ε relationships under reversed loading are best described by the following examples.

(a) Construction of first reversal curve. - Shown in Fig. A5.9(b) and illustrating two cases:

Case 1 Loading reversed at A in plastic plateau range; loading path described by S→A→B→X.

Case 2 Loading reversed at A' in strain-hardening range; loading path described by S→A'→A"→B'→X'.

The initial monotonic loading from S→A or S→A' follows the monotonic σ-ε curve established from the input. As loading reverses, the following rules apply:

(1) At the beginning of unloading, as the magnitude of stress is reduced to the initial yielding stress level from A' to A" (Case 2), the σ-ε relationship is assumed to be linear-elastic.

(2) For the reversal curve between A and B or A" and B' (points B and B' are referred to as the reversal yield points), the σ-ε relationship is given by a Ramberg-Osgood equation:

$$\bar{\varepsilon}_s = \beta(\bar{\sigma}_s + \alpha|\bar{\sigma}_s|^n) \qquad \text{(A5.1)}$$

where

$$\bar{\varepsilon}_s = \frac{\varepsilon_s - \varepsilon_{sA}}{2\varepsilon_y}$$

$$\bar{\sigma}_s = \frac{\sigma_s - \sigma_{sA}}{2\sigma_y}$$

σ_{sA} and ε_{sA} = stress and strain coordinates of point A, respectively

σ_s and ε_s = stress and strain coordinates of a point on the reversal curve, respectively.

Parameters β, α, and n are defined by the maximum value of plastic strain, ε_{Pmax}, during the previous loadings. This strain value is determined at each time of reversal, point A, by:

$$\varepsilon_{Pmax} = \left|\varepsilon_{sA} - \frac{\sigma_{sA}}{E_s}\right| \qquad \text{(A5.2)}$$

where E_s is the elastic modulus of steel.

The reversal yield point, B or B', is the point at which the magnitude of steel stress reaches the yield stress level during loading (Case 1), or where the magnitude of the strain, $\Delta\varepsilon_s$, that occurs during loading reaches the value of ε_{sh} (Case 2).

If loading continues beyond point B, the stress-strain relationship is assumed to be given by the monotonic strain-hardening curve, CY, shown in Fig. A5.9(a). For example, the cyclic strain-hardening curve, BX, shown in Fig. 5.9(b) is constructed by rotating curve CY 180 degrees and shifting it to point B with point C matching point B.

(b) Construction of the second and subsequent reversal curves. - If loading reverses a second time, similar to that which occurred at point E in Fig. A5.9(c), the stress-strain relationship of the ascending reversal curve, EF, will be assumed to be given by the previous descending curve, AE. This rule is applicable where there is no change in the value of ε_{Pmax}

from the last reversal of loading. For example, ascending reversal curve EF is established by rotating curve SE 180 degrees and shifting it to point E with point A matching point E. For loading beyond point F, the stress-strain relationship is assumed to be given by the monotonic stress-strain curve [Fig. A5.9(a)]. If loading continues to point G [Fig. A5.9(c)], there will be an increase in the value of $\varepsilon_{p_{max}}$. The stress-strain relationships of the new reversal curve, GH, would then be constructed according to the $\varepsilon_{p_{max}}$ reached at point G, wherein $\varepsilon_{p_{max}} = |\varepsilon_{sG} - \sigma_{sG}/E_s|$.

(c) Determination of initiation of cyclic strain-hardening in plastic plateau range. - The σ-ε response of Specimen 1 (Fig. A5.5) under monotonic loading shows that strain-hardening is initiated at a strain value of 0.012 in./in. Strain-hardening of Specimen 3 under cyclic loading occurred earlier at a strain value of 0.007 in./in. (point A, Fig. A5.7). This difference in strain-hardening behavior was not observed when the σ-ε response of monotonically loaded Specimen 1 was compared with that of cyclically loaded Specimen 2 (Fig. A5.6). The reason for this could be that before reaching point A, Specimen 3 underwent considerable plastic deformation in the opposite compressive sense, whereas Specimen 2 did not. This was because the small magnitudes of stress reversal in the tensile plastic plateau range of Specimen 2 did not induce much plastic deformation in compression. Therefore, the possibility of cyclic strain-hardening was determined by the amount of plastic strain increment that occurred during loading in the opposite sense, or the strain difference, $|\Delta\varepsilon_s'|$, between two sequential zero stress points in a cycle of stress reversal [Fig. A5.10(a)]. This parameter is compared with the plastic strain value at which strain-hardening is initiated under the monotonic loading condition, $|\varepsilon_{sh} - \varepsilon_y|$ [Fig. A5.10(a)]. The rules used in the analysis are illustrated in Fig. A5.10 for two cases and described below.

Case A Shown in Fig. A5.10(a) and using the value $|\Delta\varepsilon_s'| > 0.5|\varepsilon_{sh} - \varepsilon_y|$.* Cyclic strain-hardening is initiated during reloading to tension in the plastic plateau range and the cyclic strain-hardening curve 3-4 is constructed by shifting curve CY to point 3, with 3 matching C.

Case B Shown in Fig. A5.10(b) and using the value $|\Delta\varepsilon_s'| < 0.5|\varepsilon_{sh} - \varepsilon_y|$.* Cyclic strain-hardening is suppressed during reloading to tension in the plastic plateau range. The strain-hardening is initiated at the same strain value as that under monotonic loading conditions.

(d) Stress relaxation. - The cyclic mean stress relaxation is shown in Fig. A5.9(c) and is accounted for in the following manner. At the completion of a full cycle between two opposite stresses, σ_{sA} and σ_{sE}, the stress at point F, σ_{sF}, is reduced by an amount, $\Delta\sigma_x$, from the stress, σ_{sA}, at the previous peak point, A. Based on experimental observations, the value of $\Delta\sigma_x$ is taken to be 0.05 $|\sigma_{sA} + \sigma_{sE}|$. It was found that a slightly better correlation with MTS experimental results can be obtained using this rule.

The phenomenon of stress relaxation was found to have little effect on the results of predicted moment-curvature examples shown in Sect. 5.7.

A5.1.5 Comments on Hysteretic Rules

(a) Ramberg-Osgood Nonlinear Equation. - This equation (Eq. A5.1) is used to establish the reversal curve in the stress interval, wherein, $\sigma_y > \sigma_s > -\sigma_y$. The nonlinear term on

*The factor of 0.5 is used because it provides a good correlation with experimental results.

the right-hand side of Eq. A5.1 represents the plastic part of the steel strain, $\bar{\varepsilon}_s$ while the linear term represents the elastic part. Parameter α of the nonlinear term determines the amount of plastic strain relative to elastic strain. Parameter n controls the sharpness of departure of the reversed curve from linear behavior, or the rate of softening of the steel modulus, $\Delta\sigma_s/\Delta\varepsilon_s$.

For the large value of n used in the model, i.e., 6 to 7 (Fig. A5.11), the contribution of the nonlinear term, $\alpha|\bar{\sigma}_s|^n$, to $\bar{\varepsilon}_s$ during unloading from A to O [Fig. A5.9(b)] is not significant. The degradation in steel modulus during unloading is mainly determined by parameter β (Fig. A5.11), which is the average value of the slope of the unloading curve. After the stress is reversed, the relative contribution of the plastic strain, $\alpha|\bar{\sigma}_s|^n$, becomes increasingly greater. The three parameters, β, α, and n in Eq. A5.1 are expressed in terms of the maximum amount of plastic strain, $\varepsilon_{P_{max}}$, induced from previous loadings (Fig. A5.11). A similar approach has been adopted by other investigators [1.5, 5.4, 5.5]. The reason for assuming this approach can be seen from the test results shown in Figs. A5.6 to A5.8. The obtained hysteretic σ-ε loops show that the softening effect or the plastic flow tends to increase and to occur early in the reversed loading as the amount of plastic strain increases.

A simple relationship between n, α, and $\varepsilon_{P_{max}}$ (Fig. A5.11) was determined using a trial-and-error procedure. Note that for a value of $\varepsilon_{P_{max}}$ greater than ε_{sh}, the values of parameters α and n are constant while β becomes constant for an $\varepsilon_{P_{max}} > 35 \times 10^{-5}$ in./in. This is due to the insensitivity of the Bauschinger effect to the increase in plastic strain as the steel was strained beyond the plastic plateau range (Figs. A5.6 and A5.7).

(b) Construction of cyclic strain-hardening curve. - This curve represents the portion of the reversal curve beyond reverse yielding point B or B' [Fig. A5.9(b)]. The criterion used to determine the location of this point on the curve is based on observations of the monotonic stress-strain response [Fig. A5.9(a)], wherein yielding occurs at a stress level of σ_y and strain-hardening is initiated at a strain value of ε_{sh}. It was found that the portion of the reversal curve beyond the reverse yielding point can be reasonably approximated by the monotonic strain-hardening curve.

A5.1.6 Accuracy of Model

The accuracy of the postulated hysteretic rules and the assumed relationships between the residual plastic strain parameter, $\varepsilon_{P_{max}}$, and parameters α, β, and n of the Ramberg-Osgood equation can be seen by comparing the experimental and analytical results shown in Figs. A5.8, A5.12, and A5.13. Analytical results are indicated by solid lines and the corresponding experimental results by dashed lines. The analytically predicted curves are in good agreement with the experimental results.

A5.2 MODEL FOR CONCRETE STRESS-STRAIN RELATIONSHIPS

Numerious models for the concrete stress-strain response under monotonic loading have been suggested. More recently, refined models have been proposed by Sargin [1.16] and Kent and Park [5.8], in which the confinement effect of the lateral reinforcement on the concrete σ-ε response is considered. In addition to stipulating a concrete σ-ε relationship under monotonic loading, rules regarding unloading, loading, crack opening, and crack closing of concrete under cyclic loading must also be established.

A5.2.1 Model for Monotonic Stress-Strain Curve

For concrete confined by rectangular hoops, the monotonic compressive σ-ε curve is defined by the relationship given by Kent and Park [5.8]. The corresponding curve is shown in Fig. A5.14(a) and is used here as an envelope for concrete under cyclic loading (Sect. A5.2.2). For the ascending branch, AB($|\varepsilon_c| < |\varepsilon_o|$), the stress-strain relationship is given as:

$$\sigma_c = f'_c\left[2\left(\frac{\varepsilon_c}{\varepsilon_o}\right) - \left(\frac{\varepsilon_c}{\varepsilon_o}\right)^2\right] \tag{A5.3}$$

where

σ_c = concrete stress

f'_c = concrete cylinder strength

ε_o = strain at maximum strength

ε_c = concrete strain

The falling branch of the curve is expressed as:

$$\sigma_c = f'_c\,[1 - Z(\varepsilon_c - \varepsilon_o)] \quad \text{for } |\varepsilon_o| \leq |\varepsilon_c| \leq |\varepsilon_{20c}| \tag{A5.4}$$

$$\sigma_c = 0.2\, f'_c \quad \text{for } |\varepsilon_{20c}| < |\varepsilon_c| \tag{A5.5}$$

where $Z = \dfrac{0.5}{\varepsilon_{50_t} - \varepsilon_o \text{ (in./in.)}}$

and

$$\varepsilon_{20c} = \left(\frac{3 + \varepsilon_o f'_c \text{ (psi)}}{f'_c - 1000}\right) + \frac{3}{4}\,\rho''\,\sqrt{b''/s} \tag{A5.6}$$

in which

ρ'' = ratio of volume of stirrup ties to volume of concrete core

b'' = width of confined core

s = stirrup spacing

ε_{20c} = strain at 0.2 of f'_c on the falling branch of the σ_c- ε_c curve [Fig. A5.14(a)]

ε_{50_t} = similar to ε_{20_t}, except at 0.5 of f'_c [Fig. A5.14(a)]

A5.2.2 Model for Concrete Behavior under Cyclic Loading

The assumed model for concrete behavior under cyclic loading is illustrated in Fig. A5.14(a). In this model, unloading of compressed concrete from points 1 to 2 (zero stress point) is assumed to take place elastically. As loading proceeds beyond point 2 to the tensile strain range at point 3, cracking is assumed to initiate in the concrete layer. This cracking results in the loss of concrete stiffness and renders it incapable of carrying the load [Fig. A5.14(a)]. The model therefore does not account for the tensile strength of concrete. This strength can, however, be easily accomodated in the model, but because its effect on the overall behavior is negligible, it is not included.

As loading reverses at point 3 and proceeds into the compressive strain range, the cracks are assumed to close at point 2 or 4. By point 5, the elastic stiffness of the concrete is regained and loading proceeds elastically until reaching the previous level of maximum compressive strain. Henceforth, the concrete σ-ε relation is governed by the monotonic σ-ε curve of the ABCD envelope curve.

The assumed model is similar to that reported by Wakabayashi [5.9] except that a different equation for the envelope curve is used.

To check the accuracy of this model (Model 1), the analytical results are compared with test results of the concrete control cylinder of Beam R-6 where the cylinder was subjected to a series of repeated loadings in compression [Fig. A5.14(b)]. Comparison generally shows good agreement despite the disagreement for unloading and reloading observed in the range of large compressive strain where $|\varepsilon_c| > |\varepsilon_o|$. By using Model 1 and another model (Model 2) to compare the analytical M-ϕ response of a section, this lack of agreement was found to have very little effect on the results (Sect. 5.6). In Model 2 it was assumed that loading began and unloading ended at the point of zero stress and strain (Fig. 5.14).

A5.2.3 Crushing of Unconfined Concrete

If the compressive strain in the unconfined concrete layer reaches -0.005 in./in., this layer will be assumed to start crushing and to have a reduced resistance of only 0.2 f'_c [Fig. A5.14(a)]. The assumed crushing strain of -0.005 in./in. is comparable to the value used by other investigators [1.5 and 1.16]. Some resistance of the unconfined crushed concrete is assumed since concrete may not los complete resistance as crushing begins. However, a complete loss of resistance could occur if the compressive strain reaches a value large enough to cause the unconfined concrete to spall off physically. It is recognized that more experimental investigations are needed to establish a realistic concrete cracking model.

A5.3 DATA INPUT TO PROGRAM CYCMC (CYCLIC MOMENT-CURVATURE ANALYSIS PROGRAM)

A5.3.1 Heading Card (12A6)

columns	entry
1-72	enter heading information for use in labeling output

A5.3.2 Data Cards

(a) Card 1 Steel areas, control information (6F10.0)

variable	columns	entry
AS(1)	1-10	top steel area (in.^{2})
AS(2)	11-20	bottom steel area (in.^{2})
PUNCH	21-30	flag for punching output Default = no punching $\neq$ 0.0 punch moment-curvature data points and stress-strain data points
PAX	31-40	applied axial load on section (kips)
FACC	41-50	scale factor for curvature values [Sect. A5.3.2(g)]. Default = 1.0
TOL	51-60	percentage tolerance in internal force balance to be used in equilibrium iteration.

(b) Card 2 Dimensions of cross-section (6F10.0) [Fig. A5.15(a)]

variable	columns	entry
DD	1-10	distance from top fiber to centroid of top steel (in.)
D	11-20	distance from top fiber to centroid of bottom steel (in.)
H	21-30	height of cross-section (in.)
WB	31=40	width of stem (in.)
WF	41-50	width of flange (slab) (in.)
DF	51-60	thickness of flange (slab) (in.)

(c) Data for monotonic stress-strain curve [Fig. A5.15(b)]

(i) Top steel stress-strain curve

Card 3 Stress Values (7F10.0)

variable	columns	entry
FV1RG (1,1)	1-10	stress value, point 1 (ksi)
FV1RG (1,2)	11-20	stress value, point 2
.		.
.		.
.		.
FV1RG (1,7)	61-70	stress value, point 7

Card 4 Strain values (7F10.0)

variable	columns	entry
EV1RG (1,1)	1-10	strain value, point 1 (10^{-3} in./in.)
EV1RG (1,2)	11-20	strain value, point 2
.		.
.		.
.		.
EV1RG (2,7)	61-70	strain value, point 7

(ii) Bottom steel stress-strain curve

Card 5 Stress values (7F10.0)

variable	columns	entry
FV1RG (2,1)	1-10	stress value, point 1 (ksi)
FV1RG (2,2)	11-20	stress value, point 2
.		.
.		.
.		.
FV1RG (2,7)	61-70	stress value, point 7

Card 6 Strain values (7F10.0)

variable	columns	entry
FV1RG (2,1)	1-10	strain value, point 1 (10^{-3} in./in.)
EV1RG (2,2)	11-20	strain value, point 2
.		.
.		.
.		.
EV1RG (2,7)	61-70	strain value, point 7

(d) Card 7 Concrete properties (4F10.0)

variable	columns	entry
FCD	1-10	concrete compressive strength, f'_c (ksi)
EO	11-20	strain corresponding to f'_c
ECR	21-30	strain at which concrete crushes
PPB	31-40	binding ratio (volume of lateral tie/volume of concrete).

(e) Card 8 Control information on discretization (2I5)

variable	columns	entry
NB	1-5	No. of concrete layers in beam (stem)
NF	6-10	No. of concrete layers (NB + NF) < 60

(f) Card 9 Number of curvature values (I5)

variable	columns	entry
NPT	1-5	No. of curvature values

(g) Card 10, etc. Curvature values (8F10.0)

variable	columns	entry
CCR (1)	1-10	1st curvature value (10^{-3} in./in.)
CCR (2)	11-20	2nd curvature value (10^{-3} in./in.)
.		.
.		.
.		.

A5.4 DATA INPUT TO PROGRAM BAUSH (PROGRAM FOR CALCULATION OF CYCLIC STRESS-STRAIN RESPONSE OF REINFORCING STEEL

A5.4.1 Heading Cards (12A6) two cards

columns	entry
1-72	enter heading information for use in labeling output

A5.4.2 Data for Monotonic Stress-Strain Curve [Fig. A5.15(b)]

Card 3 Stress values (7F10.0)

variable	columns	entry
FV1RG (1,1)	1-10	stress value, point 1 (ksi)
FV1RG (1,2)	11-20	stress value, point 2
.		.
.		.
.		.
FV1RG (1,7)	61-70	stress value, point 7

Card 4 Strain values (7F10.0)

variable	columns	entry
EV1RG (1,1)	1-10	strain value, point 1 (10^{-3} in./in.)
EV1RG (1,2)	11-20	strain value, point 2
.		.
.		.
.		.
EV1RG (1,7)	61-70	strain value, point 7

A5.4.3 Steel Strain Values Defining Cyclic History

Card 5 Control information (I5)

variable	columns	entry
NPTS	1-5	No. of strain values NPTS < 500

Card 6 (8F.10.0) Strain value at points of reversal [Fig. A5.15(c)]

variable	columns	entry
ESE (1)	1-10	strain value, point 1 = 0
ESE (2)	11-20	strain value, point 2
.		.
.		.
.		.
ESE (8)	71-80	strain value, point 8

Card 7, etc. (8F10.0)

variable	columns	entry
ESE (9)		strain value, point 9
.		.
.		.
.		.
ESE (NPTS)		strain value, point NPTS

6. EVALUATION OF BEHAVIOR OF ANCHORED MAIN BARS

6.1 GENERAL REMARKS

Test results from the experimental program indicate that flexural and shearing deformations are not the only sources of beam tip deflection, δ, in R/C beams. A significant part of the δ was due to slippage or pull-out of the main reinforcement from its anchorage. On the basis of experimental data (Tables 4.3a-4.3i), it was found that the amount of tip deflection due to this slippage, δ_{FE}, accounted for 20 to 50 percent of the total tip deflection. Since the slippage of steel reinforcement relative to concrete mainly occurred due to bond deterioration [6.1, 6.2], knowledge of the basic mechanism and factors controlling the bond deterioration is essential.

Many studies have been conducted on bond deterioration under general loading [6.3-6.8]. These studies have contributed significantly to an understanding of the mechanism of bond deterioration. Some of the more pertinent findings are reviewed here briefly, followed by a discussion of a proposed mechanism of bond deterioration under general loading.

The behavior of anchored main bars in the experimental beams is discussed on the basis of the measured steel strains along these bars and the corresponding stress values predicted from the hysteretic steel stress-strain model developed in Appendix A5. These data offer a good opportunity to study the bond deterioration and stress transfer from anchored steel to concrete. To gain further insight into the mechanical behavior of the concrete boundary layer around the anchored bars, a finite element analysis of both the elastic and inelastic behavior of the layer is carried out in Appendix A6.

6.2 NATURE OF BOND BETWEEN STEEL AND CONCRETE

The nature of the bond between steel and concrete has been extensively studied [6.1 and 6.2]. For the type of reinforcement used in the present tests on deformed bars, bond is mainly due to the bearing of bar lugs on concrete and the strength of concrete between lugs. Some of the bond resistance comes from friction and from the chemical adhesion between the concrete and bar surface [6.1]. The variables that have been known to affect bond effectiveness are: local stress level, history of loading, lug geometry and spacing, size of bar, amount of concrete cover surrounding the bar, properties of concrete surrounding the bar (i.e., tensile and compressive concrete strength), and type of aggregate (normal or lightweight).

The design and anchorage of the main longitudinal #5 or #6 steel bars were similar in all beams (Sect. 2.1.1). The main variable affecting the slippage of an anchored bar is the history of the force acting on the bar at the beam-column interface, which in turn depends on the prescribed loading history applied on the beam.

6.2.1 Effect of Loading History on Bond Deterioration

The most significant studies on the effect of loading history and bond deterioration can be divided into three groups according to the method of loading and the type of specimen selected: (1) Tests carried out to study the flexural bond deterioration along the embedded bar between two crack surfaces (flexural cracks), with loading applied at the two ends of the bar, Fig. 6.1(a) [6.3-6.5]. The strain distribution along the steel is measured to check the bond deterioration along the bar. (2) Tests on the local bond stress-slip relationship [6.6]. In these tests the reinforcing bar is embedded in concrete over a short length (several bar diameters long) and the bar is loaded only at one end [see Fig. 6.1(b)]. (3) Tests on

Preceding page blank

the anchored bar embedded in concrete with an anchored length sufficient to develop the strength of the bar [6.4, 6.7, 6.8]. These tests were conducted to study the bond slip taking place along flexural steel anchored in an exterior column [Fig. 6.1(c)].

The types of loading history investigated were monotonic loading [6.4-6.8], cyclic loading in tension [6.3-6.8], and cyclic loading in tension and compression [6.4-6.8].

The general conclusions on the effect of loading on bond resistance can be summarized as follows:

(1) Bond deterioration is sensitive to the previous loading history. The greater the magnitude of the previous peak stress, the greater the disruption of the local bond and the less effective the bond at lower stress levels [6.3-6.8].

(2) A limited number of repeated loading and unloading cycles in tension, below the proportional limit of the steel does not induce appreciable bond deterioration. However, once the steel has undergone several complete stress reversals from tension to compression, bond deterioration can be readily observed [6.3-6.8].

(3) Bond deterioration contributes to the degradation of axial stiffness of a rebar embedded in concrete. As the bond along the embedded bar deteriorates, the effect of the concrete surrounding the bar on axial stiffness diminishes [6.3-6.5].

(4) Yielding of steel along the embedded length of the bar further contributes to the stiffness degradation. Upon loading reversal, the stiffness is affected by the Bauschinger effect of steel [6.5-6.7].

6.2.2 Bond Deterioration Mechanism

Bresler and Bertero [6.3] have proposed a theory which explains the mechanism of bond deterioration under repeated loading as a failure in the concrete boundary layer adjacent to the steel-concrete interface. This failure occurs when the stress reaches a critical value and local fracture and inelastic deformation take place. Damage to the concrete boundary layer from previous loadings tends to accumulate and is irreversible. Therefore, the greater the magnitude of the previous peak stress and number of cycles, the greater the softening of the concrete boundary layer and the less effective the bond at lower stress levels. Once a bar experiences stress reversal, further damage to the concrete boundary is inflicted and, therefore, results in further bond deterioration.

Although the failure theory mentioned above is useful for explaining the phenomenon of bond deterioration under repeated loading, further studies are needed to identify the actual physical bond failure mechanism.

Goto [6.9] has studied the internal cracking development in concrete around a deformed tension bar. His study has helped to identify the physical bond resistance and progressive failure mechanisms which cause bond deterioration. Based on his findings and information gained from other investigators, a theory on the mechanism of bond deterioration under general loading is proposed.

6.3 THEORY ON BOND DETERIORATION MECHANISM

To illustrate this theory, some of the test results on the local bond stress-slip relationship under different loading histories obtained by Morita and Kaku [6.6] are reproduced in Fig. 6.2. These curves were obtained from monotonic loading, repeated loading in

one sense, and loading reversals. The tests were carried out on a 25-mm diam. (#8) deformed bar embedded in the center of an R/C beam. The embedment length (bond length) was 66 mm (2.6 in.). The deformations (lugs) of the bar have a height of 2.6 mm (0.102 in.), a 45-degree lug face inclination, and are spaced at 16.7 mm (0.66 in.).* The bar is loaded at one end and the slip is measured at the other end (free end of the bar). The bond stress, u, is calculated from the applied load, F, by:

$$u = \frac{F}{\Sigma_0 \Delta x} \tag{6.1a}$$

where Σ_0 is the perimeter of the bar and Δx, the embedment length. The relationship between the applied stress, σ, and the u, obtained by substituting $\sigma_s = F/A_b$ (A_b is the area of the bar) into Eq. 6.1a and rearranging, becomes:

$$\sigma_s = u \frac{\Sigma_0 \Delta x}{A_b} \tag{6.1b}$$

In no test did the applied steel stress exceed the yielding stress of the bar.

6.3.1 Monotonic Response (Specimen A25-4-MN)

This specimen is shown in Fig. 6.2(a). As this bar was subjected to a monotonically increasing tensile force, cracks would initiate in the concrete around the tip of the bar lugs due to stress concentration [Fig. 6.3(a)].** At this stage of loading, the force (stress) transfer from bar to concrete was mainly provided by the wedging action of bar lugs and, to a lesser degree, by friction between the steel and concrete. Wedging action was provided by lugs bearing on the concrete "teeth," which caused compression of the concrete in the directions shown in Fig. 6.3(a).

As indicated by the dashed line in Fig. 6.2(a), continuous stiffness degradation was observed in the monotonic response. This degradation can be explained by the increasing internal cracking and inelastic deformation of the compressed concrete. As the applied load on the bar increases so does the magnitude of stresses in the concrete boundary layer. An increase in tensile stress will cause further propagation of internal cracks. As concrete is compressed inelastically by the wedging action of the deformed bar, there will be a reduction in the tangent modulus of the concrete boundary layer. This reduction can be observed in the typical concrete compressive stress-strain relationship of Fig. 2.10. For the above reasons, there will be a continuing degradation in stiffness as shown in the monotonic stress-slip bond response.

6.3.2 Repeated Loading in One Sense (Specimen A25-12-RP)

This bar was subjected to a series of unloadings and reloadings in tension with increasing slippage. The response curves indicated by solid lines in Fig. 6.2(a) show that each time the load was removed some residual slippage remained. This can be explained by the fact that some inelastic deformations were generated in the concrete boundary layer around the bar as the concrete teeth were subjected to large concentrated compression forces exerted from the tension bar [Fig. 6.3(a)]. These inelastic deformations were not recovered after releasing

---

* These data were obtained through private communication with Messrs. Morita and Kuku in July, 1974.

** The crack pattern indicated in Fig. 6.3(a) is drawn according to the observed crack pattern formed in the concrete boundary layer around deformed bars reported by Goto [6.9].

the load ; thus, the previously opened cracks were not closed [Fig. 6.3(b)].

It can also be seen from Fig. 6.2(a) that at reloading, the average loading stiffness is not significantly different from that of the previous unloading stiffness. This behavior can again be explained by the similar reloading and unloading stiffness characteristics of the compressed concrete [Fig. A5.14(b)].

6.3.3 Behavior under Reversed Loading (Specimen A25-11-RV)

This specimen was subjected to a series of loading reversals of increasing magnitude. The typical response during the loading reversal can be studied in three distinct stages, AB, BC, and CD [Fig. 6.2(b)].

As the load was reversed from A to B, there was some bond resistance which could have been due to friction between steel and concrete. Afterwards, as most of the friction was overcome, there was only slight bond resistance during loading from B to C due to open cracks, Δ_c, which originated in the previous loading as shown in Fig. 6.3(b). The bar had to move a distance over the open cracks before bar lugs could make contact with the concrete tooth, at which time the stiffness increased again [range CD, Fig. 6.2(b)].

The internal crack development during loading reversal in range CD, is illustrated in Fig. 6.3(c). As the bar lugs made contact with the surrounding concrete and traveled farther inward, the previously developed transverse cracks were forced to close. As the load increased further, a new set of transverse cracks developed in the directions of principal tensile stress, normal to the previous set of cracks [Fig. 6.3(c)]. If the applied load or deformations during reversal had been sufficiently large, some transverse cracks might have joined with the previously formed cracks.

As the load reversed again after point D, a process similar to that from A to D took place [Fig. 6.2(b)]. Frictional resistance was smaller than before, however, because the concrete tooth was broken up [Fig. 6.3(d)], resulting in a different crack pattern.

Test results for another case of reversed loading are shown in Fig. 6.2(c). The bar (A25-13-RR) was subjected to loading reversals in which the applied compressive force was smaller than the tensile force. The applied compressive force was not intense nor was it long enough to induce reversal in slippage. The bar did not move enough under compression to make bar lugs contact with the concrete. Consequently, the stiffness increase observed in stage CD of Specimen A25-11-RV did not occur.

6.4 ANCHORAGE BEHAVIOR OF TEST BEAMS

Figure 6.4 shows the arrangement and loading of anchored main bars in a typical anchorage zone of a test beam. The anchorage of the main bars is similar for all test beams (Sect. 2.1.1). The characteristics of bar anchorage include: (1) a long, straight anchorage length of 26.25 in. which corresponds to 35 times the diameter of a #6 bar or 42 times the diameter of a #5 bar; (2) a 180-degree standard end hook provided at the end of the anchored bar; and (3) a massive anchorage block which provides a minimum of a 5-in. side cover and a 4-in. rear cover backed up by a 1-1/8 - in. steel plate of the reaction fixture box (Fig. 3.1).

The forces acting on the anchored steel bar are the internal forces carried by the main steel reinforcement (Fig. 6.4). These forces are axial force T or C and shear force V_{dw}. The slippage of anchored steel is mainly caused by the applied axial load deformation. The shear at the beam-column interface tends to produce more local disruption of the concrete,

thus accelerating bond degradation along the anchored bars near the interface. The behavior of bond deterioration along anchored steel is examined mainly on the basis of the measured steel strain distribution along the anchored bars of Beams T-2 and T-3. The steel strain distribution curves and the corresponding stress distribution curves are shown in Figs. 6.5-6.14.

6.4.1 Reduction of Steel Strain Distribution Data

Microdot weldable strain gages (approximately 1-3/4 in. in length) were used to determine the strain variation along the anchored main bars. These gages were spaced far enough apart to minimize the interference of gages and their connecting wires with the development of the bond along the bar. Three gages were used to measure the top and bottom steel strains. The first and third strain gages were placed on the same bar about 11.5 in. apart and the second gage, on the adjacent bar 5 in. from the beam interface, as shown in Fig. 6.5. In this figure, the portion of the anchored bar between the first and the second gages is referred to as Region I, and that between the second and third gages, as Region II.

6.4.2 Computation of Steel Strain and Average Bond Stress

Steel stress distribution along the anchored bars (Fig. 6.6, 6.11, and 6.14) is computed from the corresponding steel strain distribution using the steel stress-strain model described in Sect. A5.1.

The average bond stress between gages is computed as follows:

$$u \text{ (average bond stress)} = \frac{A_b}{\Sigma_o} \frac{\Delta\sigma_s}{\Delta x} \tag{6.2}$$

where

A_b = area of bar

$\Delta\sigma_s$ = difference in steel stress between two gage points

Σ_o = perimeter of bar

Δx = distance over which u is computed, i.e., distance between two gage points

6.4.3 Behavior under Monotonic Loading

Figs. 6.5 and 6.6 show the distributed strain and stress curves for the anchored top #6 bar of Beam T-2 loaded under monotonically increasing tension. Using this bar as an example, the following observations can be made.

(1) As the applied stress increased to 26 ksi at LP 2 (Fig. 6.6), most stress transfer took place along the bar in the first 11.5 in. from the beam-column interface which is about 34 percent of the total equivalent anchorage length (34.2 in.*). As the applied stress increased further, increasingly more stress was transferred in the remaining anchorage length of 22.7 in. This fact can be seen by the steady increase of stress value at gage T3 with the increase of the applied stress (Fig. 6.6). This behavior indicates that as the applied force on the anchored bar increases, there is a redistribution of resisting forces along the bar from the highly stressed region near the loaded end (beam-column interface) to the remaining

---

* This includes 26.25 in. of straight embedment length plus an equivalent embedment length of 7.93 in. for the end hook (Sect. 2.1.1).

anchorage. This redistribution may be due to the softening caused by the development of internal cracking and inelastic deformations in the concrete boundary layer of the highly stressed regions of the beam.*

(2) After the steel yielded at the interface at LP 4, inelastic strain developed first along Region I and then along Region II (Fig. 6.5). The propagation of inelastic strains inside the anchored bar could have been caused by the strain-hardening of steel and/or local bond failure along the anchored bar as the maximum bond-stress transfer capacity was exceeded. This fact is indicated in the results shown in Fig. 6.6. After maximum bond stress was reached at about 490 psi in Region I at LP 3, the bond stress started to drop, and yielding of steel occurred in Region I at LP 4 and at subsequent load points (Fig. 6.5). The maximum bond stress reached in Region II was 690 psi at LP 5, about 41 percent higher than that in Region I (Fig. 6.6). After LP 5, the bond stress decreased and yielding occurred within Region II (Fig. 6.5). The code specifies an ultimate bond stress for the top tension bar of 560 psi [6.10], which is about 14 percent higher than the maximum bond stress observed in Region I and 19 percent lower than that in Region II.** The reason for the smaller stress transfer capacity in Region I could be due to the fact that the V_{dw} carried by the main bar (Fig. 6.4), tends to produce local disruption of the bond near the beam-column interface, i.e., in Region I. Therefore, the bond stress that can be developed in Region I is less than that in Region II.

6.4.4 Behavior under Cyclic Loading

(a) Behavior of anchored bars. - The experimental results on stress distribution along cyclically loaded anchored top and bottom main bars of Beams T-1 and T-3 (Figs. 6.11 and 6.14) indicate that the anchorage lengths of these bars have more than sufficient capacity to develop the compressive force applied on the bar at peaks of loading reversals. Most of the applied compression was transferred along the first 11.5 in. of embedment length out of an equivalent available anchorage length of about 33 in. to 36 in. (Sect. 2.1.1).

On the other hand, when these bars were loaded in tension at the peaks of loading reversals, the first 11.5 in. of anchorage length was not enough to transfer all the applied stress; a large part of the applied stress had to be transferred along the remaining anchorage length (Figs. 6.11 and 6.14). More anchorage length is required to transfer tension than to transfer compression for the following reasons: (1) The force or deformation induced in compression bars is generally smaller than that in tension bars [Figs. 6.7(a), 6.9(a), 6.12(a), and 6.13(a)]. This is because once the crack at the beam-column interface closes due to flexure, concrete in the beam will take a part of the compression, thus relieving the amount of compression to be carried by the anchored compression bars. (2) A higher bond stress can be developed along compression bars than along tension bars [6.1 and 6.2]. The maximum bond stresses observed in the compression bars were 1110 psi for the #5 bars [Fig. 6.14(b)] and 940 psi for the #6 bars [Fig. 11(a)]. On the other hand, the observed maximum bond stress along the tension bars did not exceed 830 psi (Figs. 6.11 and 6.14).

---

* See the analytical studies in the appendix to this chapter.

** In view of the fact that the presence of strain gages, together with their connecting wires and wrappings, tends to interfere with bond development, it is possible that the bond stress developed in Region I without the presence of gages could be higher than the code specified value for ultimate bond stress (560 psi).

(b) Effect of cyclic loading on bond deterioration. - To study the effect of cyclic loading on bond deterioration, the steel strain distribution curve of the top and bottom tensile #6 bars of Beams T-1 and T-3 are compared with the corresponding computed monotonic curves having the same steel strain value at the interface (Figs. 6.7-6.10 and 6.12).

These monotonic curves are established from steel strain data of monotonically loaded tensile #6 bars of Beam T-2 as follows: for a given steel strain at the interface, the strain at the second and third gage positions can be determined from the curves in Fig. 6.15. These curves are established from the three strain gage readings of the #6 bars of Beam T-2 (Fig. 6.5).

To establish a quantitative index for estimating bond deterioration, the parameter λ is introduced. This parameter is defined as the bond deterioration index due to cylic loading; thus:

$$\lambda = \frac{\Delta_{cy} - \Delta_m}{\Delta_m} = \frac{\Delta_\lambda}{\Delta_m} \tag{6.3}$$

where Δ_{cy} is the integral of steel strain ($\int \varepsilon_s(x)\, dx$) along the first 11.5 in.* of the cyclically loaded anchored bar, and Δ_m is the integral of steel strain along the first 11.5 in. of the monotonically loaded anchored bar which has the same steel strain value at the beam-column interface as that of the cyclically loaded anchored bar. The value of Δ_m is also equal to the area under the monotonic curves indicated in Figs. 6.7-6.10, and 6.12. The quantity Δ_λ ($= \Delta_{cy} - \Delta_m$) represents the increase in the amount of bar elongation due to the effect of cyclic loading.

The bond deterioration caused by cyclic loading prior to the yielding of steel can be seen by the behavior of the bottom #6 bars of Beam T-3 (Fig. 6.7). The results show that after the bars had undergone a compressive stress of -5 ksi at LP 2 and were then loaded to a tensile stress of 22 ksi at LP 4 in the first cycle, some bond deterioration occurred as indicated by the λ value (Eq. 6.3) of 0.16 [Fig. 6.7(b)]. This bond deterioration is apparently due to damage produced on the bond as these bars were subjected to compression at LP 2.

After LP 4, the bars underwent two more similar cycles of tension and compression. These two repeated cycles did not appear to produce further bond deterioration: the steel strain distribution at LP 8 and LP 12 remained essentially unchanged [Fig. 6.7(b)].

The results confirm the previous finding (Sect. 6.2.1) that if the magnitude of applied deformation is small, a limited number of repeated reversals would not produce much further bond deterioration.

Bond deterioration caused by cyclic loading after the yielding of steel is examined for the anchored top bars and bottom bars of Beam T-3 (Figs. 6.8 to 6.10) and those of Beam T-1 (Figs. 6.12 and 6.13). As loading reached LP 16 at a δ/δ_y of one [Fig. 6.8(a)], the anchored bottom bars of Beam T-3 yielded and the strain at the interface increased to about 13.5 x 10^{-3} in./in. Yielding of the steel penetrated to the position of gage B2, which is located 5 in. inward from the beam-column interface. Afterwards, when the loading was reversed to LP 18 at a δ/δ_y of one, the bar was subjected to a compressive stress of

* This length of 11.5 in. was used because it is the length where steel strains were measured.

-51 ksi, and the steel strain at the beam-column interface was reduced to about 2.7 x 10^{-3} in./in. [Fig. 6.8(a)]. The steel stress distribution curve at LP 18 [Fig. 6.11(b)] shows that the average bond stresses that occurred along Regions I and II were about 600 psi and 720 psi, respectively. At this level of bond stress, the newly developed cracks under compression could have joined the internal cracks that were previously developed under tension [Fig. 6.3(c)]. As a consequence, when the bar was again loaded in tension to LP 20 at a δ/δ_y of -1 [Fig. 6.8(a)], significant bond deterioration occurred as indicated by the λ value of 0.44, and the Δ_λ value of 0.018 in. In the following two repeated cycles at a δ/δ_y of one [LP 20 to LP 26, Fig. 6.8(a)], no further bond deterioration was observed in the measured regions, I and II.

In the next three cycles at a δ/δ_y of two [LP 28 to LP 36, Fig. 6.8(b)], the applied peak tensile stress increased to about 72 ksi and the tensile strain, to about 22 x 10^{-3} in./in. At the compression peaks (LP's 30 and 34), the stress changed to about -62 ksi, and the strain was reduced to about 6 x 10^{-3} in./in. The amount of bond deterioration at this level of ductility is reflected in the λ value of 0.24 and the Δ_λ value of 0.024 in. The increase in bar elongation due to the effect of cyclic loading was about 33 percent greater than that at the lower ductility ratio of one (0.018 in.). The value of λ at a δ/δ_y of two (0.24) was actually 46 percent smaller than that at a δ/δ_y of one (0.44). The reason can be seen in the expression for λ, where $\lambda = \Delta_\lambda/\Delta_m$ according to Eq. 6.3. Since the value of Δ_m is 0.10 in. at a δ/δ_y of two and only 0.04 in. at a δ/δ_y of one, the ratio Δ_λ/Δ_m is actually smaller, despite the larger value of Δ_λ at a δ/δ_y of two.

The series of stress reversals applied on the anchored top bars of Beam T-3 was less severe than that applied on the bottom bars of the same beam. This can be seen in the stress and strain limits reached in these top and bottom bars during the history of cyclic loading [compare loading histories in Figs. 6.9(a) and 6.7(a)]. The amount of bond deterioration that occurred in the top bars of Beam T-3 was considerably smaller than that in the bottom bars. For example, after six cycles of gradually increasing inelastic reversals, bond deterioration was first observed in the top bars at a δ/δ_y of three [LP 38, Fig. 6.10(b)]. The λ value and the Δ_λ value at this point were about 0.114 and 0.011 in., respectively. In comparison, considerably more bond deterioration had occurred in the bottom bars of the same beam at the lower ductility ratios of one and two.

The degree of bond deterioration occurring in the top #6 bars of Beam T-1 was as small as that in the top #6 bars of Beam T-3 since the applied loading histories in these bars were similar in intensity and characteristics [see loading histories in Figs. 6.9(a) and 6.12(a)]. On the other hand, the applied series of stress reversals on the bottom #5 bars of Beam T-1 was more severe than that of the bottom #6 bars of Beam T-3. This can be seen clearly by the stress and strain limits reached at comparable peak points [Figs. 6.7(a) and 6.13(a)]. During the series of stress reversals in the inelastic range, the strain of the anchored bottom bars of Beam T-1 actually reversed at the beam-column interface. This reversal was not observed to occur in the bottom bars of Beam T-3.

For this reason, although the bottom #5 bars of Beam T-1 had inherently better bond characteristics than the larger, bottom #6 bars of Beam T-3, the bond deterioration occurring in the #5 bars was more pronounced than that in the #6 bars.* This fact can be observed

---

* For the same length of the bar, the bond stress required to resist a given amount of applied steel stress, $\Delta\sigma_s$, is proportional to the ratio, A_b/Σ_0 (Eq. 6.1). For #5 bars, this ratio is 0.158, and for the #6 bars, it is 0.187, or 18 percent higher.

from comparing the ratios between the measured steel strain at the first gage, ε_1, at the beam-column interface and that at the second gage, ε_2, located 5 in. inward from the interface. The third gage readings were not available for comparison due to its early failure on the bottom bar of Beam T-1.

LP	Beam	Strain at 1st Gage ε_1 (10^{-3}in./in.)	Strain at 2nd Gage ε_2 (10^{-3} in./in.)	Ratio of ε_2 and ε_1 $\frac{(\varepsilon_2/\varepsilon_1)_{T-1}}{(\varepsilon_2/\varepsilon_1)_{T-3}}$
16	T-1/T-3	12.5/13.5	4.10/ 2.25	0.33/0.167
24	T-1/T-3	12.3/14.6	9.90/ 6.20	0.81/0.425
28	T-1/T-3	26.5/22.2	9.10/11.30	0.72/0.510

The ratio $\varepsilon_2/\varepsilon_1$ indicates that due to a larger bond deterioration occurring along the anchored bottom bars of Beam T-1, the strain that developed at the second gage position of these bars was higher than that at the same position on the bottom bars of Beam T-3 for a similar amount of steel strain at the interface.

6.5 CONCLUDING REMARKS

From the results presented in this chapter and in Appendix A6, the following observations can be made:

(1) The finite element analysis of the mechanical behavior of the concrete boundary layer around an anchored main #6 bar (Appendix A6) provided data and results that lead to a better understanding of the behavior of the anchored main bars of the experimental beams. The results show that cracks can initiate in the concrete boundary layer around the deformed tensile #6 bars at a very low steel stress level (about 2.3 ksi). The resulting crack development in the concrete boundary layer is the reduction of the contribution of concrete to the axial stiffness of the embedded steel reinforcing bar and the ensuing redistribution of stress from the cracked region to the uncracked region that exists along the remaining length of the bar. Stress is transferred along the cracked concrete boundary layer mainly through radial compressive stress in the concrete. The general inclination of the predicted crack pattern correlated well with that observed in the test results reported by Goto [6.9].

(2) Analysis of the results on anchored main bars of the experimental beams shows that a larger maximum bond stress can develop along compression bars than along tension bars. The values of the maximum nominal bond stress, u_{max}, observed were 960 psi along compressive #6 bars (the corresponding ACI code value is 800 psi), and 690 and 830 psi along top and bottom tensile #6 bars, respectively (the code values are 560 psi and 800 psi, respectively).

(3) There are two areas where bond stress could not develop effectively: (a) Near the beam-column interface, where bond disruption occurs due to dowel action developed as a consequence of the shear action at the interface. The results obtained from the top tensile #6 bars show a 30 percent decrease in the value of u_{max} toward the interface. (b) Along the embedment length where yielding takes place at the peaks of cyclic loading. Not much stress transfer can be developed along this length because as the strain increases in the range of the plastic plateau, there is no stress increase, i.e., very early strain-hardening.

(4) Test results show that when anchored main bars are subjected to a number of gradually increasing inelastic stress reversals, the amount of bond degradation depends on the magnitude

of tensile and compressive stresses, as well as the magnitude of strain limits reached during the stress reversals. Bond degradation is especially severe when both the applied stress and strain are reversed at the loaded end.

(5) If the anchorage failure can be delayed or prevented, the development of inelastic deformations along the anchored main bars could provide an important source of energy dissipation for the beam. In Beam T-3, for example, the amount of energy dissipated in the anchored bars computed from the M-θ_{FE} diagram [Fig. 4.11(b)] constituted about 44 percent of the total energy dissipated in the beam. It is doubtful that the same amount of dissipation would occur in the case of actual beam-to-column joints. In such joints, the straight anchorage length* of main bars is usually determined by the width of the column. In order to delay anchorage failure caused by progressive penetration of inelastic deformation (yielding) along the anchored bar of these interior and exterior beam-column joints, it is recommended to use a small diameter bar with a large plastic plateau and a small rate of strain-hardening.

---

* The straight anchorage length used in the half-scale beam was 26.25 in. This length was large compared to the 17-in. width of the half-scale prototype frame column to which the beam was connected.

A6. APPENDIX TO CHAPTER 6
ANALYTICAL STUDY OF BOND BEHAVIOR

A6.1 GENERAL REMARKS

As pointed out in Chapter 6, the bond behavior along anchored bars is directly affected by the development of internal cracking in the concrete boundary layer around the bar. The objective of this analytical study is to solve specific problems related to the mechanical behavior of such a concrete boundary layer. These problems include defining the stress level at which internal cracking initiates in the concrete around an anchored deformed bar (such as the #6 bar used in the beam tests), and determining how the internal cracking in concrete around such an anchored bar develops (propagates) and what the quantitative effect of this cracking is on the bond behavior.

An existing nonlinear finite element analysis program, NONPLAX [6.11], which can take into account the effect of concrete cracking, was used for the present study. The significance of the results are discussed and suggestions for future studies are presented.

A6.2 BRESLER AND BERTERO STUDY

In the study reported by Bresler and Bertero [6.3], a centrally reinforced concrete prism fixed at one end was analyzed using an axisymmetric linear-elastic finite-element model. The deformed #8 bar was modeled as a plain bar. Hence, the effect of the bar lugs was not studied.

The results of their study show that the stress developed at the steel-concrete interface near the loaded end of the concrete prism was considerably higher than that in the remainder of the prism, and that cracking can be initiated at a low level of applied steel stress.

To study the effect of the cracking and inelastic deformations that occurred in the concrete boundary layer, the material characteristics of concrete around the bar were modified to give a "softer" resistance. On that basis the results indicate that relatively more deformation would occur in the softer concrete boundary layer. This caused a redistribution of stress away from the highly stressed region to the remainder of the concrete prism.

A6.3 FINITE-ELEMENT MODEL

To predict the steel stress level which will initiate internal cracking in concrete surrounding a main #6 bar, an axisymmetric finite-element model is adopted. The dimensions of this model are shown in Fig. A6.1. The model is made of a bar embedded in concrete with load applied at one end. The length and diameter of the concrete prism were chosen to be about five times the diameter of the #6 bar (or 4 in.) It was thought that with a prism of this size different boundary support conditions would not significantly affect results obtained for local stresses in the steel-concrete interface near the loaded end where internal cracking was expected to initiate. To prove this point, two support conditions were studied. In one case, the concrete prism was supported at the end of the prism (Model 1); in the other, it was supported at the longitudinal surface (Model 2) (Fig. A6.1). These stresses were therefore similar to those developed in the vicinity of the anchored #6 bar in the tested beam. Based on the analytical results, conclusions could therefore be made regarding the steel stress level at which internal cracking would initiate along the anchored #6 bar.

To study the internal crack development, crack pattern, and quantitative effect of this cracking on bond behavior, Model 2 was used. This model approximately represents a 4-in.

segment of the actual anchored #6 bar embedded in the massive concrete anchorage block which provided a minimum concrete cover thickness of 5 in. (Fig. A6.2). The applied force, F, on the model represents the force transferred from steel to concrete over the 4-in. segment of the anchored bar (Fig. A6.2).

A6.4 FINITE ELEMENTS

The deformed #6 bar and the surrounding concrete are modeled as shown in Fig. A6.1. The finite element used to represent the steel bar and concrete was the 4-node linear strain axisymmetric quadrilateral element. This element can also be collapsed into a triangular element by specifying two nodes at the same location.

For the 4-node linear-strain axisymmetric isoparametric quadrilateral element (Fig. A6.3), the relationship between the displacement field inside the element (u_r, u_z) and the displacement at nodes (u_{ri}, u_{zi}) is given by:

$$u_r = \sum_{i=1}^{4} h_i \, u_{ri} \tag{A6.1a}$$

$$u_z = \sum_{i=1}^{4} h_i \, u_{zi} \tag{A6.1b}$$

where the displacement interpolation functions, h_i, are:

$$h_1 = \frac{1}{4}(1-s)(1-t)$$

$$h_2 = \frac{1}{4}(1+s)(1-t)$$

$$h_3 = \frac{1}{4}(1+s)(1+t)$$

$$h_4 = \frac{1}{4}(1+s)(1+t)$$

where s and t are local element coordinates. In mapping the local coordinates to r-z structural coordinates, identical interpolation functions are used:

$$r = \sum_{i=1}^{4} h_i \, r_i \tag{A6.2a}$$

$$z = \sum_{i=1}^{4} h_i \, z_i \tag{A6.2b}$$

In the axisymmetric problem, the shear strains, $\gamma_{r\theta}$ and $\gamma_{z\theta}$, are zero using symmetry. The relationship between the non-zero strains and the displacement is:

$$\underline{\varepsilon} = \begin{Bmatrix} \varepsilon_{zz} \\ \varepsilon_{rr} \\ \varepsilon_{\theta\theta} \\ \gamma_{rz} \end{Bmatrix} = \begin{Bmatrix} u_{z,z}{}^{*} \\ u_{r,r} \\ u_r/r \\ r_r/z + u_{z,r} \end{Bmatrix} \tag{A6.3}$$

$^{*}u_{z,z} = \dfrac{\partial u_z}{\partial z}$

Now substitute Eq. A6.1 into Eq. A6.3, to obtain the strain and nodal displacement relationships:

$$\underline{\varepsilon} = \underline{H}(s,t)\underline{u} = \begin{bmatrix} \underline{H},z & \underline{0} \\ \underline{0} & \underline{H},r \\ \underline{0} & \underline{H}/r \\ \underline{H},r & \underline{H},z \end{bmatrix} \begin{Bmatrix} u_z \\ \\ u_r \end{Bmatrix} \tag{A6.4}$$

where u_z and u_r are nodal displacement vectors, and

$$\underline{H} = [h_1 \quad h_2 \quad h_3 \quad h_4]$$

$$\underline{H},z = [h_{1,z} \; h_{2,z} \; h_{3,z} \; h_{4,z}]$$

$$\underline{H},r = [h_{1,r} \; h_{2,r} \; h_{3,r} \; h_{4,r}]$$

The internal stresses, σ_{rr}, σ_{zz}, $\sigma_{\theta\theta}$, and σ_{rz} (Fig. A6.3), are computed by multiplying the strain vector, $\underline{\varepsilon}$ (Eq. A6.4), by the appropriate material property matrices specified in Sect. A6.5.

A6.5 MATERIAL MODEL FOR CONCRETE

The basic assumptions for the concrete material behavior are listed below [6.11]:

(1) Under uniaxial stress, concrete is assumed to be elasto-perfectly plastic in compression where the elastic limit is defined by f'_c, and to fail in compression when reaching a specified crushing strain.* Cracking (tensile failure) is assumed to occur as the principal tensile stress reaches a specified tensile strength * and the internal element force in the cracked direction is redistributed to the remainder of the structure.

(2) Under a triaxial stress, cracking is allowed to occur at the principal stress directions in the r-z plane and in the hoop direction (Fig. A6.3); thus,

Elastic, uncracked concrete element:

$$\begin{Bmatrix} \sigma_{rr} \\ \sigma_{zz} \\ \sigma_{\theta\theta} \\ \sigma_{rz} \end{Bmatrix} = \frac{E_c}{(1+\nu)(1-2\nu)} \begin{bmatrix} 1-\nu & \nu & \nu & 0 \\ & 1-\nu & \nu & 0 \\ & & 1-\nu & 0 \\ \text{sym} & & & \frac{1-2\nu}{2} \end{bmatrix} \begin{Bmatrix} \varepsilon_{rr} \\ \varepsilon_{zz} \\ \varepsilon_{\theta\theta} \\ \gamma_{rz} \end{Bmatrix} \tag{A6.5}$$

---

*For the specified values used in the analysis, see Fig. A6.1.

Concrete element cracked perpendicular to principal stress direction 1 in the r-z plane:

$$\begin{Bmatrix} \sigma_1 \\ \sigma_2 \\ \sigma_3 \\ \sigma_{12} \end{Bmatrix} = \frac{E_c}{1-\nu^2} \begin{bmatrix} 0 & 0 & 0 & 0 \\ & 1 & \nu & 0 \\ & & 1 & 0 \\ & & & \frac{G^*(1-\nu^2)}{E_c} \end{bmatrix} \begin{Bmatrix} \varepsilon_1 \\ \varepsilon_2 \\ \varepsilon_3 \\ \gamma_{12} \end{Bmatrix} \tag{A6.6}$$

where G^* is the shear modulus of the cracked element = 0.0.

Concrete element cracked perpendicular to principal stress direction 2 in the r-z plane:

$$\begin{Bmatrix} \sigma_1 \\ \sigma_2 \\ \sigma_3 \\ \sigma_{12} \end{Bmatrix} = \frac{E_c}{1-\nu^2} \begin{bmatrix} 1 & 0 & & 0 \\ & 0 & 0 & 0 \\ & & 1 & 0 \\ \text{sym} & & & \frac{G^*(1-\nu^2)}{E_c} \end{bmatrix} \begin{Bmatrix} \varepsilon_1 \\ \varepsilon_2 \\ \varepsilon_3 \\ \gamma_{12} \end{Bmatrix} \tag{A6.7}$$

Concrete cracked in the hoop direction:

$$\begin{Bmatrix} \sigma_{rr} \\ \sigma_{zz} \\ \sigma_{\theta\theta} \\ \sigma_{rz} \end{Bmatrix} = \frac{E_c}{1-\nu^2} \begin{bmatrix} 1 & \nu & 0 & 0 \\ & 1 & 0 & 0 \\ & & 0 & 0 \\ & & & G \end{bmatrix} \begin{Bmatrix} \varepsilon_{rr} \\ \varepsilon_{zz} \\ \varepsilon_{\theta\theta} \\ \gamma_{rz} \end{Bmatrix} \tag{A6.8}$$

A6.6 MATERIAL MODEL FOR STEEL

In the present study, the steel was modeled by plane stress elements. A linear-elastic stress-strain relationship (Eq. A6.5) was used. In the cases studied here, the steel was not strained to yielding; the linear-elastic assumption therefore remains valid.

A6.7 MATERIAL PROPERTIES AND REBAR CHARACTERISTICS USED IN THE MODEL

The material properties used in the analytical model are typical of those of the test beams. The values are indicated in Fig. A6.1. The modulus of rupture of concrete (462 psi) was used for determining the cracking strength of the concrete elements.

The finite element mesh for the reinforcing bar was constructed to reflect the actual geometry of the deformed #6 bar with lugs. The lugs on the bar have a spacing of 0.45 in., a height of 0.10 in., and a lug face inclination of 45 degrees.

A6.8 NONLINEAR ANALYSIS SOLUTION PROCEDURE

The standard step-by-step nonlinear analysis solution procedure was used. For each loading increment, Newton-Raphson equilibrium iterations were carried out using a force convergence criterion. The structural stiffness was reformed at each iteration for a more rapid convergence.

A6.9 ANALYTICAL RESULTS

The analytical results are shown in Figs. A6.4 to A6.8. The stress distribution throughout the concrete prism is illustrated by the plots of stress components σ_{rr}, σ_{zz}, $\sigma_{\theta\theta}$, and σ_{rz}, as well as principal stress components σ_1 and σ_2 in the r-z plane. In Figs. A6.6 and A6.7, the crack pattern obtained from the analysis is also shown in Figs. A6.6 and A6.7.

It was assumed in the analysis that the amount of initial self-equilibrating internal stresses that might develop due to shrinkage and temperature variation in the prism were small and could be neglected.

A6.9.1 Stress Distribution in Uncracked Prism - Linear-elastic Solution

The stress distributions in Models 1 and 2 shown in Figs. A6.4 and A6.5 correspond to an applied steel bar displacement of 0.00005 in. The corresponding applied steel stresses were 760 psi for Model 1 and 890 psi for Model 2. The results indicate that the difference in the boundary conditions for the two models did not greatly affect the stress developed in the concrete boundary layer near the loaded end.

The results for both models indicate that high local stresses occurred at the steel concrete interface near the loaded end of the prism. The ratio between the applied steel stress and the maximum concrete principal tensile stress in both models was about 5 [Figs. A6.4(a)] and A6.5(a)]. Assuming that a crack initiated at 462 psi (a typical value of modulus of rupture for the concrete used in the present R/C beam tests), the magnitude of applied steel stress would have had to have been 5 x 462 = 2310 psi. This value is about 1/10 of that normally considered as the working steel stress level.

In Model 1, where the prism is fixed at the end, some of the applied load is transferred to the fixed end by axial tension in both steel and concrete. This is indicated in the longitudinal distribution of σ_z along the prism [Fig. A6.4(b)]. In Model 2, the end of the prism cannot resist forces; stress σ_z approaches zero at the free end, and all the applied force must be transferred by shear stresses across the steel-concrete interface [Fig. A6.5(b)].

Both models indicate that stresses σ_r and σ_θ, developed in the concrete boundary layer near the loaded end, are in tension [Figs. A6.4(c) and A6.5(c)]. This is caused by the radial displacement of the steel bar surface due to the Poisson effect having a steel ratio of 0.30.

A6.9.2 Predicted Crack Development in Concrete Layer around Anchored Main Bar and Its Effect On Bond Behavior

As discussed in Sect. A6.3, Model 2 was selected in order to study crack development in the concrete boundary layer and the effect of this cracking on bond behavior along an anchored main #6 bar.

The model was loaded incrementally at one end of the steel bar to cause cracks to develop along the surrounding concrete. The crack patterns at different loading stages are shown in Fig. A6.6. In Fig. A6.7, typical stress distribution in the cracked concrete prism is illustrated. The relationship between the applied stress, σ_s, and the axial displacement, $\Delta\delta_b$, of the steel bar at the loaded end is plotted in Fig. A6.8.

To find the average bond stress or the amount of stress transfer from steel to concrete corresponding to a given stress level, σ_s, the relationship given by Eq. 6.2 was used:

$$u = \frac{\sigma_s A_b}{\Sigma o \Delta x}$$

The values of A_b and Σ_o are those for the main #6 bar under study and that of Δx = 4 in., for the embedment length of this bar in Model 2.

Based on the results shown in Figs. A6.6 to A6.8, the following observations can be made.

(1) With increasing load, cracks propagate along the concrete boundary layer around the steel (Fig. A6.6). Most of the cracks that developed could be described as "inclined ring" cracks as illustrated in Fig. A6.6. Because of stress concentration at the tip of the bar lugs, these inclined cracks usually initiated in the concrete directly above the lugs [Figs. A6.6(a) - A6.6(d)].

(2) The formation of these inclined ring cracks was due to the fact that the principal tensile stress exceeded the cracking strength of the concrete (Sect. A6.7). As cracking took place, the stress previously carried in the principal tensile stress direction was redistributed to the remainder of the structure. No tension could then be transmitted across the cracked planes. This can be observed in the principal stress vectors in the cracked concrete boundary layer where zero tensile stress is indicated in the cracked direction perpendicular to the principal compressive stress direction, σ_2 [Fig. A6.7(a)].

(3) The angle and direction of the predicted inclined crack pattern [Figs. A6.6 and 6.7(b)] correlated reasonably well with that indicated in the experimentally observed crack pattern reported by Goto [6.9]. The latter is shown in Fig. 6.3(a).

(4) The results in Fig. A6.7(a) demonstrate that as inclined cracking occurred in the concrete layer, the stress transfer from steel to the surrounding concrete was achieved through the radial compression of concrete at inclined angles. A large part of this compression was transferred through the wedge action of the deformed bar.

(5) As concrete surrounding the steel was compressed radially by the wedge action of the bar, tensile hoop stresses, σ_θ, were induced, as shown in Fig. A6.7(c). Splitting cracks formed as the tensile hoop stress exceeded the cracking strength of the concrete [Figs. A6.6(c), A6.6(d) and A6.7(b)].

(6) The quantitative effect of internal cracking on bond behavior can be seen in Fig. A6.8 by comparing the responses of nonlinear and linear-elastic (perfect bond) stress-displacement with cracking. The departure of the nonlinear σ_s versus the δ_b curve from the linear-elastic one shown in Fig. A6.8 was due to the development of internal cracking alone. This is because the applied stress level was not high enough to cause either the concrete to compress beyond f'_c (-4510 psi*) or the steel bar to be stressed (in tension or in compression) beyond the yield stress value of 65,000 psi. Therefore, except for concrete cracking, concrete and steel are still in the linear-elastic range. Internal cracking caused a softening of the concrete boundary layer around the bar; this led to a bar displacement, $\Delta\delta_{bc}$, greater than that for the linear-elastic solution at the same stress level (Fig. A6.8). For example, before the first cracking at about 2.3 ksi, the value of $\Delta\delta_{bc}$ was zero since concrete cracking had not yet occurred (Fig. A6.8). However, after the crack initiated displacement, the value of $\Delta\delta_{bc}$ becam increasingly large; for example, at a bond stress of 400 psi, the contribution of $\Delta\delta_{bc}$ to the total bar displacement, δ_b, was about 26 percent. Stiffness degradation caused by internal cracking was also observed. The slope (stiffness)

* The concrete compressive strength is assumed to be the elastic limit for concrete in compression (Sect. A6.5).

of the σ_s vs. δ_b curve before the first cracking was about 18 ksi/in. After cracking had been initiated and the bar was loaded to about σ_s = 5 ksi (u = 240 psi), the stiffness was reduced to about 12 ksi/in. and then decreased to 9.3 at σ_s = 10 ksi (u - 480 psi) (Fig. A6.8).

A6.9.3 Significance of Results Related to Pull-out of Anchored Main Bars

The analytical results indicate that internal cracks could initiate at a low level of steel stress, i.e., about 2.3 ksi near the loaded end of the anchored #6 bar.

The analytical results from Model 2 indicate that the increase in stress transfer from steel to concrete along a segment of the anchored bar will cause propagation of internal cracking in the concrete boundary layer. A reduction of the axial stiffness of the embedded bar takes place due to softening of the cracked concrete boundary layer. Along a real anchored bar this concrete cracking, accompanied by local concrete crushing and inelastic deformation, will cause disruption of the bond, resulting in bond slippage which will then lead to the pull-out (slippage) of the rebars from their anchorage zone.

A6.10 SUGGESTIONS FOR FUTURE STUDIES

In future studies, it will be desirable to model the whole anchored bar with the surrounding concrete to study the effect of crack propagation, crushing and inelastic deformation along the concrete boundary layer as well as the effect of inelastic deformations developing along a steel rebar on the slippage of the anchored bar. Under cyclic loadings in which inelastic deformation is expected to be induced in both concrete and steel, the hysteretic models for steel and concrete must be incorporated in the analytical model. Finally, experimental data on the slippage of anchored rebars under such loadings are needed to qualify analytical procedures and assumptions.

7. EVALUATION OF SHEAR BEHAVIOR

7.1 GENERAL REMARKS

In the past a large number of tests have been performed to study the behavior and strength of concrete beams failing in shear. Theories pertaining to shear failure and possible shear transfer and shear-resisting mechanisms have been extensively discussed in the literature. A summary of the knowledge gathered from past studies can be found in review papers of the ACI-ASCE Joint Committee 326 in 1962 [7.1], by Bresler and MacGregor in 1967 [7.2], and more recently, by the ACI-ASCE Joint Committee 426 [7.3], and the ACI Special Publication No. 42 [7.4].

Most of the past studies on shear behavior of R/C beams have mainly been experimental and concerned with behavior under monotonic loading. Very few studies have actually been made in the area of shear behavior under earthquake-induced load reversal.

The experiments of the research reported herein were planned to provide data on the overall shear force-shear distortion hysteretic behavior of R/C beams as well as to obtain detailed photogrammetric measurements of the deformation pattern of the beam critical region. Using these data, the following problems related to shear behavior of R/C beams can be investigated:

(1) How the shear is transferred along cracked regions and the general shear-resisting mechanisms under monotonic and reversed loadings.

(2) The nature and magnitude of the shear distortion which occurs in the critical region subjected to reversed bending and shear.

(3) The shear degradation mechanism under repeated inelastic load reversals and/or deformations to define its main parameters and to formulate a mechanical or mathematical model for its implementation.

7.2 BASIC MECHANISMS OF SHEAR TRANSFER AND SHEAR RESISTANCE IN CRACKED REGIONS

The shear resistance in cracked R/C elements can be developed through the following shear transfer mechanisms: (1) shear transfer across the uncracked concrete; (2) interface shear transfer across crack faces by aggregate interlocking and friction; (3) combination of bending of the main longitudinal steel reinforcement, commonly referred to as the dowel action; and (4) shear transfer through web reinforcement.

7.2.1 Mechanisms under Monotonic Loading (Beam T-2)

Before flexural cracking occured at a V_{cr} of 9 kips (Table 4.1), Beam T-2 [Fig. 7.1(a)] behaved as an elastic composite beam. Shear was primarily transferred by the uncracked concrete. As flexural cracks developed in the cracked beam section, part of the shear was carried across the crack by aggregate interlocking, friction, and dowel action. The remaining shear was carried by the uncracked concrete.

As the load reached about 15 kips at V_c (Table 4.1), inclined cracks were observed to extend from the previous flexural cracks. These cracks are referred to as flexure-shear cracks [Fig. 7.1(a)].

Where the inclined cracks intersected the stirrups [marked by circles in Fig. 7.1(a)], a part of the shear was transferred through the web reinforcement (stirrups) across cracks, from the stirrups to the uncracked concrete either through bond or through the support offered to the tie by the longitudinal steel around which the stirrup was hooked. The remaining shear was transferred through aggregate interlocking, dowel action, and the uncracked concrete in the compression zone.

7.2.2 Mechanisms under Loading Reversals (Beam T-3)

The typical crack pattern developed under reversed loading is shown in Fig. 7.1(b). After the beam underwent numerous reversals, some of the cracks in the lower part joined the previously opened cracks in the upper part, forming continuous cracks traversing the whole beam section. Along the vertical cracks, shear was transferred by aggregate interlocking, friction, and dowel action alone. Along the inclined cracks which intersect one or more stirrups, the shear was transferred across the crack through web reinforcement, dowel action, and aggregate interlocking -- especially in the regions where the cracks reclosed. In these regions the friction that can develop may constitute a significant source of shear resistance [Fig. 7.1(b)].

7.3 MECHANISM OF SHEAR DISTORTION IN R/C BEAMS

7.3.1 Uncracked Beam

The tip deflection, $\Delta\delta^e_{tip}$ (Fig. 7.2), of an uncracked beam can be expressed as:

$$\Delta\delta^e_{tip} = \Delta\delta^e_{sh} + \Delta\delta^e_{flex} \tag{7.1a}$$

where

$\Delta\delta^e_{sh}$ is the shear deformation of the uncracked beam, and $\Delta\delta^e_{flex}$ signifies the flexural deformation of the uncracked beam.

From ordinary beam theory, the values of $\Delta\delta^e_{sh}$ and $\Delta\delta^e_{flex}$ are given by:

$$\Delta\delta^e_{sh} = n\,\frac{V\ell}{GA}\,, \tag{7.1b}$$

where n is 6/5 for rectangular beam sections and:

$$\Delta\delta^e_{flex} = \frac{1}{3}\,\frac{P\ell^3}{EI} \tag{7.1c}$$

7.3.2 Cracked Beam

After a crack has developed across the entire beam section due to reversed bending and shear (Fig. 7.3), the change in tip deflection can be expressed as:

$$\Delta\delta_{tip}\ (\text{after cracking}) = \Delta\delta^e_{tip} + \Delta\delta_{crk} \tag{7.2}$$

where $\Delta\delta^e_{tip}$ is the contribution from the flexural and shear deformations of concrete pieces A and B separated by the crack, and $\Delta\delta_{crk}$ represents the contribution of concentrated deformations occurring at the crack. The $\Delta\delta_{crk}$ component can be subdivided into a rigid body translation of piece B with respect to piece A which is the shear deformation at a crack, $\Delta\delta_{crack}$, [Fig. 7.3(a)], and $\Delta\delta_{flex,\ crk}$ is the flexural deformation due to the concentrated rotation of piece B with respect to piece A, i.e., $\Delta\theta x\ell'$ [Fig. 7.3(b)].

When the crack remains open the amount of shear deformation, $\Delta\delta_{crack}$, that occurs at the crack is controlled by the following factors [Fig. 7.3(c)]: (1) dowel deformation of longitudinal reinforcement (top, bottom, and intermediate, if any); (2) stirrup elongation, which in turn depends upon the width of crack and upon the effectiveness of stirrup anchorage (bond and/or mechanical); and (3) effectiveness of aggregate interlocking and frictional resistance

along the crack.

On the other hand, the flexural deformation, $\Delta\delta_{flex,crk}$, at the crack is controlled by: (1) width of the crack; (2) stresses developed in the longitudinal reinforcing bars; (3) effectiveness of the longitudinal reinforcement anchorage; (4) resistance offered by the ties; and (5) condition of concrete in the compression zone, i.e., the degree of crushing, splitting, and cracking.

Once the crack closes due to bending, the effectiveness of aggregate interlocking and frictional resistance of the confined concrete along the crack increases rapidly, and the contribution of shear deformation at the crack to the tip deflection diminishes.

7.4 MEASUREMENT OF SHEAR DISTORTION BY DIAGONAL CLIP GAGES

The device used for measuring shear distortion in the present study is indicated in Fig. 3.6(a). The value of the shear distortion is computed from the changes in diagonal distance as measured by the clip gages (Eq. 3.1).

Under pure flexure or flexure with small shear, cracks usually form perpendicular to the longitudinal axis. The opening of these cracks will cause similar amounts of displacement, Δ and $\bar{\Delta}$ for diagonal distances AC and BD. Thus, $\Delta = \bar{\Delta}$ [Fig. 7.4(a)]. The measuring device will correspondingly indicate no shear distortion.

The measuring device will indicate the shear deformation of the concrete and the shear displacement at the crack [Fig. 7.4(b)]. This can be shown by simple geometric analysis as given in Fig. 7.4(b). However, if an inclined crack develops in an instrumented region, the device will also measure some of the flexural deformation taking place at this crack. This is demonstrated by geometry in Fig. 7.4(c) for an idealized crack running diagonally across the instrumented region. The measured contribution from actual flexural deformation occurring at an inclined crack tends to increase with increasing shear-to-moment ratio.* Although this deformation is not a pure shear deformation, it is measured as a form of shear distortion by the adopted device. Consequently, data obtained from this device should be carefully interpreted in view of the actual crack pattern.

7.5 PHOTOGRAMMETRIC STUDY OF DEFORMATION PATTERNS IN CRITICAL REGION

A photogrammetric study of the deformation pattern of the critical region of Beam T-3 during a half-cycle at a δ/δ_y of four [LP 49 to LP 51, Fig. 4.9(i)] is presented in Figs. 7.5 to 7.7. The displacement of the grid points are plotted on a scale larger than that used for constructing the reference grid so that the characteristics of the deformation fields can be easily observed. Two successive deformation fields are plotted in each figure to show the incremental changes in deformation. The deformation field corresponding to the earlier load point is drawn in dashed lines and the later one, by solid lines.

7.5.1 LP 49 to LP 49A (From 0 kips to 6 kips)

During this stage of the response, the amount of shear resistance was small while the amount of shear distortion was large. Figure 7.5 indicates that the deformation pattern of the critical region was distinctly translational and the deformation caused by the rotation of

*For beams subjected to bending with small shear, cracks are almost vertical; thus, this contribution from flexural deformation cannot be induced, as shown in Fig. 7.4(a). This is not the case, however, when beams are subjected to bending with high shear. In such cases, cracks become inclined [Fig. 7.4(c)].

the beam was relatively small.* The translational deformation is mainly derived from the shear displacement across the cracks. Significant shear displacement (about 0.1 in.) not crossed by the lateral ties took place at the vertical crack. The total beam deflection at about 25.5 in. away from the beam fixed-end was 0.44 in.

7.5.2 LP 49A to LP 50 (From 6 kips to 35 kips)

In contrast to the incremental deformation observed from 0 kips to 6 kips (Fig. 7.5), the incremental deformation pattern at this stage of the response was largely rotational (Fig. 7.6). Although some rotation of the beam had already occurred from LP 49 to LP 49A, it was very small compared to the amount of shear deformation. As the loading continued beyond LP 49A, the cracks in the compression zone started to close under the increasing compression due to flexure. Aggregate interlocking could thus develop more effectively and shear resistance is seen to have increased in the shear force-shear distortion, V-γ_{av}, response (Fig. 7.6). The increase in beam deflection, δ_{crit}, at 25.5 in. from the support was 1.25 in. (Fig. 7.6). The calculated δ_{crit} based on the average rotation of the vertical grid lines is 1.06 in. The difference between these values suggests that the deflection due to shear distortion was relatively small, i.e. 1.25 - 1.06 = 0.19 in.

7.5.3 LP 59 to LP 51 (From P = 35 kips to 0 kips)

During the release of load, beam deflection was reduced. The results shown in Fig. 7.7 indicate that the incremental deformation during unloading was mainly the result of beam rotation. The amount of shear deformation at this stage was small compared to the amount of shear deformation at the initial stage of loading. The reason for this is that during the unloading process, the cracks in the compression zone, which were closed at LP 50, stayed in contact during unloading; hence, aggregate interlocking and friction were effective. Therefore, the magnitude of shear distortion taking place during unloading was small. This fact is also indicated in the recorded V-γ_{av} response shown in Fig. 7.7.

7.6 SHEAR DEGRADATION MECHANISM UNDER REPEATED REVERSED LOADINGS

The shear force-shear distortion response of test beams subjected to stepwise increasing load/deformation indicated that the degradation in shearing stiffness of the critical region occurred progressively from cycle to cycle. This can be seen in Figs. 4.12(a) to 4.12(g) which plot the steady increase in magnitude of measured shear distortion with each applied reversal. This increasing magnitude suggests that degradation in shear resistance is the result of accumulated damages incurred in the critical regions from previous loadings.

A qualitative explanation for the observed degradation in shear resistance follows. The shear degradation mechanisms involved in the different stages of response are illustrated in Fig. 7.8 and are discussed below under the general heading of Shear Degradation Mechanism.

7.6.1 Shear Degradation Mechanism

(a) Stage I (Initial loading stage). - The end of the initial loading stage is defined as the time when there is a distinct increase in shearing stiffness, i.e., in the slope of the shear force-shear distortion loading curve. After the beam has undergone one or more loading reversals barely inducing yielding of the main reinforcement, some vertical and inclined

---

*Rotation of the beam is caused by the fixed-end rotation and bending of the beam (flexural deformation).

cracks* open through the entire cross-section in the critical region due to residual tensile strain accumulated in the steel. Large shear deformations (relative translational movements) at these open cracks may lead to progressive grinding of the concrete and development of considerable dowel action. The development of dowel action usually leads to the splitting of concrete, causing bond deterioration along the main reinforcing bars. As a result, aggregate interlocking and dowel action will become less effective as the number of reversals increases.

(b) Stage II (Advanced loading stage). - At this stage of loading cracks in the compression zone are closed under increasing compression due to flexure. The shear force acting at the contacted crack faces can cause progressive grinding of concrete which smoothes the contacting surface along the cracks; hence, the resistance of aggregate interlocking and friction will become less effective as the number of reversals increases.

The restraint offered by the stirrup ties across the crack could become less effective due to degradation of the bond along their anchorage (embedment) lengths in the concrete beam. Furthermore, as a result of high compression developed at the peak loading of each cyclic reversal as well as the lateral swelling of the concrete core, the concrete cover shell may crush and spall around the beam near the support. This would reduce the effectiveness of the compression zone to transfer shear. Only the confined core in compression would remain effective but this compression is usually small. Therefore, the computation of the v_u by the code recommended equation wherein $v_u = V_u/bd$ [1.2,1.11], should not be applied at this stage unless modified by replacing b, d of the gross section area by those of the confined core.

(c) Stage III (Unloading stage). - Upon release of external loads the deformations in the critical region are reduced, although the change in deformation during this unloading is usually smaller than that which occurs during loading (Sect. 7.5.3). It is unlikely that any significant shear degradation could occur during the unloading stage.

The damages that occur during loading stages I and II accumulate and cause an increase in shear distortion with each repetition of loading reversal (Fig. 7.8).

7.6.2 Shear Degradation due to Increase in Applied Beam Displacement

If the amplitude of the full reversal deformation cycle is increased, it can reach such a magnitude that the main reinforcement will strain-harden. This, in turn, will cause the yielding of the main reinforcement to spread further along the beam, thereby increasing the length of the critical region. Furthermore, the existing cracks will widen , causing greater shear distortion at the cracks. The increase in shear distortion due to an increase in peak beam displacement is indicated by range EF in Fig. 7.8.

7.7 SHEAR DISTORTION RESPONSE OF TEST BEAMS

To study the effects of the different parameters affecting the shear behavior of the test beams, the peak shear distortion, δ_{sh}, for each inelastic loading cycle is plotted against the tip deflection of the beam, δ (Fig. 7.9). All the peak shear distortion values are derived from the V-γ_{av} diagrams and the peak tip deflection values, from the P-δ diagrams. The shear distortion vs. tip deflection points in the same loading sense are connected by straight lines; thus, the history of change of shear distortion from cycle to cycle can be easily observed.

---

*Inclined cracks have more opportunity to offer shear resistance because they can cross one or more ties.

7.7.1 Effect of Loading History

Monotonic cyclic loading curves are compared in Figs. 7.9(a) and 7.9(c). This comparison shows that under cyclic loading, shear distortion tends to increase with each repeated cycle of inelastic load reversal, i.e. from LP 26 to LP 34, and from LP 38 to LP 46. This effect caused more shear distortion to occur in cyclically loaded beams T-1 and R-3 than in monotonically loaded Beam R-4.

7.7.2 Effect of Relative Amounts of Top and Bottom Steel Reinforcement

The effect can be seen by comparing the results of Beams T-1 and T-3, having similar amounts of top reinforcement but with different amounts of bottom reinforcement (four #6 bars for Beam T-3 and three #5 bars for Beam T-1).

The results are comparable at the same load point having similar values of beam displacement ductility. The results shown in Figs. 7.9(d) and 7.9(f) indicate that the larger amount of steel at the bottom of Beam T-3 caused more shear distortion to occur in the peak upward load points, i.e., LP 28 to LP 52. At peak downward loadings from LP 14 to LP 50, the amount of shear distortion reached by the two beams were similar, as shown in Figs. 7.9(e) and 7.9(c), respectively. However, a detailed analysis of the recorded V-γ_{av} diagrams of Beams T-3 and T-1 [Figs. 4.12(g) and 4.12(f)] reveals that the amount of shear distortion taking place during inelastic downward loading phases (from zero to peak) is generally a little larger in Beam T-3 than in Beam T-1. The larger amount of shear distortion occurring in Beam T-3 was due to the higher ratio of shear force that developed in this beam during upward loadings. This higher ratio of shear force tended to cause more shear degradation.

7.7.3 Effect of Slab in T-beam

The effect of the slab on shear distortion behavior can be seen by comparing results for Beams T-1 and R-3. The results are comparable at the same load point having similar beam displacement ductility values. The results indicate that the value of shear distortion occurring in the downward direction of Beam T-1 is larger than that in Beam R-3. For example, at LP 50 with a δ/δ_y of four, the magnitude of shear distortion in Beam T-1 was about 35 percent higher [Fig. 7.9(a) and 7.9(c)]. This can be explained by the larger amount of shear force which developed in Beam T-1 as a consequence of its large moment capacity in the downward loading direction. The large moment capacity was due to slab reinforcement. Table 4.1 indicates that the v_{max} for Beam T-1 was $4.0\sqrt{f'_c}$, while it was only $3.1\sqrt{f'_c}$ for Beam R-3.

7.7.4 Effect of High Shear Force

Beams R-6 and R-5 were both symmetrically reinforced but had different beam spans (Table 2.1). The maximum nominal shear stress developed in Beam R-6 was about $3.5\sqrt{f'_c}$ and in Beam R-5, about $5.3\sqrt{f'_c}$. The effect of high shear can be seen by comparing the shear force-shear distortion loading curves of the two beams at comparable ductilities (Fig. 7.10). The curves obtained from Figs. 4.12(d) and 4.12(e) are shifted to the same origin for ease of comparison.

As the deflection ductility of the loading reversals increased, there was increasingly more degradation in the shearing stiffness occurring in Beam R-5 during the initial loading stages. Thus, there is a greater amount of shear distortion at comparable cycles. The value of average shear stiffness, K_{sh}, during the initial stage of loading to a δ/δ_y of about two was 200 k/in. for Beam R-6, while shear distortion at peak loading constituted about 8 percent

of the total tip deflection.* The corresponding values for Beam R-5 were 130 k/in. and about 17 percent of the total tip deflection.

After loading reached a δ/δ_y of about four, the values of K_{sh} and δ_{sh}/δ were 63 k/in. and 0.12, respectively, for Beam R-6; and 7 k/in. and 0.37, respectively, for Beam R-5.

Since there was a higher shear force acting in the critical region of Beam R-5 during inelastic reversals, the grinding of cracked surfaces would be more severe, and the ties across the shear crack would have to resist higher shear force. This caused greater tie deformations across the crack and more degradation in the tie anchorage. Consequently, a more pronounced degradation of shearing stiffness and a larger magnitude of shear distortion was observed in Beam R-5.

A quantitative analysis of the degradation of shearing stiffness in Beam R-5 is presented in the appendix to this chapter.

7.8 CONCLUDING REMARKS

(1) Comparison of the shear force-shear distortion behavior of different test beams indicates that the magnitude of shear distortion increases in beams with (a) a shorter shear span, as in Beam R-5; and (b) with a larger amount of main reinforcement as in the case of Beam T-3 vs. Beam T-1. When fully reversed inelastic cycles were applied, the shear force acting in the short beam was higher in both loading directions. For beams with a larger reinforcement area in the bottom, the shear force developed was higher in the loading direction which induced tension in the bottom reinforcing bars. Consequently, in these cases, there was more degradation in shear resistance. The results further reveal that if the maximum nominal shear stress induced during inelastic reversals reached $5.3\sqrt{f'_c}$ in the two loading directions, as in Beam R-5, the degree of shear degradation would become very significant. For example, the shear distortion constituted about 37 percent of the tip deflection as the displacement ductility reached four. In the similar beam, R-6, with a maximum nominal shear stress of $3.5\sqrt{f'_c}$, this value was less than 13 percent.

(2) The shear resistance in cracked R/C critical regions subjected to monotonically increasing load is developed through (a) shear stresses of uncracked concrete; (b) aggregate interlocking and frictional resistance along cracked faces; (c) web reinforcement resistance at inclined cracks; and (d) dowel action of the main steel reinforcement. As the beam is subjected to several loading reversals, flexural and/or flexure-shear cracks may develop across the entire beam section; therefore, the shear must be resisted by web reinforcement, dowel action, and aggregate interlocking and friction. The last two resistances become less effective as the crack width increases and concrete crushes in the compression zone. As a result, large shear distortion could occur and become an important source of beam deflection as well as a significant parameter in the overall behavior of the flexural member. It should be re-emphasized, however, that this degradation occurs because of the opening of the cracks induced by yielding of the main reinforcement and is therefore a combined flexure-shear type of degradation mechanism.

(3) Photogrammetric study of a half-cycle of Beam T-3 at a ductility level of four indicates that during the initial loading stage, the deformation pattern in the critical region is essentially translational due to the shear deformation at those cracks which remain open

---

*See Tables 4.3f and 4.3e.

throughout the entire beam section.

(4) The recorded shear force-shear distortion diagrams indicate that after flexural yielding occurred in both loading directions, the degradation of shear resistance and the amount of shear distortion increased with the magnitude of applied load and/or deformation as well as with each repeated cycle of reversal. The possible shear degradation mechanisms include (a) the opening of cracks due to yielding or slippage of the main reinforcement; (b) the spalling of the concrete cover around the periphery of the flexural critical region; (c) the degradation in stirrup-tie anchorage due to large variations in the strains where it is crossed by inclined cracks (Fig. 4.13), and/or by the splitting and spalling of the concrete cover; (d) the crushing and grinding of concrete at the crack surfaces which could lead to a less effective aggregate interlocking resistance along the open cracks; and (e) the local disruption of bond between the longitudinal steel and concrete due to the dowel action along the open cracks.

(5) The shear force-shear deformation model developed in Appendix A7 offers a reasonable prediction of the shear degradation that occurred during the initial stage of loading reversals at a beam displacement ductility ratio of one, and the first reversal at a ductility level of two. The most important parameters for determining the shear stiffness degradation appear to be the aggregate interlocking along the large cracks and the dowel action of the longitudinal steel. When loading reversals were carried out at a displacement ductility of two, the aggregate interlocking resistance could not be predicted by the analytical model since it does not account for the effect of degradation due to reversals.

A7. APPENDIX TO CHAPTER 7 - ANALYSIS OF THE HYSTERETIC SHEAR FORCE-SHEAR DEFORMATION RELATIONSHIP IN R/C BEAMS SUBJECTED TO INELASTIC LOAD REVERSALS

A7.1 GENERAL REMARKS

Since the contribution of shear deformation to the tip deflection of the short beam, R-5, was found to be significant during inelastic load reversals, it is desirable to investigate in more detail this beam's response in terms of formulating a model for the analytical prediction of its hysteretic shear force-shear deformation relationship. Predicting the entire history of such a relationship is difficult because of the large number of factors which it would involve. These factors are often complex in nature and difficult to formulate mathematically. Consequently, many simplifications must be introduced to make the analysis feasible.

As discussed in Chapter 7, after the beam has cracked through its entire section during inelastic reversals, shear deformation at the cracks can become significant during the initial stage of loading reversal before cracks start to close. Therefore, it is desirable to predict, however approximately, the amount of shear deformation that can occur before the cracks close, and the value of shearing stiffness together with its possible variation during such a stage.

In this appendix, a mathematical model for predicting the hysteretic shear force-shear deformation relationship of Beam R-5 is described.* The predicted results are compared with the measured ones. The significance of the analytical studies is summarized at the end of the appendix.

A7.2 ANALYTICAL METHOD

The value of shearing stiffness at the initial stage of an inelastic load reversal and the shear deformation range of this stage are estimated on the basis of the observed crack pattern, measured crack widths, and measured yield lengths of the main bars. The following factors were considered in estimating shearing stiffness: (1) aggregate interlocking resistance; (2) stirrup-tie resistance at inclined cracks; (3) dowel action of main reinforcing bars; and (4) shear resistance of R/C pieces separated by a crack.

Two general assumptions are made in the analysis:

(a) Components of shear deformations. - The increment of shear deformation, $\Delta\delta_{sh}$, of the critical region (Fig. 7.10), can be expressed as a sum of the shear deformation due to cracks, $\Delta\delta_{crack}$ (Fig. 7.3), and the shear deformation of R/C pieces separated by cracks, $\Delta\delta_{sh}^{c}$.

$$\Delta\delta_{sh} = \Delta\delta_{crack} + \Delta\delta_{sh}^{c} \tag{A7.1}$$

The value of $\Delta\delta_{crack}$ is calculated from the shear displacement at the cracks assuming no shear deformation can occur in R/C pieces separated by cracks. This value is related to the load increment, ΔV, by:

$$\Delta\delta_{crack} = \Delta V \,/\, K_{crack} \tag{A7.2}$$

---

* Despite many modifications, the model presented in this appendix remains conceptually the same as that originally suggested by Ma in his Ph.D. Dissertation[A7.1]. More recent studies on the problems of aggregate interlocking and friction have been conducted by Loeber and Paulay and Mattock. The results of these studies have been incorporated in a new, refined model to be discussed in a separate paper.

where K_{crack} is the total shearing stiffness contributed by the elements offering resistance to the shear at cracks (Sects. A7.3.3-A7.3.5).

The value of $\Delta\delta_{sh}^{c}$ is approximated by the shear deformation corresponding to the uncracked critical region, given by an equation similar to Eq. 7.1b:

$$\Delta\delta_{sh}^{c} = K^{c}\Delta V = (\eta \frac{\ell_{crit}}{GA})\Delta V \tag{A7.3}$$

where

ΔV	=	load increment
ℓ_{crit}	=	length of critical region
A	=	cross-sectional area of beam
G	=	shear modulus of concrete
η	=	cross-sectional shape factor = 6/5 for rectangular beam section.

(b) Material behavior. - As the critical region is subjected to inelastic reversals, the reinforcing steel and concrete could be strained inelastically, causing a change of material characteristics. At the initial stage of loading reversal, however, the stress levels in the steel and concrete would generally be below the stress levels which can cause significant inelastic (plastic) deformation in the material. Therefore, it is assumed that the steel and concrete behave linear-elastically during the initial stage of reversal. Thus, elastic moduli, E_s for steel (Fig. 2.9) and $E_{c_{0.45}}$ for concrete (Fig. 2.10), were used for computing stiffness. It should be noted that due to the effect of the previous inelastic strain history, the moduli of steel and concrete at the initial stage of loading reversal could be lower than these respective initial linear-elastic moduli. Therefore, such an assumption tends to overestimate the stiffness of steel and concrete elements.

A7.3 MATHEMATICAL MODEL FOR COMPUTING SHEAR DEFORMATION AT CRACKS

The model used for computing shear deformation at cracks is illustrated in Fig. A7.1(a). The model for the critical region of Beam R-5 with two large cracks, A and B, is shown in Fig. A7.1(c). The two blocks, I and II, in the model represent the corresponding R/C blocks, I and II, in the beam [Fig. A7.1(c)]. These blocks are connected to each other and to the beam fixed-end by springs. The spring represents the shear resistance offered by aggregate interlocking, K_{ag}; stirrup-ties, K_{st}; and dowel action of the main reinforcement, K_{dw}. Downward and upward displacement represent downward and upward shear displacement of the beam.

The linkage connecting blocks I and II controls the closure of flexure-shear crack B on the inclined plane during loading in either upward or downward direction. The crack is closed when the center pin reaches the end of the slot. The distance, Gap^{S}, required to reach crack closure from the neutral (zero shear displacement) position is related to the crack width, Δ_c, by geometry as illustrated in Fig. A7.1(c):

$$Gap^{S} = \Delta_c \ / \ \sin\theta \tag{A7.4}$$

where θ is the angle (with respect to a vertical line) of the inclined plane on which the crack is expected to close.

Vertical crack A and flexure-shear inclined crack B may be closed due to the increase in shear displacements which causes a large percentage of aggregates on the two faces of the cracks to contact. This assumption is discussed in Sect. A7.3.1. The effect of flexural

rotations in closing up the crack (Fig. 3) is neglected in this model. The importance of this effect should be the object of future studies.

The linkages along the top steel spring, K_{dw}^{t}, and the bottom steel spring, K_{dw}^{b}, are used to control the possible contact of dowel with concrete blocks, and the contact of dowel with stirrup-ties. Before these contacts are made during the initial stage of loading reversal, there is only one dowel spring for the top reinforcement and one for the bottom reinforcement, spanning across the two cracks, A and B [Fig. A7.1(b)]. This is because at this time no bond was assumed between the main reinforcement and the concrete in the yielded lengths of the main bars. (This is discussed in greater detail in Sect. A7.3.5). After contacts are made, the dowel stiffness will be recomputed according to the new (contacted) boundary conditions, i.e. dowel stiffness will be associated with each crack (Sect. A7.3.5).

The gap distance, Gap^{t}, controls the contact of dowel (main reinforcing bars) with ties, while Gap^{c} controls the contact of dowel with the concrete block. The actual gaps represented by these linkages are shown in Figs. A7.1(c) and A7.1(d).

The representations of contact in the analytical model between dowel and ties, and between dowel and concrete for both the downward and the upward loading directions are shown in Fig. A7.2. To help further clarify the proposed model, a comparison between the free-body diagram of the model and that of the beam is given in Fig. A7.3.

A7.3.1 End of Initial Loading Stage

The end of the initial stage of an inelastic load reversal is defined as the time when all the large cracks [A and B in Fig. A7.4(a)] which were open, are closed due to flexural deformation and shear displacement along these cracks. As these cracks close, the aggregate interlocking resistance and friction become effective due to the contact of the particles protruding in the two surfaces along each crack. This action reduces the tendency toward further shear deformation.

For simplicity, the contribution of flexural deformation in closing the crack is neglected. It is therefore assumed that a large vertical or inclined crack will close when the $\Delta\delta_{crack}$ at the crack reaches the value given by:

$$\Delta\delta_{crack} \geq \Delta_c \qquad \text{(A7.5)}$$

where Δ_c is the crack width.

If the above condition is reached at a large open crack, the majority of coarse aggregates on the two faces of this crack could reach contact. Since the tensile strength of normal weight aggregates is usually greater than that of mortar, cracks will form around the aggregates [Fig. A7.4(b)]. The amount of shear displacement requried to bring a certain aggregate into contact, with concrete on the other face of the crack, depends on the shape of the aggregate and its position with respect to the crack. Examination of the cracked surfaces of the test beams shows that the slope, θ, of exposed aggregates along a crack could vary from 0 degrees to 90 degrees with respect to the cracked face [Fig. A7.4(b)]. If it is assumed that most of the aggregates have slopes in the neighborhood of 45 degrees, then it can be seen by geometry that it takes a shear displacement of the magnitude of crack width Δ_c to establish contact on the 45-degree surface of the aggregate [Fig. A7.4(c)]. Therefore, as the shear displacement reaches this value, contact could have been established on the majority of the aggregates along the crack. As an increase in shear resistance brings an increase in bending moment, large flexural deformation could then develop, causing the crack to

close since compression can be effectively transmitted through the contacted aggregates in the compression zone [Fig. A7.4(a)]. It is important to emphasize that crack closure is due to the combined effect of shear and flexural deformation.

The closure of an inclined crack on its inclined plane is also possible when the condition given by Eq. A7.4 is reached. By then, stiffness K_{ag} will increase. More shear displacement along the crack is required to reach this condition than to reach the condition given by Eq. A7.5 since Δ_c (Eq. A7.5) is less than or equal to $\Delta_c/\sin\theta$ (Eq. A7.4). Hence, Eq. A7.4 does not generally control the contact along an inclined crack.

In summary, the end of the initial loading stage is reached when all large open cracks (vertical and inclined) in the beam start to close. This occurs when the conditioning given by Eq. A7.5 is satisfied at each of these cracks.

A7.3.2 Shear Deformation after Initial Loading Stage of Inelastic Load Reversal

The amount of shear deformation occurring after the initial loading and during unloading is assumed to be negligible compared with that occurring during the initial loading stage [Fig. A7.4(d)]. The reason for this assumption is that when all the cracks are closed after the initial loading stage, the shearing stiffness becomes closer to the stiffness given by Eq. A7.3. The given stiffness is very large and remains so during the unloading (see discussion of a typical half-cycle of a V-γ_{av} response in Sect. 7.5. Therefore, after a half-cycle of loading, the amount of residual shear deformation is equal to the shear deformation at the end of the last initial loading stage [Fig. A7.4(d)]:

$$\delta_{res} = \delta_{crack} \tag{A7.6}$$

Thus, during the next half-cycle of loading reversal, it is necessary to overcome this amount of residual shear deformation in order to reach the zero shear deformation position.

A7.3.3 Aggregate Interlocking Resistance (Stiffness)

The aggregate interlocking resistance, K_{ag}, along the cracked surface of the concrete is known to be affected by the concrete properties, crack width, and loading history. However, only a few studies on this phenomenon have been conducted [7.3.7.4]. An experimental study of the effect of crack width on the aggregate interlocking resistance has been reported by Fenwick and Paulay [7.5]. The test specimen used by these researchers is shown in Fig. A7.5(a). The compressive strength of concrete used was 4810 psi, a value similar to that used in the present study (Table 2.1). The shear stress vs. shear displacement curves obtained from a large number of tests are shown in Fig. A7.5(a).

The results show that the smaller the crack width, the higher the value of the aggregate interlocking resistance. This is due to an increase in the available contact area against which aggregate particles across the crack can bear [7.5]. The K_{ag} as a function of the Δ_c is calculated and shown in Fig. A7.5(b). The value of K_{ag} is obtained by taking the average slope of the shear stress vs. shear displacement curves [Fig. A7.5(a)] and multiplying this slope by the gross area of the beam section.

In estimating the aggregate interlocking resistance the effect of the loading history is not accounted for since there are presently few available data that can be used to quantify this effect. However, it is expected that the degradation of aggregate interlocking resistance

will increase with the number of loading reversals and with the magnitude of applied relative displacement across the crack. As the number of applied reversals and the magnitude of displacement increases, the damage produced by the abrasion of the contact area will increase.

A7.3.4 Stirrup Resistance (Stiffness)

Flexural and shear displacements across a crack tend to pull out the ties from the two adjacent concrete blocks separated by the crack. This pull-out is resisted by the bond along the tie and by the mechanical anchorage of the tie to the longitudinal steel. Therefore, to estimate the resistance of ties to shear displacement across a crack during the initial stage of a loading reversal, it is necessary to determine the effectiveness of the bond along the tie and of the tie anchorage in the two adjacent R/C blocks.

As discussed in Chapter 6, the bond between reinforcing steel and concrete is sensitive to the previous loading history, particularly to the peak value of the stress or strain developed in the tie. The effectiveness of the stirrup-tie anchorage along the concrete block here is assumed to be controlled by the peak value of the tie deformation stretching across the crack and to other parameters described below.

As illustrated in Fig. A7.6(a), tie deformation at the crack interface reached a value of Δ_p at peak loading (LP 26). This can be expressed as a sum of the pull-outs from the two concrete blocks separated by the crack:

$$\Delta_p = \Delta^{\ell} + \Delta^{r} \tag{A7.7}$$

where Δ^{ℓ} corresponds to pull-out from the left block and Δ^{r}, that from the right block.

Assuming that the steel strain variation along the tie is linear (triangular) [Fig. A7.6(a)*] and the compatible deformations of the two concrete blocks are neglected, the pull-outs from the R/C blocks separated by the crack can be expressed as a function of the steel strain, ε_o, at the crack interface by the following equations:

$$\text{for the left block,} \quad \Delta^{\ell} = \frac{1}{2}\,\varepsilon_o\,\ell_x^{\ell} \tag{A7.8a}$$

$$\text{for the right block,} \quad \Delta^{r} = \frac{1}{2}\,\varepsilon_o\,\ell_x^{r} \tag{A7.8b}$$

where ℓ_x^{ℓ} and ℓ_x^{r} are the effective lengths requried to develop the stirrup force, F, at the crack interface corresponding to ε_o.

The effective lengths, ℓ_x^{ℓ} and ℓ_x^{r}, can be calculated on the basis of the available bond resistance along the tie:

$$\text{for the left block,} \quad \ell_x^{\ell} = \frac{F}{\Sigma o u_{\ell}} = \frac{\varepsilon_o E_s A_s}{\Sigma o u_{\ell}} \tag{A7.9a}$$

$$\text{for the right block,} \quad \ell_x^{r} = \frac{F}{\Sigma o u_{r}} = \frac{\varepsilon_o E_s A_s}{\Sigma o u_{r}} \tag{A7.9b}$$

---

* An improved solution would be to use strain distribution obtained from analytical studies such as those conducted in Appendix A6 (Figs. A6.4 to A6.8).

where

u_ℓ, ur = estimated maximum average bond resistance (psi) along lengths ℓ_s^ℓ and ℓ_x^r, respectively

A_s = cross-sectional area of ties

Σo = perimeter of ties (#2 bars).

The expression for ℓ_x^ℓ and ℓ_x^r in terms of Δ_p can be obtained by making use of Eqs. A7.7, A7.8, and A7.9:

for the left block, $$\ell_x^\ell = \left[\frac{2A_sE_s}{\Sigma o\ u_\ell}\ \Delta_p/(1+\frac{u_\ell}{u_r})\right]^{1/2} \quad \text{(A7.10a)}$$

for the right block, $$\ell_x^r = (\frac{u_\ell}{u_r})\ \ell_x^\ell \quad \text{(A7.10b)}$$

The main objective of the analytical model is to determine the possibility of predicting the shear force-shear deformation in the inelastic range of Beam R-5, i.e., beyond LP 26 of Fig. 4.12(d). At this loading point, it can be assumed that the local bond stress, u_i, along ℓ_x^i (i=r, ℓ) has reached its maximum value [Fig. A7.6(a)]. Thus, internal concrete cracks along this length could open up as illustrated in Fig. 6.3(a). Then, as applied force F [Fig. A7.6 (a)] is released, the internal cracks would remain open as shown in Fig. 6.3(b). At the beginning of loading in the upward direction (LP 27 to LP 27A), internal cracks did not close; consequently, the bond along ℓ_x^i is not assumed to be effective, i.e., $u_i = 0$ [Fig. A7.6(b)]. Stirrup resistance, K_{st} (LP 27 to LP 27A) to the relative displacement along the crack must then be derived from the remaining unslipped length. The stiffness of this stirrup-tie may be approximated by:

$$K_{st} = \frac{A_sE_s}{\ell_x^r + \ell_x^\ell} \quad \text{(A7.11a)}$$

If the length, ℓ_x^i, exceeds the anchored length of the tie, ℓ_d^i (i=r, ℓ) [Fig. A7.6(b)], then ℓ_d^i will not be sufficient to develop force F at the crack interface, and bond resistance could fail along the entire length, ℓ_d^i. Resistance of the ties to the shear displacement taking place along the inclined crack would then be assumed to be lost:

$$K_{st} = 0 \quad \text{(A7.11b)}$$

for either $\ell_x^r > \ell_d^r$ or $\ell_x^\ell > \ell_d^\ell$

A7.3.5 Dowel Stiffness of Longitudinal Steel

The shear displacement across the crack is also resisted by the dowel action of the main longitudinal reinforcing bars, K_{dw}. Factors that can influence this dowel action are: (1) restraints provided to the bars by lateral ties; (2) support to the bars by the surrounding concrete; and (3) material characteristics, size, and shape of the bars [7.5, 7.7].

Dowel action of the main bars at the beginning of loading reversal is computed assuming that along the length of these bars where steel has been strained beyond yielding, the bond is lost and dowel deflection is free from the restraint of ties and surrounding concrete. The reasons for this assumption are illustrated in Fig. A7.7(a) and are explained below.

(a) Gap between main bars and ties. - Inspecting the steel reinforcement cages of the test beam during the time of construction indicated that there was usually some gap left between the main bar and the ties, Gap^t. The maximum gap width was about 1/4 in. As the longitudinal bars were strained beyond yielding, concrete around the bar between the bar and tie could undergo early crushing (because it usually consisted solely of mortar) and/or grinding which could leave a gap around the bar [Fig. A716(b)]. Therefore, at the beginning of a loading reversal, the resistance offered by the tie to the dowel action of the yielded length of main bars could be very small. Gap^t used in the model [Fig. A7.1(a)] was assumed to be 0.10 in.

(b) Gap between main bars and confined concrete core. - The larger gap between the surface of the bars and the confined concrete core, Gap^c, occurred near cracks. This gap was assumed to be equal to 0.10 in. or about the same thickness as the concrete boundary layer around the bar between the bar lugs [Figs. A7.7(a) and A7.7(b)]. This assumption was made after the concrete boundary layer between and around the bar lugs was observed to have crushed, following large deformation reversals along the yielded length of the steel. Furthermore, as the cracks open up, the dowel action (kinking) of the main bars induces splitting cracks, and relative movement between bars and concrete can occur, thus grinding out a gap around the bar.

(c) Concrete cover along yielded lengths of main bars. - As splitting cracks (Fig. A7.7) developed along the yielded lengths of the main bars, the restraint of the concrete cover to the bending of the dowel is assumed to be ineffective.

Based on the above assumptions, the dowel stiffness of the top and bottom main bars at the beginning of inelastic load reversal is given by:*

$$K_{dw} = 12\, E_s I_s \left(\frac{1}{\ell_p^3}\right) \tag{A7.12}$$

where ℓ_p is the yielded length of the steel and I_s is the moment of inertia of the main bars. If the dowel displacement is such that Gap^c or Gap^t starts to close, the value of K_{dw} must be recomputed to account for the dowel support at contact points. An example of a computed dowel stiffness after contact was established between the dowel and concrete block and between the dowel and ties, is shown in Fig. A7.8.

An outline of the analytical procedure for determining shear force-shear deformation relationships is shown in Fig. A7.9. The analytical examples are given in Sects. A7.5 through A7.6.

A7.4 COMPARISON BETWEEN PREDICTED SHEAR FORCE-SHEAR DEFORMATION AND MEASURED SHEAR FORCE-SHEAR DISTORTION RESPONSE

When comparing the predicted shear force-shear deformation relationship with the measured shear force-shear distortion response, it should be realized that the measured values could contain not only shear deformation but also some contribution from flexural deformations. On the other hand, the predicted values using the present model are based on shear deformations alone. Comparison can still be made in the initial stages of inelastic reversals, however, where the results of photogrammetric analysis [Sect. 7.5] have shown that beam displacement consists mainly of shear deformations at cracks. Thus, in terms of the amount of shear displacement that occurred, the comparable aspects are: (1) the value of shearing stiffness, and (2) the range of initial loading stage.

---

*The assumed dowel deflection shape corresponds to that of a beam fixed at both ends under a differential support settlement. The expression for the deflected shape of the dowel is: $\Delta\delta_{dw}(x) = [2(x/\ell_p)^2 - 3(x/\ell_p)^3]\Delta\delta_{dw}$ [Fig. A7.7(c)].

A7.5 LOADING REVERSALS AT A DUCTILITY OF ONE

After the beam has yielded in both loading directions in the first inelastic cycle of loading reversal, two large open cracks (A and B) developed in the beam [Fig. A7.10(a)]. Distinct degradation in shearing stiffness can be observed during initial stages of the second and third cycles conducted at the same peak tip displacement [Fig. A7.10(b)]. The assumed deformation pattern of the critical region at the initial loading stage of the second cycle, LP 29 to LP 29A, is shown in Fig. A7.10(a), and the corresponding mathematical model, in Fig. A7.1(a). The computed values are listed in Table A7.1.

(a) Aggregate interlocking stiffness. - At the initial loading stage from LP 29 to LP 29A, the major cracks observed were the vertical crack, A, at the beam-column interface; and the inclined crack, B [Fig. A7.10(a)]. Both were about uniform in width across the beam section. The values were 0.01 in. for crack A and 0.004 in. for crack B. The corresponding values of aggregate interlocking stiffness obtained from K_{ag} vs. the crack-width curve [Fig. A7.5(b)] were about 400 k/in. for K_{ag}^{A} and 1400 k/in. for K_{ag}^{B}.

(b) Stirrup-tie stiffness at inclined crack B. - The resistance of tie ② [Fig. A7.10(a)] to the shear displacement at inclined crack B, K_{st}, was assumed to be ineffective. Since the concrete cracked along this tie at its upper anchorage length [Fig. A7.10(a)], no bond was assumed along this length. The mechanical anchorage of tie ② around the top bars was also ineffective since the top bars in the tie/bar connection were strained beyond yielding, and according to assumptions made in Sect. A7.3.5(a), there were some gaps between tie ② and the top bars.

(c) Dowel stiffness of longitudinal steel. - Dowel stiffness for the top and bottom bars, K_{dw}, is computed from Eq. A7.12 using the following values:

I_s : moment of inertia of top or bottom bars (four #6 bars) = 4 x 0.0155 = 0.062 in.^{4}

E_s : modulus of elasticity of #6 bar = 29,100 ksi (Fig. 2.9)

ℓ_p : yielded length of reinforcing bar in beam critical region = 7 in. [Fig. A7.10(a)].*

Since the yielded lengths of the top and bottom bars were about the same (7 in.), the computed values of their dowel stiffness were identical, i.e., $K_{dw}^{t} = K_{dw}^{b} = 64$ k/in.

A7.5.1 Determination of Overall Shearing Stiffness at Beginning of Loading

Shearing stiffness of the cracked critical region of Beam R-5 was derived on the basis of the assumption in Sect. A7.2(a), and the following compatibility and equilibrium relationships corresponding to the assumed deformation pattern of this critical region [Fig. A7.10(a)]:

(a) Compatibility. -

$$\Delta\delta_{crack} = \Delta\delta_{dw} = \Delta\delta_{crack}^{A} + \Delta\delta_{crack}^{B} \tag{A7.13}$$

where

$\Delta\delta_{dw}$ = dowel displacement

$\Delta\delta_{crack}^{A}$ = shear displacement at crack A

$\Delta\delta_{crack}^{B}$ = shear displacement at crack B

---

* Yielded length was determined by measuring the elongations of the top and bottom bars by clip gages.

(b) Equilibium (Fig. A7.3). -

$$\text{Block II:} \quad \Delta V = \Delta V^B_{ag} + \Delta V^B_{st} + \Delta V^t_{dw} + \Delta^b_{dw} \tag{A7.14a}$$

$$\text{Block I :} \quad \Delta V^A_{ag} = \Delta V^B_{ag} + \Delta V^B_{st} \tag{A7.14b}$$

where

$\Delta V = K_{crack}\Delta\delta_{crack}$ = applied shear (A7.14c)

$\Delta V^A_{ag} = K^A_{ag}\ \Delta\delta^A_{crack}$ = shear resisted by aggregate interlocking at crack A (A7.14d)

$\Delta V^t_{dw} = K^t_{dw}\ \Delta\delta^t_{dw}$ = shear resisted by top bars (A7.14e)

$\Delta V^b_{dw} = K^b_{dw}\ \Delta\delta^b_{dw}$ = shear resisted by bottom bars (A7.14f)

$\Delta V^B_{ag} = K^B_{ag}\ \Delta\delta^B_{crack}$ = shear resisted by aggregate interlocking at crack B (A7.14g)

$\Delta V^B_{st} = K^B_{st}\ \Delta\delta^B_{crack}$ = shear resisted by stirrup-tie at crack B (A7.14h)

By using Eqs. A7.13 and A7.14, the expression for K_{crack}, the shearing stiffness contributed by the resistance to shear at the cracks (Eq. A7.2), can be obtained as:

$$K_{crack} = K^t_{dw} + K^b_{dw} + \frac{1}{1/K^A_{crack} + 1/K^B_{crack}} \tag{A7.15a}$$

where

$$K^A_{crack} = K^A_{ag} \tag{A7.15b}$$

and

$$K^B_{crack} = K^B_{ag} + K^B_{st} \tag{A7.15c}$$

Substituting the values of $K^t_{dw} = K^b_{dw} = 64$ k/in. $K^A_{crack} = K^A_{ag} = 400$ k/in, and $K^B_{crack} = K^B_{ag} + K^B_{st} = 1400 + 0 = 1400$ k/in. into Eq. A7.15a, we obtain:

$$K_{crack} = 64 + 64 + \frac{1}{1/400 + 1/1400}$$

$$= 128 + 311 = 439 \text{ k/in.}$$

The shearing stiffness, K^c, of R/C pieces separated by cracks is computed on the basis of Eq. A7.3:

$$K^c = \frac{5}{6}\frac{GA}{\ell_{crit}} = \frac{E_c A}{2(1+\nu)\ell_{crit}}$$

$$K^c = \frac{5}{6}\frac{(4300 \text{ ksi})(144 \text{ in.}^2)}{2(1+0.2)(7 \text{ in.})} = 29{,}9000 \text{ k/in.}$$

where

E_c = 4300 ksi (Beam R-5, Fig. 2.10)

A = 144 in.^{2} beam cross-sectional area

ν = 0.20

$\ell_{crit} = \ell_p$ of 7 in.

Comparison of the values of K^c (29,900 k/in.) and K_{crack} (439 k/in.) indicates that K^c is about 70 times as large as K_{crack}. Similar results were found during initial loadings at a δ/δ_y of two (Sect. A7.6). This means that the shear deformation of the cracked critical region primarily results from shear displacement at the cracks. The shear deformation of solid R/C pieces separated by cracks is very small by comparison. The latter deformation is subsequently neglected in the analyses, i.e., $\Delta\delta^c_{sh} = 0$, in Eq. A7.1. It follows therefore that the shearing stiffness of the cracked critical region could be given by K_{crack} (Eq. A7.15a) without sacrificing much accuracy.

The results also indicate that in determining the value of K_{crack}, the most important parameters are the aggregate interlocking in the vertical crack, K^A_{ag}, and the dowel action of the main bars. The aggregate interlocking at the inclined crack, K^B_{ag}, is of less importance in determining K_{crack} since the value of K^B_{ag} is much greater than K^A_{ag}. Being the greater value, K^B_{ag} cannot affect the third term of Eq. A7.15a, and will thereby have no influence on the value of K_{crack}.

A7.5.2 Estimation of End of Initial Loading Stage

The end of the initial loading stage is determined when both cracks A and B reach the contact condition defined by Eq. A7.5 (Sect. A7.3.1). The amount of shear displacement, $\Delta\delta_{crack}$, required to reach this condition can be derived from the following equations:

Eq. A7.13: $\Delta\delta_{crack} = \Delta\delta_{crack} + \Delta\delta^B_{crack}$

Eq. A7.14(b): $\Delta V^A_{ag} = \Delta V^B_{ag} + \Delta V^B_{st}$:

$$K^A_{ag}\,\Delta\delta^A_{crack} = K^B_{ag}\,\Delta\delta^B_{crack} + K^B_{st}\,\Delta\delta^B_{crack}$$

Therefore,

$$\Delta\delta^A_{crack} = \left(\frac{K^B_{ag} + K^B_{st}}{K^A_{ag}}\right)\Delta\delta^B_{crack} \tag{A7.16a}$$

or

$$\Delta\delta^B_{crack} = \left(\frac{K^A_{ag}}{K^B_{ag} + K^B_{st}}\right)\Delta\delta_{crack} \tag{A7.16b}$$

Substituting Eq. A7.16 into Eq. A7.13 and considering Eqs. A7.15:

$$\Delta\delta_{crack} = \left(1 + \frac{K^A_{crack}}{K^B_{crack}}\right)\Delta\delta_{crack} \tag{A7.17a}$$

$$\Delta\delta_{crack} = \left(1 + \frac{K^B_{crack}}{K^A_{crack}}\right)\Delta\delta^B_{crack} \tag{A7.17b}$$

By substituting the $\Delta\delta_{crack}$ in Eq. A7.5, necessary for cracks to reach contact, into Eq. A7.17, the following is obtained:

To develop contact at crack A,

$$\Delta\delta_{crack} \geq (1 + 400/1400)(0.01 \text{ in.}) = 0.0128 \text{ in.}$$

To develop contact at crack B,

$$\Delta\delta_{crack} \geq (1 + 1400/400)(0.004 \text{ in.}) = 0.018 \text{ in.}$$

Thus, the value of $\Delta\delta_{crack}$ required to develop the first contact is at crack A. When effective interlocking is developed at this crack, i.e., for a $\Delta\delta_{crack}$ = 0.0128., there is actually an increase in its interlocking stiffness, K^A_{ag}. This increase is neglected herein since there is very little difference between 0.0128 in. and 0.014 in. (= 0.018 - 0.004) which is the shear displacement at crack A when contact is also developed at crack B. Thus, the range of shear deformation for the initial loading from LP 29 to LP 29A is 0.018 in. (Fig. A7.11).

Since very little shearing stiffness degradation occurred in the initial loading stages prior to LP 29,* residual shear deformations were neglected at these stages in the analyses, δ_{res} = 0 (Fig. A7.11).

A7.5.3 Check for Gap Closures

Possible gap closures during the predicted initial loading stage are analyzed in Table A7.1. The results show that no contact was reached either between the tie and the dowel, or between the dowel and the tie concrete blocks. Gap^s at inclined crack B was not closed during this initial loading.

A7.5.4 Repeated Cycles at a Ductility of One

During the application of the two successive cycles of loading reversals (LP 30 to LP 36) at a displacement ductility ratio of one, there was a small decrease in shearing stiffness at the initial loading stage [Fig. A7.10(b)]. This decrease could have been caused by the degradation of aggregate interlocking resistance along cracks A and B during the repetition of loading reversal.

The predicted values of shearing stiffness at the initial loading stages of two successive cycles were the same as those at the last initial loading, LP 29 to LP 29A, since the crack width and beam deformation limits in the two repeated cycles were observed to remain the same as in the last half-cycle. The predicted shear deformation range of the initial loading stage at the two successive cycles was increased by an amount equal to $\Delta\delta_{crack}$ = 0.018 in. (Fig. A7.11) which is the residual shear deformation, δ_{res} (Eq. A7.6) that remained after unloading at LP's 31, 33, and 35.

A7.5.5 Comparison of Analytical Results with Measured Values

(a) Validity of comparison. - The shear deformation was measured by diagonal clip gages mounted on the longitudinal steel in a region extending from 1.5 in. to 14 in. of the beam support (Fig. A7.12). To compare the analytical with the experimental results, i.e. with the shearing stiffness indicated in the V-δ_{sh} diagram of Fig. A7.10(b), it is necessary to compute the shearing stiffness corresponding to the region over which the measurement was taken.

As shown in Fig. 7.4(b), the value of shear deformations measured by the diagonal clip gages is given by:

$$\Delta\delta_{sh} = \frac{1}{2}\left(\Delta\delta^t_{sh} + \Delta\delta^b_{sh}\right) \tag{A7.18}$$

Assuming negligible shear deformation in the solid R/C pieces (Sect. A7.5.1), the quantities $\Delta\delta^t_{sh}$ and $\Delta\delta^b_{sh}$ shown in Fig. A7.12 can be approximated by:

$$\Delta\delta^t_{sh} = \Delta\delta_{crack} - \frac{e^2_{\ell_p,t}}{4E_s I_s}\Delta V^t_{dw} \tag{A7.19a}$$

---

* Since the top and bottom steel did not reach yielding in the previous stages of initial loading, the steel strains were insufficient to cause large crack openings across the beam section.

and

$$\Delta\delta^b_{sh} = \Delta\delta_{crack} - \frac{e^2 \ell'^b_p}{4E_s I_s} \Delta V^b_{dw} \tag{A7.19b}$$

where e is the distance from the beam fixed-end to the first gage point on the steel equal to 1.5 in., $\ell'^t_p = \ell^t_p - \frac{2}{3}$ e, and $\ell'^b_p = \ell^b_p - \frac{2}{3}$ e.

By defining $K'_{crack} = \Delta V/\Delta\delta_{sh}$ and substituting Eqs. A7.14e, A7.14f, A7.12, A7.13, and A7.2 into Eqs. A7.19 and A7.18, the following expression for K'_{crack} is obtained:

$$K'_{crack} = \left\{ \frac{1}{1-1.5\left[\left(\frac{e}{\ell^t}\right)^2 \left(\frac{\ell'^t_p}{\ell^t_p}\right) + \left(\frac{e}{\ell^b_p}\right)^2 \left(\frac{\ell'^b_p}{\ell^b_p}\right)\right]} \right\} K_{crack} \tag{A7.20}$$

where $K'_{crack} = Z\ K_{crack}$. For the problems studied here, the value of e is relatively small compared to that of ℓ^t_p and ℓ^b_p and the value of Z is a little greater than one, ranging from 1.03 (for ℓ^t_p, ℓ^b_p = 14 in.) to 1.13 (for ℓ^t_p, ℓ^b_p = 7 in.) For simplicity, the value of K_{crack} obtained from Eq. A7.20 is compared with the measured shearing stiffness, K_{sh} [Figs. A7.10(b), A7.14(a), and A7.15(b)].

It should be noted, however, that once the length of the critical region extends beyond the instrumented region (14 in., Fig. A7.12), the measured shear deformation cannot represent the shear deformation of the whole critical region, and the analytical and experimental results are no longer comparable.

(b) Comparison of results. - The shearing stiffness indicated in the measured shear force-shear distortion curve [Fig. A7.10(b)] is about 400 k/in., which correlates fairly well with the computed value of 438 k/in. (K_{crack}, Table A7.1).

The comparison of the predicted deformation range of the initial loading stage with the corresponding range indicated in the measured shear force-shear distortion curve (Fig. A7.11) is also reasonable. The end of the initial loading stage in the measured response is indicated by the distinct increase in the stiffness (slope) of the loading curve.

The actual behavior indicated that the increase in stiffness after the initial loading stage was not as abrupt as predicted by the model since, in the actual case, there was gradual contact and closure of the crack.

A7.6 INELASTIC LOADINGS AT A DUCTILITY OF TWO

After cycling at a ductility ratio of one, Beam R-5 was deflected upward to a δ/δ_y of -2 at LP 36. Larger crack openings in the lower side of the beam were developed due to a more extensive yielded length of the main bottom steel. As a consequence, during the initial loading from LP 37 to LP 37A [Fig. A7.13(a)] in the downward direction, cracks A and B became wider [Fig. A7.13(b)], causing a decrease in shearing stiffness and a longer range of the initial loading stage. The computation of the values for the shearing stiffness of the critical region and the range of the initial loading stage is in accordance with the procedure presented in Sect. A7.5. The results and parameters used in the computation are listed in Table A7.2. Note that although the available data regarding K_{ag} contains values for Δ_c up to only 0.015 in. [Fig. A7.5(a)], the extrapolation made in Fig. A7.5(b) permits consideration of a K_{ag} = 200 k/in. for a crack width of 0.02 in.

(a) Comparison of shearing stiffness at initial loading stage. - The results in Table A7.2 show that the computed value for K'_{crack} from LP 37 to LP 37A was 177 K/in. As indicated in Fig. A7.13(a), the value of shearing stiffness in the corresponding stage of the measured shear force-shear distortion response was about 130 k/in., 32 percent less than the computed value. This discrepancy could be due to overestimating the aggregate interlocking stiffness of cracks A and B since some local concrete crushing due to flexure could have occurred along the cracks in the previous and first peak upward loading (LP 36) at a δ/δ_y of -2. The damage produced by this crushing could have led to a lower aggregate interlocking stiffness in loadings from LP 37 to LP 37A. Since aggregate interlocking stiffness is computed in the analysis on the basis of the width of the cracks only (Sect. A7.3.3) and does not account for damage induced from the previous history of loading, it could have overestimated the aggregate interlocking resistance.

As the beam is deflected downward to LP 38, another major crack, C [Figs. A7.13(b) and A7.14(b)] opened up. During the initial loading in the upward direction from LP 39 to LP 39A, further degradation in shearing stiffness was observed [Fig. A7.14(a)].

The calculations of shearing stiffness and range of initial loading are listed in Tables A7.3 and A7.4. Since the widths of cracks A and B [Fig. A7.14(b)] were about 0.04 in. at the initial loading stage, the value of K_{ag} of each crack cannot be estimated from the K_{ag} vs. Δ_c data in Fig. A7.5 which only includes crack widths up to 0.015 in. Therefore, the results for LP 39 to LP 39A are calculated using what can be denoted as upper- and lower-bound values of K^A_{ag} and K^B_{ag} (Table A7.3 and A7.4). The upper-bound values of K^A_{ag} and K^B_{ag} are taken to be 200 k/in. based on the K_{ag} vs. Δ_c data in Fig. A7.5(b), and the lower-bound value is taken to be zero. Furthermore, in the latter case, it is also assumed that as contact between protruding particles at the two surfaces of cracks A and B had been made, no increase in stiffness, K_{ag}, could be developed.

The predicted upper-and lower-bound shear force-shear deformation relationships are shown in Fig. A7.15(a). The indicated upper- and lower-bound shearing stiffnesses at the beginning of loading are about 83 k/in. and 16 k/in., respectively. The corresponding shearing stiffness value indicated in the measured shear force-shear distortion curve at the same loading stage is 71 k/in. [Fig. A7.15(b)] which lies within the predicted bounds, 16 k/in. and 83 k/in.

After three repeated reversals at a δ/δ_y of two, the measured shear force-shear distortion loops showed that the value of shearing stiffness decreased to about 17 k/in. at the initial loading stage [Fig. A7.15(b)]. This measured value of shearing stiffness is close to the computed value of shearing resistance, K_{dw} (16 k/in.), offered by the dowel action of the top and bottom steel alone. This finding indicates that probably after three repeated reversals at a δ/δ_y of two, there was practically no aggregate interlocking resistance at the large cracks (the vertical crack, A, and perhaps the inclined cracks, B and C, as well). This could have been due to the increased grinding and crushing of the concrete mortar as well as that of the weak, coarse aggregates along the wide open cracks. Since there was little aggregate interlocking and tie resistance along these cracks, the shear must be resisted by the dowel action of the main bars. Only tie 3 may offer some resistance near the mid-height of inclined crack C. The other possible tie resistances along cracks B and C were not effective due to cracking along the tie [Fig. A7.14(b)]. In computing the K_{st} value of tie 3 a maximum bond stress of 500 psi was used [Fig. A7.14(b)]. This value was based on the observed maximum bond stress developed along the main top tension bar close to the crack interface

(Sect. 6.4.3). Because the required length, ℓ_x^i, was greater than the available anchorage length, ℓ_d^i, no resistance could be developed (Sect. A7.3.4).

(b) Comparison of deformation range of initial loading. - The analytical results for LP 37 to LP 37A show that shearing stiffness increased abruptly after the shear displacement, $\Delta\delta_{crack}$, reached 0.058 in. from the beginning of loading [Fig. A7.15(a)].

The experimental results for this stage of loading show a distinct increase of shearing stiffness as the shear distortion, $\Delta\delta_{sh}$, reached about 0.045 in. [Fig. A7.13(a)] and the stiffness increased gradually afterwards. The upper-bound analytical results for LP 39 to LP 39A show that the shearing stiffness increased rapidly after the shear displacement reached 0.16 in. from the beginning of loading [Fig. A7.15(a)], whereas the lower-bound results indicate that the first significant stiffness increased at a $\Delta\delta_{crack}$ of 0.172 in., where K_{crack} changed from 16 k/in. to 112 k/in. and then to 234 k/in. at a $\Delta\delta_{crack}$ of 0.211 in. The end of the initial loading stage was reached at a $\Delta\delta_{crack}$ of 0.277 in. [Fig. A7.15(a)].

The experimental results for the loading stage from LP 39 to LP 39A show a distinct rise in the shearing stiffness after shear distortion reached 0.08 in. from the beginning of loading, and stiffness continued to increase gradually up to about a $\Delta\delta_{sh} \doteq 0.150$ in. where a sharp increase in stiffness was observed [Figs. A7.14(a) and A7.15(b)].

Judging from the above results, it is clear that the analytical model tends to predict a somewhat later and more abrupt increase in shearing stiffness than that observed in the experiments. This could be due to several factors:

(1) The analytical model did not account for the possible concrete granules entrapped in the cracks, which flaked off from the cracked surfaces. Entrapped granules could possibly establish contact across the crack sooner, thus causing an earlier rise in interface shear resistances (aggregate interlocking, friction) along the cracks.

(2) Contact of main bars with the surrounding tie and confined concrete core in the critical region may occur earlier during the initial loading stage. This could be due to the fact that there may be some crushed concrete granules entrapped in the gaps, Gap^c and Gap^t [Fig. A7.1(c)]; hence, contact between the tie and main bar and the confined concrete and main bar could occur earlier.

A7.7 INELASTIC LOADINGS AT A DUCTILITY GREATER THAN TWO

The observed degradation of shearing stiffness which occurred in the experiments due to loading reversals at a δ/δ_y of three and four is reflected in the decrease of the value of K_{sh} from 13 k/in. to about 4 k/in. near the failure at LP 62 (Fig. A7.16).

After loading exceeded the deflection ductility ratio of three, the yielded length of the longtudinal steel, ℓ_p, extended beyond the last flexural clip gage (which is about 14 in. from the column face). Therefore, it was not possible to estimate the value of ℓ_p to compute the dowel stiffness, K_{dw}. Thus, the computation of K_{crack} at these stages of loading were not made. It is expected, however, that during the initial stages of loading reversal at large deflection ductility ratios of three and four, shearing stiffness will be provided mainly by the dowel action of the main steel. As was pointed out before, this is because the aggregate interlocking resistance at large cracks (crack width > 0.02 in.), such as that at vertical crack A or even inclined cracks B and C, had already been lost due to loading reversals at a ductility of two.

A7.8 CONCLUDING REMARKS

The findings obtained from the preceding analytical studies are summarized below.

(1) The analysis of the inelastic shear force-shear distortion response of Beam R-5 in which the nominal unit shear stress attained a maximum value on the order of $5.3\sqrt{f'_c}$, indicates the following behavior. During reversals at a displacement ductility ratio of one, the shearing stiffness of the initial loading stage was controlled by aggregate interlocking resistance along the large cracks that opened up across the entire cross-section of the beam critical region (particularly along the vertical one that opened up at the face of the column) and by the dowel action of the main reinforcement. As the beam was loaded to a displacement ductility ratio of two and repeated loading reversals were applied, the aggregate interlocking along large cracks was reduced rapidly. The shearing stiffness at the initial loading stage was then controlled almost entirely by the dowel action of the main bars.

(2) The analytical model used was capable of predicting reasonably well the shear-degradation which occurred at the initial loading of reversals at a displacement ductility ratio of one, and in the first cycle at a displacement ductility ratio of two. It could not, however, predict the shear degradation occurring during reversals at a displacement ductility of two. This is because the model used for the shear resistance elements, i.e., aggregate interlocking, tie resistance across the crack, and the dowel action of the main bars, did not account for the effect of their degradation due to reversals. It seems that in order to predict shear degradation at the initial loading due to repeated reversals at a displacement ductility of two or greater, it is essential to incorporate into the analysis a degradation model for the elements resisting shear along the large open cracks. More specifically, it is essential to obtain data regarding the hysteretic behavior of all such resisting elements. The analytical results indicate that the formulation of a degrading aggregate interlocking resistance model is necessary to predict the initial shear stiffness degradation that occurs under reversals. It is also necessary to have better information regarding gaps that can be developed between the ties and main bars and the main bars and confined concrete.

(3) Since the shear force-shear deformation response was predicted on the basis of the observed crack pattern, measured crack width, and yielded length of main steel, it would be desirable to be able to predict these parameters analytically. To do this requires predicting not only the shear but also the flexural behavior together with their interaction, as well as the behavior of the anchored main bars (slippage). Prediction of these types of behavior are required because (a) the crack width at the beam-column interface is determined by flexure of the beam as well as by the amount of the pull-out of the main steel from the anchorage zone; (b) the inclined crack pattern is dependent on the interaction of flexure and shear in the beam; and (c) the yielded length of steel is controlled by flexure and the amount of shear in the yielded region. The greater the amount of shear in this region, the greater will be the crack inclination, which in turn will produce a longer yielded length [1.4, 1.5].

(4) In order to reduce shear degradation during the initial loading stage, it is essential to maintain or to strengthen the shear resistances along all the large vertical and inclined cracks that open up. These resistances include tie resistance along the inclined cracks and aggregate interlocking, friction, and dowel action of the main bars. The analysis of the experimental behavior of Beam R-5 shows that aggregate interlocking resistance reduces rapidly due to the opening of cracks as the beam displacement ductility ratio increases beyond one as well as to the full reversals at displacement ductilities equal to or

greater than two. This means that the aggregate interlocking resistance is not reliable during reversals at high ductility. In order to reduce shear degradation under this condition, the following measures are recommended:

(i) To use for main reinforcement (at the top and the bottom of beam) large diameter bars tied together with a continuous spiral. This will not only decrease the opening of cracks but will also strengthen considerably the dowel resistance.

(ii) To use closely spaced vertical ties with or without supplementary ties for strengthening shear resistance at the inclined cracks. However, as these ties will not directly increase the shear resistance along a vertical crack, a better solution would be

(iii) To use a special web reinforcement scheme, for example, a rectangular spiral, or even better, an inclined bracing bar system, to provide an alternate shear resistance capability in the critical region, especially where vertical cracks can open up.

8. CONCLUSIONS, RECOMMENDATIONS FOR IMPROVING DESIGN CODE PROVISIONS, AND SUGGESTIONS FOR FUTURE RESEARCH

8.1 CONCLUSIONS FROM EXPERIMENTAL STUDIES

Due to the large number of parameters involved, a comprehensive study of the seismic behavior of R/C flexural members generally requires a wide-range investigation. However, a significant understanding of the behavior may be obtained from a relatively small investigation, if it is performed through well coordinated experimental and analytical efforts. It is with this belief that the present investigation was carried out. The observations are drawn as follows.

8.1.1 Performance of Testing Facility and Instrumentation

In general, the performance of the testing facility was satisfactory. The large amount of instrumentation (mostly electronic transducers) provided valuable data for obtaining the overall response of the test beams, as well as for studying in detail most of their deformation and resistance mechanisms. Data from the continuously recorded hysteretic force-deformation diagrams provided excellent information on the overall beam behavior since the history of stiffness degradation, strength degradation and energy dissipation were easily deduced using such data.

Photogrammetric techniques proved useful for studying the deformation pattern of critical regions in order to detect the nature of shear distortion. Large shear displacements along cracks were detected in critical regions during the initial loading of inelastic reversals. Such displacements were due to the reduction of the interface shear resistances along the cracks which remained open across entire beam sections.

8.1.2 Performance of R/C Beams

For the experimental beams designed according to present seismic code provisions [1.2,1.11], the application of a limited number of cycles of loading reversals in the working stress range did not cause significant stiffness degradation or affect the development of the moment capacity of the beam. Beams which were subjected to repeated applications of loading reversals failed only after considerable flexural yielding took place in both the top and bottom steel reinforcements. The lowest displacement ductility ratio attained was 4.1. In all cases, the ACI Code predicted value of flexural strength, M_u, was exceeded, the lowest excess being 7 percent, and the highest, 30 percent.

Some of the most important observations on the performance of the test beams in the inelastic range are listed below.

(1) Inelastic rotations. - The maximum inelastic rotation, θ_{PL}, achieved in the test beams ranged from 0.026 to 0.058 rad. The lowest value of θ_{PL} was obtained by the short beam, R-5, in which a maximum nominal shear stress, v_{max}, of $5.3\sqrt{f'_c}$ was induced under cycles of inelastic reversals. The highest value of θ_{PL} was attained by Beam R-4, which was subjected to a monotonically increasing load. Since an efficient design of a ductile moment-resisting space frame requires the inelastic hinge rotation to be on the order of 0.03 rad. [1.7], the experimentally obtained range of inelastic rotation is considered to be adequate.

(2) Stiffness degradation. - The observed stiffness degradation occurring in R/C beams was very sensitive to the loading history. Once the peak deformation of a cycle increased in either direction during inelastic load reversals, the initial stiffness and

energy dissipation per cycle were observed to degrade during subsequent reversals. Stiffness degradation also occurred due to repeated applications of loading reversals at constant large beam displacement ductilities. If the maximum nominal shear stress is greater than $3.5\sqrt{f'_c}$, stiffness degradation will be accentuated by the presence of the shear. The degree of shear degradation increases with the increase of shear stress during inelastic reversals. For example, the value of v_{max} reached in Beam R-5 was $5.3\sqrt{f'_c}$; in the similar, but longer beam, R-6, v_{max} was $3.5\sqrt{f'_c}$. The shearing stiffness of Beam R-5 at the initial stage of loading reversal was about 52 percent of the stiffness corresponding to Beam R-6. At a displacement ductility level of four, it was 12 percent. When the value of v_{max} is less than $3.5\sqrt{f'_c}$, the Bauschinger effect of steel and bond deterioration are considered the main sources of stiffness degradation.

(3) Mechanism of failure. - Failure of the unsymmetrically reinforced beams ($\rho'/\rho < 1.0$), subjected to reversals after flexural yielding, was precipitated--or accelerated--by local buckling of the bottom #5 bars near the beam support when these bars were compressed during downward loadings. For the symmetrically reinforced beams (R-5 and R-6), failure appears to have been caused by the gradual loss of shear transfer capability along large cracks which opened up across the entire beam section. These cracks developed during cyclic load reversals at a beam displacement ductility ratio ≥ 2. For Beams T-3 with four #6 bars at the bottom, failure was initiated along a plane at the interface between the slab and the beam stem. The failure plane was formed during deformation reversals at a δ/δ_y of four and was the result of stress concentration caused by the presence of top bars at the level of the beam-slab interface [Fig. 4.8(b)].

(4) Energy dissipation. - The energy dissipation capacity of R/C beams can be increased by delaying the degradation of stiffness and the early failure of the beam which may result from buckling of the compression bars. More specifically, this can be achieved in the following ways: (a) by providing supplementary cross-ties to support the compression bars unrestrained by corners ties. A 74 percent increase in the energy dissipation capacity was attained by Beam R-3, which used supplementary ties, over Beam R-1, which utilized no such ties. Codes should incorporate stringent requirements for main bars not restrained by corner ties; (b) by increasing the amount of bottom steel. In Beam T-3 the amount of bottom steel was increased 89 percent over that of Beam T-1; the result of which was an improvement in the energy dissipation capacity by 55 percent; (c) by increasing the shear span ratio (a/d) of the R/C beam in order to reduce the magnitude of shear force acting in the beam during inelastic load reversals. The nominal shear stress induced in Beam R-6 (a/d = 4.46) during inelastic load reversals was 34 percent less than that in Beam R-5 (a/d = 2.75), i.e., $3.5\sqrt{f'_c}$ vs. $5.3\sqrt{f'_c}$. The resulting energy dissipation capacity was thereby improved by 120 percent.

(5) Behavior of anchored main bars. - The length required to develop applied compression forces along cyclically loaded anchored main bars was less than that required to develop tension, i.e., a larger maximum bond stress was developed along compression bars than along tension bars. The values of the maximum nominal bond stress, u_{max}, observed were 960 psi along compressive #6 bars (the corresponding ACI Code value is 800 psi), and 690 and 830 psi along the top and bottom tensile #6 bars, respectively (the ACI Code values are 560 psi and 800 psi, respectively). There were two areas where bond stress could not develop effectively. One was near the beam-column interface, where bond disruption occurred as a consequence of the shear that developed in the bar due to dowel action at the interface crack. The results obtained from the top tensile #6 bars showed a 30 percent decrease in the

value of u_{max} toward the interface. The other area where bond could not properly develop was along the length where yielding takes place at the peaks of cyclic loading. Here, bond disruption was mainly due to considerable contraction of the bar--there was an increase in Poisson's ratio. Bond degradation along the anchored tension bars depends on the applied loading history. For anchored bars subjected to a number of gradually increasing inelastic stress reversals, degradation depends on the values of the peak tensile and compressive stresses, as well as the peak values that the strain reaches during inelastic reversals. Bond degradation was especially severe when both the applied stress and strain are fully reversed at the loaded end of the anchored bar.

(6) Influence of slab. - The main influence of the slab on the inelastic behavior of T-beams was the contribution of slab reinforcement to the top tensile steel area The increase in downward moment capacity due to slab reinforcement caused more energy dissipation per cycle. However, this increase imposed higher compression in the bottom compression zone, and a higher shear force acting in the downward direction. These increased compression and shear forces could cause early buckling of bottom bars and increase the amount of shear degradation. These factors should be considered in the analysis and design of the critical regions near girder-column connections.

8.2 CONCLUSIONS FROM ANALYTICAL STUDIES

Analytical studies were carried out to formulate a reliable mathematical model for predicting hysteretic behavior at critical regions of R/C beams. From these studies, the following observations can be made.

(1) The mathematical model developed for the reinforcing steel offers very good predictions of the hysteretic stress-strain relationship observed in the MTS tests (Appendix A5). The model uses a Ramberg-Osgood equation for describing the Bauschinger effect of steel and several rules for describing strain-hardening behavior under cyclic loading.

(2) The moment-curvature model for R/C sections, which is based on the developed reinforcing steel model and a simplified concrete model, offers a reasonable prediction of the average moment-curvature hysteretic loops obtained from beams tested under cyclic loading with small shear. The moment-curvature analysis shows that under inelastic load reversals, the moment-curvature relationship is mainly controlled by the hysteretic behavior of the top and bottom reinforcement. This points out the importance of developing an accurate model for the stress-strain hysteretic behavior of the steel reinforcement. Further work is needed to apply this moment-curvature model along the critical regions of an R/C beam so that beam displacement caused by flexure can be predicted.

(3) Applying an existing nonlinear finite-element method to the study of the mechanical behavior of the concrete boundary layer around a #6 reinforcing bar subjected to monotonically increasing tension helped to better understand the bond behavior along anchored main bars. The results indicated that increasing stress transfer from steel to concrete will cause propagation of internal cracking in the concrete boundary layer. This cracking could initiate in the concrete at very low stress levels (about 2.3 ksi). The general inclination of the predicted internal concrete crack pattern correlates reasonably well with that indicated in the test results reported by Goto [6.9]. The analysis also shows that internal concrete cracking reduces the stiffness of the concrete boundary layer, and thus the axial stiffness of the embedded bar. Along a real anchored bar this concrete cracking accompanied by local concrete crushing and inelastic deformation will cause disruption of bond, resulting in bond slippage. This, in turn, can lead to undesirable slippage (pull-out) of the rebars

from their anchorage zone. Further work is needed to extend this analytical method to the prediction of bond behavior along the entire length of the anchored bars under general loading.

(4) Although the shear force-shear deformation model developed in Appendix A7 is based on simplified assumptions and, in some cases, arbitrarily selected values, it offers a reasonable prediction of the effect of shear. This was particularly true for predicting the degradation that occurred during the initial stage of loading reversals at a beam displacement ductility ratio of one, and the first reversal at a δ/δ_y of two. This model, however, could not predict the large shear degradation that occurred during repeated reversals at a δ/δ_y of two. In order to predict the shear degradation at initial loading stages due to repeated reversals, it is essential to account for the degrading aggregate interlocking resistance, to have a more accurate estimation of dowel action and to obtain more conclusive data regarding gaps that can develop between the main bars and the ties and the confined concrete.

8.3 RECOMMENDATIONS FOR IMPROVING PRESENT SEISMIC DESIGN PROVISIONS

Based on the reported experimental and analytical findings, the following recommendations can be made for improving present seismic design provisions.

(1) Design of ties or of web and lateral reinforcement. - Comparison of the hysteretic behavior of Beams R-1 and R-3 indicated the advantages of providing lateral supports for main compression bars by means of stirrup-tie corners or by supplementary cross-ties. It is recommended, therefore, that current provisions for the arrangement of lateral ties for longitudinal bars in the columns also apply to compression bars in beams or girders:

> "...ties shall be so arranged that every corner and alternative longitudinal bar shall have lateral support provided by the corner of a tie having an inclined angle of not more than 135 deg. and no bar shall be further than 6 in. clear on either side from such a laterally supported bar."*

However, because the rationale of this code recommendation is questionable, a more logical specification should be developed [8.1].

(2) Design for interaction between slab and girder. - Comparison between the behavior of Beams T-1 and R-3 has revealed that nearly all longitudinal slab reinforcements contribute to the downward moment capacity during full inelastic reversals. In an actual building, the amount of slab reinforcement contributing to the tensile steel of the girder depends upon the type of floor construction and method used to anchor the slab reinforcement in the spandrel beams. Under large lateral reversals, flexural cracks that originate near the column connection can extend over the whole slab span between girders as shown in Fig. 8.1. Thus as a conservative practice, all the slab reinforcment in the strip of slab extending halfway to the adjacent girders should be considered when designing for critical regions near girder-column connections. This is necessary in order to satsify the following seismic code requirements [1,2,1.11]: (a) The value of the tensile steel ratio, ρ (A_s/bd) shall not exceed 0.50 of that producing balanced conditions. (The contribution of slab reinforcement should be included in the tensile steel area, A_s.) (b) The positive moment capacity of the bottom steel shall be not less than 50 percent of the negative moment capacity of the top steel. (The contribution of the slab reinforcement should be considered in estimating the negative moment capacity.) (c) Enough web (shear) reinforcement shall be provided to develop the shears resulting from the moment capacities of plastic hinges (critical regions) at the ends of the member. (In calculating these moment capacities, the contribution of slab reinforcement

*Sect. 7.12.3 of ACI Code 318-71 [1.11].

should be included.)

(3) Placement of main top reinforcement in thickness of floor slab. - As indicated in Fig. 4.8(b), a beam-slab separation failure could occur in the critical region of beams integrally cast with the floor slab when it is subjected to loading reversals of large ductility. The failure shown in this figure occurred as a direct result of stress concentration introduced by the presence of all the top main reinforcements near the beam-slab interface.* Therefore, it is recommended that all top bars be placed further away from the interface, i.e., toward the middle surface of the slab and distributed over an effective slab width as specified in Sect. 10.6.2 of Ref. 1.11. One advantage of this approach is that the stirrup-ties going through the horizontal beam-slab interface could serve as effective reinforcement for transferring horizontal shear from the slab to the beam.

(4) Selection of amount of bottom (positive moment) steel. - When full deformational reversals are expected to occur in the beam critical regions near the column connections to improve energy dissipation capacity, it is recommended that the bottom (positive moment) steel be at least 75 percent of the top (negative moment) steel.

8.4 SUGGESTIONS FOR FUTURE RESEARCH

While experimental and analytical studies reported herein have clarified some aspects of the inelastic behavior of R/C critical regions near girder-column connections subjected to earthquake-like loads, some areas have not yet been fully explored and should be the subject of future research.

(1) More realistic models, such as beam-column subassemblages, should be tested to study the effect of critical regions near girder-column connections and the contribution of different types of floor systems in the overall behavior of these assemblages.

(2) Closely spaced stirrup-ties are commonly used to reduce the distress of high shear reversals in R/C beams. However, because of the possibility that a vertical crack could develop between the two ties, there is the danger of a sliding shear failure in cases where only vertical ties are used. The efficiency of other types of web reinforcement such as inclined bars, should be investigated (some preliminary experimental studies have already been carried out, see Ref. 1.7).

(3) Most of the effort spent in this study was devoted to explaining the physical mechanisms of flexure, shear, and bond resistance under both monotonically increasing loads and loading reversal conditions. Attempts were also made to develop mathematical models for these mechanisms, considering each of these mechanisms independently. The interaction of these mechanisms should be investigated. In this way a practical, integral mathematical model can be developed for R/C flexural members under high shear, accounting for the effects of slippage in the main reinforcing bars when members are subjected to general excitations.

(4) In order to develop a workable model for an R/C flexural member under general excitations, there is an urgent need to obtain further experimental data for the purpose of determining the cyclic hysteretic behavior of bond slippage, of aggregate interlocking

---

*It should be noted that the placement of top bars in the tested T-beams did not satisfy the requirement of Sect. 10.6.2 of the ACI 318-71 Code [1.11] for controlling the width of flexural cracking in the tension zone. The code specifies that a part of the main top tensile reinforcement shall be distributed over the effective flange (slab) width or a width equal to 1/10 of the span whichever is smaller. (For the half-scale beam model, this width is 14.4 in. vs. a 9-in. width of the beam stem.)

resistance of the dowel action, and of confined and unconfined concrete. In addition, a general member failure criterion, considering the effect of loading history (path dependent characteristics), needs to be established.

REFERENCES

CHAPTER 1

[1.1] Seismology Committee, Recommended Lateral Force Requirements and Commentary, Structural Engineers Association of Calif., 1969.

[1.2] International Conference of Building Officials, Uniform Building Code, 1970 ed., Vol. 1, Pasadena, California.

[1.3] Bertero, V. V., "Experimental Studies Concerning Reinforced, Prestressed and Partially Prestressed Concrete Structures and Their Elements," Symposium on Resistance and Ultimate Deformability of Structures Acted on by Well Defined Repeated Loads, International Association for Bridge and Structural Engineering, Lisbon, 1973.

[1.4] Brown, R. H., and Jirsa, James O., "Reinforced Concrete Beams Under Load Reversals," Structural Research at Rice, Report No. 7, Rice University, Houston, Texas, October 1970; also ACI Journal, Proceedings, Vol. 68, No. 5, May 1971.

[1.5] Park, R., Kent, D., and Sampson, R., "Reinforced Concrete Members with Cyclic Loading," Journal of the Structural Division, ASCE, Vol. 98, No. ST7, July 1972.

[1.6] Bertero, V. V., Bresler, B., and Liao, H. "Stiffness Degradation of Reinforced Concrete Members Subjected to Cyclic Flexural Moments," Earthquake Engineering Research Center Report No. EERC 69-12, University of California, Berkeley, December, 1969.

[1.7] Bertero, V. V., Popov, E. P., and Wang, T. Y., "Hysteretic Behavior of Reinforced Concrete Flexural Members with Special Web Reinforcement," Earthquake Engineering Research Center, Report No. EERC 74-9, University of California, Berkeley, August 1974.

[1.8] Celebi, M., and Penzien, J., "Experimental Investigation into the Seismic Behavior of Critical Regions of Reinforced Concrete Components as Influenced by Moment and Shear," Earthquake Engineering Research Center, Report No. EERC 73-4, University of California, Berkeley, January 1973.

[1.9] Burns, N. H., and Siess, C. P., "Repeated and Reversed Loading in Reinforced Concrete," Journal of the Structural Division, ASCE, Vol. 92, No. ST5, October 1969.

[1.10] ACI Committee 439, "Effect of Steel Strength and of Reinforcement Ratio on the Mode of Failure and Strain Energy Capacity of Reinforced Concrete Beams," ACI Journal, Proceedings, Vol. 66, No. 3, March 1969.

[1.11] ACI Standard Building Code Requirements for Reinforced Concrete (ACI 318-71), American Concrete Institute, Detroit, Michigan, 1971.

[1.12] ACI Committee 318, "Commentary on Building Code Requirements for Reinforced Concrete (ACI 318-71)," American Concrete Institute, Detroit, Michigan, 1970.

[1.13] Mahin, S. A., and Bertero, V. V., "Rate of Loading Effects on Uncracked and Repaired Reinforced Concrete Members," Earthquake Engineering Research Center, Report No. EERC 72-9, University of California, Berkeley, December 1972.

[1.14] Clough, R. W. and Johnston, S. B., "Effect of Stiffness Degradation on Earthquake Ductility Requirements," Proceedings of Japan Earthquake Engineering Symposium, October 1966.

[1.15] Takeda, T., Sozen, M. A. and Nielsen, N. N., "Reinforced Concrete Response to Simulated Earthquakes," Journal of the Structural Division, ASCE, Vol. 96, No. ST-12, December 1970.

[1.16] Sargin, M., "Stress-Strain Relationships for Concrete and the Analysis of Reinforced Concrete Sections," Study No. 4, Solid Mechanics Division, University of Waterloo, Ontario, 1971.

[1.17] Cervenka, V., "Inelastic Finite Element Analysis of Reinforced Concrete Panels Under In-Plane Loads," Ph.D. Dissertation, Department of Civil Engineering, University of Colorado, Boulder, 1970.

[1.18] Franklin, H. A., "Non-linear Analysis of Reinforced Concrete Frames and Panels," Ph.D. Dissertation, Division of Structural Engineering and Structural Mechanics, Department of Civil Engineering, University of California, Berkeley, March 1970.

[1.19] Suidan, M., and Schnobrich, W., "Finite Element Analysis of Reinforced Concrete," Journal of the Structural Division, ASCE Vol. 99, No. ST10, October 1973.

[1.20] Scordelis, A. C., "Finite Element Analysis of Reinforced Concrete Structures," Speciality Conference on the Finite Element Method in Civil Engineering, Montreal, Canada, 1972.

CHAPTER 2

[2.1] Soleimani, D., "Reinforced Concrete Ductile Frames Under Earthquake Loading with Stiffness Degradation," Ph.D. Dissertation, Division of Structural Engineering and Structural Mechanics, Department of Civil Engineering, University of California, Berkeley. (in preparation).

CHAPTER 3

[3.1] Popov, E. P., and Stephen, R. M., "Cyclic Loading of Full Size Steel Connections," Earthquake Engineering Research Center, Report No. EERC 70-3, University of California, Berkeley, July 1970.

[3.2] Krawinkler, H., Bertero, V. V., and Popov, E. P., "Inelastic Behavior of Steel Beam to Column Subassemblages," Earthquake Engineering Research Center, Report No. EERC 71-7, University of California, Berkeley, October 1971.

CHAPTER 5

[5.1] Kent, D. C., "Inelastic Behavior of Reinforced Concrete Members with Cyclic Loading," Ph.D. Dissertation, Univeristy of Canterbury, Christchurch, New Zealand, 1969.

[5.2] Morrow, JoDean, "Cyclic Plastic Strain Energy and Fatigue on Metals," Internal Friction, Damping and Cyclic Plasticity, ASTM, STP-378, 1965.

[5.3] Morrow, JoDean and Sinclear G. M., "Cyclic Dependent Stress Relaxation," Symposium on Basic Mechanics of Fatigue, ASTM, STP-237, 1959.

[5.4] Singh, A., Gerstle, K. H., and Tulin, L. G., "The Behavior of Reinforcing Steel Under Reversed Loading", Journal of ASTM, Materials Research and Standards, Vol. 5, No. 1, January, 1965.

[5.5] Akten, A. E., Karlson, B. J. and Sozen, M. A., Stress-Strain Relationships of Reinforcing Bars Subjected to Large Strain Reversals, Civil Engineering Study No. 397, University of Illinois, June 1973.

[5.6] Ramberg-Osgood, W. R., "Description of Stress Strain Curves by Three Parameters," NACA, Technical Note 902, July 1943.

[5.7] Kato, B., Akiyama, H., Yamanouchi, Y., "Predictable Properties of Material Under Incremental Cyclic Loading," IABSE Symposium,Lisbon, September 1973.

[5.8] Kent, D. C., and Park, R., "Flexural Members With Concrete Confined Concrete," Journal of the Structural Division, ASCE, Vol. 97, No. ST7, July 1971.

[5.9] Wakabayashi, M., "Review of Current Research on Earthquake Resistant Design of Composite Steel and Reinforced Concrete Structures in Japan", U.S.-Japan Seminar on Earthquake Engineering with Emphasis on Safety of Reinforced Concrete Structures, September 1973, Berkeley, California, U.S.A.

CHAPTER 6

[6.1] ACI Committee 408, "Bond Stress - The State of the Art", ACI Journal, Vol. 63, No. 11, November 1966.

[6.2] Watstein, D., and Bresler, B., "Bond and Cracking in Reinforced Concrete," Chapter 4, Reinforced Concrete Engineering, John Wiley International, 1974.

[6.3] Bresler, B., and Bertero, V. V., "Behavior of Reinforced Concrete Under Repeated Loading", Journal of the Structural Division, ASCE, Vol. 94, No. ST6, June 1968.

[6.4] Ismail, M. A. F., and Jirsa, J. O., "Bond Deterioration in Reinforced Concrete Subject to Low Cycle Loads", ACI Journal, Proceedings, Vol. 69, June 1972.

[6.5] Zagajeski, S., "Deterioration of Bond in Reinforced Concrete Beams due to Cyclic Load reversals", Graduate Student Report No. 608, Division of Structural Engineering and Structural Mechanics Department of Civil Engineering, University of California, Berkeley, California, Winter 1974.

[6.6] Morita, S. and Kaku, T., "Local Bond Stress-Slip Relationshiop Under Repeated Loading," IASBE Symposium Lisbon, September 1973.

[6.7] Hassan, F. M. and Hawkins, N. M., "Effects of Post-Yield Loading Reversals on Bond Between Reinforcing Bars and Concrete", Report SM73-2, Dept. of Civil Engineering, University of Washington, Seattle, Washington, March 1973.

[6.8] Jirsa, J. O., "Bond and Anchorage in Reinforced Concrete Frame Joints", U.S.-Japan Seminar on Earthquake Engineering with Emphasis on Safety of Reinforced Concrete Structures, September 1973, Berkeley, California, U.S.A.

[6.9] Goto, Y., "Cracks Formed in Concrete Around Deformed Tension Bars", ACI Journal, Proceedings, Vol. 68, No. 4, April 1971.

[6.10] Building Code Requirements for Reinforced Conctete, ACI Committee 318-63, American Concrete Institute, Detroit, Michigan 1963.

[6.11] Liu, D., "Nonlinear Analysis of Axisymmetric Reinforced Concrete Structures," Graduate Student Report No. 559, Division of Structural Engineering and Structural Mechanics, Department of Civil Engineering, University of California, Berkeley, California, Fall 1972.

CHAPTER 7

[7.1] ACI-ASCE Committee 326, "Shear and Diagonal Tension," ACI Journal, Proceedings, Vol. 59, February and March 1962.

[7.2] Bresler, B., and MacGregor, J. G., "Review of Concrete Beams Failing in Shear," Journal of the Structural Division, ASCE, Vol. 93, No. ST1, February 1967.

[7.3] ACI-ASCE Committee 426, "The Shear Strength of Reinforced Concrete Members," Journal of the Structural Division, ASCE, Vol. 99, No. ST6, June 1973.

[7.4] "Shear in Reinforced Concrete," Vol. 1 and 2, Special Publication No. 42, American Concrete Institute, 1974.

[7.5] Fenwick, R. C., and Paulay, T., "Mechanism of Shear Resistance of Concrete Beams" Journal of the Structural Division, ASCE, Vol. 94, No. ST10, October 1968.

[7.6] Johnston, D., and Zia, P., "Analysis of Dowel Action", Journal of the Structural Division, ASCE, Vol. 97, No. ST5, May 1971.

[7.7] Krefeld, W. J., and Thurston, C. W., "Contribution of Longitudinal Steel to Shear Resistance of Reinforced Concrete Beams," ACI Journal, Proceedings, Vol. 63, No. 3 March 1966.

APPENDIX A7

[A7.1] Ma, Shao-yeh Marshall, "Experimental and Analytical Studies of Hysteretic Behavior of Reinforced Concrete Rectangular and T-Beams," Ph.D. Dissertation, Department of of Civil Engineering, University of California, Berkeley, 1975.

CHAPTER 8

[8.1] Bertero, V. V. and Collins, R. G., "Investigation of the Failures of the Olive View Stairtowers during the San Fernando Earthquake and their Implications in Seismic Design," Earthquake Engineering Research Center, Report No. EERC 73-26, University of California, Berkeley, 1973.

Preceding page blank

TABLE 2.1 SPECIMEN PROPERTIES

SPECIMEN	ℓ (in.)	h (in.)	b (in.)	d (in.)	ℓ/d (in/in.)	ρ	ρ'	ρ_b	top* Reinf. (bars)	bot.** Reinf. (bars)	Stirrup*** tie (bars)	tie Spacings (in.)	ρ''	f_c' (Ksi)	f_r (Psi)	Slab Size (in. x in.)	Slab reinf. (bars)
BEAM R-1	62.5	16.0	9.0	14.0	4.5	.014	.0074	.030	4#6	3#5	#2	3.5	.0053	5.07	510	None	None
BEAM R-2	62.5	16.0	9.0	14.0	4.5	.014	.0074	.026	4#6	3#5	#2	3.5	.0053	4.19	455	None	None
BEAM R-3	62.5	16.0	9.0	14.0	4.5	.014	.0074	.028	4#6	3#5	#2	3.5	.010	4.58	475	None	None
BEAM R-4	62.5	16.0	9.0	14.0	4.5	.014	.0074	.027	4#6	3#5	#2	3.5	.010	4.38	460	None	None
BEAM R-5	38.5	16.0	9.0	14.0	2.8	.014	.014	.028	4#6	4#6	#2	3.5	.010	4.58	480	None	None
BEAM R-6	62.5	16.0	9.0	14.0	4.5	.014	.014	.027	4#6	4#6	#2	3.5	.010	4.34	450	None	None
BEAM T-1	62.5	16.0	9.0	14.0	4.5	.014	.0074	.030	4#6	3#5	#2	3.5	.010	4.79	530	36 x 2.25	12#2
BEAM T-2	62.5	16.0	9.0	14.0	4.5	.014	.0074	.028	4#6	3#5	#2	3.5	.010	4.61	462	36 x 2.25	12#2
BEAM T-3	62.5	16.0	9.0	14.0	4.5	.014	.014	.028	4#6	4#6	#2	3.5	.010	4.47	470	36 x 2.25	12#2

ℓ = length of the cantilever

h = height of the beam section

b = width of the beam section

d = effective depth

ρ = top steel reinf. ratio

ρ' = bottom steel reinf. ratio

ρ'' = volume of ties/volume of bound concrete core

ρ_b = balanced steel ratio

f_c' = concrete cylinder strength

f_r = modulus of rupture of concrete

* Yield strength = 65.5 Ksi
** Yield strength = 66.5 Ksi
*** Yield strength = 60.0 Ksi
} ref. Fig. 2.9

TABLE 2.2 COMPUTED STRENGTH OF SPECIMENS

SPECIMEN	V_{cr} (kips)	$V_{w\ell}^{+}$ (kips)	$V_{w\ell}^{-}$ (kips)	V_c (kips)	V_u^{+} (kips)	V_u^{-} (kips)	V_s (kips)	$V_{ult}=V_c+V_s$ (kips)
BEAM R-1	3.8	8.4	4.9	18.0	23.0	13.0	24.8	42.8
BEAM R-2	3.3	7.5	4.9	16.6	22.5	12.6	24.8	41.4
BEAM R-3	3.5	8.0	4.9	17.3	22.7	12.9	49.6	66.9
BEAM R-4	3.4	7.7	4.9	17.0	22.6	12.8	49.6	66.6
BEAM R-5	5.8	13.0	13.0	17.3	37.0	39.0	49.6	66.9
BEAM R-6	3.3	7.6	7.6	16.9	22.6	23.8	49.6	66.5
BEAM T-1	8.1	9.8	4.9	17.6	30.2	12.9	49.6	67.2
BEAM T-2	7.1	9.4	4.9	17.3	29.8	12.9	49.6	66.9
BEAM T-3	7.2	9.2	4.9	17.1	29.6	23.9	49.6	66.7

SPECIMEN	M_{cr} (kip-in)	$M_{w\ell}^{+}$ (kip-in)	$M_{w\ell}^{-}$ (kip-in)	M_c (kip-in)	M_u^{+} (kip-in)	M_u^{-} (kip-in)
BEAM R-1	237.	525.	305.	1125.	1440.	812.
BEAM R-2	205.	460.	305.	1038.	1405.	795.
BEAM R-3	221.	500.	305.	1081.	1420.	805.
BEAM R-4	214.	480.	305.	1063.	1410.	798.
BEAM R-5	223.	500.	500.	666.	1420.	1500.
BEAM R-6	209.	475.	475.	1056.	1410.	1490.
BEAM T-1	506.	610.	304.	1100.	1880.	807.
BEAM T-2	441.	585.	304.	1081.	1860.	805.
BEAM T-3	449.	575.	304.	1069.	1850.	1495.

NOTATIONS

M_{cr}, V_{cr} - flexural cracking load based on f_r (Table 2.1)

$M_{w\ell}$, $V_{w\ell}$ - working stress load*

M_u, V_u - ultimate flexural strength*

V_s - shear carried by web reinf.*

V_c - shear carried by concrete*

M_c - $V_c \cdot \ell$

superscript + = top reinf. in tension
- = bottom reinf. in tension

*Computed from ACI 318-71 Code [1.11]

TABLE 2.3 VARIABLES STUDIED IN THE EXPERIMENTAL PROGRAM

Specimen \ Variables		Loading history*	ρ'/ρ ratio**	shear span ratio ℓ/d (in./in.)	Section Shape	Stirrup-tie	ρ'' **
BEAM	R-1	REV1	0.53	4.5	Rect.	1#2 hoop	0.0053
BEAM	R-2	REV2	0.53	4.5	Rect.	1#2 hoop	0.0053
BEAM	R-3	REV1	0.53	4.5	Rect.	2#2 hoops	0.010
BEAM	R-4	MONO	0.53	4.5	Rect.	2#2 hoops	0.010
BEAM	R-5	REV1	1.00	2.8	Rect.	2#2 hoops	0.010
BEAM	R-6	REV1	1.00	4.5	Rect.	2#2 hoops	0.010
BEAM	T-1	REV1	0.53	4.5	Tee	2#2 hoops	0.010
BEAM	T-2	MONO	0.53	4.5	Tee	2#2 hoops	0.010
BEAM	T-3	REV1	1.00	4.5	Tee	2#2 hoops	0.010

* REV1: stepwise-increasing symmetrical loading reversals

REV2: stepwise-increasing unsymmetrical loading reversals

MONO: cycling between large deflection limits, of ±6 to ±7 δ/δ_y

** ρ : top steel reinforcement ratio

ρ' : bottom steel reinforcement ratio

ρ'' : volume of stirrup-ties to the volume of bound concrete core

TABLE 4.1 PRINCIPAL EXPERIMENTAL RESULTS

SPECIMEN	V_{cr} (kips)	V_c' (kips)	V_y^+ (kips)	V_{max}^+ (kips)	V_y^- (kips)	V_{max}^- (kips)	v_{max} (Psi)	δ_y (in.)	δ_{max} (in.)	δ_{max}/δ_y (in./in.)
BEAM R-1	4.2	12.2	22.0	26.1	13.9	15.5	$3.1\sqrt{f_c'}$	0.57	2.44	4.3
BEAM R-2	4.1	11.3	22.5	24.0	13.3	15.2	$3.0\sqrt{f_c'}$	0.56	2.72	4.9
BEAM R-3	4.4	11.6	24.2	26.7	13.5	16.1	$3.1\sqrt{f_c'}$	0.64	3.16	4.9
BEAM R-4	4.5	10.6	22.8	28.2	-	16.7	$3.3\sqrt{f_c'}$	0.60	4.30	7.2
BEAM R-5	8.0	21.0	39.3	44.0	39.2	43.8	$5.3\sqrt{f_c'}$	0.36	1.58	4.4
BEAM R-6	4.5	11.6	24.0	29.5	24.0	26.5	$3.5\sqrt{f_c'}$	0.62	2.70	4.4
BEAM T-1	10.2	13.7	32.9	33.5	12.3	16.6	$4.0\sqrt{f_c'}$	0.72	2.92	4.1
BEAM T-2	9.0	15.0	32.0	37.5	-	19.0	$4.4\sqrt{f_c'}$	0.75	4.15	5.5
BEAM T-3	10.0	13.0	31.2	35.2	22.5	28.5	$4.2\sqrt{f_c'}$	0.75	3.12	4.2

SPECIMEN	M_{cr} (kip-in)	M_c (kip-in)	M_y^+ (kip-in)	M_{max}^+ (kip-in)	M_y^- (kip-in)	M_{max}^- (kip-in)	Mode of failure
BEAM R-1	262.	760.	1375.	1631.	850.	969.	flexure
BEAM R-2	256.	705.	1406.	1500.	832.	950.	flexure
BEAM R-3	275.	725.	1513.	1669.	844.	1006.	flexure
BEAM R-4	281.	661.	1425.	1763.	-	1044.	flexure
BEAM R-5	308.	810.	1513.	1694.	1509.	1686.	shear
BEAM R-6	281.	725.	1500.	1844.	1500.	1656.	shear
BEAM T-1	637.	855.	2056.	2094.	769.	1037.	flexure
BEAM T-2	569.	940.	2000.	2344.	-	1187.	flexure
BEAM T-3	625.	815.	1950.	2200.	1406.	1781.	flexure

NOTATIONS

Sign + - loading in downward dir.
Sign - - loading in upward dir.
M_c, V_c - approximate load at which first inclined cracking was observed
M_y, V_y - flexural yielding load
M_{max}, V_{max} - max. load reached
v_{max} - max. nominal shear stress $= V_{max}/bd$
δ_y - tip deflection @ yield
δ_{max} - max. tip deflection

TABLE 4.2 DUCTILITY, ROTATION CAPACITY, AND ENERGY DISSIPATION CAPACITY

Specimen	Material (Steel) Ductility Factor $(\varepsilon_s/\varepsilon_y)$ Max. 1	Curvature Ductility Factor (ϕ/ϕ_Y) Max. 2	Deflection Ductility Factor (in/in)μ_δ 3	Cyclic Deflection Ductility Factor (in/in)μ_δ 4	Max. Plastic Rotation, θ_{PL} (Radians) 4	Cyclic Plastic Rotation θ^c_{PL} (Radians) 4	Energy Dissipation Capacity (kips-in) 5
BEAM R-1	$37.9/\varepsilon'_y = 16.1$	$2.37/\phi_y = 8.3$	4.3	6.8	.030	.053	335.
BEAM R-2	$39.0/\varepsilon'_y = 16.6$	$2.42/\phi_y = 8.5$	4.9	6.7	.037	.051	267.
BEAM R-3	$51.6/\varepsilon'_y = 22.0$	$2.37/\phi_y = 8.3$	4.9	8.1	.039	.073	583.
BEAM R-4	$42.6/\varepsilon_y = 18.9$	$4.21/\phi_y = 14.7$	7.2	12.8	.058	.114	336.
BEAM R-5	NO DATA	$3.00/\phi_y = 10.5$	4.4	5.6	.026	.043	349.
BEAM R-6	NO DATA	$2.67/\phi_y = 9.3$	4.4	6.6	.036	.056	738.
BEAM T-1	$44.1/\varepsilon'_y = 18.8$	$2.14/\phi'_y = 8.6$	4.1	6.7	.035	.065	519.
BEAM T-2	NO DATA	$5.02/\phi'_y = 20.2$	5.5	9.7	.054	.104	234.
BEAM T-3	$47.0/\varepsilon'_y = 20.0$	$2.78/\phi'_y = 11.2$	4.2	6.7	.038	.068	803.

1 Average value over $d/_2$ from Beam Support ε'_y = .00235 in/in (#5 bar), ε_y = .00225 in/in (#6 bar)

2 Average value over $d/_2$ from Beam Support ϕ'_y = (upward loading) = $.248 \times 10^{-3}$ Rad/in.

ϕ_y (downward loading) = $.286 \times 10^{-3}$ Rad/in.

3 δ_y, measured deflection at first flexural yielding in the downward (strong) direction

4 Ref. Fig. 4.15

5 Sum of area enclosed by P-δ loops before failure of beam

TABLE 4.3a ESTIMATION OF COMPONENTS OF TIP DISPLACEMENT (BEAM R-1)

Load Point	δ_{Shear} (in) ①	δ_{FE} (in) ②	$\delta_{Flex\ 1}$ (in) ③	$\delta_{Flex\ 2}$ (in) ④	δ_{Sum} (in) Σ①-④	$\delta_{Meas.}$ (in)	% Agreement (in/in) $\delta_{Sum}/\delta_{Meas.}$	P (kips)	δ/δ_y (in/in) δ_y=0.57"
14	↑	.125	.172	0.140	0.44	0.51	86.	22.0	0.90
26	Data	.325	.532	0.152	1.01	1.16	87.	24.0	2.04
38	Not	.393	.930	0.159	1.48	1.75	85.	25.0	3.07
50	Avail-	.730	1.220	0.165	2.12	2.44	87.	26.1	4.28
	able								
16		-.197	- .197	-0.103	-0.50	-0.61	82.	-13.9	-1.07
28		-.300	- .746	-0.106	-1.15	-1.25	92.	-14.4	-2.19
40		-.495	- .978	-0.112	-1.59	-1.89	84.	-15.3	-3.32
52	↓	-.515	-1.134	-0.114	-1.76	-2.28	77.	-15.5	-4.00

		% ① δ_{FE} (in/in)	% ② $\delta_{Flex\ 1}$ (in/in)	% ③ $\delta_{Flex\ 2}$ (in/in)	δ/δ_y (in/in)
14		24.5	33.7	27.5	0.90
26		28.0	45.9	13.1	2.04
38		22.4	53.1	9.1	3.07
50		29.9	50.0	6.8	4.28
16		32.2	32.3	16.9	-1.07
28		24.0	59.7	6.9	-2.19
40		26.2	51.7	5.9	-3.30
52		22.6	49.7	5.0	-4.00

① % $\delta_{FE} = (\delta_{FE}/\delta_{Meas})$ % ② % $\delta_{Flex\ 1} = (\delta_{Flex\ 1}/\delta_{Meas})$ %

③ % $\delta_{Flex\ 2} = (\delta_{Flex\ 2}/\delta_{Meas})$ %

TABLE 4.3b ESTIMATION OF COMPONENTS OF TIP DISPLACEMENT (BEAM R-2)

Load Point	δ_{Shear} (in.) ①	$\delta_{FE+Flex\ 1}$ (in.) ②	$\delta_{Flex\ 2}$ (in.) ③	δ_{Sum} (in.) ④	δ_{Meas} (in.) Σ①~③	% Agreement $\delta_{Sum}/\delta_{Meas.}$ (in./in)	P (kips)	δ/δ_y (in./in) δ_y=0.56"
14	-.01	- .39	-.102	-0.50	-0.54	93.	-13.3	-0.97
26	-.03	- .83	-.103	-0.97	-1.08	90.	-13.9	-1.93
38	-.06	-1.36	-.106	-1.53	-1.60	96.	-14.2	-2.86
50	-.10	-1.82	-.114	-2.03	-2.16	94.	-15.2	-3.86
62	-.18	-2.22	-.114	-2.50	-2.72	92.	-15.2	-4.86
40	.025	+ .25	.143	0.42	0.56	75.	22.5	1.00
52	.050	+ .69	.142	0.89	0.96	93.	24.0	1.71
64	.150	+ 1.13	.151	1.43	1.59	90.	23.8	2.84

	% δ_{Shear} (in./in.)	% $\delta_{FE+Flex\ 1}$ (in./in.)	% $\delta_{Flex\ 2}$ (in./in.)	δ/δ_y (in./in.)
14	1.9	72.2	18.9	-0.97
26	2.8	77.0	9.5	-1.93
38	3.8	85.0	6.7	-2.86
50	4.6	84.3	5.3	-3.86
62	6.4	81.6	4.2	-4.86
40	4.5	44.6	25.5	1.00
52	5.2	71.9	15.8	1.71
64	9.4	71.1	9.5	2.84

TABLE 4.3c ESTIMATION OF COMPONENTS OF TIP DISPLACEMENT (BEAM R-3)

Load Point	δ_{Shear} (in) ①	δ_{FE} (in) ②	$\delta_{Flex\ 1}$ (in) ③	$\delta_{Flex\ 2}$ (in) ④	δ_{Sum} (in) Σ①~④	$\delta_{Meas.}$ (in)	% Agreement (in/in) $\delta_{Sum}/\delta_{Meas.}$	P (kips)	δ/δ_y (in/in) δ_y=0.64"
14	0.012	.245	.208	.154	0.62	0.66	94.	24.2	1.03
26	0.045	.429	.555	.158	1.19	1.25	95.	24.8	1.95
38	0.110	.570	.950	.163	1.79	1.87	96.	25.7	2.92
50	0.170	.820	1.175	.169	2.33	2.47	95.	26.6	3.86
62	0.25+	.855	1.515	.170	2.79	3.12	89.	26.7	4.88
16	-0.010	-.193	- .258	-.103	-0.57	-0.62	92.	-13.8	-0.97
28	-0.080	-.320	- .695	-.106	-1.20	-1.25	96.	-14.2	-1.96
40	-0.175	-.535	-1.013	-.114	-1.84	-1.88	98.	-15.2	-2.93
52	-0.290	-.770	-1.100	-.118	-2.28	-2.43	94.	-15.8	-3.80
64	-0.310+	-1.53	- .998	-.121	-2.96	-3.16	94.	-16.1	-4.93

	% δ_{Shear} (in/in)	% δ_{FE} (in/in)	% $\delta_{Flex\ 1}$ (in/in)	% $\delta_{Flex\ 2}$ (in/in)	δ/δ_y (in/in)
14	1.8	37.3	31.6	23.3	1.03
26	3.6	34.2	44.4	12.6	1.95
38	5.9	30.5	50.6	8.7	2.92
50	7.0	33.2	47.5	6.9	3.86
62	8.0	27.3	48.5	5.5	4.88
16	1.6	31.1	41.5	16.6	-0.97
28	6.4	25.5	55.5	8.5	-1.96
40	9.3	28.5	54.0	6.1	-2.93
52	12.0	31.7	45.2	4.9	-3.80
64	9.8+	48.5	31.6	3.8	-4.93

TABLE 4.3d ESTIMATION OF COMPONENTS OF TIP DISPLACEMENT (BEAM R-4)

Load Point	δ_{Shear} (in) ①	δ_{FE} (in) ②	$\delta_{Flex\ 1}$ (in) ③	$\delta_{Flex\ 2}$ (in) ④	δ_{Sum} (in) Σ①~④	$\delta_{Meas.}$ (in)	% Agreement (in/in) $\delta_{Sum}/\delta_{Meas.}$	P (kips)	δ/δ_y (in/in) δ_y=0.60"
7	0.012	0.183	0.26	0.144	0.060	0.60	100.	22.8	1.00
8	0.04	0.375	0.55	0.163	1.13	1.20	94.	24.5	2.00
9	0.10	0.497	1.07	0.177	1.84	1.90	97.	25.3	3.17
10	0.13	0.585	1.47	0.184	2.39	2.44	97.	26.0	4.07
11	0.16	0.756	1.85	0.215	2.98	3.06	98.	27.0	5.10
12	0.20	0.838	2.20	0.318	3.57	3.68	97.	27.7	6.13
13	0.23	1.025	2.56	0.425	4.24	4.20	101.	28.2	7.00
14	-0.228	-0.375	0.46	0.060	- .09	0.0	-	-15.3	-
15	-0.408	-1.40	-1.85	-0.51	-4.17	-4.30	97.	-16.7	-7.17
16	0.50+	2.04	2.00	-0.14	4.40	+4.40	100.	24.0	7.33

	% δ_{Shear} (in/in)	% δ_{FE} (in/in)	% $\delta_{Flex\ 1}$ (in/in)	% $\delta_{Flex\ 2}$ (in/in)	δ/δ_y (in/in)
7	2.0	30.5	43.5	24.0	1.00
8	3.3	31.2	46.0	13.5	2.00
9	5.3	26.2	56.5	9.7	3.17
10	5.3	23.9	60.2	7.5	4.07
11	5.2	24.9	60.5	7.0	5.10
12	5.5	22.8	59.6	8.7	6.13
13	5.5	24.4	61.0	10.1	7.00
14	-	-	-	-	-
15	9.5	32.5	43.0	11.8	-7.17
16	11.4+	46.4	45.5	3.2	7.33

TABLE 4.3e ESTIMATION OF COMPONENTS OF TIP DISPLACEMENT (BEAM R-5)

Load Point	δ_{Shear} (in) ①	$\delta_{FE+Flex\ 1}$ (in) ②	$\delta_{Flex\ 2}$ (in) ③	δ_{Sum} (in) Σ①~③	$\delta_{Meas.}$ (in)	% Agreement (in/in) $\delta_{Sum}/\delta_{Meas.}$	P (kips)	δ/δ_y (in/in) δ_y=0.36"
26	0.033	0.233	0.032	0.30	0.39	77.	39.3	1.08
38	0.132	0.535	0.034	0.70	0.793	89.	41.5	2.20
50	0.252	0.818	0.036	1.11	1.25	88.	44.0	3.47
62	0.530	0.758	0.034	1.32	1.45	91.	41.5	4.03
28	-0.026	-0.291	-0.032	-0.35	-0.43	81.	-39.2	-1.19
40	-0.144	-0.542	-0.034	-0.72	-0.81	89.	-41.0	-2.25
52	-0.250	-0.886	-0.036	-1.17	-1.27	92.	-43.8	-3.53
64	-0.420	-0.975	-0.0325	-1.43	-1.58	90.	-40.0	-4.39

	% δ_{Shear} (in/in)	% $\delta_{FE+Flex\ 1}$ (in/in)	% $\delta_{Flex\ 2}$ (in/in)	δ/δ_y (in/in)
26	8.6	59.7	8.3	1.08
38	16.7	67.7	4.3	2.20
50	20.0	65.5	2.9	3.47
62	36.5	52.2	2.3	4.03
28	6.2	67.7	7.4	-1.19
40	17.8	66.9	4.2	-2.25
52	19.6	69.8	2.8	-3.53
64	26.6	61.7	2.1	-4.39

TABLE 4.3f ESTIMATION OF COMPONENTS OF TIP DISPLACEMENT (BEAM R-6)

Load Point	δ_{Shear} (in) ①	δ_{FE} (in) ②	$\delta_{Flex\ 1}$ (in) ③	$\delta_{Flex\ 2}$ (in) ④	δ_{Sum} (in) Σ①~④	$\delta_{Meas.}$ (in)	% Agreement (in/in) $\delta_{Sum}/\delta_{Meas.}$	P (kips)	δ/δ_y (in/in) δ_y=0.62"
14	0.015	.185	.217	.162	0.58	0.62	94.	24.0	1.00
26	0.085	.308	.506	.166	1.07	1.10	97.	24.5	1.77
38	0.190	.337	.997	.168	1.69	1.97	86.	27.5	3.18
50	0.330	.796	1.30	.287	2.71	2.70	100.	29.5	4.36
16	-0.025	- .059	-.218	-.148	-0.45	-0.42	107.	-24.0	-0.68
28	-0.060	- .303	-.315	-.146	-0.82	-0.80	103.	-24.5	-1.29
40	-0.100	- .659	-.706	-.141	-1.61	-1.56	104.	-25.5	-2.52
52	-0.280	-1.040	-.90	-.077	-2.30	-2.30	100.	-26.5	-3.71

	% δ_{Shear} (in/in)	% δ_{FE} (in/in)	% $\delta_{Flex\ 1}$ (in/in)	% $\delta_{Flex\ 2}$ (in/in)	δ/δ_y (in/in)
14	2.4	29.8	35.0	36.1	1.00
26	7.7	28.0	46.0	15.1	1.77
38	9.6	17.1	50.6	8.5	3.18
50	12.2	29.5	48.2	10.6	4.36
16	6.0	14.1	51.9	35.2	-0.68
28	7.5	37.9	39.4	18.3	-1.29
40	6.4	42.2	45.3	9.0	-2.52
52	12.2	45.2	39.1	3.3	-3.71

TABLE 4.3g ESTIMATION OF COMPONENTS OF TIP DISPLACEMENT (BEAM T-1)

Load Point	δ_{Shear} (in) ①	δ_{FE} (in) ②	$\delta_{Flex\ 1}$ (in) ③	$\delta_{Flex\ 2}$ (in) ④	δ_{Sum} (in) Σ①~④	$\delta_{Meas.}$ (in)	% Agreement (in/in) $\delta_{Sum}/\delta_{Meas.}$	P (kips)	δ/δ_y (in/in) δ_y=0.72"
14	0.015	0.358	0.281	0.151	0.81	0.98	82.	32.4	1.36
26	0.055	0.584	0.677	0.162	1.48	1.46	101.	33.2	2.03
38	0.120	0.812	1.040	0.172	2.14	2.17	99.	33.5	5.01
50	0.225	1.237	1.043	0.168	2.68	2.92	92	32.8	4.06
16	-0.030	-0.190	-0.383	-0.111	-0.71	-0.72	99.	-13.9	-1.00
28	-0.095	-0.495	-0.835	-0.150	-1.58	-1.55	102.	-15.2	-2.15
40	-0.175	-0.445	-1.08	-0.402	-2.11	-2.19	96.	-16.1	-3.04
52	-0.250	-0.990	-1.10	-0.498	-2.84	-2.94	97.	-16.6	-4.0

	% δ_{Shear} (in/in)	% δ_{FE} (in/in)	% $\delta_{Flex\ 1}$ (in/in)	% $\delta_{Flex\ 2}$ (in/in)	δ/δ_y (in/in)
14	1.5	36.5	28.7	15.4	1.36
26	3.8	40.0	46.4	11.1	2.03
38	5.5	37.4	47.9	7.94	3.01
50	7.8	42.4	35.7	5.75	4.06
16	4.2	26.4	53.2	15.4	-1.00
28	6.1	32.0	53.9	9.7	-2.15
40	8.0	20.3	49.3	18.4	-3.04
52	8.5	33.7	37.4	16.9	-4.08

TABLE 4.3h ESTIMATION OF COMPONENTS OF TIP DISPLACEMENT (BEAM T-2)

Load Point	δ_{Shear} (in) ①	δ_{FE} (in) ②	$\delta_{Flex\ 1}$ (in) ③	$\delta_{Flex\ 2}$ (in) ④	δ_{Sum} (in) Σ①~④	$\delta_{Meas.}$ (in)	% Agreement (in/in) $\delta_{Sum}/\delta_{Meas.}$	P (kips)	δ/δ_y (in/in) δ_y=0.75"
5	0.018	0.183	0.266	0.147	0.614	0.80	77.	32.0	1.07
6	0.06	0.293	0.857	0.148	1.36	1.48	92.	32.5	1.97
7	0.10	0.460	1.560	0.164	2.284	2.30	99.	34.2	3.07
8	0.138	0.560	2.01	0.197	2.90	2.95	98.	35.4	3.93
9	0.20	0.785	2.81	0.331	4.13	4.10	100.	37.5	5.47
10	0.163	0.59	2.42	0.170	3.34	3.15	106.	0.0	4.2
11	-0.05	0.355	1.44	0.147	1.99	2.10	95.	-11.5	7.8
12	-0.40	-1.71	-1.87	-0.167	-4.15	-4.15	100.	-19.0	-5.53

	% δ_{Shear} (in/in)	% δ_{FE} (in/in)	% $\delta_{Flex\ 1}$ (in/in)	% $\delta_{Flex\ 2}$ (in/in)	δ/δ_y (in/in)
5	2.3	22.9	33.3	18.4	1.07
6	4.1	19.8	57.9	10.0	1.97
7	4.4	20.0	67.8	7.1	3.07
8	4.7	18.9	68.1	6.7	3.93
9	4.9	19.1	68.5	8.1	5.47
10	5.2	18.7	76.8	5.4	4.2
11	-2.4	16.9	68.6	7.0	2.8
12	9.6	41.2	45.1	4.1	-5.53

TABLE 4.3i ESTIMATION OF COMPONENTS OF TIP DISPLACEMENT (BEAM T-3)

Load Point	δ_{Shear} (in) ①	δ_{FE} (in) ②	$\delta_{Flex\ 1}$ (in) ③	$\delta_{Flex\ 2}$ (in) ④	δ_{Sum} (in) Σ①~④	$\delta_{Meas.}$ (in)	% Agreement (in/in) $\delta_{Sum}/\delta_{Meas.}$	P (kips)	δ/δ_y (in/in) δ_y=0.75"
14	0.017	0.40	0.357	0.136	0.91	1.02	89.	32.0	1.36
26	0.065	0.57	0.621	0.127	1.38	1.52	91.	31.8	2.03
38	0.125	0.90	1.020	0.121	2.17	2.30	94.	34.0	3.07
50	0.225	1.35	1.135	0.150	2.86	3.12	92.	35.2	4.16
16	-0.040	-0.35	-0.283	-0.140	-0.81	-0.75	108.	-24.0	-1.00
28	-0.120	-0.57	-0.72	-0.142	-1.55	-1.56	99.	-25.8	-2.08
40	-0.235	-1.00	-0.97	-0.242	-2.45	-2.28	108.	-28.5	-3.04
52	-0.350	-1.52	-1.29	-0.208	-3.37	-3.10	109.	-28.5	-4.13

	% δ_{Shear} (in/in)	% δ_{FE} (in/in)	% $\delta_{Flex\ 1}$ (in/in)	% $\delta_{Flex\ 2}$ (in/in)	δ/δ_y (in/in)
14	1.67	39.2	35.0	13.3	1.36
26	4.3	37.5	40.9	8.4	2.03
38	5.4	39.1	44.4	5.3	3.07
50	7.2	43.3	36.4	4.8	4.16
16	5.3	46.7	37.7	18.7	-1.00
28	7.7	36.5	46.2	9.1	-2.08
40	10.3	43.9	42.5	10.6	-3.04
52	11.3	49.0	41.6	6.7	-4.13

TABLE 5.1 RESULTS FROM THEORETICAL MOMENT-CURVATURE (M-ϕ) ANALYSIS [Fig. 5.5-5.8]

Parameter \ Beam Section	T-2	R-4	T-3	R-6
Top Steel/Bottom Steel	(4#6 +12#2)/3#5	4#6/3#5	(4#6 +12#2)/4#6	4#6/4#6
Steel ratio ρ/ρ_t	0.39	0.53	0.75	1.00
Moment @ 1st Yield (Kip-in)*	1970.	1460.	1980.	1465.
ϕ 1st Yield (10^{-3}rad/in)*	0.261	0.237	0.244	0.225
ϕ_{max} (10^{-3}rad/in)	±5.0	±5.0	±5.0	±5.0
N.A. @ ϕ_{max} (in)*	6.16	3.13	2.82	1.75
ε_{cmax} (10^{-3}in/in)*	-30.8	-15.6	-14.1	-8.8
ϕ@concrete crushing (10^{-3}rad/in)*	1.67	2.2	2.3	2.7
MAXIMUM RANGE OF STEEL STRAINS IN THE 1st AND 2nd CYCLES (10^{-3} in/in)				
(top bars)	0.0 to 40.4	0.0 to 55.0	0.0 to 58.0	0.0 to 61.2
(bottom bars)	-24.0 to 97.9	-8.8 to 106.2	-7.3 to 92.7	-1.92 to 69.8

TABLE 5.2 ENERGY DISSIPATION VALUES (E_{diss}) FROM M-ϕ ANALYSIS

E_{diss} due to \ Section		T-2	R-4	T-3	R-6
		(K-in/in)/%	(K-in/in)/%	(K-in/in)/%	(K-in/in)/%
1st cycle	(top bars)	6.4 / 35.2**	7.27/ 44.5	13.60/ 52.4	13.62/ 62.4
	(bottom bars)	9.80/ 53.6	8.17/ 50.5	12.00/ 46.0	7.95/ 36.3
	(concrete)	2.00/ 11.2	0.90/ 5.5	0.40/ 1.6	0.30/ 1.3
	(M-ϕ)	18.2 /100.0	16.34/100.0	26.00/100.0	21.87/100.0
2nd cycle	(top bars)	0.52/ 3.0	1.13/ 6.8	6.40/ 22.1	11.60/ 42.2
	(bottom bars)	16.60/ 97.0	15.40/ 93.2	22.60/ 77.9	15.90/ 57.8
	(concrete)	0. / 0.	0. / 0.	0. / 0.	0. / 0.
	(M-ϕ)	17.12/100.0	16.53/100.0	29.00/100.0	27.50/100.0
E_{diss}(bottom bars) / E_{diss} (top bars)					
Cycle \ Section		T-2	R-4	T-3	R-6
1st cycle		1.5	1.5	0.9	0.6
2nd cycle		32.6	13.7	3.5	1.4

* These values are obtained in the first half-cycle of loading.

** (E_{diss}/E_{diss} of M-ϕ)%, i.e., (6.4/18.2) = 35.2%.

TABLE 5.3 EFFECT OF INCREASING AMOUNT OF FLEXURAL STEEL ON ENERGY DISSIPATION CAPACITY - (MOMENT-CURVATURE ANALYSIS RESULTS)

Sections Compared	Increase In Total Steel Areas (in^2)	% Increase In Steel Area	Change In ρ'/ρ_t Ratio	Increase in E_{diss} (M-ϕ) Due to Increase in Steel Area	
				1st Cycle	2nd Cycle (Shakedown Cycle)
R-4 vs. T-2	2.69 to (2.69 + 0.60) (increase in top steel)	22.%	0.53 to 0.39	11.%	4.%
T-2 vs. T-3	3.29 to (3.29 + 0.83) (increase in bot. steel)	25.%	0.39 to 0.75	43.%	69.%
R-4 vs. R-6	2.69 to (2.69 + 0.83) (increase in bot. steel)	31.%	0.53 to 1.00	34.%	66.%
T-2 vs. R-6	3.29 to (3.29 + 0.23) (net increase in steel area)	7.%	0.39 to 1.00	20.%	61.%

TABLE A7.1 COMPUTED VALUES OF SHEAR STIFFNESS AT INITIAL LOADING STAGE (BEAM R-5) LP29-29A

(1) Aggregate Interlocking (K_{ag}) [Sect. A7.5.1(a)]

Crack	Crack Width (in.)	K_{ag} [Fig. A7.5(b)] (K/in.)
A	0.010	400
B	0.004	1400

(2) Stirrup Resistance Across Crack (k_{st}) [Fig. A7.1 (c)] [Sect. A7.5.1(b)]

Tie	Parameters for Determining Slipped Length (Eq. A7.11)			Slipped Length/ Available Anchor (in./in.)		K_{st} (K/in) (Eq.A7.11)
	Max Stretching (Δ_p)	available bond				
		left anchor.	right anchor.	left anchor.	right anchor.	
Tie 2 @ crack B	0.012 in. (@LP 26)	0.0	-	-	-	0.0

(3) Dowel Resistance of Longitudinal Steel (K_{dw}) [Sect. A7.5.1(c)]

	ℓ_p	K_{dw}	
top steel	7 in.	64 K/in. (K^t_{dw})	128 K/in.
bottom steel	7 in.	64 K/in. (K^b_{dw})	

(4) Shear Resistance of R/C Blocks (K^c) [Sect. A7.5.2(b)]

$$K^c = \frac{5}{6}\,\frac{GA}{\ell_{crit}} = 29{,}900 \text{ K/in}, \quad \ell_{crit} = \ell_p = 7 \text{ in.}$$

(5) Shear Resistance at Cracks (K_{crack}) [Sect. A7.5.2(b)]

$$K^A_{crack} = K^A_{ag} = 400 \text{ K/in}, \quad K^B_{crack} = K^B_{ag} + K^B_{st} = 1400 + 0 = 1400 \text{ k/in.}$$

(Eq. A7.15) $$K_{crack} = K^t_{dw} + K^b_{dw} + \frac{1}{\frac{1}{K^B_{crack}} + \frac{1}{K^B_{crack}}} = 64 + 64 + 310 = 438 \text{ K/in.}$$

(6) Range of Initial Loading Stage (LP29-29A) [Sect. A7.5.3]

δ_{res}, Residual shear deformation at LP 29 = 0

Eq. A7.5: $\Delta\delta^A_{crack}$ (contact) = Δ^A_c = 0.01 in, $\Delta\delta^B_{crack}$ (contact) = Δ^B_c = 0.004 in.

TABLE A7.1 (cont'd.)

(6) Cont'd.

to develop contact at crack A, $\Delta\delta_{crack} = \left(1 + \frac{K^A_{crack}}{K^B_{crack}}\right)(0.01) = 0.0128$ in.

to develop contact at crack B, $\Delta\delta_{crack} = \left(1 = \frac{K^B_{crack}}{K^A_{crack}}\right)(0.004) = 0.018$ in.

Therefore, to develop contact at both cracks A and B requires $\Delta\delta_{crack}$=0.018 in.
Thus the deformation range of initial loading is: $\Delta\delta_{crack}$
(LP29 - 29A) = δ_{res} + 0.018 in.= 0.018 in. [Fig. A7.11]
The shear displacements occurred at the cracks are:

$\Delta\delta^B_{crack}$ = 0.004 in.
$\Delta\delta^A_{crack}$ = 0.018 - 0.004 = 0.014 in } shear displ. from zero shear displ.

(7) Check for Gap Closure (all shear displ. indicated in (7) are incremental values from zero shear displ. position)

Contact along bottom steel [Figs. A7.1(c) and A7.8]

Contact with	(a) dowel displacement*	(b) block displacement	|(a)-(b)|	Gap^c	Closure
block I @X = 0.01 in. (Δ^A_c)	≈0.00 in.	0.014 in. ($\Delta\delta^A_{crack}$)	0.014 in.<	0.10 in.	no
block II @X = 4.5 in. (Fig. A7.8)	0.01 in.	0.018 in. ($\Delta\delta^A_{crack}$ + $\Delta\delta^B_{crack}$)	0.008 in.<	0.10 in.	no

Contact along top steel [Figs. A7.1(c) and A7.8]

Contact with	(a) dowel displacement*	(b) tie or block displacement	|(a)-(b)|	Gap	Closure
tie ① x = 1.0 in	0.0008 in.	0.014 in. ($\Delta\delta^A_{crack}$)	0.0132 in.	<0.10 in. (Gap^t)	no
block I = 4.5 in	0.010 in.	0.014 in. ($\Delta\delta^A_{crack}$)	0.004 in.	<0.10 in. (Gap^c)	no

Closure of crack B on inclined plane [Fig. A7.1(c)]

Eq. A7.4: $Gap^s = (\Delta^B_c/\sin\theta) = 0.004/\sin 20° = 0.0116$ in

Since 0.0116 in > $\Delta\delta^B_{crack}$ (=0.004 in), therefore Gap^s is not closed

*dowel displacement computed from:

$$\Delta\delta_{dw}(x) = \left(3\left(\frac{x}{\ell_p}\right)^2 - 2\left(\frac{x}{\ell_p}\right)^3\right)\Delta\delta_{crack}$$ (notations [Fig. A7.1(c)])

TABLE A7.2 COMPUTED VALUES OF SHEAR STIFFNESS AT INITIAL LOADING STAGE (BEAM R-5) LP 37-37A [Sect. A7.6]

(1) Aggregate Interlocking (K_{ag})

Crack	Crack Width (in.)	K_{ag} [Fig. A7.5(b)] (K/in.)
A	0.02	200
B	0.02	200

(2) Stirrup Resistance Across Crack (K_{st})

Tie	
Tie 2 @ crack B	No Resistance [Table A7.1(2)]

(3) Dowel Resistance of Longitudinal Steel (K_{dw})

	ℓ_p	K_{dw}
top steel	7 in.	64 K/in. (K^t_{dw})
bottom steel	14 in.	8 K/in. (K^b_{dw})

$\Big\}$ 72 K/in.

(4) Shear Resistance of R/C Blocks (K^c)

$$K^c = \frac{5}{6}\,\frac{GA}{\ell_{crit}} = 14{,}950 \text{ K/in.},\quad \ell_{crit} = \ell_p^b = 14 \text{ in.}$$

(5) Shear Resistance at Cracks (K_{crack})

$$K^A_{crack} = K^A_{ag} = 200 \text{ K/in},\quad K^B_{crack} = K^B_{ag} + K^B_{st} = 200 + 0 = 200 \text{ K/in.}$$

(Eq. A7.15) $$K_{crack} = K^t_{dw} + K^b_{dw} + \left(\frac{1}{\frac{1}{K^A_{crack}} + \frac{1}{K^B_{crack}}}\right) 64 + 8 + 100 = 172 \text{ K/in.}$$

(6) Range of Initial Loading Stage (LP37-37A) [Fig. A7.15(a)]

δ_{res}, Residual shear deformation at LP37 = 0.018 in. (Eq. A7.6)

Eq. A7.5: $\Delta\delta^A_{crack}$ (contact) = Δ^A_c = 0.02 in, $\Delta\delta^B_{crack}$ (contact) = Δ^B_c = 0.02 in.

to develop contact at crack A, $\Delta\delta_{crack} = \left(1 + \frac{200}{200}\right)(0.02) = \underline{0.04}$ in.

to develop contact at crack B, $\Delta\delta_{crack} = \left(1 + \frac{200}{200}\right)(0.02) = \underline{0.04}$ in.

TABLE A7.2 (cont'd.)

(6) Cont'd.

$\Delta\delta_{crack}$ (LP37-37A) = δ_{res} + 0.04 in.= 0.018 + 0.04 = 0.058 in. ANS

$\Delta\delta^{B}_{crack}$ = 0.02 in.
$\Delta\delta^{A}_{crack}$ = 0.02 in.
> increments from zero shear displ.

(7) Check for Gap Closure (all shear displ. indicated in (7) are incremental values from zero shear displ.)

Contact along bottom steel [Fig. A7.1(c)]

Contact with	(a) dowel displacement*	(b) block displacement	|(a)-(b)|	Gap	Closure
block I @X = 0.02" (Δ^{A}_{c})	≈ 0.00 in.	0.02 in. ($\Delta\delta^{A}_{crack}$)	0.02 in. <	0.10 in. (Gap^{c})	no
block II @X = 4.5"	0.056 in.	0.02 in. ($\Delta\delta^{A}_{crack}$ + $\Delta\delta^{B}_{crack}$)	0.016 in. <	0.10 in. (Gap^{c})	no

Contact along top steel [Fig. A7.13(b)]

Contact with	(a) dowel displacement*	(b) block or tie displacement	|(a)-(b)|	Gap	Closure
tie 1 @X = 1.0"	0.00058 in.	0.020 in. ($\Delta\delta^{A}_{crack}$)	0.019 in.	0.100 in. (Gap^{t})	no
block I @X = 4.5"	0.0097 in.	0.040 in. ($\Delta\delta^{A}_{crack}$ + $\Delta\delta^{B}_{crack}$	0.030 in.	0.100 in. (Gap^{c})	no

Closure of crack B on inclined plane [Fig. A7.1(c)]

Eq. A7.4: $Gap^{s} = \Delta^{B}_{c}/\sin\theta = 0.02/\sin 20^{\circ} = 0.058$ in.

Since 0.058 in. > $\Delta\delta^{B}_{crack}$ (=0.02 in.)

Gap^{s} is not closed

*dowel displacement computed from:

$$\Delta\delta_{dw}(X) = \left(3\left(\frac{X}{\ell_p}\right)^2 - 2\left(\frac{X}{\ell_p}\right)^3\right)\Delta\delta_{crack}$$ (Notations [Fig. A7.1 (c)])

TABLE A7.3 COMPUTED VALUES OF SHEAR STIFFNESS AT INITIAL LOADING STAGE (BEAM R-5) LP39-39A (USING UPPER BOUND VALUES FOR K^A_{ag} , K^B_{ag})

(1) Aggregate Interlocking (K_{ag})

Crack	Crack Width (in.)	K_{ag} [Fig. A7.5(b)] (K/in.)
A	0.04	200 (upper bound value)
B	0.04	200 (upper bound value)
C	0.02	200

(2) Stirrup Resistance Across Crack (K_{st}) [Fig. A7.14(b)]

Tie	Parameters for Determining Slipped Length (Eq. A7.11)			Slipped Length/ Available Anchor		K_{st} (K/in) (Eq. A7.11)
	Max Stretching (Δ_p)	available bond		ℓ^ℓ_x/ℓ^ℓ_d	ℓ^r_x/ℓ^r_d	
		left anchor.	right anchor.	left anchor.	right anchor.	
tie 1 @ crack B	No resistance [Table A7.1(s)]					0.0
tie 4 upper @ crack C	Ineffective due to cracking along tie					0.0
tie 3 center @ crack C	0.02 in. @ LP 38	500 psi	500 psi	8.6"/6.0"	8.6"/5.0"	$\ell^l_x > \ell^l_d, (i=\ell,r)$ $\therefore K_{st} = 0.$
tie 3 lower @ crack C	Ineffective due to cracking along tie					0.0

(3) Dowel Resistance of Longitudinal Steel (K_{dw})

	ℓ_p	K_{dw}	
top steel	14 in.	8 K/in.	(K^t_{dw})
bottom steel	14 in.	8 K/in.	(K^b_{dw})

K_{dw} = 16 K/in.

(4) Shear Resistance of R/C Blocks (K^c)

$$K^c = \frac{5}{6}\frac{GA}{\ell_{crit}} = 14{,}950 \text{ K/in.}, \ell_{crit} = \ell_p = 14 \text{ in.}$$

(5) Shear Resistance at Cracks (K_{crack})

$$K^A_{crack} = K^A_{ag} = 200 \text{ K/in}, \quad K^B_{crack} = K^B_{ag} + K^B_{st} = 200 \text{ K/in.}$$

$$K^C_{crack} = K^C_{ag} + K^C_{st} = 200 + 0 = 200 \text{ K/in.}$$

Considering the force and deformation of the model [Fig. A7.17(b)], the expression for K_{crack} is:

TABLE A7.3 (cont'd.)

(5) Cont'd.

$$K_{crack} = K^t_{dw} + K^b_{dw} + \left(\frac{1}{\frac{1}{K^A_{crack}} + \frac{1}{K^B_{crack}} + \frac{1}{K^C_{crack}}} \right)$$

$$= 8 + 8 + 66.7 = 82.7 \text{ K/in.}$$

(6) Range of the Initial Loading Stage (LP39-39A) [Fig. A7.15(a)]

δ_{res}, residual shear deformation at LP37 = 0.04 in. (Eq. A7.6)

Eq. A7.5: $\Delta\delta^A_{crack}$ (contact) = Δ^A_C = 0.04 in, $\Delta\delta^B_{crack}$ (contact) = Δ^B_C = 0.04 in.

$\Delta\delta^C_{crack}$ (contact) = Δ^C_c = 0.02 in

to develop contact at crack A, $\Delta\delta_{crack} = \left(1 + \frac{K^A_{crack}}{K^B_{crack}} + \frac{K^A_{crack}}{K^C_{crack}}\right)(0.04) = 0.120$ in.

to develop contact at crack B, $\Delta\delta_{crack} = \left(1 + \frac{K^B_{crack}}{K^A_{crack}} + \frac{K^B_{crack}}{K^C_{crack}}\right)(0.04) = 0.120$ in.

to develop contact at crack C, $\Delta\delta_{crack} = \left(1 + \frac{K^C_{crack}}{K^A_{crack}} + \frac{K^C_{crack}}{K^B_{crack}}\right)(0.02) = 0.06$ in.

After a $\Delta\delta'_{crack}$ of 0.06" $\Delta\delta^A_{crack}$ closed at 0.02"
$\Delta\delta^B_{crack}$ closed at 0.02"
$\Delta\delta^C_{crack}$ closed at 0.02"

Whereupon K^C_{ag} increases considerably; presumably approaching ∞.

Therefore, to close the remaining 0.02" at cracks A and B to obtain contact of aggregates at these cracks it is necessary to have:

for A $\Delta\delta''_{crack} = (1 + 1 + 0)\ (0.02") = 0.04"$
for B $\Delta\delta''_{crack} = (1 + 1 + 0)\ (0.02") = 0.04"$
for C $= (1 + \infty + \infty)\ (0.0) = 0$

Thus, total $\Delta\delta_{crack}$ = 0.06" + 0.04" = 0.10"
(Contact at crack A will occur when $\Delta\delta_{crack}$ = 0.10 in.) and

$$K''_{crack} = 8 + 8 + \frac{1}{\frac{1}{200} + \frac{1}{200}} = 8 + 8 + 100 = 116 \text{ k/in.}$$

TABLE A7.3 (cont'd.)

(7) Check for Gap Closure (all shear displ. indicated in (7) are incremental values from zero shear displ.)
(LP39-LP39A)

Contact along top steel [Fig. A7.14(b)]

Contact with	(a) dowel displacement* (in.)	(b) block displacement (in.)	|(a)-(b)| (in.)	Gap (in.)	Gap Closure
block I @X = 0.04" (Δ_c^A)	≈ 0.00	0.040 ($\Delta\delta^A_{crack}$)	0.04	<0.10 (Gap^c)	no
block II @X = 4.5"	0.025	0.080 ($\Delta\delta^A_{crack} + \Delta\delta^B_{crack}$)	0.055	<0.10 (Gap^c)	no
block III @X = 11.5"	0.092	0.100 ($\Delta\delta_{crack}$)	0.08	<0.10 (Gap^c)	no

Contact along bottom steel [Fig. A7.14(b)]

Contact with	(a) dowel displ.* (in.)	(b) block or tie displ. (in.)	|(a)-(b)| (in.)	Gap (in.)	Gap Closure
tie 1 @ X = 1.0"	0.0017	0.04 ($\Delta\delta^A_{crack}$)	0.0383	<0.10 (Gap^t)	no
block I @ X = 4.5"	0.025	0.04 ($\Delta\delta^A_{crack}$)	0.015	<0.10 (Gap^t)	no
tie 2 @ X = 4.5"	0.025	0.08 ($\Delta\delta^A_{crack} + \Delta\delta^B_{crack}$)	0.055	<0.10 (Gap^t)	no
block II @ X = 8.0"	0.061	0.08 ($\Delta\delta^A_{crack} + \Delta\delta^B_{crack}$)	0.019	<0.10 (Gap^t)	no
tie 3 @ X = 8.0"	0.061	0.10 ($\Delta\delta_{crack}$)	0.039	<0.10 (Gap^t)	no
tie 4 @ X = 11.5"	0.092	0.10 ($\Delta\delta_{crack}$)	0.008	<0.10 (Gap^t)	no

Closure of cracks B and C on inclined plane [Fig. A7.14(b)

Crack	@	Crack Width	Gap^s (Eq. A7.4)	Shear displ.	Gap Closure
B	20°	Δ_c^B = 0.04 in.	0.12 in.	> 0.04 in.	no
C	45°	Δ_c^C = 0.02 in.	0.04 in.	= 0.04 in.	just closing

* dowel displacement computed from [Fig. A7.15(c)]:

$$\delta_{dw}(X) = \left(3\left(\frac{X}{\ell_p}\right)^2 - 2\left(\frac{X}{\ell_p}\right)^3\right)\Delta\delta_{crack}$$

TABLE A 7.4 COMPUTED VALUES OF SHEAR STIFFNESS AT INITIAL LOADING STAGE (BEAM R-5) LP39-39A (USING LOWER BOUND VALUES FOR K^A_{ag} , K^B_{ag})

(1) Aggregate Interlocking (K_{ag})

Crack	Crack Width (in.)	K_{ag} [Fig. A7.5(b)] (K/in.)
A	0.04	0 (lower bound value)
B	0.04	0 (lower bound value)
C	0.02	200

(2) Stirrup Resistance Across Crack (K_{st})

No resistance [Table A7.3(2)]

(3) Dowel Resistance of Longitudinal Steel (K_{dw})

	ℓ_p	K_{dw}
top steel	14 in.	8 K/in. (K^t_{dw})
bottom steel	14 in.	8 K/in. (K^b_{dw})

$> K_{dw} = 16$ K/in.

(4) Shear Resistance of R/C Blocks (K^c)

$$K^c = \frac{5}{6}\,\frac{GA}{\ell_{crit}} = 14{,}950 \text{ K/in}, \quad \ell_{crit} = \ell_p = 14 \text{ in.}$$

(5) Shear Resistance at Cracks (K_{crack})

$$K^A_{crack} = K^A_{ag} = 0 \text{ K/in}, \quad K^B_{crack} = K^B_{ag} + K^B_{st} = 0 + 0 = 0 \text{ K/in.}$$

$$K^C_{crack} = K^C_{ag} + K^C_{st} = 200 + 0 = 200 \text{ K/in.}$$

Consider the force - deformation of the model [Fig. A7.17(b)] the expression

$$\text{for } K_{crack} = K^t_{dw} + K^b_{dw} + \left(\frac{1}{\frac{1}{K^A_{crack}} + \frac{1}{K^B_{crack}} + \frac{1}{K^C_{crack}}}\right)$$

$$= 8 + 8 + 0 = 16 \text{ K/in.}$$

(6) 1st Contact Point ($LP39^1$) [Fig. A7.18(a)]

(block I contacts top steel, bottom steel contacts 1st stirrup-ties)

Shear displ. at the 1st contact point ($LP39^1$)

Most shear displ. occurred along crack A ($K^A_{crack} = 0$) [Fig. A7.18(b)]

TABLE A7.4 (cont'd.)

(6) Cont'd.

	Shear displ. of	Shear displ. (in.)
1	block I = $\Delta\delta^A_{crack}$	0.10
2	$\Delta\delta^B_{crack}$	0.00
3	block II	0.10
4	$\Delta\delta^C_{crack}$	0.00
5	block III = $\Delta\delta_{crack}$	0.10

Gaps Along Top Steel (LP39[1]) [Fig. A7.18(b)]

Contact	dowel displ. (in.)	Gap (in.)	Gap Closure
@ X = 0.04" (Δ^A_c)	6 0.00$^+$	Gap^c -(1 - 6) = 0.00$^+$	Closes
@ X = 4.5"	7 0.024	Gap^c -(3 - 7) = 0.024	no
@ X = 11.5"	8 0.091	Gap^c -(5 - 8) = 0.091	no

Gaps Along Bottom Steel (LP39[1]) [Fig. A7.18(b)]

Contact	dowel displ. (in.)	Gap (in.)	Gap Closure
@ X = 1.0 (in)	9 .0015	Gap^t -(1 - 9) ≐ 0.0	Closes
@ X = 4.5	10 .024	Gap^c -(3 - 10) = .18	no
@ X = 4.5	11 .024	Gap^t -(3 - 11) = .02	no
@ X = 8.0	12 .061	Gap^c -(3 - 12) = .14	no
@ X = 8.0	13 .061	Gap^t -(5 - 13) = .06	no
@ X = 11.5	14 .091	Gap^t -(5 - 14) = .09	no

K_{crack} after 1st contact point (LP39[1]) [Fig. A7.18(a)]

Most of shear displ. occurred along crack B (K^B_{crack} = 0) [Fig. A7.18(b)] [Fig. A7.19(a)]

The shear stiffness is offered by dowel action [Fig. A7.18(b)]:

$$K_{crack} = K^t_{dw} + K^b_{dw} = \frac{12E_sI_s}{\ell_p^3} + \frac{12E_sI_s}{\ell_p^3}$$

$$= 8 + 8 = 16 \text{ K/in.}$$

TABLE A7.4 (cont'd.)

(7) 2nd Contact Point ($LP39^2$) [Fig. A7.18(a)]

(block II contacts top steel, bottom steel contacts the 2nd tie, Fig. A7.19(a)

Shear displ. at the 2nd contact point ($LP39^2$)

	Shear displ. of	Shear displ. (in.)
1	block I = $\Delta\delta^A_{crack}$	0.100
2	$\Delta\delta^B_{crack}$	0.032
3	block II	0.132
4	$\Delta\delta^B_{crack}$	0.000
5	block III = $\Delta\delta_{crack}$	0.132

Gaps Along Top Steel ($LP39^2$) [Fig. A7.19(a)]

Contact		dowel displ. (in.)	Gap (in.)	Gap Closure
@ X = 0.04" (Δ_c^A)	6	0.0^+	Gap^C -(1 - 6) = 0.0^+	reopens due to dowel displ. ($LP39^1$-39^2)
@ X = 4.5"	7	0.032	Gap^C -(3 - 7) = 0.0	closed at 2nd contact pt($LP39^2$)
@ X = 11.5"	8	0.121	Gap^C -(5 - 8) = 0.1	no

Gaps Along the Bottom Steel ($LP39^2$) [Fig. A7.19(a)]

Contact		dowel displ. (in)	Gap(in)	Gap Closure
@ X = 1.0(in)	9	.002	Gap^t -(1 - 9) = .002	reopens due to dowel displ.($LP39^1$-39^2)
@ X = 4.5	10	.032	Gap^C -(3 - 10) = .200	no
@ X = 4.5	11	.032	Gap^t -(3 - 11) = .00	closes @ 2nd contact pt($LP39^2$)
@ X = 8.0	12	.081	Gap^C -(3 - 12) = .151	no
@ X = 8.0	13	.081	Gap^t -(5 - 13) = .049	no
@ X = 11.5	14	.121	Gap^t -(5 - 14) = .089	no

K_{crack} after 2nd contact point ($LP39^2$) [Fig. A7.18(a)][Fig. A7.19(a),(b),(c)]

$$K^B_{crack} = K^{t^B}_{dw} + K^{b^B}_{dw} = 2\,K^B_{dw} = 2\,\frac{3E_sI_s}{(4.5)^3}\left(\frac{4 + (9.5/4.5)}{1 + (9.5/4.5)}\right)^{**} = 234 \text{ K/in.}$$

** Fig. A7.8(b), Fig. A7.19

TABLE A7.4 (cont'd.)

(7) cont'd.

$$K^C_{crack} = (K^C_{ag} + K^C_{st} + K^{t^C}_{dw} + K^{b^C}_{dw})^{**} = 200 + 0 + \frac{12\ E_s I_s}{14^3} + \frac{12\ E_s I_s}{14^3} = 200 + 16 = 216\ \text{K/in.}$$

$$K_{crack} = \left(\frac{1}{\frac{1}{K^A_{crack}} + \frac{1}{K^B_{crack}}}\right) = 112\ \text{K/in.}$$

** Ref. Fig. A7.8(c)

(8) <u>3rd Contact Point (LP 39^3)</u> [Fig. A7.18(a)]

Eq. A7.4 $\Delta\delta^B_{crack}$ (to close crack B on inclined plane) $= \frac{0.04}{\sin 20°} = 0.117$ in.

Eq. A7.5 $\Delta\delta^C_{crack}$ (contact crack C on aggregates) $= \Delta^C_c = 0.02$ in.

At the 2nd contact point (LP 39^2), the values of shear displacements at the cracks are:

$$\Delta\delta^A_{crack} = 0.10\ \text{in.},\ \Delta\delta^B_{crack} = 0.032\ \text{in.},\ \Delta\delta^C_{crack} = 0.0\ \text{in.}$$

Crack A is already closed. Since $\Delta\delta^A_{crack} > \Delta^A_c$, the amount of additional shear displacement required to close crack B and C are:

$$\Delta\delta^B_{crack} = (0.117 - 0.032) = 0.085\ \text{in.}$$

$$\Delta\delta^C_{crack} = (0.02 - 0.0) = 0.02\ \text{in.}$$

The amount of $\Delta\delta_{crack}$ required to close crack B and crack C is:

to close crack B, $\Delta\delta_{crack} = \left(1 + \frac{K^B_{crack}}{K^C_{crack}}\right)\Delta\delta^B_{crack} = (1 + 234/216) = 2.08\ \Delta\delta^B_{crack}$

$$= 2.08(0.085) = 0.177\ \text{in.}$$

to close crack C, $\Delta\delta_{crack} = \left(1 + \frac{K^C_{crack}}{K^B_{crack}}\right)\Delta\delta^C_{crack} = (1 + 216/234) = 1.923\ \Delta\delta^C_{crack}$

$$= 1.923(0.02) = 0.039\ \text{in.}$$

The amount of $\Delta\delta_{crack}$ required to bring crack C into contact is then 0.039 in. and the corresponding values of shear displacement at the cracks are:

$$\Delta\delta^C_{crack} = 0.02\ \text{in. and}\ \Delta\delta^B_{crack} = 0.039 - 0.02 = 0.019\ \text{in.}$$

TABLE A7.4 (cont'd.)

(8) cont'd.

Shear displ. at end of initial loading stage (LP 39^3)

$\Delta\delta_{crack}$ = 0.132 (@ LP 39^2) + 0.039 = 0.171 in.

$\Delta\delta^A_{crack}$ = 0.10 in.

$\Delta\delta^B_{crack}$ = 0.032 (@ LP 39^2) + 0.019 = 0.051 in.

$\Delta\delta^C_{crack}$ = 0.0 (@ LP 39^2) + 0.02 = 0.02 in.

(9) Last Contact Point (LP 39A) [Fig. A7.18(a)]

From LP 39^3 to LP 39A, $k^C_{crack} = \infty$, and the stiffness, k_{crack}, corresponds to that of the dowel stiffness along crack B, k^B_{crack} [Fig. A7.18(b)]

$$k_{crack} = k_{crack} = 2\,\frac{3E_sI_s}{(4.5)^3}\left(\frac{4 + (9.5/4.5)}{1 + (9.5/4.5)}\right) = 234 \text{ K/in.}$$

and $\Delta\delta_{crack} = \Delta\delta^B_{crack}$ since $\Delta\delta^A_{crack} = \Delta\delta^C_{crack} \doteq 0$

Closure of crack B on the inclined plane requires

$$\Delta\delta_{crack} \text{ or } \Delta\delta^B_{crack} = \frac{0.04''}{\sin 20°} - 0.032''(\text{LP } 39^1 \rightarrow \text{LP } 39^2) - 0.019''(\text{LP } 39^2 \rightarrow \text{LP } 39^3)$$

$$= 0.066 \text{ in.}$$

Therefore, the deformation range of the initial loading stage is:

$$\Delta\delta_{crack}(\text{LP } 39 - 39A) = \underbrace{\delta_{res}}_{0.04} + \underbrace{0.171 + 0.066}_{0.237} = 0.277 \text{ in. [Fig. A7.18(a)]}$$

Check for possible contact along top steel (LP 39^2-LP 39^3) [Fig. A7.29(a)]

Steel contacting with tie 3 is possible if $\Delta h \geq (Gap^t + Gap^c)$ = 0.20 in.

Since $\Delta h < \Delta h'$ = 0.12 in. < 0.20 in., there is no contact.

Possible contact along bottom steel [Fig. A7.20(b)]

Steel contacting with tie 3 is possible if $\Delta h \leq 0$.

Since $\Delta h < \Delta h'$ = 0.04 in., there is no contact.

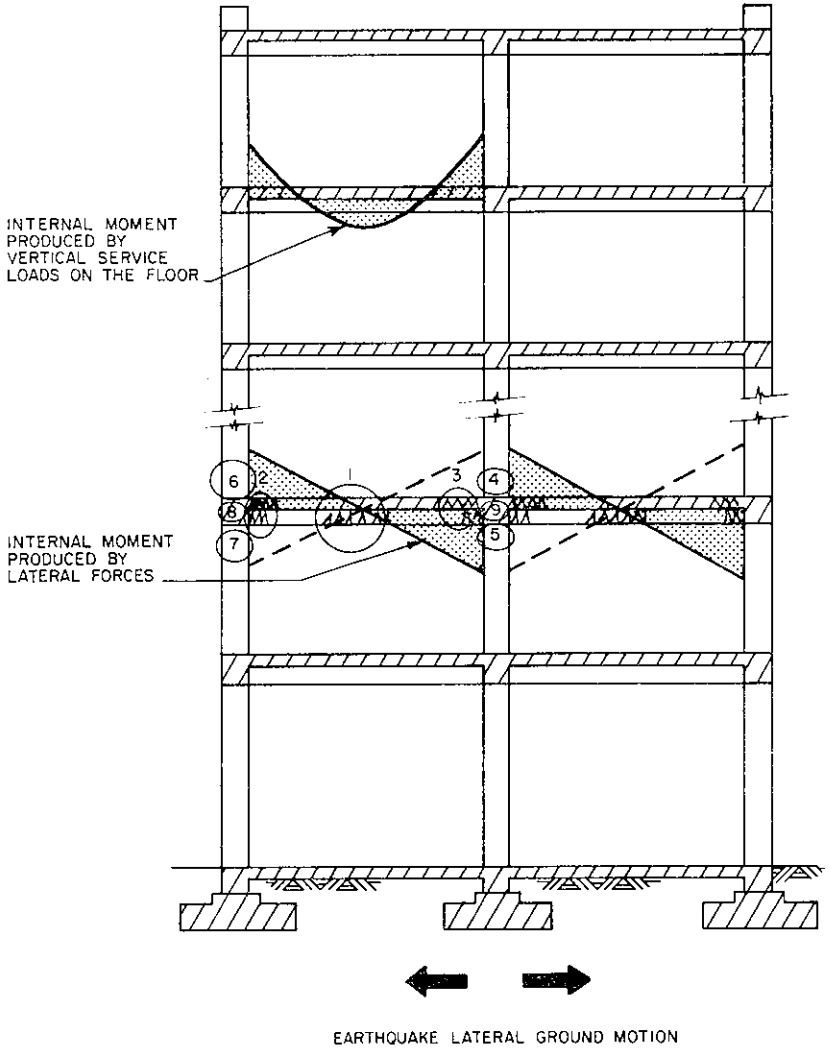

FIG. 1.1 CRITICAL REGIONS DEVELOPED UNDER EARTHQUAKE MOTION [1.3]

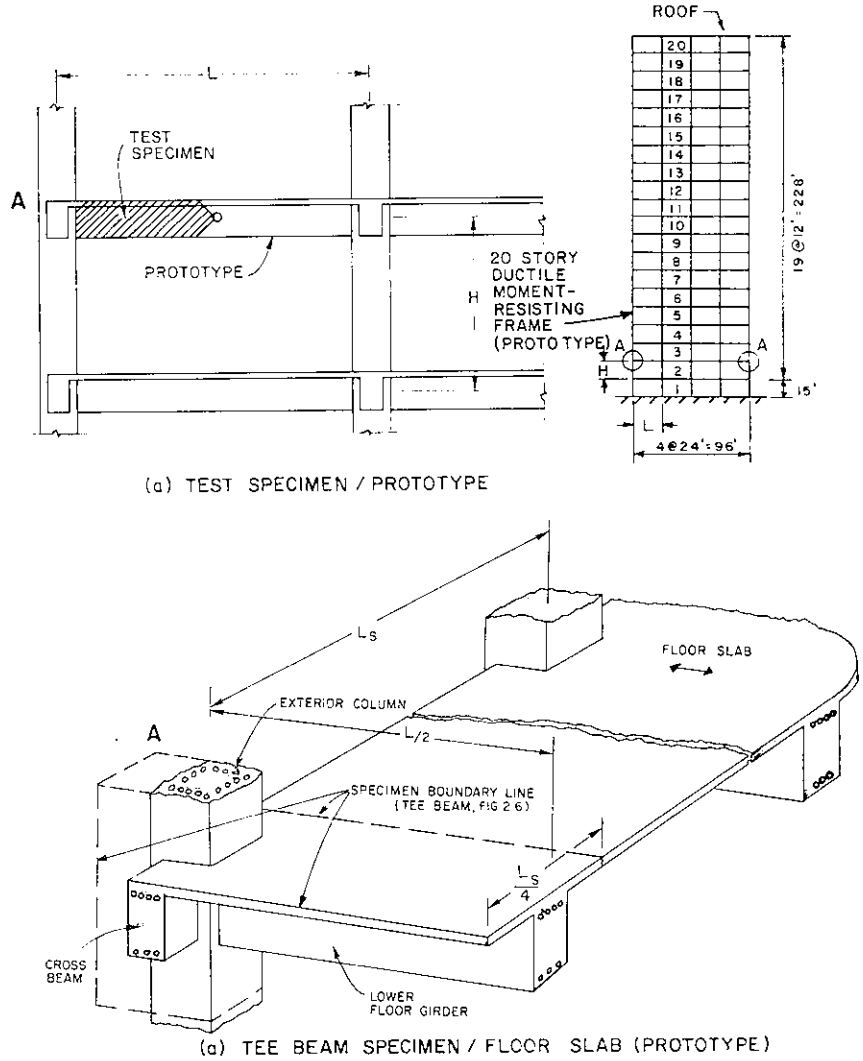

FIG. 2.1 TEST SPECIMEN

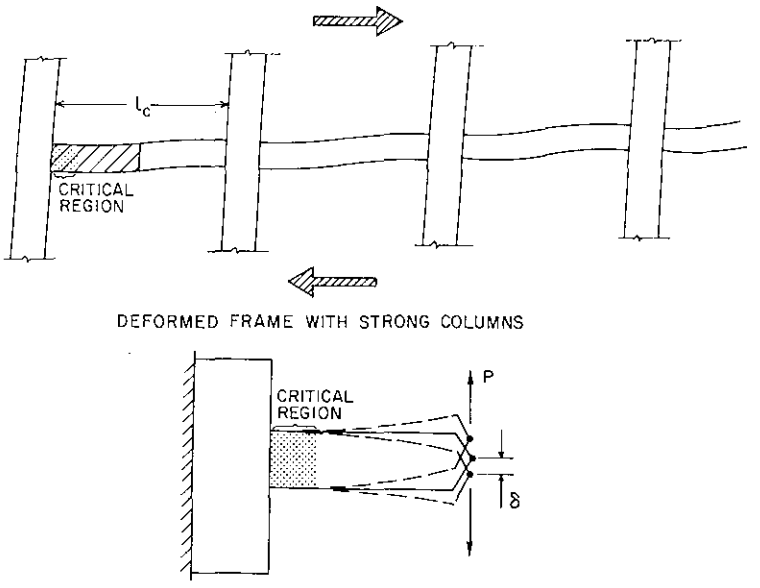

FIG. 2.2 LOADING METHOD

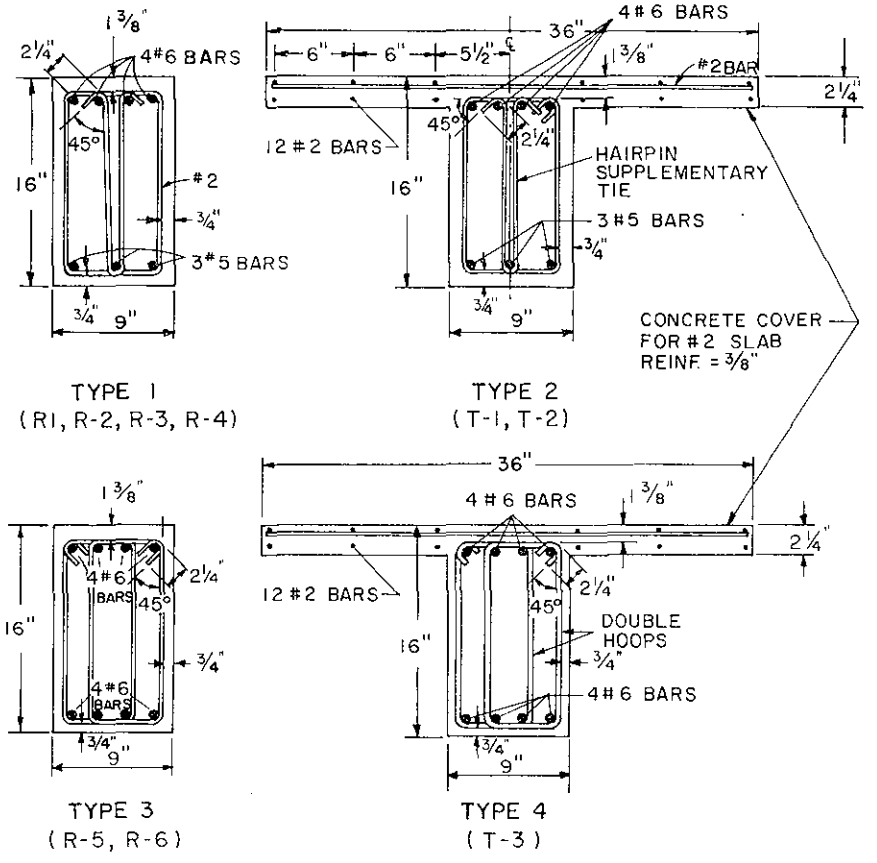

(ALL TIES ARE #2 BARS SPACED AT d/4.)

FIG. 2.3 BEAM SECTION DETAILS

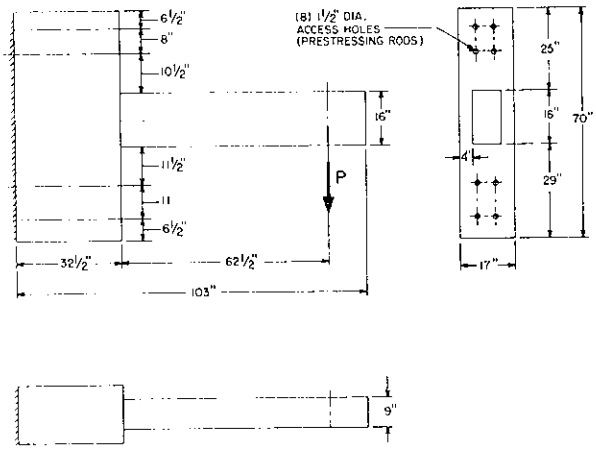

FIG. 2.4 SPECIMEN DIMENSIONS (BEAMS R-1 TO R-4, AND R-6)

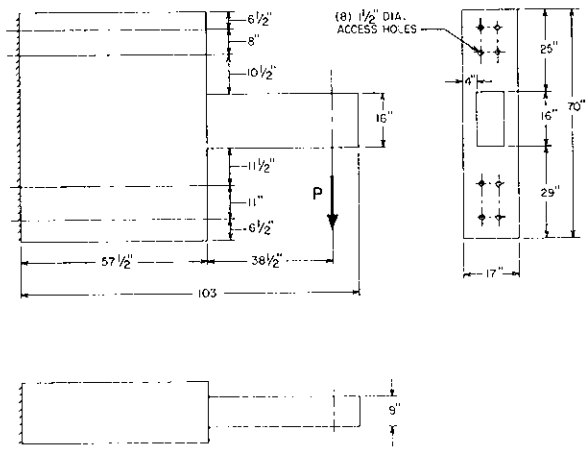

FIG. 2.5 SPECIMEN DIMENSIONS (BEAM R-5)

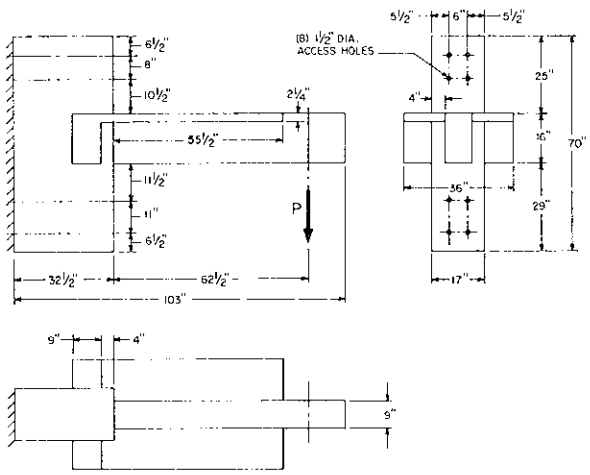

FIG. 2.6 SPECIMEN DIMENSIONS (BEAMS T-1 TO T-3)

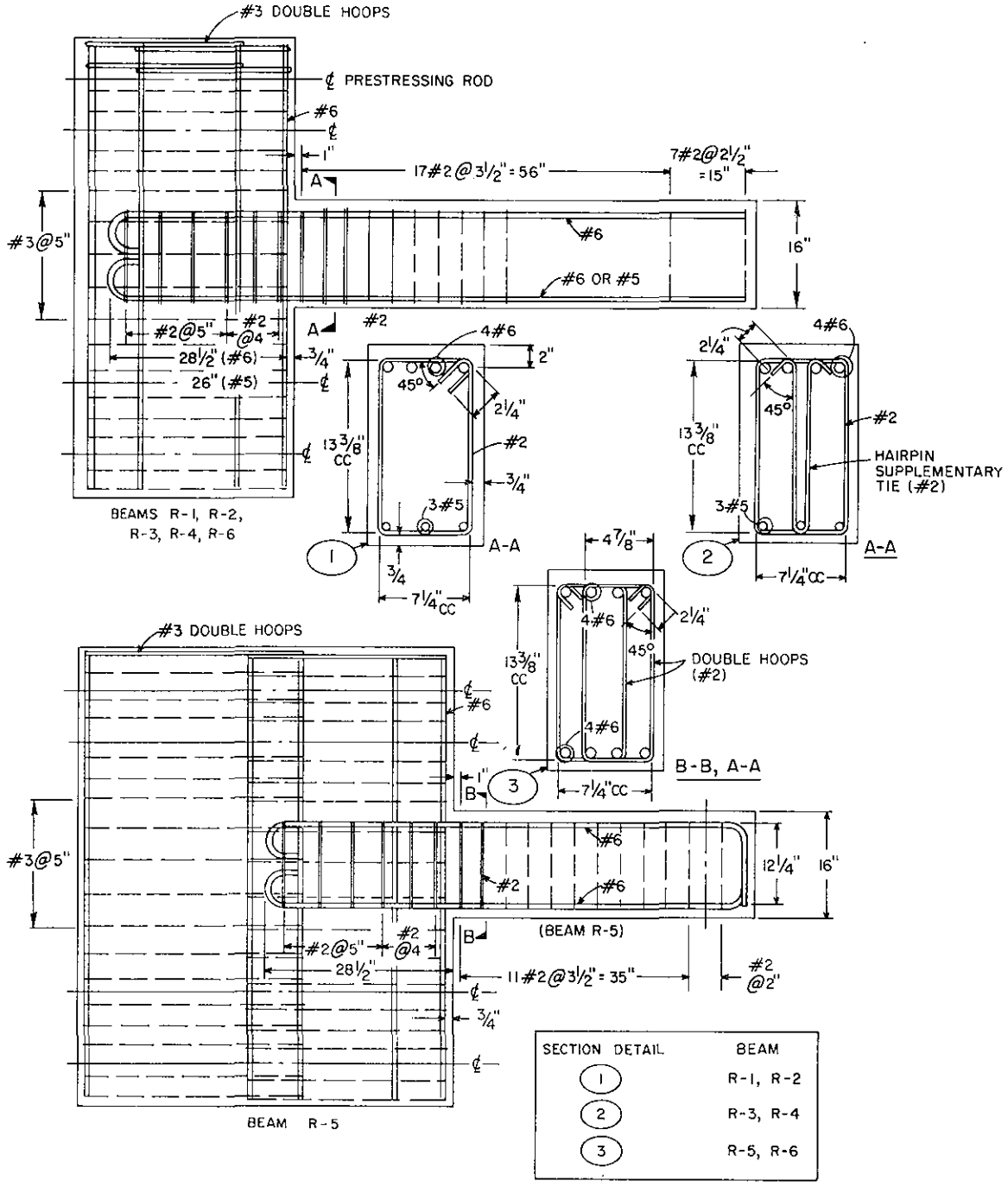

FIG. 2.7 REINFORCEMENT DETAILS (RECTANGULAR BEAMS)

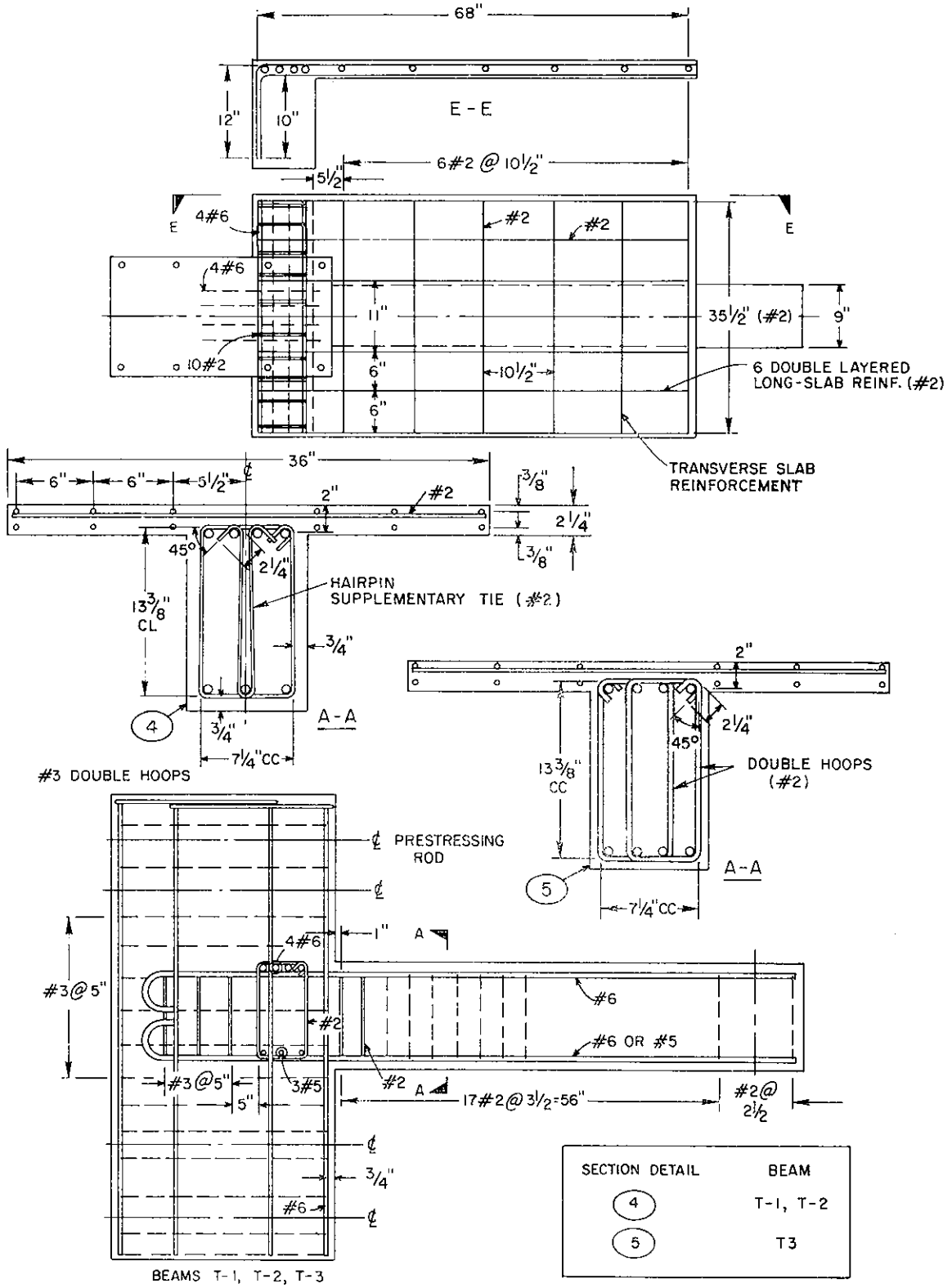

FIG. 2.8 REINFORCEMENT DETAILS (T-BEAMS)

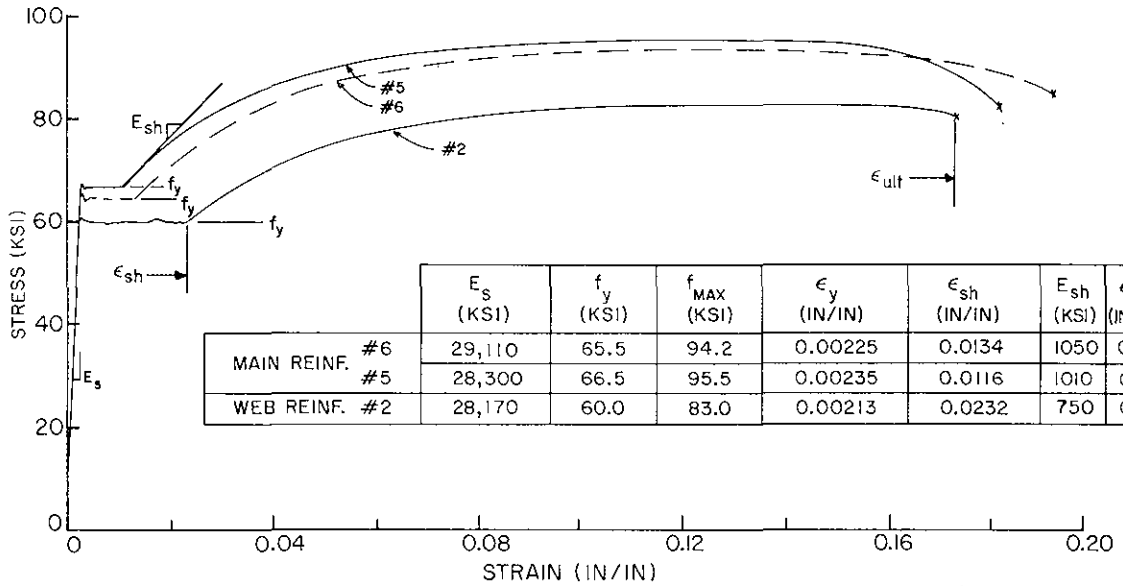

		E_s (KSI)	f_y (KSI)	f_{MAX} (KSI)	ϵ_y (IN/IN)	ϵ_{sh} (IN/IN)	E_{sh} (KSI)	ϵ_{ult} (IN/IN)
MAIN REINF.	#6	29,110	65.5	94.2	0.00225	0.0134	1050	0.19
	#5	28,300	66.5	95.5	0.00235	0.0116	1010	0.18
WEB REINF.	#2	28,170	60.0	83.0	0.00213	0.0232	750	0.17

FIG. 2.9 STRESS-STRAIN CURVES OF BEAM REINFORCEMENT

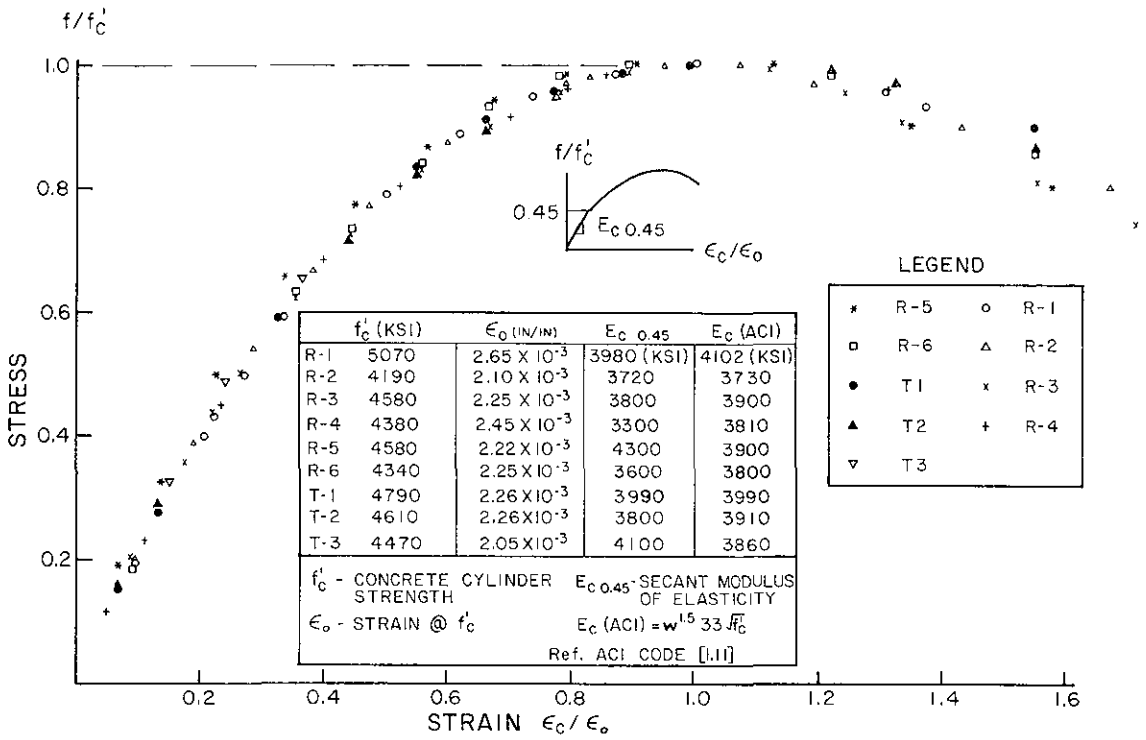

	f'_c (KSI)	ϵ_o (IN/IN)	$E_{c\,0.45}$	E_c (ACI)
R-1	5070	2.65×10^{-3}	3980 (KSI)	4102 (KSI)
R-2	4190	2.10×10^{-3}	3720	3730
R-3	4580	2.25×10^{-3}	3800	3900
R-4	4380	2.45×10^{-3}	3300	3810
R-5	4580	2.22×10^{-3}	4300	3900
R-6	4340	2.25×10^{-3}	3600	3800
T-1	4790	2.26×10^{-3}	3990	3990
T-2	4610	2.26×10^{-3}	3800	3910
T-3	4470	2.05×10^{-3}	4100	3860

f'_c - CONCRETE CYLINDER STRENGTH

ϵ_o - STRAIN @ f'_c

$E_{c\,0.45}$ - SECANT MODULUS OF ELASTICITY

E_c (ACI) $= w^{1.5}\, 33 \sqrt{f'_c}$

Ref. ACI CODE [1.11]

FIG. 2.10 CONCRETE STRESS-STRAIN CURVES (COMPRESSION TEST RESULTS)

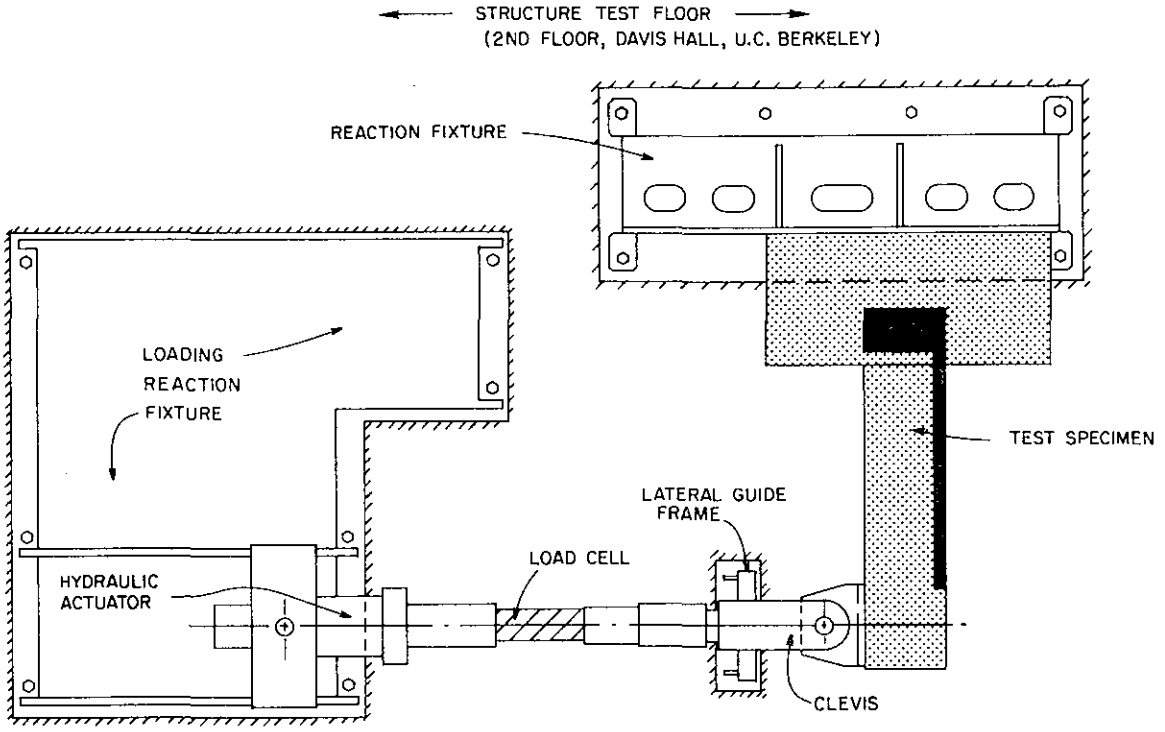

FIG. 3.1 LOADING AND SUPPORT OF TEST SPECIMENS

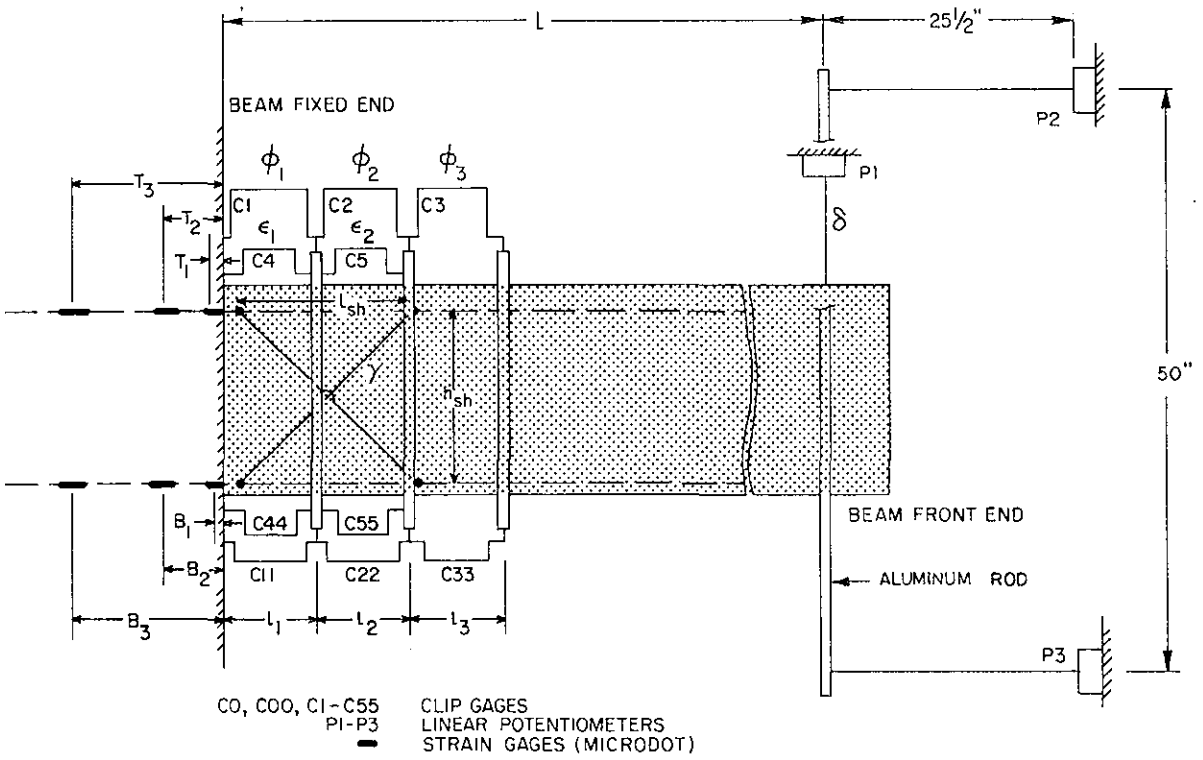

FIG. 3.2 SCHEMATIC INSTRUMENTATION OF TEST SPECIMEN

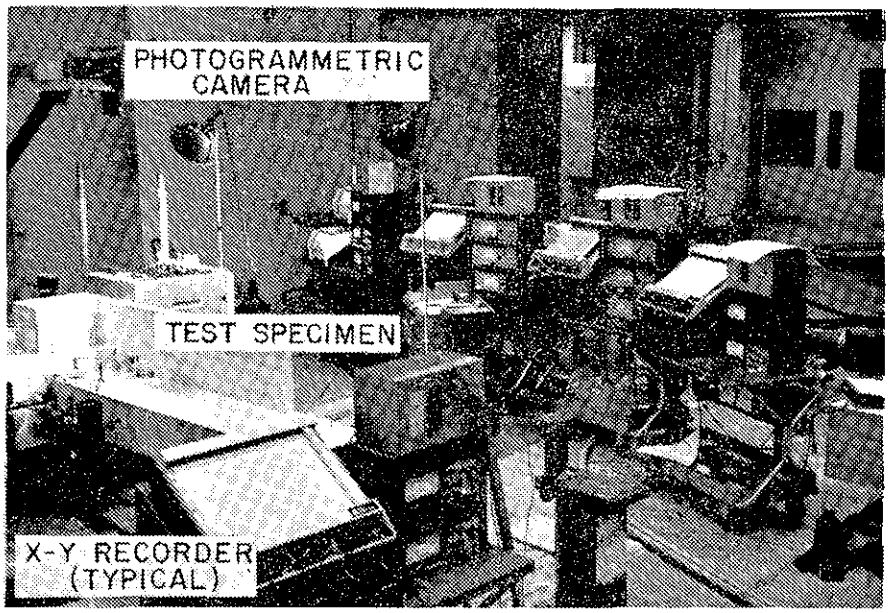

(a) GENERAL TEST SETUP

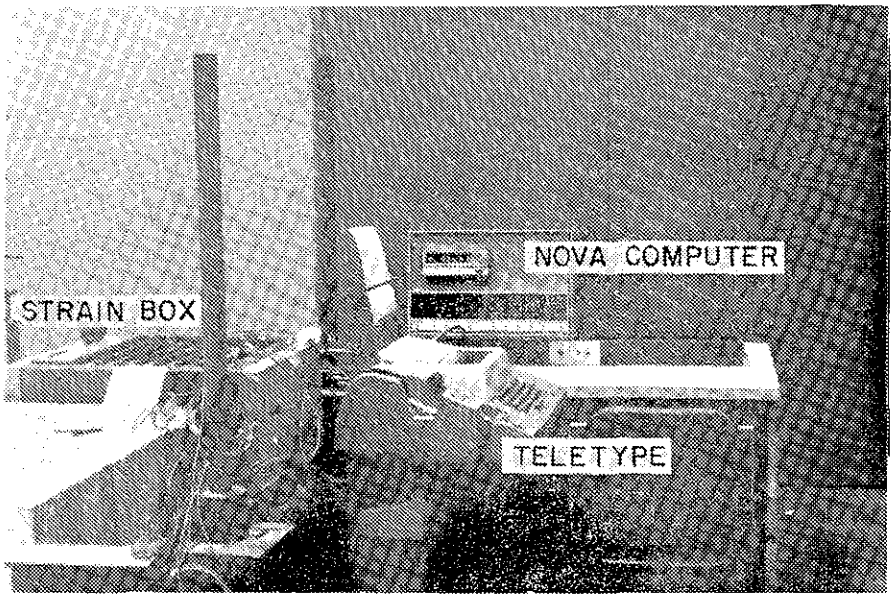

(b) LOW-SPEED SCANNER EQUIPMENT

FIG. 3.3 TEST SETUP AND EQUIPMENT

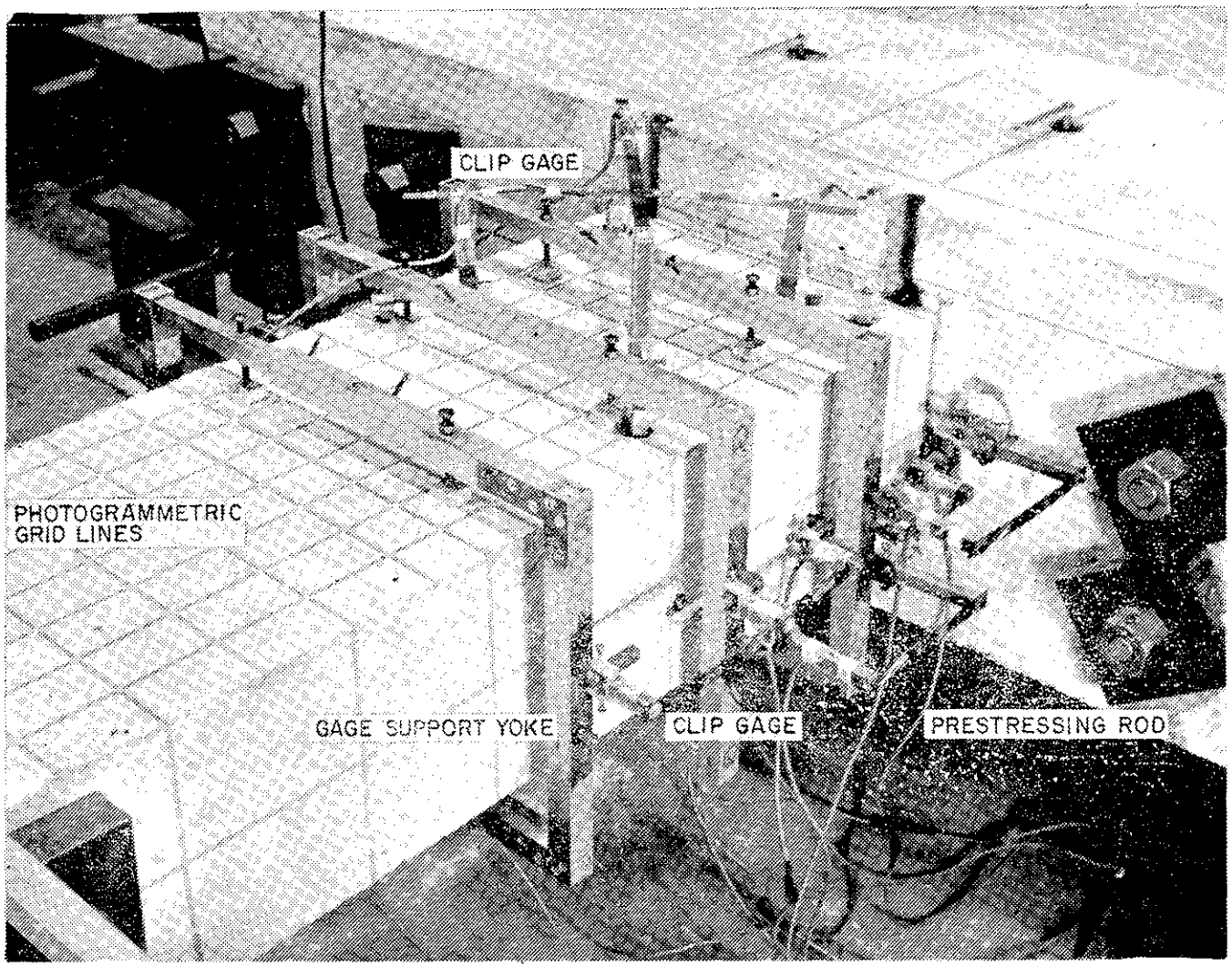

FIG. 3.4 INSTRUMENTATION FOR MEASURING SHEAR AND BENDING DEFORMATIONS

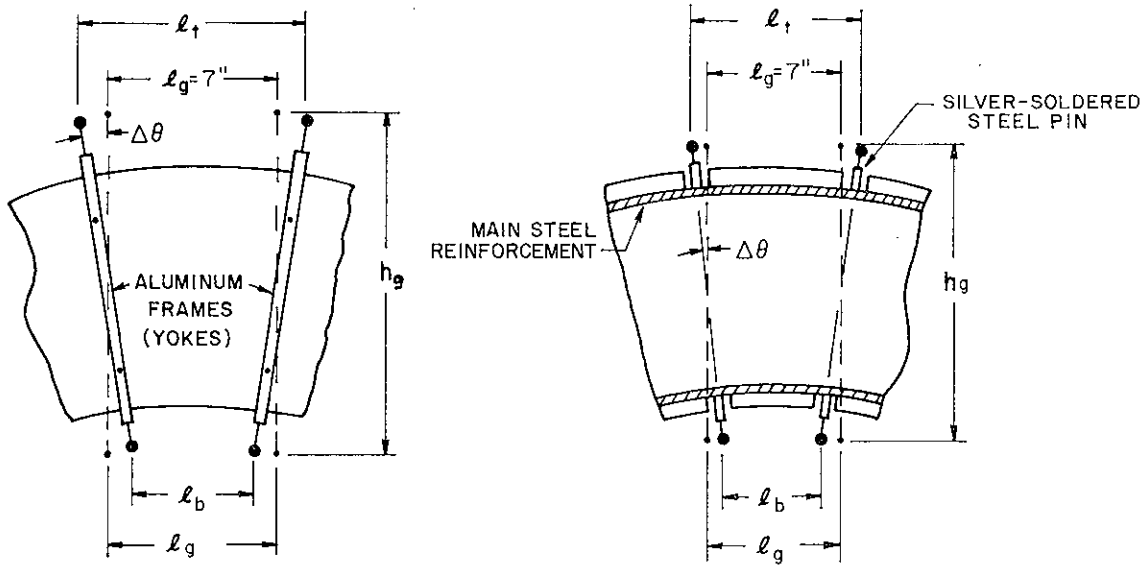

RELATIVE ROTATION $\Delta\theta = \dfrac{\Delta + \bar{\Delta}}{h_g}$ $\quad \left.\begin{array}{l}\Delta = (\ell_t - \ell_g) \\ \bar{\Delta} = (\ell_b - \ell_g)\end{array}\right]$ MEASURED BY CLIP GAGES

AVERAGE CURVATURE $\phi_{av} = \Delta\theta / \ell_g$

FIG. 3.5 ROTATIONAL DEFORMATION MEASUREMENTS

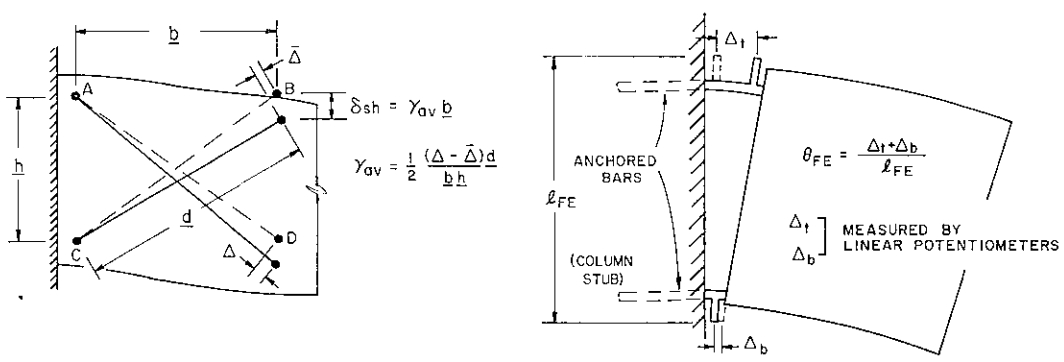

(a) SHEAR DISTORTION γ_{av} MEASUREMENT (b) FIXED END ROTATION θ_{FE} MEASUREMENT

FIG. 3.6 DEFORMATION MEASUREMENTS

FIG. 3.7 INSTRUMENTATION FOR MEASURING REBAR PULL-OUT

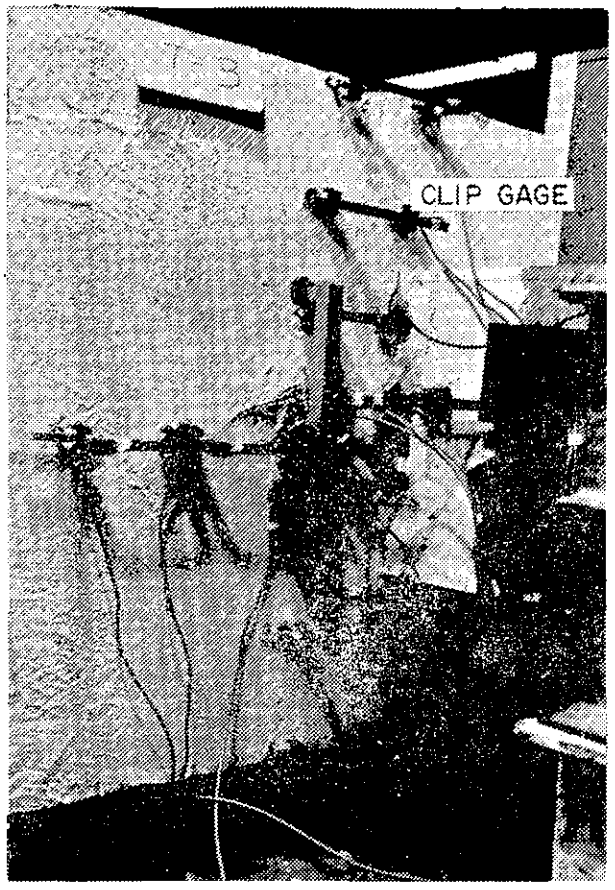

FIG. 3.8 INSTRUMENTATION ON SLAB

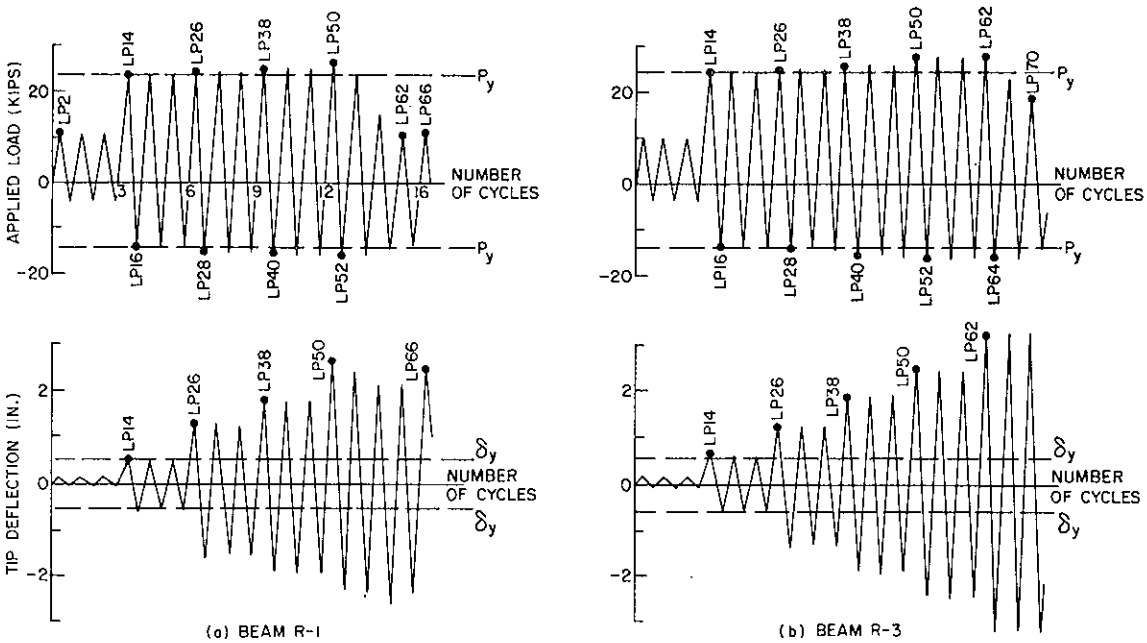

FIG. 3.9 LOADING HISTORIES (BEAMS R-1 AND R-3)

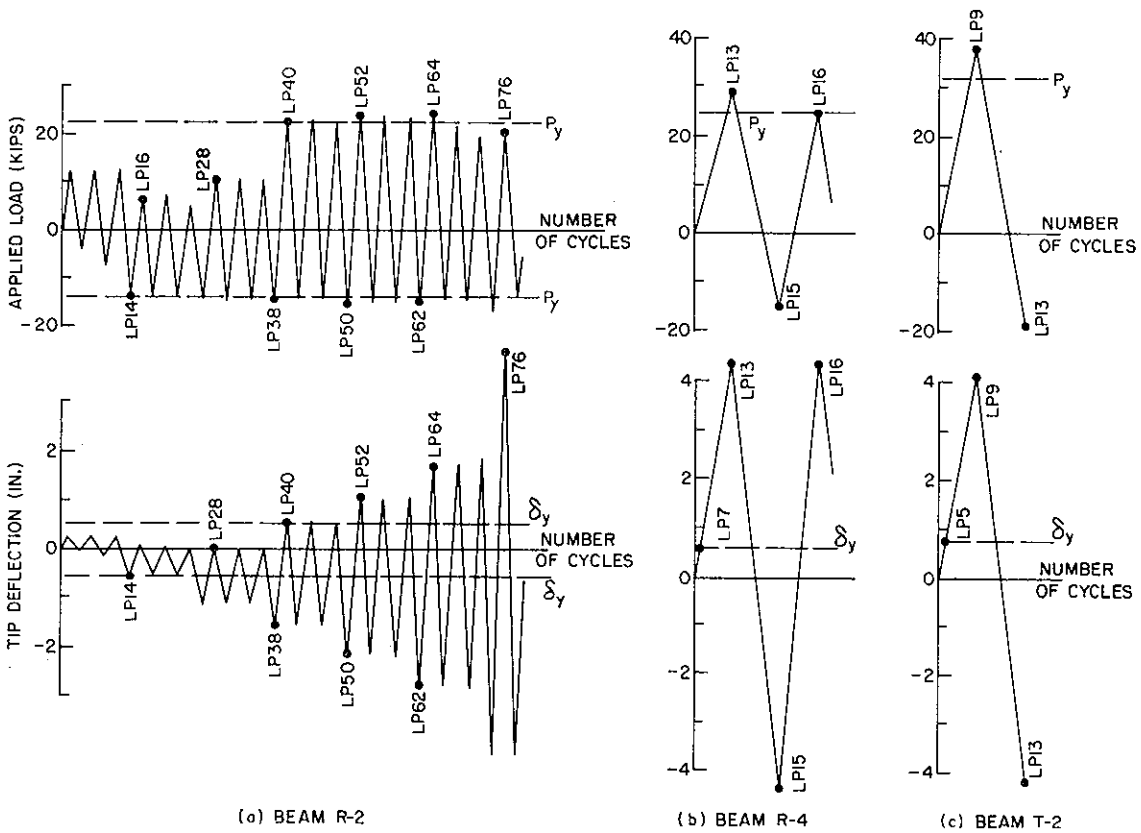

FIG. 3.10 LOADING HISTORIES (BEAMS R-2, R-4 AND T-2)

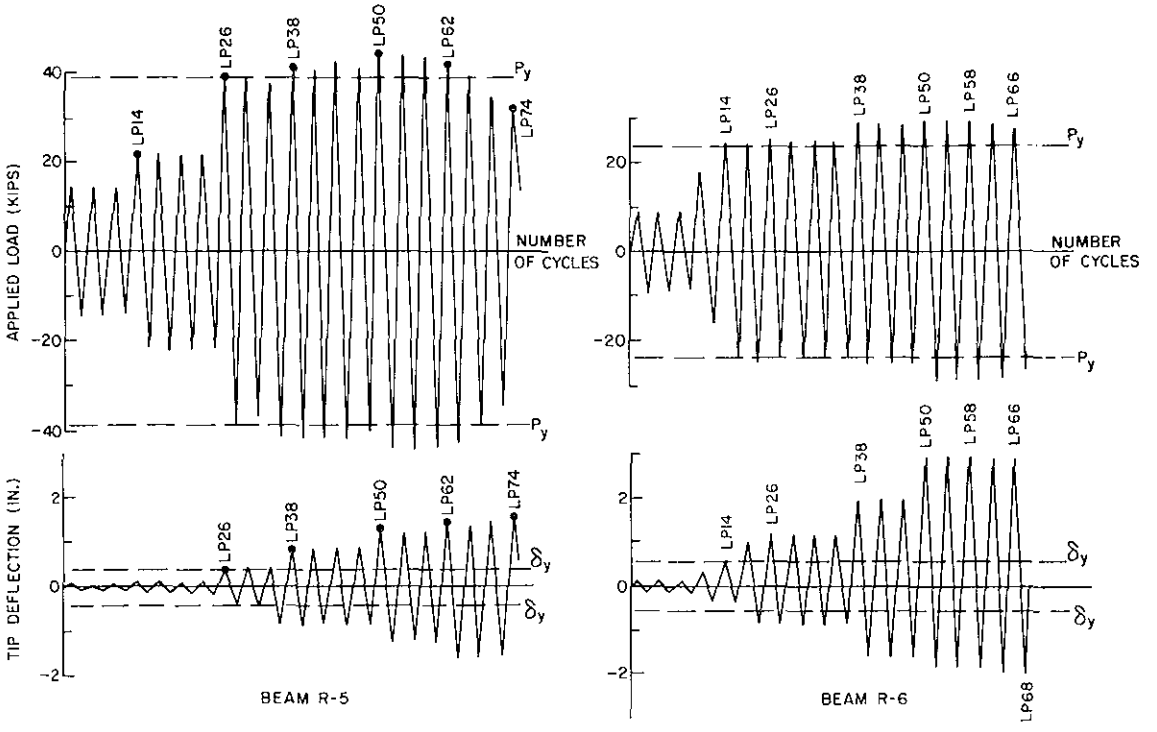

FIG. 3.11 LOADING HISTORIES (BEAMS R-5 AND R-6)

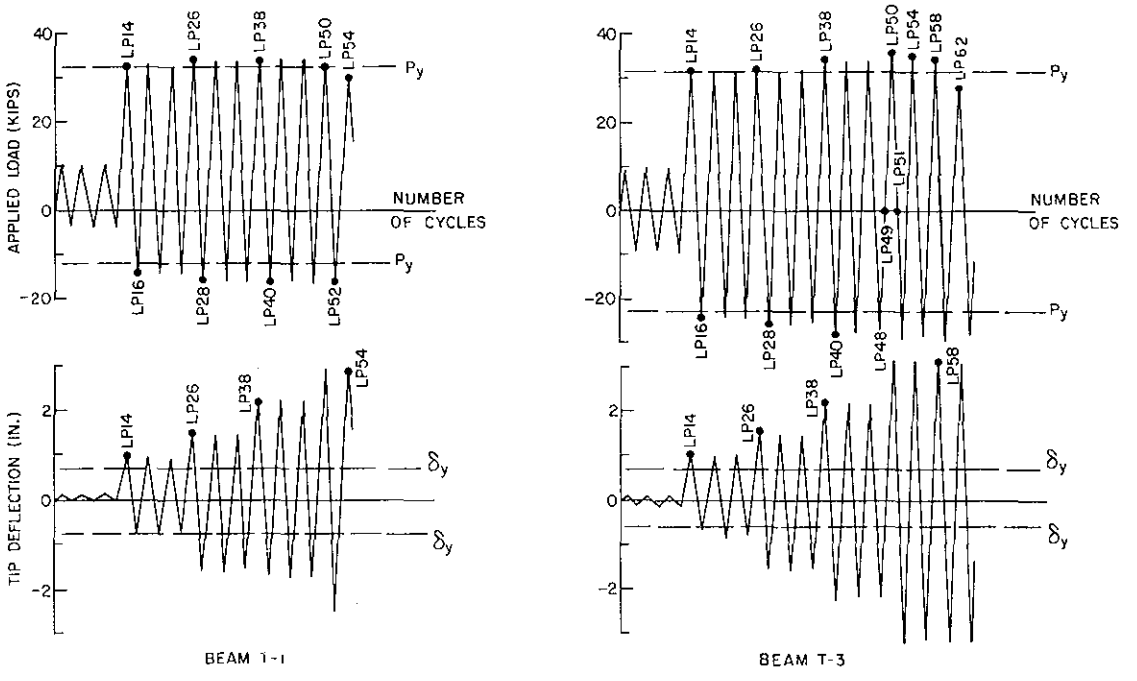

FIG. 3.12 LOADING HISTORIES (BEAMS T-1 AND T-3)

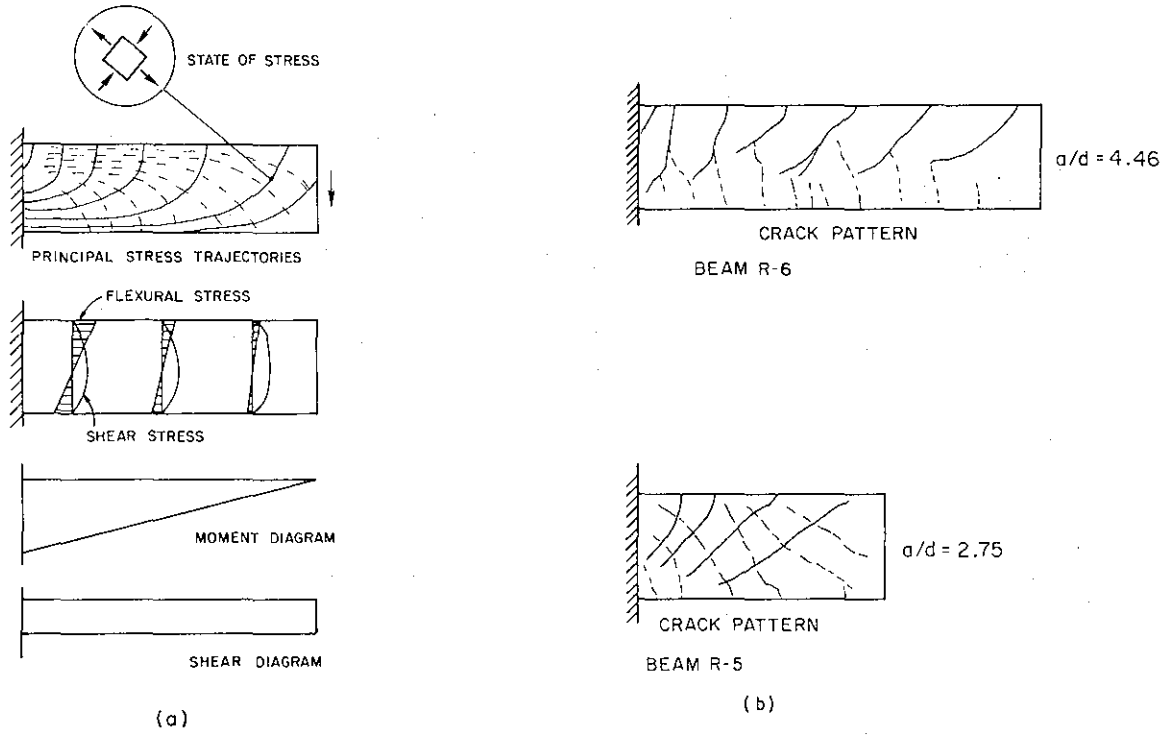

FIG. 4.1 CRACKING IN CONCRETE BEAMS

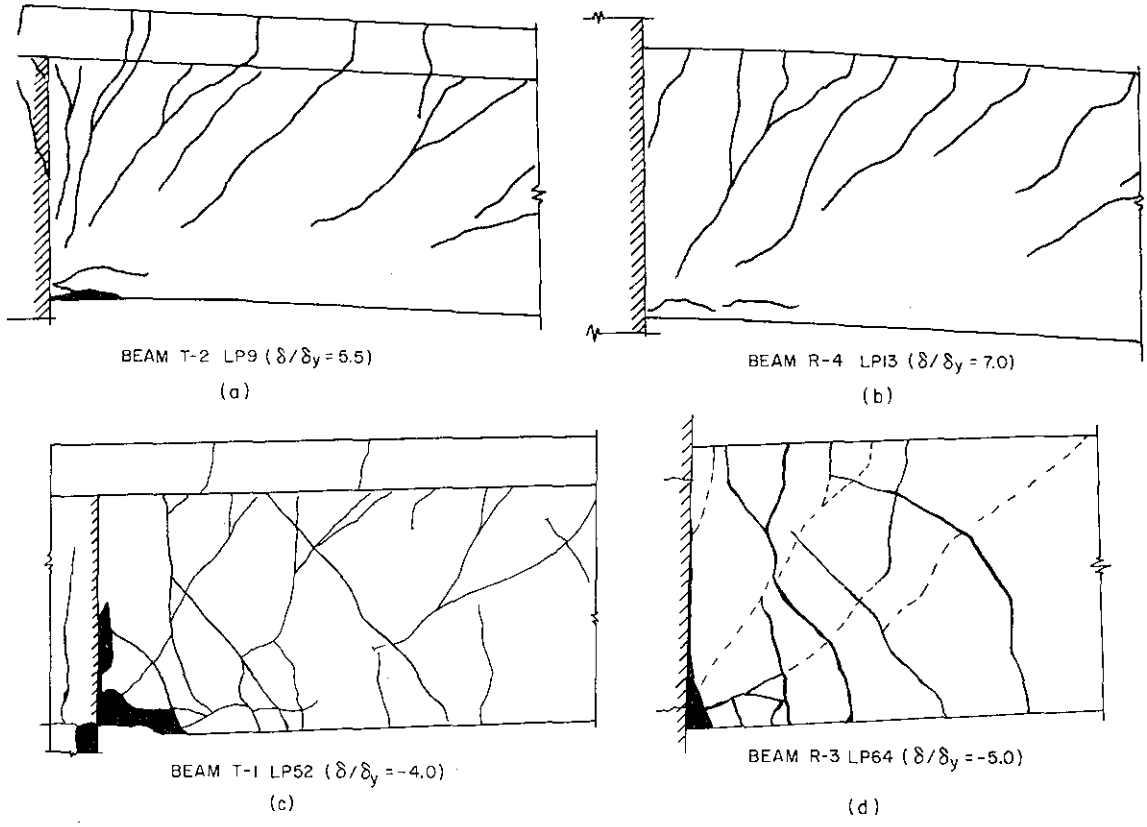

FIG. 4.2 CRACK PATTERNS (BEAMS T-2, R-4, T-1 AND R-3)

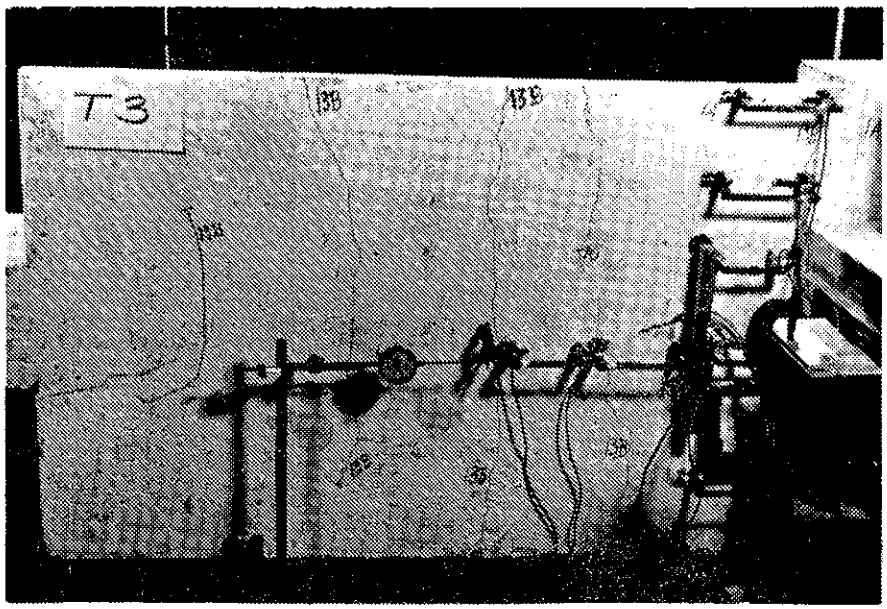

P = 15.7 KIPS

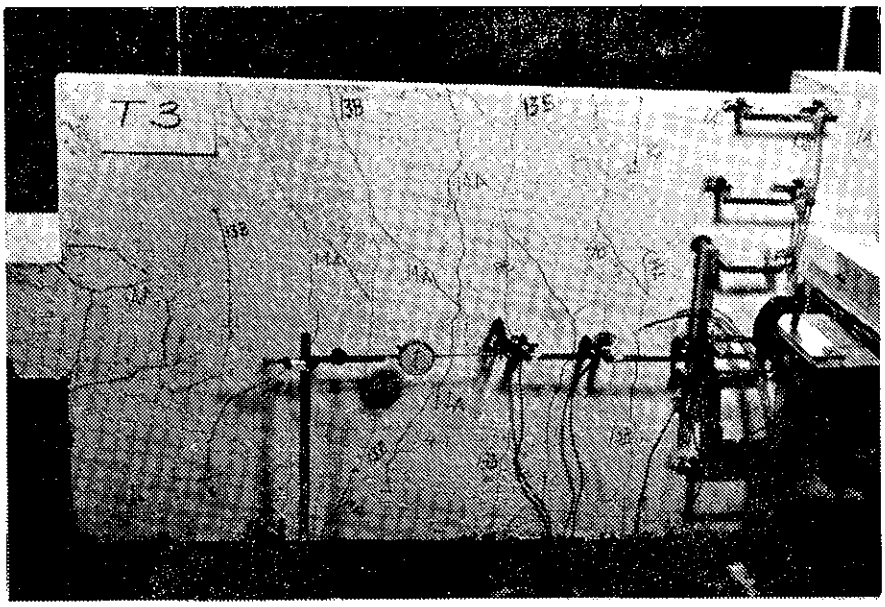

P = 32 KIPS (YIELD LOAD)

FIG. 4.3 CRACK PATTERN ON SLAB (BEAM T-3)

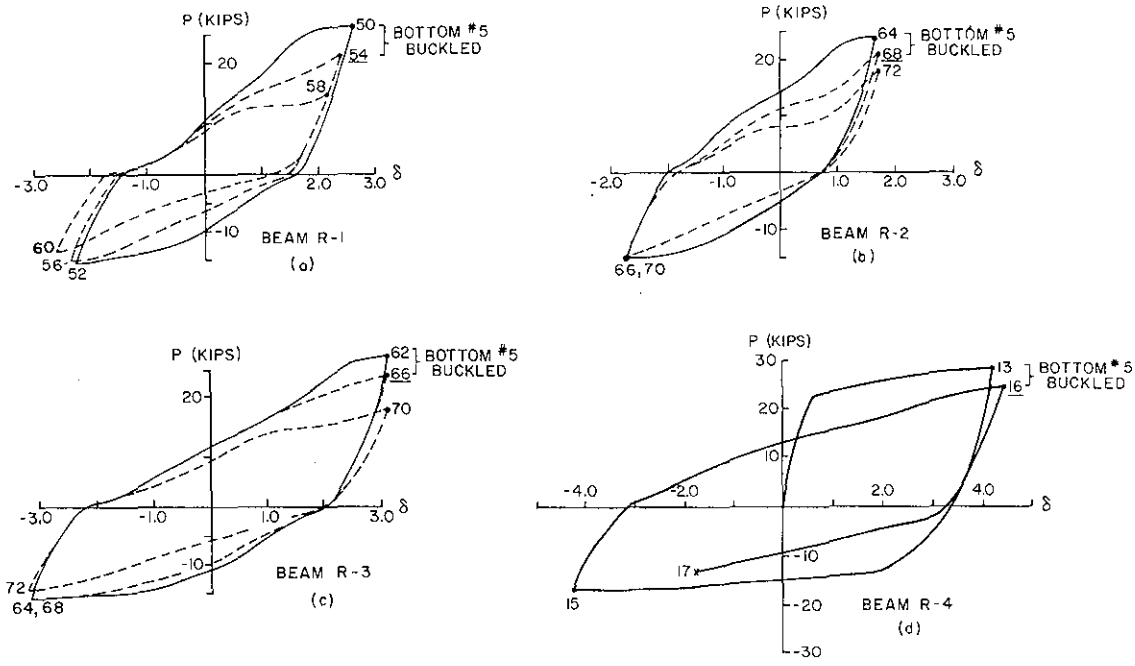

FIG. 4.4 P-δ HYSTERETIC LOOPS NEAR FAILURE (BEAMS R-1 TO R-4)

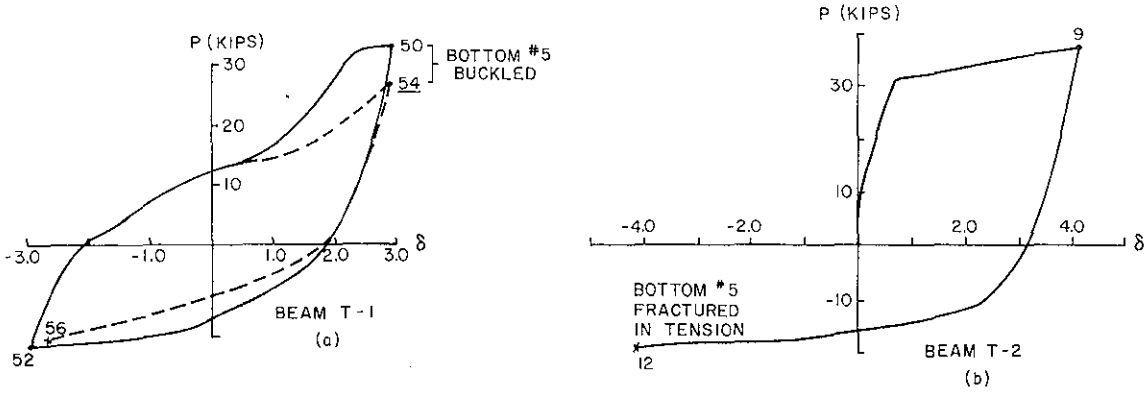

FIG. 4.5 P-δ HYSTERETIC LOOPS NEAR FAILURE (BEAMS T-1 AND T-2)

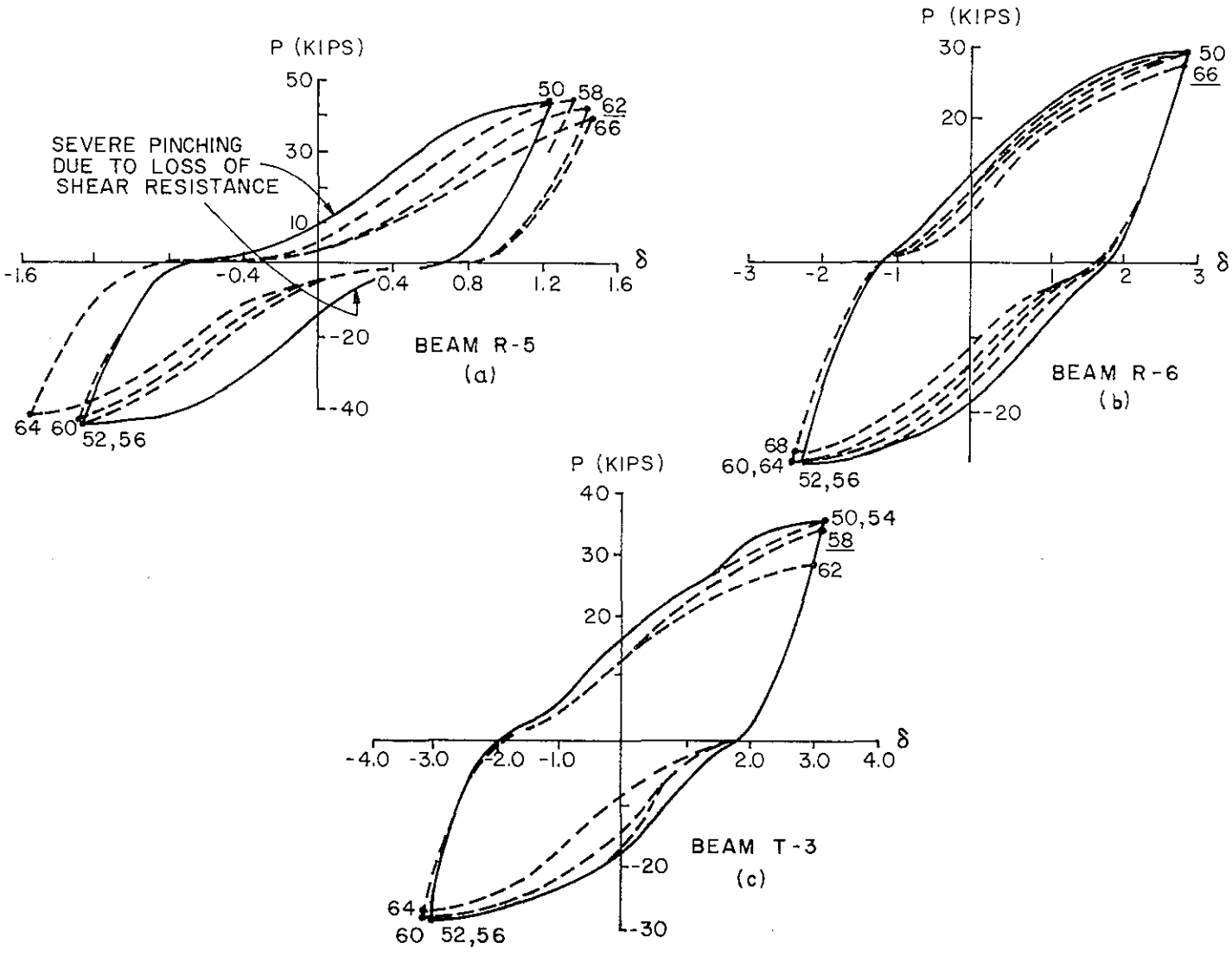

FIG. 4.6 P-δ HYSTERETIC LOOPS NEAR FAILURE (BEAMS R-5, R-6 AND T-3)

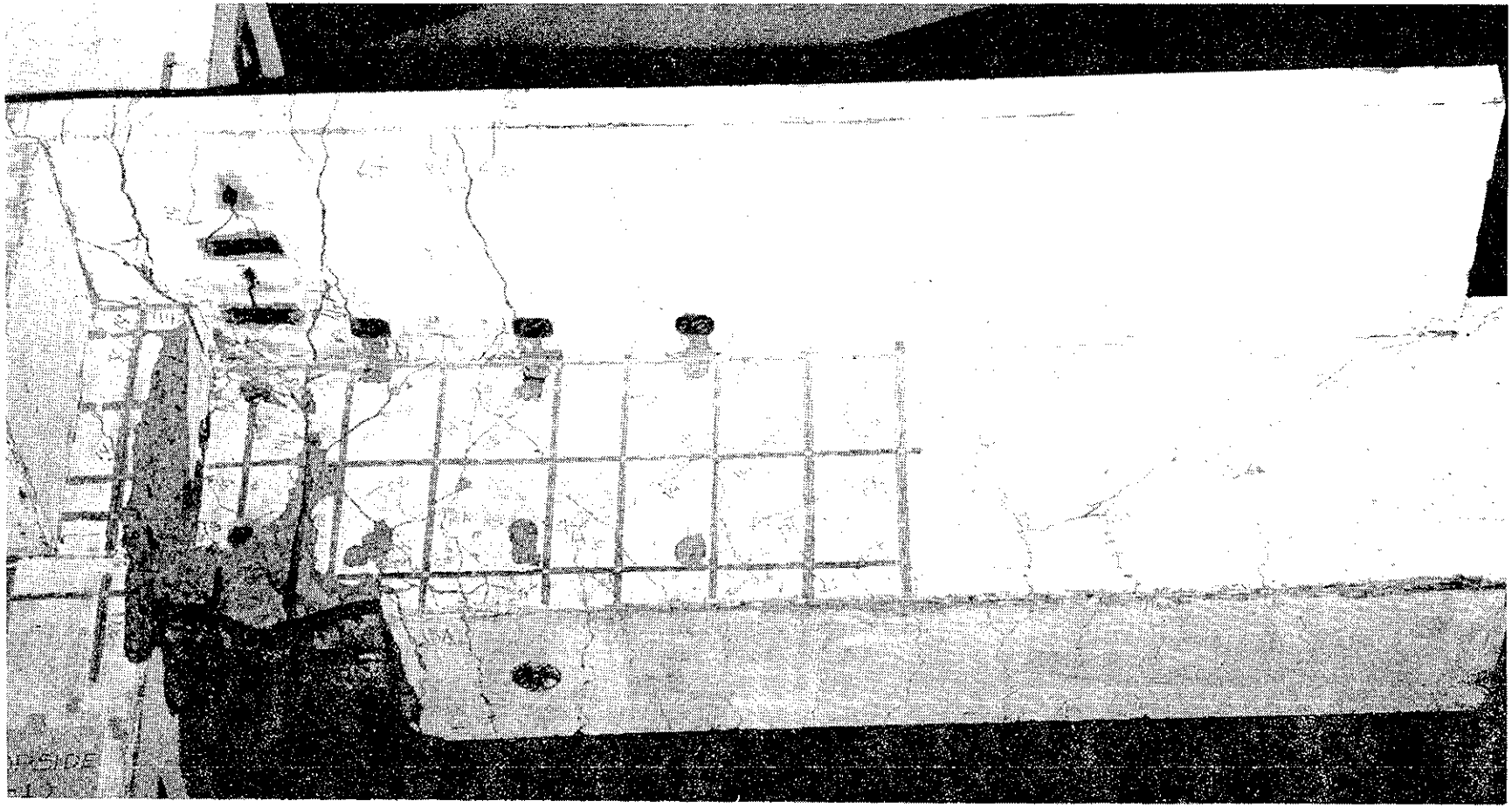

FIG. 4.7 FAILED BEAM (BEAM T-1)

FIG. 4.8(a) BEAM R-5 NEAR FAILURE (LP 62)

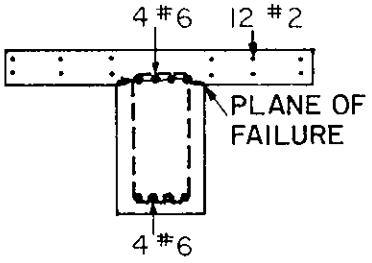

CROSS SECTION
(BEAM T-3)

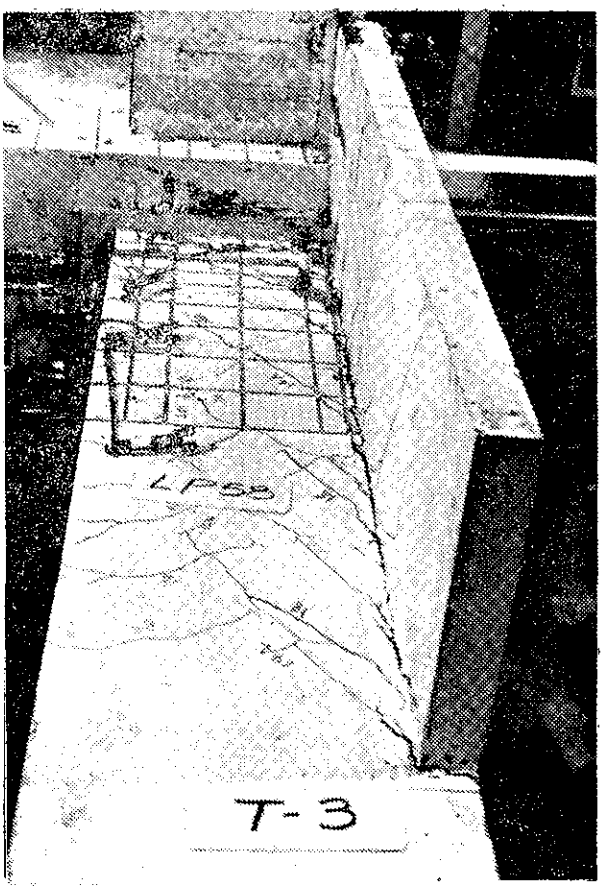

FIG. 4.8(b) BEAM T-3 NEAR FAILURE (LP 58)

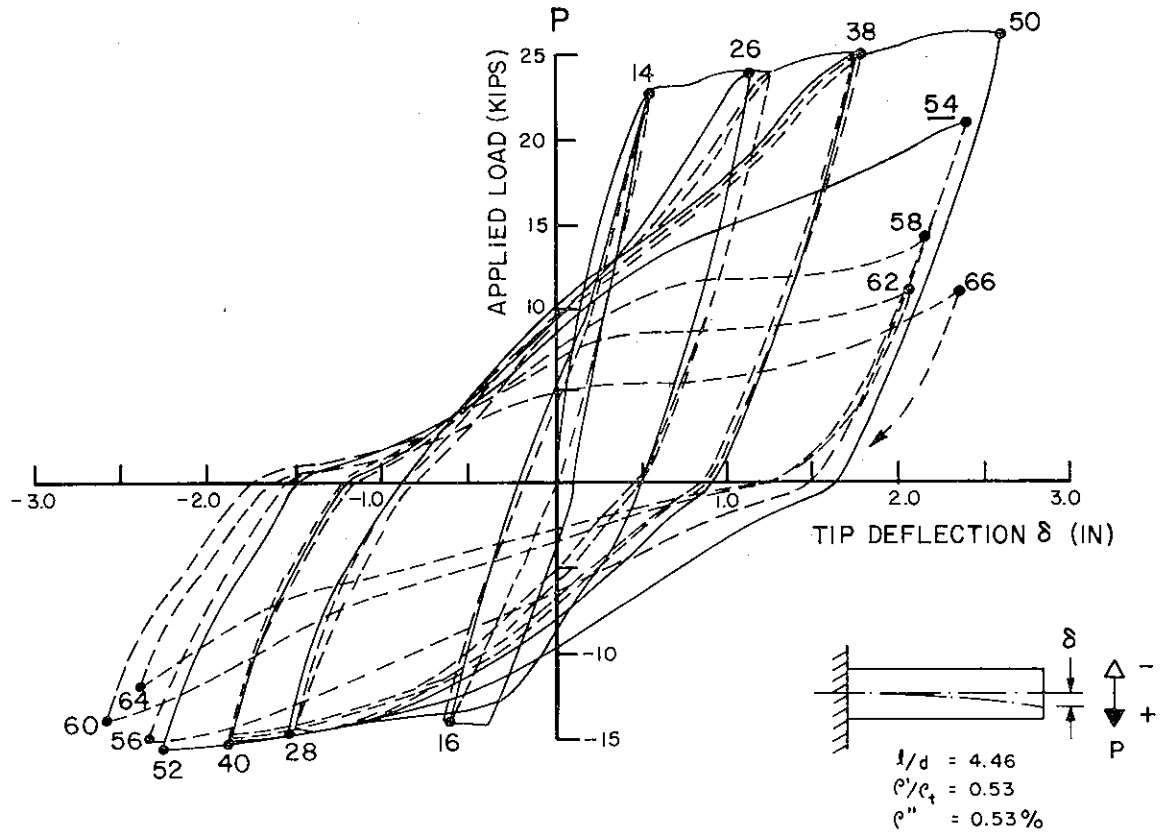

FIG. 4.9(a) P-δ DIAGRAM (BEAM R-1)

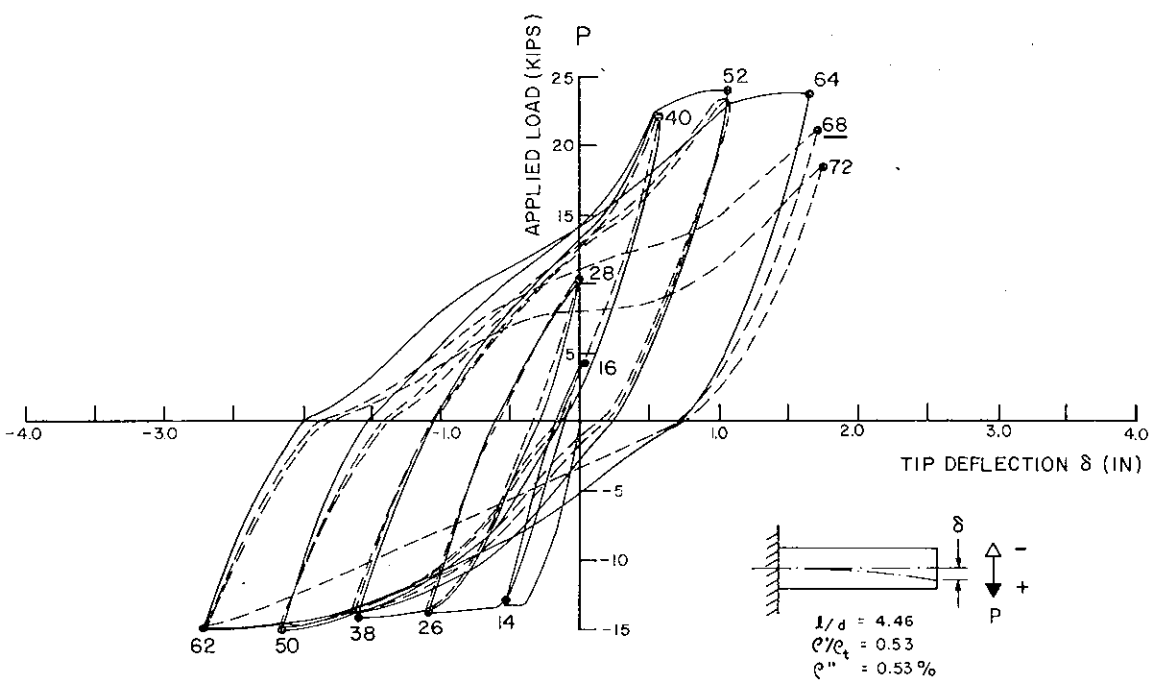

FIG. 4.9(b) P-δ DIAGRAM (BEAM R-2)

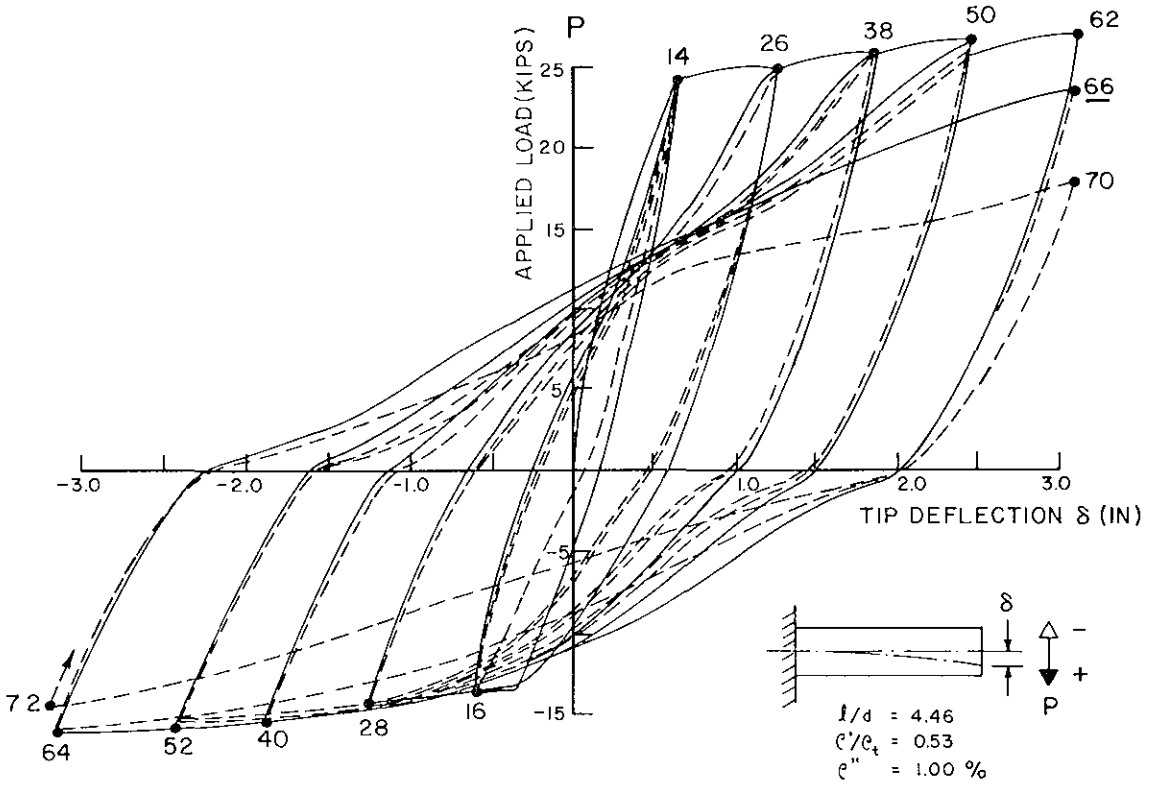

FIG. 4.9(c) P-δ DIAGRAM (BEAM R-3)

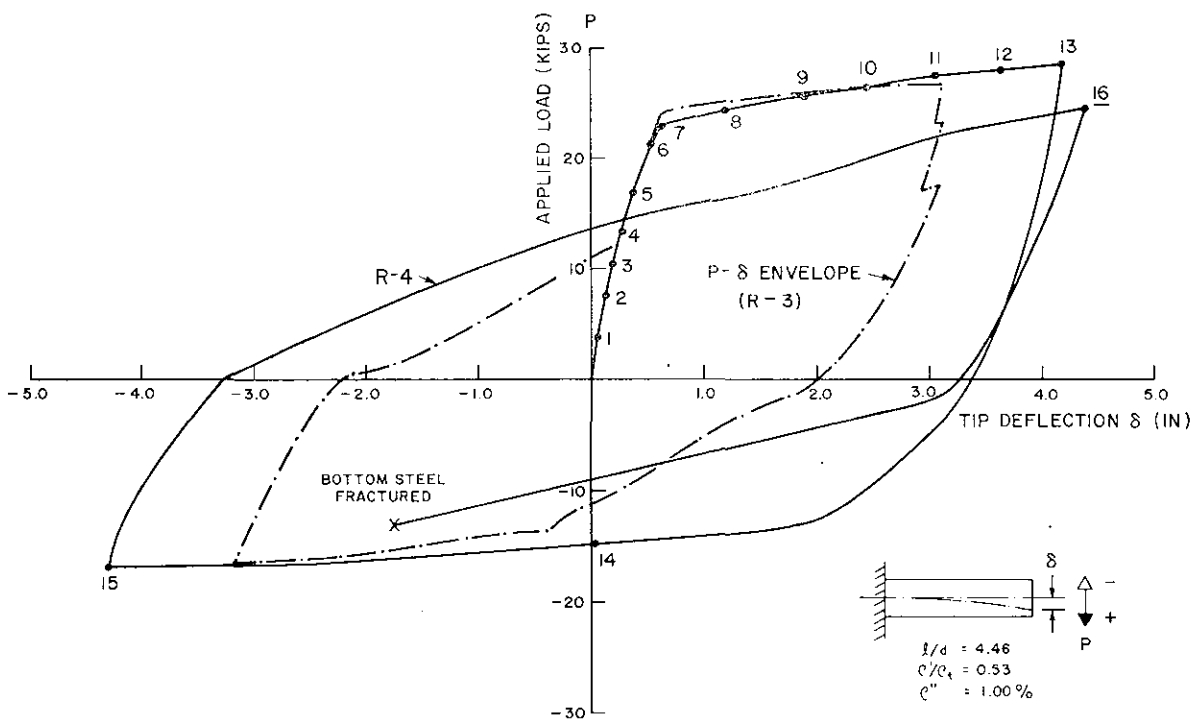

FIG. 4.9(d) P-δ DIAGRAM (BEAM R-4)

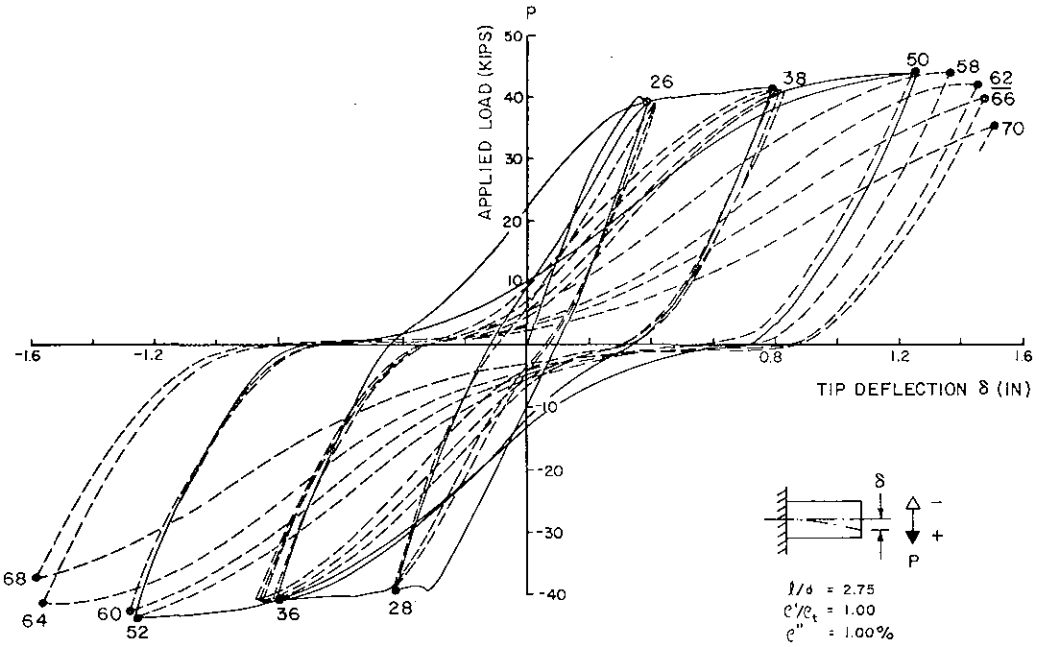

FIG. 4.9(e) P-δ DIAGRAM (BEAM R-5)

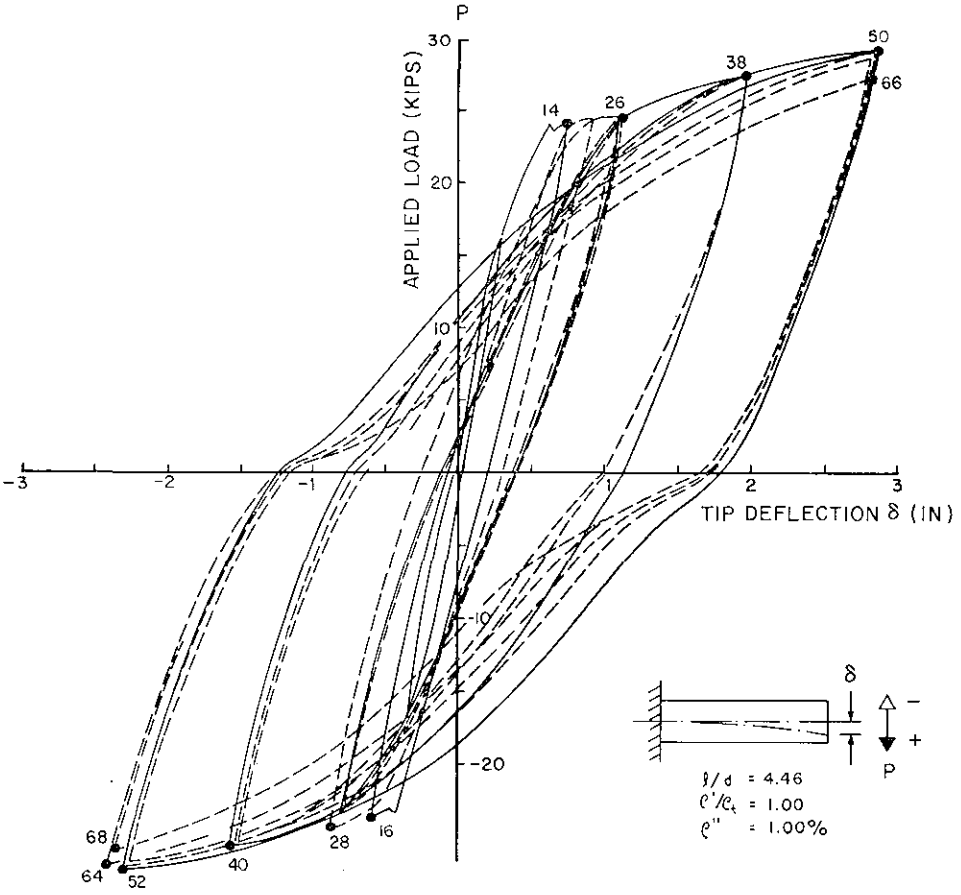

FIG. 4.9(f) P-δ DIAGRAM (BEAM R-6)

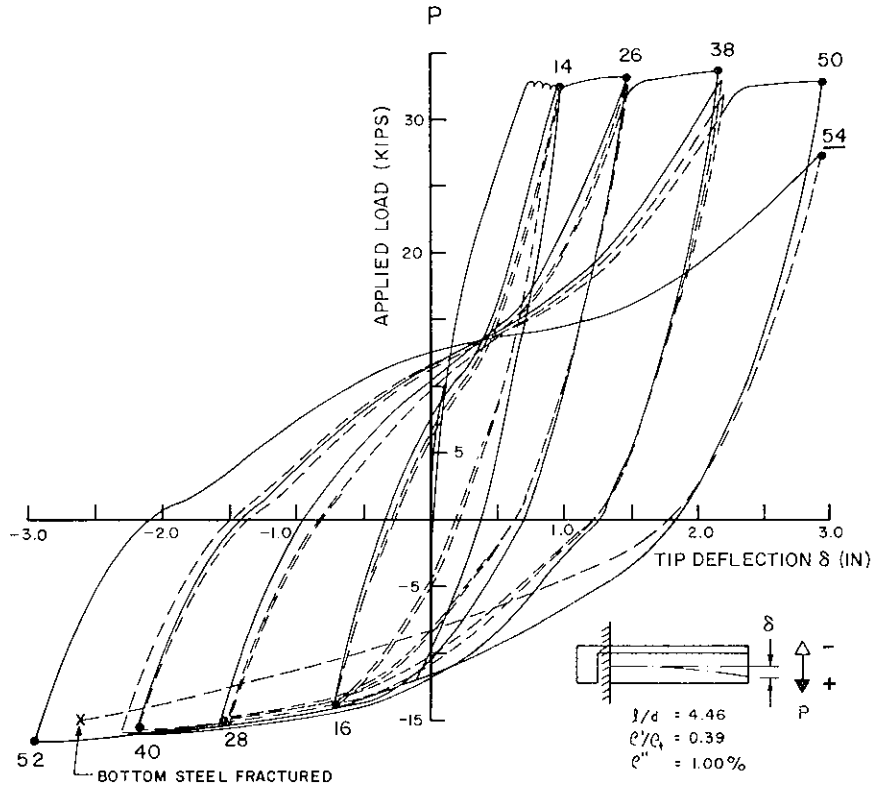

FIG. 4.9(g) P-δ DIAGRAM (BEAM T-1)

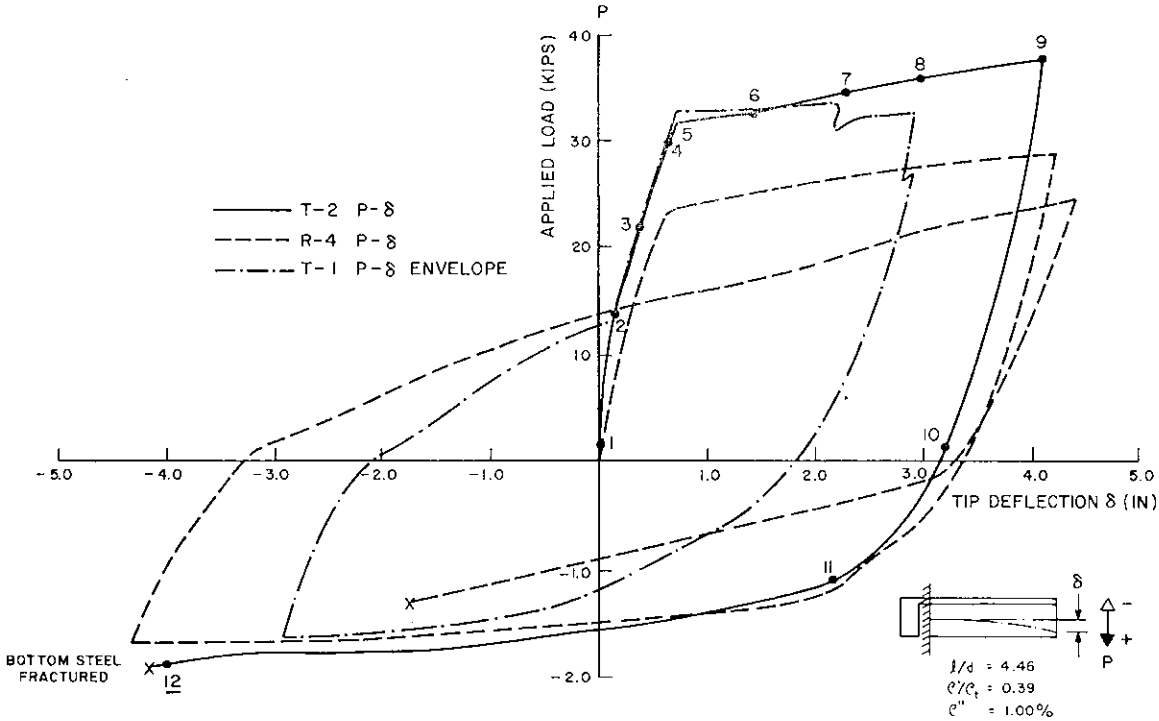

FIG. 4.9(h) P-δ DIAGRAM (BEAM T-2)

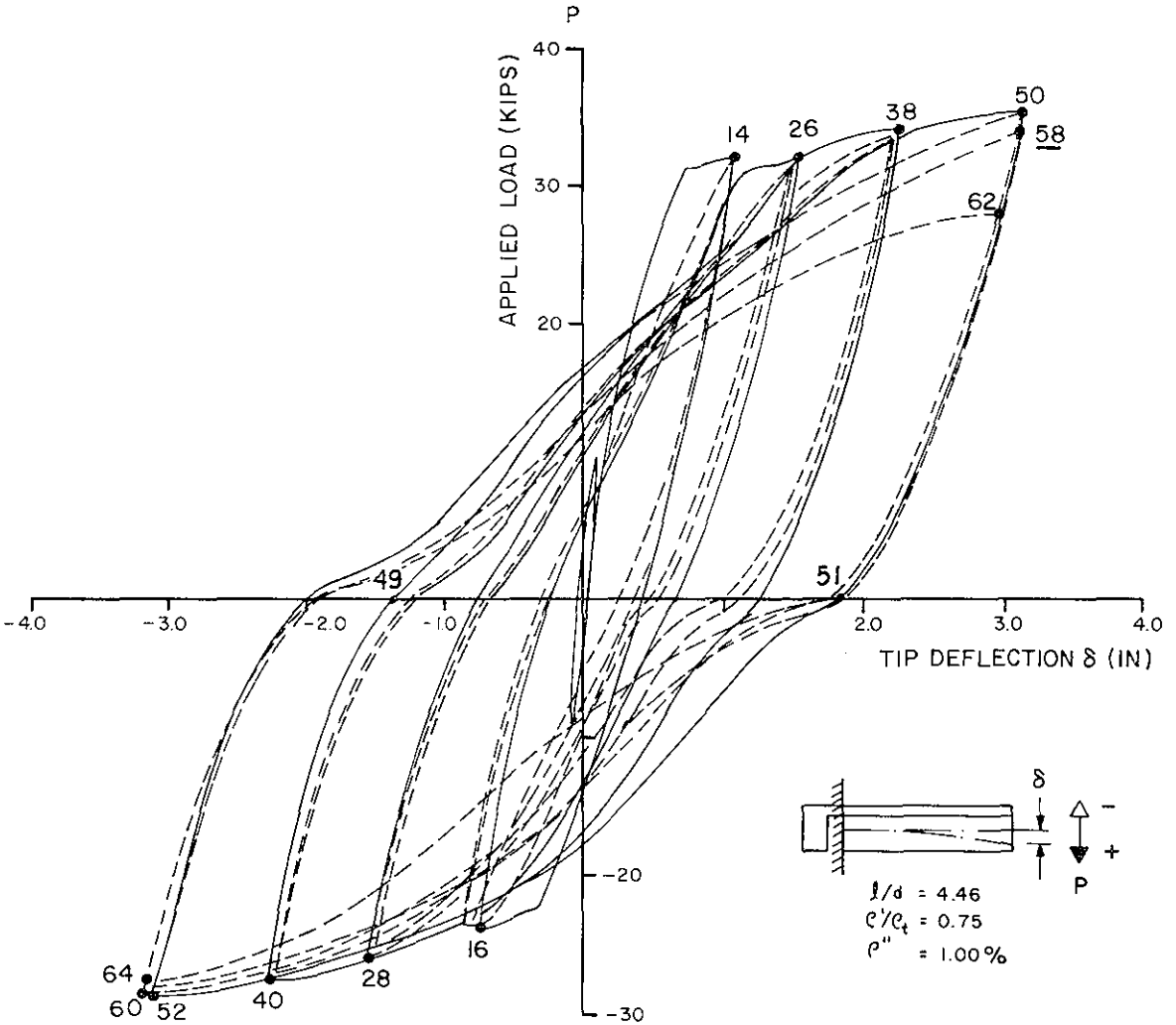

FIG. 4.9(i) P-δ DIAGRAM (BEAM T-3)

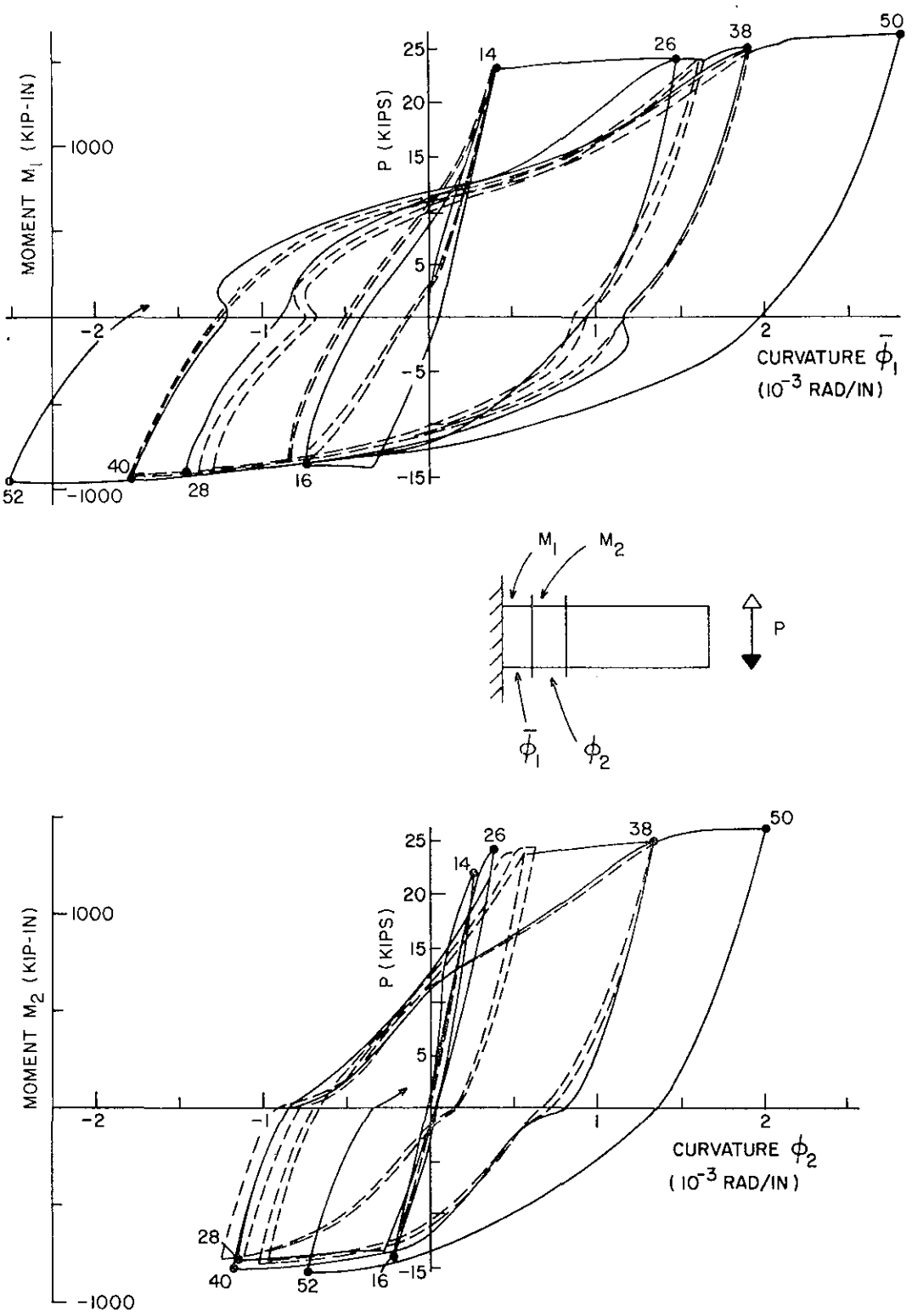

FIG. 4.10(a) M-ϕ DIAGRAMS (BEAM R-1)

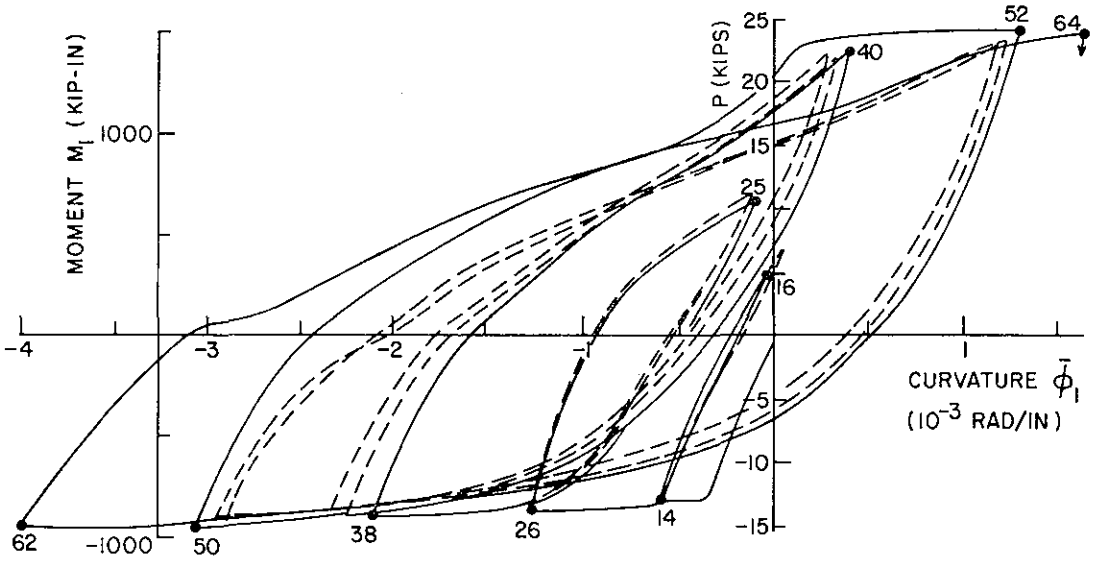

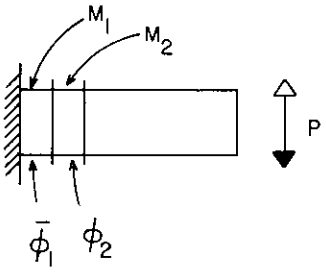

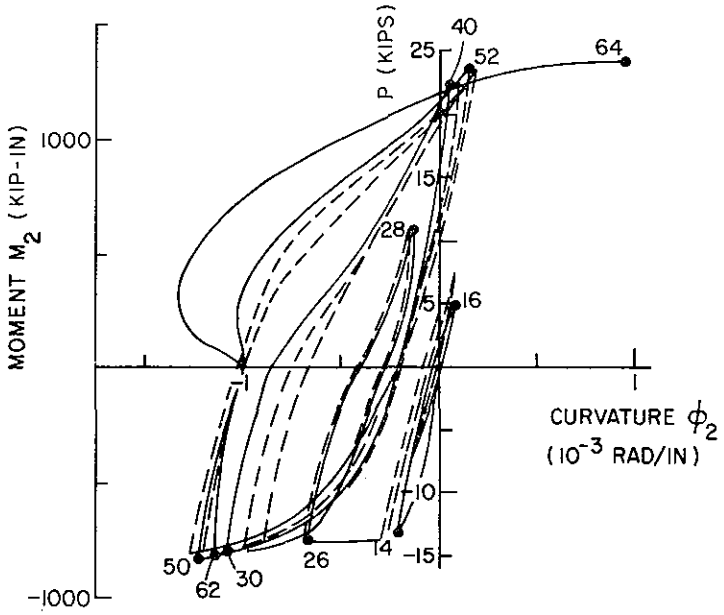

FIG. 4.10(b) M-ϕ DIAGRAMS (BEAM R-2)

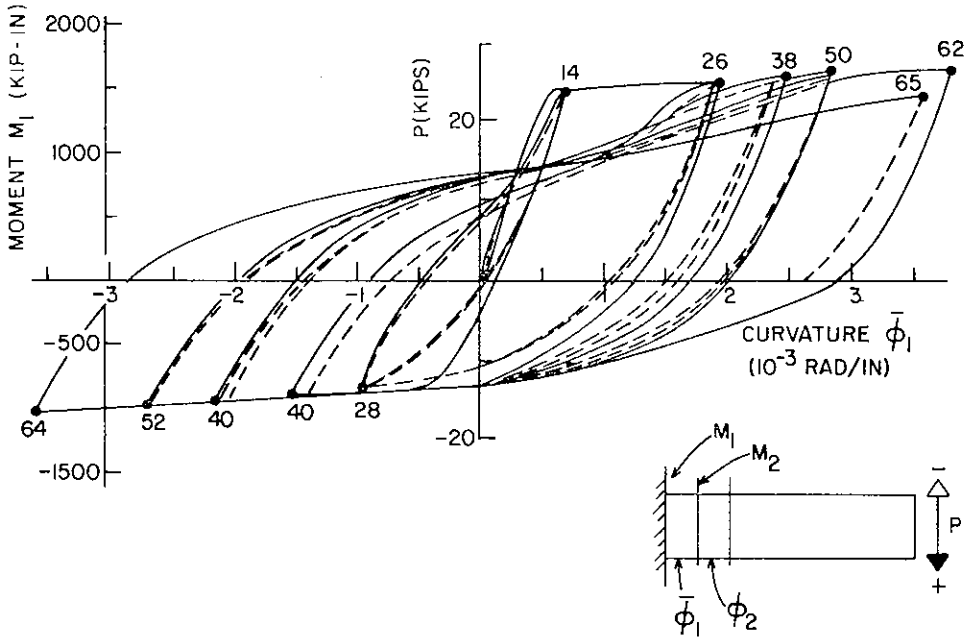

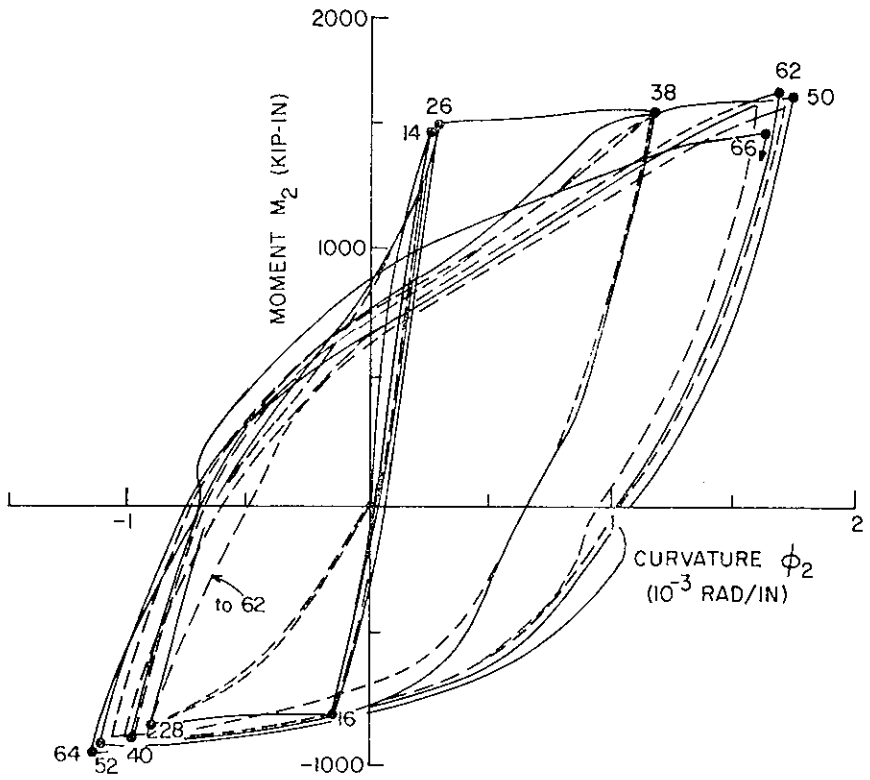

FIG. 4.10(c) M-ϕ DIAGRAMS (BEAM R-3)

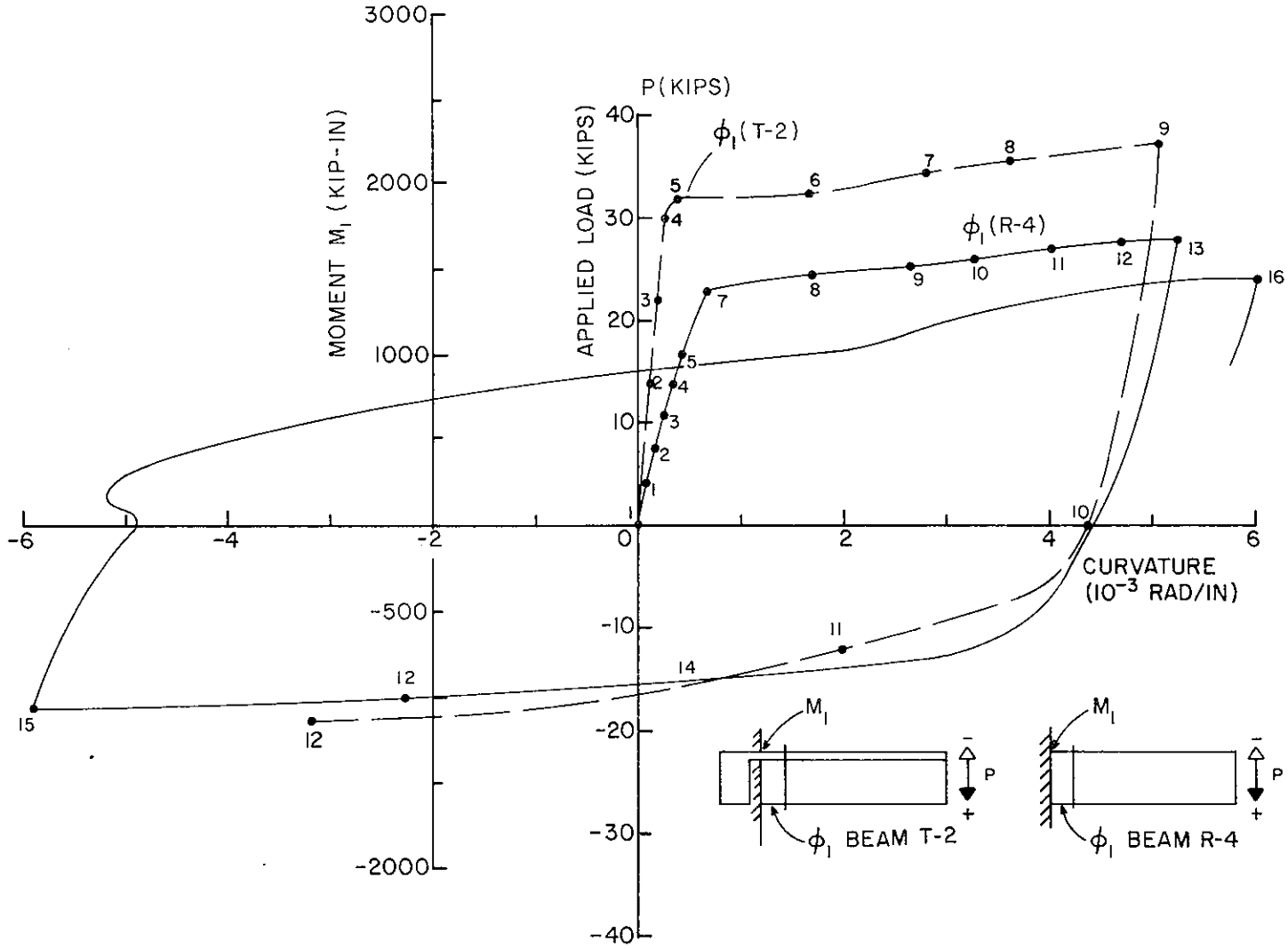

FIG. 4.10(d) M-ϕ DIAGRAM (BEAMS R-4 AND T-2)

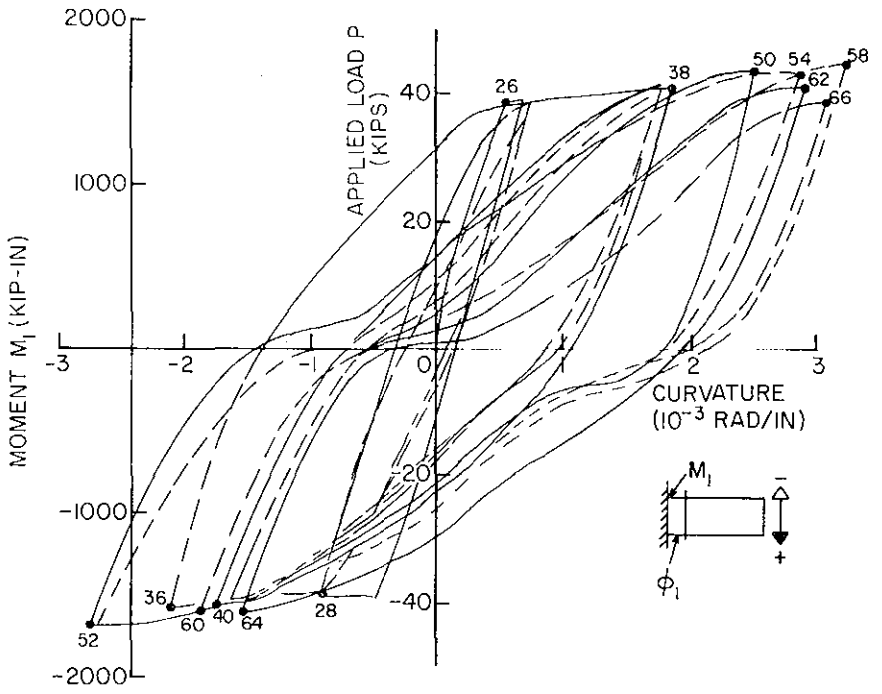

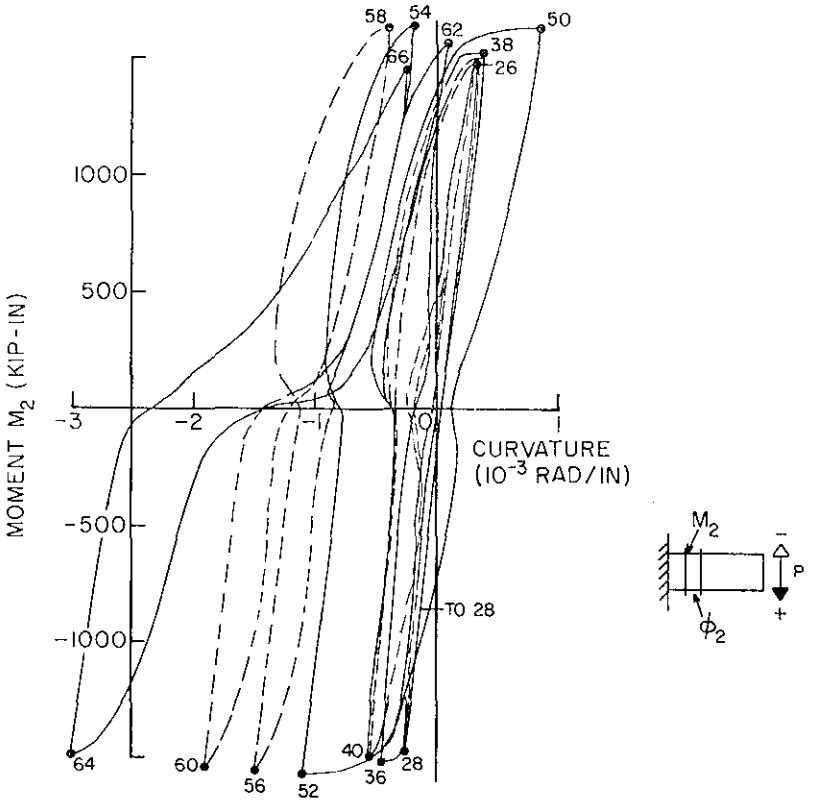

FIG. 4.10(e) M-ϕ DIAGRAMS (BEAM R-5)

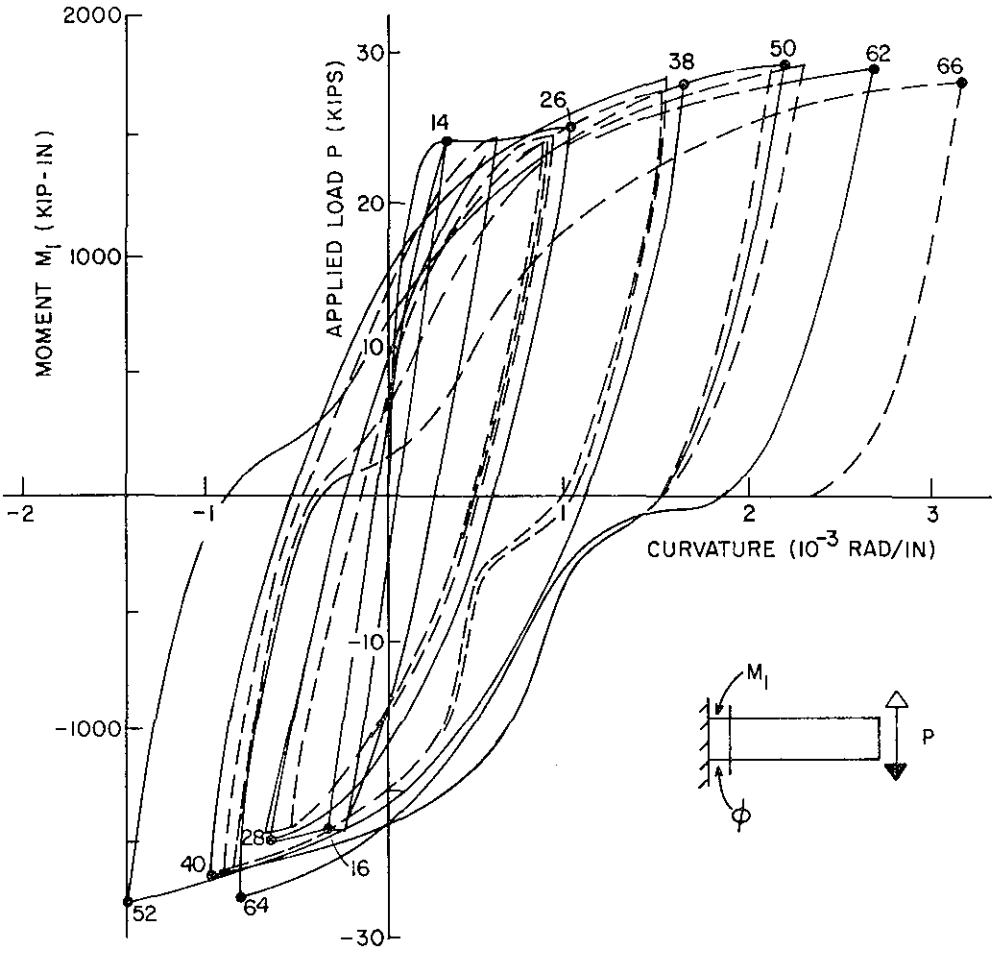

FIG. 4.10(f) M-ϕ DIAGRAMS (BEAM R-6)

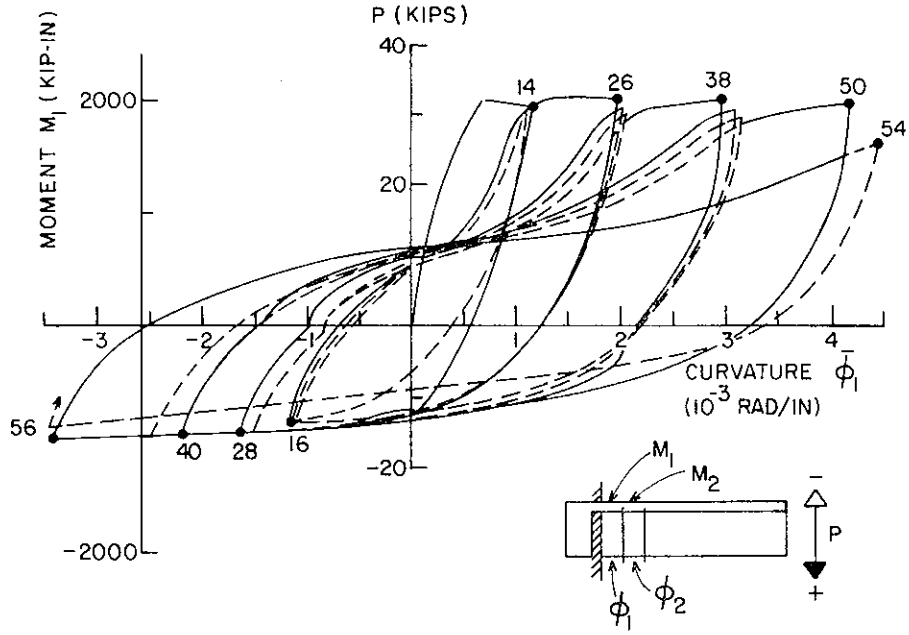

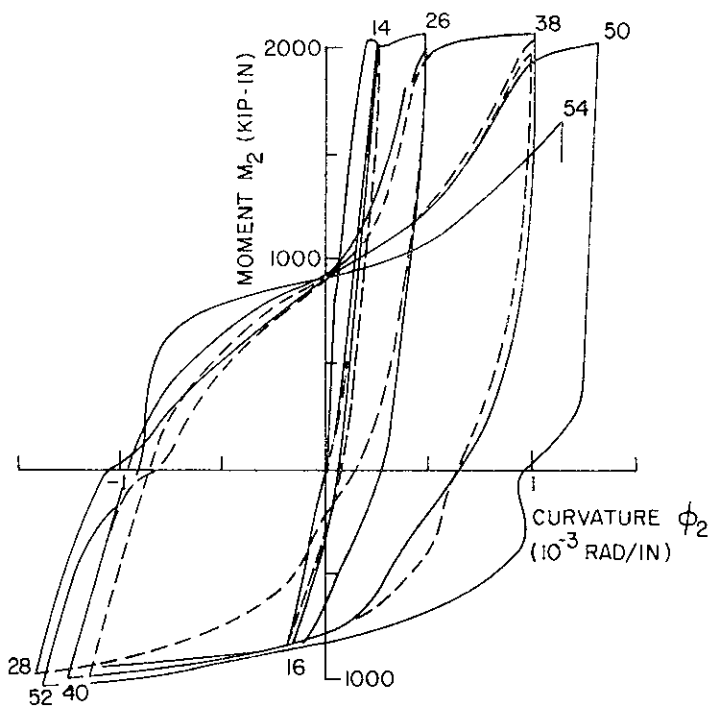

FIG. 4.10(g) M-ϕ DIAGRAMS (BEAM T-1)

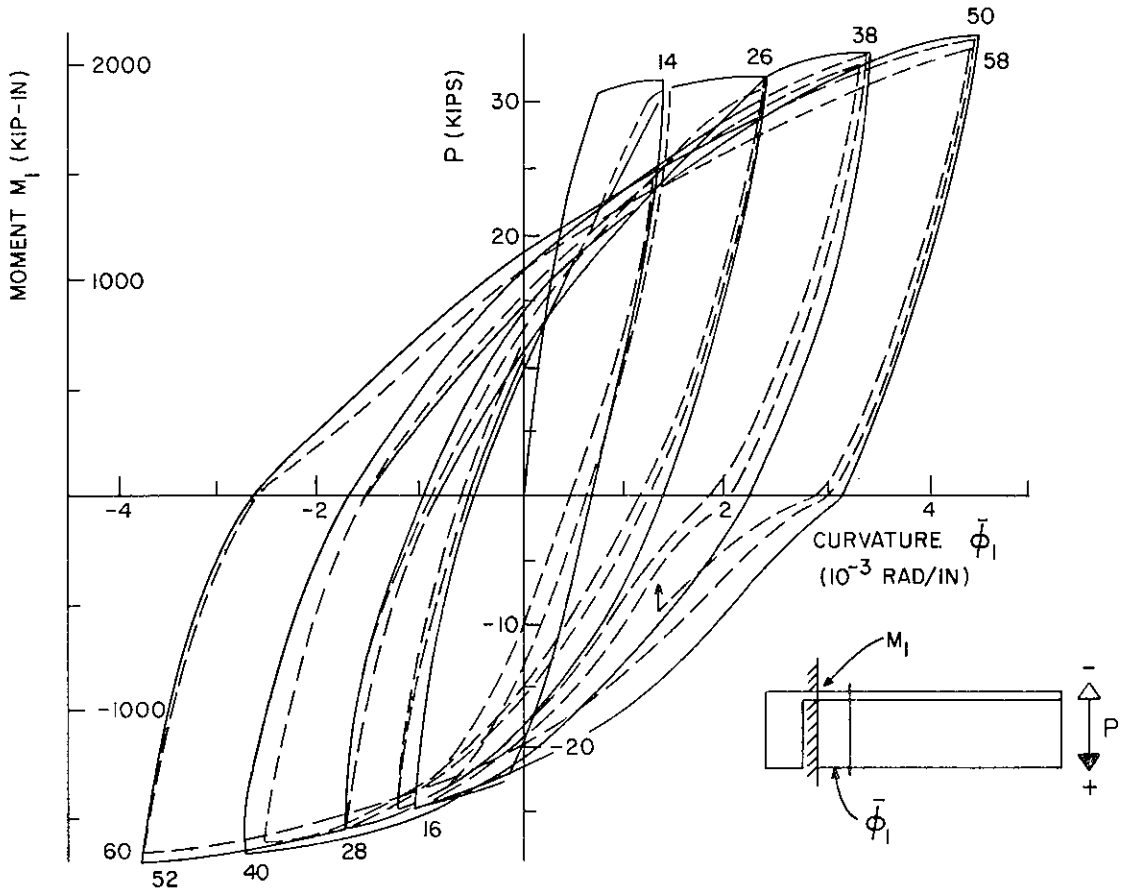

FIG. 4.10(h) M-ϕ DIAGRAM (BEAM T-3)

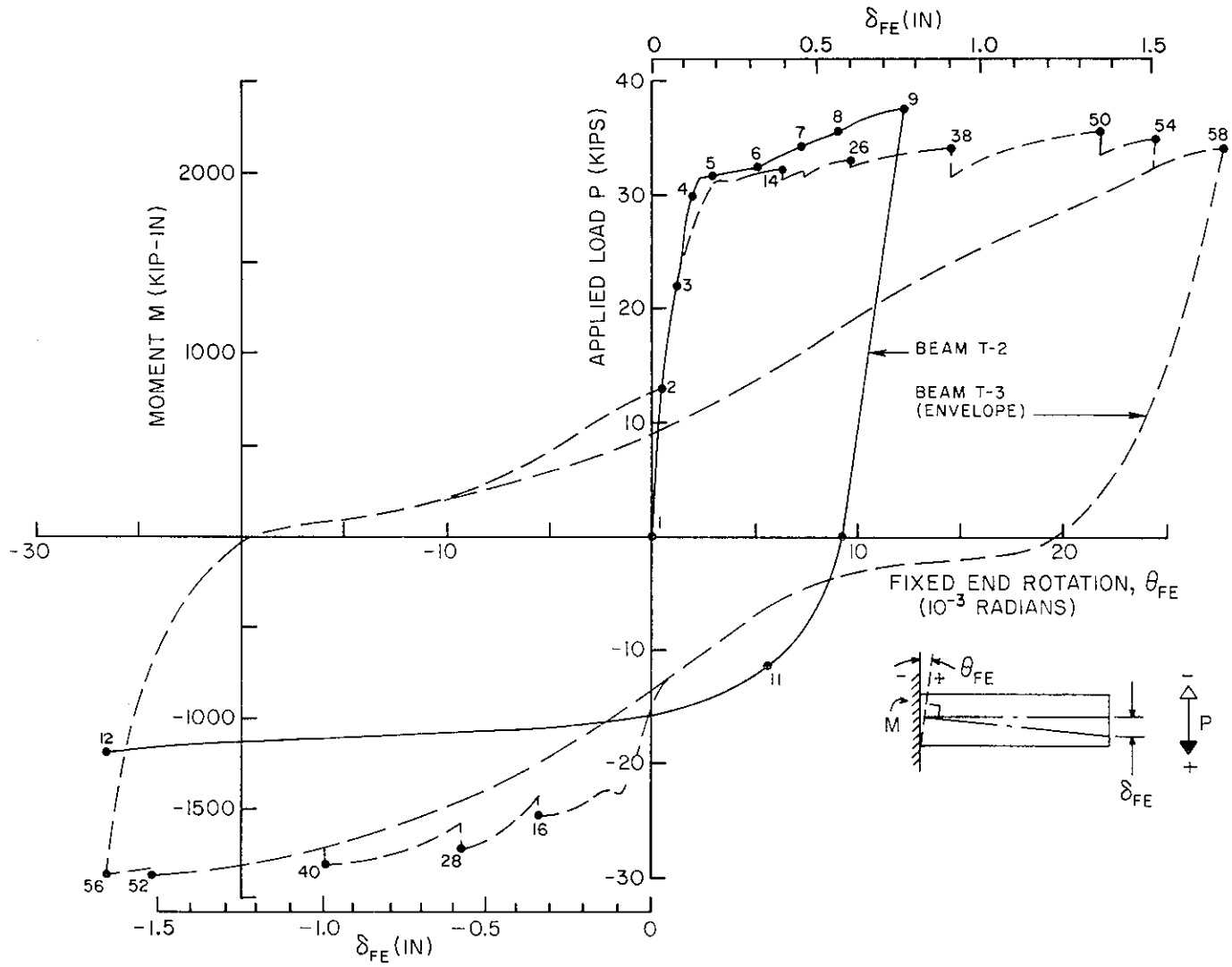

FIG. 4.11(a) M-θ_{FE} DIAGRAM (BEAM T-2)

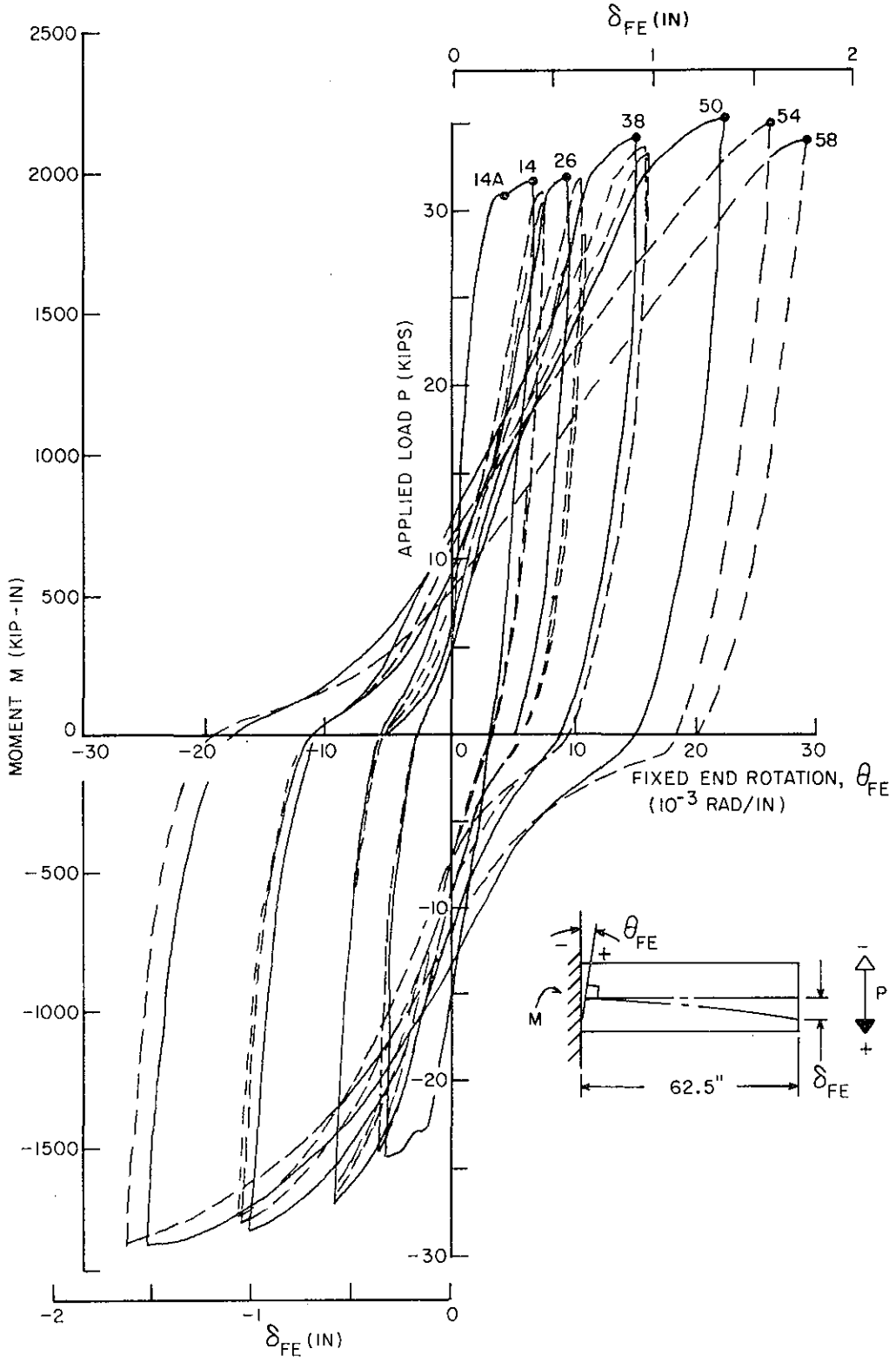

FIG. 4.11(b) M-θ_{FE} DIAGRAM (BEAM T-3)

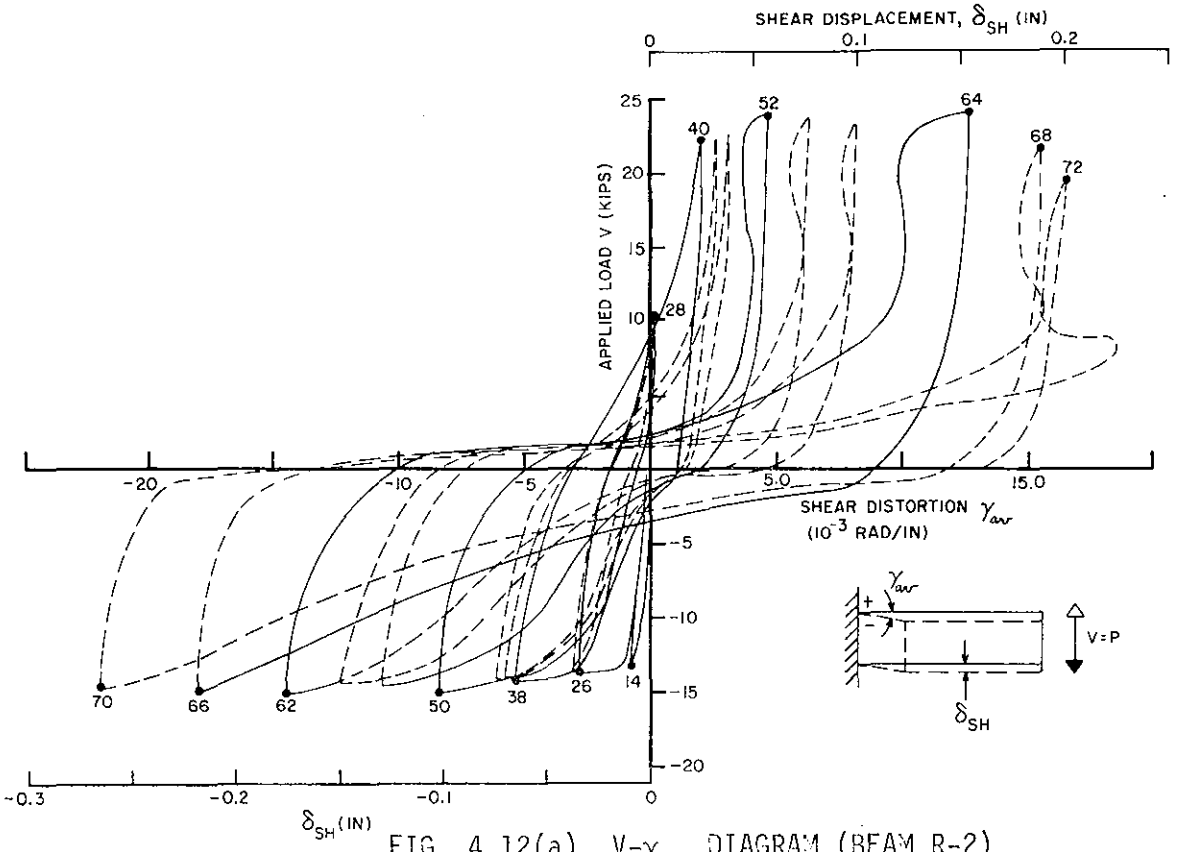

FIG. 4.12(a) V-γ_{av} DIAGRAM (BEAM R-2)

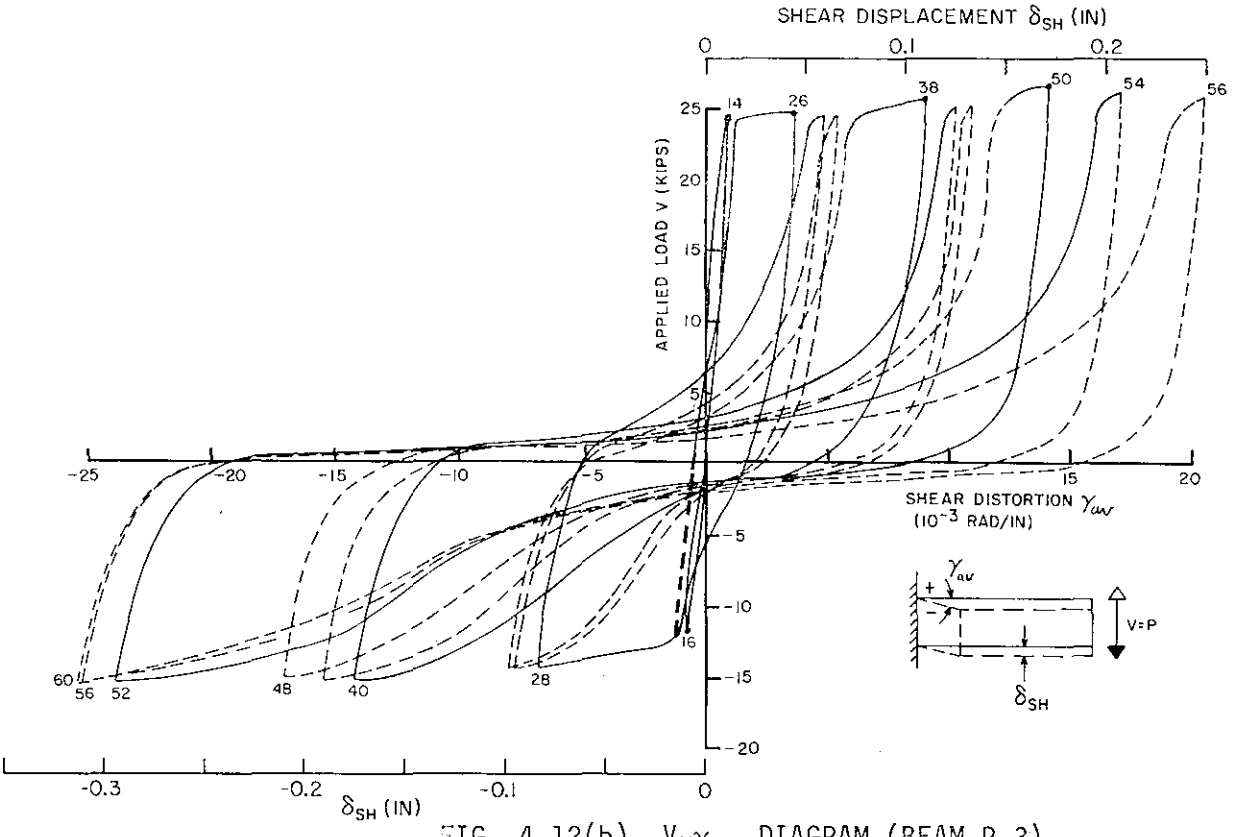

FIG. 4.12(b) V-γ_{av} DIAGRAM (BEAM R-3)

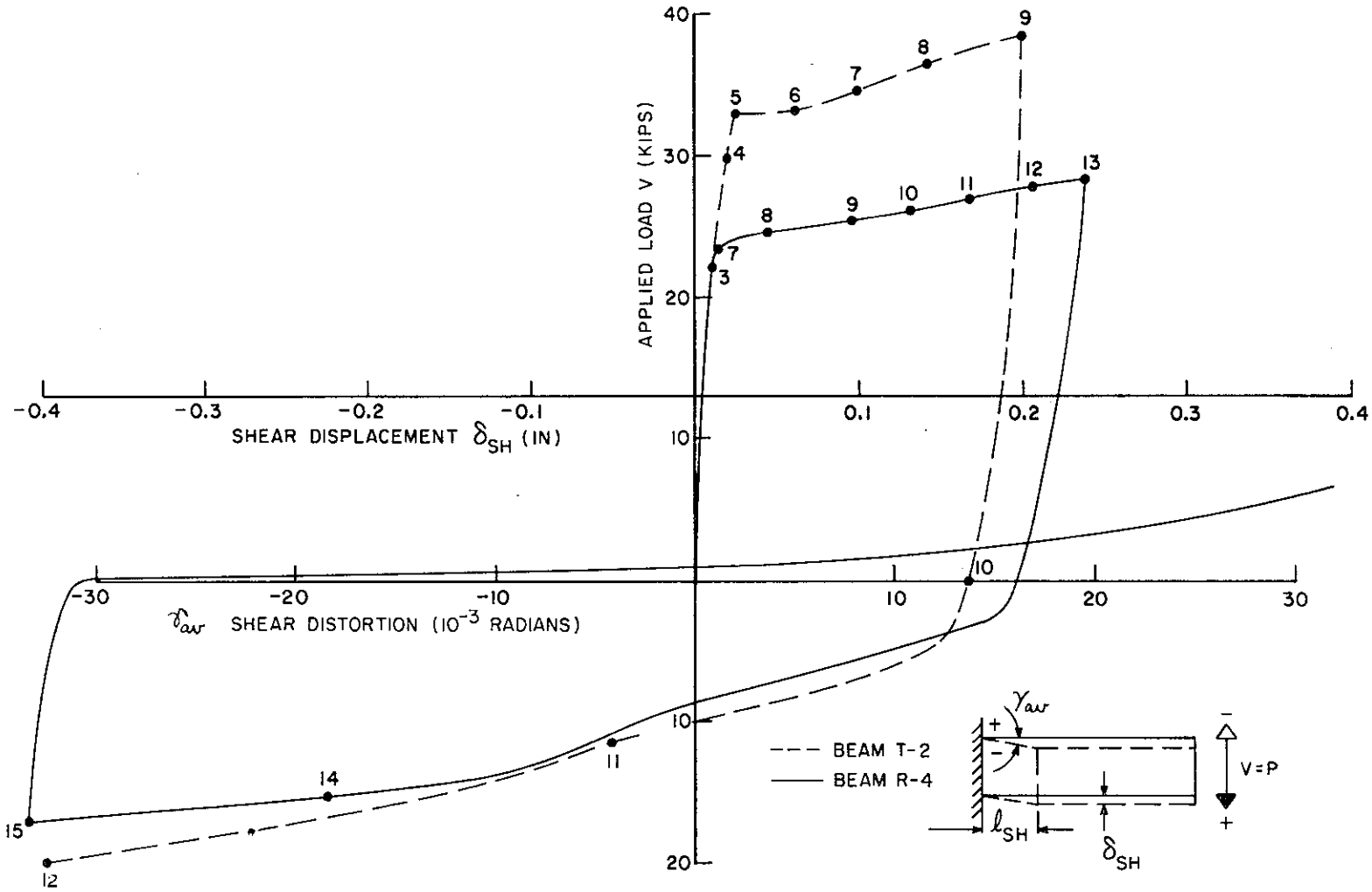

FIG. 4.12(c) V-γ_{av} DIAGRAM (BEAMS R-4 AND T-2)

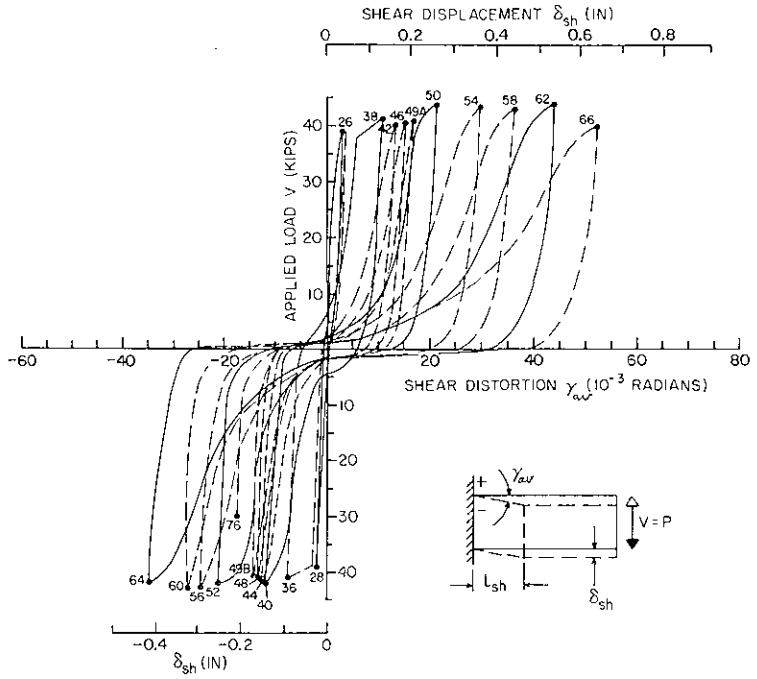

FIG. 4.12(d) V-γ_{av} DIAGRAM (BEAM R-5)

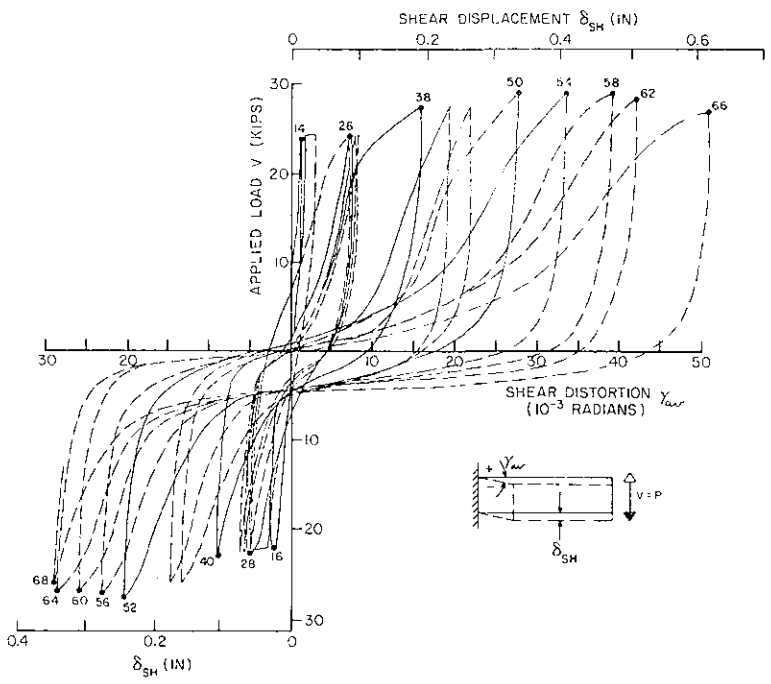

FIG. 4.12(e) V-γ_{av} DIAGRAM (BEAM R-6)

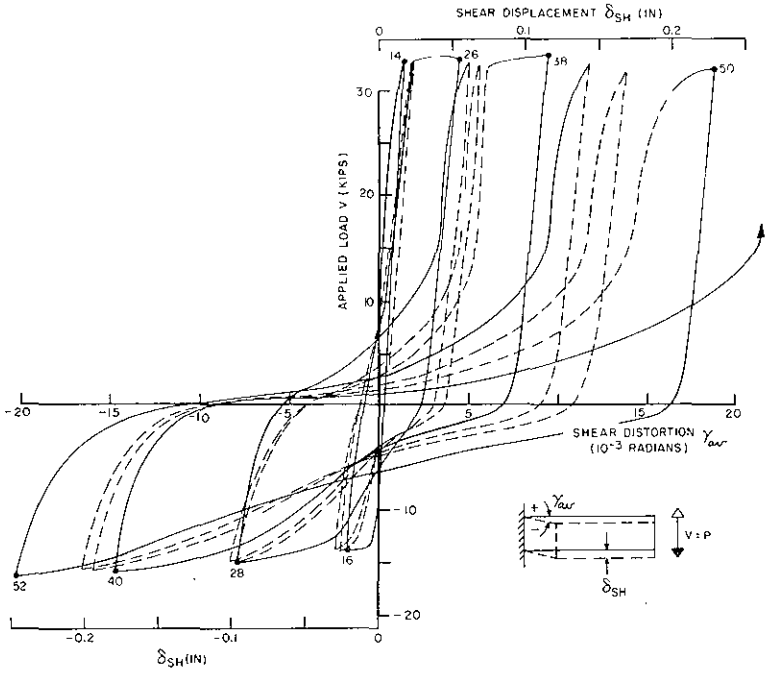

FIG. 4.12(f) V-γ_{av} DIAGRAM (BEAM T-1)

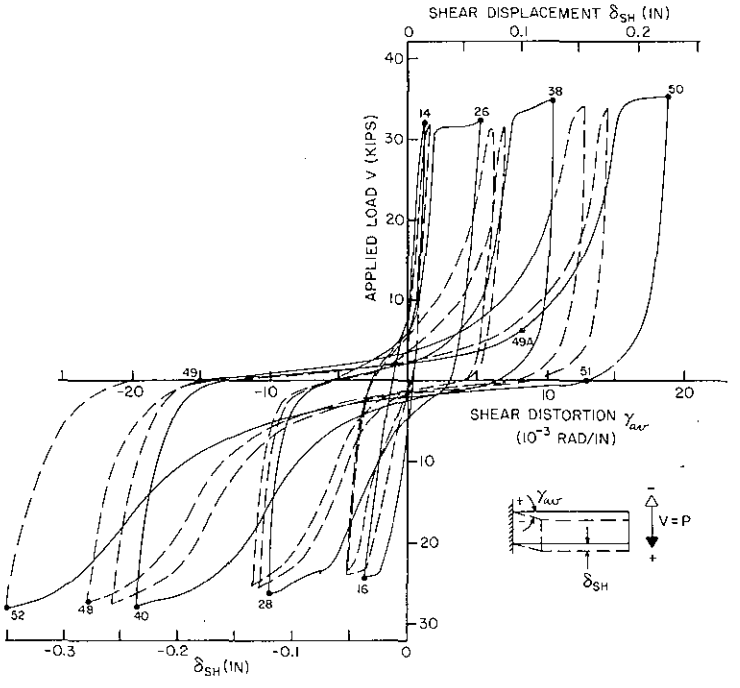

FIG. 4.12(g) V-γ_{av} DIAGRAM (BEAM T-3)

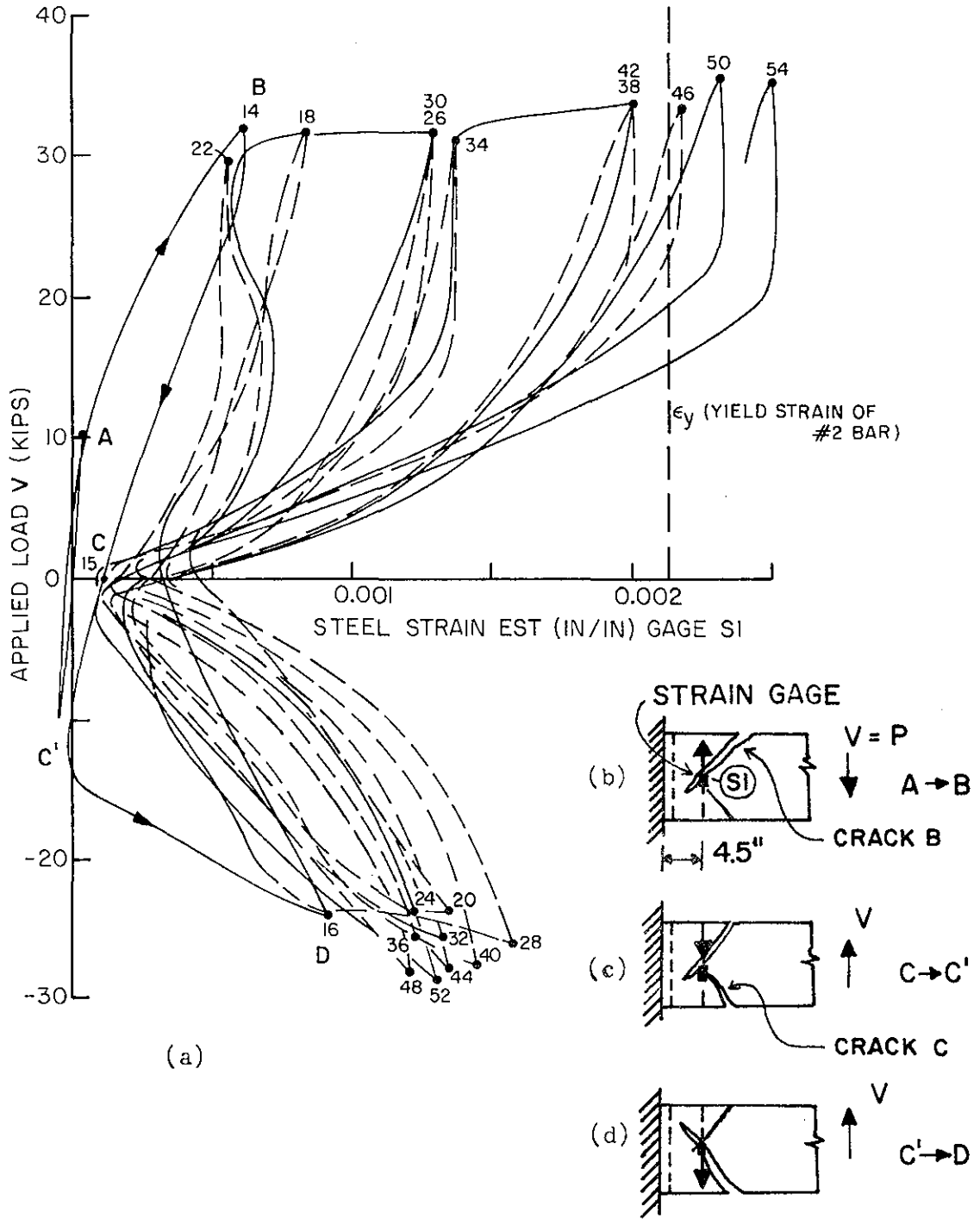

FIG. 4.13 V-ε_{st} DIAGRAM (BEAM T-3)

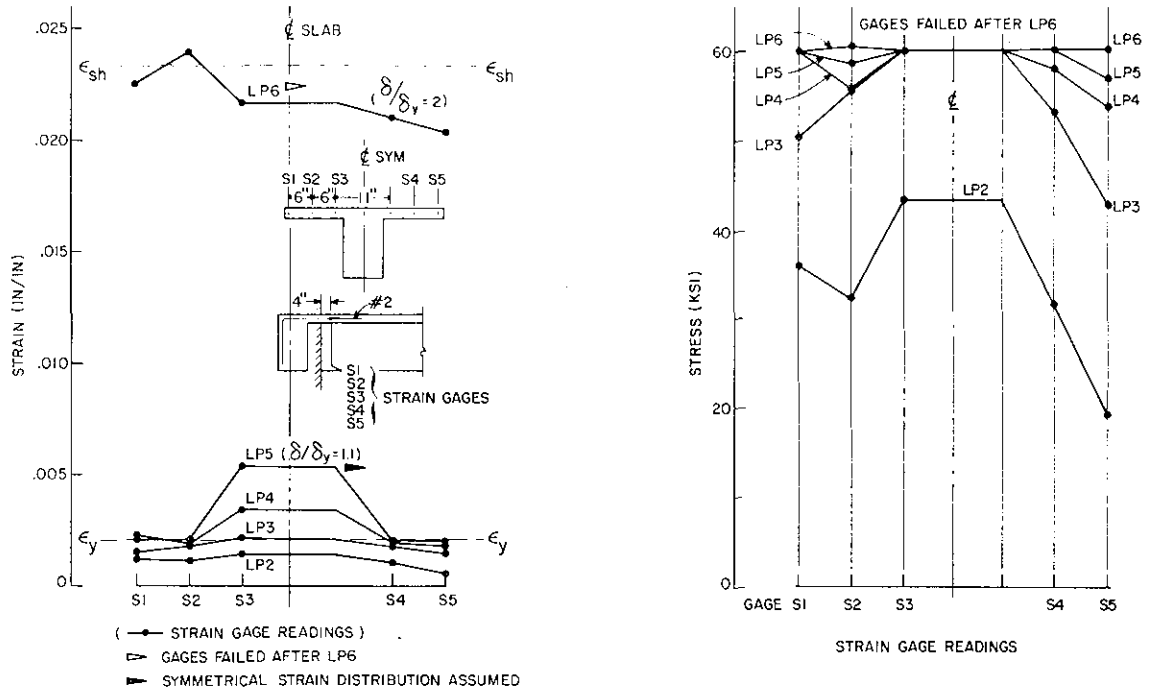

FIG. 4.14(a) STRAIN VARIATION IN SLAB REINFORCEMENT - TOP #2 REINFORCEMENT (BEAM T-2)

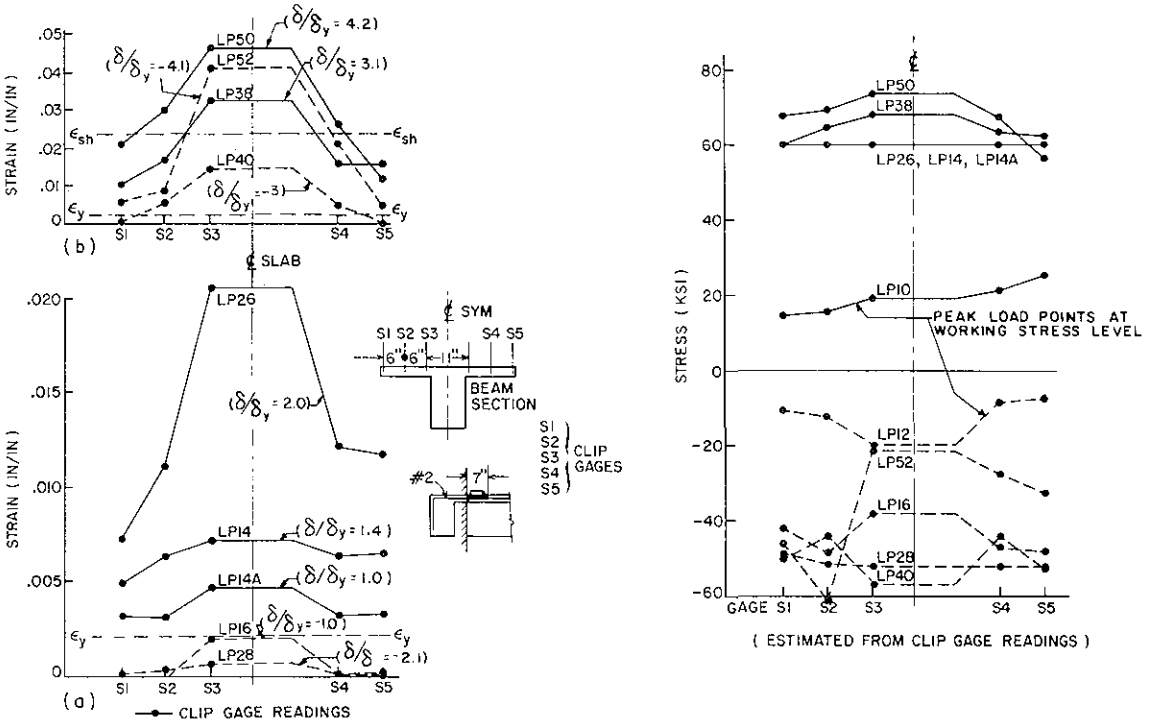

FIG. 4.14(b) STRAIN VARIATION IN SLAB REINFORCEMENT - TOP #2 REINFORCEMENT (BEAM T-3)

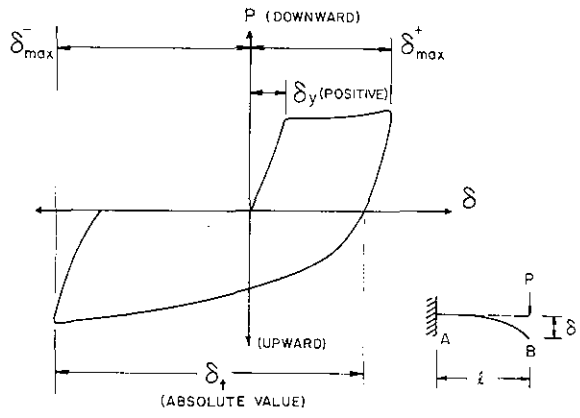

MAXIMUM PLASTIC ROTATION

$$\theta_{PL} = \frac{|\text{MAX}\,|\delta^+_{MAX}, \delta^-_{MAX}| - \delta_y|}{\ell}$$

CYCLIC MAXIMUM PLASTIC ROTATION

$$\theta^t_{PL} = |\delta_t - \delta_y| / \ell$$

DEFLECTION DUCTILITY FACTOR

$$\mu_\delta = \frac{\text{MAX}\,|\delta^+_{MAX}, \delta^-_{MAX}|}{\delta_y}$$

CYCLIC DUCTILITY FACTOR [1.6]

$$\mu^t_\delta = \delta_t / \delta_y$$

FIG. 4.15 DEFORMATIONAL PARAMETERS

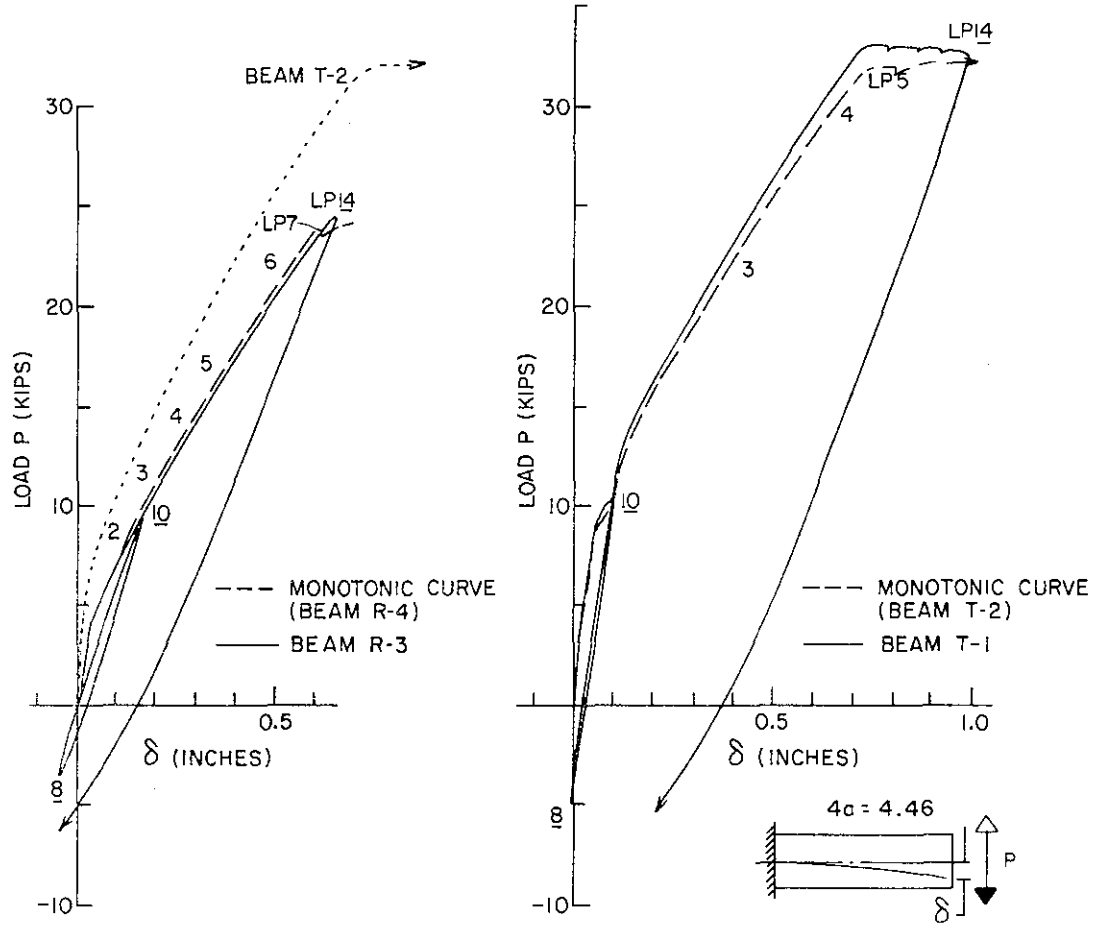

FIG. 4.16 INITIAL P-δ RELATIONSHIPS

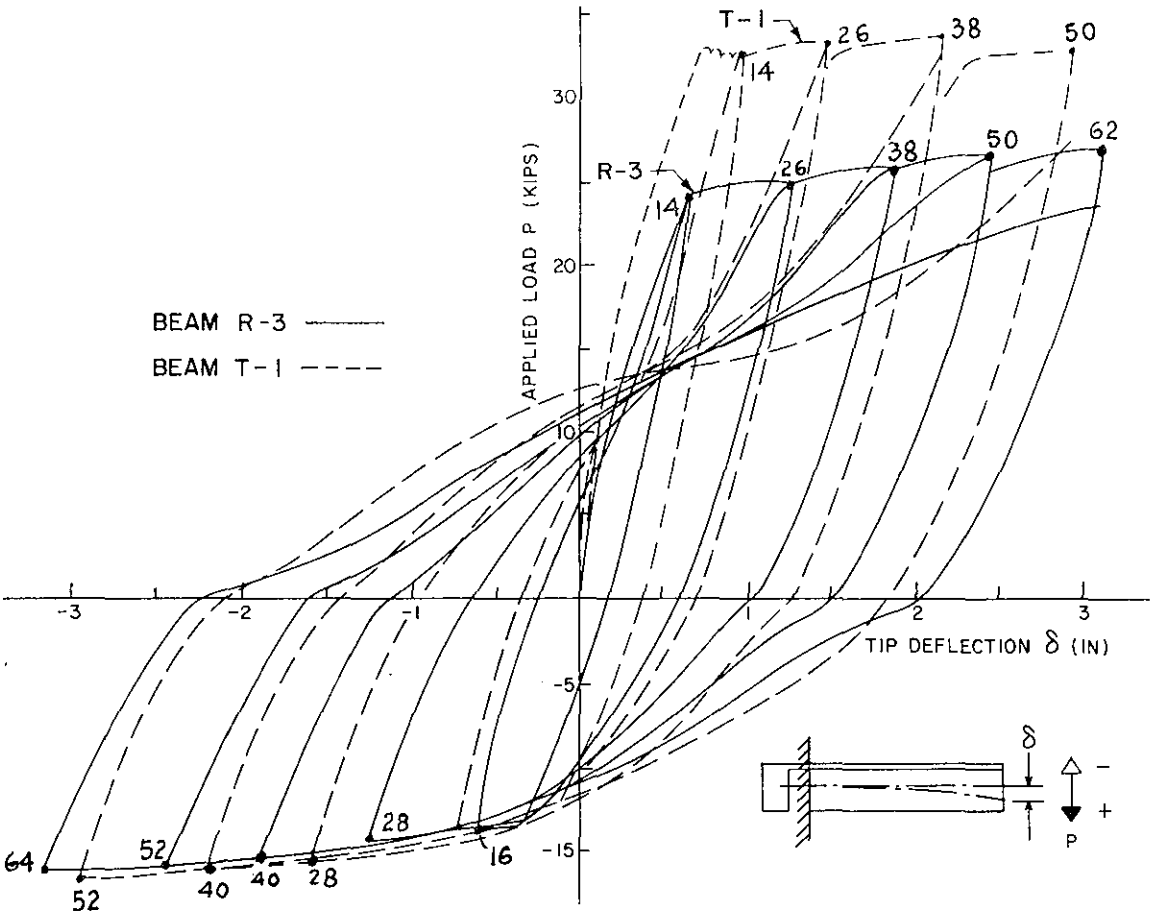

FIG. 4.17(a) COMPARISON OF P-δ HYSTERETIC LOOPS OF BEAMS T-1 AND R-3

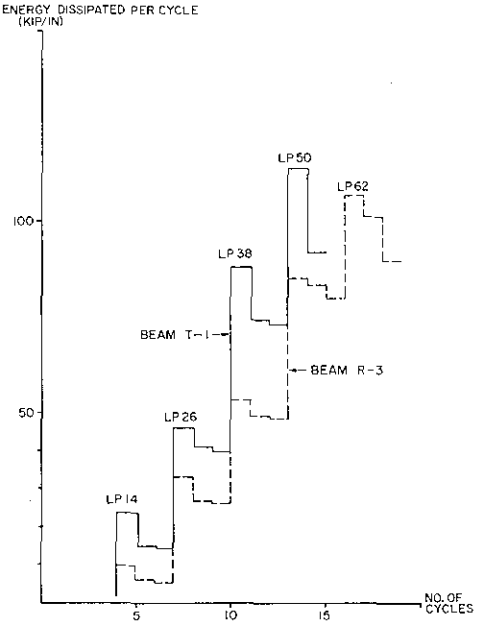

FIG. 4.17(b) ENERGY DISSIPATION
VS. NUMBER OF CYCLES
(BEAMS T-1 AND R-3)

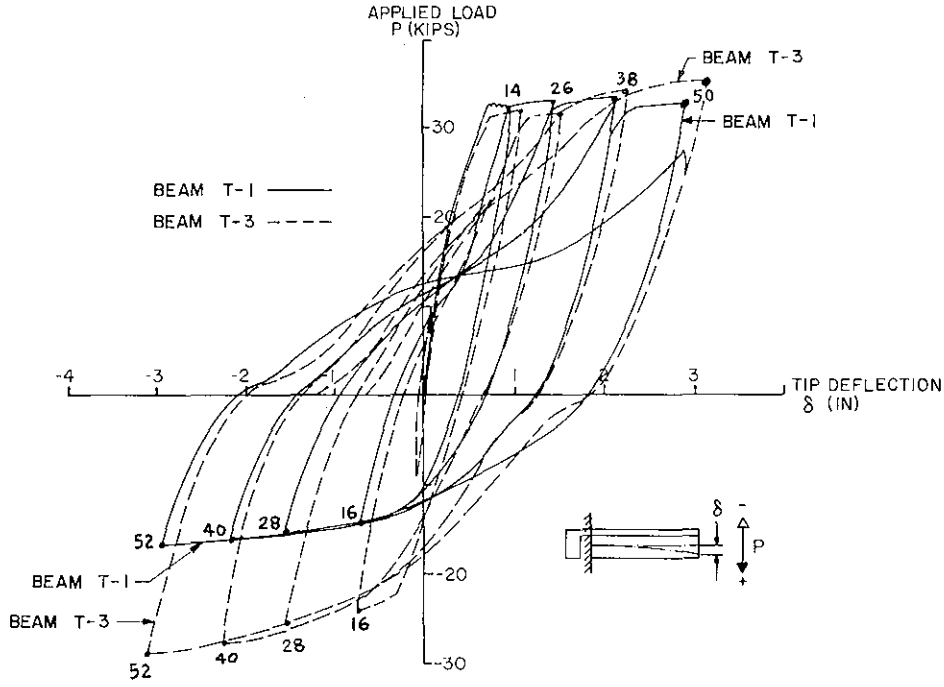

FIG. 4.18 COMPARISON OF P-δ HYSTERETIC LOOPS OF BEAMS T-1 AND T-3

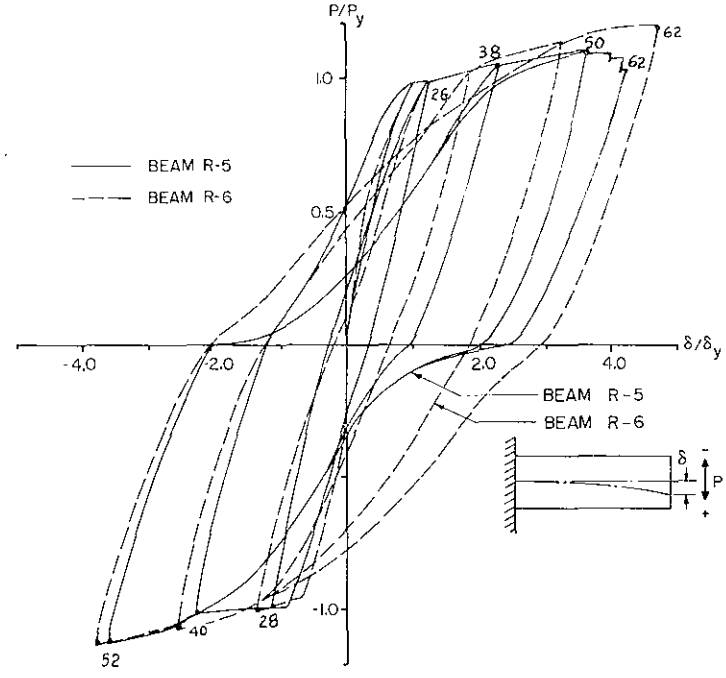

FIG. 4.19 COMPARISON OF P-δ HYSTERETIC LOOPS OF BEAMS R-5 AND R-6

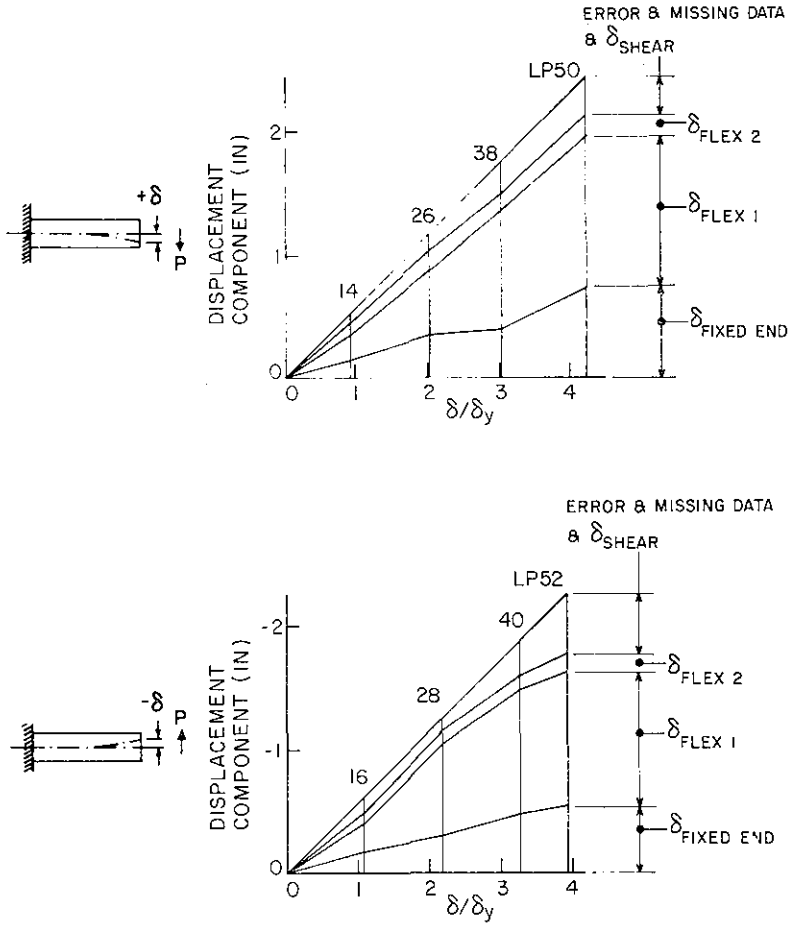

FIG. A4.1 CONTRIBUTION OF DIFFERENT SOURCES OF DEFORMATION TO TIP DEFLECTION AND ITS VARIATIONS WITH INCREASING DUCTILITY RATIOS (BEAM R-1)

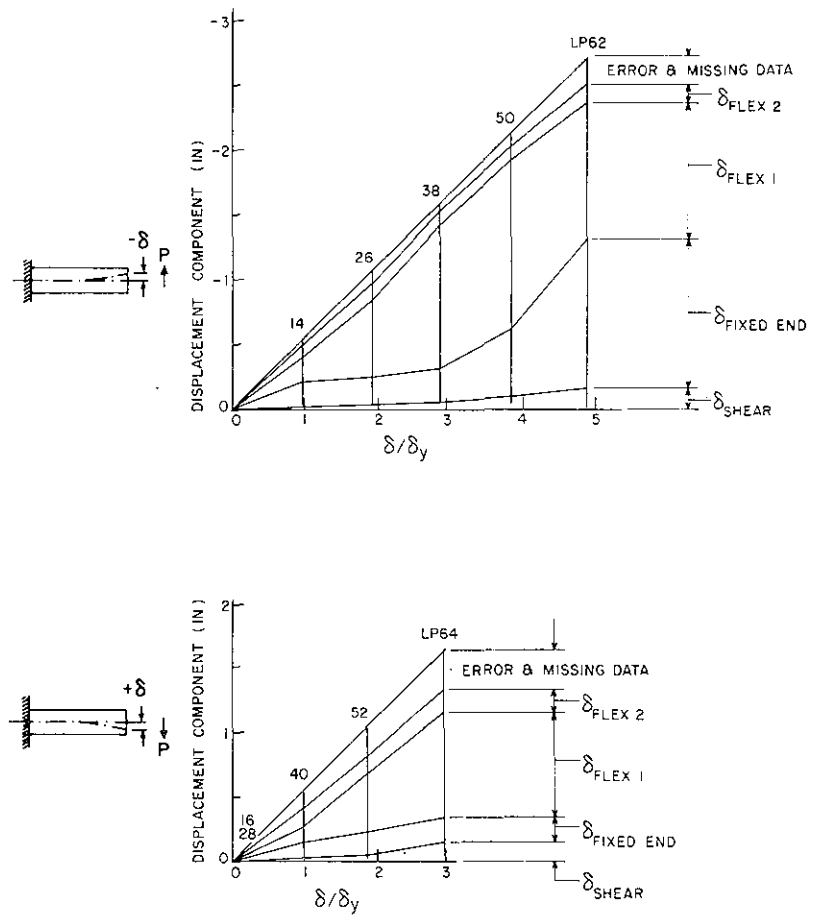

FIG. A4.2 CONTRIBUTION OF DIFFERENT SOURCES OF DEFORMATION TO TIP DEFLECTION AND ITS VARIATIONS WITH INCREASING DUCTILITY RATIOS (BEAM R-2)

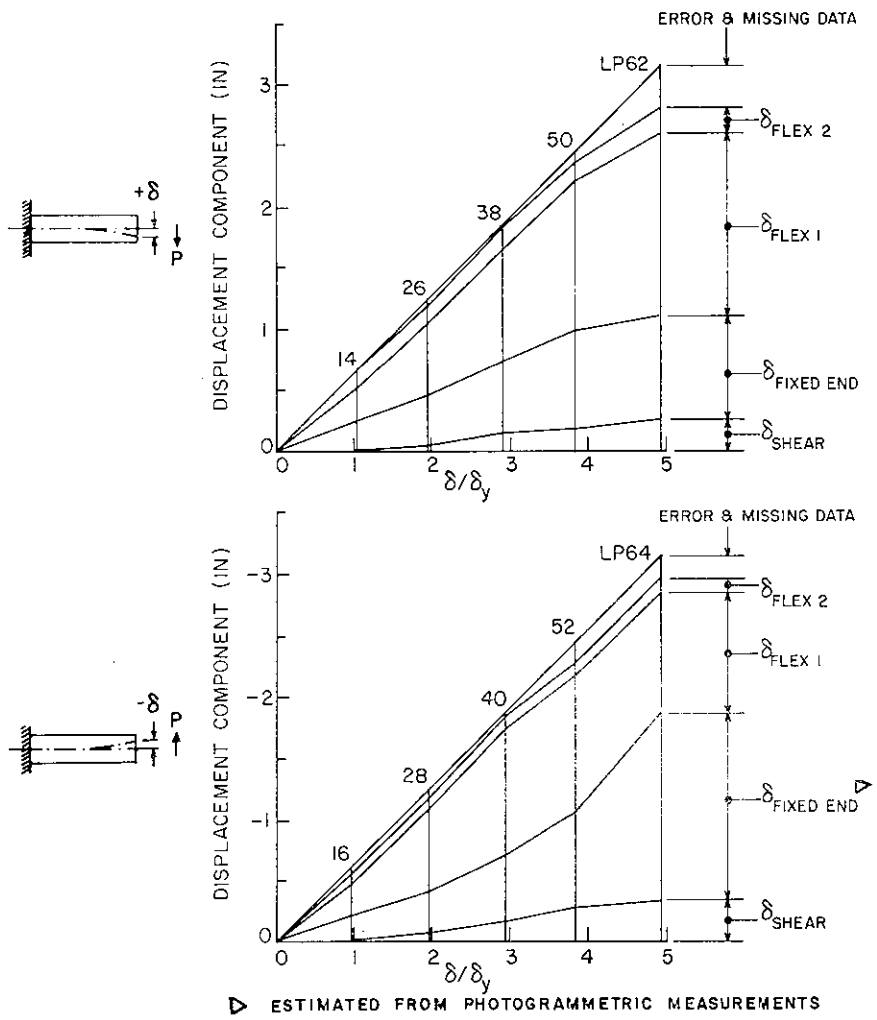

FIG. A4.3 CONTRIBUTION OF DIFFERENT SOURCES OF DEFORMATION TO TIP DEFLECTION AND ITS VARIATIONS WITH INCREASING DUCTILITY RATIOS (BEAM R-3)

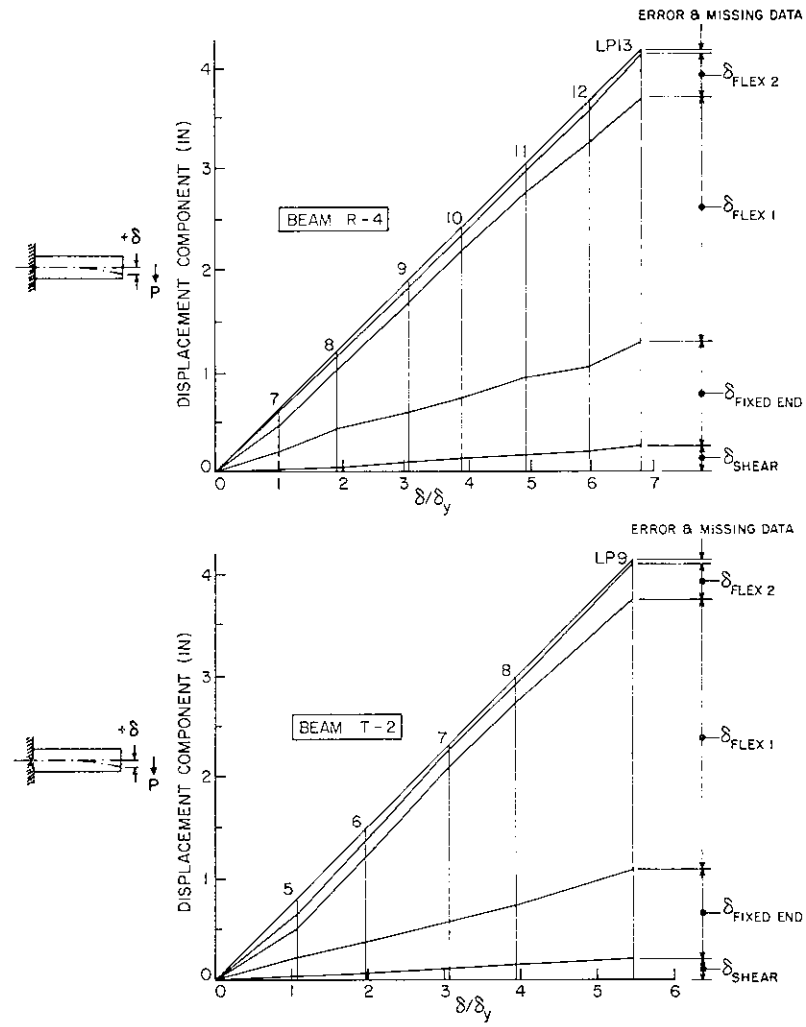

FIG. A4.4 CONTRIBUTION OF DIFFERENT SOURCES OF DEFORMATION TO TIP DEFLECTION AND ITS VARIATIONS WITH INCREASING DUCTILITY RATIOS (BEAMS R-4 AND T-2)

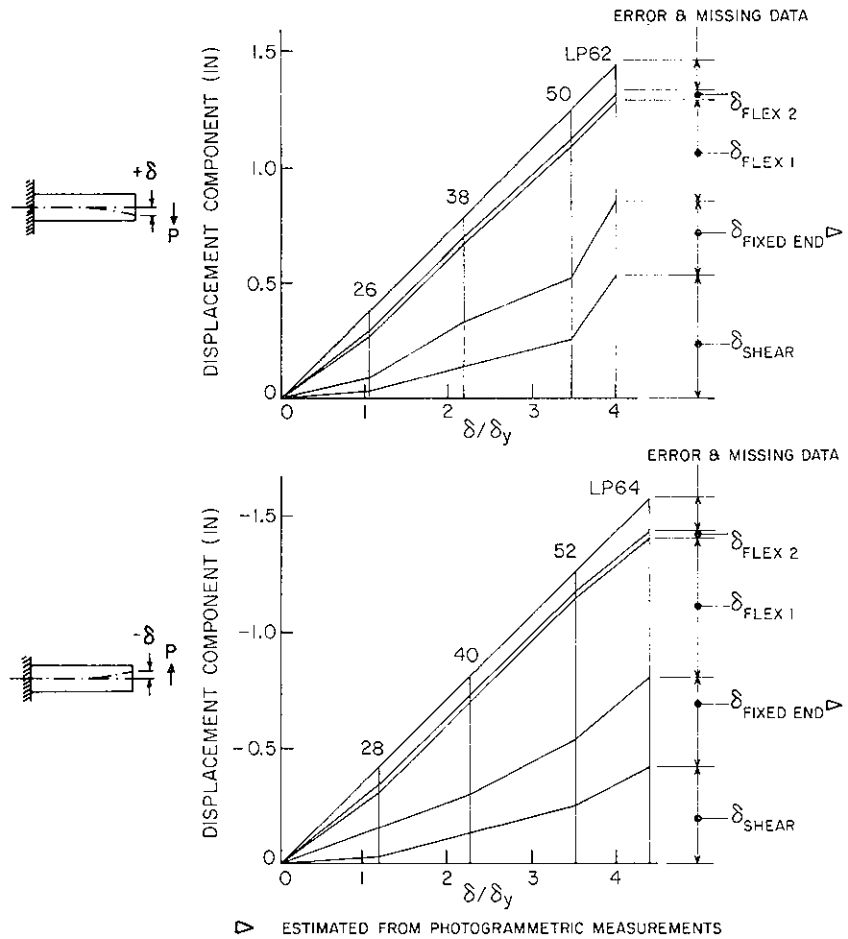

FIG. A4.5 CONTRIBUTION OF DIFFERENT SOURCES OF DEFORMATION TO TIP DEFLECTION AND ITS VARIATIONS WITH INCREASING DUCTILITY RATIOS (BEAM R-5)

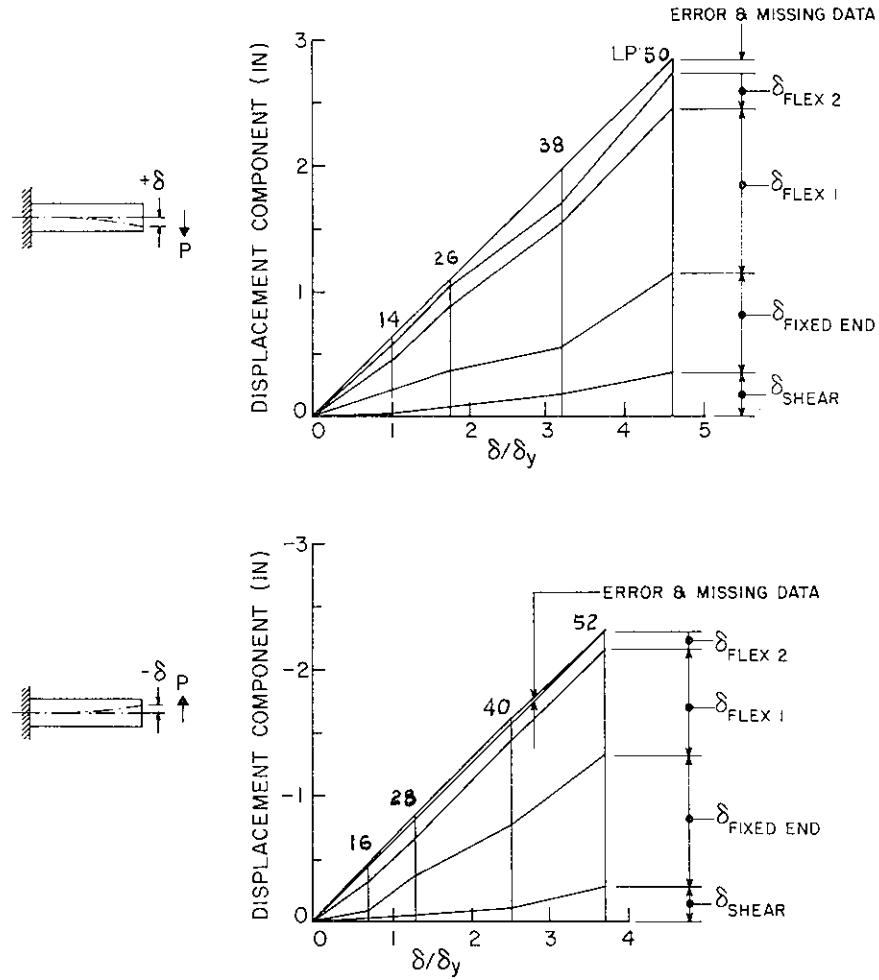

FIG. A4.6 CONTRIBUTION OF DIFFERENT SOURCES OF DEFORMATION TO TIP DEFLECTION AND ITS VARIATIONS WITH INCREASING DUCTILITY RATIOS (BEAM R-6)

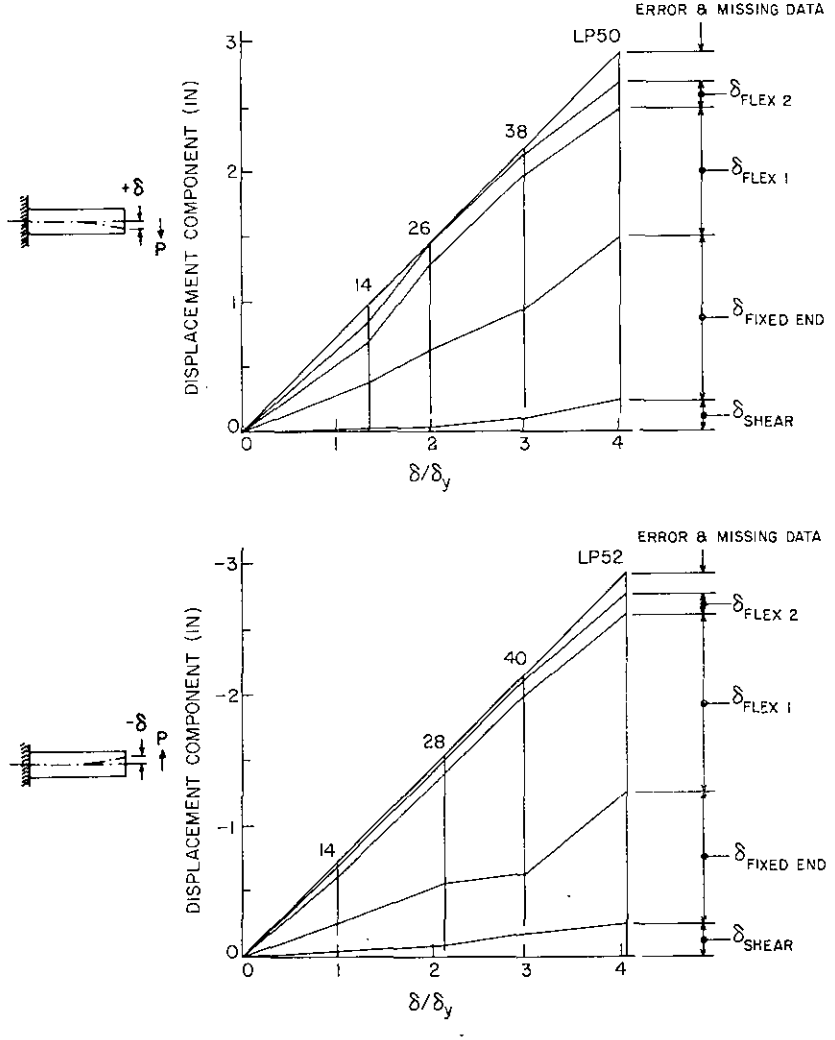

FIG. A4.7 CONTRIBUTION OF DIFFERENT SOURCES OF DEFORMATION TO TIP DEFLECTION AND ITS VARIATIONS WITH INCREASING DUCTILITY RATIOS (BEAM T-1)

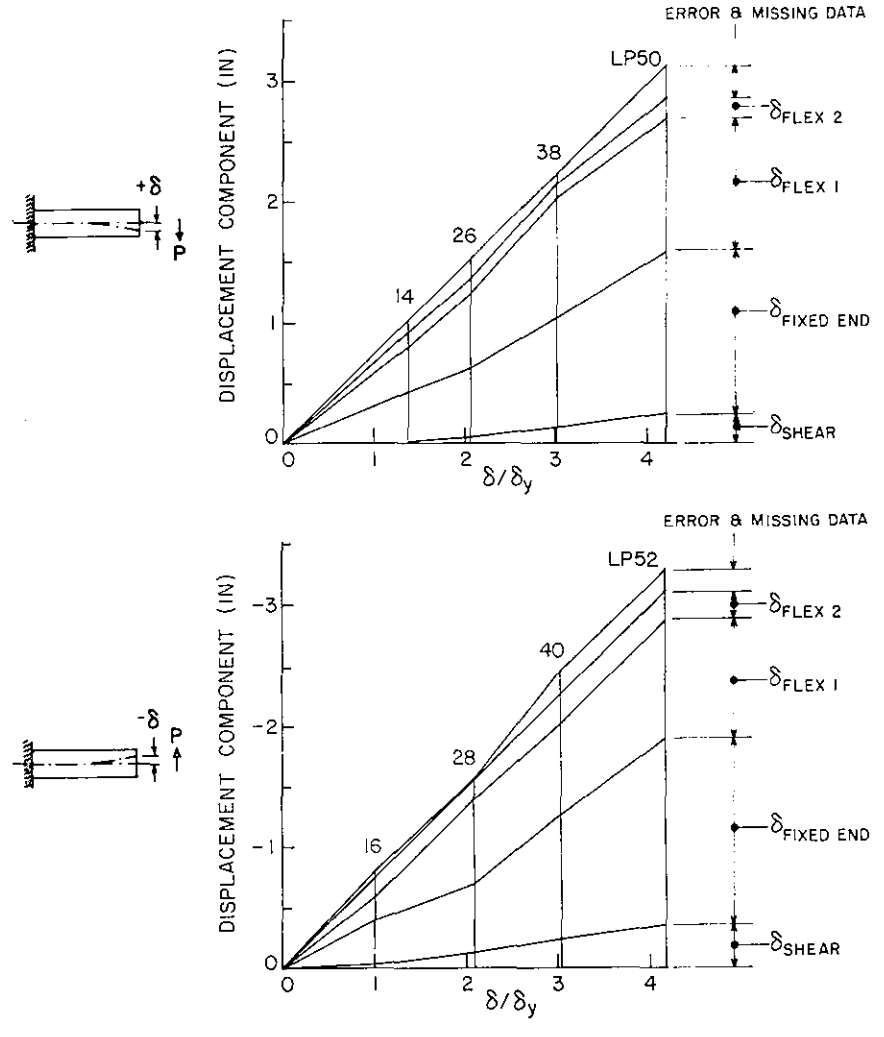

FIG. A4.8 CONTRIBUTION OF DIFFERENT SOURCES OF DEFORMATION TO TIP DEFLECTION AND ITS VARIATIONS WITH INCREASING DUCTILITY RATIOS (BEAM T-3)

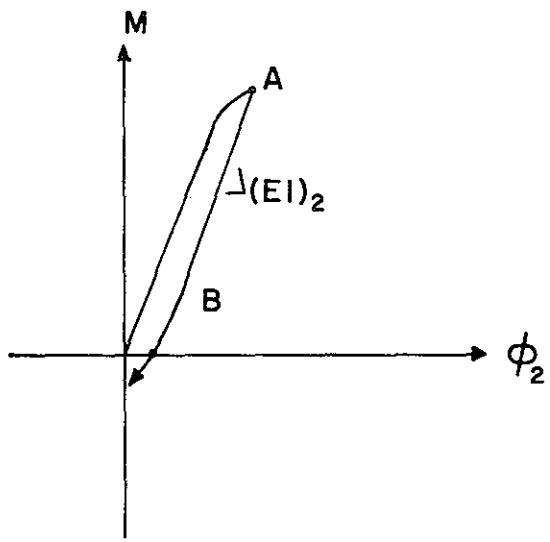

FIG. A4.9 ESTIMATION OF FLEXURAL STIFFNESS $(EI)_2$

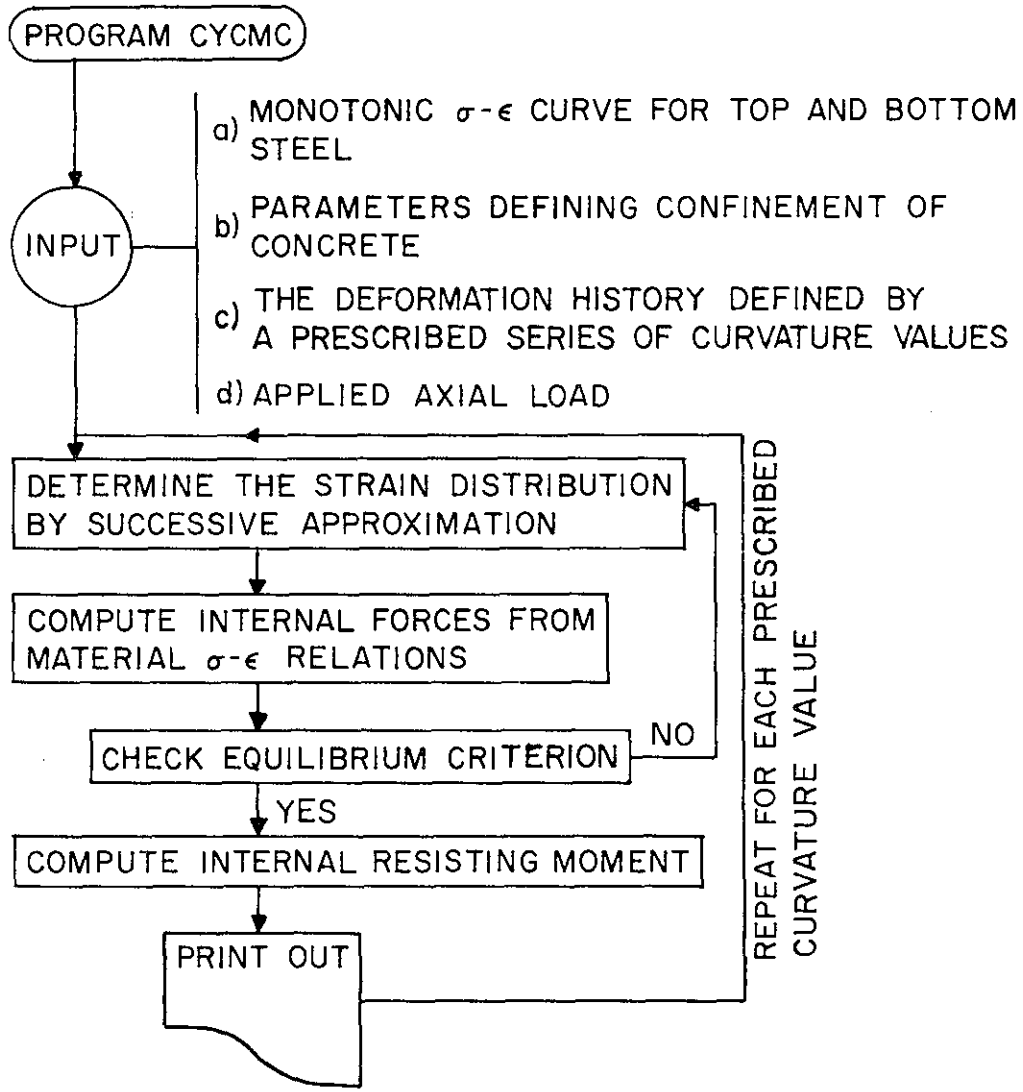

FIG. 5.1 FLOW CHART FOR CYCLIC MOMENT-CURVATURE ANALYSIS

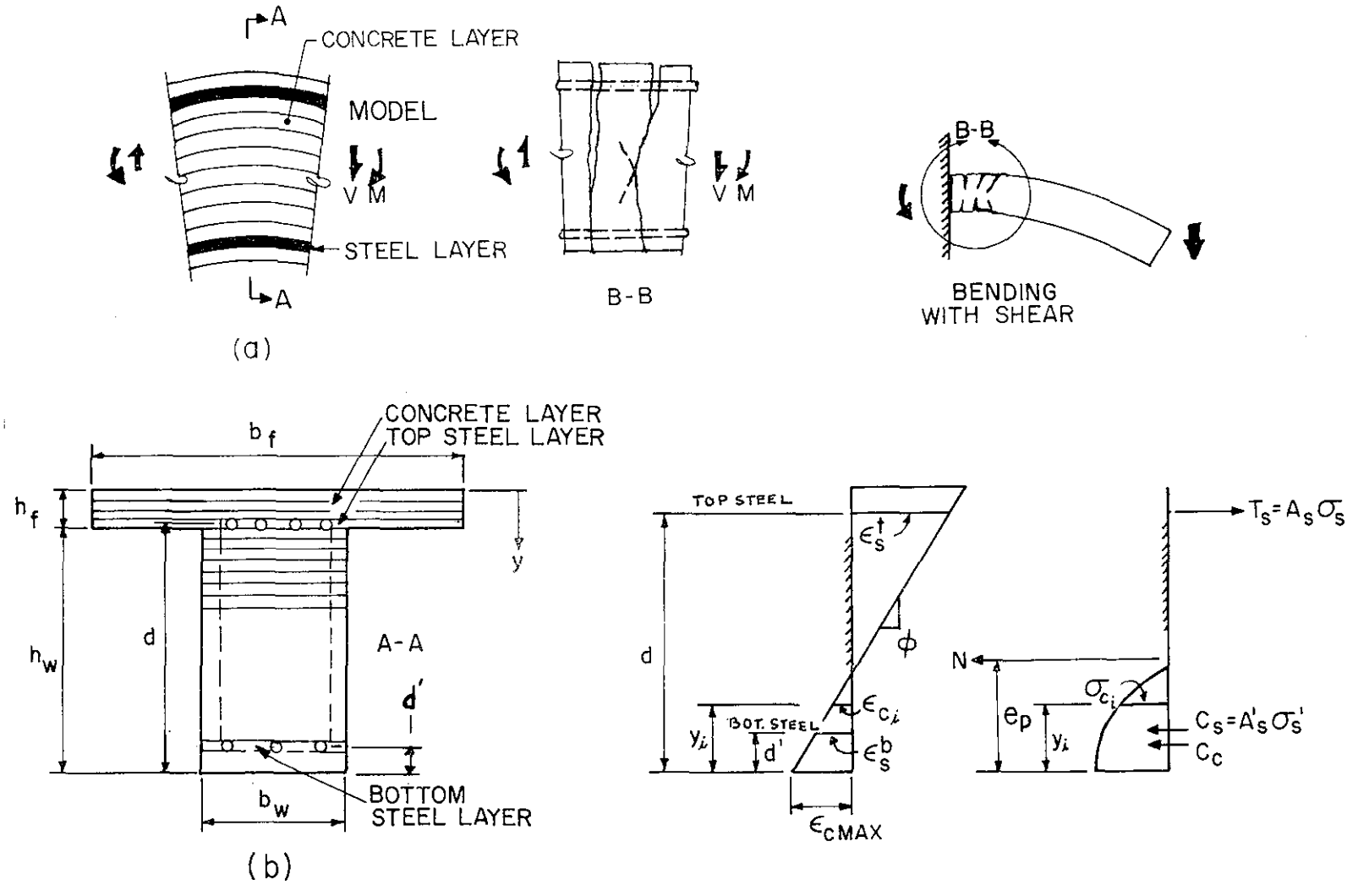

FIG. 5.2 IDEALIZATION OF A R/C FLEXURAL REGION

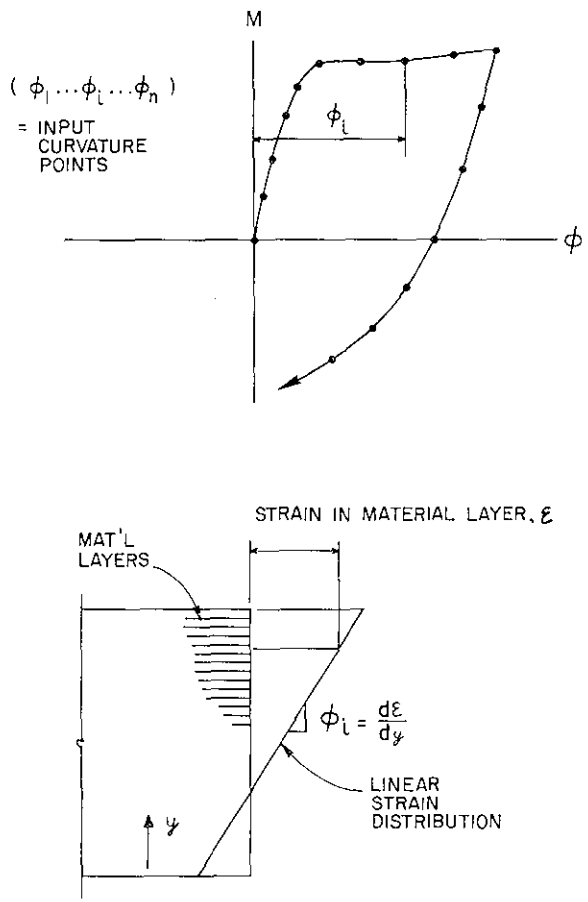

FIG. 5.3 STEP-BY-STEP DETERMINATION OF M-ϕ RELATIONSHIP

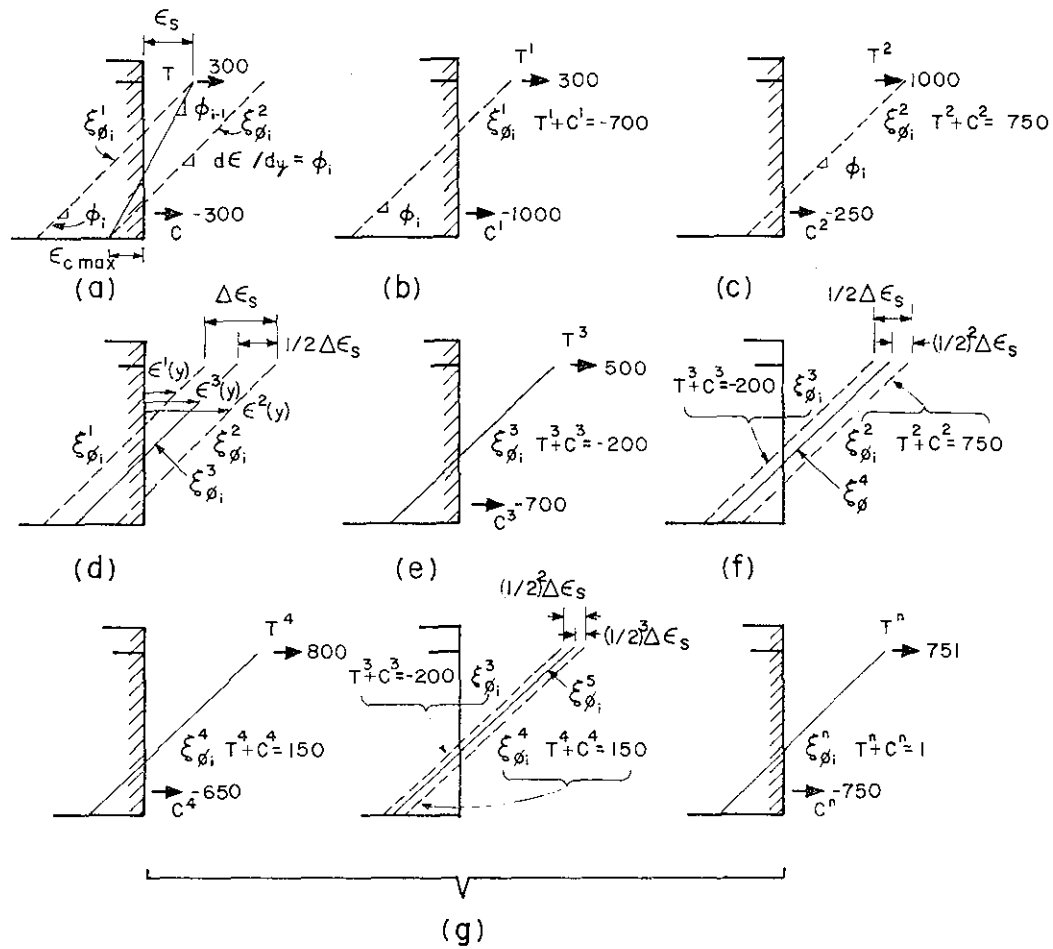

FIG. 5.4 NUMERICAL PROCEDURE FOR DETERMINING STRAIN DISTRIBUTION CORRESPONDING TO A SELECTED CURVATURE

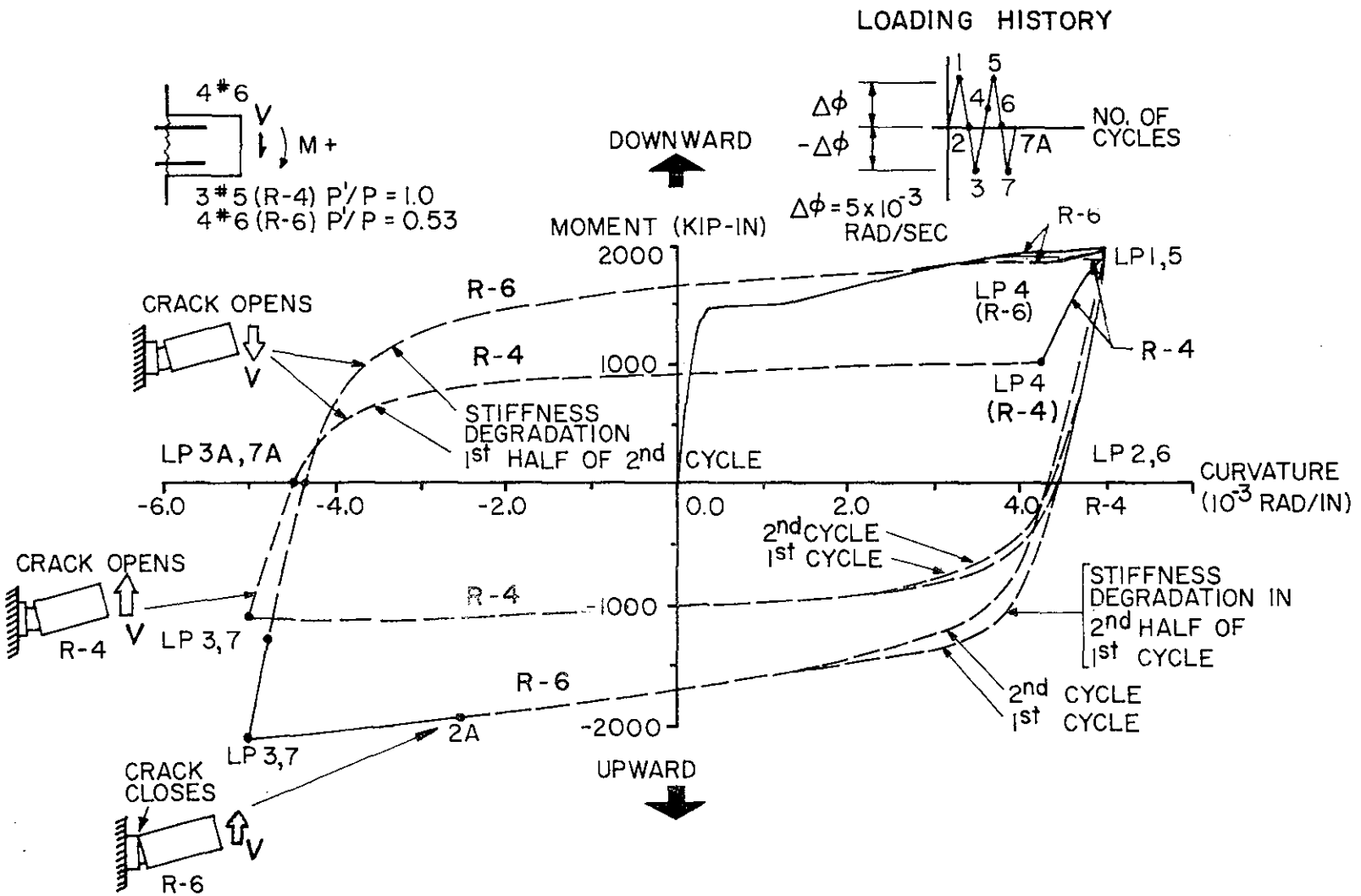

FIG. 5.5 THEORETICAL M-φ HYSTERETIC LOOPS (BEAMS R-4 AND R-6)

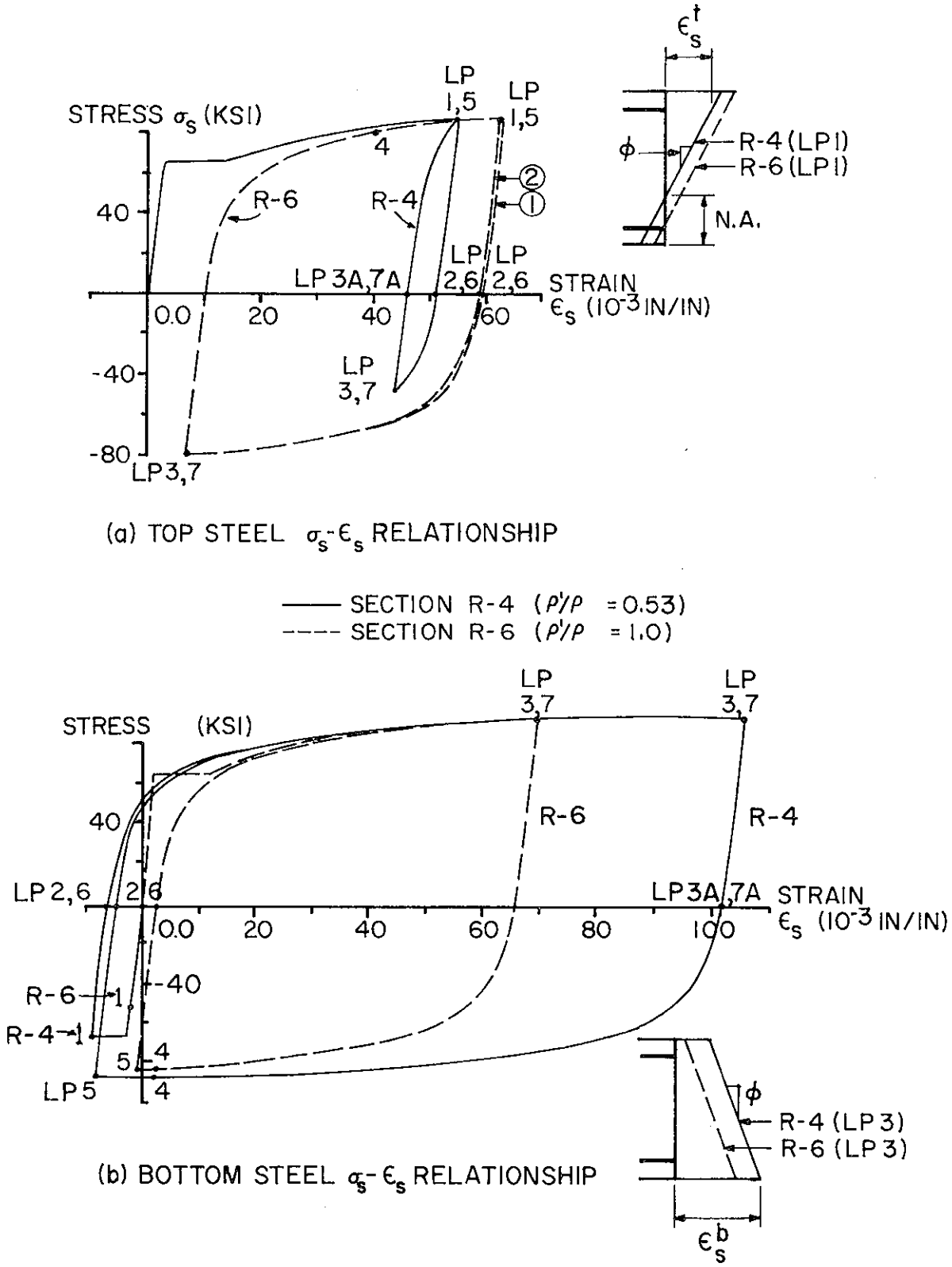

FIG. 5.6 STRESS-STRAIN HYSTERETIC LOOPS OF BEAMS R-4 AND R-6 (M-ϕ) ANALYSIS RESULTS)

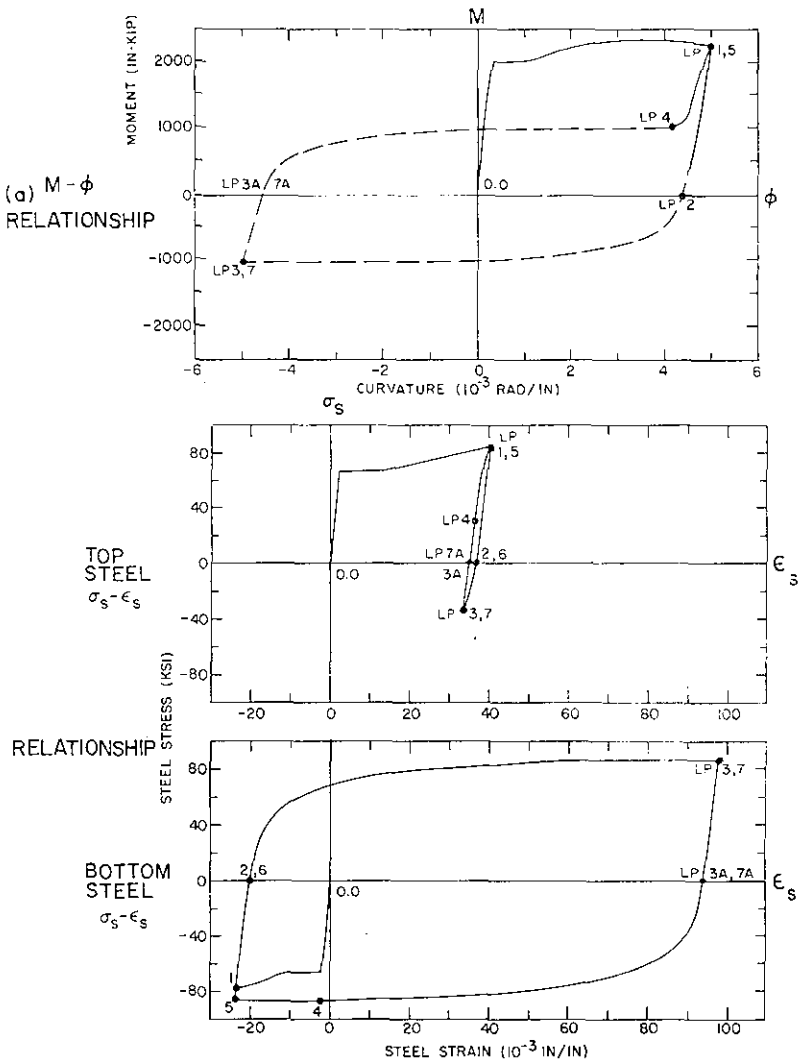

FIG. 5.7 MOMENT-CURVATURE ANALYSIS RESULTS (BEAM T-2) ρ'/ρ_t = 0.39

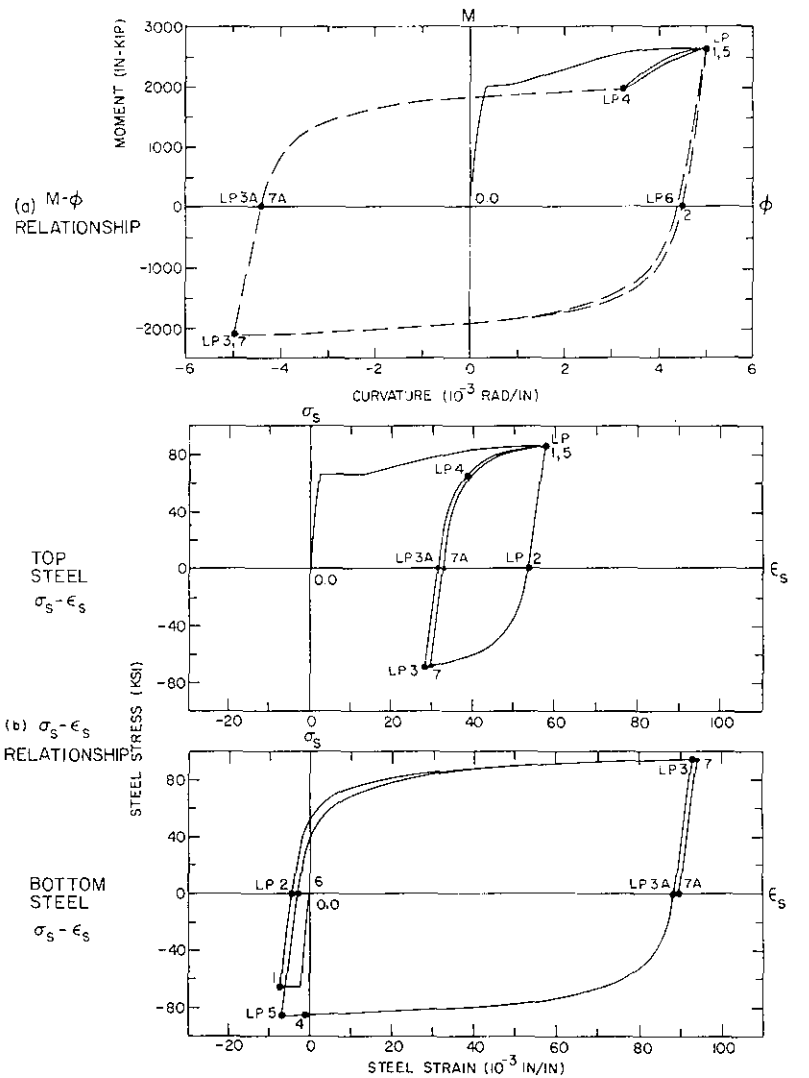

FIG. 5.8 MOMENT-CURVATURE ANALYSIS RESULTS (BEAM T-3) ρ'/ρ_t = 0.75

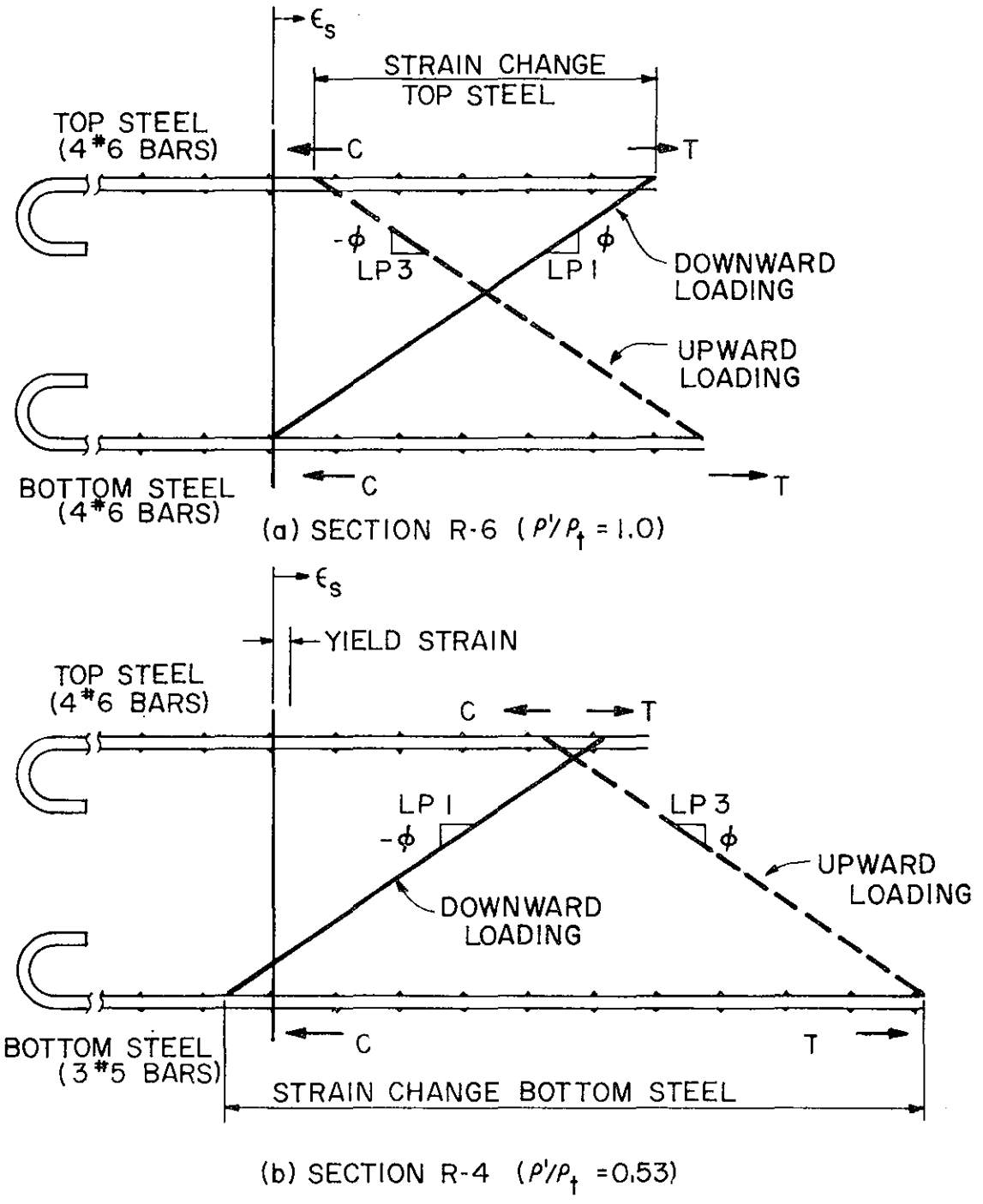

FIG. 5.9 EFFECT OF STEEL RATIO, ρ'/ρ_t,
(OR RATIO BETWEEN MOMENT CAPACITIES IN TWO DIRECTIONS)
ON RELATIVE STRAINING OF TOP AND BOTTOM STEEL REINFORCEMENTS

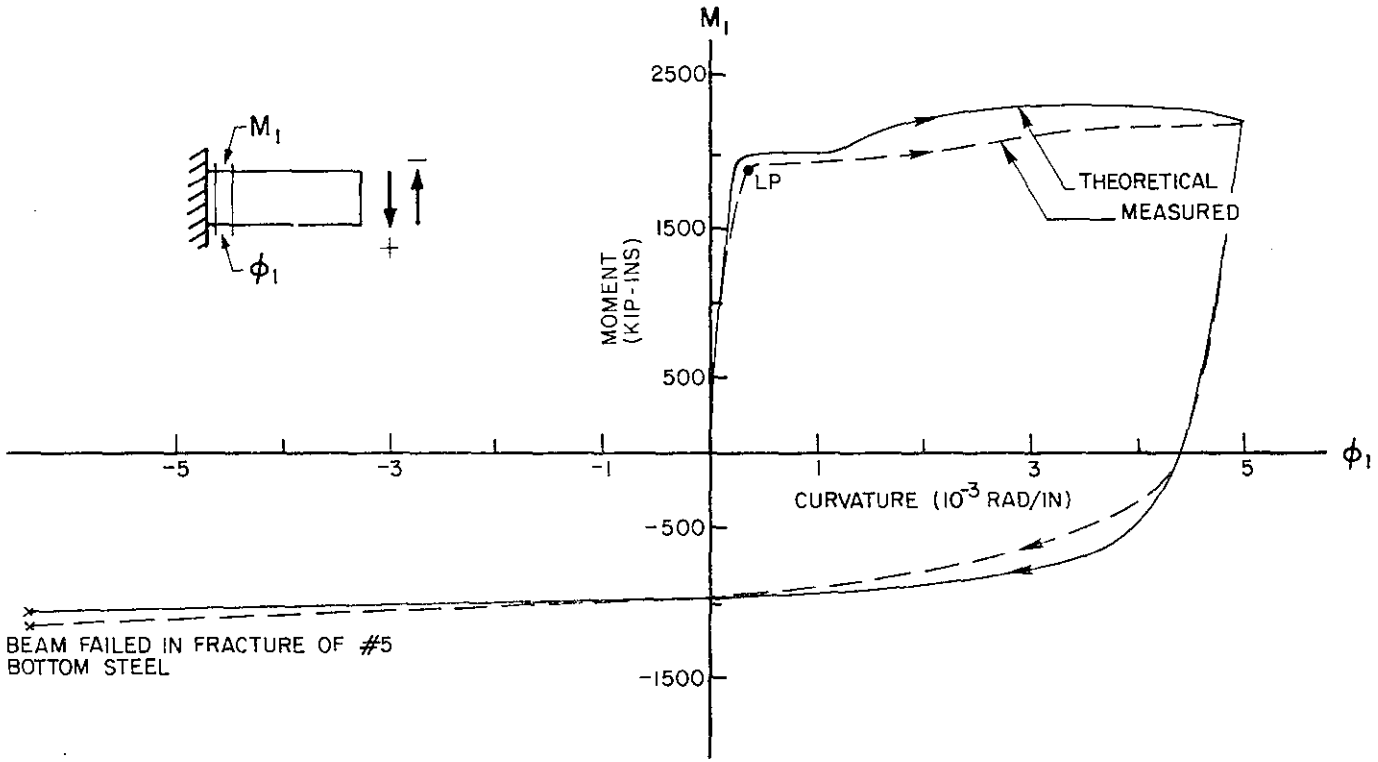

FIG. 5.10 COMPARISON BETWEEN THEORETICAL $M\text{-}\phi_{av}$ AND MEASURED RELATIONSHIPS ($M\text{-}\phi_1$, BEAM T-2) $\rho'/\rho_t = 0.34$

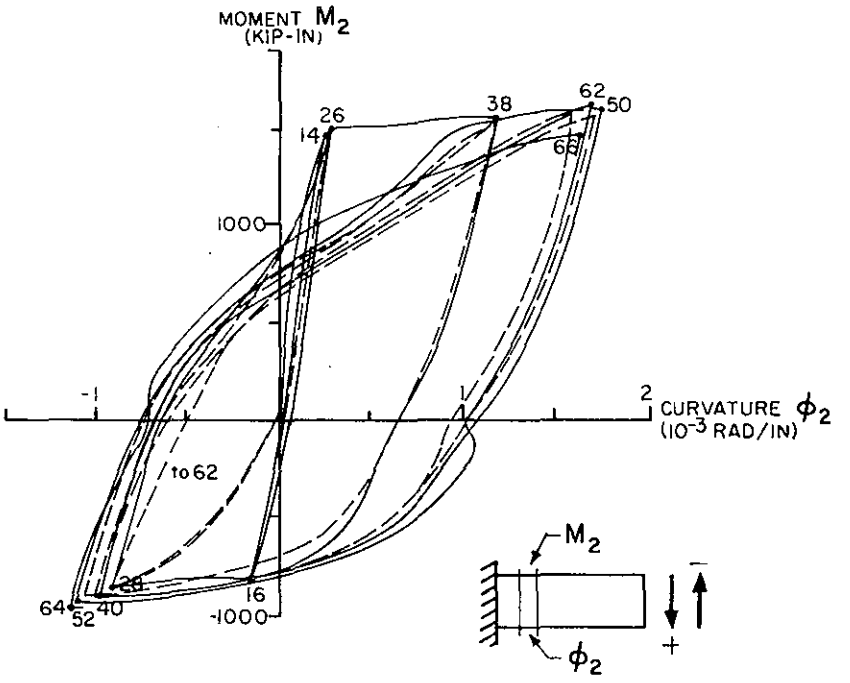

M-ϕ DIAGRAMS – BEAM R-3
(EXPERIMENTAL RESULTS)

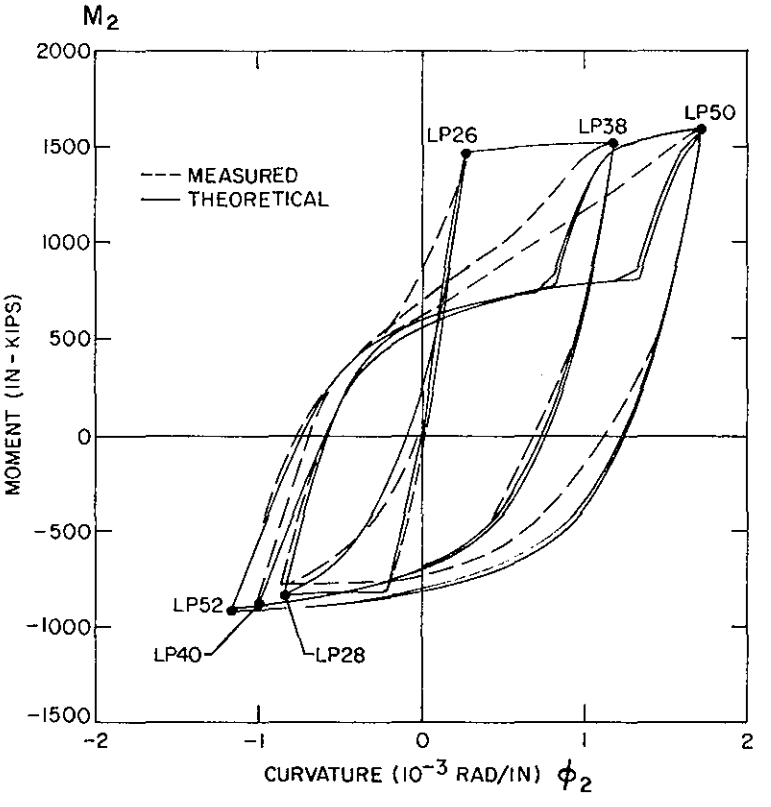

FIG. 5.11 COMPARISON BETWEEN THEORETICAL M-ϕ_{av} AND MEASURED RELATIONSHIPS (M-ϕ_2, BEAM R-3) ρ'/ρ_t = 0.53

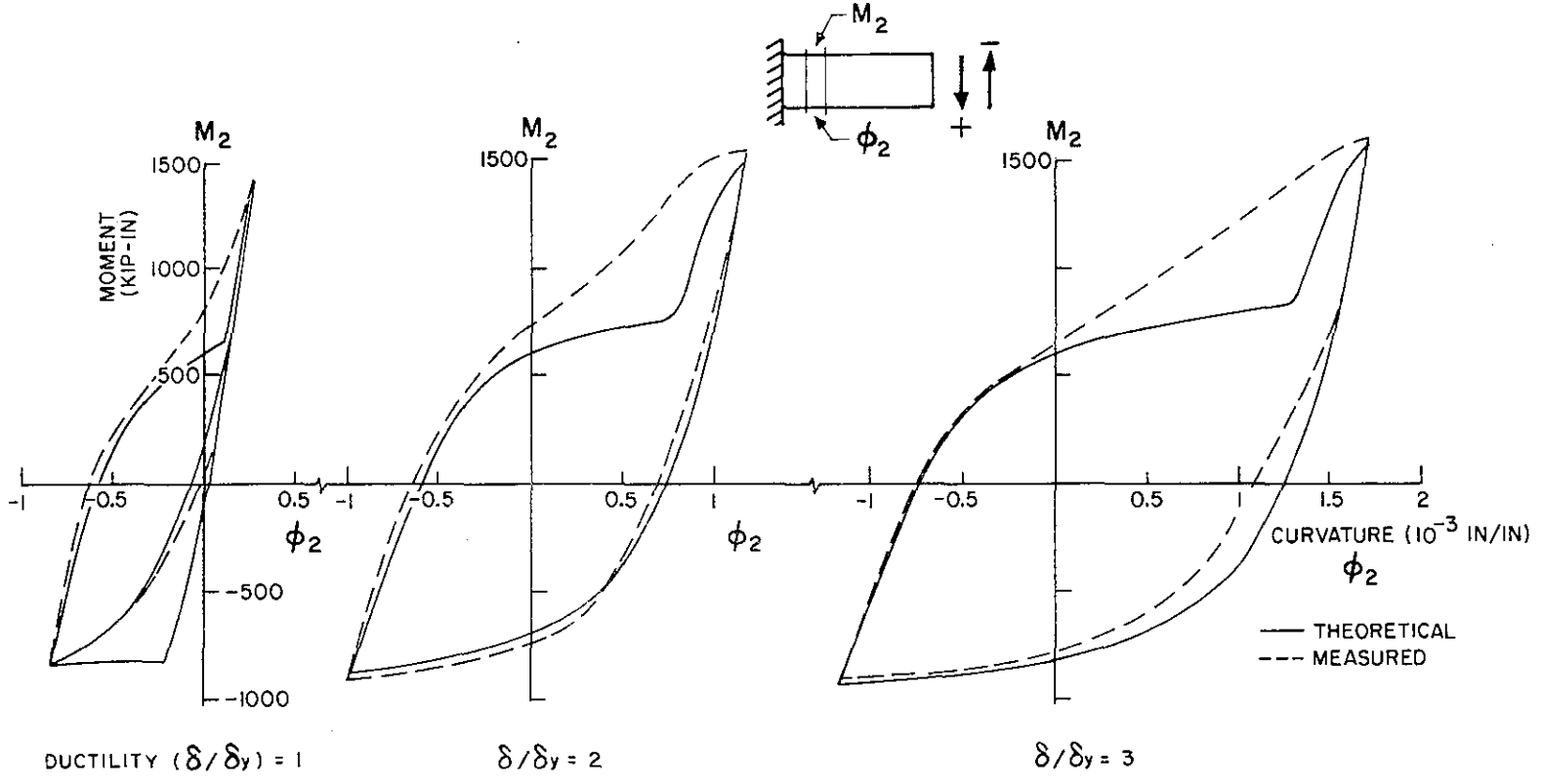

FIG. 5.12 LOOP-BY-LOOP COMPARISON BETWEEN THEORETICAL $M\text{-}\phi_{av}$ AND MEASURED RELATIONSHIPS ($M\text{-}\phi_2$, BEAM R-3) $\rho'/\rho_t = 0.53$

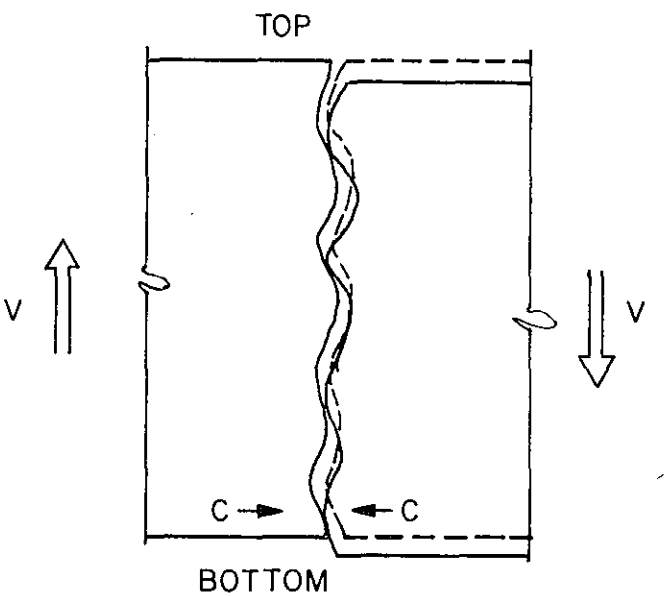

FIG. 5.13 CONTACT OF CRACK FACES DUE TO VERTICAL SHEAR DISPLACEMENT

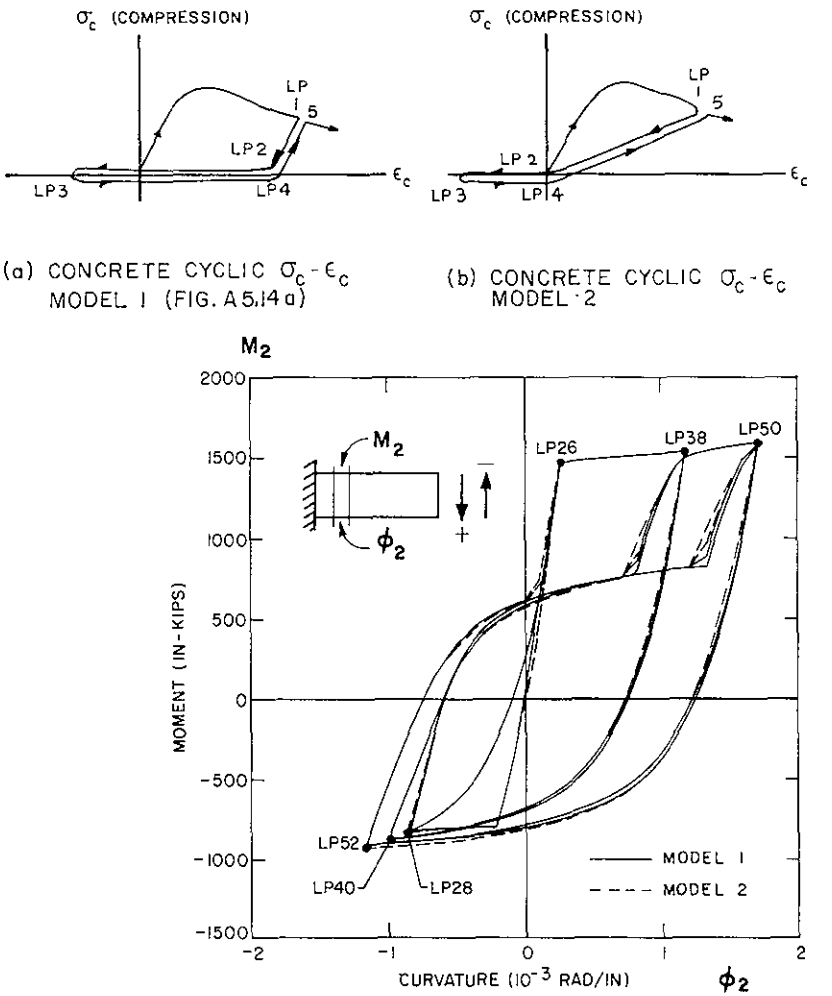

(a) CONCRETE CYCLIC σ_c-ϵ_c MODEL 1 (FIG. A5.14a)

(b) CONCRETE CYCLIC σ_c-ϵ_c MODEL 2

(c) THEORETICAL M-ϕ_2 RESPONSE (BEAM R-3)

FIG. 5.14 PREDICTED M-ϕ_{av} HYSTERETIC LOOPS USING DIFFERENT CONCRETE CYCLIC σ-ε MODELS

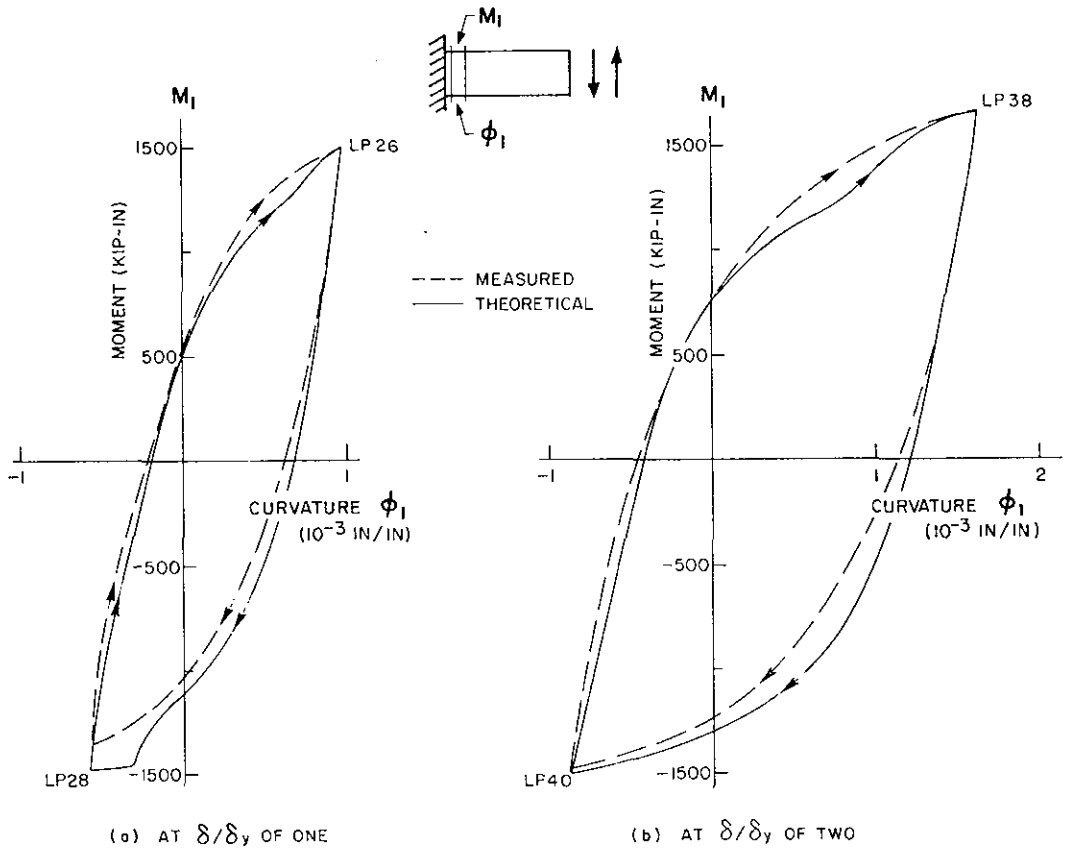

FIG. 5.15 LOOP-BY-LOOP COMPARISON BETWEEN THEORETICAL $M\text{-}\phi_{av}$ AND MEASURED RELATIONSHIPS ($M\text{-}\phi_1$, BEAM R-6) $\rho'/\rho_t = 1.00$

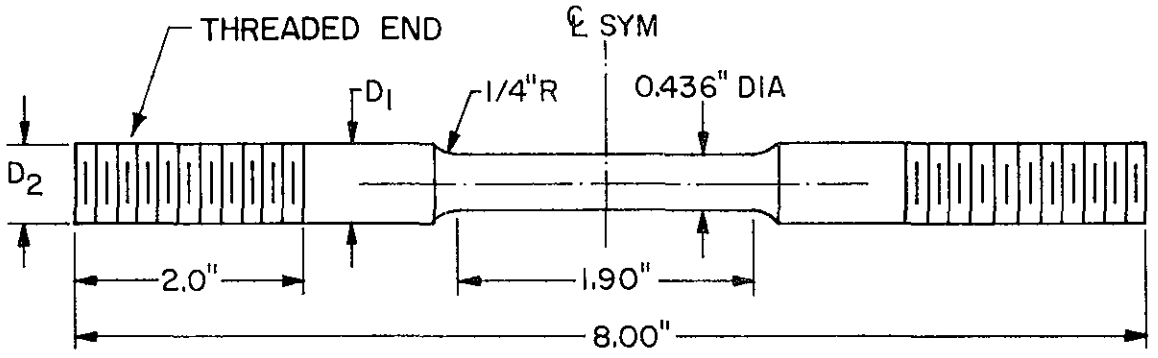

	D_1	D_2
#6 REBAR SPECIMENS	0.625"	0.625"
#5 REBAR SPECIMENS	0.587"	0.500"

FIG. A5.1 DIMENSIONS OF MACHINED REBAR SPECIMENS

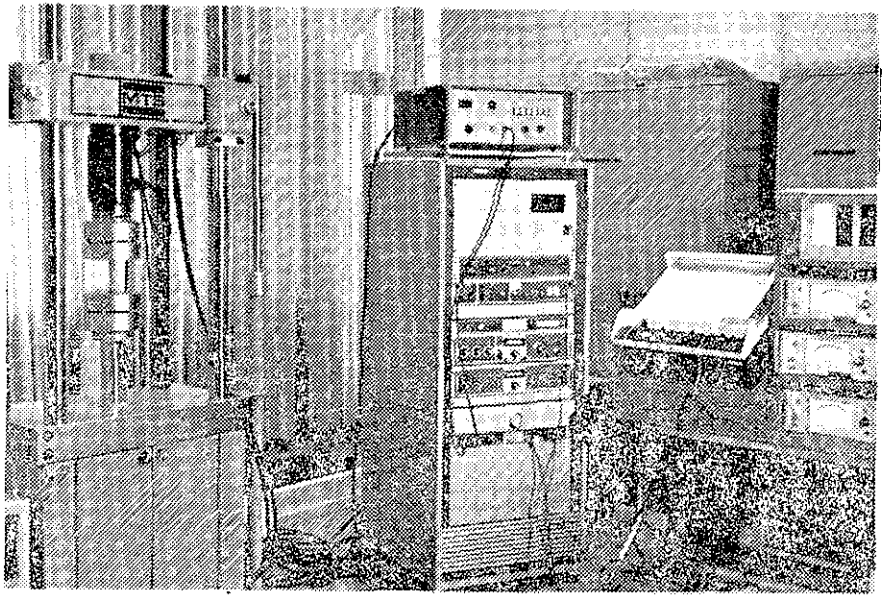

(a) MTS TEST MACHINE, CONTROL CONSOLE, AND X-Y RECORDER

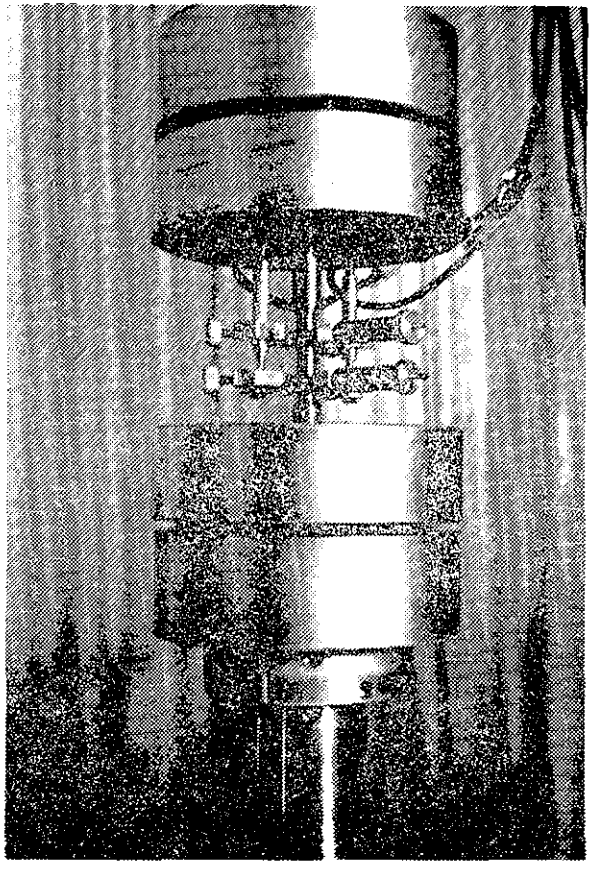

(b) STRAIN MEASURING TRANSDUCERS (LVDTS)

FIG. A5.2 TEST SETUP (STEEL REINFORCEMENT σ-ε HYSTERETIC RELATIONSHIP STUDY)

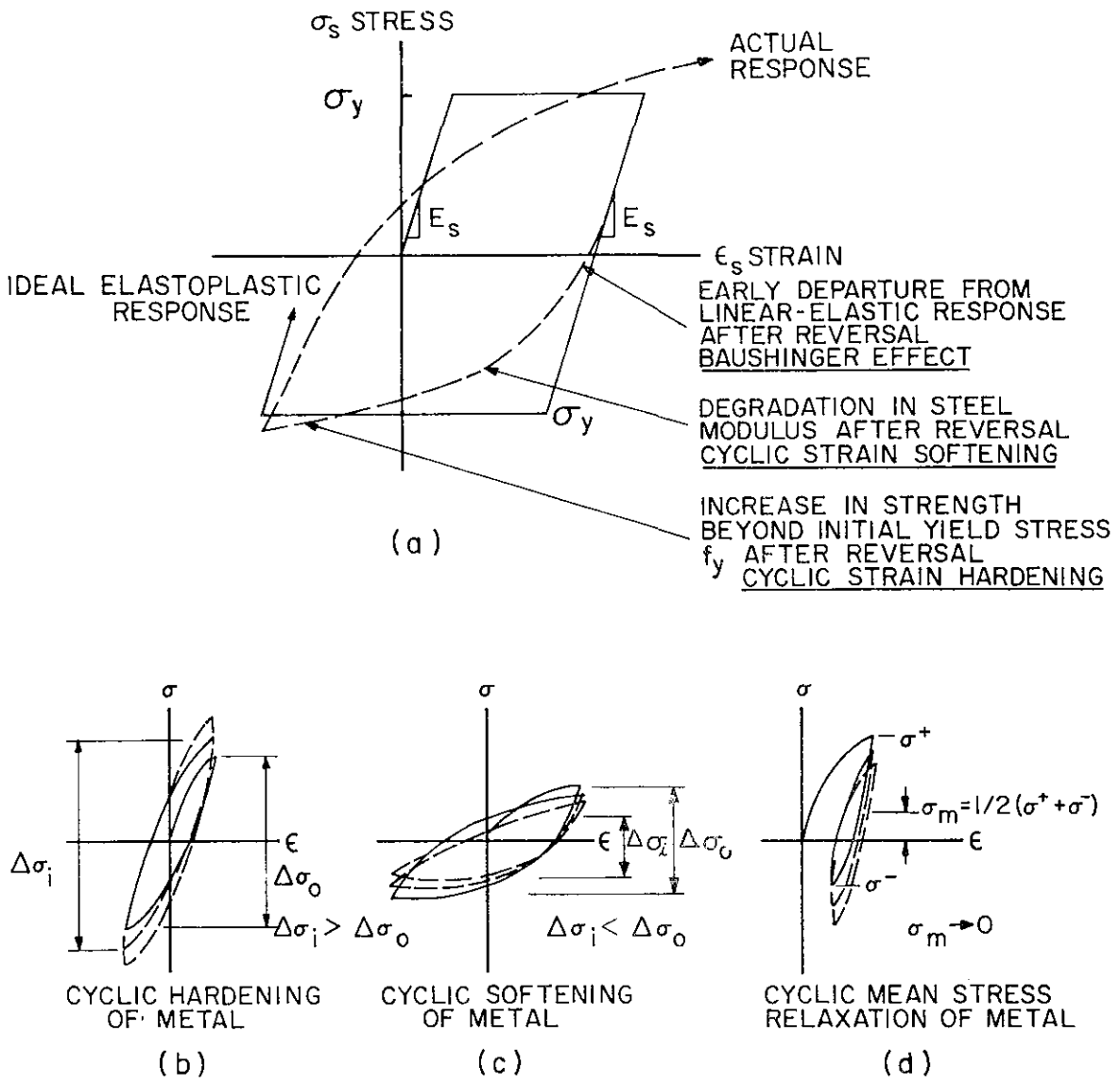

FIG. A5.3 DEFINITION OF TERMS CHARACTERIZING STRESS-STRAIN HYSTERETIC BEHAVIOR OF REINFORCING STEEL

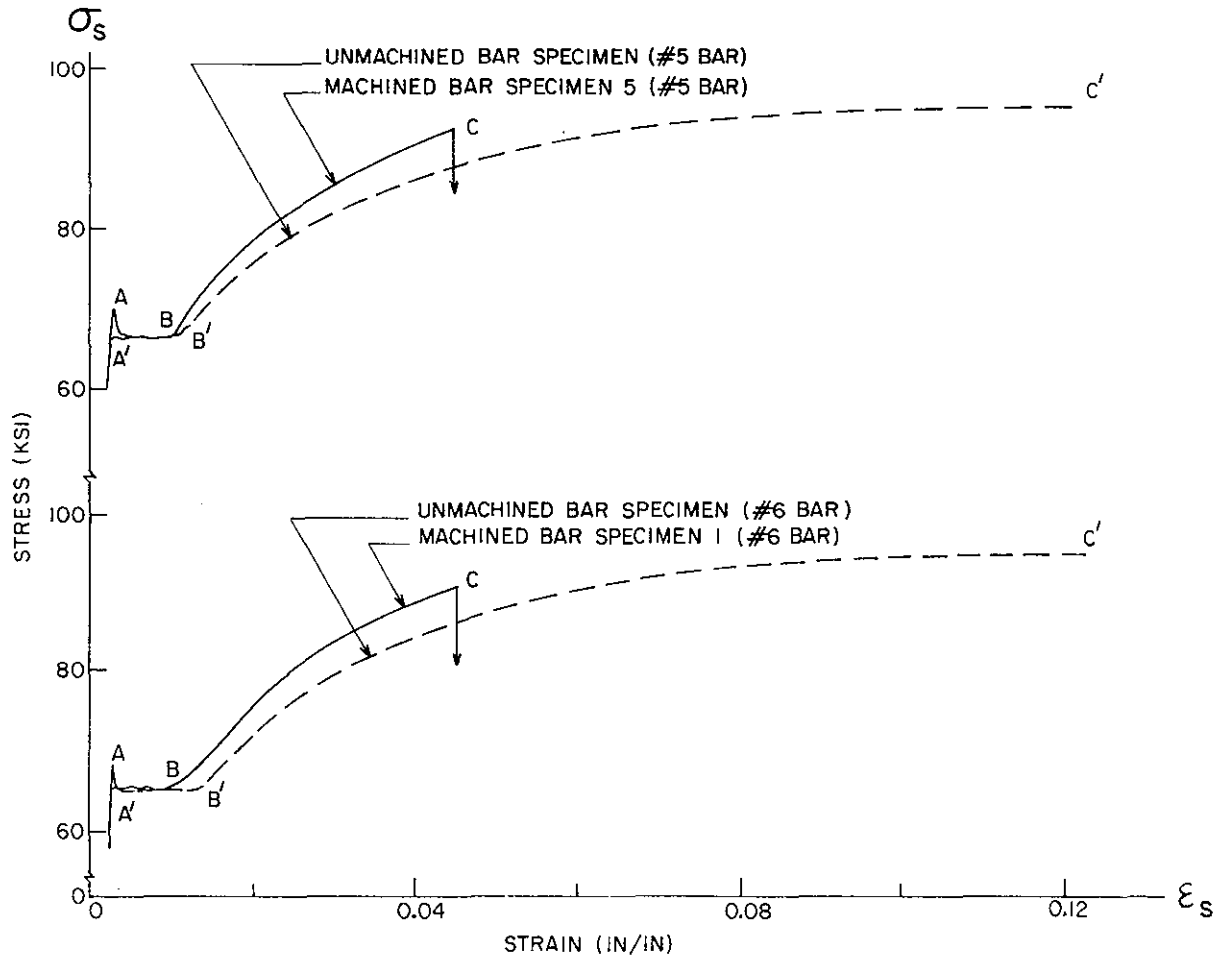

FIG. A5.4 COMPARISON BETWEEN σ_s-ε_s CURVES OF MACHINED AND UNMACHINED REBAR SPECIMENS

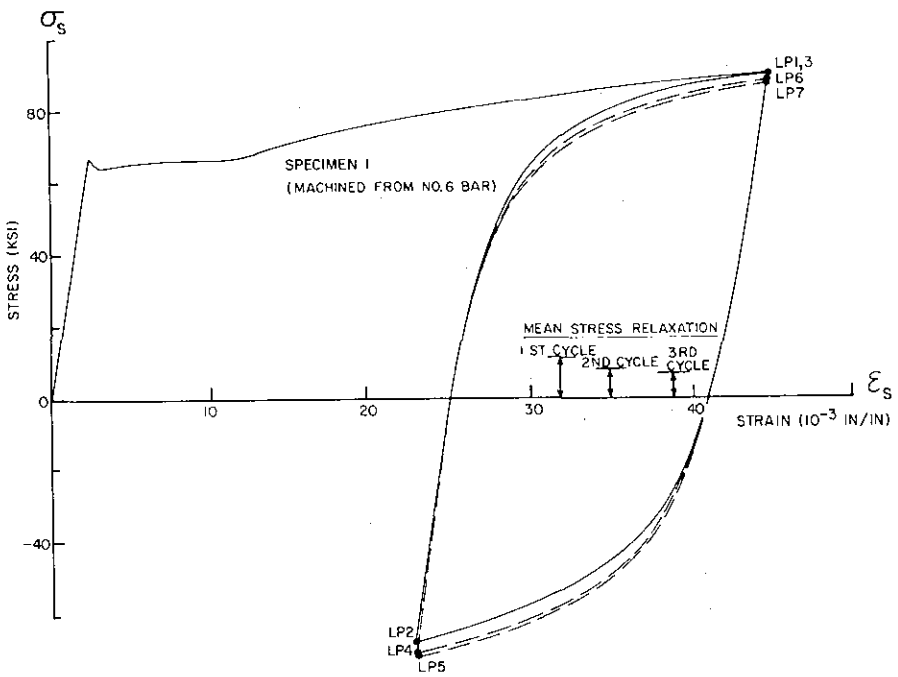

FIG. A5.5 HYSTERETIC σ_s-ε_s DIAGRAM (SPECIMEN 1)

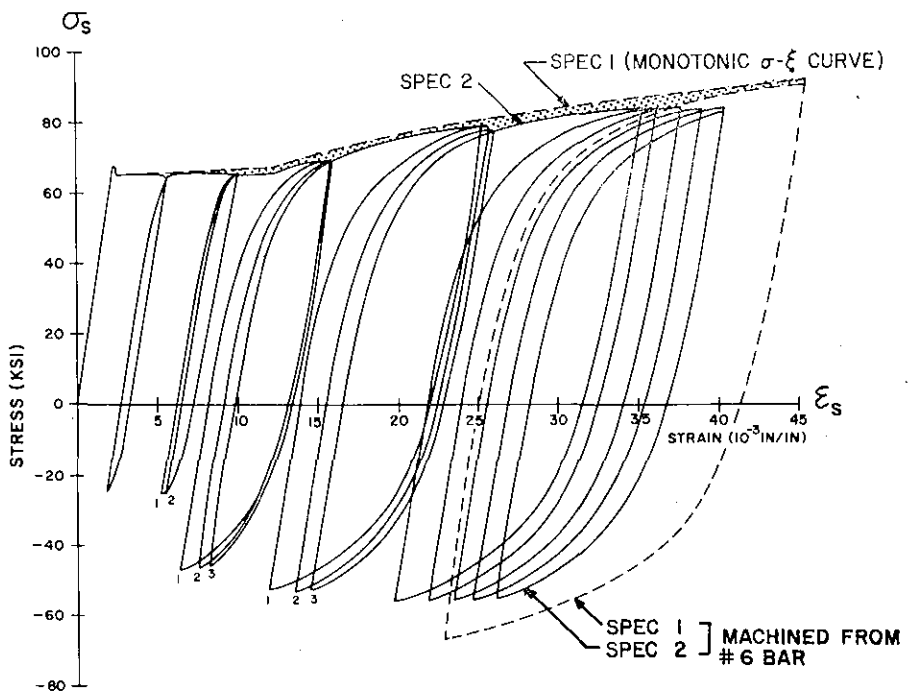

FIG. A5.6 HYSTERETIC σ_s-ε_s DIAGRAM (SPECIMENS 1 AND 2)

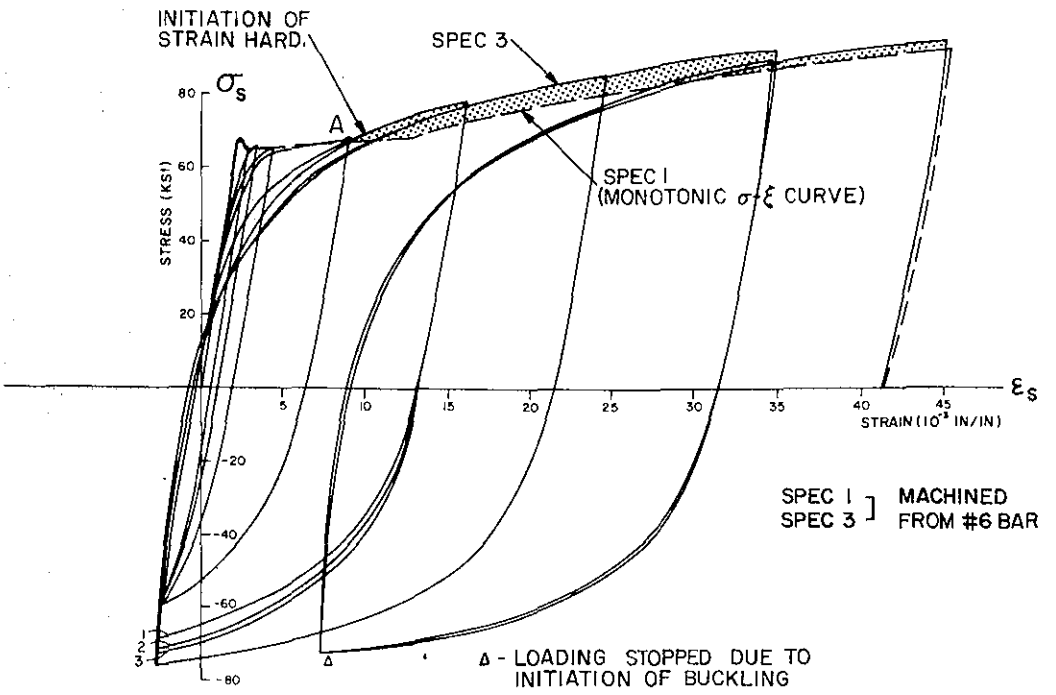

FIG. A5.7 HYSTERETIC σ-ε DIAGRAM (SPECIMENS 1 AND 3)

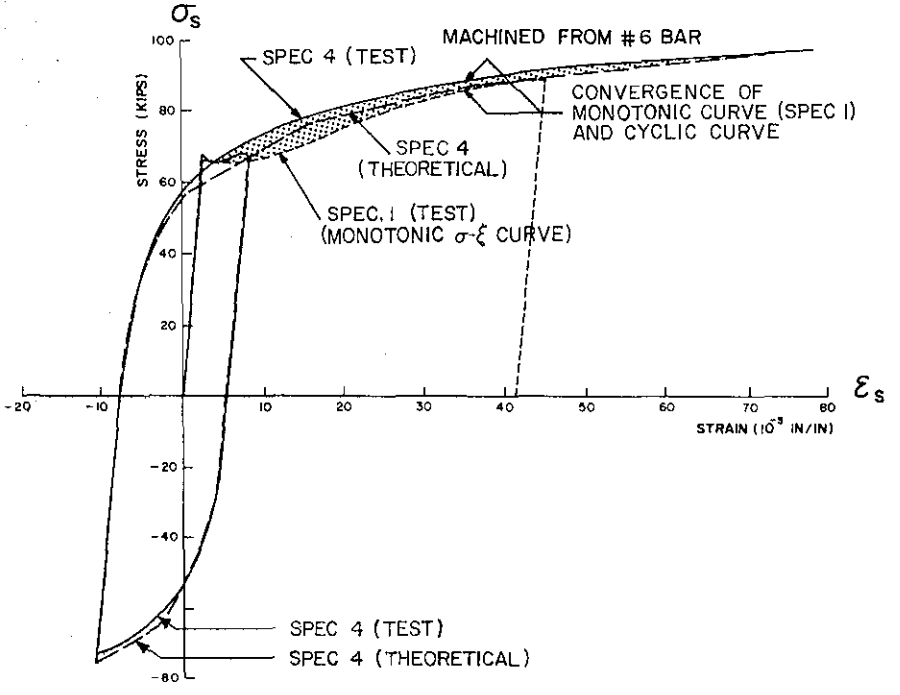

FIG. A5.8 HYSTERETIC σ_s-ε_s DIAGRAM (SPECIMEN 4)

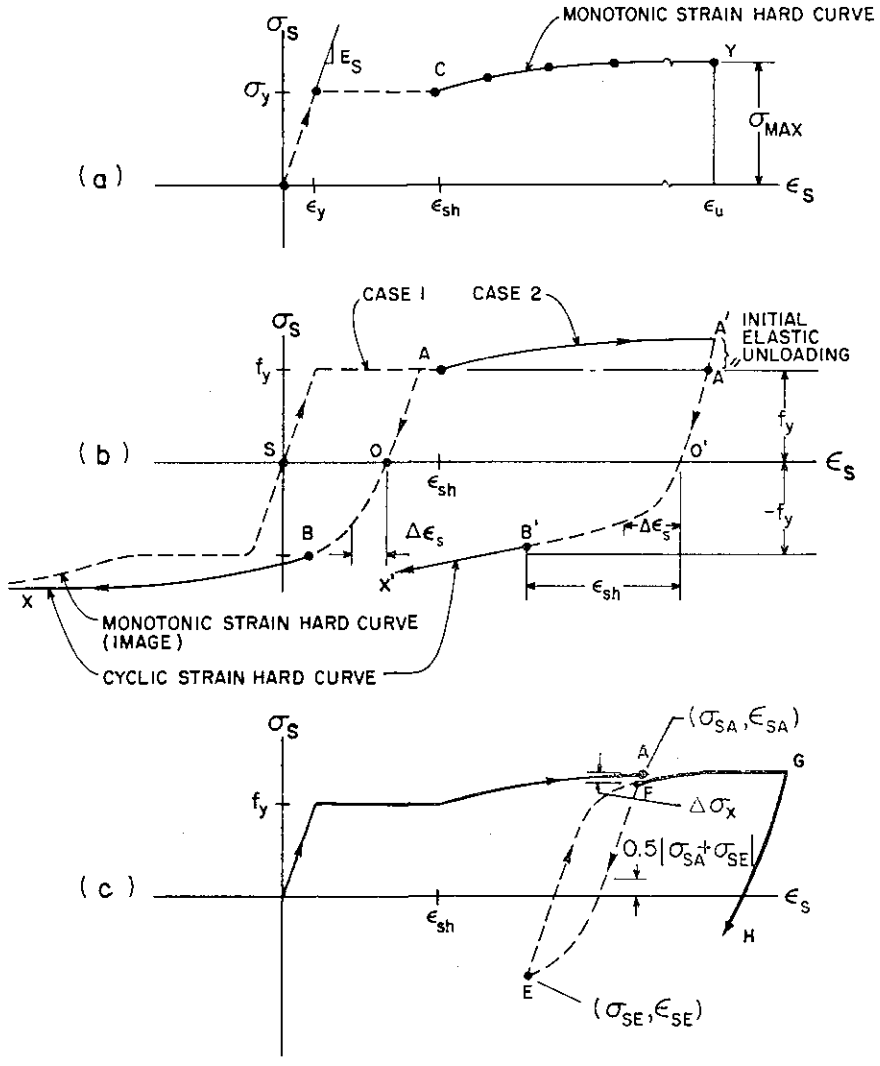

FIG. A5.9 CONSTRUCTION OF ANALYTICAL HYSTERETIC σ-ε RELATIONSHIP OF REINFORCING STEEL

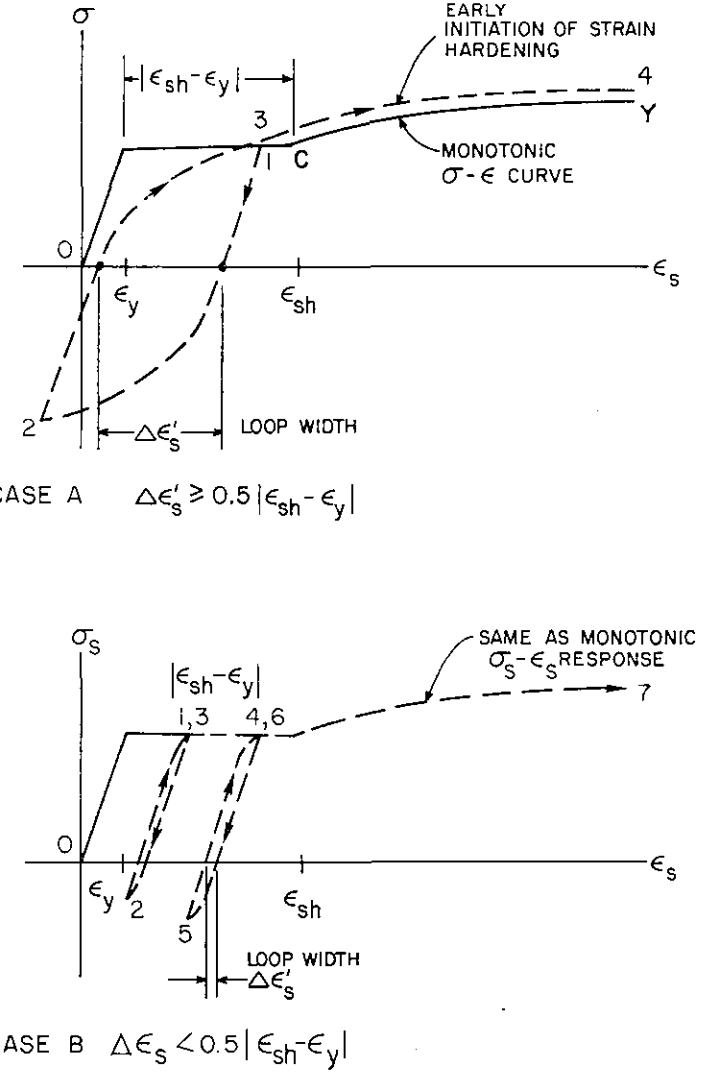

FIG. A5.10 STRAIN-HARDENING INITIATION FOR REVERSALS CARRIED OUT IN PLASTIC PLATEAU RANGE (REINFORCING STEEL σ_s-ε_s HYSTERETIC MODEL)

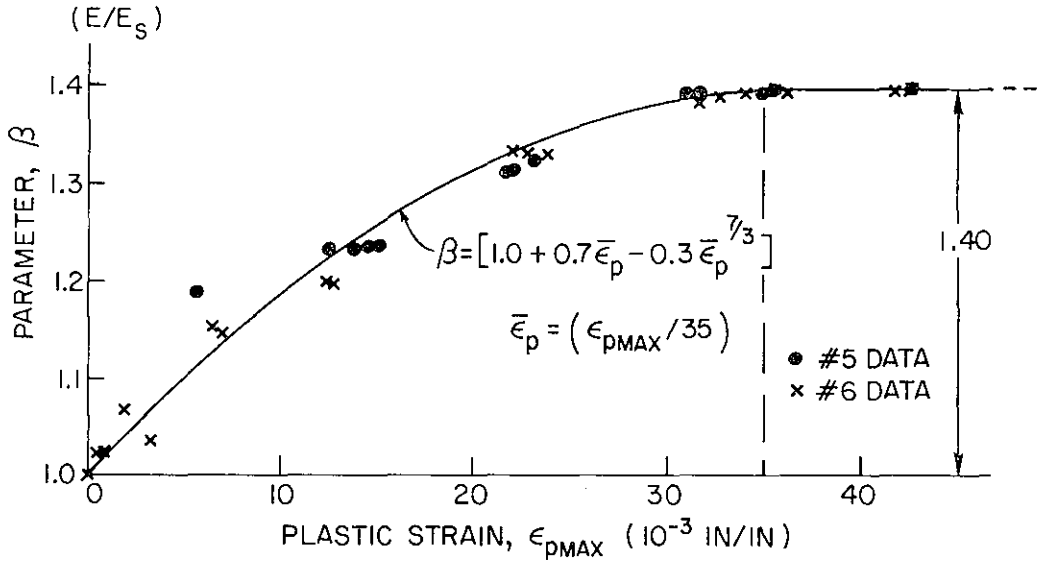

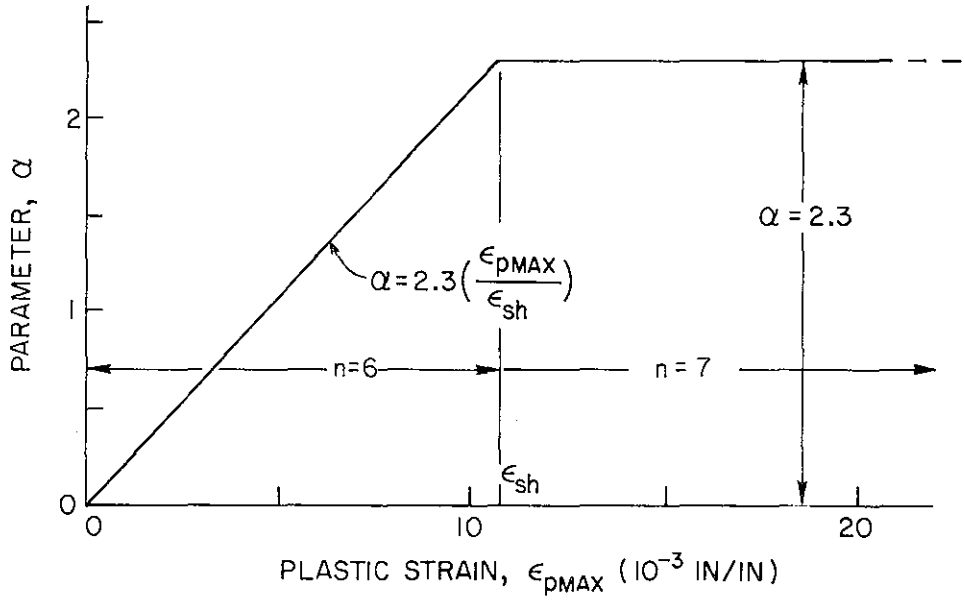

FIG. A5.11 ASSUMED RELATIONSHIP BETWEEN RAMBERG-OSGOOD FUNCTION PARAMETERS (n, α, β) AND MAXIMUM PLASTIC STRAIN (εpmax)

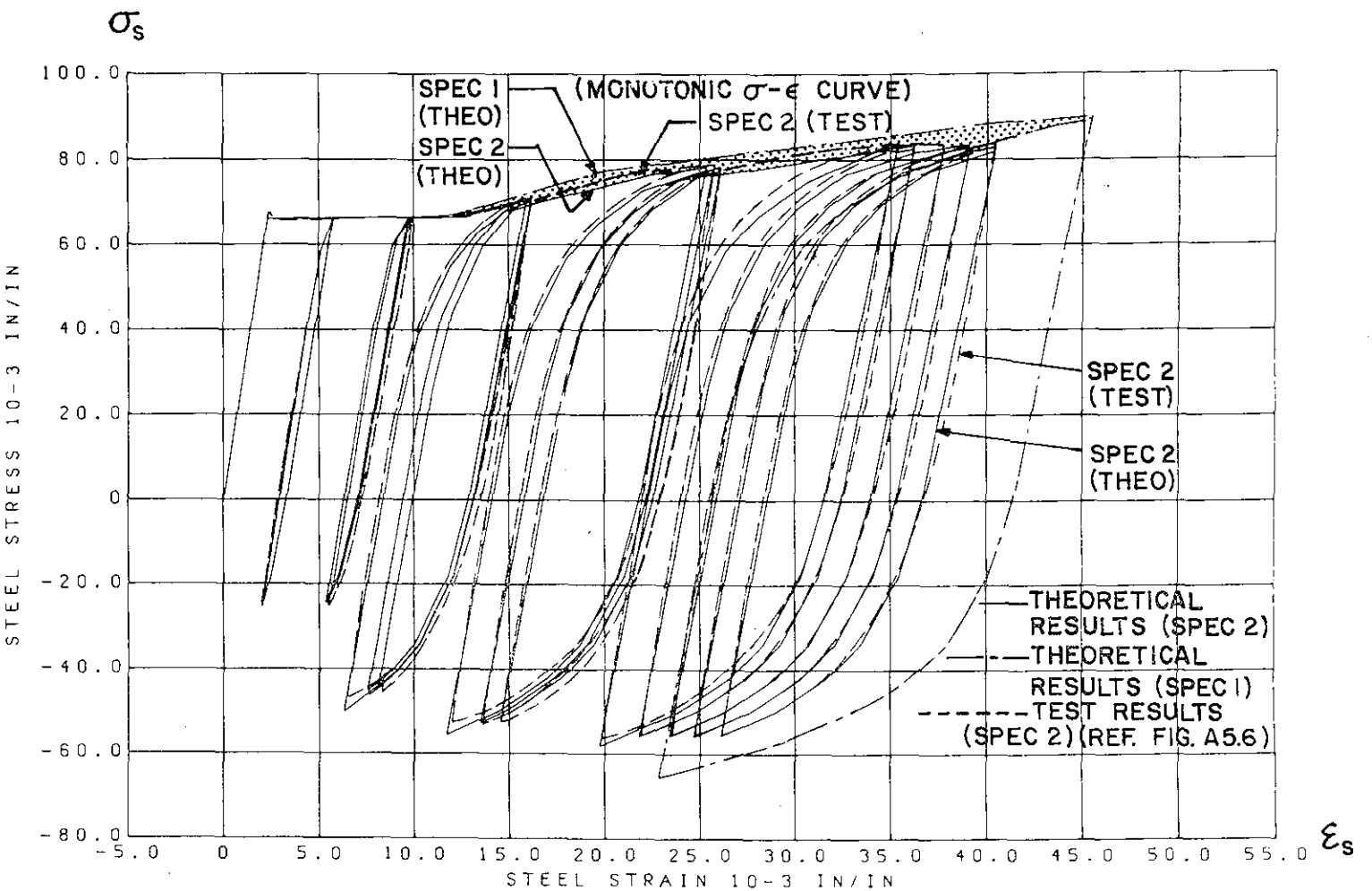

FIG. A5.12 COMPARISON OF PREDICTED AND EXPERIMENTAL σ_s-ε_s HYSTERETIC LOOPS (SPECIMEN 2)

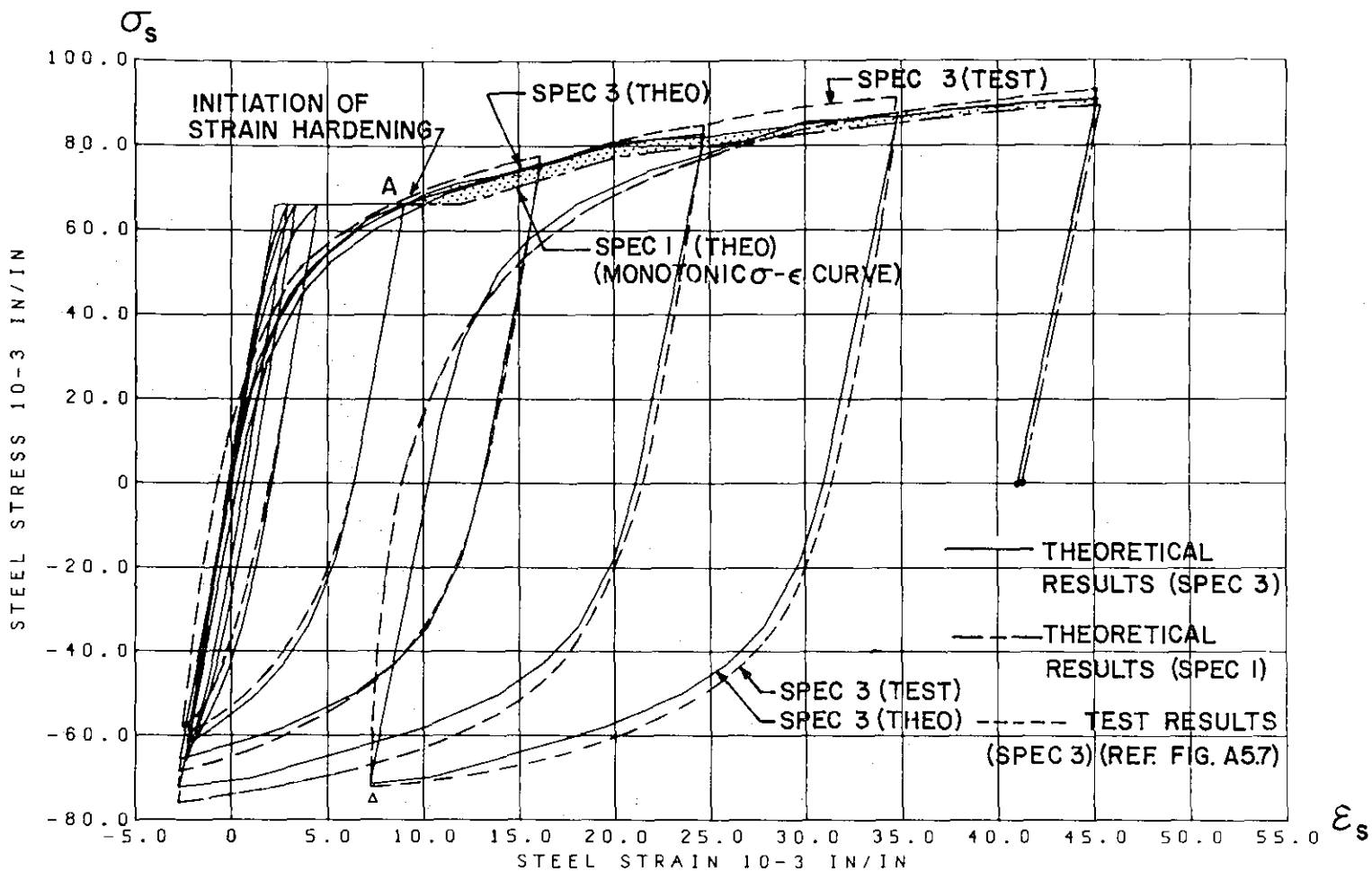

FIG. A5.13 COMPARISON OF PREDICTED AND EXPERIMENTAL σ_s-ε_s HYSTERETIC LOOPS (SPECIMEN 3)

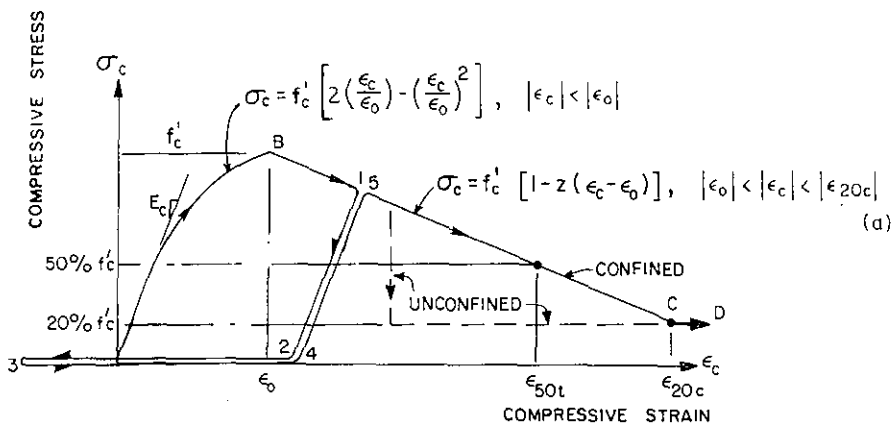

(a)

FIG. A5.14(a) PROPOSED MODEL FOR σ_c-ε_c RELATIONSHIP OF CONFINED AND UNCONFINED CONCRETE UNDER GENERALIZED (CYCLIC) ACTIONS

(b)

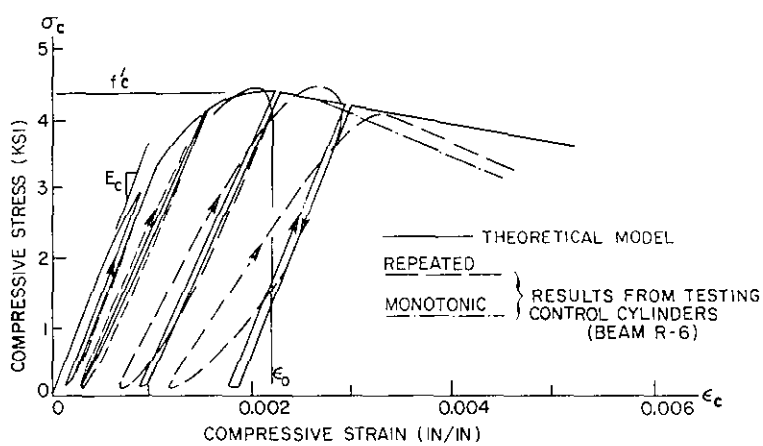

(c)

FIG. A5.14(b) COMPARISON BETWEEN THEORETICAL AND MEASURED CONCRETE σ_c-ε_c RESPONSE UNDER REPEATED LOADING

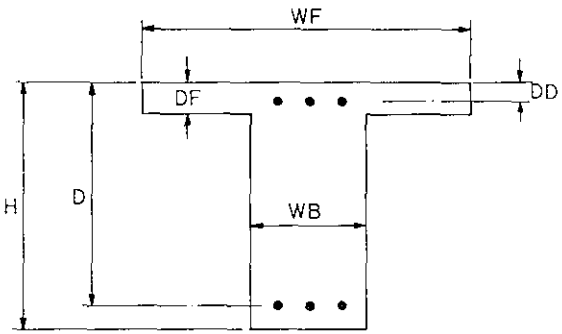

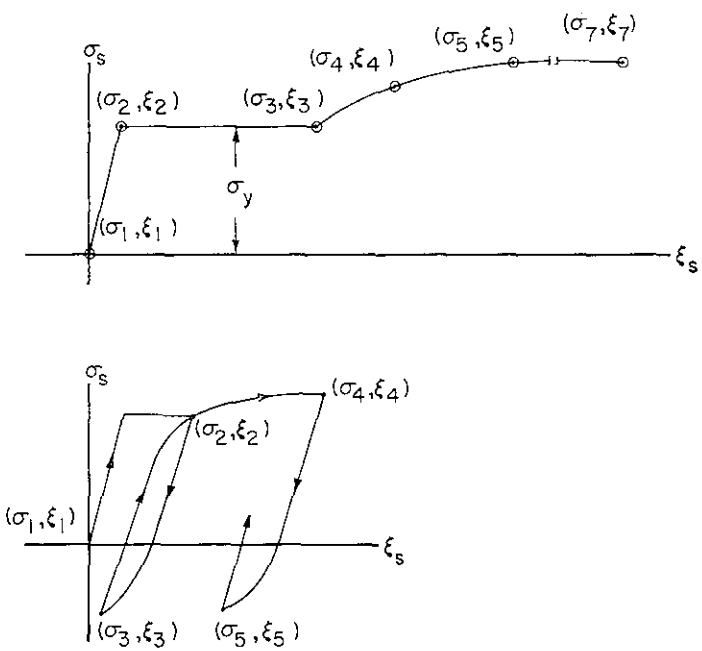

FIG. A5.15 INPUT PARAMETERS (COMPUTER PROGRAMS CYCMC AND BAUSH)

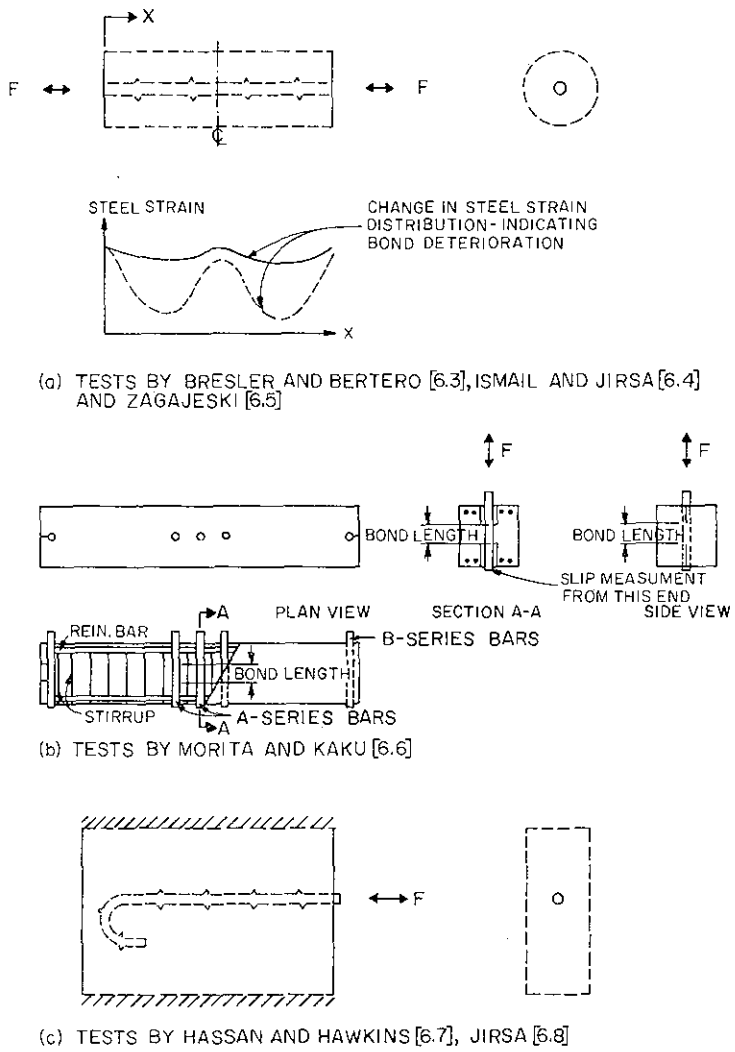

FIG. 6.1 TESTS ON BOND DETERIORATION UNDER CYCLIC LOADING

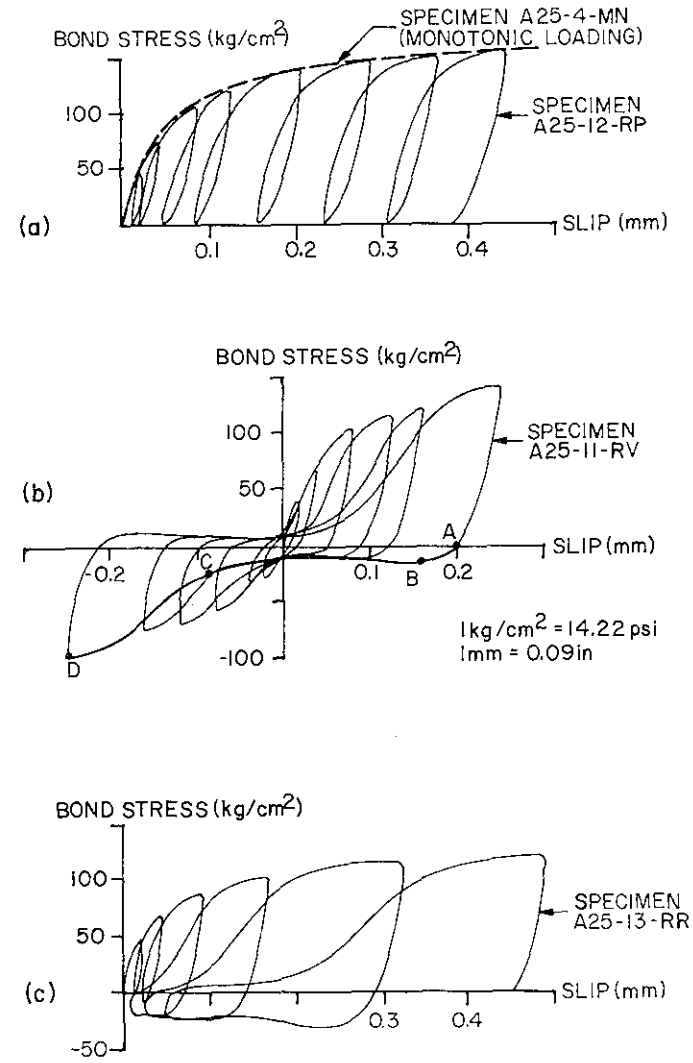

FIG. 6.2 BOND STRESS-SLIP RELATIONSHIPS FROM MORITA AND KAKU'S TESTS [6.6]

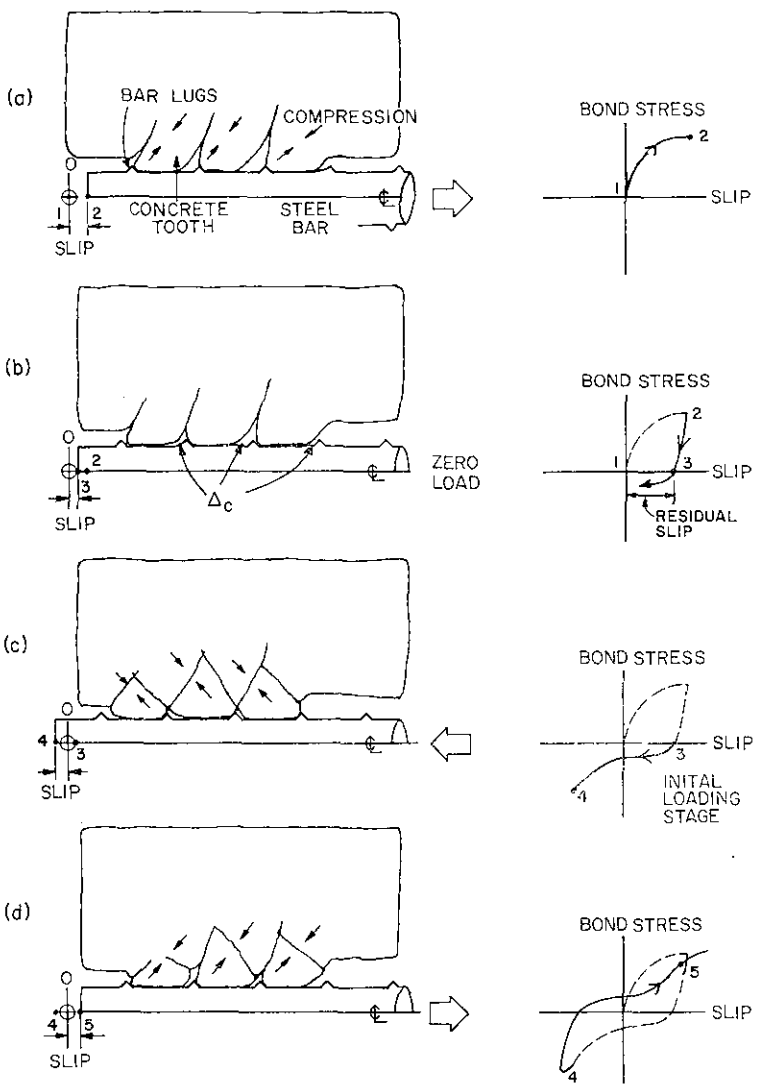

FIG. 6.3 MECHANISMS OF BOND RESISTANCE

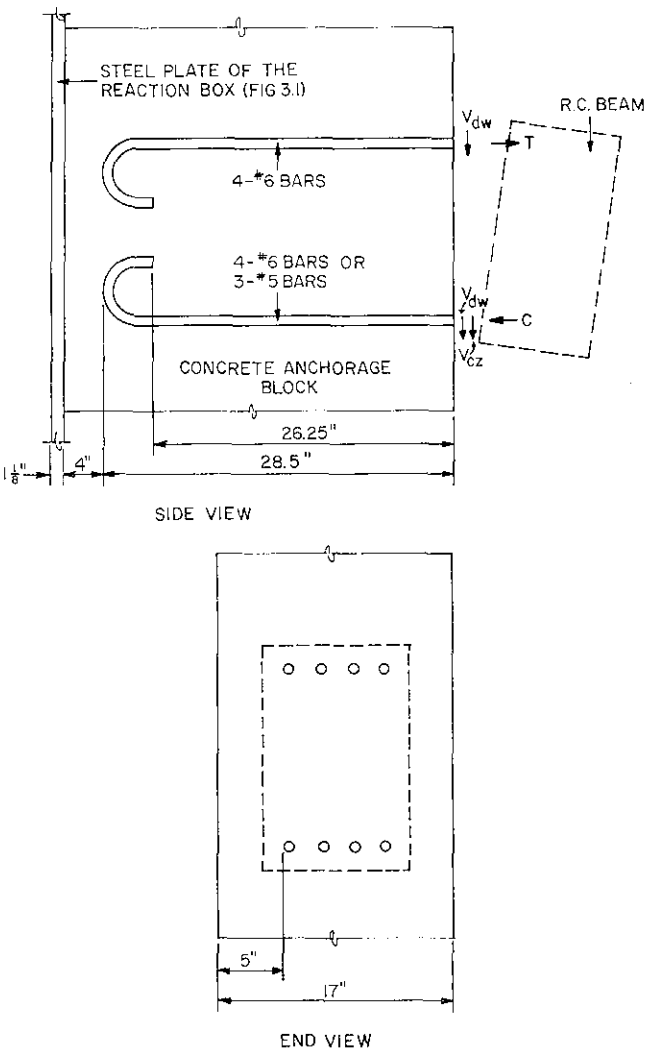

FIG. 6.4 ARRANGEMENT AND LOADING OF ANCHORED BAR

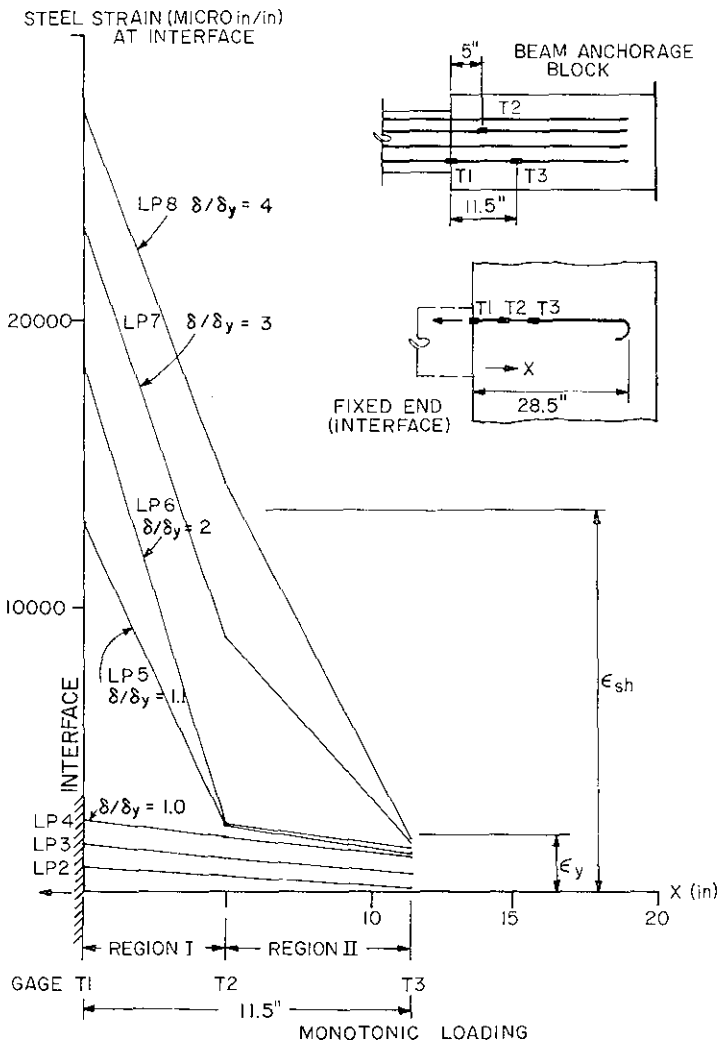

FIG. 6.5 STRAIN VARIATION ALONG ANCHORED LONGITUDINAL REINFORCEMENT - TOP #6 STEEL (BEAM T-2)

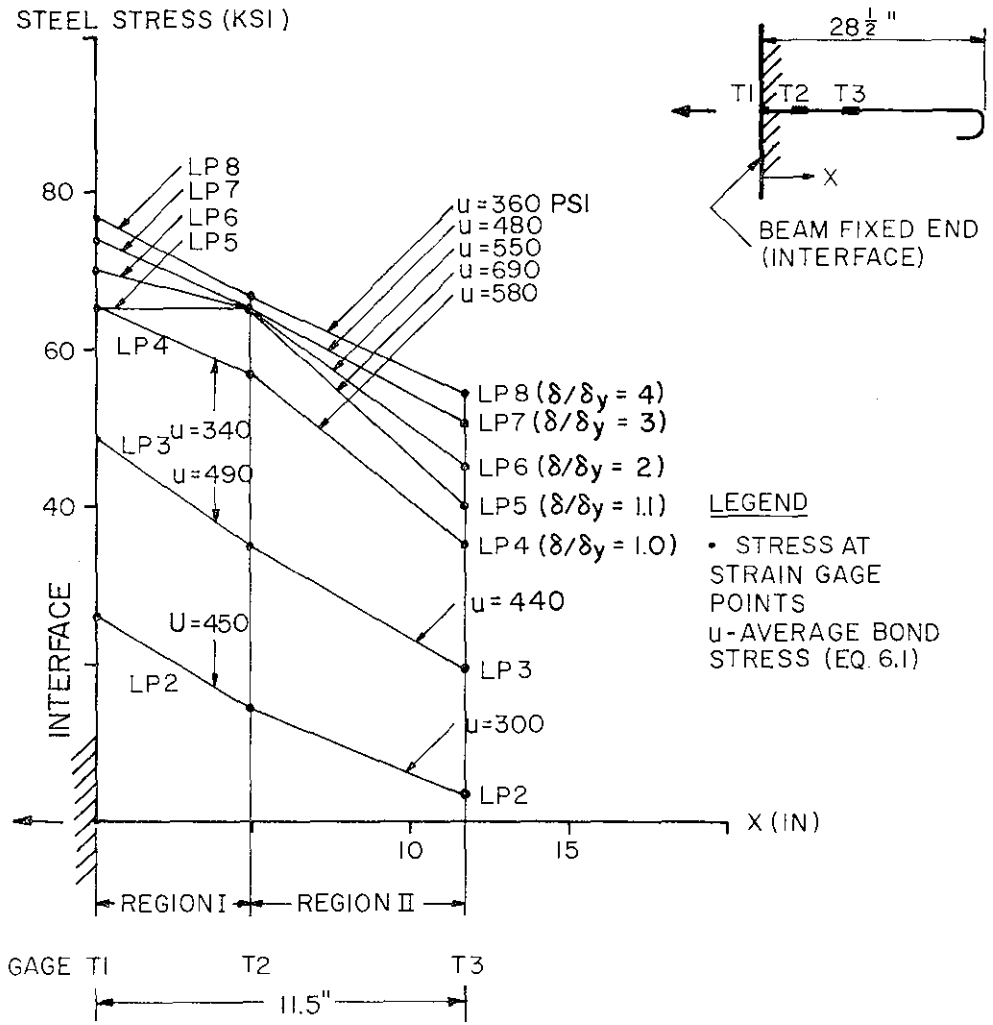

FIG. 6.6 STRESS VARIATION ALONG ANCHORED TOP REINFORCEMENT - #6 BAR (BEAM T-2)

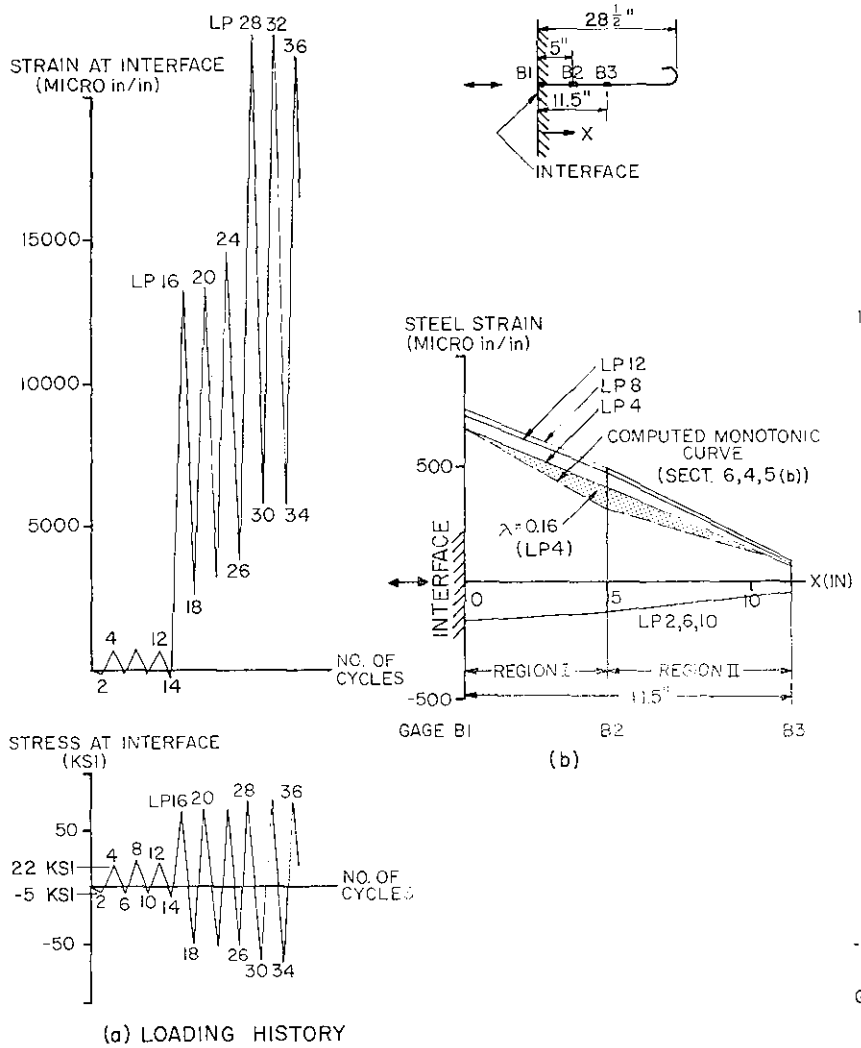

FIG. 6.7 STRESS VARIATION ALONG ANCHORED BOTTOM REINFORCEMENT - #6 BAR (BEAM T-3)

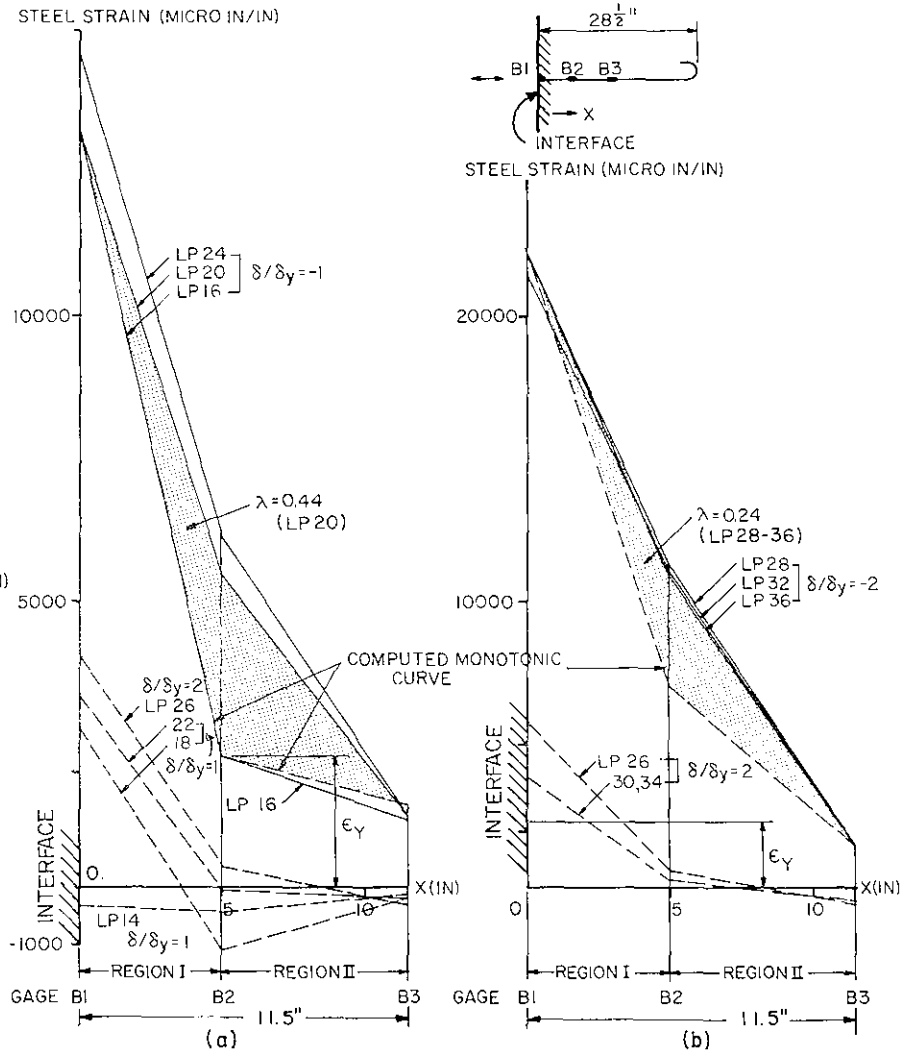

FIG. 6.8 STRAIN VARIATION ALONG ANCHORED BOTTOM REINFORCEMENT - #6 BAR (BEAM T-3)

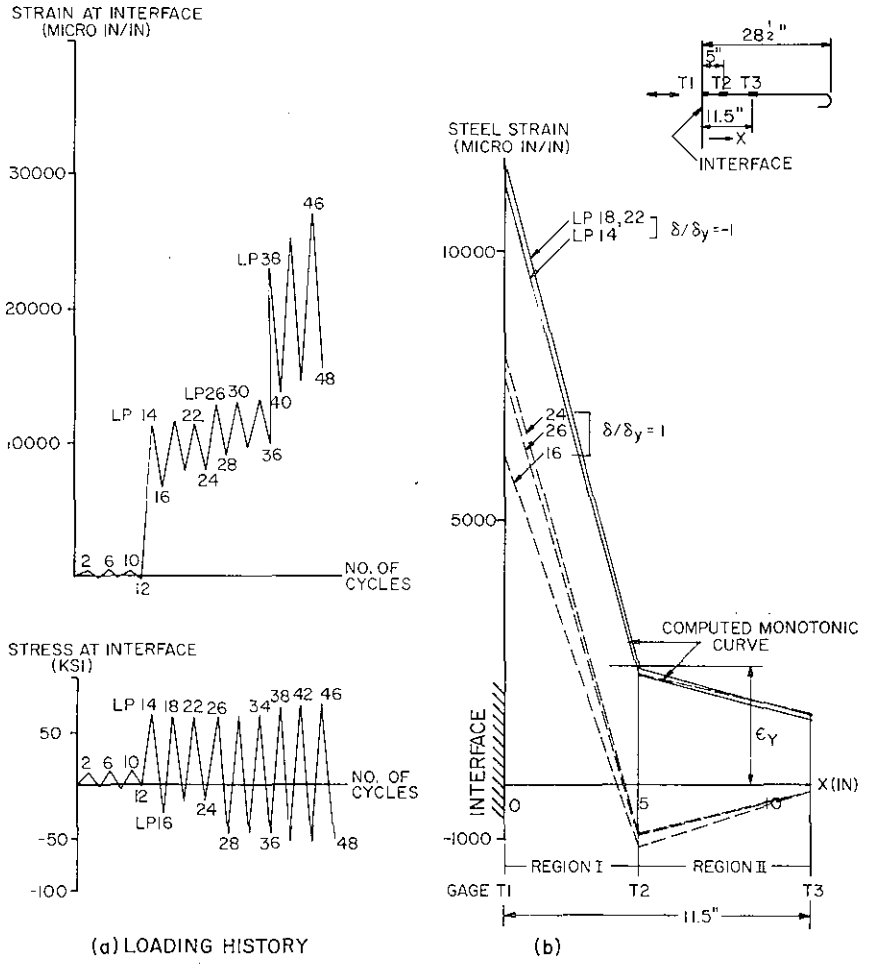

FIG. 6.9 STRESS VARIATION ALONG ANCHORED TOP REINFORCEMENT - #6 BAR (BEAM T-3)

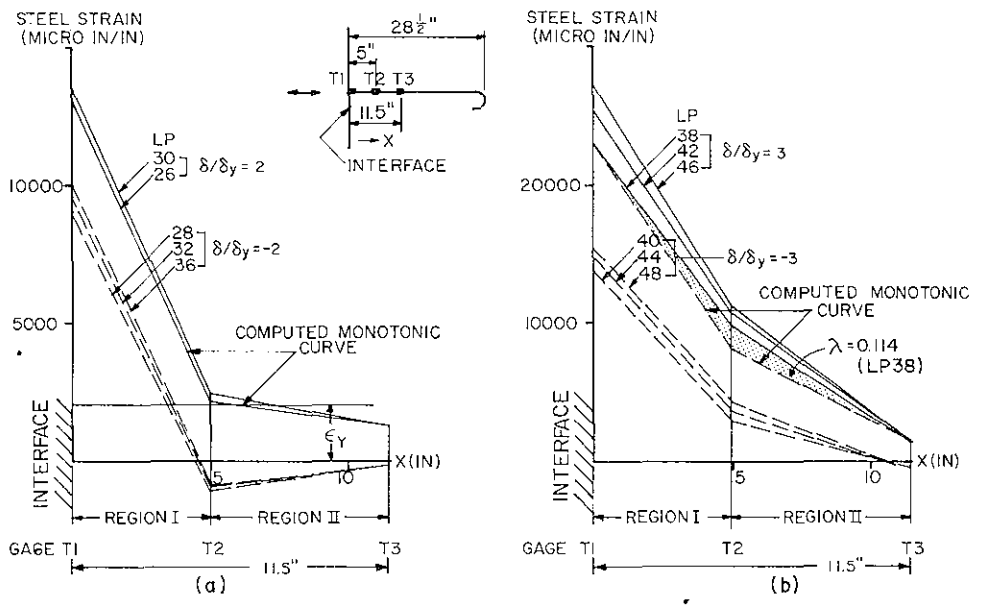

FIG. 6.10 STRAIN VARIATION ALONG ANCHORED TOP REINFORCEMENT - #6 BAR (BEAM T-3)

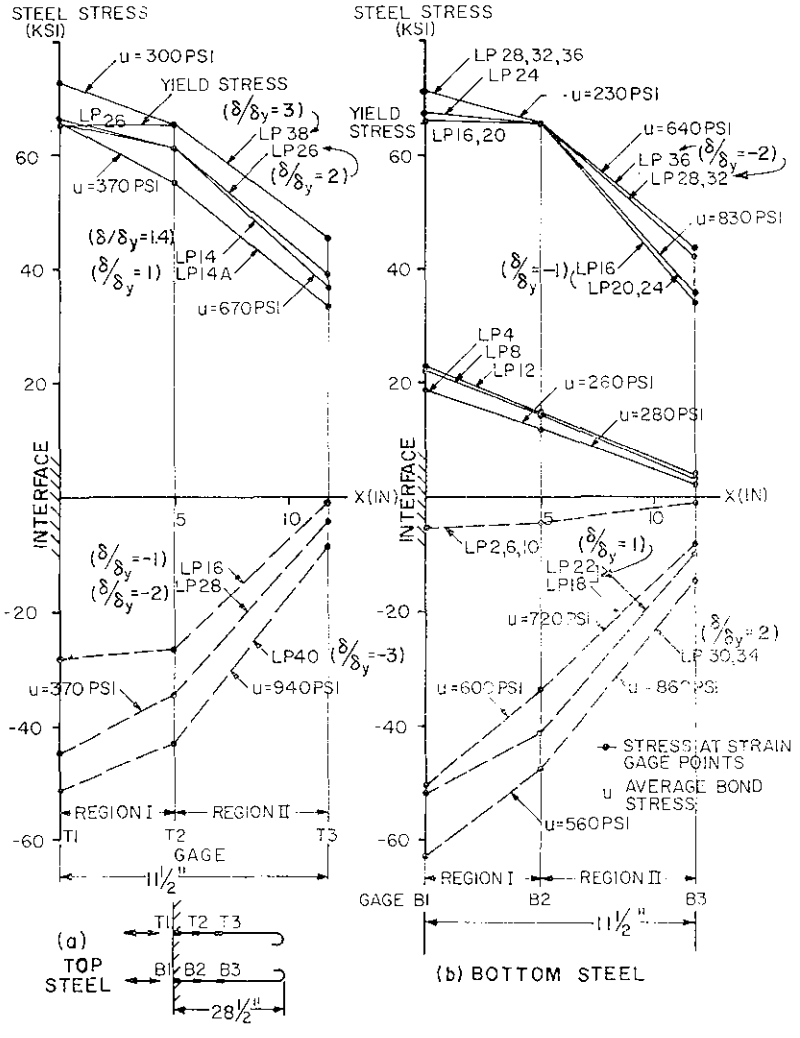

FIG. 6.11 STRESS VARIATION ALONG ANCHORED LONGITUDINAL REINFORCEMENTS (BEAM T-3)

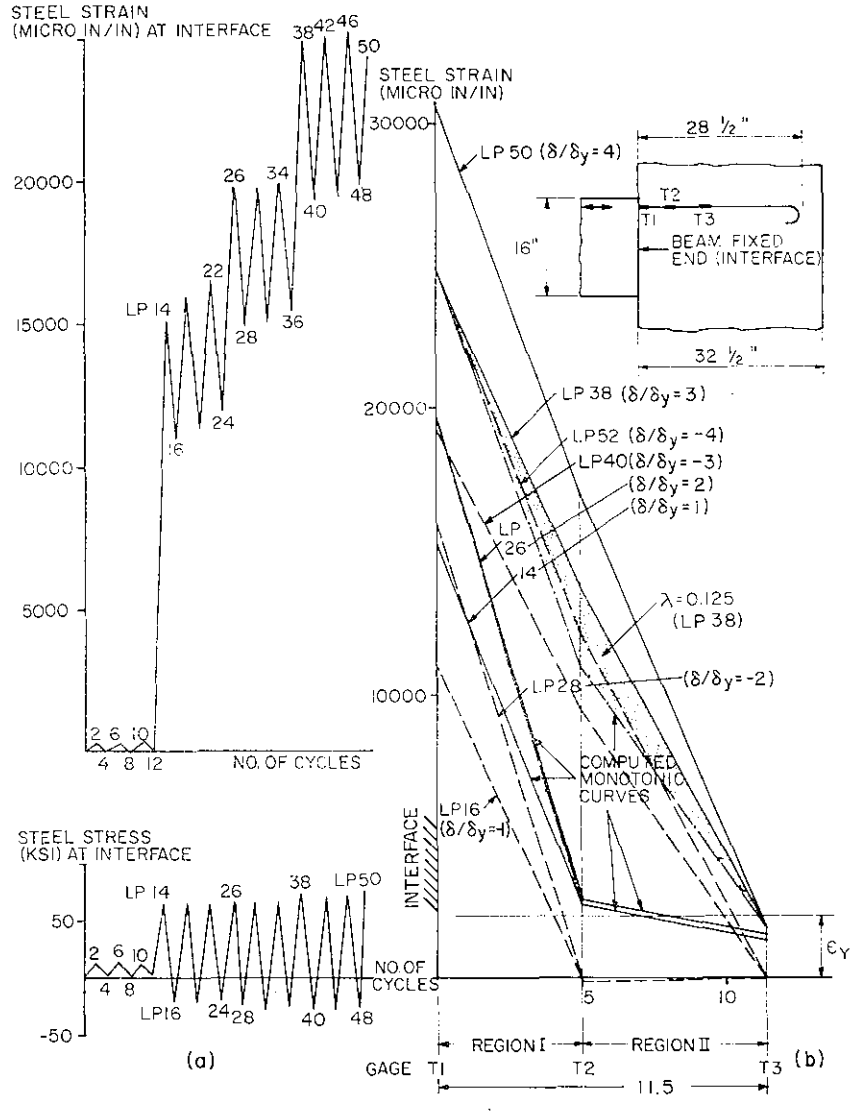

FIG. 6.12 STRAIN VARIATION ALONG ANCHORED LONGITUDINAL REINFORCEMENT - TOP #6 STEEL (BEAM T-1)

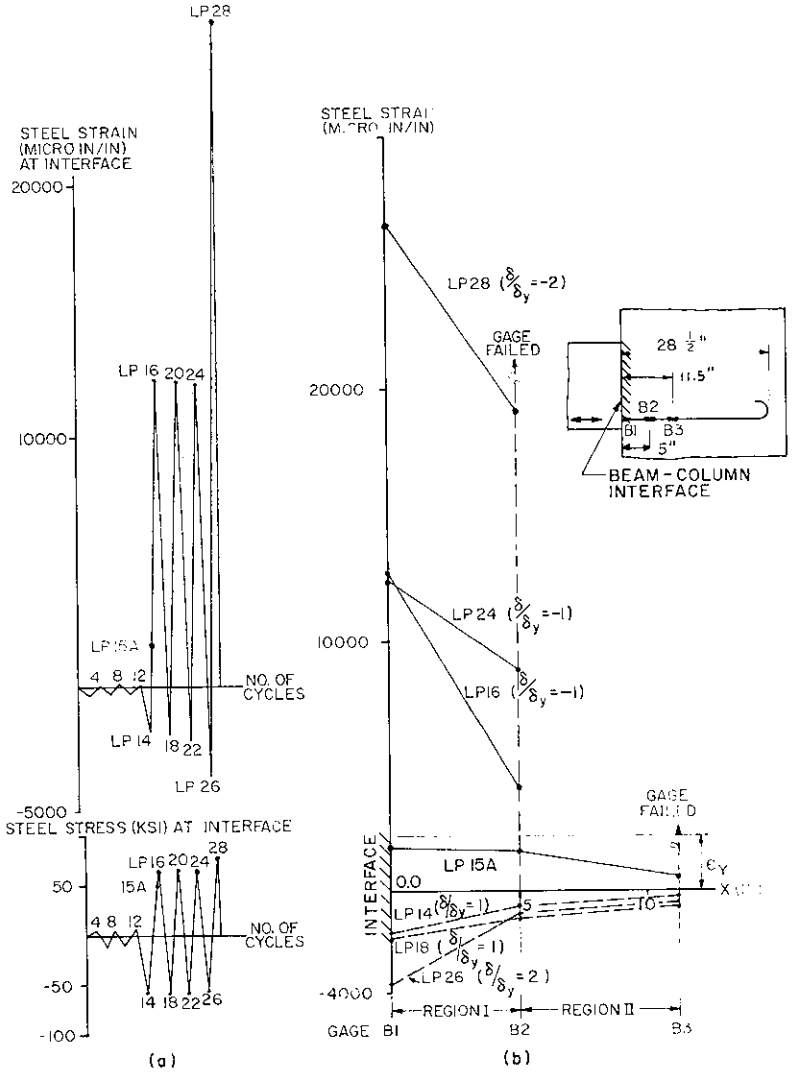

FIG. 6.13 STRAIN VARIATION ALONG ANCHORED LONGITUDINAL REINFORCEMENT - BOTTOM #5 STEEL (BEAM T-1)

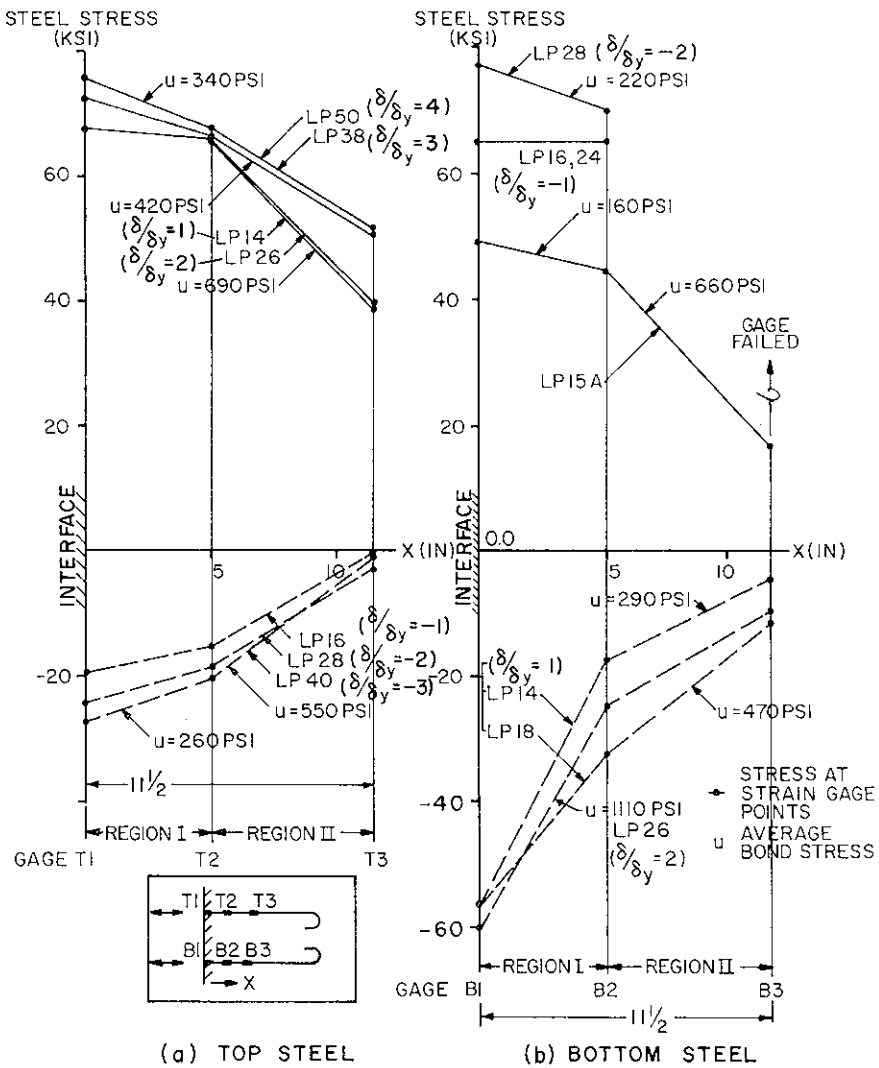

FIG. 6.14 STRESS VARIATION ALONG ANCHORED LONGITUDINAL REINFORCEMENT - (BEAM T-1)

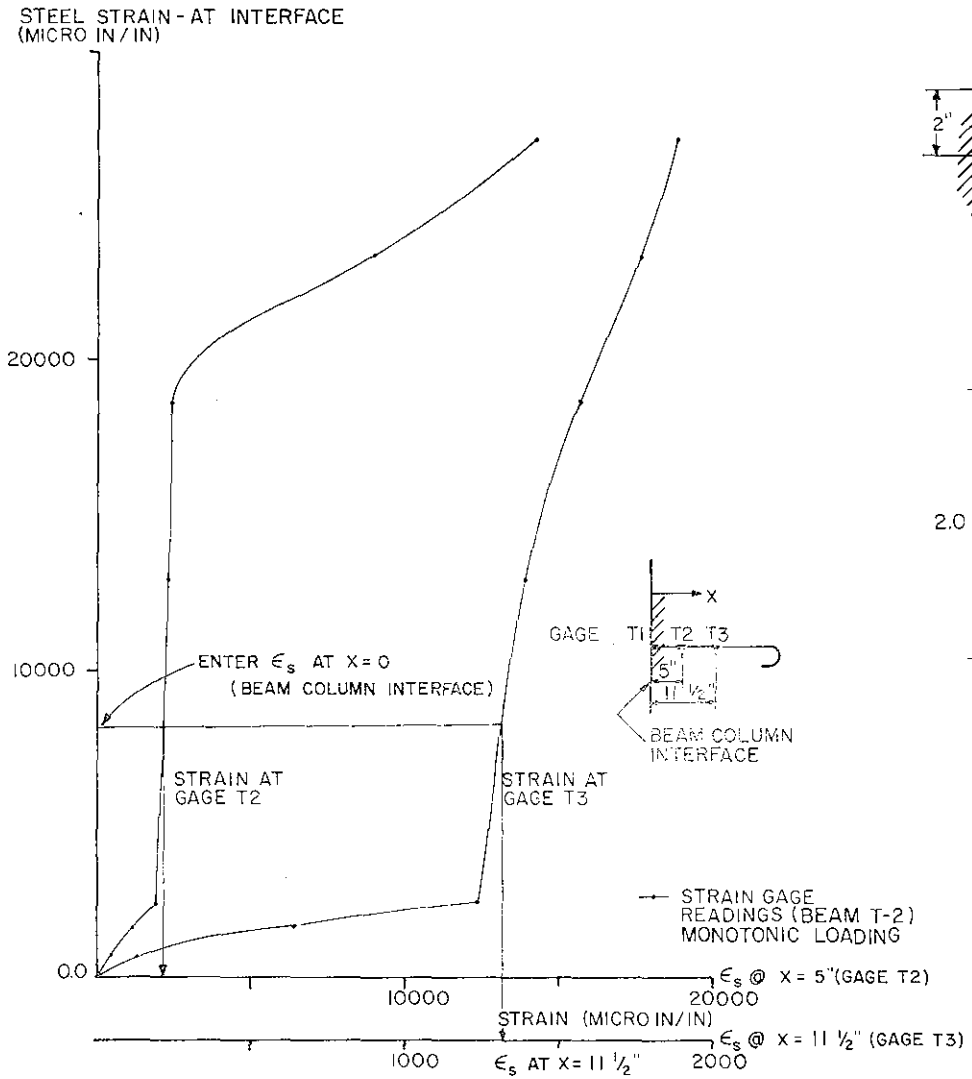

FIG. 6.15 METHOD OF ESTABLISHING STEEL STRAIN INSIDE ANCHORED #6 BAR UNDER MONOTONIC LOADING CONDITION

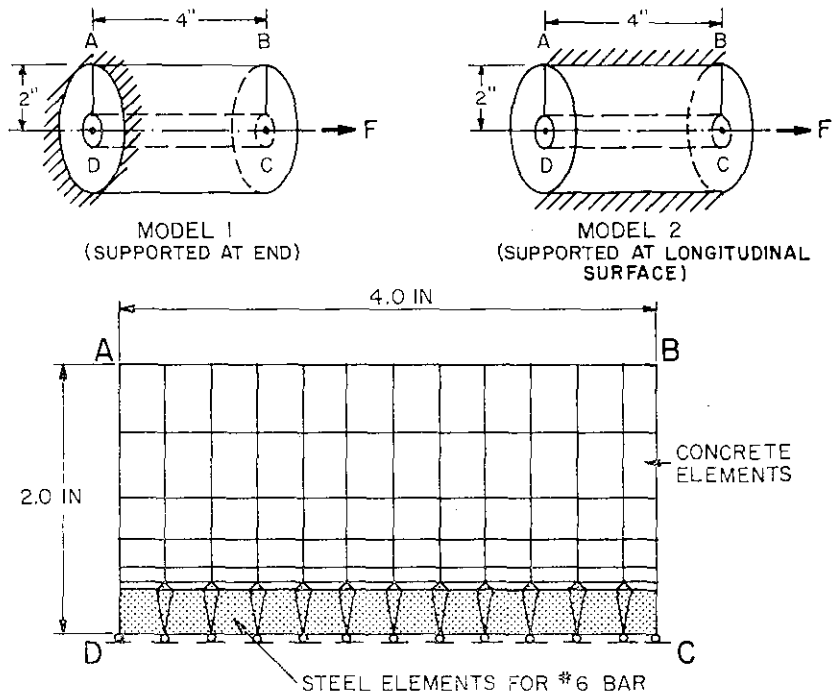

AXISYMMETRIC FINITE ELEMENT MESH

MATERIAL CHARACTERISTICS

ELASTIC MODULUS OF STEEL = 29100 KSI
POISSON'S RATIO OF STEEL = 0.30
CONCRETE COMPRESSION STRENGTH = 4610 PSI
CONCRETE CRACKING STRENGTH = 462 PSI
POISSON'S RATIO OF CONCRETE = 0.20
ELASTIC MODULUS OF CONCRETE = 3800 KSI
CONCRETE CRUSHING STRAIN = -0.005 IN/IN

FIG. A6.1 FINITE-ELEMENT MODEL FOR STUDYING BOND BETWEEN CONCRETE AND #6 BAR

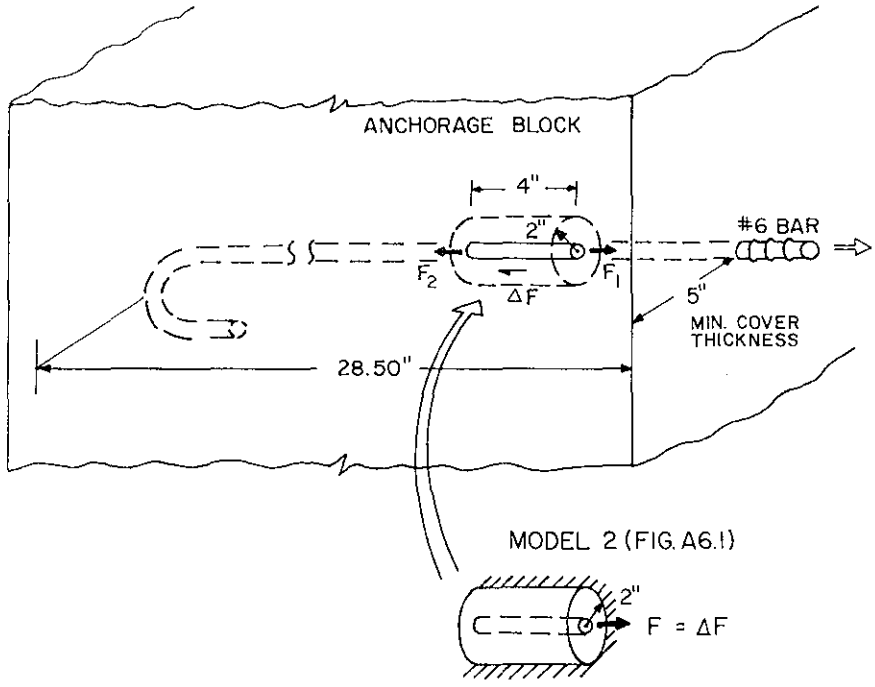

FIG. A6.2 MODEL USED FOR STUDYING CRACK DEVELOPMENT IN ANCHORED BAR

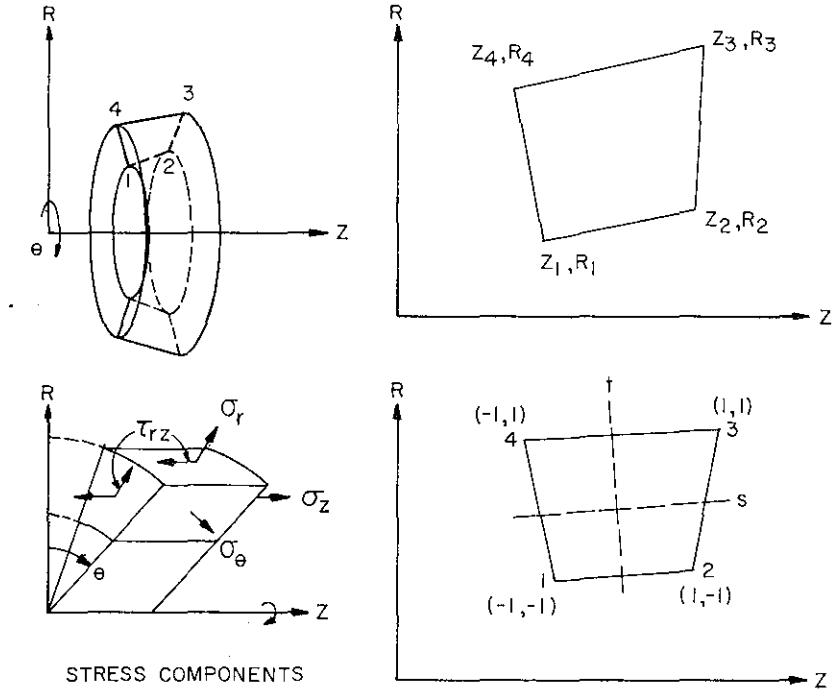

FIG. A6.3 QUADRILATERAL ISOPARAMETRIC AXISYMMETRIC ELEMENT

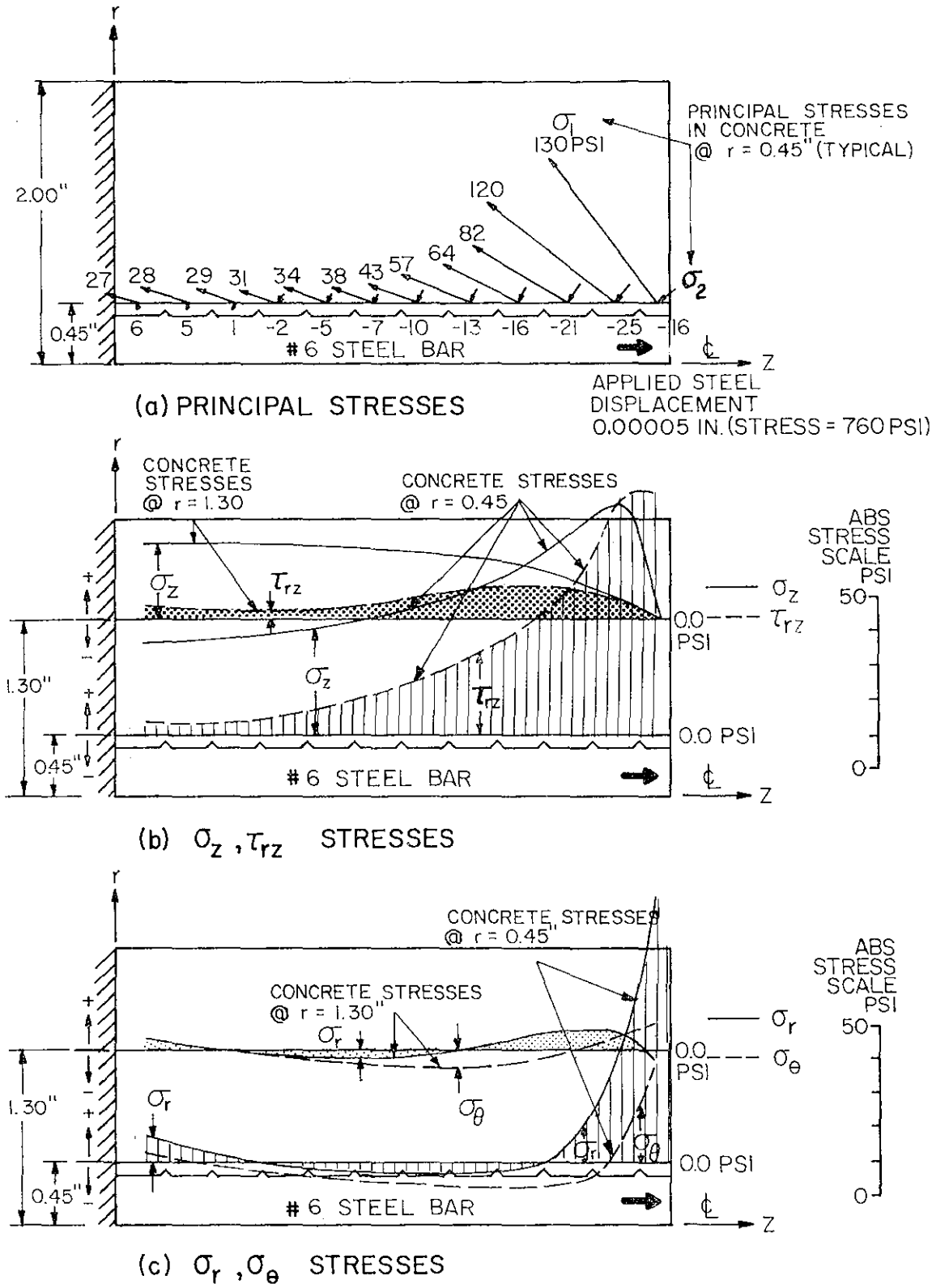

FIG. A6.4 LINEAR-ELASTIC FINITE ELEMENT ANALYSIS RESULTS (MODEL 1) - BOND STUDY

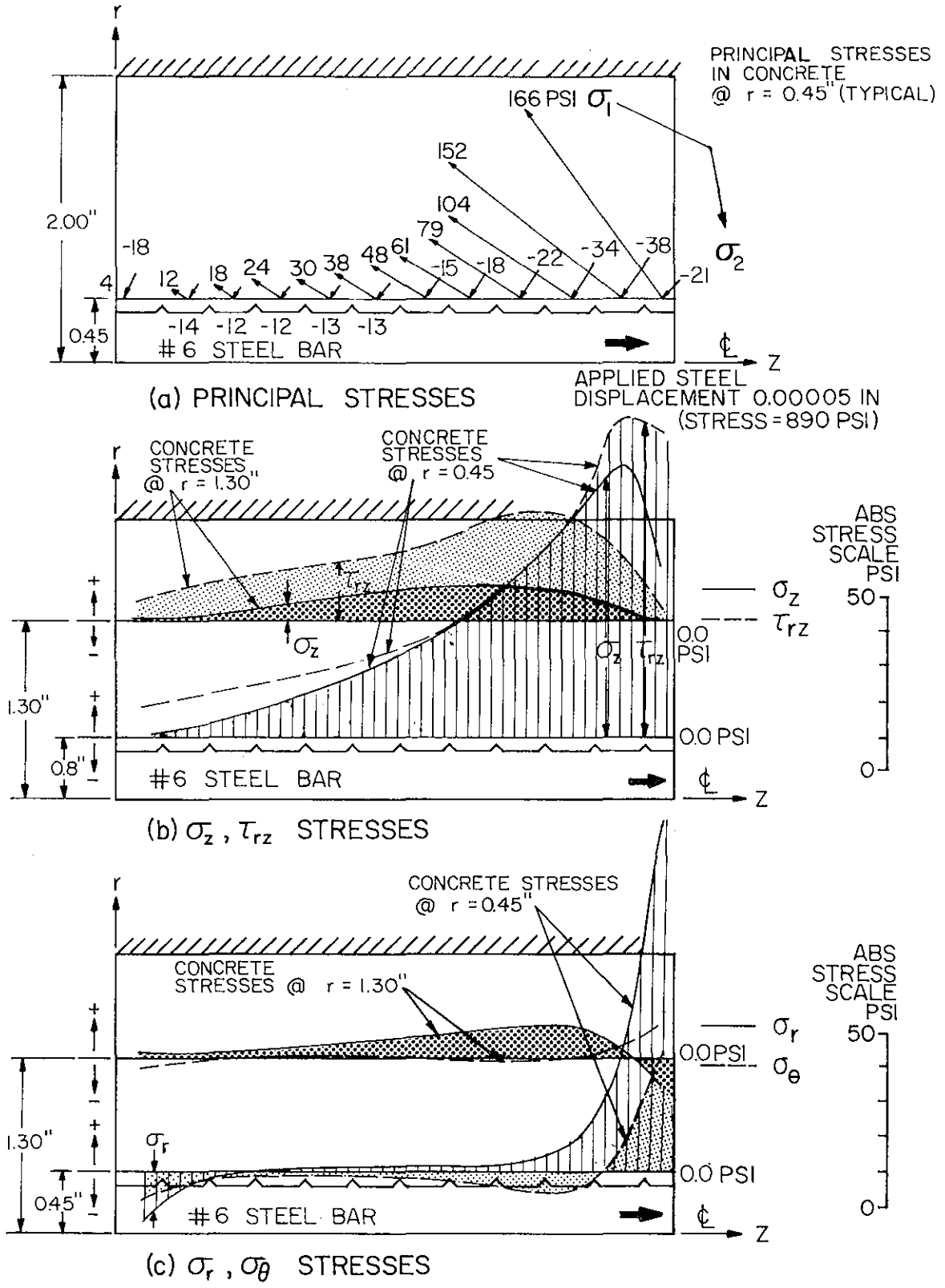

FIG. A6.5 LINEAR-ELASTIC FINITE ELEMENT ANALYSIS RESULTS (MODEL 2) - BOND STUDY

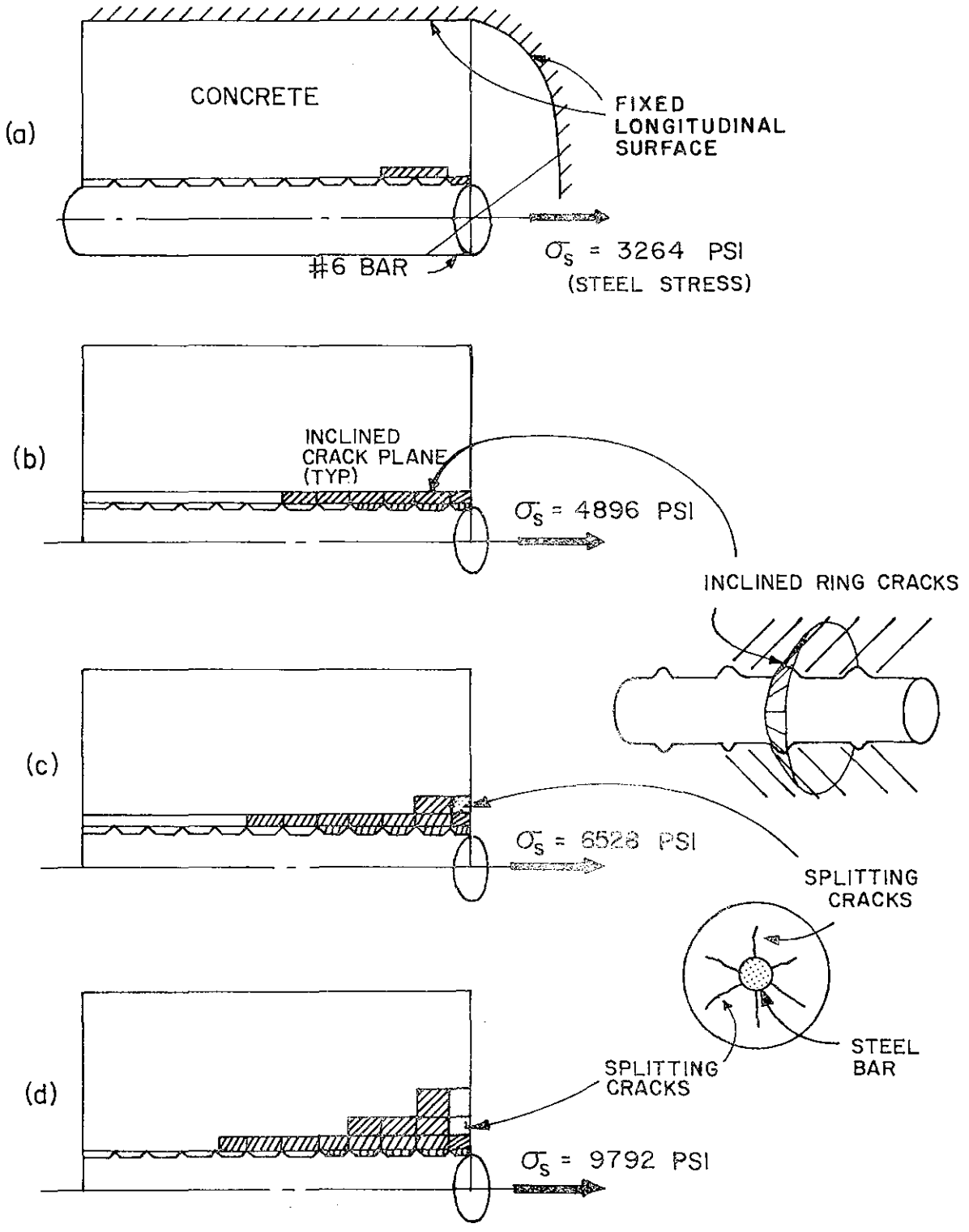

FIG. A6.6 CRACK DEVELOPMENT IN CONCRETE SURROUNDING #6 REBAR (MODEL 2) - FINITE ELEMENT ANALYSIS RESULTS

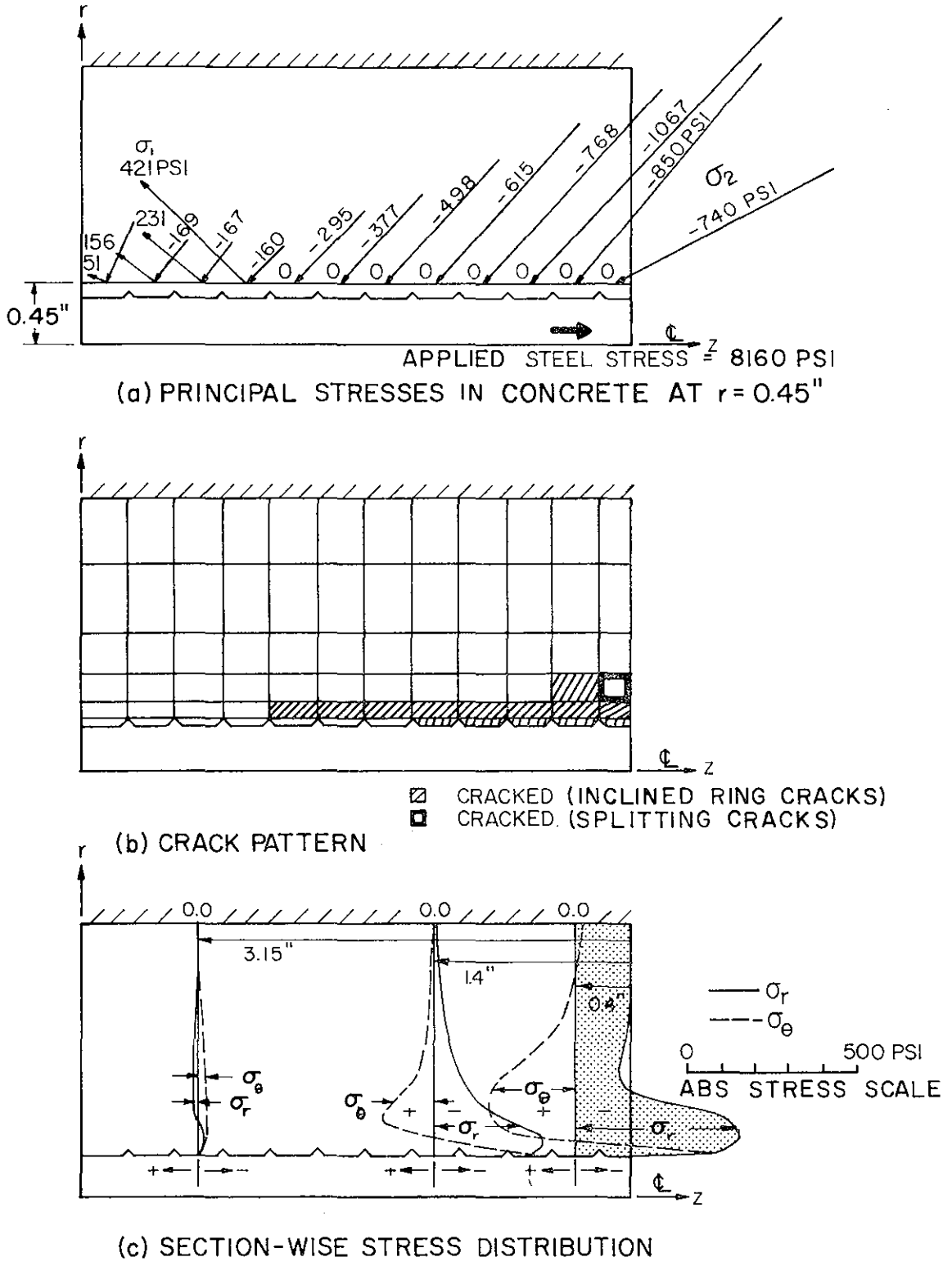

FIG. A6.7 NONLINEAR FINITE ELEMENT ANALYSIS RESULTS (MODEL 2) - BOND STUDY

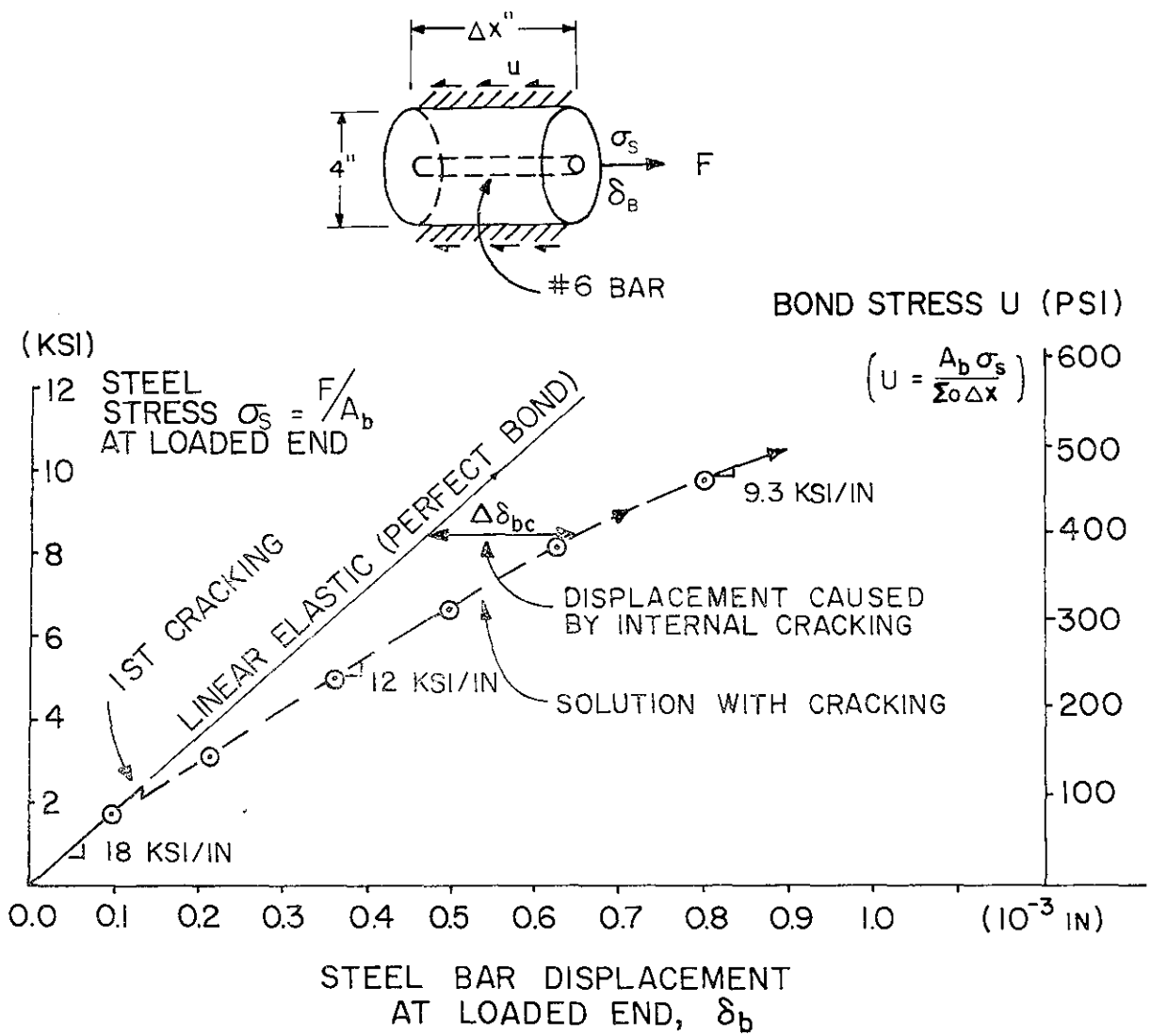

FIG. A6.8 APPLIED FORCE VS. BAR DISPLACEMENT - FINITE ELEMENT ANALYSIS RESULTS

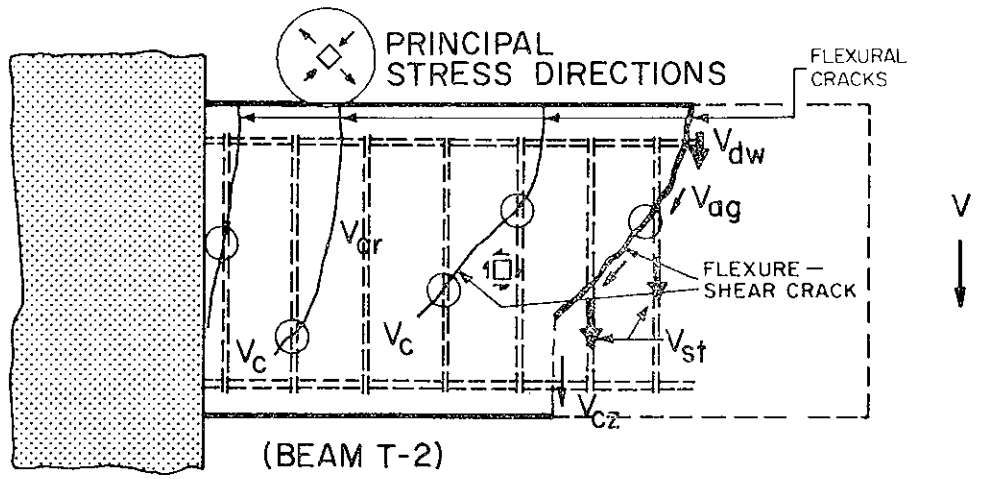

$V = V_{dw} + V_{ag} + V_{st} + V_{cz}$

V_{dw} = SHEAR CARRIED BY DOWEL

V_{ag} = SHEAR CARRIED BY AGGREGATE INTERLOCKING

V_{st} = SHEAR CARRIED BY STIRRUPS

V_{cz} = SHEAR CARRIED BY COMPRESSION ZONE

(a) UNDER MONOTONIC LOADING

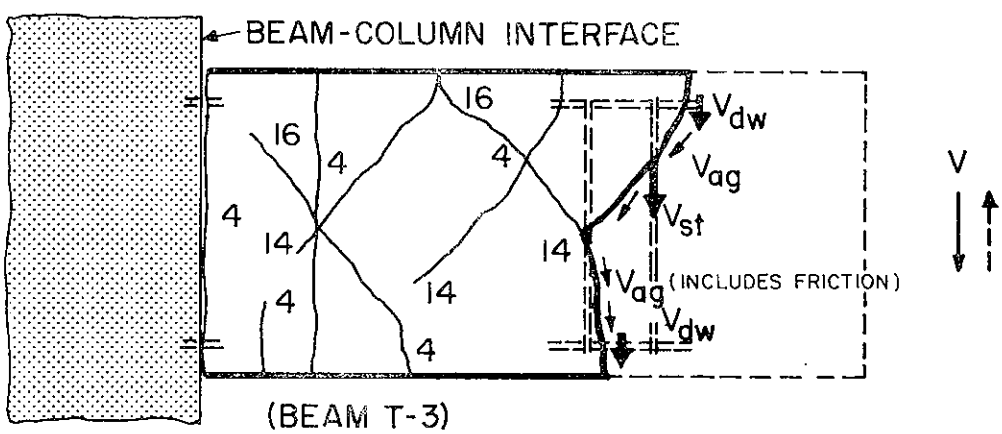

(b) UNDER REVERSED LOADING

FIG. 7.1 SHEAR TRANSFER MECHANISM

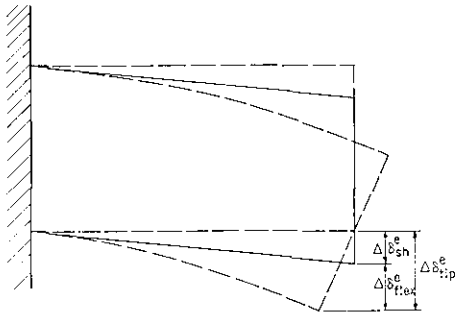

FIG. 7.2 DEFORMATION IN AN ELASTIC BEAM

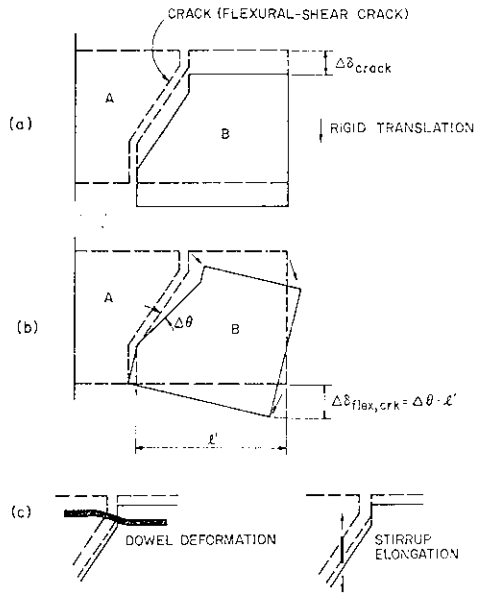

FIG. 7.3 DEFORMATIONS AT A CRACK

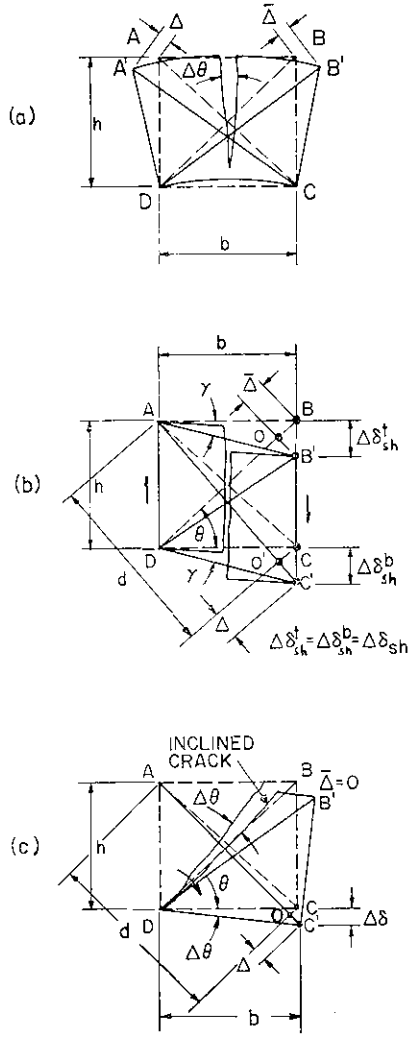

FLEXURAL DEFORMATION AT VERTICAL CRACK

$\Delta - \bar{\Delta} = 0$

MEASURED SHEAR DISTORTION

$= \frac{1}{2}\frac{(\Delta-\bar{\Delta})d}{h} = 0$

TRANSLATION-SHEAR DEFORMATIONS ($\Delta\delta_{sh}$)

TRIANGLE B B'O

$\Delta\delta^t = \frac{\bar{\Delta}}{\sin\theta} = -\bar{\Delta}\frac{d}{h}$

TRIANGLE C C'O'

$\Delta\delta^b = \frac{\Delta}{\sin\theta} = \Delta\frac{d}{h}$

MEASURED SHEAR DISTORTION

$= \frac{1}{2}\frac{(\Delta-\bar{\Delta})d}{h} = \frac{1}{2}(\Delta\delta^t_{sh} + \Delta\delta^b_{sh}) = \Delta\delta_{sh}$

FLEXURAL DEFORMATION AT INCLINED CRACK

TRIANGLE O C C'

$\Delta\theta\, b \doteq \Delta\delta \doteq \frac{\Delta}{\sin\theta} \doteq \Delta\frac{d}{h}$

$\Delta\theta \doteq \Delta\frac{d}{bh}$

MEASURED SHEAR DISTORTION

$= \frac{1}{2}\frac{(\Delta-\bar{\Delta})d}{h} = \Delta\theta\frac{b}{2}$

FIG. 7.4 DEFORMATIONS MEASURED BY DIAGONAL GAGES

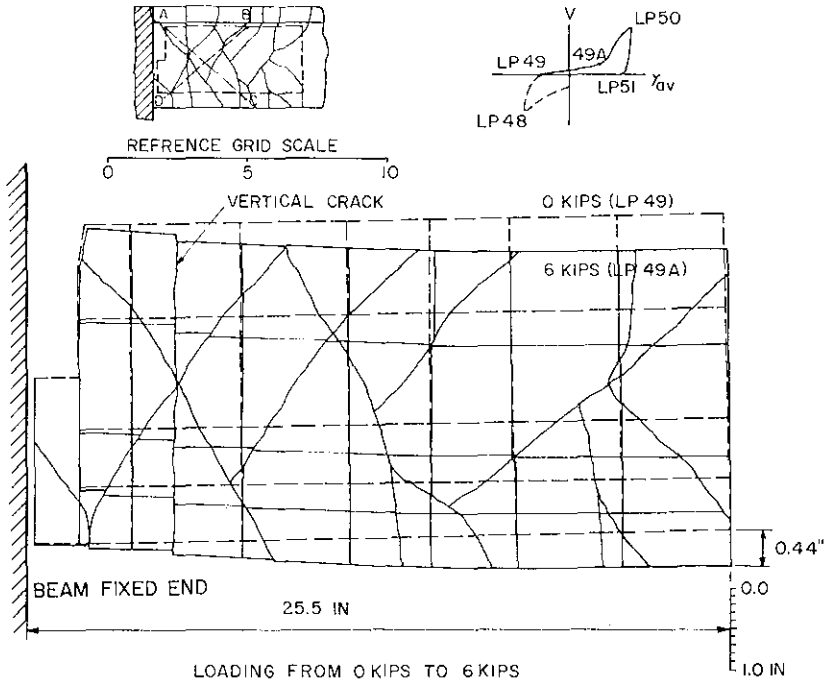

FIG. 7.5 PHOTOGRAMMETRIC RESULTS
(BEAM T-3) - LP #49 - LP #49A

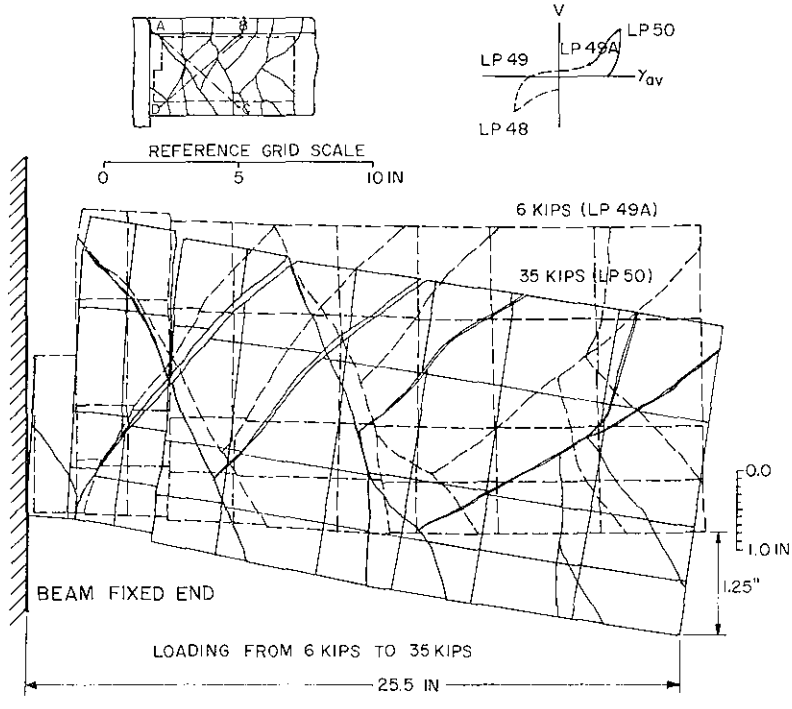

FIG. 7.6 PHOTOGRAMMETRIC RESULTS
(BEAM T-3) - LP #49A - LP #50

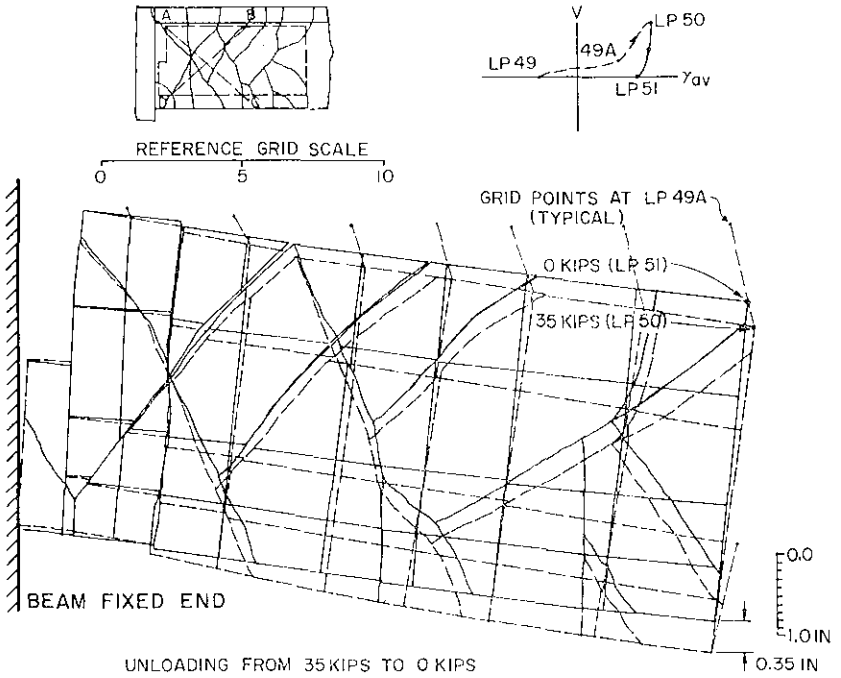

FIG. 7.7 PHOTOGRAMMETRIC RESULTS
(BEAM T-3) - LP #50 - LP #51

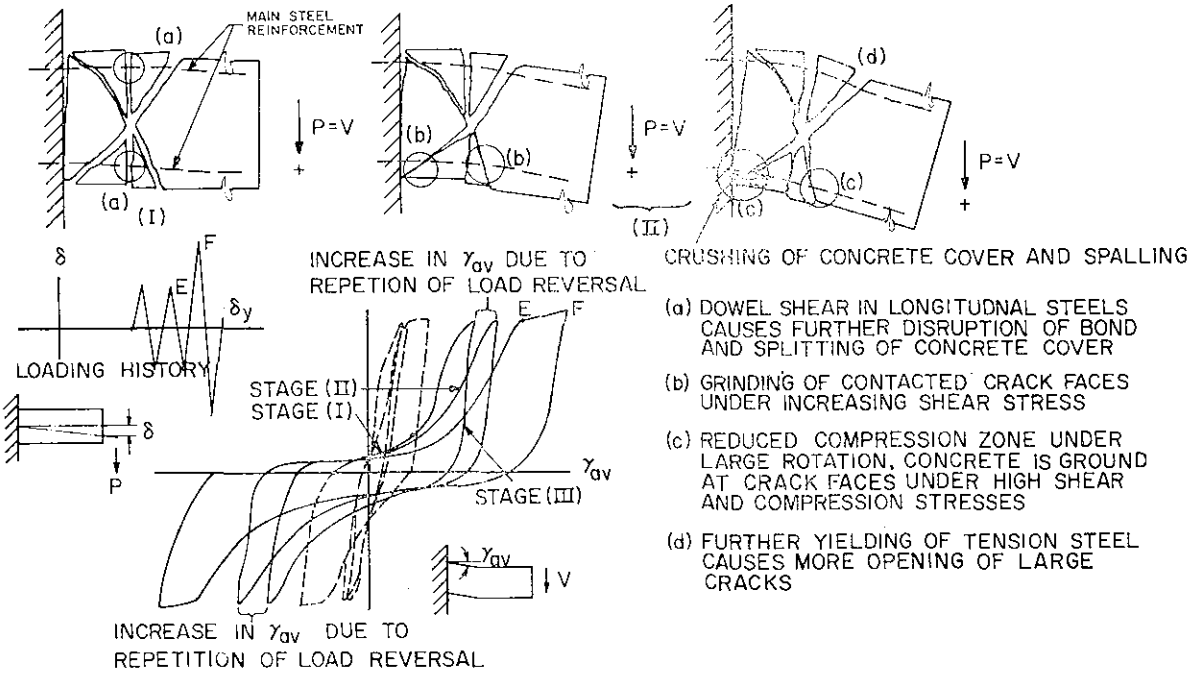

FIG. 7.8 SHEAR DEGRADATION MECHANISM

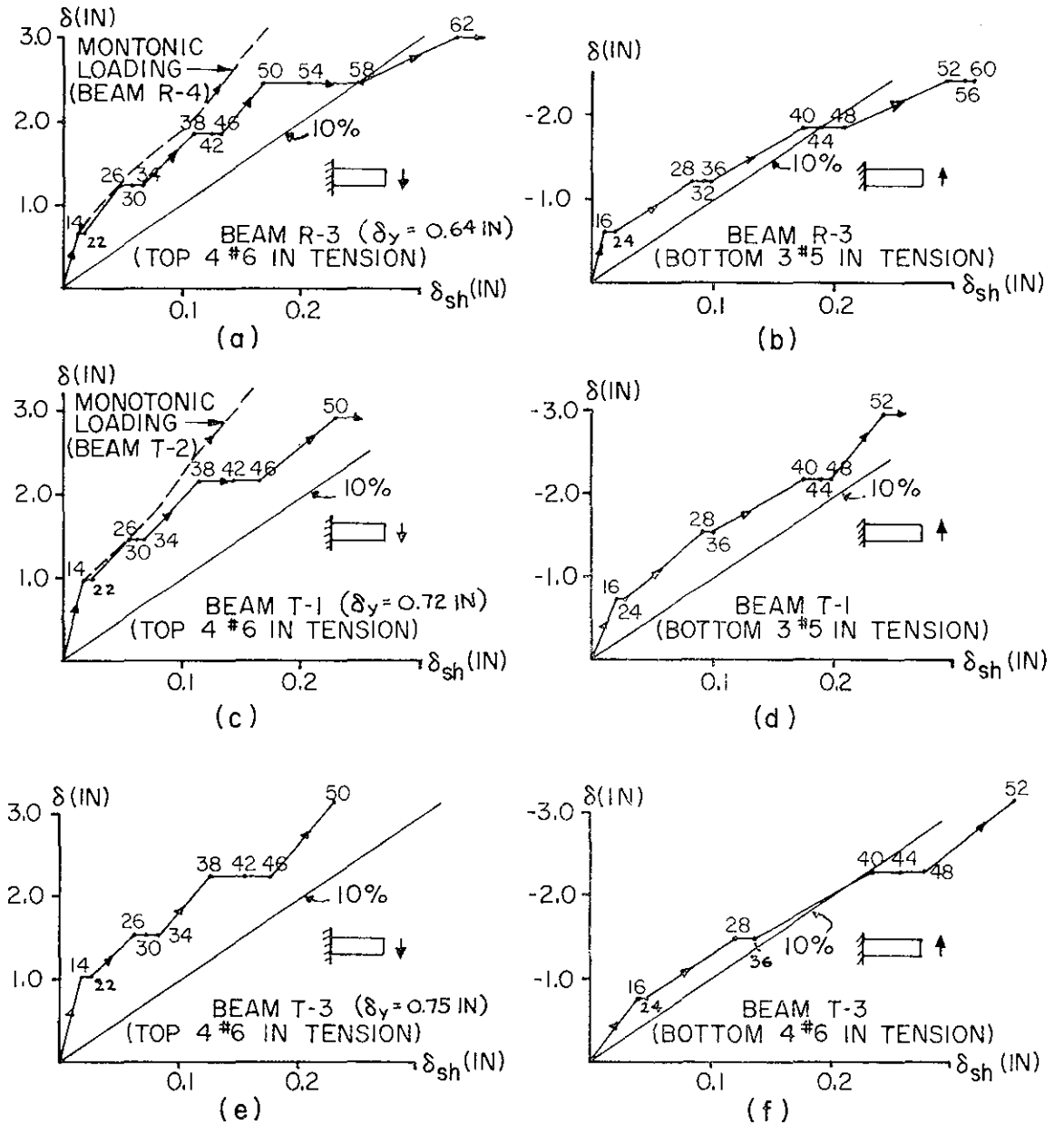

FIG. 7.9 MAGNITUDE OF MEASURED SHEAR DISTORTION (δ_{sh}) VS. TIP DEFLECTION (δ)

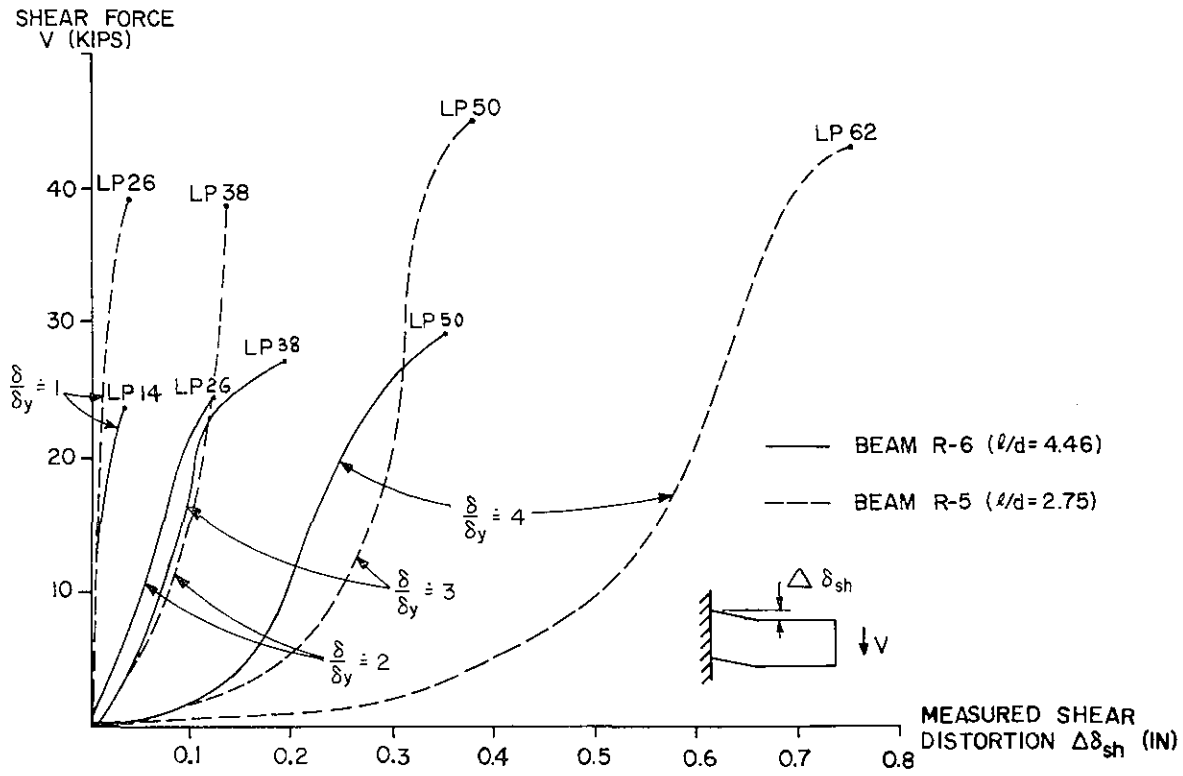

FIG. 7.10 COMPARISON BETWEEN SHEAR FORCE-SHEAR DISTORTION RESPONSE OF BEAM R-6 AND BEAM R-5

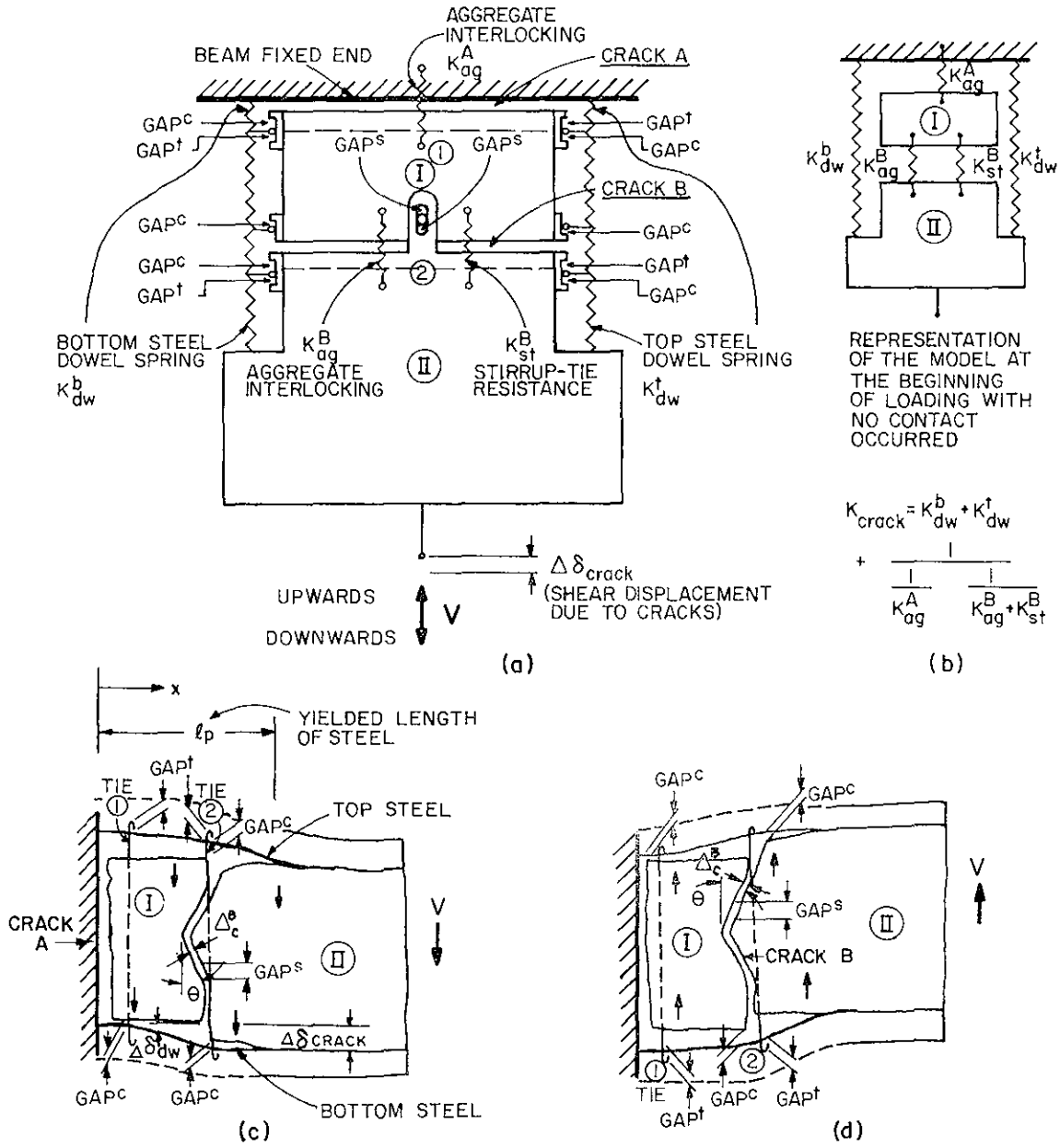

FIG. A7.1 SHEAR FORCE-SHEAR DEFORMATION MODEL FOR CRITICAL REGION OF BEAM R-5 WITH TWO LARGE CRACKS

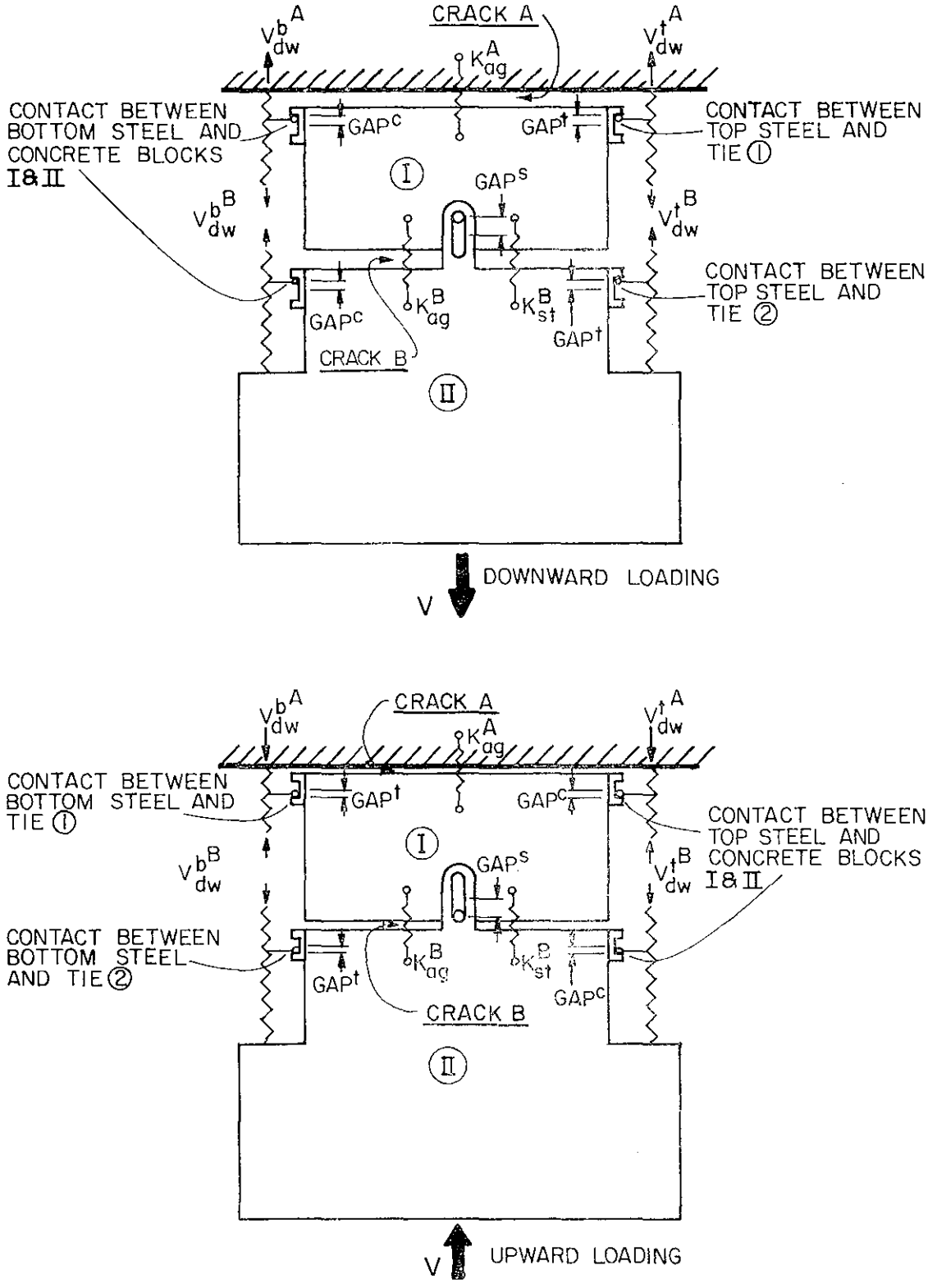

FIG. A7.2 REPRESENTATION OF CONTACTS IN SHEAR FORCE - SHEAR DEFORMATION MODEL

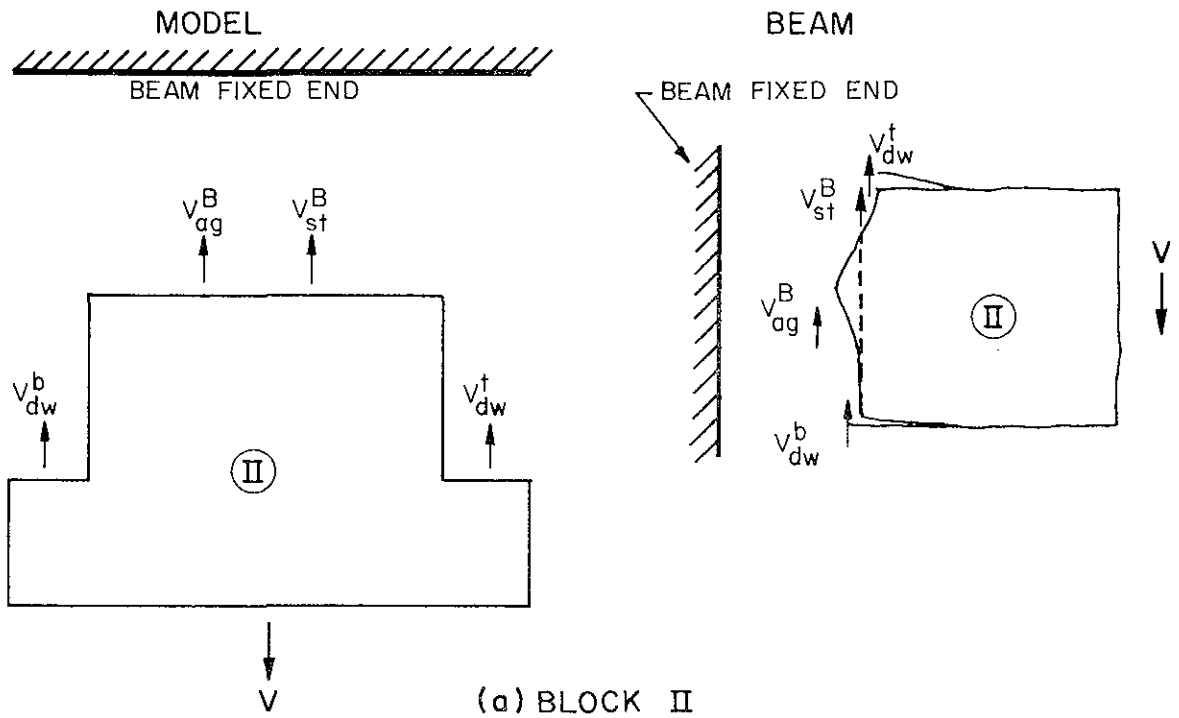

(a) BLOCK II

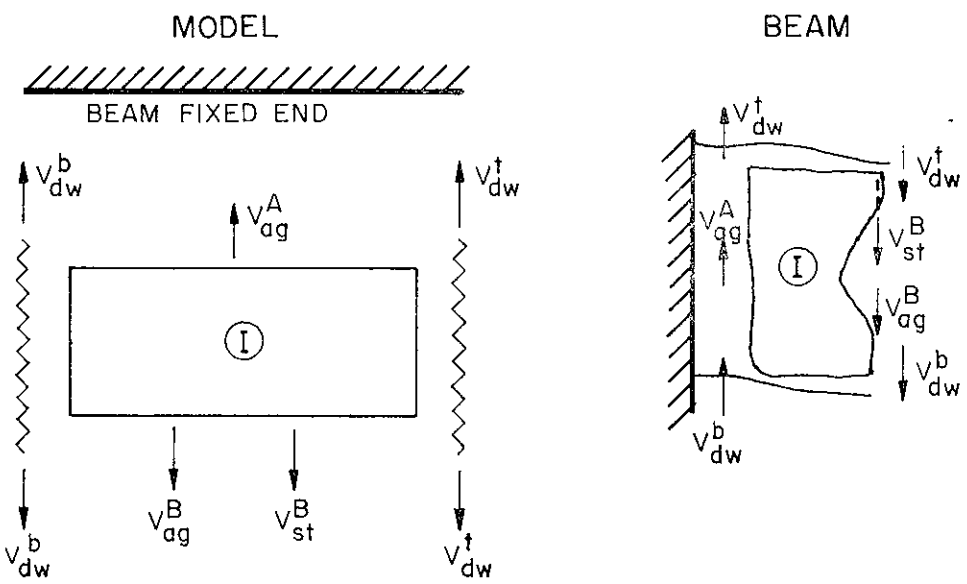

(b) BLOCK I

FIG. A7.3 COMPARISON BETWEEN FREE BODY DIAGRAM OF SHEAR FORCE-SHEAR DEFORMATION MODEL AND THAT OF ACTUAL BEAM

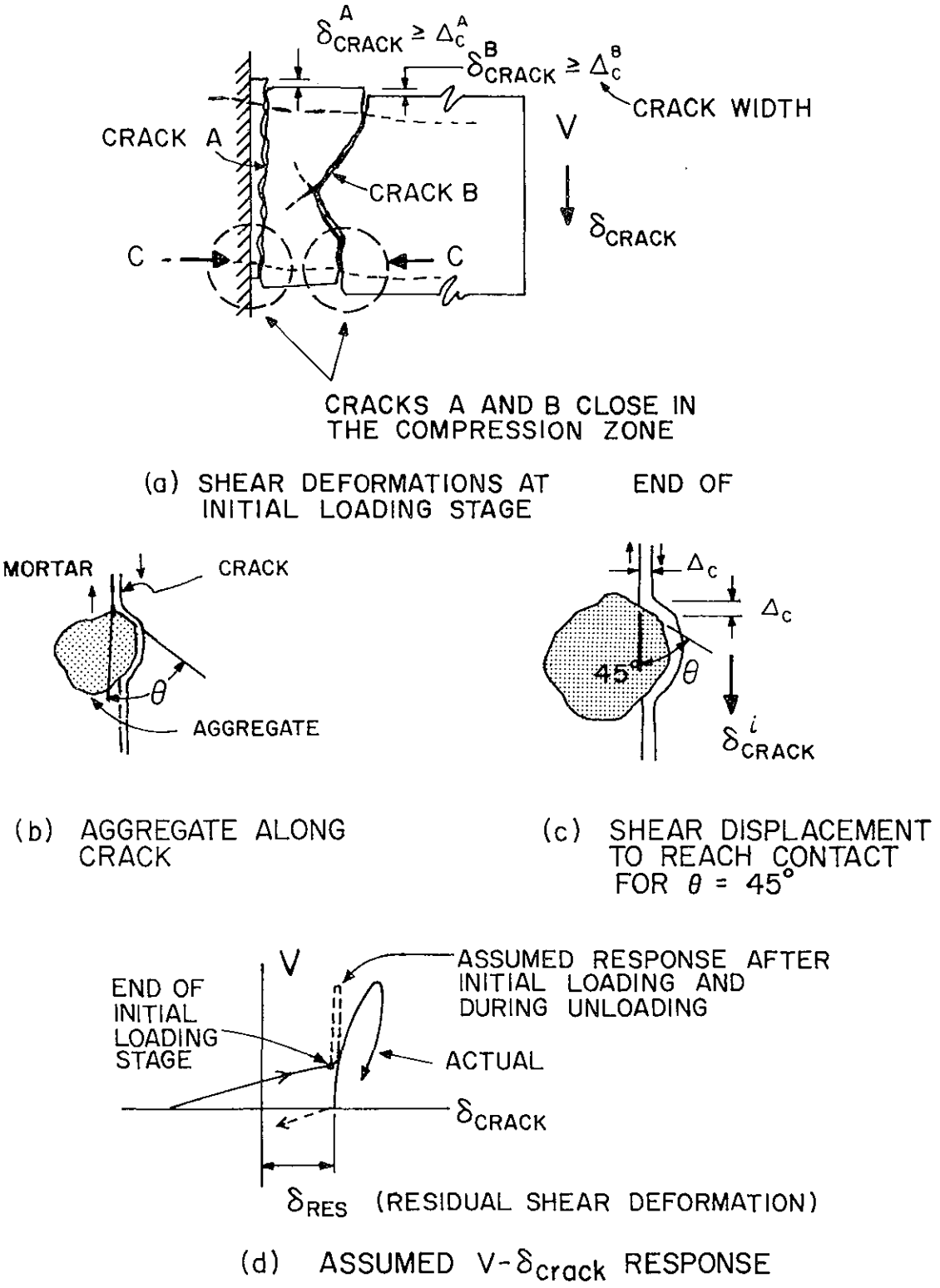

FIG. A7.4 END OF INITIAL LOADING STAGE

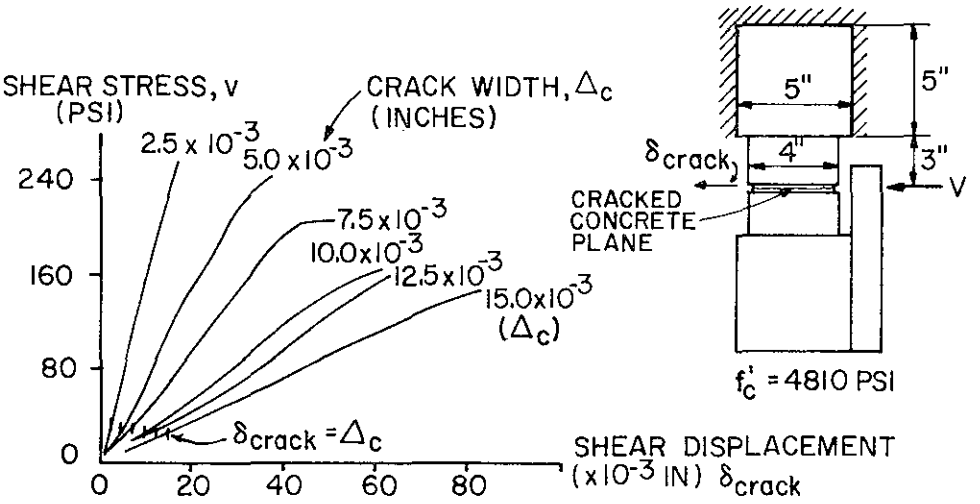

(a) FENWICK AND PAULAY'S TEST RESULTS [7.5]

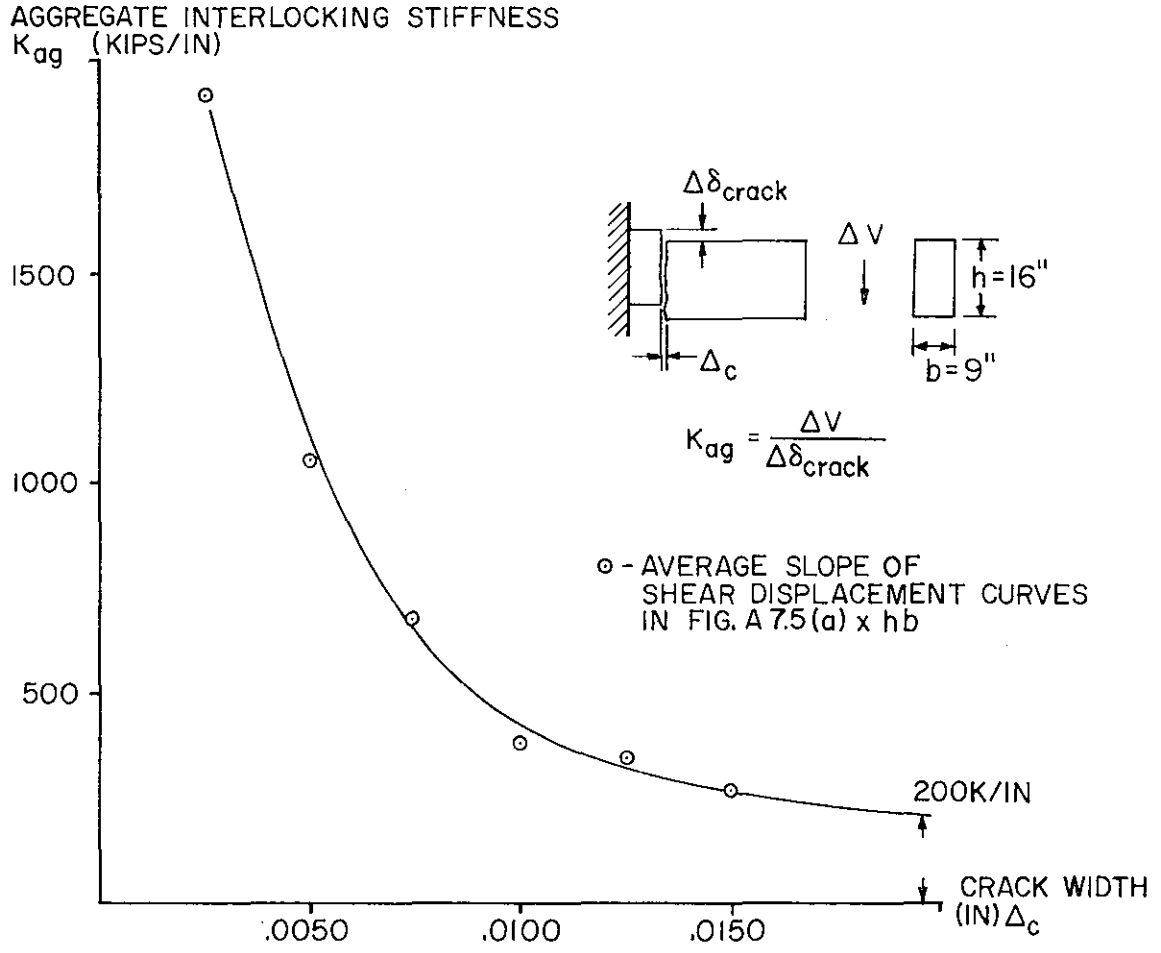

(b) COMPUTED CRACK AGGREGATE INTERLOCKING STIFFNESS

FIG. A7.5 AGGREGATE INTERLOCKING STIFFNESS

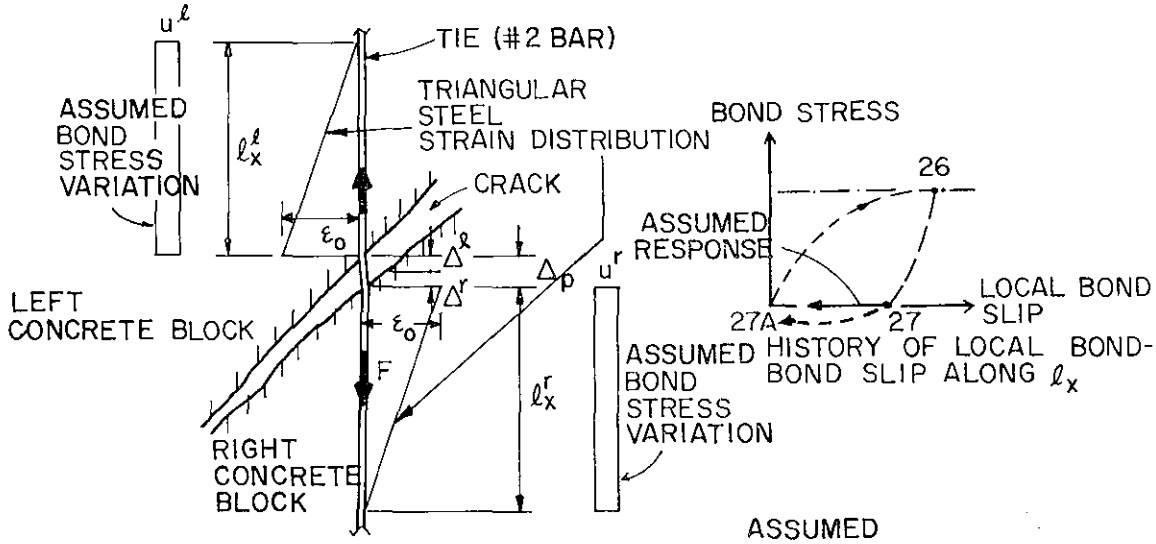

(a) STIRRUP-TIE RESISTANCE AT PEAK LOADING STAGE (LP 26)

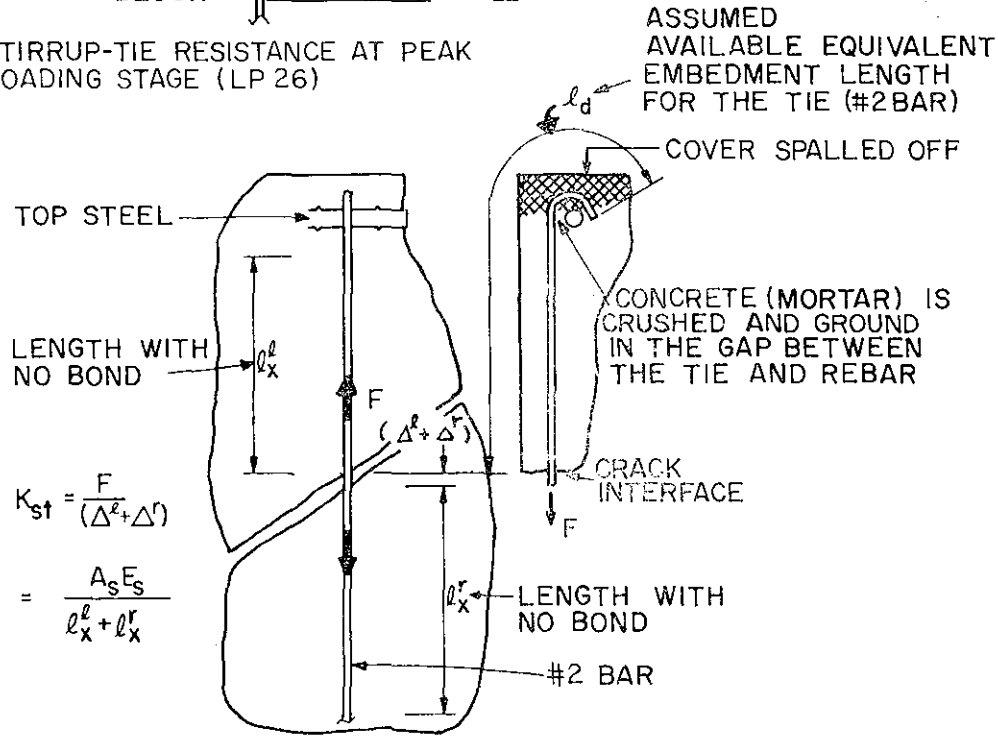

(b) STIRRUP-TIE STIFFNESS AT INITIAL LOADING STAGE (LP 27-27A)

FIG. A7.6 SHEAR STIFFNESS OF TIE ACROSS INCLINED CRACK

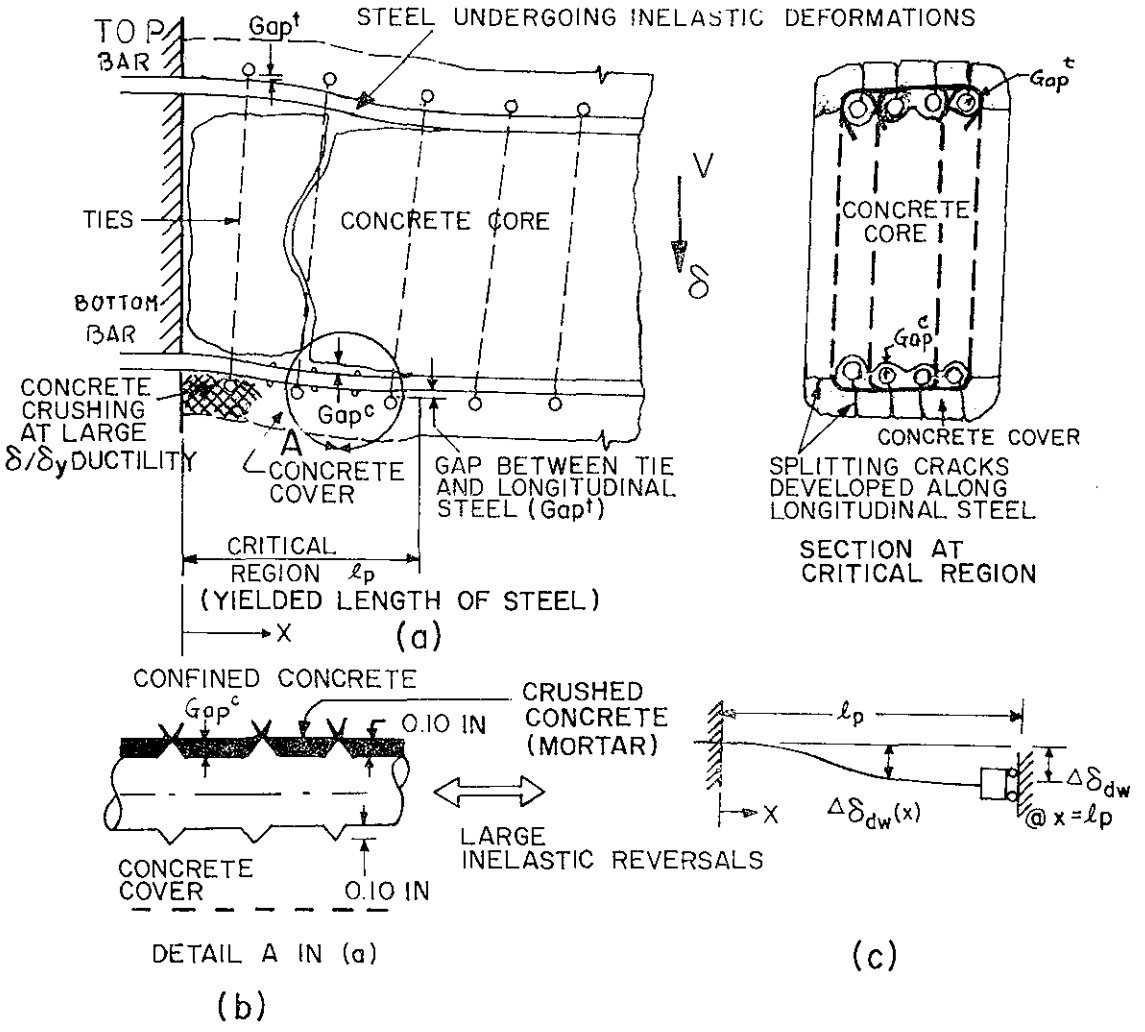

FIG. A7.7 DOWEL STIFFNESS IN CRITICAL REGION

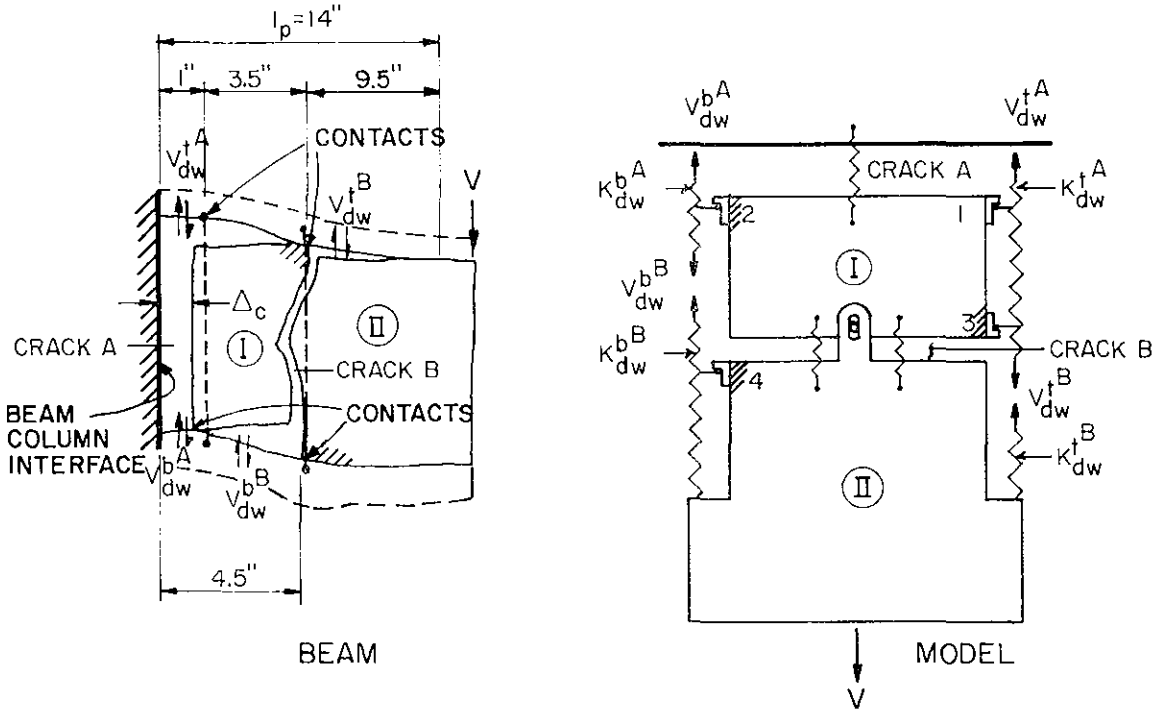

CRACK A	$K_{dw}^{t\,A}$ (approx)		$\frac{3E_sI_s}{e^3}$, e = 1"
	$K_{dw}^{b\,A}$ (approx)	DOWEL AT BEAM COLUMN INTERFACE	$\frac{3E_sI_s}{e^3}$, e = Δ_c
CRACK B	$K_{dw}^{t\,B}$ (APPROX)	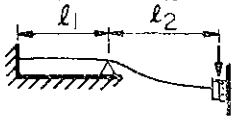	$\frac{3E_sI_s}{\ell_2^3}\left(\frac{4+\ell_1/\ell_2}{1+\ell_1/\ell_2}\right)$ ℓ_1 = 3.5", ℓ_2 = 9.5
	$K_{dw}^{b\,B}$ (APPROX)	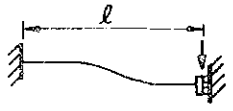	$\frac{12E_sI_s}{\ell^3}$, ℓ = 4.5"

FIG. A7.8 FORMULAS FOR ESTIMATING DOWEL STIFFNESS AS MAIN BARS ARE BROUGHT INTO CONTACT WITH SURROUNDING CONCRETE AND TIES

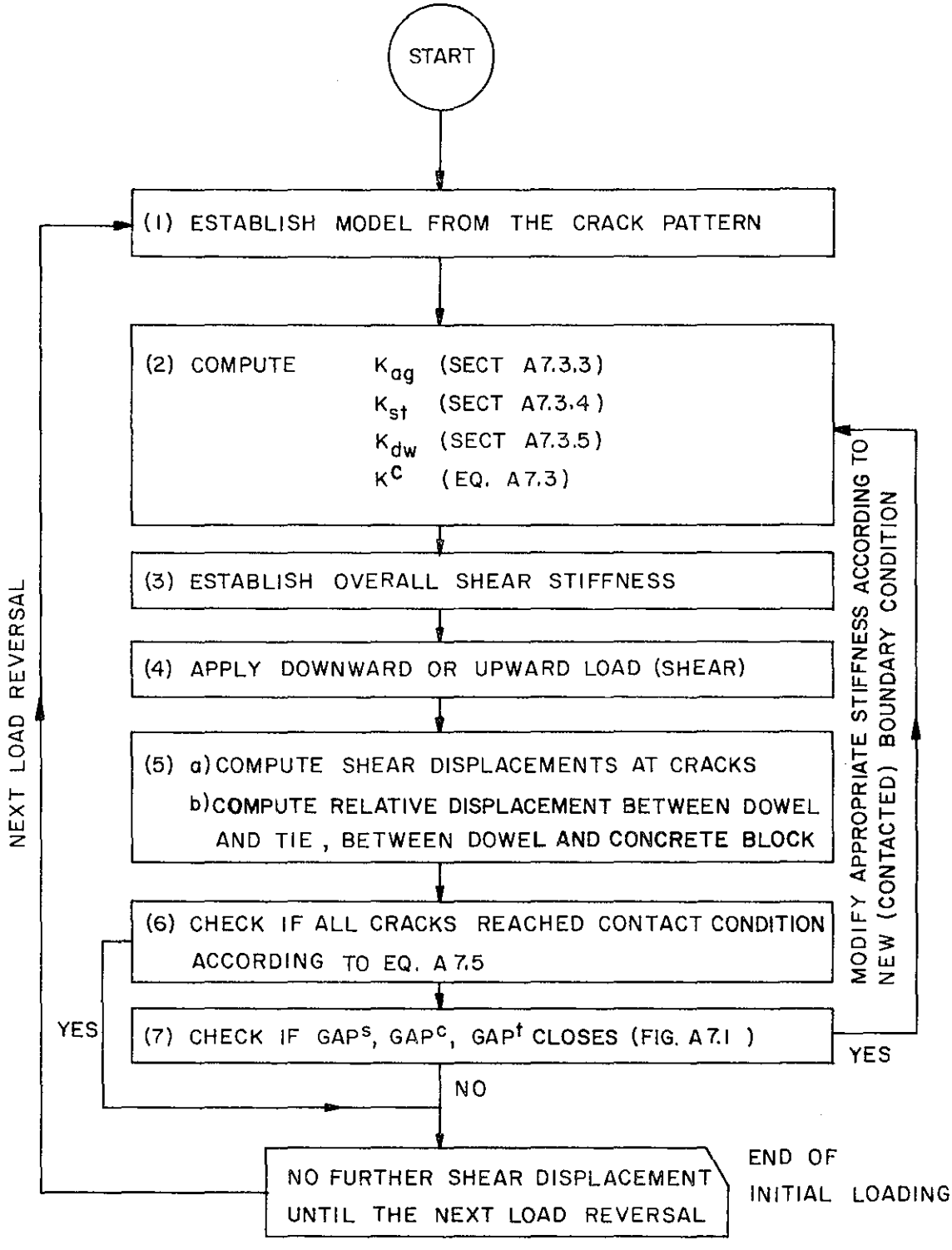

FIG. A7.9 PROCEDURE FOR DETERMINING SHEAR FORCE-SHEAR DEFORMATION RELATIONSHIPS

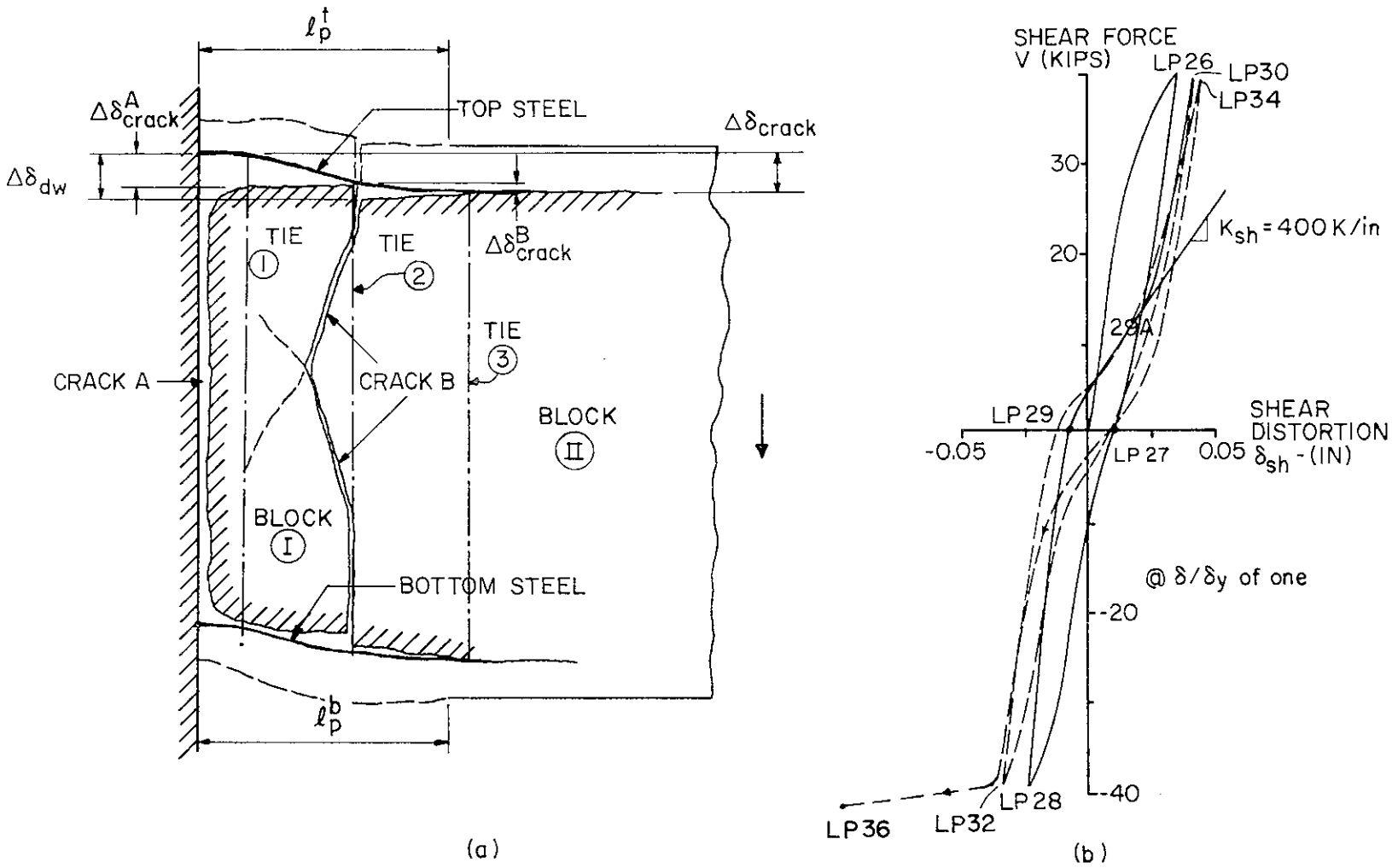

FIG. A7.10 ASSUMED DEFORMATION PATTERN DURING INITIAL LOADING STAGE (BEAM R-5) - LP #29 - LP #2AA

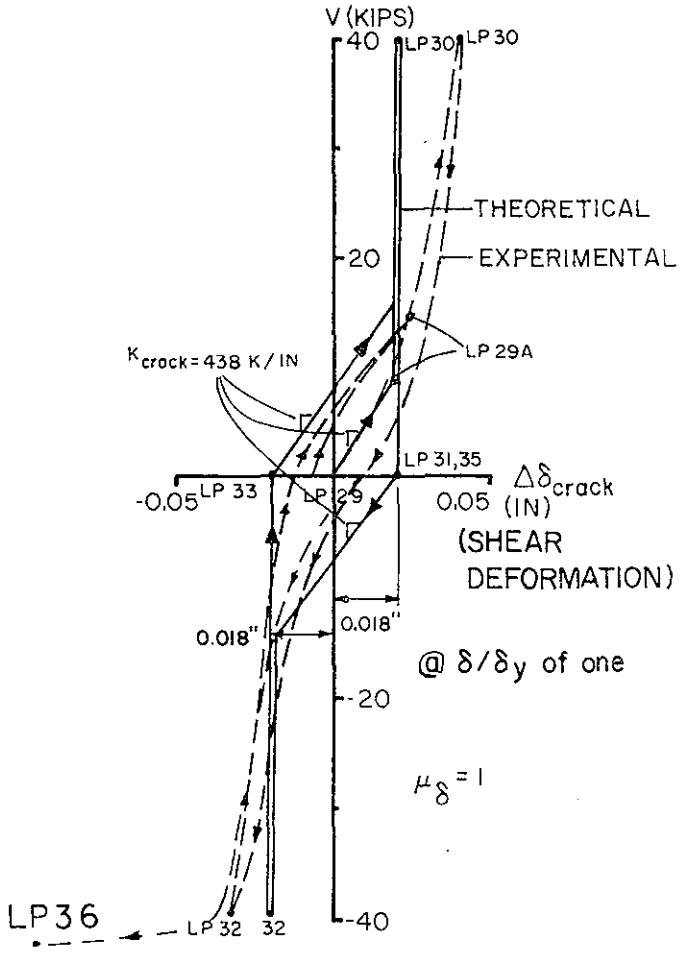

FIG. A7.11 PREDICTED SHEAR FORCES-SHEAR DEFORMATION RELATIONSHIP (δ/δ_y = 1)

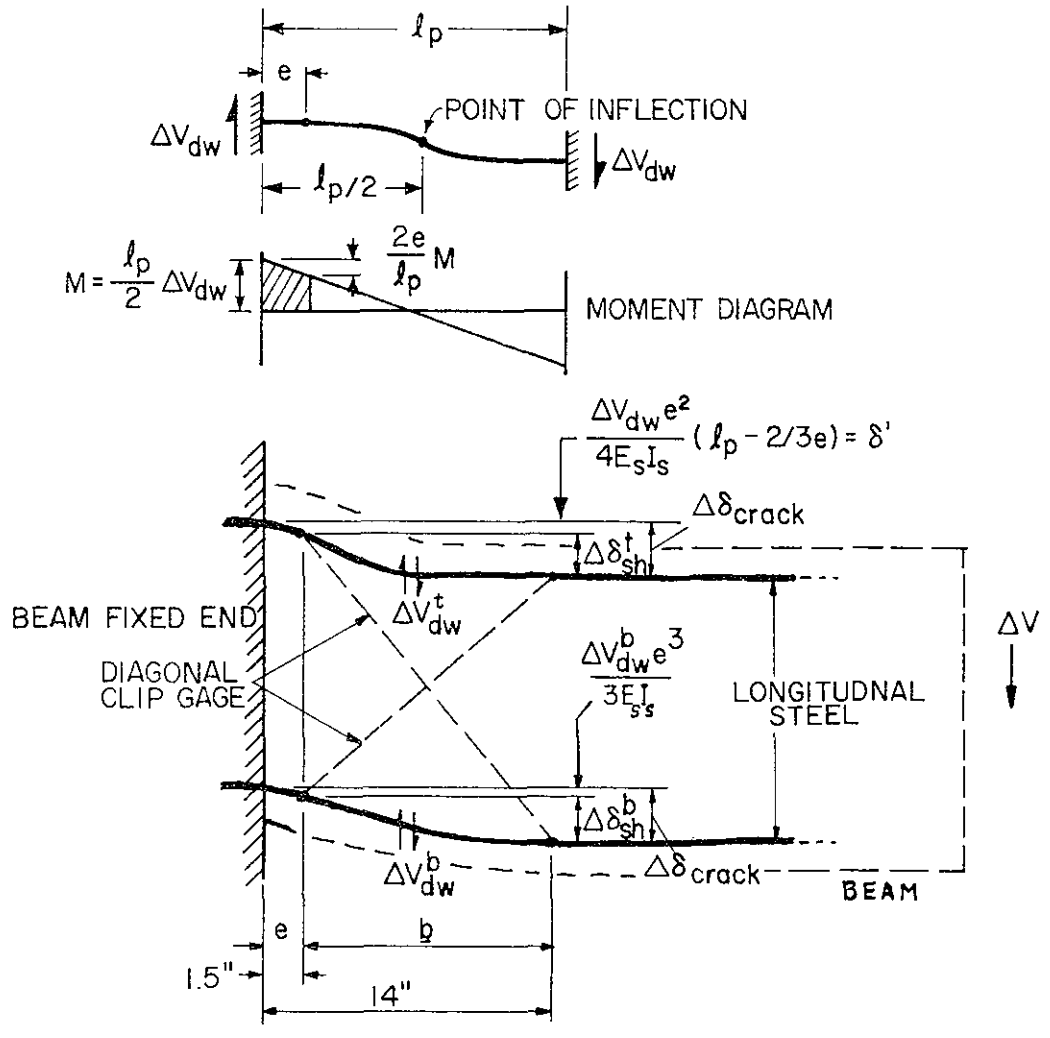

FIG. A7.12 SHEAR DEFORMATION MEASURED BY DIAGONAL CLIP GAGES

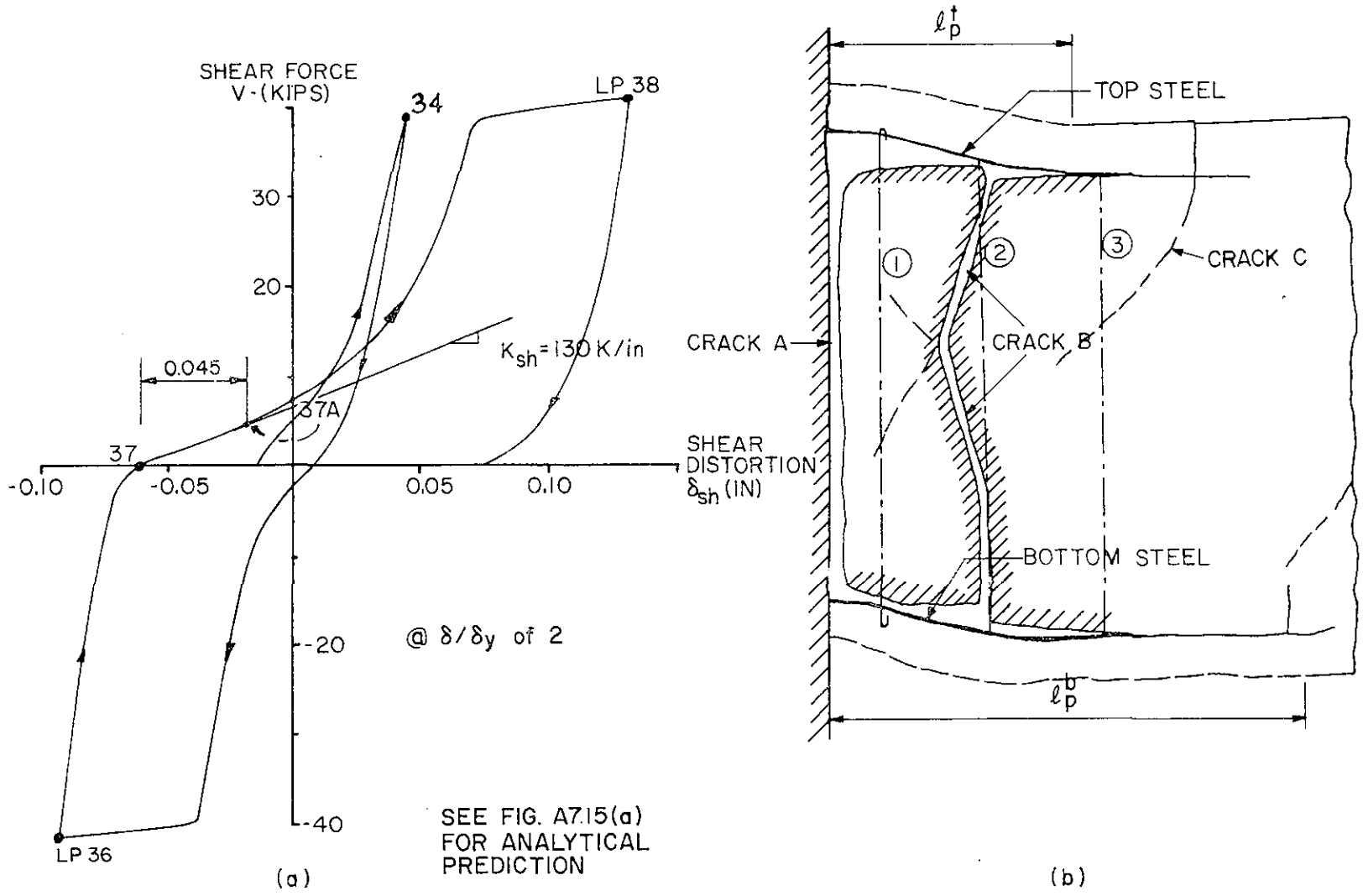

FIG. A7.13 ASSUMED DEFORMATION PATTERN DURING INITIAL LOADING STAGE. (BEAM R-5) - LP #37 - LP #37A

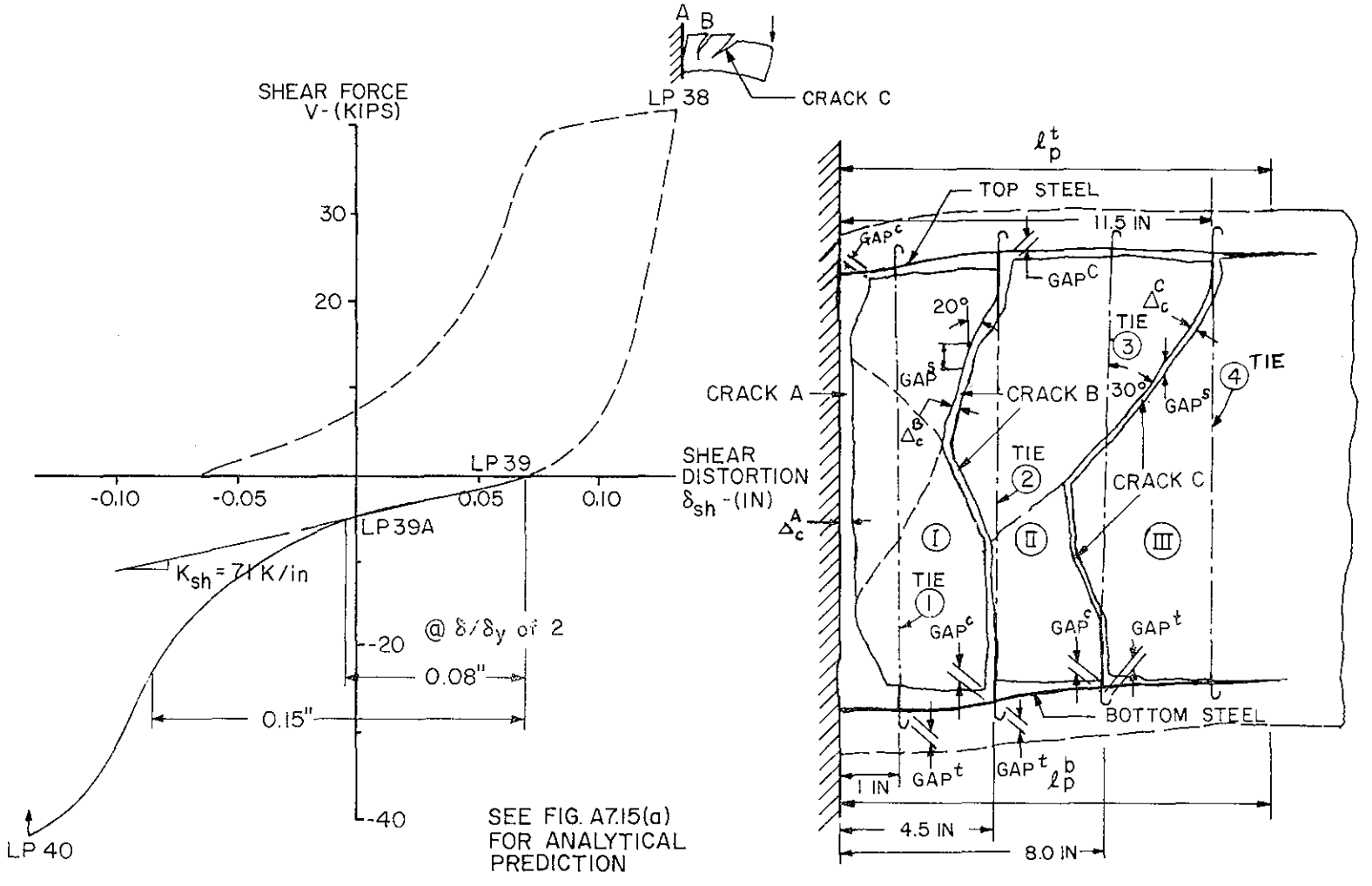

(a) EXPERIMENTAL $V-\delta_{sh}$ CURVE

(b) DEFORMATION PATTERN

FIG. A7.14 ASSUMED DEFORMATION PATTERN DURING INITIAL LOADING STAGE (BEAM R-5) - LP #39 - LP #39A

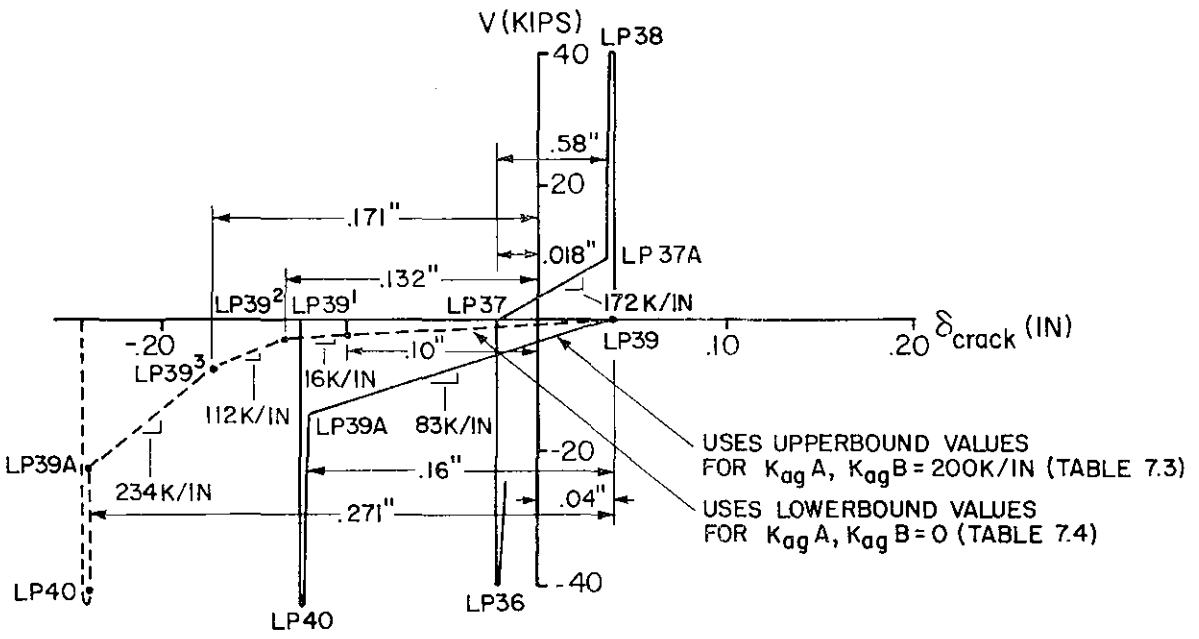

(a) ANALYTICAL RESULTS

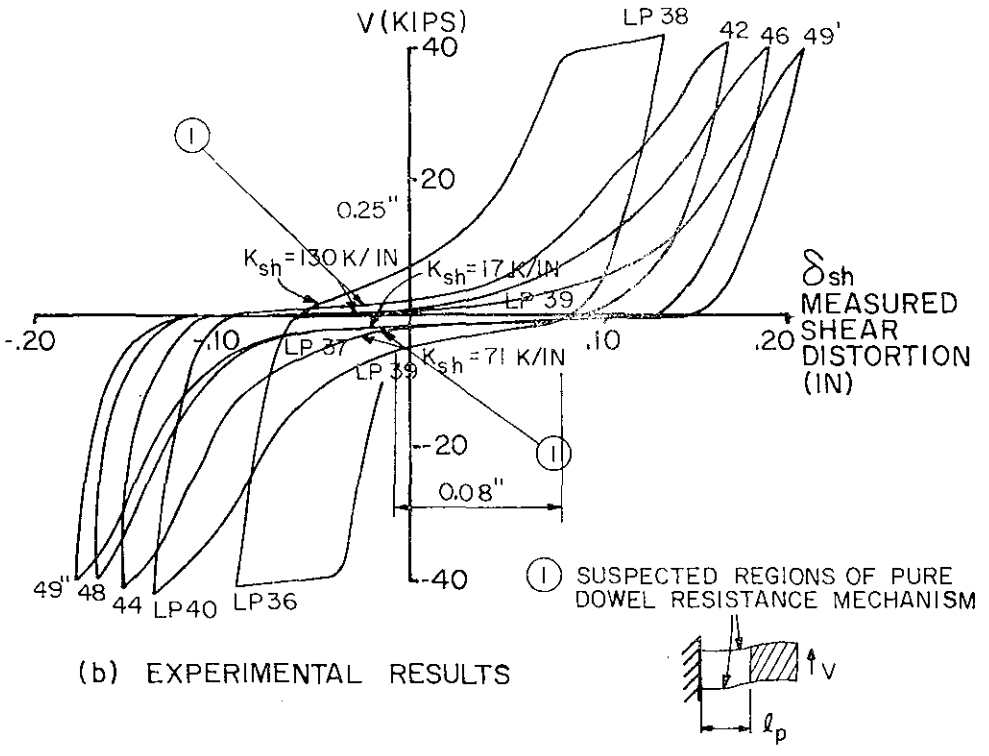

(b) EXPERIMENTAL RESULTS

FIG. A7.15 ANALYTICAL AND EXPERIMENTAL RESULTS ON SHEAR FORCE-SHEAR DISPLACEMENT HYSTERETIC LOOPS AT DUCTILITY RATIO (δ/δ_y) OF TWO

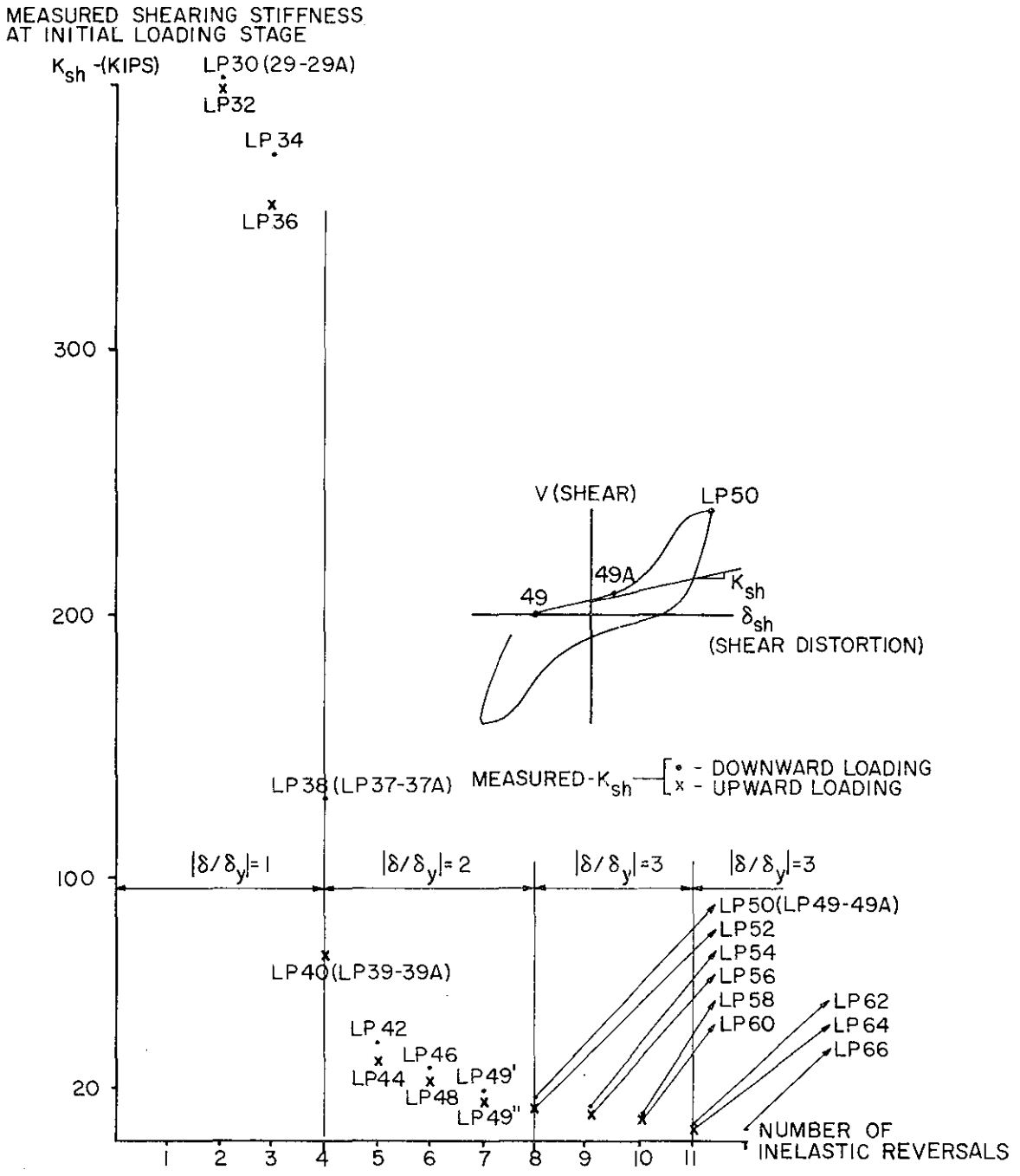

FIG. A7.16 VARIATION OF MEASURED SHEARING STIFFNESS AT INITIAL LOADING STAGES VS. NUMBER OF INELASTIC REVERSALS

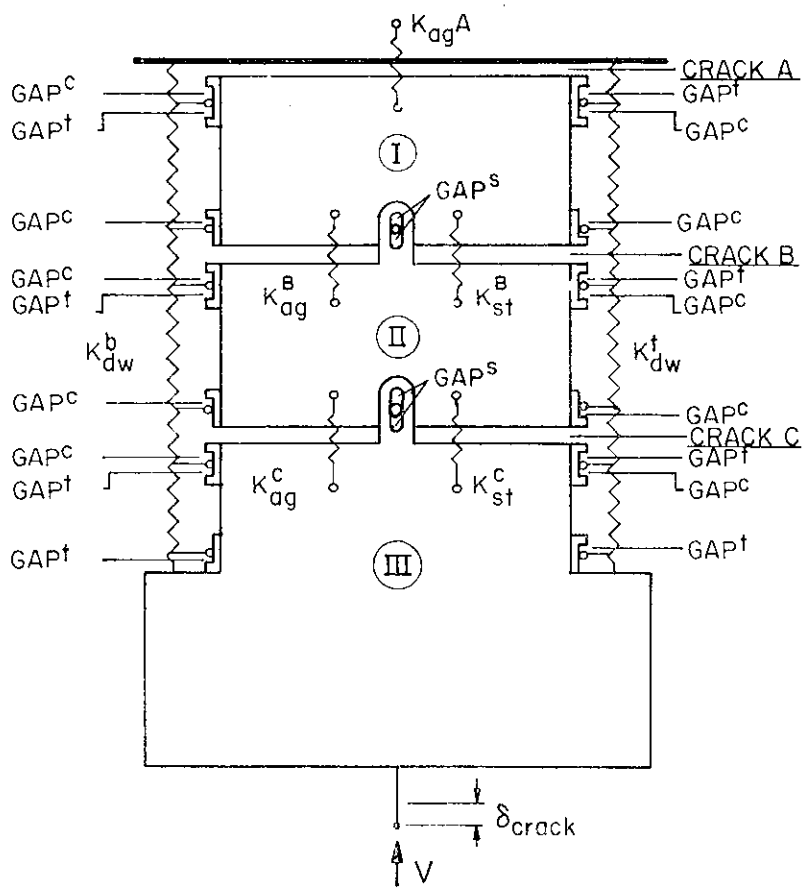

(a) GENERAL MODEL

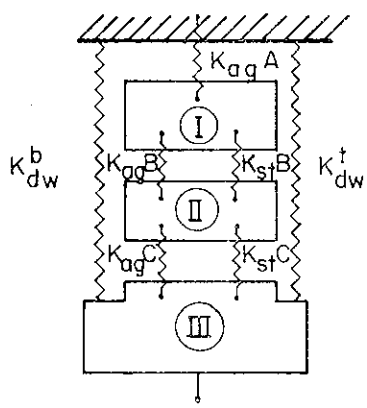

$$K_{crack}^A = K_{ag}^A$$

$$K_{crack}^B \cong K_{ag}^B + K_{st}^B$$

$$K_{crack}^C \cong K_{ag}^C + K_{st}^C$$

K_{crack} (of the model)

$$= K_{dw}^t + K_{dw}^b + \frac{1}{\frac{1}{K_{crack}^A} + \frac{1}{K_{crack}^B} + \frac{1}{K_{crack}^C}}$$

(b) AT THE BEGINNING OF LOADING WITH NO CONTACT OCCURRING

FIG. A7.17 SHEAR FORCE-SHEAR DEFORMATION MODEL FOR CRITICAL REGION OF BEAM R-5 WITH THREE LARGE CRACKS (LP #39 - LP #39A)

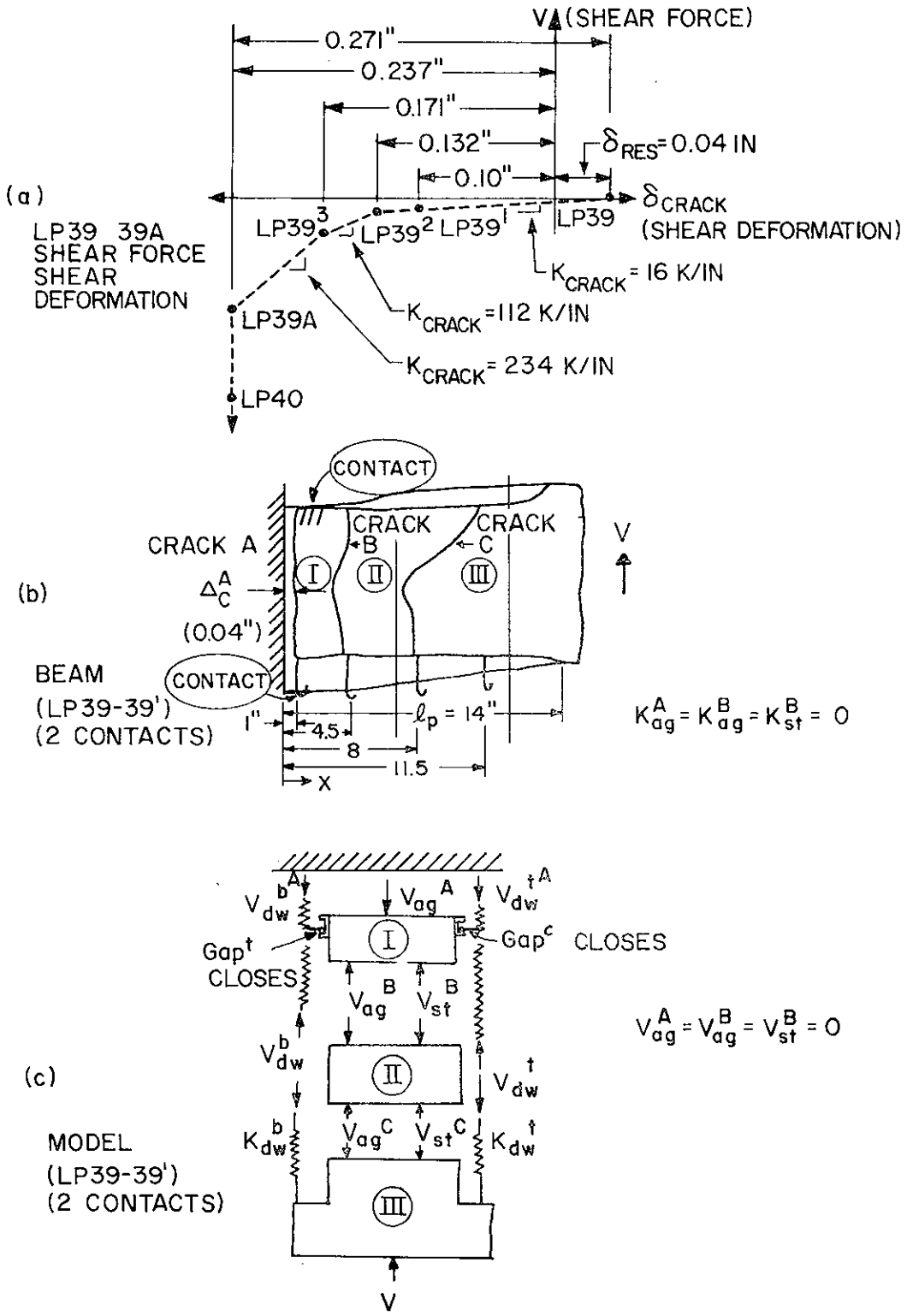

FIG. A7.18 ILLUSTRATIONS [TABLE A7.4]

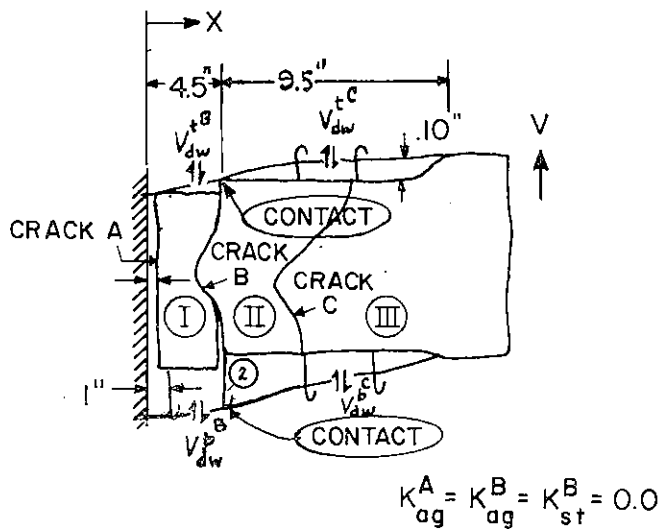

(a) BEAM FROM LP39[1] TO LP39[2] (2 CONTACTS)

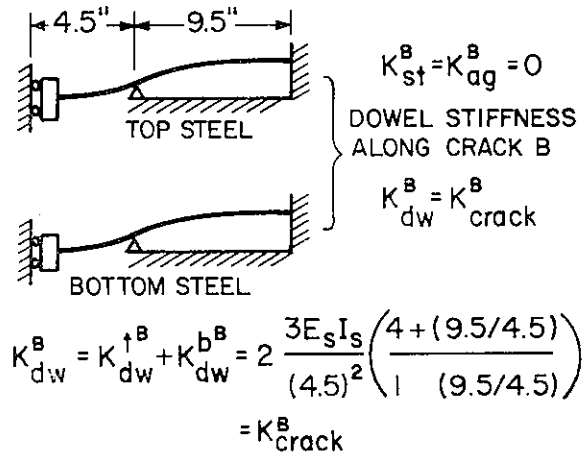

(b) CRACK STIFFNESS ALONG CRACK B

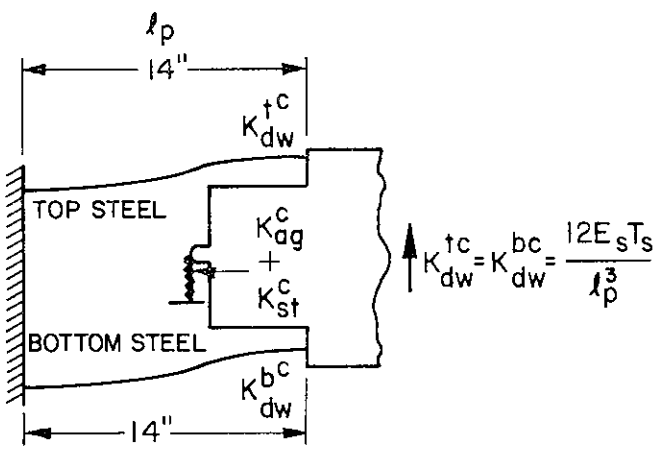

(c) CRACK STIFFNESS ALONG CRACK C

FIG. A7.19 ILLUSTRATIONS [TABLE A7. 4]

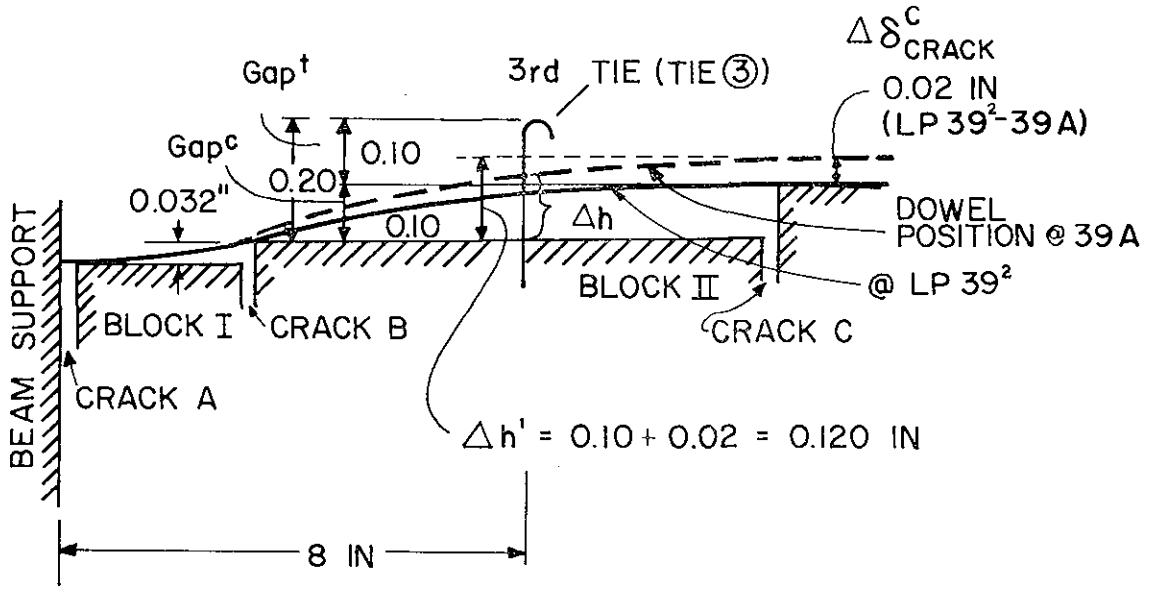

(a) TOP STEEL (LP 39²-39³)

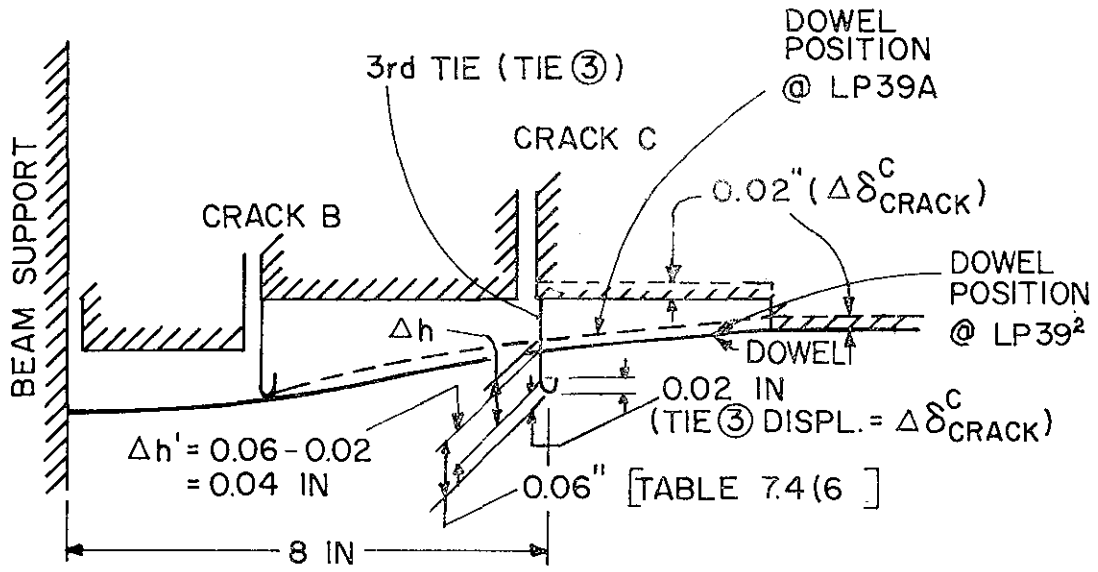

(b) BOTTOM STEEL (LP39²-39³)

FIG. A7.20 ILLUSTRATIONS (TABLE 7.4)

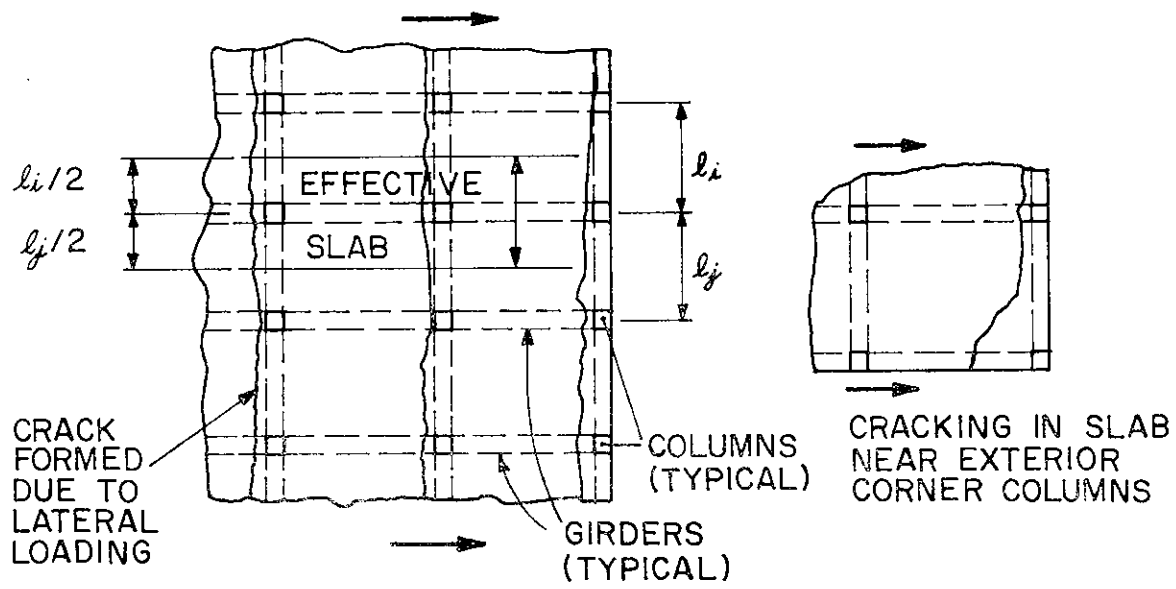

FIG. 8.1 CRACKING IN FLOOR SLAB UNDER LATERAL LOADING

EARTHQUAKE ENGINEERING RESEARCH CENTER REPORTS

$5.75	EERC 67-1	"Feasibility Study Large-Scale Earthquake Simulator Facility," by J. Penzien, J. G. Bouwkamp, R. W. Clough and D. Rea - 1967 (PB 187 905)
	EERC 68-1	Unassigned
$4.75	EERC 68-2	"Inelastic Behavior of Beam-to-Column Subassemblages Under Repeated Loading," by V. V. Bertero - 1968 (PB 184 888)
$3.75	EERC 68-3	"A Graphical Method for Solving the Wave Reflection-Refraction Problem," by H. D. McNiven and Y. Mengi 1968 (PB 187 943)
$5.75	EERC 68-4	"Dynamic Properties of McKinley School Buildings," by D. Rea, J. G. Bouwkamp and R. W. Clough - 1968 (PB 187 902)
$3.75	EERC 68-5	"Characteristics of Rock Motions During Earthquakes," by H. B. Seed, I. M. Idriss and F. W. Kiefer - 1968 (PB 188 338)
$7.50	EERC 69-1	"Earthquake Engineering Research at Berkeley," - 1969 (PB 187 906)
$6.25	EERC 69-2	"Nonlinear Seismic Response of Earth Structures," by M. Dibaj and J. Penzien - 1969 (PB 187 904)
$5.25	EERC 69-3	"Probabilistic Study of the Behavior of Structures During Earthquakes," by P. Ruiz and J. Penzien - 1969 (PB 187 886)
$3.25	EERC 69-4	"Numerical Solution of Boundary Value Problems in Structural Mechanics by Reduction to an Initial Value Formulation," by N. Distefano and J. Schujman - 1969 (PB 187 942)
$3.75	EERC 69-5	"Dynamic Programming and the Solution of the Biharmonic Equation," by N. Distefano - 1969 (PB 187 941)

Note: Numbers in parentheses are Accession Numbers assigned by the National Technical Information Service. Copies of these reports may be ordered from the National Technical Information Service, 5285 Port Royal Road, Springfield, Virginia, 22161. Accession Numbers should be quoted on orders for the reports (PB --- ---) and remittance must accompany each order. (Foreign orders, add $2.50 extra for mailing charges.) Those reports without this information listed are not yet available from NTIS. Upon request, EERC will mail inquirers this information when it becomes available to us.

Preceding page blank

$7.00	EERC 69-6	"Stochastic Analysis of Offshore Tower Structures," by A. K. Malhotra and J. Penzien - 1969 (PB 187 903)
$3.25	EERC 69-7	"Rock Motion Accelerograms for High Magnitude Earthquakes," by H. B. Seed and I. M. Idriss - 1969 (PB 187 940)
$4.25	EERC 69-8	"Structural Dynamics Testing Facilities at the University of California, Berkeley," by R. M. Stephen, J. G. Bouwkamp, R. W. Clough and J. Penzien - 1969 (PB 189 111)
$3.75	EERC 69-9	"Seismic Response of Soil Deposits Underlain by Sloping Rock Boundaries," by H. Dezfulian and H. B. Seed - 1969 (PB 189 114)
$7.25	EERC 69-10	"Dynamic Stress Analysis of Axisymmetric Structures under Arbitrary Loading," by S. Ghosh and E. L. Wilson - 1969 (PB 189 026)
$7.25	EERC 69-11	"Seismic Behavior of Multistory Frames Designed by Different Philosophies," by J. C. Anderson and V. V. Bertero - 1969 (PB 190 662)
$5.75	EERC 69-12	"Stiffness Degradation of Reinforcing Concrete Structures Subjected to Reversed Actions," by V. V. Bertero, B. Bresler and H. Ming Liao - 1969 (PB 202 942)
$3.75	EERC 69-13	"Response of Non-Uniform Soil Deposits to Travel Seismic Waves," by H. Dezfulian and H. B. Seed - 1969 (PB 191 023)
$5.25	EERC 69-14	"Damping Capacity of a Model Steel Structure," by D. Rea, R. W. Clough and J. G. Bouwkamp - 1969 (PB 190 663)
$3.75	EERC 69-15	"Influence of Local Soil Conditions on Building Damage Potential during Earthquakes," by H. B. Seed and I. M. Idriss - 1969 (PB 191 036)
$5.75	EERC 69-16	"The Behavior of Sands under Seismic Loading Conditions," by M. L. Silver and H. B. Seed - 1969 (AD 714 982)
$3.75	EERC 70-1	"Earthquake Response of Concrete Gravity Dams," by A. K. Chopra - 1970 (AD 709 640)
$4.75	EERC 70-2	"Relationships between Soil Conditions and Building Damage in the Caracas Earthquake of July 29, 1967," by H. B. Seed, I. M. Idriss and H. Dezfulian - 1970 (PB 195 762)

$4.25	EERC 70-3	"Cyclic Loading of Full Size Steel Connections," by E. P. Popov and R. M. Stephen - 1970 (PB 213 545)
$5.25	EERC 70-4	"Seismic Analysis of the Charaima Building, Caraballeda, Venezuela," by Subcommittee of the SEAONC Research Committee: V. V. Bertero, P. F. Fratessa, S. A. Mahin, J. H. Sexton, A. C. Scordelis, E. L. Wilson, L. A. Wyllie, H. B. Seed and J. Penzien, Chairman - 1970 (PB 201 455)
$4.75	EERC 70-5	"A Computer Program for Earthquake Analysis of Dams," by A. K. Chopra and P. Chakrabarti - 1970 (AD 723 994)
$3.75	EERC 70-6	"The Propagation of Love Waves across Non-Horizontally Layered Structures," by J. Lysmer and L. A. Drake - 1970 (PB 197 896)
$3.75	EERC 70-7	"Influence of Base Rock Characteristics on Ground Response," by J. Lysmer, H. B. Seed and P. B. Schnabel - 1970 (PB 197 897)
$3.75	EERC 70-8	"Applicability of Laboratory Test Procedures for Measuring Soil Liquefaction Characteristics under Cyclic Loading," by H. B. Seed and W. H. Peacock - 1970 (PB 198 016)
$3.75	EERC 70-9	"A Simplified Procedure for Evaluating Soil Liquefaction Potential," by H. B. Seed and I. M. Idriss - 1970 (PB 198 009)
$3.75	EERC 70-10	"Soil Moduli and Damping Factors for Dynamic Response Analysis," by H. B. Seed and I. M. Idriss - 1970 (PB 197 869)
$5.25	EERC 71-1	"Koyna Earthquake and the Performance of Koyna Dam," by A. K. Chopra and P. Chakrabarti - 1971 (AD 731 496)
$3.75	EERC 71-2	"Preliminary In-Situ Measurements of Anelastic Absorption in Soils Using a Prototype Earthquake Simulator," by R. D. Borcherdt and P. W. Rodgers - 1971 (PB 201 454)
$5.25	EERC 71-3	"Static and Dynamic Analysis of Inelastic Frame Structures," by F. L. Porter and G. H. Powell - 1971 (PB 210 135)
$4.25	EERC 71-4	"Research Needs in Limit Design of Reinforced Concrete Structures," by V. V. Bertero - 1971 (PB 202 943)
$5.25	EERC 71-5	"Dynamic Behavior of a High-Rise Diagonally Braced Steel Building," by D. Rea, A. A. Shah and J. G. Bouwkamp - 1971 (PB 203 584)

$5.25	EERC 71-6	"Dynamic Stress Analysis of Porous Elastic Solids Saturated with Compressible Fluids," by J. Ghaboussi and E. L. Wilson - 1971 (PB 211 396)
$9.25	EERC 71-7	"Inelastic Behavior of Steel Beam-to-Column Subassemblages," by H. Krawinkler, V. V. Bertero and E. P. Popov - 1971 (PB 211 335)
$3.75	EERC 71-8	"Modification of Seismograph Records for Effects of Local Soil Conditions," by P. Schnabel, H. B. Seed and J. Lysmer - 1971 (PB 214 450)
$4.75	EERC 72-1	"Static and Earthquake Analysis of Three Dimensional Frame and Shear Wall Buildings," by E. L. Wilson and H. H. Dovey - 1972 (PB 212 904)
$3.75	EERC 72-2	"Accelerations in Rock for Earthquakes in the Western United States," by P. B. Schnabel and H. B. Seed - 1972 (PB 213 100)
$6.25	EERC 72-3	"Elastic-Plastic Earthquake Response of Soil-Building Systems," by T. Minami - 1972 (PB 214 868)
$4.75	EERC 72-4	"Stochastic Inelastic Response of Offshore Towers to Strong Motion Earthquakes," by M. K. Kaul - 1972 (PB 215 713)
$4.75	EERC 72-5	"Cyclic Behavior of Three Reinforced Concrete Flexural Members with High Shear," by E. P. Popov, V. V. Bertero and H. Krawinkler - 1972 (PB 214 555)
$6.25	EERC 72-6	"Earthquake Response of Gravity Dams Including Reservoir Interaction Effects," by P. Chakrabarti and A. K. Chopra - 1972 (AD 762 330)
$4.75	EERC 72-7	"Dynamic Properties on Pine Flat Dam," by D. Rea, C.-Y. Liaw and A. K. Chopra - 1972 (AD 763 928)
$5.25	EERC 72-8	"Three Dimensional Analysis of Building Systems," by E. L. Wilson and H. H. Dovey - 1972 (PB 222 438)
$6.25	EERC 72-9	"Rate of Loading Effects on Uncracked and Repaired Reinforced Concrete Members," by S. Mahin, V. V. Bertero, D. Rea and M. B. Atalay - 1972 (PB 224 520)
$4.25	EERC 72-10	"Computer Program for Static and Dynamic Analysis of Linear Structural Systems," by E. L. Wilson, K.-J. Bathe, J. E. Peterson and H. H. Dovey - 1972 (PB 220 437)

$11.25	EERC 72-11	"Literature Survey - Seismic Effects on Highway Bridges," by T. Iwasaki, J. Penzien and R. W. Clough - 1972 (PB 215 613)
$5.25	EERC 72-12	"SHAKE-A Computer Program for Earthquake Response Analysis of Horizontally Layered Sites," by P. B. Schnabel and J. Lysmer - 1972 (PB 220 207)
	EERC 73-1	"Optimal Seismic Design of Multistory Frames," by V. V. Bertero and H. Kamil - 1973
$9.25	EERC 73-2	"Analysis of the Slides in the San Fernando Dams during the Earthquake of February 9, 1971," by H. B. Seed, K. L. Lee, I. M. Idriss and F. Makdisi - 1973 (PB 223 402)
	EERC 73-3	"Computer Aided Ultimate Load Design of Unbraced Multistory Steel Frames," by M. B. El-Hafez and G. H. Powell - 1973
$7.00	EERC 73-4	"Experimental Investigation into the Seismic Behavior of Critical Regions of Reinforced Concrete Components as Influenced by Moment and Shear," by M. Celebi and J. Penzien - 1973 (PB 215 884)
$3.75	EERC 73-5	"Hysteretic Behavior of Epoxy-Repaired Reinforced Concrete Beams," by M. Celebi and J. Penzien - 1973 (PB 239 568)
$6.25	EERC 73-6	"General Purpose Computer Program for Inelastic Dynamic Response of Plane Structures," by A. Kanaan and G. H. Powell - 1973 (PB 221 260)
$4.25	EERC 73-7	"A Computer Program for Earthquake Analysis of Gravity Dams Including Reservoir Interaction," by P. Chakrabarti and A. K. Chopra - 1973 (AD 766 271)
$8.50	EERC 73-8	"Behavior of Reinforced Concrete Deep Beam-Column Subassemblages under Cyclic Loads," by O. Kustu and J. G. Bouwkamp - 1973 (PB 246 117)
$5.75	EERC 73-9	"Earthquake Analysis of Structure-Foundation Systems," by A. K. Vaish and A. K. Chopra - 1973 (AD 766 272)
$6.25	EERC 73-10	"Deconvolution of Seismic Response for Linear Systems," by R. B. Reimer - 1973 (PB 227 179)
$7.00	EERC 73-11	"SAP IV: A Structural Analysis Program for Static and Dynamic Response of Linear Systems," by K.-J. Bathe, E. L. Wilson and F. E. Peterson - 1973 (PB 221 967)
$7.25	EERC 73-12	"Analytical Investigations of the Seismic Response of Long, Multiple Span Highway Bridges," by W. S. Tseng and J. Penzien - 1973 (PB 227 816)

$3.75	EERC 73-13	"Earthquake Analysis of Multi-Story Buildings Including Foundation Interaction," by A. K. Chopra and J. A. Gutierrez - 1973 (PB 222 970)
$7.00	EERC 73-14	"ADAP: A Computer Program for Static and Dynamic Analysis of Arch Dams," by R. W. Clough, J. M. Raphael and S. Mojtahedi - 1973 (PB 223 763)
$6.25	EERC 73-15	"Cyclic Plastic Analysis of Structural Steel Joints," by R. B. Pinkney and R. W. Clough - 1973 (PB 226 843)
$4.75	EERC 73-16	"QUAD-4: A Computer Program for Evaluating the Seismic Response of Soil Structures by Variable Damping Finite Element Procedures," by I. M. Idriss, J. Lysmer, R. Hwang and H. B. Seed - 1973 (PB 229 424)
$5.25	EERC 73-17	"Dynamic Behavior of a Multi-Story Pyramid Shaped Building," by R. M. Stephen and J. G. Bouwkamp - 1973 (PB 240 718)
	EERC 73-18	"Effect of Different Types of Reinforcing on Seismic Behavior of Short Concrete Columns," by V. V. Bertero, J. Hollings, O. Kustu, R. M. Stephen and J. G. Bouwkamp - 1973
$5.25	EERC 73-19	"Olive View Medical Center Material Studies, Phase I," by B. Bresler and V. V. Bertero - 1973 (PB 235 986)
	EERC 73-20	"Linear and Nonlinear Seismic Analysis Computer Programs for Long Multiple-Span Highway Bridges," by W. S. Tseng and J. Penzien - 1973
$3.25	EERC 73-21	"Constitutive Models for Cyclic Plastic Deformation of Engineering Materials," by J. M. Kelly and P. P. Gillis - 1973 (PB 226 024)
$4.75	EERC 73-22	"DRAIN - 2D User's Guide," by G. H. Powell - 1973 (PB 227 016)
$7.50	EERC 73-23	"Earthquake Engineering at Berkeley - 1973" - 1973 (PB 226 033)
	EERC 73-24	Unassigned
$7.00	EERC 73-25	"Earthquake Response of Axisymmetric Tower Structures Surrounded by Water," by C.-Y. Liaw and A. K. Chopra - 1973 (AD 773 052)
$8.75	EERC 73-26	"Investigation of the Failures of the Olive View Stairtowers during the San Fernando Earthquake and Their Implications in Seismic Design," by V. V. Bertero and R. G. Collins - 1973 (PB 235 106)

$5.25	EERC 73-27	"Further Studies on Seismic Behavior of Steel Beam-Column Subassemblages," by V. V. Bertero, H. Krawinkler and E. P. Popov - 1973 (PB 234 172)
$5.25	EERC 74-1	"Seismic Risk Analysis," by C. S. Oliveira - 1974 (PB 235 920)
	EERC 74-2	"Settlement and Liquefaction of Sands under Multi-Directional Shaking," by R. Pyke, C. K. Chan and H. B. Seed - 1974
$4.75	EERC 74-3	"Optimum Design of Earthquake Resistant Shear Buildings," by D. Ray, K. S. Pister and A. K. Chopra - 1974 (PB 231 172)
$4.75	EERC 74-4	"LUSH - A Computer Program for Complex Response Analysis of Soil-Structure Systems," by J. Lysmer, T. Udaka, H. B. Seed and R. Hwang - 1974 (PB 236 796)
$5.25	EERC 74-5	"Sensitivity Analysis for Hysteretic Dynamic Systems: Applications to Earthquake Engineering," by D. Ray - 1974 (PB 233 213)
$4.25	EERC 74-6	"Soil-Structure Interaction Analyses for Evaluating Seismic Response," by H. B. Seed, J. Lysmer and R. Hwang - 1974 (PB 236 519)
	EERC 74-7	Unassigned
$3.75	EERC 74-8	"Shaking Table Tests of a Steel Frame - A Progress Report," by R. W. Clough and D. Tang - 1974 (PB 240 869)
$5.75	EERC 74-9	"Hysteretic Behavior of Reinforced Concrete Flexural Members with Special Web Reinforcement," by V. V. Bertero, E. P. Popov and T. Y. Wang - 1974 (PB 236 797)
$5.25	EERC 74-10	"Applications of Reliability-Based, Global Cost Optimization to Design of Earthquake Resistant Structures," by E. Vitiello and K. S. Pister - 1974 (PB 237 231)
$3.75	EERC 74-11	"Liquefaction of Gravelly Soils under Cyclic Loading Conditions," by R. T. Wong, H. B. Seed and C. K. Chan 1974 (PB 242 042)
$3.75	EERC 74-12	"Site-Dependent Spectra for Earthquake-Resistant Design," by H. B. Seed, C. Ugas and J. Lysmer - 1974 (PB 240 953)

$8.75	EERC 74-13	"Earthquake Simulator Study of a Reinforced Concrete Frame," by P. Hidalgo and R. W. Clough - 1974 (PB 241 944)
$5.25	EERC 74-14	"Nonlinear Earthquake Response of Concrete Gravity Dams," by N. Pal - 1974 (AD/A006583)
$5.25	EERC 74-15	"Modeling and Identification in Nonlinear Structural Dynamics, I - One Degree of Freedom Models," by N. Distefano and A. Rath - 1974 (PB 241 548)
	EERC 75-1	"Determination of Seismic Design Criteria for the Dumbarton Bridge Replacement Structure, Vol. I: Description, Theory and Analytical Modeling of Bridge and Parameters," by F. Baron and S.-H. Pang - 1975 ( )
	EERC 75-2	"Determination of Seismic Design Criteria for the Dumbarton Bridge Replacement Structure, Vol. 2: Numerical Studies and Establishment of Seismic Design Criteria," by F. Baron and S.-H. Pang - 1975 ( )
$7.50	EERC 75-3	"Seismic Risk Analysis for a Site and a Metropolitan Area," by C. S. Oliveira - 1975 (PB 248 134)
$7.00	EERC 75-4	"Analytical Investigations of Seismic Response of Short, Single or Multiple-Span Highway Bridges," by Ma-chi Chen and J. Penzien - 1975 (PB 241 454)
$10.00	EERC 75-5	"An Evaluation of Some Methods for Predicting Seismic Behavior of Reinforced Concrete Buildings," by Stephen A. Mahin and V. V. Bertero - 1975 (PB 246 306)
$8.75	EERC 75-6	"Earthquake Simulator Study of a Steel Frame Structure, Vol. I: Experimental Results," by R. W. Clough and David T. Tang - 1975 (PB 243 981)
$4.75	EERC 75-7	"Dynamic Properties of San Bernardino Intake Tower," by Dixon Rea, C.-Y. Liaw, and Anil K. Chopra - 1975 (AD/A008406)
$6.00	EERC 75-8	"Seismic Studies of the Articulation for the Dumbarton Bridge Replacement Structure, Vol. I: Description, Theory and Analytical Modeling of Bridge Components," by F. Baron and R. E. Hamati - 1975 (PB 251 539)
$7.75	EERC 75-9	"Seismic Studies of the Articulation for the Dumbarton Bridge Replacement Structure, Vol. 2: Numerical Studies of Steel and Concrete Girder Alternates," by F. Baron and R. E. Hamati - 1975 (PB 251 540)

$6.25	EERC 75-10	"Static and Dynamic Analysis of Nonlinear Structures," by Digambar P. Mondkar and Graham H. Powell - 1975 (PB 242 434)
$8.00	EERC 75-11	"Hysteretic Behavior of Steel Columns," by E. P. Popov, V. V. Bertero and S. Chandramouli - 1975 (PB 252 365)
$15.25	EERC 75-12	"Earthquake Engineering Research Center Library Printed Catalog" - 1975 (PB 243 711)
$5.75	EERC 75-13	"Three Dimensional Analysis of Building Systems," Extended Version, by E. L. Wilson, J. P. Hollings, and H. H. Dovey - 1975 (PB 243 989)
	EERC 75-14	"Determination of Soil Liquefaction Characteristics by Large-Scale Laboratory Tests," by Pedro De Alba, Clarence K. Chan and H. Bolton Seed - 1975
$8.00	EERC 75-15	"A Literature Survey - Compressive, Tensile, Bond and Shear Strength of Masonry," by Ronald L. Mayes and Ray W. Clough - 1975 (PB 246 292)
$5.00	EERC 75-16	"Hysteretic Behavior of Ductile Moment Resisting Reinforced Concrete Frame Components," by V. V. Bertero and E. P. Popov - 1975 (PB 246 388)
$4.00	EERC 75-17	"Relationships Between Maximum Acceleration, Maximum Velocity, Distance from Source, Local Site Conditions for Moderately Strong Earthquakes," by H. Bolton Seed, Ramesh Murarka, John Lysmer and I. M. Idriss - 1975 (PB 248 172)
	EERC 75-18	"The Effects of Method of Sample Preparation on the Cyclic Stress-Strain Behavior of Sands," by J. Paul Mulilis, Clarence K. Chan and H. Bolton Seed - 1975
	EERC 75-19	"The Seismic Behavior of Critical Regions of Reinforced Concrete Components as Influenced by Moment, Shear and Axial Force," by M. B. Atalay and J. Penzien - 1975
$4.50	EERC 75-20	"Dynamic Properties of an Eleven Story Masonry Building," by R. M. Stephen, J. P. Hollings, J. G. Bouwkamp and D. Jurukovski - 1975 (PB 246 945)
$6.00	EERC 75-21	"State-of-the-Art in Seismic Shear Strength of Masonry - An Evaluation and Review," by Ronald L. Mayes and Ray W. Clough - 1975 (PB 249 040)
$6.00	EERC 75-22	"Frequency Dependencies Stiffness Matrices for Viscoelastic Half-Plane Foundations," by Anil K. Chopra, P. Chakrabarti and Gautam Dasgupta - 1975 (PB 248 121)
	EERC 75-23	"Hysteretic Behavior of Reinforced Concrete Framed Walls," by T. Y. Wong, V. V. Bertero and E. P. Popov - 1975

	EERC 75-24	"Testing Facility for Subassemblages of Frame-Wall Structural Systems," by V. V. Bertero, E. P. Popov and T. Endo - 1975
	EERC 75-25	"Influence of Seismic History on the Liquefaction Characteristics of Sands," by H. Bolton Seed, Kenji Mori and Clarence K. Chan - 1975
$4.00	EERC 75-26	"The Generation and Dissipation of Pore Water Pressures During Soil Liquefaction," by H. Bolton Seed, Phillippe P. Martin and John Lysmer - 1975 (PB 252 648)
$5.00	EERC 75-27	"Identification of Research Needs for Improving a Seismic Design of Building Structures," by V. V. Bertero - 1975 (PB 248 136)
	EERC 75-28	"Evaluation of Soil Liquefaction Potential during Earthquakes," by H. Bolten Seed, I. Arango and Clarence K. Chan 1975
$4.00	EERC 75-29	"Representation of Irregular Stress Time Histories by Equivalent Uniform Stress Series in Liquefaction Analyses," by H. Bolton Seed, I. M. Idriss, F. Makdisi and N. Banerjee 1975 (PB 252 635)
	EERC 75-30	"FLUSH - A Computer Program for Approximate 3-D Analysis of Soil-Structure Interaction Problems," by J. Lysmer, T. Udaka, C.-F. Tsai and H. B. Seed - 1975
	EERC 75-31	"ALUSH - A Computer Program for Seismic Response Analysis of Axisymmetric Soil-Structure Systems," by E. Berger, J. Lysmer and H. B. Seed - 1975
	EERC 75-32	"TRIP and TRAVEL - Computer Programs for Soil-Structure Interaction Analysis with Horizontally Travelling Waves," by T. Udaka, J. Lysmer and H. B. Seed - 1975
$4.00	EERC 75-33	"Predicting the Performance of Structures in Regions of High Seismicity," by J. Penzien - 1975 (PB 248 130)
	EERC 75-34	"Efficient Finite Element Analysis of Seismic Structure - Soil - Direction," by J. Lysmer, H. Bolton Seed, T. Udaka, R. N. Hwang and C.-F. Tsai - 1975
$5.00	EERC 75-35	"The Dynamic Behavior of a First Story Girder of a Three-Story Steel Frame Subjected to Earthquake Loading," by Ray W. Clough and Lap-Yan Li - 1975 (PB 248 841)
$7.75	EERC 75-36	"Earthquake Simulator Study of a Steel Frame Structure, Volume II - Analytical Results," by David T. Tang - 1975 (PB 252 926)
$6.75	EERC 75-37	"ANSR-I General Purpose Computer Program for Analysis of Non-Linear Structural Response," by Digambar P. Mondkar and Graham H. Powell - 1975 (PB 252 386)

	EERC 75-38	"Nonlinear Response Spectra for Probabilistic Seismic Design and Damage Assessment of Reinforced Concrete Structures," by Masaya Murakami and Joseph Penzien 1975
	EERC 75-39	"Study of a Method of Feasible Directions for Optimal Elastic Design of Framed Structures Subjected to Earthquake Loading," by N. D. Walker and K. S. Pister - 1975
$4.00	EERC 75-40	"An Alternative Representation of the Elastic-Viscoelastic Analogy," by Gautam Dasgupta and Jerome L. Sackman - 1975 (PB 252 173)
	EERC 75-41	"Effect of Multi-Directional Shaking on Liquefaction of Sands," by H. Bolton Seed, Robert Pyke and Geoffrey R. Martin - 1975
	EERC 76-1	"Strength and Ductility Evaluation of Existing Low-Rise Reinforced Concrete Buildings - Screening Method," by Tsuneo Okada and Boris Bresler - 1976
	EERC 76-2	"Experimental and Analytical Studies on the Hysteretic Behavior of Reinforced Concrete Rectangular and T-Beams," by Shao-Yeh Marshall Ma, Egor P. Popov and Vitelmo V. Bertero - 1976
	EERC 76-3	"Dynamic Behavior of a Multistory Triangular-Shaped Building," by J. Petrovski, R. M. Stephen, E. Gartenbaum and J. G. Bouwkamp - 1976
	EERC 76-4	"Earthquake Induced Deformations of Earth Dams," by Norman Serff and H. Bolton Seed - 1976
	EERC 76-5	"Analysis and Design of Tube-Type Tall Building Structures," by H. de Clercq and G. H. Powell - 1976
	EERC 76-6	"Time and Frequency Domain Analysis of Three-Dimensional Ground Motions, San Fernando Earthquake," by Tetsuo Kubo and Joseph Penzien - 1976
	EERC 76-7	"Expected Performance of Uniform Building Code Design Masonry Structures," by R. L. Mayes, Y. Omote, S. W. Chen and R. W. Clough - 1976
	EERC 76-8	"Cyclic Shear Tests on Concrete Masonry Piers, Part I - Test Results," by R. L. Mayes, Y. Omote and R. W. Clough 1976
	EERC 76-9	"Stabilization of Potentially Liquefiable Sand Deposits using Gravel Drain Systems," by H. Bolton Seed and John R. Booker - 1976

EERC 76-10 "Stabilization of Potentially Liquefiable Sand Deposits Using Gravel Drain Systems," by H. Bolton Seed, and John R. Booker - 1976

EERC 76-11 "Influence of Design and Analysis Assumptions on Computed Inelastic Response of Moderately Tall Frames," by G. H. Powell and D. G. Row - 1976

EERC 76-12 "Sensitivity Analysis for Hysteretic Dynamic Systems: Theory and Applications," by D. Ray, K. S. Pister and E. Polak - 1976

EERC 76-13 "Coupled Lateral Torsional Response of Buildings to Ground Shaking," by Christopher L. Kan and Anil K. Chopra - 1976

EERC 76-14 "Seismic Analyses of the Banco de America," by V. V. Bertero, S. A. Mahin, and J. A. Hollings - 1976

EERC 76-15 "Reinforced Concrete Frame 2: Seismic Testing and Analytical Correlation," by Ray W. Clough and Jawahar Gidwani - 1976

EERC 76-16 "Cyclic Shear Tests on Masonry Piers, PartcII - Analysis of Test Results," by R. L. Mayes, Y. Omote and R. W. Clough 1976

EERC 76-17 "Structural Steel Bracing Systems: Behavior Under Cyclic Loading," by E. P. Popov, K. Takanashi and C. W. Roeder 1976

EERC 76-18 "Experimental Model Studies on Seismic Reponse of High Curved Overcrossings," by David Williams and William G. Godden - 1976

EERC 76-19 "Effects of Non-Uniform Seismic Distrubances on the Dumbarton Bridge Replacement Structure," by Frank Baron and Raymond E. Hamati - 1976